NOVEL AZOHETEROARYL PHOTOSWITCHES

AND THEIR APPLICATIONS

A thesis submitted by:

Claire Elizabeth Weston

In partial fulfilment of the requirements for the degree of:

Doctor of Philosophy

March 2016

Department of Chemistry

Imperial College London

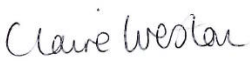
South Kensington

London

SW7 2AZ

Declaration of Originality

I, Claire Weston, hereby confirm that the work presented within this thesis is entirely my own, conducted under the supervision of Dr Matthew J. Fuchter, at the Department of Chemistry, Imperial College London, unless otherwise stated. All work performed by others has been acknowledged within the text and referenced where appropriate.



Claire E. Weston

London, 21st March 2016

Copyright Declaration

The copyright of this thesis rests with the author and is made available under a Creative Commons Attribution Non-Commercial No Derivatives licence. Researchers are free to copy, distribute or transmit the thesis on the condition that they attribute it, that they do not use it for commercial purposes and that they do not alter, transform or build upon it. For any reuse or redistribution, researchers must make clear to others the licence terms of this work.

ABSTRACT

Photoswitchable compounds have diverse applications, from photopharmacology to optical data storage. Azobenzenes are one of the most commonly used photoswitches, with a wealth of research focused on improving the photoconversion achieved upon irradiation and increasing the thermal stability of the *Z*-isomer. This work reports the development, study, and applications of the understudied azoheteroaryl photoswitches.

A new class of azoheteroarenes, the arylazopyrazoles, have been developed. These photochromic compounds undergo very slow *Z*-*E* thermal isomerisation compared to the azobenzenes and achieve good to quantitative photoswitching between the two isomers. The conformation of the *Z*-isomers of these azoheteroarenes, and hence their spectral properties, can be tuned by altering the substitution pattern on the heteroaryl ring. Building on the initial work reported, a wider range of arylazoheteroarenes have also been studied, in order to fully investigate their properties and identify factors that control their thermal isomerisation rates.

The azoheteroaryl photoswitches have been employed in two applications. The first, is the development of photoswitchable histone deacetylase (HDAC) inhibitors for use in photopharmacology, using either arylazopyrazoles or azobenzenes. Assays were carried out on human HDACs and bacterial homologues; sub-micromolar IC_{50} values were obtained for the bacterial HDACs and up to a 9-fold difference in activity between *E*- and *Z*-isomers was observed. Several tethered photoswitchable HDAC inhibitors were also developed – such compounds have potential use in industrial applications. The inhibitor-enzyme conjugates had reduced enzyme activity relative to the unbound enzyme, however no difference in activity was seen between the *E*- and *Z*-isomers.

The second application was the development of an azobisimidazole photoswitchable base. This compound exhibited a difference in basicity between the *E*- and *Z*-isomers of 1.3 pK_a units. The difference in basicity is due to the additional proton stabilisation in the protonated *Z*-isomer, which is facilitated by the basic imidazole nitrogens, and can be used to reversibly control solution pH.

ACKNOWLEDGEMENTS

First and foremost, I'd like to thank Dr Matthew Fuchter for his continued help and support throughout my PhD and for giving me the opportunity to carry out such a variety of research. I would also like to thank Dr Robert Richardson for all his help with both photochemistry and computational work, especially for his never ending patience when it came to understanding equation derivations! I hope to not let him down as self-appointed laser protégé.

I'd also like to thank Professor Meyer-Almes and his group at the University of Applied Sciences, Darmstadt for their work on the biological aspects of this project, in particular Dr Michael Korbus and Andreas Krämer for carrying out the bulk of the biological assays. Thanks also to Dr Julia Contreras-García at the Pierre and Marie Curie University and Joaquín Calbo at the University of Valencia, for their invaluable computational work. I am very grateful to both Andreas Krämer and Joaquín Calbo for their prompt and helpful answers to the many questions I had regarding the work they had carried out.

Thanks are also due to the analytical staff at Imperial College; Dr Lisa Haigh, Andrew White, Dick Sheppard and especially Pete Haycock for running so many kinetic experiments!

A big thank you to past and present members of both the Fuchter and Barrett groups for keeping me going throughout my PhD. In particular, Kate for experiencing the whole process with me, Joaquim for helping me out when I first started and Fanny for helping me through any wobbles during my first year. I am also grateful to all my labmates in the Hofmann lab over the years, especially members of the Other bay, where I made my humble beginnings, and the Superbay, whose hallowed fumehoods and well stocked cupboards Rob and Pete persuaded me I was worthy of. Thank you also to Josh who made my final year so much more enjoyable.

I am very grateful to my proof readers; Nicole, Tom, Hannah, Luiza, Alex and Josh (who got off very lightly).

Finally, I'd like to thank my family for supporting me throughout my PhD, particularly my Mum and Graham for letting me invade their house while writing up!

CONTENTS

ABSTRACT 5
ACKNOWLEDGEMENTS 7
ABBREVIATIONS 19
EQUATIONS 23
1 INTRODUCTION 25
1.1 Light as a stimulus 25
1.2 Photochromism and photoswitches 25
1.3 Azobenzenes 27
1.4 Tuning the properties of azobenzenes 30
1.5 Applications of azobenzenes 32
2 NOVEL AZOHETEROARYL PHOTOSWITCHES 37
2.1 INTRODUCTION 37
2.2 RESULTS AND DISCUSSION PART I: Arylazopyrazoles and pyrroles 38
2.2.1 Photoswitch design and aims 38
2.2.2 Synthesis 39
2.2.3 Photoswitching 41
2.2.4 Thermal isomerisation kinetics 46
2.2.5 Computational studies 49
2.2.5.1 Energy minimised conformations and calculated UV/vis spectra 49
2.2.5.2 n-π* transition intensity 51
2.2.5.3 Calculated thermal isomerisation kinetics 54
2.3 RESULTS AND DISCUSSION PART II: Further study of arylazoheteroarenes 55
2.3.1 Photoswitch design and aims 55
2.3.2 Synthesis 56
2.3.3 Photoswitching 58
2.3.4 Thermal isomerisation kinetics 61
2.3.5 Computational studies 64
2.3.5.1 Calculated thermal isomerisation kinetics 64
2.3.5.2 Non-covalent interactions and charge transfer 66
2.4 CONCLUSIONS 70
3 PHOTOSWITCHABLE HDAC INHIBITORS 73
3.1 INTRODUCTION 73

3.1.1 Epigenetics and cancer 73
3.1.1.1 Epigenetic mechanisms in normal cells 74
3.1.1.2 The role of epigenetics in cancer 75
3.1.1.3 Epigenetic cancer therapy 76
3.1.2 Photodynamic therapy 78
3.1.3 Photopharmacology 80
3.1.4 Photoswitchable HDAC inhibitors 82
3.2 RESULTS AND DISCUSSION PART I: Azobenzene-based HDAC inhibitors 83
3.2.1 Preliminary work 83
3.2.2 Design of azobenzene HDAC inhibitors and stilbene isosteres 84
3.2.3 Synthesis 84
3.2.4 Photoswitching 87
3.2.5 Thermal isomerisation kinetics 88
3.2.6 Biochemistry 89
3.3 RESULTS AND DISCUSSION PART II: Arylazopyrazole-based HDAC inhibitors 96
3.3.1 Design of arylazopyrazole HDAC inhibitors 96
3.3.2 Synthesis 96
3.3.3 Photoswitching 97
3.3.4 Thermal isomerisation kinetics 98
3.3.5 Biochemistry 99
3.4 RESULTS AND DISCUSSION PART III: Photoswitchable tethered HDAC inhibitors 101
3.4.1 Preliminary work 101
3.4.2 Synthesis 103
3.4.3 Photoswitching 107
3.4.4 Thermal isomerisation kinetics 108
3.4.5 Biochemistry 108
3.5 CONCLUSIONS 110
4 AZOBISIMIDAZOLE: A PHOTOSWITCHABLE BASE 112
4.1 INTRODUCTION 112
4.2 RESULTS AND DISCUSSION 115
4.2.1 Photoswitch design 115
4.2.2 Synthesis 117
4.2.3 Photochemistry and pK_a determination 119

4.2.4 Computational NMR predictions 122
4.2.5 pH jump 123
4.2.6 Photocontrol of a cyclisation reaction 125
4.3 CONCLUSIONS 129
5 EXPERIMENTAL 130
5.1 Synthesis – general methods 130
5.2 Synthesis – experimental procedures 131
5.2.1 General procedures 131
5.2.2 Arylazopyrazoles and pyrroles 133
5.2.3 Further study of arylazoheteroarenes 137
5.2.4 Photoswitchable azobenzene-based HDAC inhibitors 144
5.2.5 Photoswitchable arylazopyrazole-based HDAC inhibitors 157
5.2.6 Photoswitchable tethered HDAC inhibitors 162
5.2.7 Azobisimidazole: A photoswitchable base 172
5.3 Photochemistry 176
5.3.1 General methods 176
5.3.2 Quantification of PSS composition by NMR spectroscopy 177
5.3.3 Estimation of PSS composition by UV/vis spectroscopy 177
5.3.4 Photoisomerisation quantum yields 178
5.3.5 Thermal isomerisation kinetics 178
5.3.6 pK_a titration 179
5.3.7 pH jump 179
5.4 Computational 180
5.4.1 Arylazopyrazoles and pyrroles 180
5.4.2 Further study of arylazoheteroarenes 180
5.4.3 Azobisimidazole: A photoswitchable base 181
5.5 Biochemistry 182
5.5.1 General methods 182
5.5.2 Continuous HDAC assay 182
5.5.3 Endpoint HDAC assay 183
5.5.4 Chemical modification of HDAH variants 183
5.5.5 Measurement of Michaelis-Menten kinetics 183
6 REFERENCES 185

7 APPENDIX 197
7.1 Equation derivations 197
7.1.1 Thermal isomerisation kinetics 197
7.1.2 Photoisomerisation quantum yields 197
7.1.3 pK_a equation derivation 199
7.2 X-ray crystallography 202
7.3 Photochemistry 207
7.3.1 Novel azoheteroaryl photoswitches 207
Quantification of PSS composition by NMR 207
Photostationary states following broadband irradiation 216
Estimation of PSS composition by UV/vis for fast thermally isomerising compounds 217
UV/vis spectra 218
Photoisomerisation kinetics 221
Thermal isomerisation kinetics 222
7.3.2 Photoswitchable HDAC inhibitors 228
Quantification of PSS composition by NMR 228
Thermal isomerisation kinetics 236
7.3.3 Azobisimidazole: A photoswitchable base 238
Estimation of PSS compositions by UV/vis spectroscopy 238
pH titrations 238
Thermal isomerisation kinetics 239
7.4 Computational 239
7.4.1 Novel azoheteroaryl photoswitches: Arylazopyrazoles and pyrroles 239
Energy minimised structures and excitation data 239
Structures and Cartesian coordinates for optimised geometry 241
Structures and Cartesian coordinates for transition states 249
Dihedral drives 257
7.4.2 Azobisimidazole: A photoswitchable base 258
Energy minimised structures and excitation data 258
Structures and Cartesian coordinates for optimised geometry 259
GIAO ^{13}C NMR Calculations 266
7.5 Biochemistry 268

LIST OF FIGURES

Figure 1.1. Examples of the main classes of photoswitch 26

Figure 1.2. UV/vis spectra of *E*- and *Z*-azobenzene 28

Figure 1.3. Different possible isomerisation mechanisms for azobenzenes 28

Figure 1.4. Different classes of azobenzenes 29

Figure 1.5. Azo-hydrazone tautomerisation in *p*-hydroxyazobenzene (**5**). 30

Figure 1.6. Resonance structures for the push-pull (**6**) and protonated (**7**) azobenzenes 30

Figure 1.7. o*rtho*-Substituted azobenzenes with visible light switching and long half-lives 31

Figure 1.8. Bridged azobenzene **10** with a thermally stable *Z*-isomer 32

Figure 1.9. Photoswitchable analogue of propofol 33

Figure 1.10. Photoswitchable peptides 33

Figure 1.11. A) Schematic of a daisy chain rotaxane; B) Example of a daisy chain rotaxane controlled by light 34

Figure 1.12. A) An early liquid-crystalline polymer (**15**) containing azobenzene, for use in holographic optical storage, and; B) the binary test pattern stored in polymer **15**, using a polarised writing beam; C) A recovered data page using a holographic memory card 35

Figure 1.13. A) A photoswitchable acid (**16**); B) A photoswitchable base (**17**) 35

Figure 2.1. Azoheteroarenes with fast thermal half-lives 37

Figure 2.2. Arylazoimidazole **20** developed by Herges and co-workers 38

Figure 2.3. Azoheteroarenes chosen for study 39

Figure 2.4. Azo-hydrazone tautomerisation 39

Figure 2.5. UV/vis spectra of azopyrroles **21**-**22** and azopyrazoles **23**-**24** in acetonitrile 41

Figure 2.6. Estimating pure *Z*-spectrum of **22** 42

Figure 2.7. PSSs and time-resolved spectra for **24** 44

Figure 2.8. Repeated photoswitching cycles 44

Figure 2.9. Thermal isomerisation of azopyrroles **22** and **21** at 25 °C and azopyrazole **23** at 70 °C showing the effect of adding water on the rate 48

Figure 2.10. Comparison of calculated and experimental UV/vis spectra 50

Figure 2.11. A) Calculated conformations and dihedral angles for *Z*-isomers; B) Crystal structures for *Z*-**23** and *Z*-**24** 51

Figure 2.12. Energy minimised conformations of; A) *Z*-**21** with the mirror plane labelled and the calculated n- and π*-orbitals; B) *Z*-**22**, showing no symmetry in the molecule 52

Figure 2.13. Dihedral angle vs. n–π* intensity and population fraction for *Z*-isomers 53

Figure 2.14. Original azoheteroaryl photoswitches studied and new photoswitches chosen for experimental and computational study..... 55

Figure 2.15. UV/vis spectra of azoheteroarenes **31**-**38** 60

Figure 2.16**.** A) Time-resolved UV/vis spectra for photoswitching of **34** at 355 nm and 532 nm; B) Repeated photoswitching cycles for **34**..... 61

Figure 2.17. Conjugation of the heteroarene into the azophenyl moiety..... 63

Figure 2.18. Hammett values for the solvolysis of 1-arylethyl derivatives..... 63

Figure 2.19. Contribution of inductive effects and resonance effects to the electron donation in the three possible pyrazole regioisomers 64

Figure 2.20. The two optimised transition states, shown for **35**..... 65

Figure 2.21. Comparison of calculated and thermal half-lives at 25 °C..... 66

Figure 2.22. NCI surfaces for; A) *E*- and *Z*-**23**; B) *E*- and *Z*-**24**..... 67

Figure 2.23. Energy minimised *Z*-conformers for compounds with two *ortho*-nitrogens (**37** and **38**) or one *ortho*-nitrogen and one *ortho*-methyl (**32**) 69

Figure 2.24. Comparison of *Z*-isomer NPA charges and calculated thermal half-lives..... 70

Figure 3.1. Schematic showing the organisation of DNA within chromatin and positioning of epigenetic modifications..... 73

Figure 3.2. Phylogenetic tree of the classical HDAC family 74

Figure 3.3. Schematic showing the effect of HDAC overexpression..... 75

Figure 3.4. Examples of the four main classes of HDAC inhibitors 76

Figure 3.5. A) Crystal structure of HDLP and hydroxamic acid trichostatin A; B) Crystal structure of HDAC2 and benzamide inhibitor **56**..... 77

Figure 3.6. Pharmacophore for classical HDAC inhibitors 77

Figure 3.7. Mechanisms of cell death mediated by HDAC inhibition 78

Figure 3.8. Mechanism of action of photodynamic therapy at the cellular level..... 78

Figure 3.9. Structure of Photofrin, a haematoporphyrin derivative..... 79

Figure 3.10. Illustration of the photopharmacology concept for destroying a tumour. 80

Figure 3.11. Three strategies using photosensitive ligands..... 81

Figure 3.12. Illustration showing optimisation of photochemical properties of the azobenzene by red-shifting absorption wavelength 82

Figure 3.13. Initial photoswitchable HDAC inhibitor design, incorporating the cinnamyl hydroxamic acid moiety seen in several HDAC inhibitors 83

Figure 3.14. Photo- and thermal isomerisation of azobenzene **57a**. 83

Figure 3.15. *E*- and *Z*-azobenzene HDAC inhibitors and *E*- and *Z*-stilbene analogues 84

Figure 3.16. UV/vis spectra of **57a**-**c** recorded in DMSO 87

Figure 3.17. A) UV/vis spectra of **57a**; B) The ratio of isomers present in the NMR spectrum, using the alkene signal shown in C) 88

Figure 3.18. Log IC_{50} values for the *E*- and *Z*-azobenzenes and stilbenes against HDACs 92

Figure 3.19. New HDAC inhibitor design incorporating azopyrazole **24** 96

Figure 3.20. UV/vis spectra of **68a**-**c** recorded in DMSO 98

Figure 3.21. IC_{50} curves for the best results 100

Figure 3.22. Enzyme-inhibitor crystal structures of **68a** with HDAH and Pa3774 101

Figure 3.23. Schematic showing photocontrol of HDAH with a tethered azobenzene 102

Figure 3.24. Proposed designs for photoswitchable tethered HDAC inhibitors 102

Figure 3.25. UV/vis spectra of **72b**-**c** recorded in DMSO 107

Figure 3.26. Assay results for enzymatic activity of the HDAH variants with *E*- and *Z*-**72b** or **72c** tethered, and of the uncoupled enzyme as a control 109

Figure 4.1. An example of an irreversible and a reversible photo acid 112

Figure 4.2. Previous azo photoswitchable bases reported by A) Woolley, and; B) Hecht 113

Figure 4.3. Photoswitchable glycosidase mimic **90** developed by the Bandyopadhyay group 114

Figure 4.4. Positioning of basic heteroatoms for a photoswitchable azoheteroaryl base 115

Figure 4.5. The two possible regioisomers of azobisimidazole that allow hydrogen bond stabilisation in the protonated *Z*-isomer 115

Figure 4.6. A) Calculated spectra for neutral **91** and **92**; B) Energy minimised conformations of *Z*-**91** and *Z*-**92**; C) Numbering of the imidazole ring. 116

Figure 4.7. A) Energy minimised structures, and; B) Calculated UV/vis spectra of **91**H^+ 117

Figure 4.8. A) UV/vis spectra of the PSSs of **91** and est. pure *Z*-isomer spectrum; B) pH titration of *E*-**91** and the 415 nm PSS 120

Figure 4.9. The photoswitch species present at different pHs and irradiation wavelengths 120

Figure 4.10. A) UV/vis spectra for neutral and protonated *E*-**91**; B) pH titration of *E*-**91** 121

Figure 4.11. Comparison of experimental and calculated spectra for protonated **91** 122

Figure 4.12. Difference in calculated chemical shift values for protonation on the azo or imidazole and the experimental chemical shifts for *E*-**91**H^+ 123

Figure 4.13. *E*-**91** and 405 nm PSS with equimolar BCP; A) pH titration; B) Exponential fit of $A_{440\ nm/590\ nm}$ against pH; C) pH jump; D) pH oscillation 124

Figure 4.14. Reaction rates for irradiated and dark reactions 128

LIST OF SCHEMES

Scheme 2.1. Synthesis of azopyrroles....39
Scheme 2.2. Synthesis of azopyrazole **24** 40
Scheme 2.3. Synthesis of azopyrazole **23** 40
Scheme 2.4. Alternative synthesis of azopyrazole **23**....41
Scheme 2.5. Synthesis of azopyrazoles **31** and **33**, azotetrazole **37**, and azotriazole **38**....56
Scheme 2.6. Synthesis of azopyrazoles **32** and **34**....57
Scheme 2.7. Synthesis of azopyrroles **35** and **36**....58
Scheme 3.1. Proposed catalytic mechanism of HDACs for the deacetylation of acetylated lysine. .75
Scheme 3.2. Synthesis of iodoazobenzenes **60a**-**b** 85
Scheme 3.3. Synthesis of iodoazobenzene **60c** 85
Scheme 3.4. Synthesis of azobenzene-based HDAC inhibitors....85
Scheme 3.5. Synthesis of stilbene analogues 86
Scheme 3.6. Key steps of the cell-free fluorogenic assay....90
Scheme 3.7. Synthesis of arylazopyrazole-based HDAC inhibitors....97
Scheme 3.8. Retrosynthetic analysis of **72**....104
Scheme 3.9. 1st generation attempted synthesis of **72b**....104
Scheme 3.10. 2nd generation synthesis of **72b**-**c** 105
Scheme 3.11. Synthetic route towards **72a**....106
Scheme 4.1. Retrosynthetic strategies for azobisimidazole **91**....117
Scheme 4.2. Attempted synthesis of azobisimidazole **91** *via* oxidative coupling method....118
Scheme 4.3. Synthesis of azobisimidazole **91** *via* reductive coupling method 119
Scheme 4.4. Cyclisation reaction catalysed by $NaHCO_3$ 126
Scheme 4.5. Preparation of the starting material for the cyclisation reaction 126
Scheme 4.6. Cyclisation reaction using *E*- or *Z*-**91** as the base....127

LIST OF TABLES

Table 1.1. Absorption maxima and molar extinction coefficients for azobenzene 28

Table 2.1. Highest percent conversions for *E*-*Z* and *Z*-*E* photoisomerisation 42

Table 2.2. Spectral data for **21**-**24** 43

Table 2.3. Quantum yields for all compounds 45

Table 2.4. *Z*-*E* thermal isomerisation kinetics at 25 °C 47

Table 2.5. Comparison of n-π* and π-π * λ_{max} in experimental and calculated spectra 50

Table 2.6. Calculated oscillator strengths (f) for π-π* and n-π* excitation 52

Table 2.7. Comparison of calculated and experimental thermal half-lives at 25 °C 54

Table 2.8. Percent photoconversions for *E*-*Z* and *Z*-*E* photoisomerisation 59

Table 2.9. Spectral data for the azoheteroarenes 60

Table 2.10. *Z*-*E* thermal isomerisation kinetics at 25 °C 61

Table 2.11. Experimental and calculated thermal isomerisation half-lives 65

Table 2.12. SCF energies of the most stable *Z*-conformers the lowest energy transition states 66

Table 2.13. NCI and NPA calculations 68

Table 3.1. Wittig reaction with different *para*-substituents 86

Table 3.2. Spectral data for **57a**-**c**. 88

Table 3.3. Thermal isomerisation kinetics at 30 °C 89

Table 3.4. Initial fluorogenic assay of *E*-azobenzenes and *E*- and *Z*-stilbenes against HDAH 90

Table 3.5. IC_{50} values for *E*- and *Z*-azobenzenes and stilbenes against bacterial HDACs 93

Table 3.6. IC_{50} values with for *E*- and *Z*-azobenzenes and stilbenes against human HDACs 94

Table 3.7. Spectral data for **68a**-**c** 98

Table 3.8. Thermal isomerisation kinetics of **68a**-**c** at 30 °C 99

Table 3.9. IC_{50} values for **68a**-**c** against bacterial HDACs 100

Table 3.10. Residence times of the HDAH-dansyl ligand with different alkyl spacer lengths 103

Table 3.11. Attempted conditions for Hofmann rearrangement 105

Table 3.12. Spectral data for **72b**-**c** 107

Table 3.13. Thermal isomerisation kinetics of **72b**-**c** at 30 °C. 108

Table 3.14. Michaelis-Menten kinetics for **72 b**-**c** bound to the M30C or S20C HDAH mutant 109

Table 4.1. pH jump. 124

Table 4.2. Reaction conditions for cyclisation reactions. 127

ABBREVIATIONS

A	Absorption
Ac	Acetyl
AMC	Aminomethylcoumarin
APAH	Acetylpolyamine amidohydrolase
APCI	Atmospheric pressure chemical ionisation
Aq.	Aqueous
Ar	Aryl
a.u.	Atomic unit
BCP	Bromocresol purple
Bn	Benzyl
Boc	*tert*-Butyloxycarbonyl
Bu	Butyl
Calc.	Calculated
CI	Chemical ionisation
COSY	Correlation spectroscopy
CTCL	Cutaneous T-cell lymphoma
d	Days
d	Deuterated
DBU	1,8-Diazabicyclo[5.4.0]undec-7-ene
DCM	Dichloromethane
DFT	Density functional theory
DMF	Dimethyl formamide
DMSO	Dimethyl sulfoxide
DNA	Deoxyribonucleic acid
EC_{50}	Concentration of a drug where the response is reduced by half
EDG	Electron donating group
EI	Electron ionisation
Eq.	Equation
Equiv.	Equivalent
ESI	Electrospray ionisation
Et	Ethyl
EWG	Electron withdrawing group

Exp.	Experimental
FDA	Food and Drug Administration
FRET	Fluorescence resonance energy transfer
GIAO	Gauge-including atomic orbital
h	Hours
HAT	Histone acetyltransferase
HBTU	*N,N,N′,N′*-Tetramethyl-*O*-(1*H*-benzotriazol-1-yl)uronium hexafluorophosphate
HDAC	Histone deacetylase
HDAH	Histone deacetylase-like amidohydrolase
HDLP	Histone deacetylase-like protein
HEPES	4-(2-Hydroxyethyl)-1-piperazineethanesulfonic acid
HMBC	Heteronuclear multiple bond correlation
HOMO	Highest occupied molecular orbital
HPD	Haematoporphyrin derivative
HRMS	High resolution mass spectrometry
i	*iso*
IC_{50}	Concentration of an inhibitor/drug where the enzyme activity is reduced by half
IR	Infrared
LUMO	Lowest unoccupied molecular orbital
M	Molar (mol dm^{-3})
m	*meta*
m/z	Mass-to-charge ratio
*m*CPBA	*m*-Chloroperoxybenzoic acid
MD	Molecular dynamics
Me	Methyl
m.p.	Melting point
MS	Mass spectrometry
NAD	Nicotinamide adenine dinucleotide
NBO	Natural bond order
NCI	Non-covalent interactions
NLO	Non-linear optic
NMR	Nuclear magnetic resonance
NOE	Nuclear Overhauser effect

NPA	Natural population analysis
o/n	Overnight
o	*ortho*
4-PAM	4-Phenylazomaleinanil
p	*para*
PCM	Polarisable continuum model
Pdb	Protein data bank
PDT	Photodynamic therapy
PE	Petroleum ether 40-60 °C
Ph	Phenyl
PPTS	Pyridinium *p*-toluenesulfonate
PSS	Photostationary state
PTM	Post-translational modification
RDG	Reduced density
R_f	Retention factor
rfu	Relative fluorescence unit
RNA	Ribonucleic acid
ROS	Reactive oxygen species
rt	Room temperature
s	Seconds
SAHA	Suberoylanilide hydroxamic acid
SCF	Self-consistent field
t	*tert*
$t_{1/2}$	Half-life
TDDFT	Time-dependent density functional theory
TFA	Trifluoroacetic acid
THF	Tetrahydrofuran
THP	Tetrahydropyran
TLC	Thin layer chromatography
UV	Ultraviolet
wt	Wild-type
YAG	Yttrium aluminium garnet
ZBG	Zinc binding group

ε	Molar extinction coefficient
θ	Dihedral angle
λ_{max}	Absorption maxima
Φ	Quantum yield

EQUATIONS

$$PSS = \frac{\varepsilon_A \Phi_{A\rightarrow B}}{\varepsilon_B \Phi_{B\rightarrow A}} \quad (1)$$

$$A_Z = \frac{A_{PSS}\text{-}A_E \times f}{1\text{-}f} \quad (2)$$

$$\Phi_{A\rightarrow B} = \frac{k\,V}{q_{in}\varepsilon_A l\, ln10} \quad (3)$$

$$\ln\frac{k}{T} = \frac{-\Delta H^{\ddagger}}{R} * \frac{1}{T} + \ln\left(\frac{k_B}{h}\right) + \frac{\Delta S^{\ddagger}}{R} \quad (4)$$

$$k = \frac{k_B T}{h}\exp\left(\frac{-\Delta G^{\ddagger}}{RT}\right) \quad (5)$$

$$k = \frac{k_B T}{h}\exp\left(\frac{\Delta S^{\ddagger}}{R}\right)\exp\left(\frac{-\Delta H^{\ddagger}}{RT}\right) \quad (6)$$

$$K_a^Z = \frac{K_a^E K_a^{PSS} R_{PSS}^{unprot}}{K_a^E + K_a^E R_{PSS}^{unprot} - K_a^{PSS}} \quad (7)$$

$$\delta_{calc}^x = \delta_{exp}^{ref} + \sigma^{ref} - \sigma^x \quad (8)$$

$$\delta_{scaled} = \frac{\delta_{calc}\text{-intercept}}{slope} \quad (9)$$

$$f_{PSS} = \frac{A_{PSS}\text{-}A_Z}{A_E\text{-}A_Z} \quad (10)$$

1 INTRODUCTION

1.1 Light as a stimulus

Light is capable of inducing a response in a huge variety of biological systems and is believed to be one of the stimuli responsible for the origin of life on Earth.[1] Organisms have evolved to convert light into energy or biological signals; prominent examples include photosynthesis, vision, and the circadian clock, which enables organisms to coordinate their behaviour and biology with the day-night cycle.[2–4] In recent years, scientists have used light to probe biological systems. One common method is to genetically engineer a particular protein of interest so that it is fluorescent – this allows the protein to be tracked within a cell or organism using fluorescent imaging.[5–7] The 2008 Nobel Prize in Chemistry was awarded for the seminal work on fluorescent tagging, demonstrating its importance as a biological tool.[8] Genetically modified proteins and receptors are also important in the related field of optogenetics, where the addition of a light-sensitive element allows either visualisation or control of cellular function.[9,10] Biological processes can also be studied by using small molecule light-sensitive probes, such as 'caged' or photoswitchable biomolecules, termed opto*chemical* genetics.[11] Light is an extremely attractive stimulus as it is non-invasive and capable of achieving very high spatial and temporal precision. The wavelength and intensity of the light source can be tuned, and it can transfer sufficient energy to cause photochemical transformations such as electrocyclisation, ligand dissociation, and isomerisation.[12,13] As such, there are now a wide range of applications in which light is exploited, from optogenetics and photopharmacology to spin-state switching and molecular motors.[11,14–19]

1.2 Photochromism and photoswitches

Photochromism is the reversible transformation between two forms of a chemical species, caused by the absorbance of light, where the two forms have different absorption spectra.[20] This difference in absorption spectra often results in an obvious colour change. Photochromic molecules, known as photoswitches, differ from 'caged' molecules, which are irreversibly switched to a different state.[11,21] Upon continued irradiation of a photoswitch, a steady state is reached where the rates of both the forward (A→B) and reverse isomerisation (B→A) become equal – this is referred to as the photostationary state (PSS).[22] The photoisomerisation rates are proportional to two properties; the quantum yields (Φ) of the forward and reverse isomerisations, and the extinction coefficients (ε) of A and B at the irradiation wavelength. The extinction coefficient defines how strongly the substance absorbs light at a given wavelength,[22] while the quantum yield defines how many times a specific event occurs (in this case photoisomerisation) per photon

absorbed by the system,[23] with a maximum value of 1. The relationship of these two properties to the photoisomerisation rate means that the composition of isomers at the PSS depends on both the quantum yields and extinction coefficients, as shown in equation 1.[24] This is the case if both isomers are thermally stable, however if one isomer is not, then the thermal isomerisation rate may prevent the 'true' PSS being reached.[24] This is only an issue if the thermal isomerisation occurs at a similar rate to the photoisomerisation. This problem can be solved by increasing the intensity of the irradiation, as this increases the photoisomerisation rate relative to the thermal isomerisation rate.

$$PSS = \frac{\varepsilon_A \Phi_{\mathrm{A}\rightarrow\mathrm{B}}}{\varepsilon_B \Phi_{\mathrm{B}\rightarrow\mathrm{A}}} \qquad (1)$$

There are several main classes of photoswitches; spiropyrans, diarylethenes, fulgides, and azobenzenes.[13,25–28] The first three of these classes undergo electrocyclic ring opening and closing on irradiation with light, while azobenzenes undergo *E*-Z isomerisation upon irradiation (Figure 1.1).

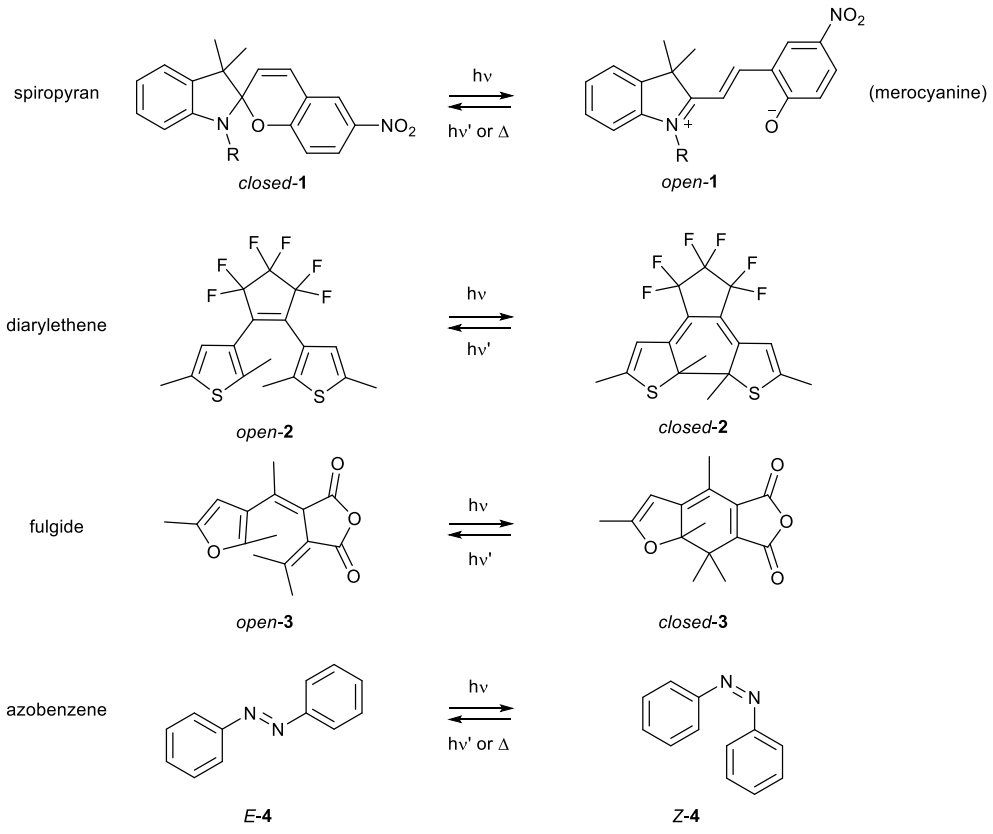


Figure 1.1. Examples of the main classes of photoswitch.

The spiropyrans and azobenzenes are classified as T-type photoswitches, as they are both thermally and photochemically reversible.[13] The merocyanine form of spiropyran (*open*-**1**) and the *Z*-isomer of azobenzene (*Z*-**4**) both slowly isomerise back to their more thermally stable

conformations (*closed*-**1** and *E*-**4** respectively). The diarylethenes (**2**) and fulgides (**3**) are classed as P-type photoswitches; these are thermally irreversible and photochemically reversible – both *open* and *closed* conformations of each photoswitch are thermally stable.[13]

Photoswitches have a huge range of potential applications, and as such, there has been a wealth of research carried out with the aim of improving the properties of the photoswitch with respect to a specific application. One of the key focuses of research is the thermal stability of the two isomers. For some applications, such as optical data storage,[29] both isomers need to be thermally stable, while for other applications, such as real-time information transmission,[30] extremely rapid thermal isomerisation rates are required. High fatigue resistance is an important property for most applications, as this allows the photoswitch to undergo multiple cycles of photoswitching without degradation occurring. For biological applications, it is important that visible light photoswitches are used, as UV light is harmful to tissue.[11] Ideally red or near-infrared photoswitches should be used as these wavelengths have much greater tissue penetration than shorter wavelength visible light. Another desirable property is a good separation of absorbances between the two isomers. The PSS reached upon irradiation depends on the ratio of absorbances of the two isomers at the irradiation wavelength. Assuming both isomers have the same quantum yield, irradiating at a wavelength where both isomers have the same absorbance, known as an isosbestic point,[22] will lead to a PSS containing 50% of each isomer, whereas if only one isomer absorbs at the irradiation wavelength, the resulting PSS will contain only the other isomer. Therefore, a good separation of absorbances allows irradiation to be carried out at a wavelength where one isomer absorbs strongly and the other isomer has negligible absorbance, resulting in quantitative switching.

1.3 Azobenzenes

Azobenzenes have emerged as the most versatile and reliable photoswitches to date, due to several desirable properties. They often have high extinction coefficients and quantum yields, so low intensity light can be used to elicit photoisomerisation.[25,31] They also have very fast rates of photoswitching, on a picosecond timescale,[25,31,32] preventing intersystem crossing and formation of triplet state diradicals.[11] If formed, these can react with triplet oxygen to produce singlet oxygen, which is a highly reactive species; as well as being cytotoxic, it causes degradation of the photoswitch itself.[11] Another important feature of azobenzenes is the significant change in shape upon isomerisation; in general the *E*-isomers are planar, while the *Z*-isomers adopt a twisted conformation in order to minimise steric repulsion (Figure 1.2).[31] This change in shape results in a substantial difference in the end-to-end distance between the two isomers. There is also a

significant change in the dipole moment; *E*-**4** has a dipole moment of near zero, while *Z*-**4** has a dipole moment of 3 Debye.[31,33] Due to the difference in shape of the two azobenzene isomers, their UV/vis spectra are considerably different (Figure 1.2).[31]

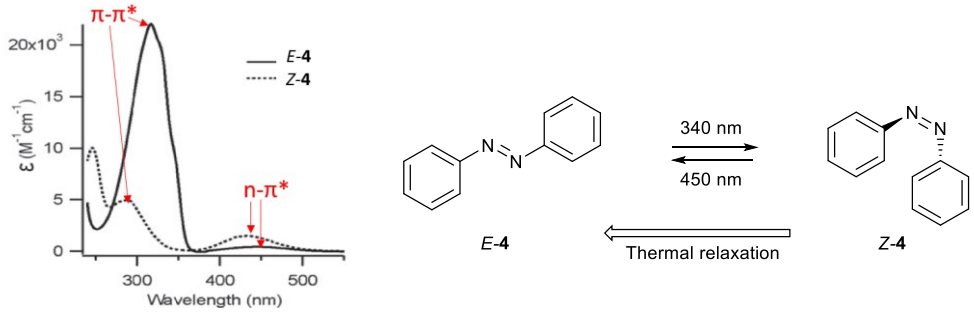


Figure 1.2. UV/vis spectra of *E*- and *Z*-**4** (left), adapted from Woolley *et al*,[31] and photoisomerisation of azobenzene (right).

E-**4**, and *E*-azobenzenes in general, have a stronger π-π* transition at lower energy (longer wavelength) than the *Z*-isomers, while the n-π* transition of the *E*-isomer is generally weaker than the *Z*-isomer but at a similar energy (Table 1.1). *E*-azobenzenes are more stable than the *Z*-isomers (with one exception – see section 1.4) and are the dominant isomer at thermal equilibrium. For azobenzene itself (**4**), irradiation of the *E*-isomer π-π* transition with UV light results in a PSS containing ~80% of the *Z*-isomer. *E*-**4** can be regenerated either by irradiation of the *Z*-isomer n-π* with visible light, producing ~95% *E*-azobenzene, or by thermal isomerisation.[31] Thermal isomerisation of *Z*-**4** occurs with a half-life of between 2 and 4 days, depending on the solvent, and results in complete conversion to the *E*-isomer.[25,34–37] The absorption spectra of the two isomers overlap, hence the incomplete photoswitching between the two.

	π-π*		n-π*	
	λ_{max} / nm	ε / M^{-1} cm^{-1}	λ_{max} / nm	ε / M^{-1} cm^{-1}
E-**4**	~320	~22000	~450	~400
Z-**4**	~270	~5000	~450	~1500

Table 1.1. Absorption maxima and molar extinction coefficients for the electronic transitions of *E*- and *Z*-**4**. Adapted from Bandara and Burdette.[25]

The two basic mechanisms by which photo- and thermal isomerisation can occur are rotation and inversion, but there are also variations on these – concerted inversion and inversion-assisted rotation (Figure 1.3).[25]

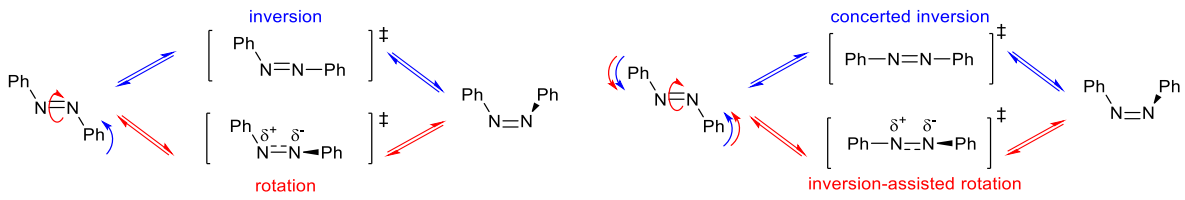


Figure 1.3. Different possible isomerisation mechanisms for azobenzenes.

In the rotation mechanism, the N=N π-bond is broken to allow N-N bond rotation. During this pathway, the dihedral angle (C-N-N-C) changes, while the N-N-C angle remains at 120°. In the inversion mechanism, the dihedral angle remains unchanged, while one N-N-C angle is increased to 180° at the transition state, resulting in a sp hybridised nitrogen. In the concerted inversion mechanism both N-N-C angles are increased to 180°, while in the inversion-assisted rotation mechanism, there is a large change in the C-N-N-C dihedral angle and smaller changes to the N-N-C angles.[25,38] The concerted-inversion mechanism is the only one of the four which has no net dipole moment in the transition state.

Over the years, there has been much debate over which pathways are followed, for both *E-Z* and *Z-E* photoisomerisation and thermal isomerisation.[38–44] Today, there is still ambiguity over the isomerisation mechanism of azobenzene, however the addition of electron donating and/or electron withdrawing substituents to azobenzene is thought to have an effect on the pathway followed.[25,39] As well as affecting the isomerisation pathway, adding substituents to azobenzene can have a large effect on the properties of the photoswitch, such as the thermal isomerisation rate or the wavelength and intensity of absorption maxima. Azobenzenes can be split into several distinct classes depending on the nature of their substituents; azobenzenes, aminoazobenzenes, push-pull azobenzenes, and protonated azobenzenes (Figure 1.4).[25]

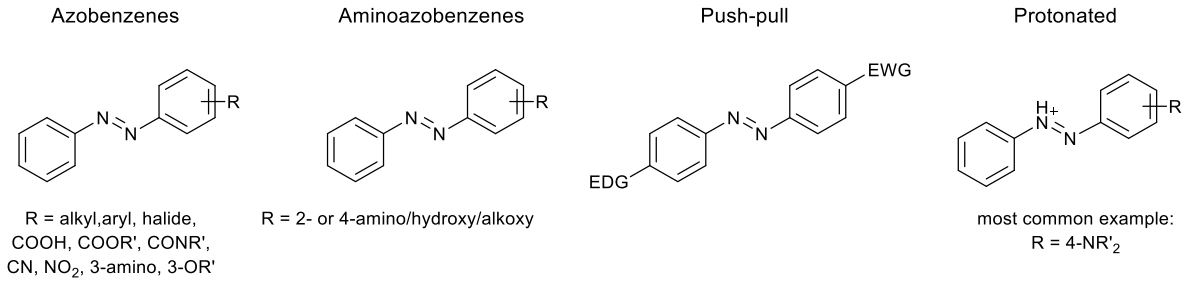


Figure 1.4. Different classes of azobenzenes.

The azobenzene class includes substituted azobenzenes whose properties are similar to those of azobenzene itself, in terms of both the absorption spectra and thermal isomerisation rates. The aminoazobenzenes have *para*- or *ortho*-amino, hydroxy, or alkoxy substituents, on either one or both benzene rings.[25] The presence of these electron donating substituents causes the π-π* absorbance to red-shift to longer wavelengths, so that it overlaps with the n-π* absorbance.[25,45] The thermal isomerisation rates are faster than for azobenzene itself, and half-lives range from several hours to milliseconds. Short half-lives are seen for *para*- and *ortho*-hydroxyazobenzenes such as **5**, where tautomerisation can lead to a single N-N bond that can rapidly rotate (Figure 1.5).[25]

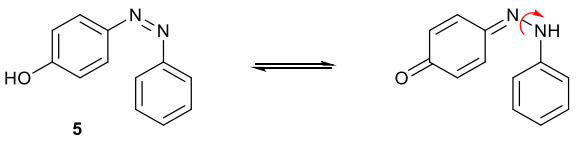


Figure 1.5. Azo-hydrazone tautomerisation in *p*-hydroxyazobenzene (**5**).

Push-pull azobenzenes have an electron withdrawing group and an electron donating group on the 4- and 4'-positions of the phenyl rings. This causes an even larger red-shift in the π-π* transition than is seen for the aminoazobenzenes, resulting in the π-π* absorbance occurring in the visible region and having a very similar energy to the n-π* absorbance.[13,25] Push-pull azobenzenes tend to have very fast thermal isomerisation rates, with half-lives in the second to millisecond timeframe.[25] This is due to resonance forms with single N-N bond character that lower the thermal energy barrier for N-N bond rotation (**6**, Figure 1.6), in a similar manner to the hydroxyazobenzenes. If an inversion mechanism were involved, as is believed to be the case in non-polar solvents,[25] the substituents would still stabilise the transition state, as inversion transition states are in general more polar than the *Z*-isomers.[46] The push-pull azobenzenes can be considered similar to the protonated azobenzenes in that they both have low lying π-π* transitions relative to the n-π* transitions – for this reason they are both referred to as pseudostilbenes.[13,25] For the push-pull azobenzenes, this is due to a lowering of π-π* energy, whereas for protonated azobenzenes it is due to an increase in n-π* energy. Protonated azobenzenes also have rapid thermal isomerisation rates, particularly the *para*-amino analogues, due to the availability of similar resonance structures to the push-pull azobenzenes (**7**, Figure 1.6).[25] For unsubstituted azobenzene the pK_a values of the *E*- and *Z*-isomer azonium ions are -2.6 and -1.6 respectively, so strong acids are required in order to obtain these species in solution.[47,48] Protonated aminoazobenzenes have considerably higher pK_a values ($pK_a \sim 0.5 - 3$) due to additional stabilisation from the *para*-amine, and can also undergo azonium-ammonium tautomerisation.[49–51]

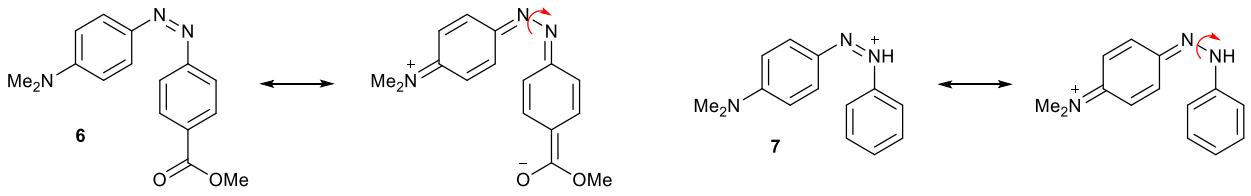


Figure 1.6. Resonance structures for the push-pull (**6**) and protonated (**7**) azobenzenes.

1.4 Tuning the properties of azobenzenes

In recent years a large amount of the research into azobenzenes has concerned tuning their properties in order to improve their suitability for certain applications. One particular focus has

been the development of photoswitches that can be switched with visible light rather than UV, while avoiding the increase in thermal isomerisation rate that is observed for amino and push-pull azobenzenes.[34,44,52,53] Woolley and co-workers recently reported that the presence of methoxy or thiol substituents on all four *ortho*-positions of the phenyl rings resulted in a significant red-shift of the *E*-isomer n-π* absorption maxima relative to the *Z*-isomer and also led to an increase in the intensity of the transition (**8**, Figure 1.7).[54–56] *E*-*Z* thermal isomerisation rates of some of these compounds were significantly slower than for azobenzene, with half-lives of up to 14 days at room temperature.[54] The separation of *E*- and *Z*-isomer n-π* absorption maxima allowed *E*-*Z* photoisomerisation to be achieved by exciting the *E*-isomer n-π* transition with green or even red light, rather than having to excite the π-π* transition using UV light.[54–56] *Z*-*E* photoisomerisation was achieved as usual by exciting the *Z*-isomer n-π* transition with blue light. Removing the requirement of UV light for photoswitching is important in biological applications, as UV light has unwanted effects on cells, such as causing DNA damage or generating reactive oxygen species.[11] The Woolley lab demonstrated the potential applications of their *ortho*-substituted compounds by synthesising azobenzene-stapled peptides and photoswitching them with red light *in vivo*.[57] In a further development, Woolley has reported protonated azobenzenes with *o*-methoxy substituents that can be switched with red or even near-infrared light.[58,59] As mentioned above, these wavelengths are the most suited for use in biological systems as they penetrate tissue further than other visible light. The *ortho*-methoxy substituents are able to stabilise the azonium proton by hydrogen bonding (see Chapter 4), so that the pK_a of the *E*-isomer is similar to physiological pH.

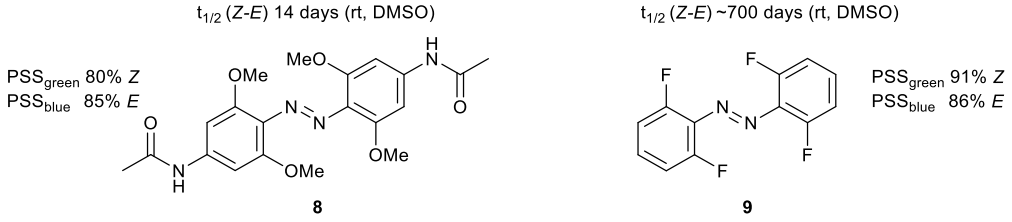


Figure 1.7. *ortho*-Substituted azobenzenes with visible light switching and long thermal half-lives.[54,60]

On a similar theme, Hecht and co-workers have developed *ortho*-tetrafluoroazobenzenes that can be photoswitched between both isomers with visible light (**9**, Figure 1.7).[60] The photoconversions achieved were comparable to or slightly improved relative to those of azobenzene, with a *para*-carboxylate *o*-tetrafluoro analogue reaching PSSs containing 90% *Z*-isomer and 97% *E*-isomer following irradiation with green and blue light respectively. In addition to this, the *Z*-isomer of *o*-tetrafluoroazobenzene itself (**9**) was very stable, with a thermal half-life of ~700 days at room temperature.[60]

Computational studies found that the presence of *ortho*-substituents leads to a significant change in the conformation and electronics of the azobenzene. For Woolley's *o*-methoxy azobenzenes, the *E*-isomer was calculated to adopt a twisted conformation rather than the planar conformation usually seen for *E*-azobenzenes, due to the unfavourable electronic interactions between the lone pairs of the *ortho*-methoxy groups and the azo nitrogens.[54] These unfavourable interactions raise the energy of the *E*-isomer non-bonding (n) HOMO which is centred on the nitrogen lone pairs, relative to the LUMO (π*), leading to a red shift in the n-π* absorption maximum. In the *Z*-isomer, the bent conformation relieves the unfavourable interactions between the azo and methoxy moieties, so a red-shift in n-π* transition is not seen.[54] In contrast to the *o*-methoxyazobenzenes, the presence of *o*-fluoro substituents barely distorts the planar geometry of the *E*-azobenzene due to the relatively small radius of the fluorine atom.[60] However, the fluorines were found to lower the energy of the *Z*-isomer n-orbital relative to that of the *E*-isomer, by reducing the electron density in the N=N bond, which reduces the repulsive interaction of the nitrogen lone pairs. This repulsive interaction is much greater in *Z*-azobenzenes than *E*-azobenzenes, hence the *Z*-isomer n-orbital energy is lowered relative to the *E*-isomer.[60] This increases the energy of the n-π* transition for the *Z*-isomer resulting in separation of *E*- and *Z*-isomer absorption maxima.

Probably the most drastic change in the properties of azobenzenes achieved to date has been a switch in the thermodynamically favoured isomer. The bridged azobenzene **10** reported by Temps and co-workers has a thermally stable *Z*-isomer, with an *E*-*Z* thermal half-life of 4.5 hours at room temperature (Figure 1.8).[61] This switch in stability relative to azobenzene is due to the high ring strain present in *E*-**10** compared to in *Z*-**10**. Photoisomerisation of both isomers can be carried out with visible light, and due to a good separation of absorption maxima, high photoconversions are achievable, with *E*-*Z* isomerisation occurring quantitatively upon irradiation with green light.[61]

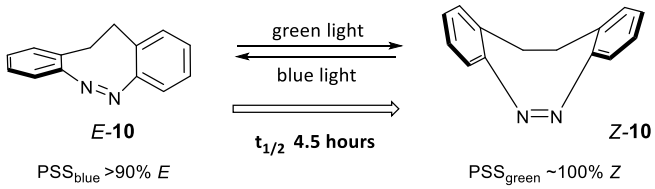


Figure 1.8. Bridged azobenzene **10** with a thermally stable *Z*-isomer.[61]

1.5 Applications of azobenzenes

One particular focus of research using azobenzenes has been in the field of photopharmacology (see Chapter 3). Incorporating a photoswitch into a known enzyme inhibitor allows the enzymatic activity to be externally controlled by light.[19,62] One conformation of the inhibitor should be less

able to access the enzyme active site than the other, resulting in a difference in enzyme activity between the two conformations. Azobenzenes are particularly suited to this application due to the significant change in shape upon isomerisation.[31] Recently, a photoswitchable analogue of the anaesthetic propofol (**11**) was developed by Trauner and co-workers (Figure 1.9),[63] where a 4-fold difference in effective dose (EC_{50}) was achieved between the *E*-isomer and the PSS, with comparative inhibitory activity to propofol itself. There have been several other examples of azobenzenes used in photopharmacology, such as a photoswitchable antibiotic reported by the Feringa group and photoswitchable anti-cataract agents reported by the Abell group.[64,65]

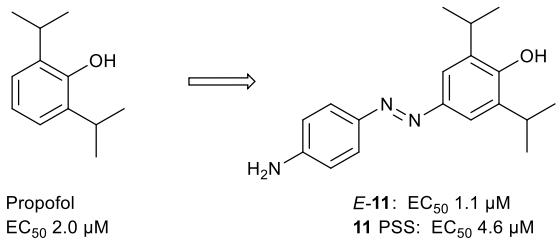


Figure 1.9. Photoswitchable analogue of propofol developed by Trauner.[63]

Azobenzenes have also been incorporated into peptide chains, resulting in large conformational changes to the peptide structure upon photoisomerisation. For example, switching between the *E*- and *Z*-isomers of an azobenzene that has been incorporated into a peptide can reversibly introduce secondary structure into a disordered peptide.[31,66] This can be achieved by 'stapling' the photoswitch onto the peptide *via* two side chains that are at an appropriate distance from each other (Figure 1.10, A), which can lead to the formation of α-helices,[67] or by incorporating the photoswitch into the peptide backbone, which tends to lead to the formation of β-hairpins upon switching to the *Z*-isomer (Figure 1.10, B).[68]

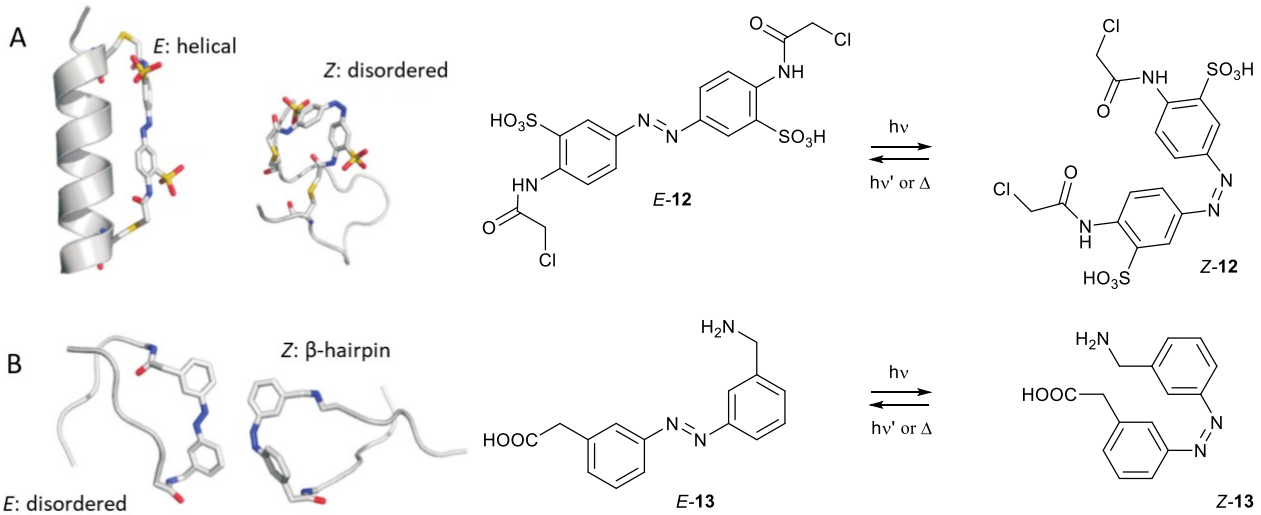


Figure 1.10. Photoswitchable peptides with: A) An azobenzene-containing peptide staple (**12**); B) An azobenzene incorporated into the primary peptide chain (**13**). Adapted from Woolley *et al*.[31]

These stapled peptides have particular use in the field of optochemical genetics, where they can be used to probe the role of specific biomolecules in their native environment.[31]

One particularly interesting use of azobenzenes is in molecular motors or machines, specifically rotaxanes.[69] Rotaxanes are a type of mechanically interlocked molecule that are able to elicit controlled translational motion on the nanoscale. One of the aims of this research is to develop artificial molecular machines that are capable of mimicking the directed motion achieved by biomolecular assemblies. Rotaxanes can be seen as analogous to muscle tissue, as they are able to contract and extend in a similar way to muscles.[69] A photochemically controlled 'daisy-chain' rotaxane (**14**) has been reported by the Kaneda lab, which exploits azobenzene *E*-*Z* isomerisation to induce contraction and extension of the chain (Figure 1.11).[70]

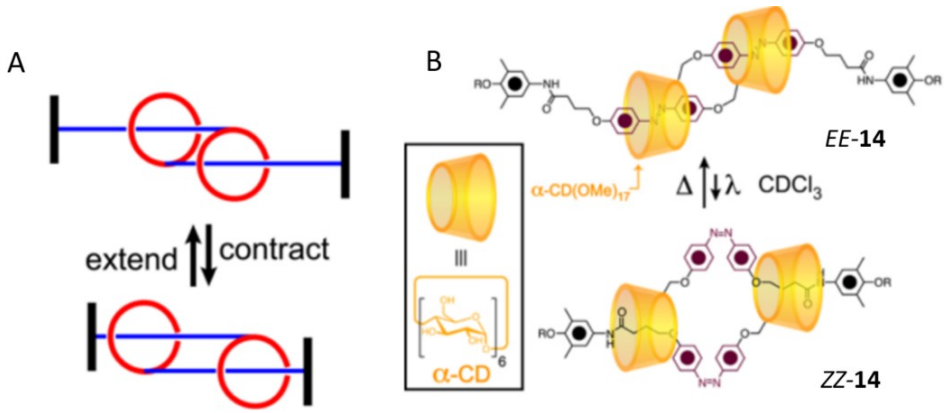


Figure 1.11. A) Schematic of a daisy chain rotaxane; B) Example of a daisy chain rotaxane controlled by light. Adapted from Stoddart *et al*.[69]

Research has also been carried out into using azobenzenes for optical data storage, with a large amount of work focusing on holographic memory.[71–76] Azobenzenes have been incorporated into polymers that are able to form liquid crystals (Figure 1.12, A).[77] By irradiating with linearly polarised light, azobenzene isomerisation can induce anisotropy in the liquid crystals (Figure 1.12, B). The presence of either *E*- or *Z*-azobenzene in the polymer changes the refractive index of the material – a property referred to as birefringence.[75] It is this property that is exploited for the storage of information. In certain examples reported in the literature, *Z*-*E* thermal isomerisation did not result in a change in the orientation of the liquid crystal, resulting in increased stability in the information stored.[77] There are several advantages of holographic memory over 2D data storage; firstly, it is 3D so allows a higher density of information to be stored; and secondly, data can be written and read as a whole data page (Figure 1.12, C) rather than bit-by-bit, resulting in much faster read-out rates.[75,76]

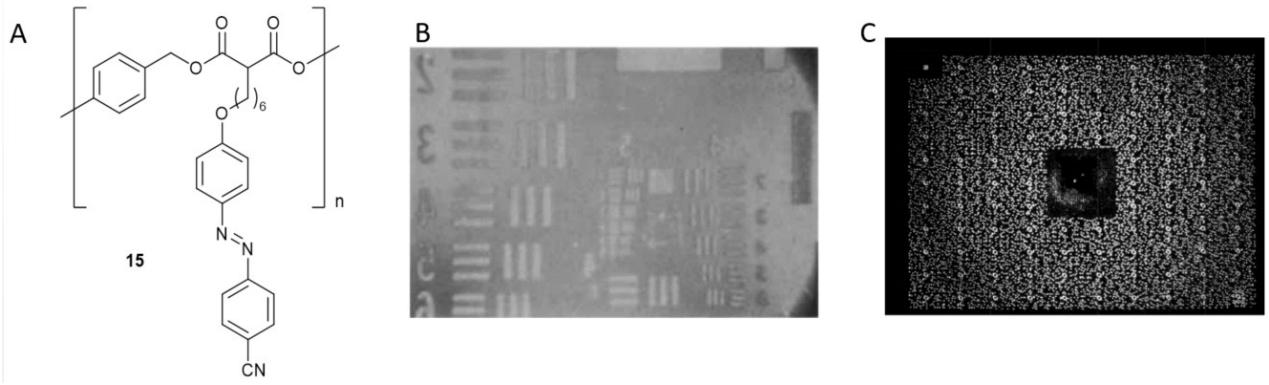


Figure 1.12. A) An early liquid-crystalline polymer (**15**) containing azobenzene, for use in holographic optical storage, and; B) the binary test pattern stored in polymer **15**, using a polarised writing beam (taken from Eich *et al*)[77]; C) A recovered data page (or bitmap) using a holographic memory card (taken from Lörincz *et al*).[78]

There have also been several examples of using azobenzenes to elicit photocontrol of chemical reactions; one way this can be achieved is by designing photoswitches with a difference in pK_a values between the two isomers (see Chapter 4).[79–81] These compounds are usually referred to as photoswitchable acids and bases and are able to control the rates of acid or base catalysed reactions. Differences in ground state acidity/basicity can be achieved by designing photoswitches where a proton is additionally stabilised in one isomer over the other by hydrogen bonding, as is the case with the 2-hydroxyazobenzenes reported by the Jullien lab (Figure 1.13, A).[81,82] Alternatively, this can be achieved through steric shielding in one isomer over the other, as is seen with the azobenzene-piperidine bases reported by Hecht and co-workers (Figure 1.13, B).[80,83,84]

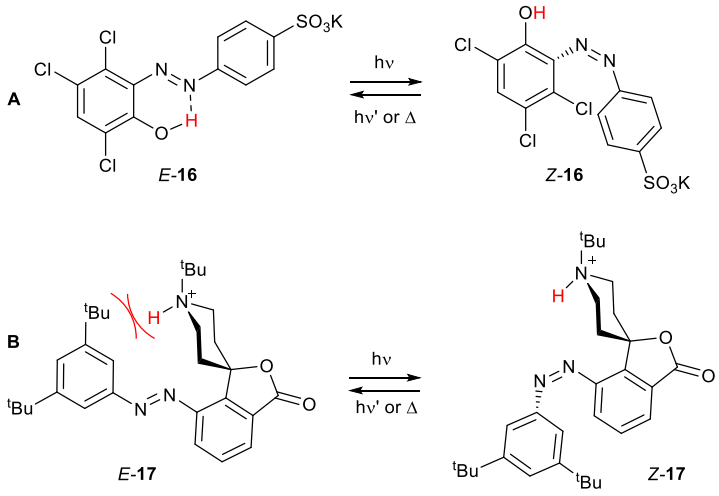


Figure 1.13. Examples of; A) A photoswitchable acid (**16**), and; B) A photoswitchable base (**17**).

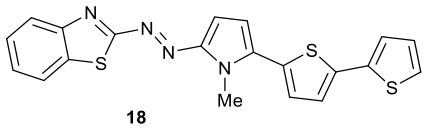
The examples that have been briefly described here demonstrate just how wide ranging the potential applications of azobenzenes are and also highlight the requirement of specific, and often very different, properties for each application. It is this tunability of properties that make azobenzene such a popular photoswitch and a continued focus for research.

2 NOVEL AZOHETEROARYL PHOTOSWITCHES

2.1 INTRODUCTION

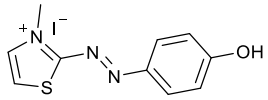
In comparison to the azobenzenes, 5-membered azoheteroarenes are far less studied, particularly in terms of their photochromism. A large part of the work on azoheteroarenes has concentrated on developing donor-π-acceptor (push-pull) systems with strong non-linear optic (NLO) and solvatochromic properties.[85–92] In NLO materials, the polarizability of the material behaves non-linearly with respect to the electric field of the light.[93] Non-linear interactions between the material and incident light lead to non-linear responses in frequency, polarization, and path/phase of the light. There are multiple NLO processes that have useful applications, such as harmonic generation and multi-photon absorption.[93] Push-pull azoheteroarenes have good second-order NLO properties with research focusing on achieving high hyperpolarizability and also high decomposition temperatures.[92]

Of the push-pull azoheteroarenes whose photoswitching behavior has been studied, incomplete *E*-*Z* conversion and fast thermal half-lives of under 1 minute were generally seen.[86,87,89] Velasco and co-workers recently exploited this property to develop extremely fast photoswitches that are able to tolerate thousands of switching cycles without decomposition (Figure 2.1).[94,95] The presence of electron withdrawing groups, such as benzothiophene, on one end of the azo group, and electron donating groups, such as bithienylpyrrole, on the opposing end (**18**, Figure 2.1) resulted in the fastest thermal isomerisation rates reported for neutral azo compounds to date, with half-lives in the microsecond range.[94] Further work in the Velasco group led to the development of thiazolium azophenolic salts such as **19**, with half-lives in the nanosecond range (Figure 2.1).[95] These push-pull azoheteroarenes have red-shifted absorption spectra relative to azobenzenes, allowing *E*-*Z* photoisomerisation with green light.



18

$t_{1/2}$ (*Z*-*E*) = 49 μs (EtOH, rt)



19

$t_{1/2}$ (*Z*-*E*) = 38 ns (EtOH, rt)

Figure 2.1. Azoheteroarenes with fast thermal half-lives, developed by Velasco and co-workers.[94,95]

For applications requiring long half-lives and high *E*-*Z* photoconversion, the arylazoimidazoles are the only 5-membered azoheteroarenes reported to date to show promise.[96–98] Herges and co-workers demonstrated that altering the position at which the azo moiety is linked to the imidazole has a large effect on the thermal properties.[96] They found that 1-methyl-5-phenylazoimidazole **20**

had a thermal half-life of 22 days (Figure 2.2), compared to 5 and 9 hours for the 4- and 2-imidazolyl analogues respectively.[96,97] Azoimidazole **20** could be photoswitched with UVA light to a PSS containing 98% *Z*-isomer, however the best PSS achieved for *Z*-*E* photoisomerisation only contained 55% *E*-isomer and required irradiation with UVB light (Figure 2.2).[96] Computational studies on this compound revealed that rather than adopting a twisted conformation like *Z*-azobenzene, *Z*-**20** adopted a conformation where the imidazole ring is co-planar to the C-N=N-C plane, while the phenyl ring is at 90° to said plane (see section 2.2.5.1 for more detailed discussion).[96]

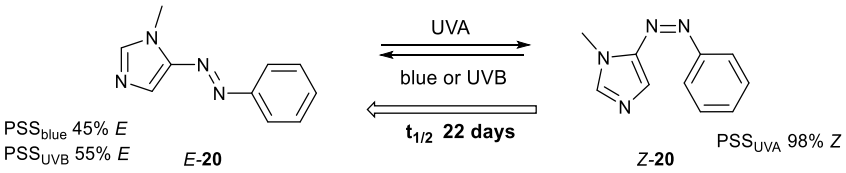


Figure 2.2. Arylazoimidazole **20** developed by Herges and co-workers.[96]

2.2 RESULTS AND DISCUSSION PART I: Arylazopyrazoles and pyrroles[i]

2.2.1 Photoswitch design and aims

Considering the limited research into 5-membered azoheteroarenes, the decision was made to develop novel photoswitches of this class with the aim of achieving quantitative photoswitching and long thermal half-lives. Compounds in which only one of the phenyl rings in azobenzene was replaced with a heteroaryl ring were chosen for study. Initially, two types of azoheteroarenes were focused on; the arylazopyrazoles, whose photochemical and thermal properties have never been studied, and the arylazopyrroles. Although the photochemistry of push-pull azoheteroarenes containing pyrroles has been studied previously, there has been less of a focus on the photochemistry of *aryl*azopyrroles where there is still a phenyl ring present on one side of the azo group.[99–101] It was thought that the difference in electronics between the pyrrole and pyrazole rings would influence the photochemical properties as well as the thermal stability of the *Z*-isomer, with regards to *Z*-*E* thermal isomerisation. In addition to this, the substitution pattern on the azoheteroaryl ring in the positions adjacent to the azo group was altered (referred to as *ortho* substituents from here on). The presence or absence of substituents would also be expected to have an effect on the photochemical and thermal properties, due to altering the sterics around the azo nitrogens. This led to four compounds being chosen for synthesis; arylazopyrroles **21** and **22** and arylazopyrazoles **23** and **24** (Figure 2.3). The specific regioisomers were chosen as they are

[i] This section is based on the following publication; C. Weston, R. Richardson, P. Haycock, A. White and M. Fuchter, *J. Am. Chem. Soc.*, 2014, **136**, 11878–11881.

synthetically accessible; the 2-position and 4-position of pyrrole and pyrazole respectively are the most reactive towards electrophiles.[102]

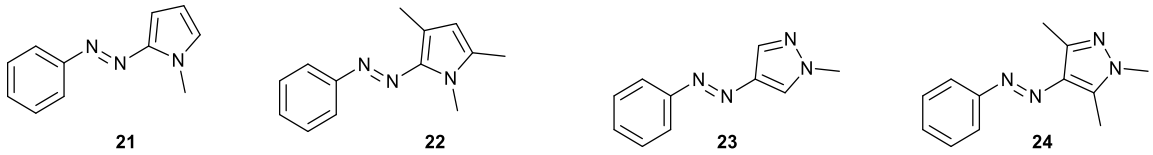


Figure 2.3. Azoheteroarenes chosen for study.

All compounds chosen were *N*-methylated to prevent assumed rapid *Z*-*E* thermal isomerisation – the presence of a heteroaryl NH allows azo-hydrazone tautomerisation to occur (Figure 2.4),[98,101] as is seen with *p*- and *o*-hydroxyazobenzenes (Figure 1.5).[25] Of the four azoheteroarenes chosen, azopyrazole **24** was the only known compound,[103] however no photochemical studies have been carried out prior to this work. As well as studying the photochemical properties of these compounds, computational studies would also be carried out in order to determine how well the spectral and thermal properties could be predicted and also to understand any experimental trends seen in these properties.

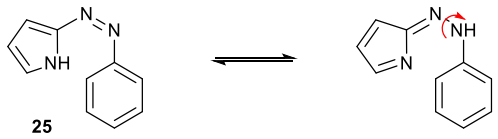
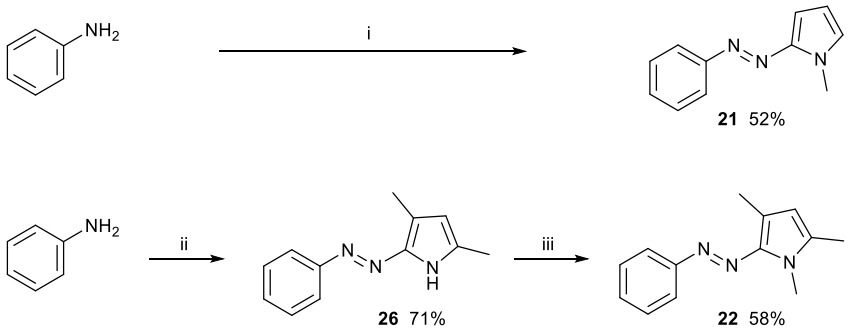


Figure 2.4. Azo-hydrazone tautomerisation that can occur when the heteroaryl ring contains a free NH.

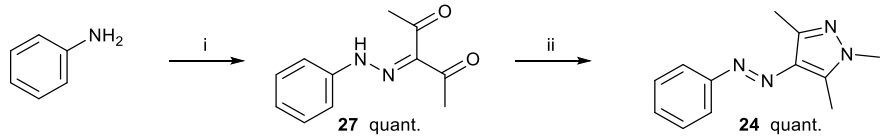
2.2.2 Synthesis

Arylazopyrroles **21** and **22** and arylazopyrazole **24** were all prepared using standard diazo coupling methods; *in situ* formation of phenyldiazonium chloride from aniline and sodium nitrite under acidic conditions.[104] Coupling the diazonium salt with *N*-methylpyrrole afforded **21** in 52% yield,[105] while coupling with 2,4-dimethylpyrrole afforded **26**,[101] which was *N*-methylated with methyl iodide to give **22** in 41% yield over the two steps (Scheme 2.1).



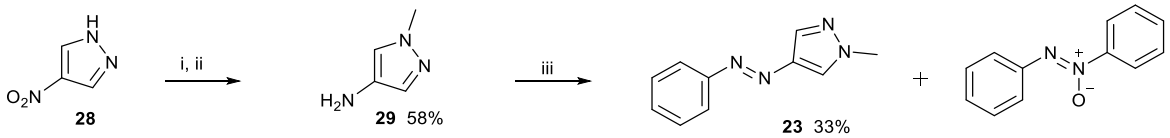
Scheme 2.1. Synthesis of azopyrroles. Reagents and conditions: (i) conc. HCl, aq. $NaNO_2$, 1:1 acetone:H_2O, 0 °C, 1 h; then add to Na_2CO_3, *N*-methylpyrrole, 1:1 acetone:H_2O, 0 °C – rt, 1 h; (ii) conc. HCl, aq. $NaNO_2$, H_2O, 0 °C, 1 h; then 2,4-dimethylpyrrole, 6:1 MeOH:pyridine, 0 °C; (iii) 60% NaH, MeI, THF, 0 – 60 °C, 2 h;

For the synthesis of **24**, the diazonium salt of aniline was coupled with acetylacetone, giving the intermediate **27** which was condensed with methylhydrazine to give the final azopyrazole in quantitative yield (Scheme 2.2).[103,106]



Scheme 2.2. Synthesis of azopyrazole **24**. Reagents and conditions: (i) conc. HCl, aq. $NaNO_2$, AcOH, 0 °C, 1 h; then add to NaOAc, acetylacetone, 2:1 EtOH:H_2O, 0 °C – rt, 1 h; (ii) NH_2NHMe, EtOH, reflux, 3 h.

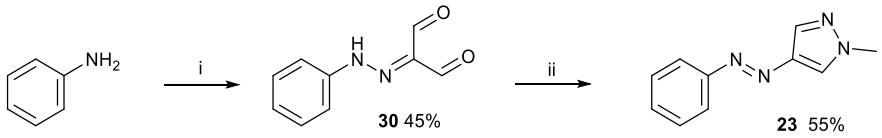
Arylazopyrazole **23** was initially prepared from 4-amino-1-methylpyrazole (**29**) and nitrosobenzene, *via* a modified Mills reaction (Scheme 2.3).[107,108] The Mills reaction was originally reported for the synthesis of azobenzenes *via* condensation of a nitrosobenzene and an aniline in acetic acid.[109] This was modified by both Campbell[107] and Brown[108] to allow for the synthesis of phenylazopyridines. Acidic solvent was not compatible with the aminopyridine starting material due to protonation of the pyridine ring, so instead they replaced it with a biphasic solvent, containing concentrated aqueous sodium hydroxide and either benzene or pyridine. The scope for this reaction has previously included various phenylazopyridines and phenylazoquinolines.[107,108] Pleasingly, the reaction also appeared to be suitable for preparing azo compounds containing 5-membered heteroarenes, such as **23**. This is especially useful considering the limited synthetic routes available for this family of compounds.[94,96,110] During the reaction of **29** with nitrosobenzene, small amounts of azoxybenzene formed (Scheme 2.3) – this side product is commonly seen in the modified Mills reaction,[107] and is presumably caused by disproportionation of nitrosobenzene to azoxybenzene and nitrobenzene, which has been reported in the absence of catalyst at a comparable temperature.[111] Difficulties in separating the product from azoxybenzene, due to co-elution during column chromatography, led to a low yield for this step (33%). The *N*-methylaminopyrazole starting material **29** was prepared in 58% over two steps from 4-nitropyrazole **28**, *via N*-methylation with methyl iodide and reduction of the nitro group with Pd/C under a hydrogen atmosphere (Scheme 2.3).



Scheme 2.3. Synthesis of azopyrazole **23**. Reagents and conditions: (i) K_2CO_3, MeI, MeCN, 60 °C, o/n; (ii) Pd/C, H_2, MeOH, rt, o/n; (iii) nitrosobenzene, 1:1 40% aq. NaOH:pyridine, 80 °C, 2 h.

As an alternative to the Mills reaction, azopyrazole **23** was later prepared in an analogous route to that of **24**, using a procedure reported for a similar compound by Makhseed and co-workers

(Scheme 2.4).[112] Instead of coupling the phenyldiazonium chloride with malondialdehyde, which is highly reactive, an equivalent reagent can be used, 3-dimethylaminoacrolein. After coupling to the diazonium chloride, the dimethylamino moiety is hydrolysed to give the phenyl-malondialdehyde adduct **30** in 45% yield. This was then condensed with methylhydrazine to give **23** in 55% yield.



Scheme 2.4. Alternative synthesis of azopyrazole **23**. Reagents and conditions: (i) conc. HCl, aq. $NaNO_2$, AcOH, 0 °C, 1 h; then add to NaOAc, dimethylaminoacrolein, EtOH, 0 °C – rt, 1 h; (ii) NH_2NHMe, EtOH, reflux, 1 h.

2.2.3 Photoswitching

The derivation of all equations in this section was carried out by Dr Robert Richardson. UV/vis spectra were obtained for the photoswitches in acetonitrile at 25 °C (Figure 2.5). Initially the spectra for the *E*-isomers were recorded. The azopyrroles **21** and **22** were found to have red-shifted π-π* absorption maxima relative to the azopyrazoles **23** and **24**, presumably because pyrroles are better π-donors to the electron withdrawing azo function than pyrazoles.[113–116] This finding is consistent with π-deficient azopyridines having a blue-shifted π-π* absorption maxima compared to azobenzene.[117] The other notable difference in the spectra of the *E*-isomers was that the *E*-pyrazoles showed a weak n-π* absorbance, well separated from the π-π* absorbance, whereas *E*-**21** and *E*-**22** had a slight shoulder on their π-π* absorbance, due to a weak n-π* transition, poorly separated from that of the π- π*.

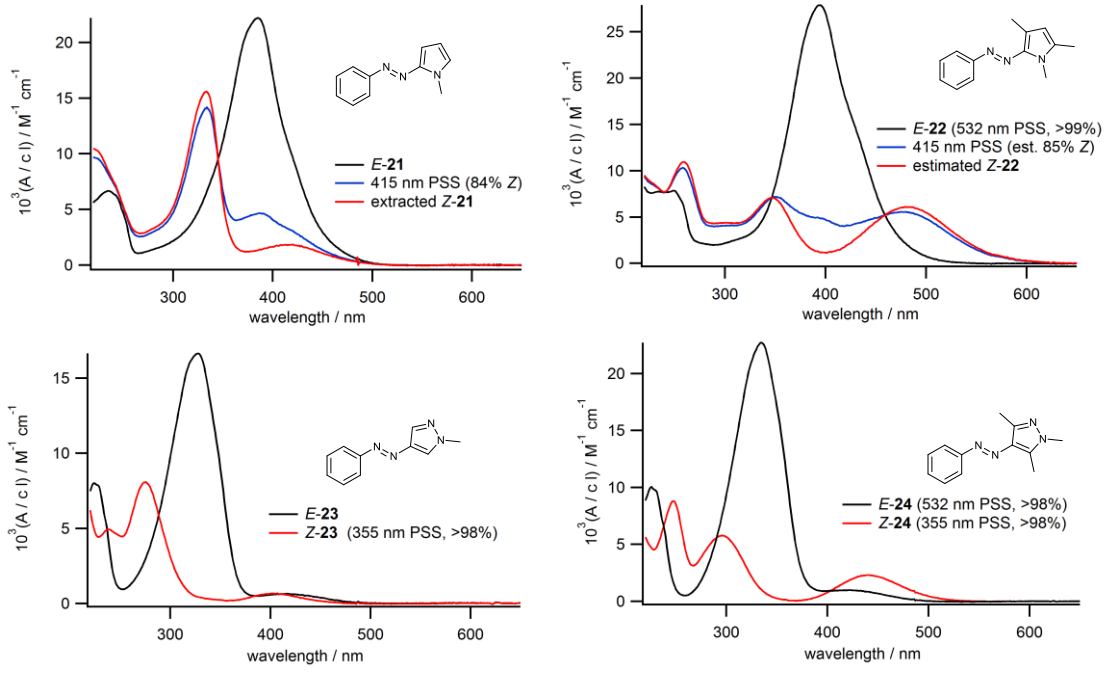


Figure 2.5. UV/vis spectra of azopyrroles **21-22** and azopyrazoles **23-24** in acetonitrile.

The *E*-isomers were irradiated with various wavelengths of light (Figure 7.15, Appendix) in order to identify the wavelengths that gave the best photoconversions; these were found to be 415 and 532 nm light for **21** and **22**, and 355 and 532 nm light for **23** and **24** (Table 2.1). The *Z*-rich PSS for each photoswitch was quantified by NMR (see Appendix 7.3.1) for all compounds except for **22**, whose thermal isomerisation rate was too fast to allow this (see below). Once the PSS had been quantified, the pure *Z*-isomer spectra were extracted using equation 2 and the other PSS compositions were obtained by interpolating between the *E*- and *Z*-isomer spectra.

$$A_Z = \frac{A_{PSS} - A_E \times f}{1 - f} \qquad (2)$$

where f = fraction of *E*-isomer present in the PSS, and A = absorbance in the PSS, *E*, or *Z* spectrum.

For **22**, the composition of the *Z*-rich (415 nm) PSS was obtained by estimating the pure *Z*-isomer spectrum. This could be achieved fairly accurately using equation 2, by varying the value of f. The maximum value was taken as the highest fraction that ensured a positive absorbance at all wavelengths, while the minimum value was taken as the lowest fraction that led to no obvious π- π* absorbance from the *E*-isomer in the estimated *Z*-isomer spectrum. This resulted in a spectrum for the pure *Z*-isomer with an estimated 3% error (Figure 2.6). Other PSS compositions for **22** were obtained as for the other photoswitches, by interpolating between the *E*- and *Z*-isomer spectra.

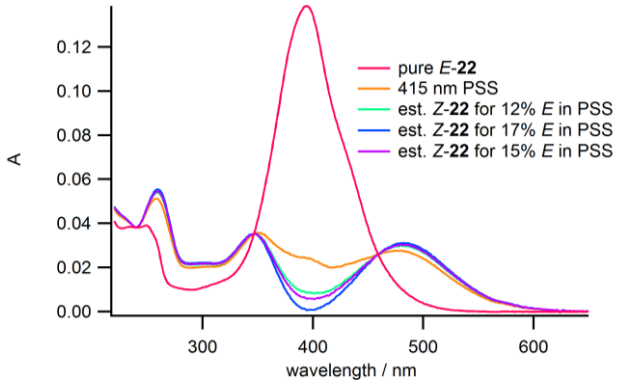


Figure 2.6. Estimating pure *Z*-spectrum of **22** with upper and lower values for fraction *E*-isomer present in PSS.

		*E-Z* (% *Z*)		*Z-E* (% *E*)
		355 nm PSS	415 nm PSS	532 nm PSS
21		-	84 ± 2	82 ± 3
22		-	85 ± 3	>99 [a]
23		>98	-	70 ± 3
24		>98	-	>98 [a]

Table 2.1. Highest percent conversions for *E-Z* and *Z-E* photoisomerisation. [a] The PSS spectra matched the pre-irradiation spectra, which were deemed to contain >99% (**22**) and >98% (**24**) *E*-isomer – see Experimental section.

Exciting the π-π* transition of azopyrazoles *E*-**23** and *E*-**24** at 355 nm using monochromatic light achieved PSSs containing >98% *Z*-isomer in both cases (*i.e.* above the limit of quantification of NMR). Near-quantitative switching was also achieved with broadband UVA (330-400 nm) light (see Appendix 7.3.1). To the best of our knowledge, the only azo compound for which ~100% *E*-*Z* photoswitching has been achieved previously is the ethylene-bridged azobenzene reported by Temps and co-workers (Figure 1.8).[61] *Z*-**24** was found to have a stronger n-π* absorbance than *E*-**24**, while the n-π* absorbance of *Z*-**23** was similar to that of *E*-**23** (Table 2.2). Irradiating the tail of the n-π* absorbance of azopyrazole *Z*-**24** at 532 nm switched it back to >98% *E*-isomer. These results show that **24** can be quantitatively switched in both directions, a result which surpasses any azo compound reported to date.[60,61] Changing the *ortho*-substitution pattern or the heteroarene resulted in less complete photoswitching. Azopyrazole *Z*-**23**, which had no methyls *ortho* to the azo nitrogen, only reached a PSS containing (70 ± 3)% *E*-isomer after excitation with 532 nm irradiation, due to overlap of the *Z*- and *E*-isomer n-π* absorbances. Irradiation of azopyrroles *E*-**21** and *E*-**22** with 415 nm light led to PSSs containing (84 ± 2)% and (85 ± 3)% *Z*-isomer respectively (Figure 2.5). As with the azopyrazoles, the bis(*o*-methylated) azopyrrole *Z*-**22** had a relatively intense n-π* absorbance compared to *Z*-**21** (Table 2.2), which had only one *ortho*-methyl. Excitation of the n-π* transition of azopyrrole *Z*-**22** using 532 nm irradiation led to quantitative (>99%) photoswitching to the *E*-isomer, whereas prolonged irradiation of the tail of the n-π* absorbance of *Z*-**21** at 532 nm led to a PSS containing (82 ± 3)% *E*-isomer.

	E-isomer π-π*		*E*-isomer n-π*		*Z*-isomer π-π*		*Z*-isomer n-π*	
	λ_{max} / nm	10^{-2} ε / M^{-1} cm^{-1}	λ_{max} / nm	10^{-2} ε / M^{-1} cm^{-1}	λ_{max} / nm	10^{-2} ε / M^{-1} cm^{-1}	λ_{max} / nm	10^{-2} ε / M^{-1} cm^{-1}
21	385	221 ± 18	~413 [a]	– [a]	333	157 ± 13 [b]	423	17.9 ± 1.4 [b]
22	394	282 ± 23	~430 [a]	– [a]	346	70.4 ± 5.7 [c]	479	60.8 ± 4.9 [c]
23	328	176 ± 14	417	6.44 ± 0.51	275	80.6 ± 6.4	403	6.66 ± 0.53
24	335	227 ± 18	425	9.63 ± 0.76	296	57.7 ± 4.6	441	23.0 ± 1.8

Table 2.2. Spectral data for **21**-**24** [a] n-π* absorbance appears as a shoulder on the π-π* absorbance, hence ε cannot be obtained. [b,c] these values are for the extracted ([b]) or estimated ([c]) pure *Z*-isomer.

The key trends seen from the UV/vis spectra were a red-shift in π-π* absorption maxima of the pyrroles relative to the pyrazoles, and a larger n-π* absorbance for the *Z*-isomers of the bis(*o*-methylated) photoswitches relative to the singly or non-*o*-methylated analogues. The red-shift in the azopyrrole absorption maxima resulted in poor separation of *E*-isomer π-π* and n-π* transitions, so poor *E*-*Z* photoconversions were seen relative to the azopyrazoles, which underwent quantitative *E*-*Z* photoisomerisation. The larger *Z*-isomer n-π* absorbance in the bis(*o*-methylated)

compounds resulted in absorbances at 532 nm that were significantly larger than in the *E*-isomers, enabling quantitative *Z*-*E* photoisomerisation.

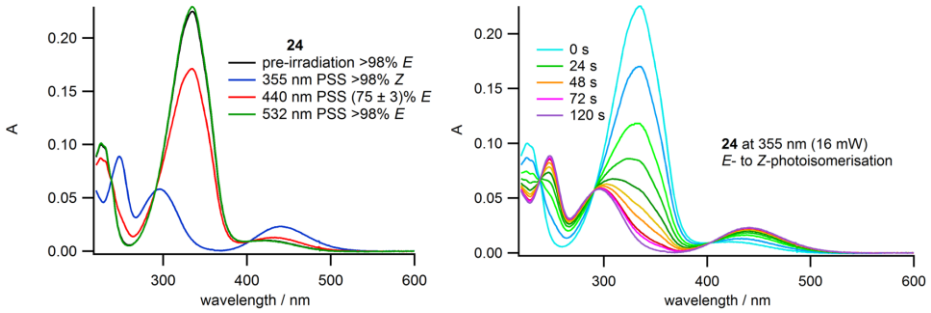


Figure 2.7. PSS for azopyrazole **24** at different irradiation wavelengths (left) and time-resolved spectra for irradiation of **24** at 355 nm (right). See Appendix 7.3.1 for spectra of other azoheteroarenes.

All compounds showed no degradation when irradiated with several different wavelengths, as shown by the presence of isosbestic points (Figure 2.7), which indicates that there are only two species present in the solution. This can also be seen for the time-resolved spectra for photoswitching (Figure 2.7). The compounds were also photoswitched multiple times in each direction in order to check their stability. After 20 switching cycles, no significant degradation was observed, demonstrating high fatigue resistance (Figure 2.8). This property is particularly important for applications such as molecular motors, where many repeated cycles of photoswitching are likely to be required.

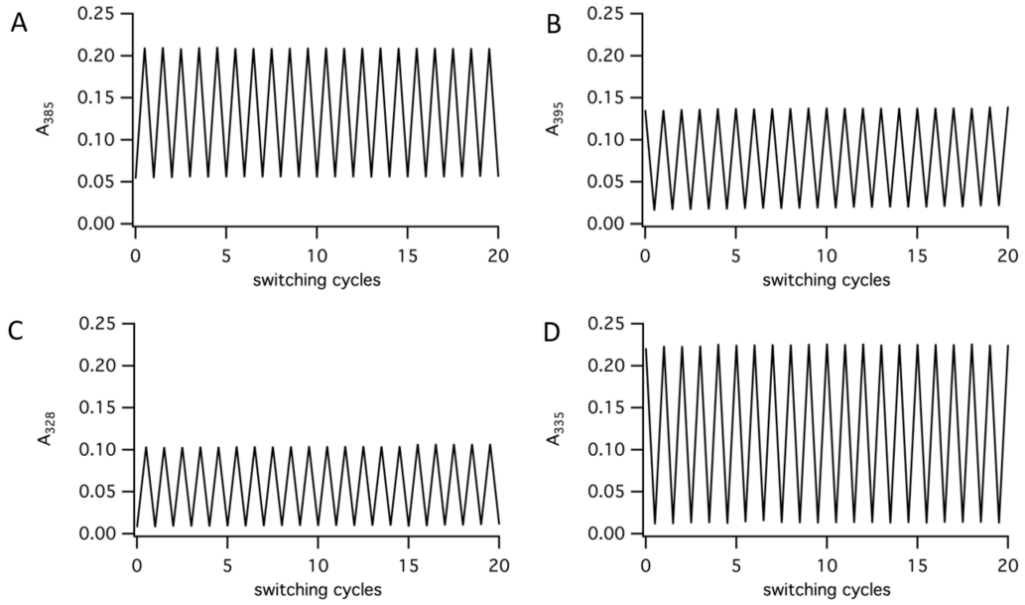


Figure 2.8. Repeated photoswitching cycles for A) **21**; B) **22**; C) **23**; D) **24**. Irradiation wavelengths of 415/532 nm were used for **21** and **22**, and wavelengths of 355/532 nm for **23** and **24**.

Quantum yields were also determined for the photoswitches using equation 3 (for derivation see Appendix 7.1), in order to compare their efficiency to azobenzenes (Table 2.3).

$$\Phi_{A\rightarrow B} = \frac{k\,V}{q_{in}\varepsilon_A l \ln 10} \qquad (3)$$

where Φ = quantum yield; k = rate constant; V = sample volume; ε = molar extinction coefficient; l = pathlength; and q = molar photon flux.

The rate constant for photoisomerisation was obtained from the exponential fit of a graph of absorbance vs. time (Figure 7.18, Appendix) and the molar photon flux was calculated using the wavelength and power of the light (eq. A8, Appendix). When incomplete photoswitching is achieved, the observed rate constant consists of the forward and reverse rate constants (*i.e. E*→*Z* and *Z*→*E*), therefore quantum yields for both the forward and reverse process can be obtained. For example, when **21** was irradiated with 415 nm light, the PSS contained a mixture of *E*- and *Z*-isomers, therefore both $\Phi_{E\rightarrow Z}$ and $\Phi_{Z\rightarrow E}$ can be calculated (Table 2.3). Whereas irradiation of **24** with 355 nm light led to quantitative photoisomerisation to the *Z*-isomer, therefore the observed rate constant is purely the rate constant for the forward process so only $\Phi_{E\rightarrow Z}$ can be obtained. The quantum yields were comparable to or better than those of azobenzene (Table 2.3).[118] Similarly, quantum yields of 1-methyl-2-(phenylazo)imidazole, reported by the Otsuki group,[97] were found to be slightly improved compared to azobenzene, suggesting a potential benefit of using azoheteroarenes over azobenzenes.

compound	wavelength / nm	transition	direction	Φ
21	415	π -π*	*E-Z*	0.50 ± 0.07
			Z-E	0.57 ± 0.10
	532	n -π*	*E-Z*	0.23 ± 0.04 [c]
			Z-E	0.41 ± 0.05 [c]
22 [a]	532	n -π*	*Z-E*	0.41 ± 0.05
23 [b]	355	π -π*	*E-Z*	0.61 ± 0.06
	415	n -π*	*E-Z*	0.72 ± 0.07
			Z-E	0.60 ± 0.06
24	355	π -π*	*E-Z*	0.46 ± 0.04
	532	n -π*	*Z-E*	0.56 ± 0.04
Azobenzene [d]	317	π -π*	*E-Z*	0.15
			Z-E	0.21
	439	n -π*	*E-Z*	0.31
			Z-E	0.46

Table 2.3. Quantum yields (Φ) for all compounds, measured in acetonitrile. Azobenzene values are included for comparison. [a] The quantum yield for *Z-E* photoisomerisation of **22** was not determined due to the competing thermal reaction. [b] The extinction coefficient for **23** at 532 nm was too small to be determined accurately, so quantum yields for *Z-E* photoisomerisation were calculated at 415 nm instead. [c] Extinction coefficients were determined from the spectra at high concentration (0.023 M) due to the weak absorbance at this wavelength and may be subject to significantly higher error. [d] Values were measured in acetonitrile, taken from Bortolus and Monti.[118]

2.2.4 Thermal isomerisation kinetics

Z-E thermal isomerisation rates and half-lives were obtained for all compounds using UV/vis (for **22**) or ^{1}H NMR (for the slower azopyrazoles and azopyrrole **21**) spectroscopy (Table 2.4), and all showed first order isomerisation. Kinetics were obtained at 25 °C in acetonitrile for the azopyrroles and azopyrazole **24**, however the isomerisation rate of **23** at this temperature was found to be too slow for this to be practical. Instead, an Eyring plot of the kinetics of thermal isomerisation of *Z*-**23** in DMSO between 80 and 120 °C was used to obtain the activation parameters $\Delta H^{\ddagger}$ and $\Delta S^{\ddagger}$, from which the thermal isomerisation rate at 25 °C was extrapolated. DMSO was chosen as it has a sufficiently high boiling point for the temperatures required and is a similar polar aprotic solvent to acetonitrile – dielectric constants at 25 °C are 46.5 and 35.9 for DMSO and acetonitrile respectively.[119] The Eyring plot uses a linear form (eq. 4) of the Eyring equation, which can be written in terms of $\Delta G^{\ddagger}$ (eq. 5) or $\Delta H^{\ddagger}$ and $\Delta S^{\ddagger}$ (eq. 6). By plotting a graph of ln(k/T) vs. 1/T, the $\Delta H^{\ddagger}$ and $\Delta S^{\ddagger}$ values can be obtained from the gradient and intercept respectively.

$$ln\frac{k}{T} = \frac{-\Delta H^{\ddagger}}{R} \times \frac{1}{T} + \ln\left(\frac{k_B}{h}\right) + \frac{\Delta S^{\ddagger}}{R} \qquad (4)$$

$$k = \frac{k_B T}{h} \exp\left(\frac{-\Delta G^{\ddagger}}{RT}\right) \qquad (5)$$

$$k = \frac{k_B T}{h} \exp\left(\frac{\Delta S^{\ddagger}}{R}\right) \exp\left(\frac{-\Delta H^{\ddagger}}{RT}\right) \qquad (6)$$

The activation parameters obtained for **23** ($\Delta H^{\ddagger}$= (+115 ± 1) kJ mol^{-1}, $\Delta S^{\ddagger}$=(−13 ± 3) J K^{-1} mol^{-1}) are similar to those obtained by Hecht and co-workers for *ortho*-tetrafluoroazobenzene (**9**) ($\Delta H^{\ddagger}$= (+109 ± 3) kJ mol^{-1}, $\Delta S^{\ddagger}$=(−29 ± 9) J K^{-1} mol^{-1});[60] the slowest thermally isomerising azobenzene known to date (Figure 1.7). Using these parameters and equation 6, the thermal isomerisation rate and half-life at 25 °C was obtained (Table 2.4). The 1000 day half-life, given as an estimate due to the extrapolation from significantly higher temperatures, compares highly favourably to the thermally irreversible diarylethenes, and suggests that azoheteroarenes may hold potential in applications such as optical data storage, where thermal stability of both isomers is needed.[120] The kinetic rate of **23** was also obtained at 70 °C in both acetonitrile and DMSO to see how comparable the values were (Figure 7.20, Appendix). The thermal isomerisation rate was found to be about 20% slower in acetonitrile than in DMSO, suggesting that the extrapolated value at 25 °C from the Eyring plot for DMSO is an underestimate of the half-life in acetonitrile. Substituted azopyrazole **24** was found to have a long half-life relative to azobenzene,[34–37] of 10 days at 25 °C in acetonitrile.

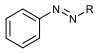
		Rate (k) / s	Half-life ($t_{1/2}$)
21 [a,d]		6.54×10^{-5}	2.95 h
22 [b,e]		3.26×10^{-2}	21.2 s
23 [c]		7.57×10^{-9}	~ 1000 d
24 [a]		7.74×10^{-7}	10 d
Azobenzene [f]		1.97×10^{-6}	4 d

Table 2.4. *Z-E* thermal isomerisation kinetics at 25 °C. Azobenzene kinetics are included for comparison. Measured using; [a] NMR; [b] UV/vis, or; [c] variable temperature NMR with values extrapolated from an Eyring plot. Values were obtained in; [a] d_3-MeCN; [b] anhydrous MeCN, or; [c] d_6-DMSO. [d] Rate was 4-fold slower when measured by UV/vis. [e] Rates were highly dependent on the water content of the solvent. [f] Values were measured in $CHCl_3$, taken from Le Fevré and Northcott.[34]

Overall, the azopyrroles had much faster thermal rates than the azopyrazoles (Table 2.4). Azopyrrole **22** had a very fast thermal rate in acetonitrile, approximately 10^3-fold faster than that of a comparable electron donating group-substituted azobenzene, 4-aminoazobenzene, in a similar solvent ($k = 8.42 \times 10^{-5}$ s^{-1} at 27 °C in acetone).[52] By substituting the phenyl ring of **22** with a *para*-electron withdrawing group, push-pull azopyrrole systems could be generated with substantially faster thermal isomerisation rates, as seen for photoswitch **18** developed by Velasco and co-workers (Figure 2.1).[94] In acetone, the thermal isomerisation rate of **18** at 25 °C was 3 s^{-1} and upon changing the solvent to ethanol, the rate underwent a substantial increase to ~14000 s^{-1}. The increase in thermal rate on moving from the azopyrazoles to the azopyrroles is presumed to be because pyrroles are better π-donors than pyrazoles,[114,115] as seen with the red-shift in π-π* absorption maxima for the azopyrroles relative to azopyrazoles (Table 2.2). This effect is seen for 4-aminoazobenzene, which has a much faster thermal rate than unsubstituted azobenzene.[52]

The thermal isomerisation rates of the azopyrroles, in particular **22**, were found to be dependent on the water, or protic solvent, content of the sample. Addition of 0.5 M water to a sample of **22** in anhydrous acetonitrile resulted in an approximately ten-fold increase in the thermal isomerisation rate of **22** (Figure 2.9). Similar treatment of an anhydrous sample of **21** only increased the thermal isomerisation rate by 10%, as measured by UV/vis spectroscopy (Figure 2.9). Doubling the water content of the NMR sample of azopyrazole **23** from 0.05 M to 0.1 M resulted in no change to the kinetics suggesting that the low water concentrations present in the NMR solvents do not significantly affect the kinetics of the pyrazoles. When measuring the thermal isomerisation kinetics of **21** by UV/vis spectroscopy at ~10^{-5} M (Figure 2.9), the rate was found to be considerably slower (~ 4-fold) than when it was measured by NMR at ~10^{-2} M (Table 2.4). This effect was still seen when the thermal isomerisation rates were measured by both NMR and UV/vis spectroscopy using the

same ~10^{-2} M stock solution of **21** in d_3-acetonitrile. For the UV/vis study, the sample was diluted ~1000-fold into d_3-acetonitrile whereas no dilution was required for NMR due to the different sensitivities of the analytical methods. This suggests that the slower rate seen by UV/vis spectroscopy may be due to a concentration effect.

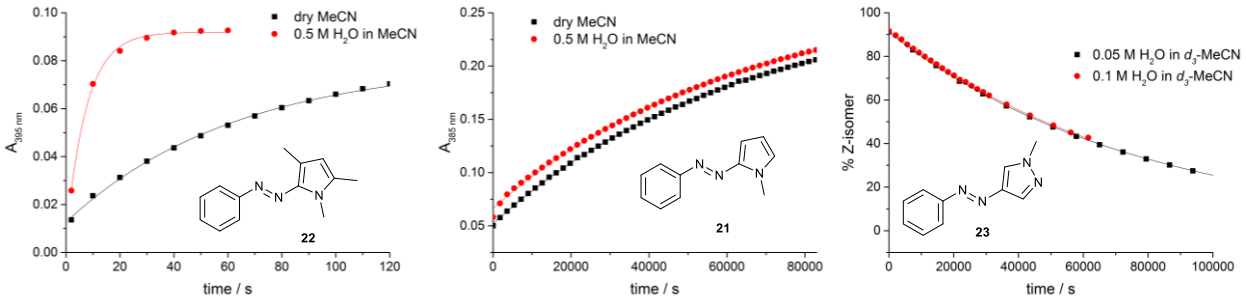


Figure 2.9. Thermal isomerisation of azopyrroles **22** and **21** at 25 °C (measured by UV/vis) and azopyrazole **23** at 70 °C (measured by NMR) showing the effect of adding water on the rate. The rate of **21** measured by UV/vis was found to be 4-fold slower than the rate measured by NMR that was used to obtain the thermal half-live in Table 2.4.

The increase in rate seen upon addition of water is similar to that seen for Velasco's push-pull azopyrroles, where switching from an aprotic solvent (acetone) to a protic solvent (ethanol) that is able to form hydrogen bonds with the azoheteroarene, leads to a substantial increase in rate, as mentioned above.[94] Similar observations have been reported for photoswitches belonging to the aminoazobenzene and push-pull azobenzene classes,[25,53,121] such as 4-aminoazobenzene, which undergoes a large increase in rate upon moving from aprotic to protic solvents, as well as upon increasing polarity of the solvent.[52] 2-(Phenylazo)imidazole has also been observed to undergo an increase in thermal isomerisation rate upon addition of methanol to a solution of the photoswitch in an aprotic solvent,[98] however this particular compound is able to tautomerise, unlike the azopyrroles reported here and in Velasco's work.[94]

Whether thermal isomerisation is occurring through an inversion or a rotation mechanism, the presence of polar and/or protic solvents is thought to stabilise the transition state in these types of photoswitch, where there is one electron rich aryl ring or a push-pull system. Computational studies of 4-aminoazobenzene identified that the lowest energy transition state for thermal isomerisation followed the inversion pathway, and found that there was greater stabilisation of this dipolar transition state relative to the *E*- or *Z*-isomer ground states upon increasing solvent polarity.[52] In contrast the thermal isomerisation rates of unsubstituted azobenzenes, or those substituted with 'electronically inactive' moieties, are independent of solvent polarity.[25,37] Out of the compounds studied in this work, azopyrrole **22**, which has the most electron donating heteroaryl ring due to the methylated pyrrole, underwent the greatest increase in rate upon addition of water. Azopyrrole **21**,

which has fewer methyl substituents on the pyrrole ring than **22**, had a much smaller increase in rate upon addition of water, while **23** which has the less electron rich pyrazole ring, did not undergo a change in rate upon addition of water.

The presence of two *ortho*-methyls on the heteroarene was found to accelerate the isomerisation, relative to the singly or non-*o*-methylated analogues (Table 2.4). This was initially presumed to be due to reduced steric interactions between the *o*-methyl substituents and the azo nitrogens in the transition state of such compounds, compared to in the ground state *Z*-isomer. Although there is some debate as to the mechanism by which thermal isomerisation of azoarenes occurs,[42–44] both the inversion and the rotation transition states (Figure 1.3) would relieve the steric strain in the bis(*o*-methylated) molecules, by increasing the distance between the methyl substituents and the azo nitrogens, thus lowering the barrier for thermal isomerisation compared to the molecules lacking the two *ortho*-methyls. More recent studies (see section 2.3.5) have revealed the presence of a favourable interaction in *Z*-**21** and *Z*-**23** that appears to be responsible for the slower thermal isomerisation rates compared to the corresponding bis(*o*-methylated) analogues *Z*-**22** and *Z*-**24**. The effect of *o*-methylation on thermal isomerisation rate has been studied for a range of methylated azobenzenes, and appears to vary considerably depending on the system involved.[121-124]

2.2.5 Computational studies

2.2.5.1 Energy minimised conformations and calculated UV/vis spectra

All computational work was carried out with the assistance of Dr Robert Richardson. Energy minimised conformations were obtained using density functional theory (DFT) calculations at the B3LYP/6-31G(d,p) level, while spectral predictions were obtained using time-dependent DFT (TDDFT) calculations at the CAM-B3LYP/6-311G(2df,2p) level. At both levels a polarisable continuum model (PCM) was used for acetonitrile, as this was the solvent used for the photochemical and thermal isomerisation studies. These methods have been well established for modelling both azobenzene and azoheteroarene systems.[54,60,96,126,127] Two energy minimised conformations were obtained for each isomer and the calculated UV/vis spectra were obtained using the Boltzmann weighted averages of these. The spectra were scaled so that the maximum peak height was equal to that for the equivalent experimental spectrum, to allow comparison (Figure 2.10).

The calculated and experimental spectra were found to be very similar, with separation of the n-π* and π-π* absorption maxima qualitatively consistent between the two. The TDDFT predictions for the π-π* transitions were slightly blue-shifted compared to the experimental spectra (Table 2.5). *Z*-**22** and *Z*-**24** were the only conformations predicted to have an appreciable n-π* transition

intensity, with absorption maxima (λ_{max}) slightly red-shifted relative to the experimental maxima. Based on these results, it would appear that the TDDFT calculations could be used to predict the separation of *E*- and *Z*-isomer absorbances that is necessary to achieve good photoswitching.

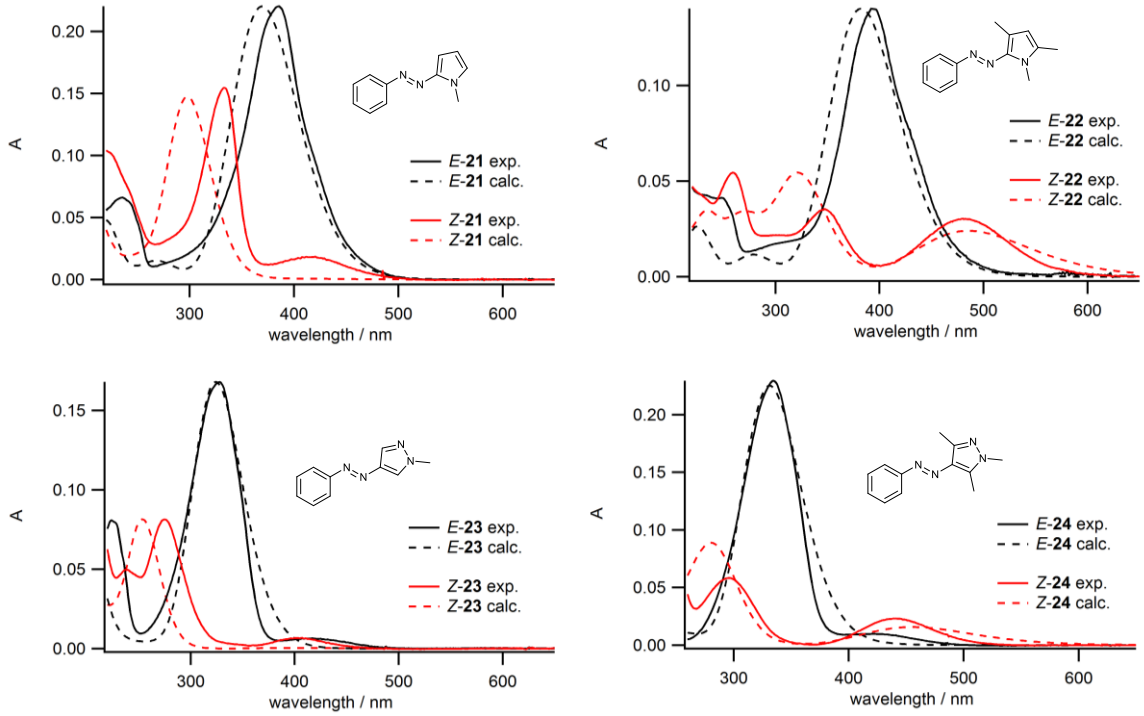


Figure 2.10. Comparison of calculated (CAM-B3LYP/6-11G(2df,2p)) and experimental UV/vis spectra.

		λ_{max} / nm							
		E-isomer π-π*		*E*-isomer n-π*		*Z*-isomer π-π*		*Z*-isomer n-π*	
		Exp.	Calc.	Exp.	Calc.	Exp.	Calc.	Exp.	Calc.
21		385	372	~413	428 [a]	333	298	423	407 [a]
22		394	383	~430	425 [a]	346	323	479	485
23		328	326	417	426 [a]	275	252	403	396 [a]
24		335	334	425	427 [a]	296	283	441	454

Table 2.5. Comparison of n-π* and π-π * λ_{max} in experimental and calculated spectra. Calculated values are for the lowest energy conformer. [a] Zero or negligible absorbance intensity calculated.

The energy minimised conformations were then used to understand the key features of the spectra. In our calculations, the *E*-isomers were all predicted to be planar, as expected for azoarenes.[25] For azopyrrole *Z*-**21** and azopyrazole *Z*-**23**, which lack the two *ortho*-methyls on the heteroarene, a 'T-shaped' conformation with the phenyl ring approximately orthogonal to the planar heteroarene-azo functionality was calculated (Figure 2.11, A). This is consistent with the findings of Herges and co-workers for 1-methyl-5-phenylazoimidazole (**20**).[96] In contrast, the two *o*-methyl groups in

azopyrrole *Z*-**22** and azopyrazole *Z*-**24** were predicted to force these species into a twisted conformation (Figure 2.11, A). To support the computational findings, crystal structures were obtained for pyrazoles *Z*-**23** and *Z*-**24**, as these were sufficiently thermally stable to allow for crystallisation (cf. *Z*-**21** and *Z*-**22**). The θ_{NNhet} dihedral angle of 25.7° for *Z*-**24** observed in the crystal structure matched well with the calculated value of 27.1° (Figure 2.11, B). Although the *Z*-**23** crystal structure was found to have a θ_{NNhet} dihedral angle of 10.8° (*c.f.* the calculated value of 0.0°), this was still considerably smaller than the value of 25.7° for *Z*-**24**, as predicted. The difference between the calculated and X-ray structure dihedral angles is consistent with the work by Jacquemin and co-workers on *E*-azobenzene,[128] which is believed to adopt a planar structure in solution and a twisted one in the solid state due to packing effects.

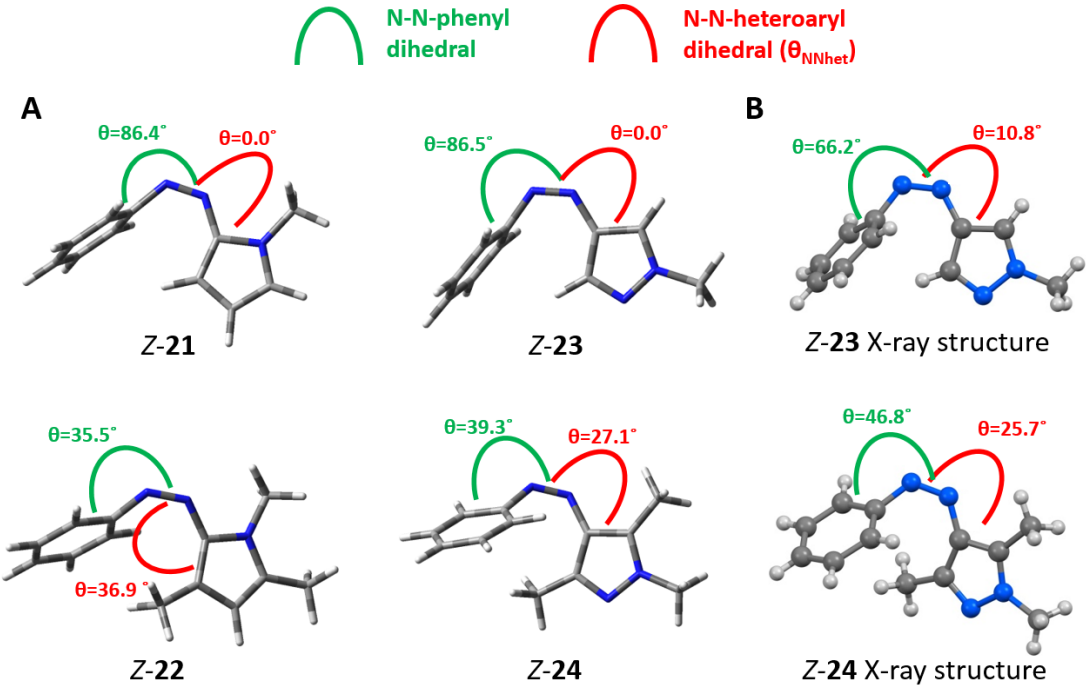


Figure 2.11. A) Calculated conformations and dihedral angles (θ) for *Z*-isomers (B3LYP/6-31G(d,p)). All values, except θ_{NNhet} for Z-**22**, are given as 180 – θ; B) Crystal structures for *Z*-**23** and *Z*-**24**.

2.2.5.2 n-π* transition intensity

From the TDDFT calculations, the oscillator strength (f) of the electronic transitions can be obtained (Table 2.6); this is a dimensionless quantity referring to the probability of an electronic transition, related directly to the intensity of the absorbance.[129] TDDFT predicts low intensity (or zero intensity) n-π* absorbances for *Z*-**21**, *Z*-**23**, and the *E*-isomers, which have the heteroarene and azo group co-planar, while the twisted azopyrrole *Z*-**22** and azopyrazole *Z*-**24** are calculated to have large n-π* absorbances (Table 2.6). Both of these predictions match those seen experimentally, although the *E*-isomers that are predicted to have zero n-π* absorbance actually have very weak absorbances experimentally. A similar trend is observed for the n-π* absorbance in planar *E*-azobenzene and

non-planar *Z*-azobenzene, where the former has a very low intensity absorbance and the latter has a larger absorbance.[25]

		E-isomer		*Z*-isomer	
		π -π* f	n-π* f	π -π* f	n-π* f
21		0.92	0	0.52	0.0023
22		0.97	0	0.30	0.14
23		0.89	0	0.53	0.0026
24		0.86	0.0017	0.32	0.058

Table 2.6. Calculated oscillator strengths (f) for π-π* and n-π* excitation for the lowest energy conformers.

In order to understand the differing n-π* intensities, the symmetry elements of the compounds need to be known. If both arenes are co-planar with the azo group, as with the *E*-isomers, a mirror plane exists through the plane of the azo function. Similarly, if one arene is co-planar with the azo group and the other is orthogonal to the azo (*i.e.* at 90°), a mirror plane also exists through the molecule, provided the second arene is symmetrically substituted, as is the case for *Z*-**21** and *Z*-**23** (Figure 2.12, A). When there is a mirror plane, or indeed any symmetry element other than identity, the two orbitals involved in the electronic transition must have the same parity about the mirror plane. The n-orbital is symmetric while the π*-orbital is antisymmetric about this plane, therefore the n-π* transition is symmetry-forbidden at the equilibrium geometry (Figure 2.12, A). Experimentally, vibrational and rotational motion results in the molecule existing in conformations with a weakly-allowed n-π* transition, thus resulting in a small absorbance. When the arenes are in a twisted conformation, as with *Z*-**22** and *Z*-**24**, there are no symmetry elements present in the molecule (Figure 2.12, B) and the n-π* transition is allowed.

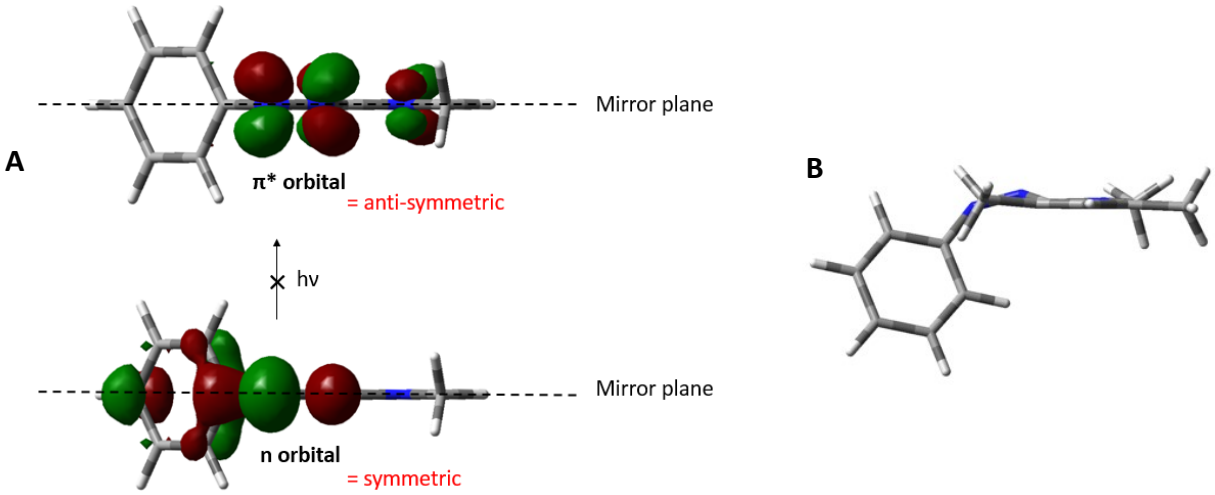


Figure 2.12. Energy minimised conformations of; A) *Z*-**21** with the mirror plane labelled and the calculated n- and π*-orbitals; B) *Z*-**22**, showing no symmetry in the molecule.

Together, the computational, spectroscopic and crystallographic findings indicate that azopyrrole *Z*-**21** and azopyrazole *Z*-**23** exist in T-shaped conformations with the phenyl ring at approximately 90° to the co-planar azoheteroarene, and the more sterically congested bis(*o*-methylated) azopyrrole *Z*-**22** and azopyrazole *Z*-**24** adopt twisted conformations. This is in contrast to *Z*-azobenzenes, where the phenyl rings always adopt a twisted conformation, due to the increased steric demand of a 6-membered ring over a 5-membered ring on the azo moiety.[25] Therefore, these 5-membered heteroarenes allow steric tuning of the spectral properties that are not available to standard azobenzenes. In order to support this argument, TDDFT calculations were performed to predict the effect of the θ_{NNhet} dihedral angle on the n-π* intensity. Energy minimised structures were calculated at constrained θ_{NNhet} values of -180° to 180°, measured at 10° increments.

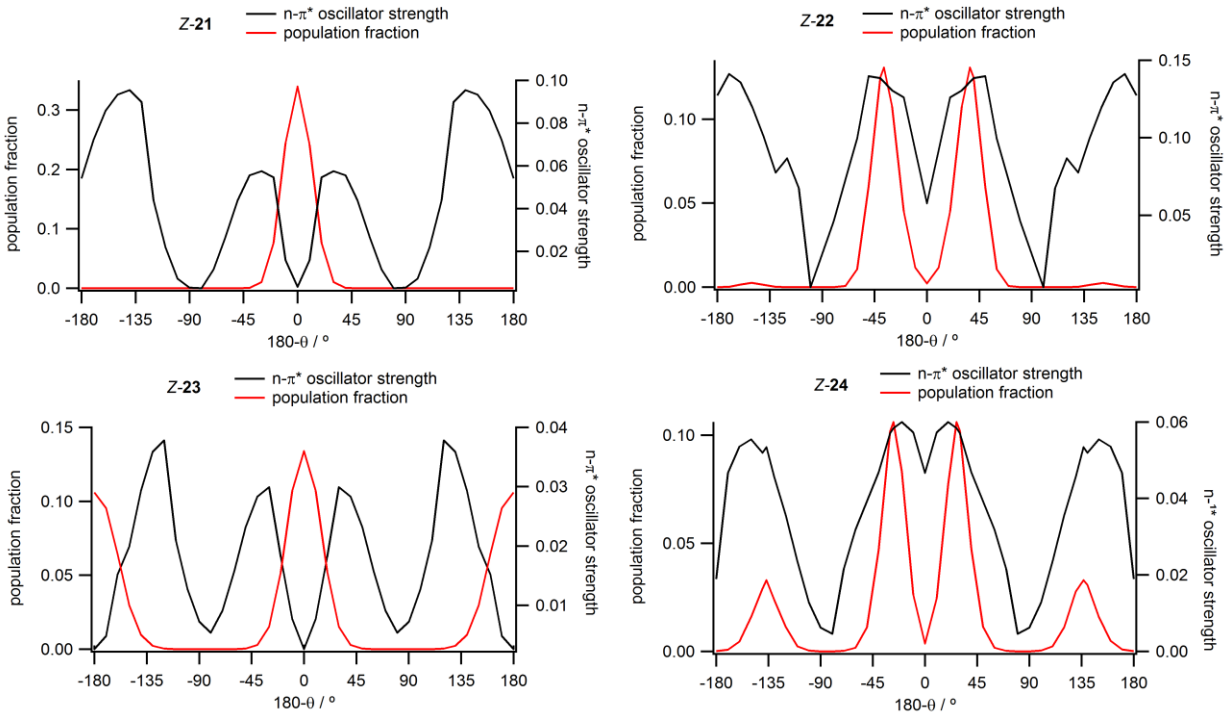


Figure 2.13. Dihedral angle (θ_{NNHet}) vs. n − π* intensity (oscillator strength) and population fraction for *Z*-isomers.

The results, shown in Figure 2.13, demonstrate that the intensity of the n-π* transition is minimal at planar (θ = 0,±180°) and orthogonal geometries (θ = ±90°). The normalised Boltzmann factor for each constrained dihedral angle was also calculated at 25 °C; this gives the fraction of the population at each geometry (Figure 2.13). *Z*-**21** and *Z*-**23** have the largest population fraction at θ = 0° (as seen in the geometry minimised structures, Figure 2.11), so most molecules will be in this conformation, however a fraction of the population is also predicted to sit outside of the equilibrium geometry (at -45° to 45°), which accounts for the weak n-π* absorbance seen in the UV/vis spectra for these isomers. Conversely, *Z*-**22** and *Z*-**24**, which have increased steric demand from the two

ortho-methyls, have a population fraction of zero at θ = 0° or 90° and the highest fraction at 20 – 40°, where the unfavourable steric interactions between the *o*-methyls and azo moiety are minimised.

2.2.5.3 Calculated thermal isomerisation kinetics

Transition state optimisations were carried out on the photoswitches, to identify how well the calculated thermal isomerisation rates matched the experimental values. All the transition states were characterised by one imaginary frequency of approximately -(400-500) cm^{-1}. Four transition states were obtained for each compound using B3LYP/6-31G(d,p) level of theory, with the initial input geometries consisting of two rotational and two inversion transition states (see Appendix 7.4.1). For all four compounds, inversion rather than rotation transition states were found to be the lowest energy. In order to obtain isomerisation rates, the Gibbs free energy of the calculated *Z*-isomer was subtracted from that of the lowest energy transition state to give the Gibbs energy of activation ($\Delta G^{\ddagger}$). This is related to isomerisation rate by the Eyring equation (eq. 5). Rates and thermal half-lives were calculated at 25 °C so that they could be directly compared to the experimental values (Table 2.7).

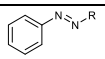
		Calculated $t_{1/2}$	Experimental $t_{1/2}$
21		1.3 h	3.0 h
22		8 s	21 s
23		62 days	1000 days
24		0.23 h	10 days

Table 2.7. Comparison of calculated and experimental thermal half-lives at 25 °C.

The calculated data matched the trends seen experimentally to an extent; the half-lives of azopyrroles **21** and **22** were correctly predicted, as were the compounds with the longest (**23**) and shortest (**22**) half-lives. The calculations also correctly predicted that bis(*o*-methylation) of each heteroarene would shorten the thermal half-life relative to the analogues without two *ortho*-methyls. For the azopyrazoles however, the calculated half-lives were 16-fold and 1000-fold shorter than the experimental values for **23** and **24** respectively. Clearly, the computational method needs to be optimised in order to allow accurate predictions of azoheteroarene half-lives (see section 2.3.5).

2.3 RESULTS AND DISCUSSION PART II: Further study of arylazoheteroarenes

2.3.1 Photoswitch design and aims

Following on from the work in section 2.2, where a significant difference in thermal half-life was seen experimentally between the azopyrazoles and the azopyrroles, the thermal kinetics of arylazoheteroarenes were studied in more detail. In particular, focusing on the effect on thermal kinetics observed upon changing the heteroarene, the position at which the azo linkage is attached, and/or the steric bulk around the azo group (*i.e. ortho*-methylation of the heteroarene). A key aim was to find a computational method that could accurately predict the thermal isomerisation rates for this class of photoswitch in order to allow analysis of the various properties that determine the rate. In light of this, several photoswitches, complementary to those studied in section 2.2, were chosen for experimental and computational study (Figure 2.14). Those chosen included pyrroles, pyrazoles, triazoles, and tetrazoles. To allow comparison with our original azopyrazoles and azopyrroles, analogues were designed with similar *ortho*-substitution patterns, but with the azo group linked to the heteroarene at different positions; at the 3-position of the pyrroles and at the 3- and 5-positions of the pyrazoles. Due to the more detailed computational work planned for these compounds, all calculations were carried out by Joaquín Calbo (University of Valencia), led by Dr Julia Contreras-García (Pierre and Marie Curie University).

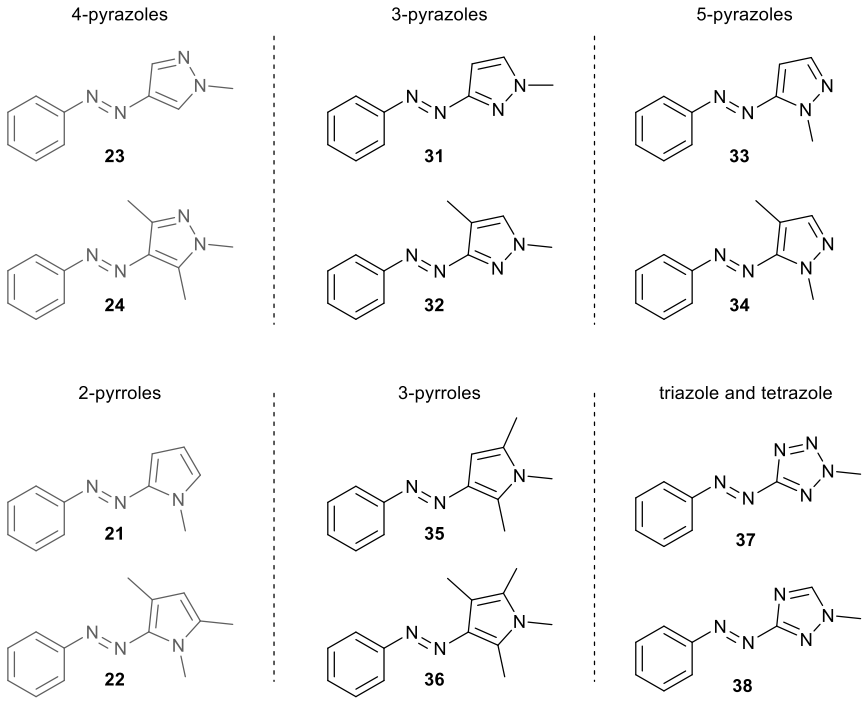
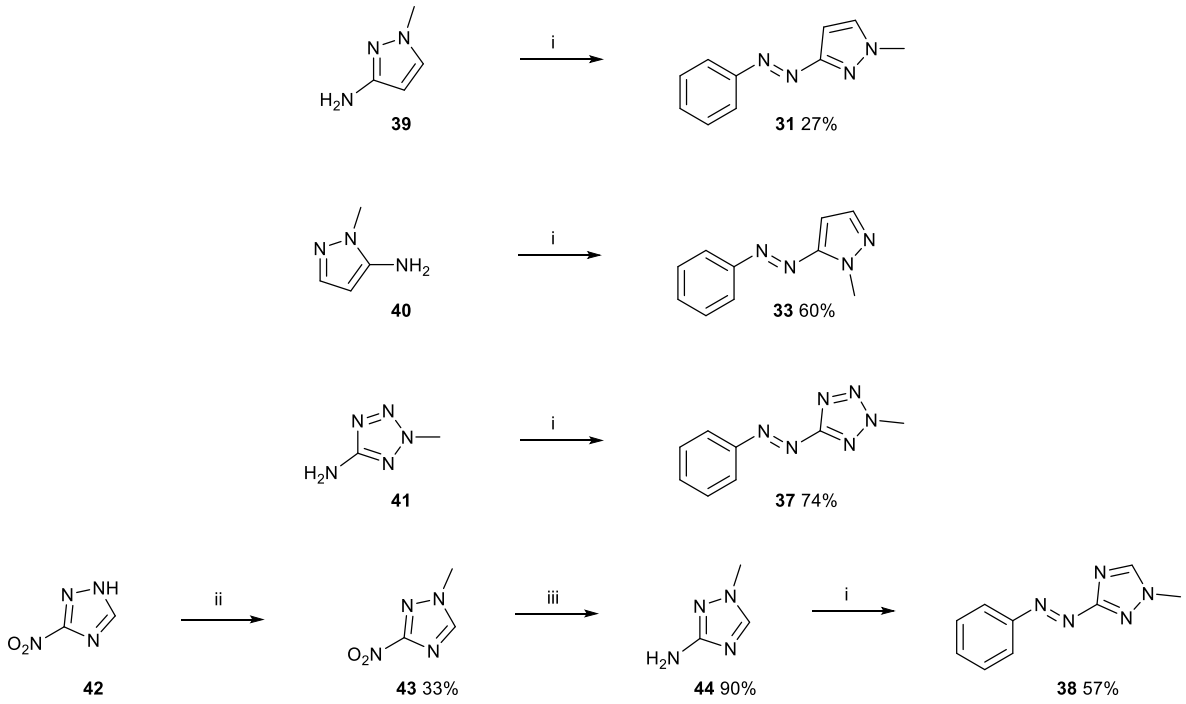


Figure 2.14. Original azoheteroaryl photoswitches studied (in grey) and new photoswitches chosen for experimental and computational study.

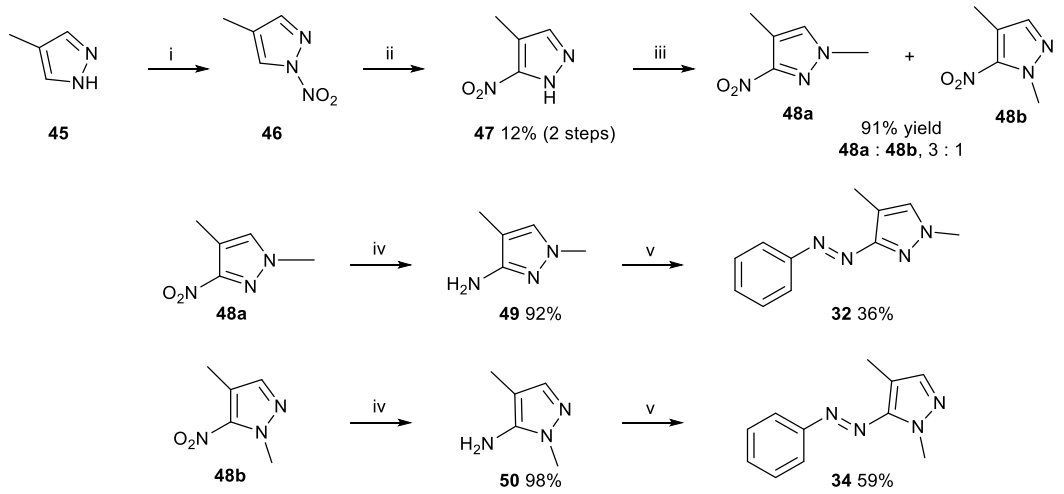
2.3.2 Synthesis

Azopyrazoles **31** and **33** and azotetrazole **37** were prepared in one step from commercially available aminoheteroarenes (**39**-**41**) and nitrosobenzene in yields of 27-74% (Scheme 2.5). The modified Mills procedure previously used for the synthesis of **23** was employed,[107,108] but the pyridine solvent was replaced with toluene. Although small amounts of azoxybenzene formed, there was no issue of co-elution with the product during purification by column chromatography, which was a problem during the purification of **23** (section 2.2.2). Aminotriazole **44**, required for the synthesis of azotriazole **38**, was not commercially available so was prepared in two steps from 3-nitrotriazole **42** (Scheme 2.5). The first step was an *N*-methylation with dimethyl sulfate, following a procedure reported by Sukhanov and Lukin.[130] The authors obtained a mixture of *N*-methylated nitrotriazole regioisomers, which they characterised and assigned by comparing to previously reported values.[131,132] Using this data, the desired 3-nitro regioisomer product (**43**) was identified. This isomer was the major product as expected, due to the unfavourable steric interactions between the methyl and nitro groups that would be present in the other two regioisomers. The assignment was confirmed by 2D NMR spectroscopy (COSY and HBMC). Nitrotriazole **43** was then reduced by transfer hydrogenation to aminotriazole **44**,[59] and coupled with nitrosobenzene to give **38** in 57% yield (Scheme 2.5).



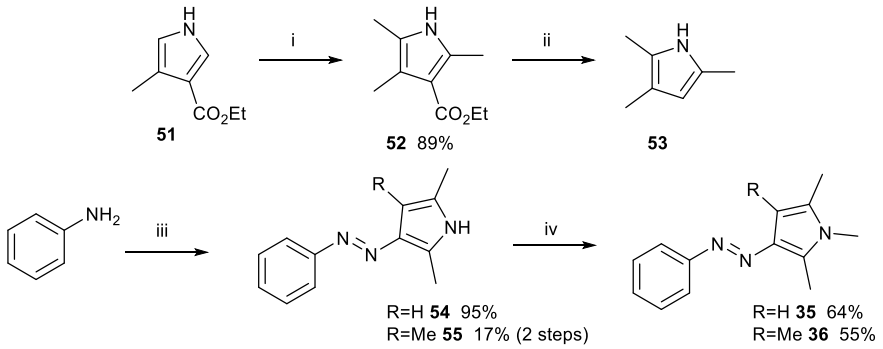
Scheme 2.5. Synthesis of azopyrazoles **31** and **33**, azotetrazole **37**, and azotriazole **38**. Reagents and conditions: (i) nitrosobenzene, 1:1 toluene:40% NaOH, 80 °C, 5 h to o/n; (ii) LiOH, Me_2SO_4, EtOH, 75 °C, o/n; (iii) Pd/C, $N_2H_4{\cdot}H_2O$, MeOH, reflux, 3 h.

Regioisomers **32** and **34** were prepared using a divergent route (Scheme 2.6). 4-Methylpyrazole **45** was *N*-nitrated to give **46**, which was then converted to 5-nitropyrazole **47** by thermal rearrangement in benzonitrile.[134] This is thought to occur *via* a [1,5] sigmatropic shift followed by tautomerisation and has also been reported for nitrotriazoles.[135] Nitropyrazole **47** was *N*-methylated to give a clean mixture of the 3- and 5-methyl regioisomers (**48a** and **48b**),[130] which were separated by Kugelrohr distillation. Initially the two regioisomers were assigned using NOE spectroscopy, and this was confirmed by obtaining an X-ray crystal structure of 3-nitropyrazole **48a** (see Appendix 7.2), which was a solid at room temperature. Both nitropyrazoles **48a** and **48b** were reduced to the corresponding amines (**49** and **50**) using Pd/C under a hydrogen atmosphere, and the amines were were then condensed with nitrosobenzene to give azopyrazoles **32** and **34** in yields of 36% and 59% respectively (Scheme 2.6).



Scheme 2.6. Synthesis of azopyrazoles **32** and **34**. Reagents and conditions: (i) aq. HNO_3, Ac_2O, AcOH, rt, 2 h; (ii) PhCN, 160 °C, 6 h; (iii) LiOH, Me_2SO_4, EtOH, 75 °C, o/n; (iv) Pd/C, H_2 (1 atm), MeOH, rt, 4 h; (v) nitrosobenzene, 1:1 toluene:40% NaOH, 80 °C, o/n.

Azopyrroles **35** and **36** were prepared using the same method as for azopyrrole **22** (section 2.2.2).[101] Phenyldiazonium chloride, formed *in situ* from aniline, was coupled with 2,5-dimethylpyrrole to give **54** in 95% yield (Scheme 2.7). This was then *N*-methylated with methyl iodide to afford **35** in 64% yield. The required 2,3,5-trimethylpyrrole (**53**) for the synthesis of azopyrrole **36** was not commercially available so was prepared in two steps from ethyl 4-methylpyrrole-3-carboxylate (**51**). Dimethylation of **51** on the remaining pyrrole carbons using paraformaldehyde under acidic conditions gave **52** in 89% yield,[136] followed by a one-pot ester hydrolysis and decarboxylation under acidic refluxing conditions to give **53** (Scheme 2.7).[137] The product was carried forward as crude material to the next step, where it was coupled with phenyldiazonium chloride (formed *in situ*) to give **55** in 17% yield over the two steps. *N*-methylation with methyl iodide gave the final photoswitch **36** in 55% yield.



Scheme 2.7. Synthesis of azopyrroles **35** and **36**. Reagents and conditions: (i) $(CH_2O)_n$, AcOH, aq. HI, aq. $H_4P_2O_6$, rt, 2 h; (ii) conc. H_2SO_4, EtOH, H_2O, reflux, 1 h; (iii) conc. HCl, aq. $NaNO_2$, H_2O, 0 °C, 1 h; then 2,5-dimethylpyrrole or **53** in 6:1 MeOH:pyridine, 0 °C, 1 h; (ii) 60% NaH, MeI, THF, 0 – 60 °C, 1 h.

2.3.3 Photoswitching

UV/vis spectra of the *E*-isomers of each compound were recorded in acetonitrile (Figure 2.15) and photoswitching was carried out using several different irradiation wavelengths (Figure 7.15, Appendix). The best photoconversions were achieved with 355 nm (*E*-*Z*) and 532 nm (*Z*-*E*) irradiation for all compounds with the exception of the *E*-*Z* photoisomerisation of **37** and the *Z*-*E* photoisomerisation of **38** (Table 2.8). Irradiation of **37** with UVB light led to a PSS containing 3% more *Z*-**37** than was present in the 355 nm PSS. Similarly, irradiation of **38** with visible light (λ_{max} ~ 420 nm) led to a PSS containing 3% more *E*-**38** than was present in the 532 nm PSS. For further photochemical study of **37** and **38**, 355 and 532 nm light was used due to the experimental set up being more suited to using a monochromatic light source rather than a broadband one, and also due to potential degradation issues when using UVB light.

Azopyrazoles **31** and **33** were quantitatively switched to the *Z*-isomers with 355 nm irradiation, while all other compounds were switched to PSSs containing a mixture of isomers. With the exception of the azopyrroles, whose thermal half-lives were too short, the 355 nm PSSs were quantified by NMR using the method adopted previously (see section 2.2.3) and the spectra for the pure *Z*-isomers were extracted (Figure 2.15). The 355 nm PSS compositions and *Z*-isomer spectra of azopyrroles **35** and **36** (Figure 2.15) were estimated by the method used previously for azopyrrole **22** (section 2.2.3). Near-quantitative to quantitative photoswitching (≥94%) to the *Z*-isomer was achieved for all four azopyrazole analogues (**31**-**34**), and these were all switched back to 79-87% *E*-isomer (Table 2.8). These results compare well to azopyrazoles **23** and **24** studied previously. Azopyrrole **36** had comparable photoconversions to those achieved for the analogous azopyrrole **22**, although the best *E*-*Z* photoconversion was achieved with 355 nm light rather than 415 nm light. In general, less complete photoswitching was achieved for the other analogues, with azotriazole **38** having the next highest photoconversions (Table 2.8).

			E-*Z* (% *Z*) 355 nm PSS	*Z*-*E* (% *E*) 532 nm PSS
Azopyrazoles	**31**		> 98	85 ± 3
	32		96 ± 2	87 ± 3
	33		> 98	79 ± 3
	34		94 ± 2	86 ± 3
Azopyrroles	**35**		77 ± 3	85 ± 5
	36		85 ± 3	98 ± 2
Azotetrazole	**37**		76 ± 2 [a]	72 ± 3
Azotriazole	**38**		90 ± 2	84 ± 3 [b]

Table 2.8. Percent photoconversions for *E*-*Z* and *Z*-*E* photoisomerisation. [a] UVB PSS was (79 ± 3)% *Z*. [b] Broadband visible light (λ~420 nm) PSS was (87 ± 3)% *E*.

Absorption maxima (λ_{max}) and molar extinction coefficients (ε) were obtained for the π-π* and n-π* absorbances of both isomers of each compound (Table 2.9). The observed trends were consistent with the findings for the azopyrroles and azopyrazoles in section 2.2.3. Photoswitches with two *ortho*-methyls on the heteroarene (**34** and **36**) had considerably larger n-π* absorbances than their non- or singly *o*-methylated analogues. It was also found that the presence of two heteroaryl basic nitrogens adjacent to the azo group (**37** and **38**), or one basic nitrogen and one *ortho*-methyl (**32**) increased the intensity of the *Z*-isomer n-π* relative to that of the *E*-isomer.

As seen previously, the azopyrroles had red-shifted π-π* absorbances compared to the other azoheteroarenes, resulting in poor separation of π-π* and n-π* absorbances in the *E*-isomers. The red-shift observed was smaller than for the 2-azopyrrole analogues (**21** and **22**) studied in section 2.2.3, suggesting that the position at which the azo moiety is attached to the heteroarene affects the amount of π-donation from the heteroaryl ring into the azo functionality. Similarly, the 5-azopyrazole analogue **33** had red-shifted π-π* absorbances relative to the 3-azopyrazole (**31**) and 4-azopyrazole (**23**) analogues, while a small red-shift was seen for bis(*o*-methylated) 5-azopyrazole *E*-**34** relative to 4-azopyrazole *E*-**24**.

To demonstrate the stability of the photoswitches with respect to photodegradation, time-resolved UV/vis spectra were obtained for all compounds (Figure 7.17, Appendix), as shown for **34** (Figure 2.16, A). Good isosbestic points were obtained, indicating that no decomposition was occurring. Repeated cycles of photoswitching were also carried out on **34** (Figure 2.16, B).

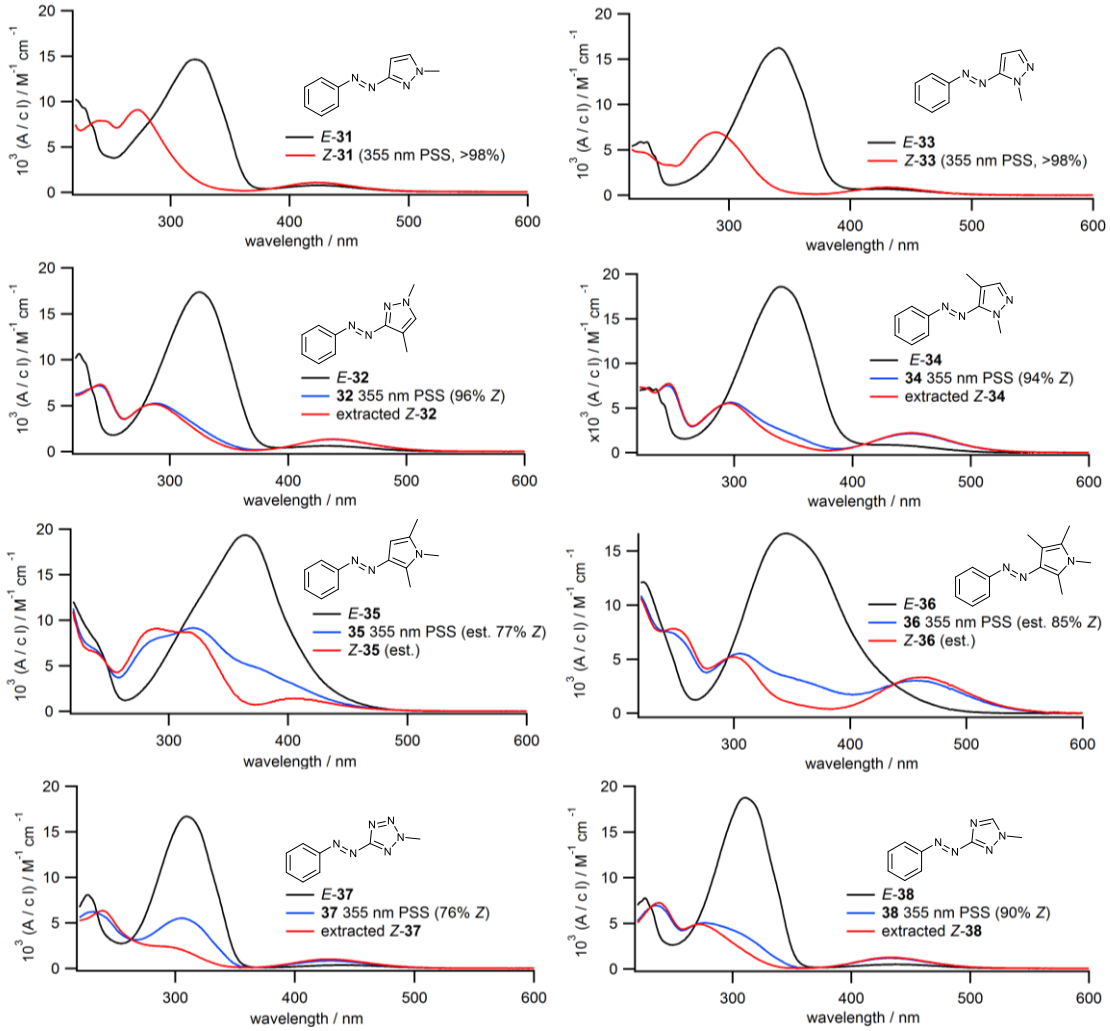


Figure 2.15. UV/vis spectra of azoheteroarenes **31**-**38**.

	E-isomer π-π*		*E*-isomer n-π*		*Z*-isomer π-π*		*Z*-isomer n-π*	
	λ_{max} / nm	$10^{-2} \times \varepsilon$ / M^{-1} cm^{-1}	λ_{max} / nm	$10^{-2} \times \varepsilon$ / M^{-1} cm^{-1}	λ_{max} / nm	$10^{-2} \times \varepsilon$ / M^{-1} cm^{-1}	λ_{max} / nm	$10^{-2} \times \varepsilon$ / M^{-1} cm^{-1}
31	320	146 ± 17	425	7.78 ± 0.91	272	90.8 ± 11	422	10.8 ± 1.3
32	325	174 ± 20	428	6.12 ± 0.72	286	51.5 ± 6.0 [b]	438	13.6 ± 1.6 [b]
33	341	162 ± 20	425	6.76 ± 0.80	289	69.4 ± 8.4	430	8.73 ± 1.1
34	340	186 ± 21	435	8.54 ± 0.95	296	55.3 ± 6.2 [b]	451	22.1 ± 2.5 [b]
35	363	193 ± 18	~410 [a]	- [a]	311	87.5 ± 7.9 [c]	405	14.2 ± 1.3 [c]
36	345	166 ± 15	~410 [a]	- [a]	300	52.0 ± 4.6 [c]	462	33.2 ± 2.9 [c]
37	310	167 ± 15	442	3.73 ± 0.34	~290	24.3 ± 2.2 [b]	428	10.1 ± 0.92 [b]
38	310	187 ± 22	438	5.05 ± 0.59	272	48.9 ± 5.7 [b]	434	12.7 ± 1.5 [b]
21	385	221 ± 18	~413 [a]	- [a]	333	162 ± 13 [b]	423	15.7 ± 1.3 [b]
22	394	282 ± 18	~430 [a]	- [a]	346	70.4 ± 5.7 [c]	479	60.8 ± 4.5 [c]
23	328	166 ± 13	417	6.40 ± 0.51	275	80.6 ± 6.4	403	6.66 ± 0.53
24	335	227 ± 18	425	9.63 ± 0.76	296	57.7 ± 4.6	441	23.0 ± 1.8

Table 2.9. Spectral data for the azoheteroarenes, including those studied in section 2.2.3. [a] n-π* absorbance appears as a shoulder on the π-π* absorbance, hence ε cannot be obtained. [b,c] These values are for the extracted ([b]) or estimated ([c]) pure *Z*-isomer.

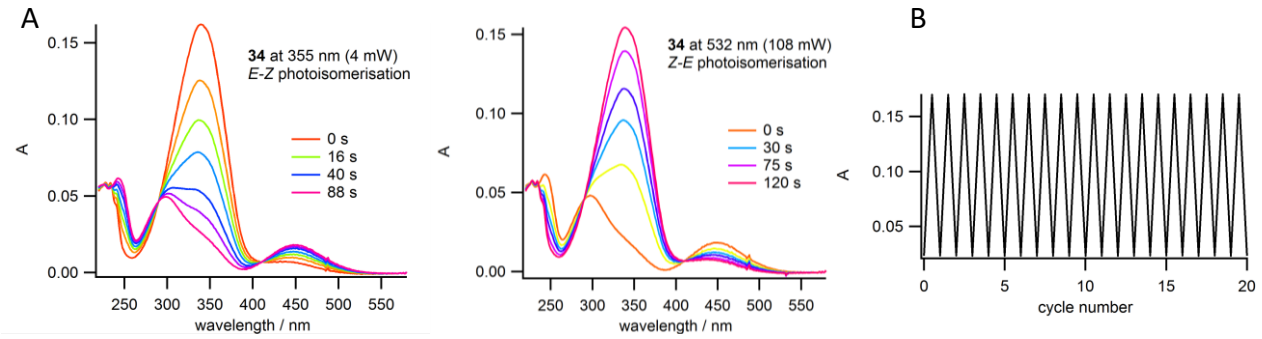


Figure 2.16. A) Time-resolved UV/vis spectra for photoswitching of **34** at 355 nm (left) and 532 nm (right). For other compounds, see Appendix; B) Repeated photoswitching cycles for **34** with 355 and 532 nm irradiation, showing no decomposition.

2.3.4 Thermal isomerisation kinetics

Thermal isomerisation rates and half-lives at 25 °C were obtained for all photoswitches using either UV/vis or NMR spectroscopy. For analogues with slow thermal isomerisation at room temperature, kinetics were measured at a range of higher temperatures (70 – 110 °C). $\Delta H^{\ddagger}$ and $\Delta S^{\ddagger}$ values were extracted using Eyring plots, as described in detail for azopyrazole **23** (see section 2.2.4), and from these the isomerisation rates and half-lives at 25 °C were calculated. Azopyrroles **35** and **36** were found to be sensitive to water content in the solvent, as seen previously with azopyrrole **22**, so the isomerisation kinetics were carried out in anhydrous acetonitrile.

	Position of azo on heteroarene			Rate (k) / s^{-1}	Half-life ($t_{1/2}$)
	4	**37** [a]		2.1×10^{-7}	39 d
	3	**38** [a]		3.8×10^{-7}	21 d
pyrazoles	3	**31** [a]		1.1×10^{-7}	74 d
	3	**32** [b]		1.4×10^{-6}	5.8 d
	4	**23** [a]		7.6×10^{-9}	1000 d
	4	**24** [b]		7.7×10^{-7}	10 d
	5	**33** [b]		7.4×10^{-7}	11 d
	5	**34** [c]		1.1×10^{-5}	17 h
pyrroles	2	**21** [b,e]		6.5×10^{-5}	3.0 h
	2	**22** [c,d]		3.3×10^{-2}	21 s
	3	**35** [c,d]		2.2×10^{-6}	3.7 d
	3	**36** [c,d]		7.6×10^{-4}	0.25 h

Table 2.10. *Z-E* thermal isomerisation kinetics at 25 °C. Measured using [a] variable temperature NMR; [b] NMR; [c] UV-vis. Values are obtained in [a] d_6-DMSO; [b] d_3-MeCN; [c] anhydrous MeCN. [d] Rates were dependent on water content of solvent. [e] Rate measured by UV/vis rather than NMR was 4-fold slower.

When comparing compounds with the same azo linkage position on the heteroarene, the bis(*o*-methylated) photoswitches had faster thermal isomerisation rates than their singly or non-methylated analogues, as expected from our previous work (section 2.2.4).[138] The position at which the azo group was attached also had a significant effect on the rate. By separating the photoswitches into those with and without two *ortho*-methyls, the 2-azopyrroles had shorter half-lives than the corresponding 3-azopyrroles ($t_{1/2}$: **22**<**36, 21**<**35**), and for the azopyrazoles, the 5-analogues had the shortest half-lives and the 4-analogues had the longest half-lives ($t_{1/2}$: **33**<**31**<**23**, **34**<**24**). Azopyrazole **32** should technically be included in the **33,31,23** series as it only has one *ortho*-methyl, however it has a basic nitrogen in the other *ortho*-position, rather than a CH, which is presumably why it does not follow the same trend. It does however fit the trend for the bis(*o*-methylated) pyrazoles – this suggests *ortho* basic nitrogens have a similar effect on the thermal isomerisation rate as *o*-methylation, presumably due to adoption of a similar twisted *Z*-conformation. This conformation would minimise unfavourable interactions between the lone electron pair on the pyrazole basic nitrogen and either the lone pairs of the azo nitrogens or the delocalised π-electron system of the phenyl ring.

The effect that altering the position of the azo group on the heteroarene has on thermal half-life can be qualitatively explained in terms of how well the *N*-methyl nitrogen lone pair is able to conjugate into the azophenyl system (Figure 2.17). For the 2-azopyrroles and the 5-azopyrazoles, the position of the *N*-methyl relative to the azo group allows better conjugation of the lone pair into the azophenyl relative to the other regioisomers. This would improve the electron donation from the heteroaryl ring and lead to faster half-lives through stabilisation of the polar transition state – generally, the dipole moment is larger in both the inversion and rotation transition states than in the *Z*-isomer. This is seen for azobenzenes with electron donating substituents on one ring, which have faster thermal isomerisation rates than unsubstituted azobenzenes.[25,52] This difference in electron donation between the different azoheteroarene regioisomers would also explain the difference in π-π* absorption maxima seen in the UV/vis spectra; the 2-azopyrrole and 5-azopyrazole π-π* absorption maxima were red-shifted relative to the other regioisomers (Table 2.9).

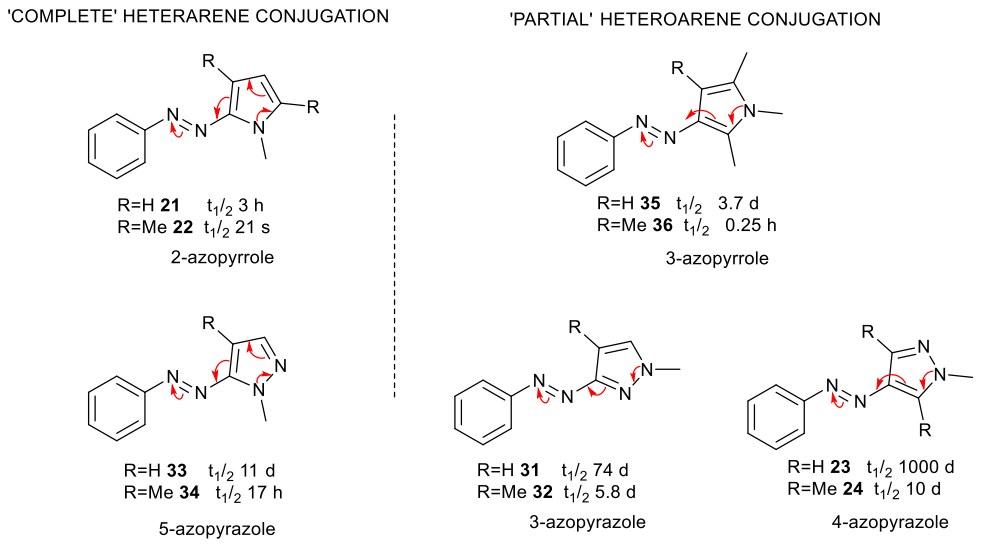


Figure 2.17. Conjugation of the heteroarene into the azophenyl moiety.

It is worth noting that the trend seen in both thermal isomerisation rate and position of π-π* absorption maxima for the different pyrazole regioisomers does not match their observed order of reactivity towards electrophiles, where the 4-position is the most reactive.[102] Using Hammett values for the reactivity of the *N*-methylated 3-, 4-, and 5-pyrazoles with respect to solvolysis of the relevant 1-arylethyl derivative (Figure 2.18), the 4-pyrazole is the most reactive regioisomer.[115] The positional reactivity is directly related to the amount of electron donation at that position, and therefore these Hammett values reveal the opposite trend to that seen for the arylazopyrazoles, where the 4-pyrazole is the least electron donating and the 5-pyrazole is the most electron donating.

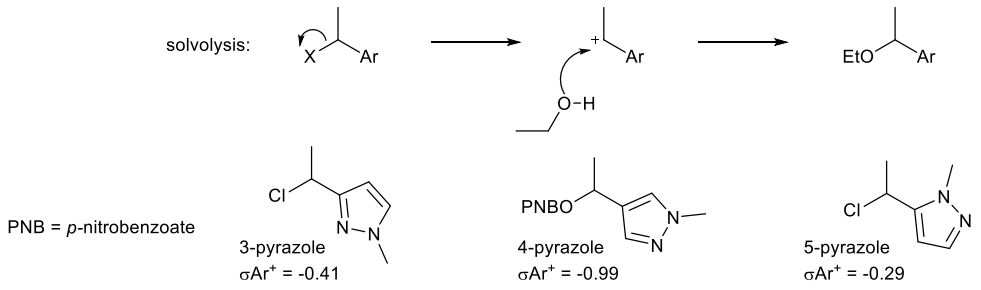


Figure 2.18. Hammett values for the solvolysis of 1-arylethyl derivatives.

The Hammett values (σ_{Ar}^{+}) shown in Figure 2.18 take into account both inductive and resonance effects.[114,115] Considering the difference in the systems involved, the relative contributions of induction or resonance to the overall electron donation is likely to differ substantially. This could explain the differences seen in terms of which pyrazole regioisomer is the most electron donating. For example, the *N*-methylpyrazole substituted in the 5-position has increased π-electron conjugation (a resonance effect) relative to the other regioisomers, but it is also adjacent to a σ-electron withdrawing nitrogen (an inductive effect). The inductive and resonance contributions to

electron donation at a particular position are shown for the different regioisomers in Figure 2.19. In our systems the 5-pyrazole is a better electron donor than the other regioisomers (*i.e.* fastest half-life, lowest energy π-π* transition), suggesting that the resonance effect dominates, whereas for the 1-arylethyl derivatives used in the solvolysis reaction, the 5-pyrazole is a less efficient electron donor (slowest solvolysis rate) than the other regioisomers, indicating that the inductive effect dominates. Although it is possible to obtain Hammett values that take into account only resonance effects,[113] these have not been reported for the heteroarenes in question.

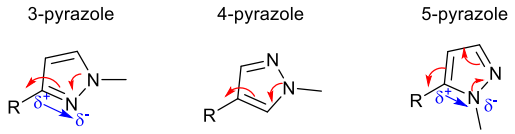


Figure 2.19. Contribution of inductive effects (blue arrows) and resonance effects (red arrows) to the electron donation in the three possible pyrazole regioisomers.

The Hammett value for solvolysis of an *N*-methyl-2-pyrrole derivative (σ_{Ar}^{+} = -1.96)[114] has been reported and the electron donation from the 2-pyrrole was found to be considerably greater than the values for the pyrazoles, as expected. A value for the *N*-methyl-3-pyrrole has not been reported, however it is assumed that it would be considerably smaller than the 2-position regioisomer, which is well documented to be the most reactive position towards electrophiles.[102]

2.3.5 Computational studies

All calculations were carried out by Joaquín Calbo (University of Valencia) and Dr Julia Contreras-García (Pierre and Marie Curie University). The aim of this collaboration was to understand the theoretical origin in the differences in experimental half-lives of the arylazoheteroarenes. Geometry optimised structures for the *E*- and *Z*-isomers and the transition states were obtained using the PBE0-D3/6-31G** level of theory in either the gas phase or using the PCM solvent model for acetonitrile. The PBE0 functional[139,140] is a hybrid functional that is very similar to B3LYP, which the Contreras-García group have found to offer identical or improved performance compared to B3LYP. The –D3 term in the hybrid functional is the Grimme correction for the dispersion interaction,[141,142] which needs to be included to take into account non-covalent interactions.

2.3.5.1 Calculated thermal isomerisation kinetics

For each compound, two optimised *Z*-isomer conformations were obtained, leading to four different isomerisation transition states. Only inversion transition states were found; either type-I (*Z*-like) with the azoheteroarene perpendicular to the phenyl ring, or type-II (*E*-like) with the two aryl rings in a co-planar conformation (Figure 2.20).

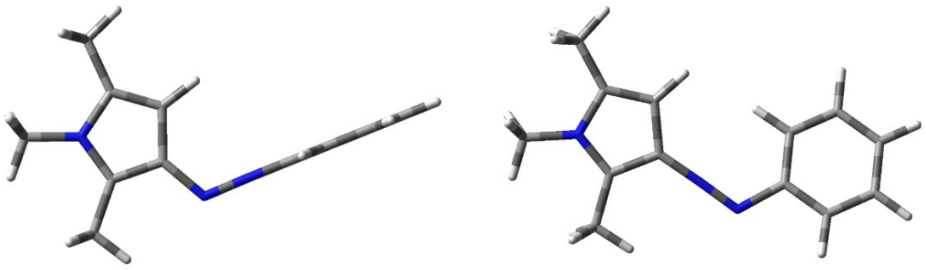


Figure 2.20. The two optimised transition states, shown for **35**: type-I (left) implying an inversion of the azo N closest to the phenyl ring (*Z*-like), and type-II (right) implying an inversion of the azo N closest to the heteroarene (*E*-like).

The Boltzmann factor of each transition state was calculated in order to obtain the contribution of each energy barrier. Thermal isomerisation rate constants for each energy barrier were obtained using the Eyring equation (eq. 5), and half-lives were calculated. The Boltzmann factors were then used to give the final weighted average half-lives, which were compared to the experimental half-lives (Table 2.11).

		Exp. $t_{1/2}$	Calc. $t_{1/2}$
23		1000 d	108 d
31		74 d	33 d
37		39 d	26 d
38		21 d	109 d
33		11 d	4.5 d
24		10 d	24 h
32		5.8 d	9.3 d
35		3.7 d	2.5 d
34		17 h	18 h
21		3.0 h	1.3 h
36		0.25 h	1.2 h
22		0.006 h	0.03 h

Table 2.11. Experimental and calculated thermal isomerisation half-lives, arranged in order of decreasing experimental half-life.

In general, the calculated half-lives were good predictions of the experimental values (*i.e.* within the same order of magnitude), and the majority of half-lives were predicted in the correct order of shortest to longest (Figure 2.21). The effect on the experimental half-lives, upon changing the position of the azo linkage on the heteroarene, was correctly predicted (see section 2.3.4), with the exception of **32**. Experimentally for the azopyrazoles, the order of increasing half-life was **34**<**32**<**24**,

whereas the calculated half-life for **32** was actually longer than for **24**. As mentioned previously, this compound differs from the other azopyrazoles studied as it has one *ortho*-methyl and one *ortho* basic nitrogen, rather than two *o*-methyls or one *o*-methyl and a CH in the other *ortho* position. The calculated half-lives of azopyrazoles **23** and **24** still did not match the experimental values as well as some of the other compounds, but they were considerably closer than the calculations carried out in section 2.2.5 using the B3LYP functional (10-fold difference, rather than 16- and 1000-fold for **23** and **24** respectively).

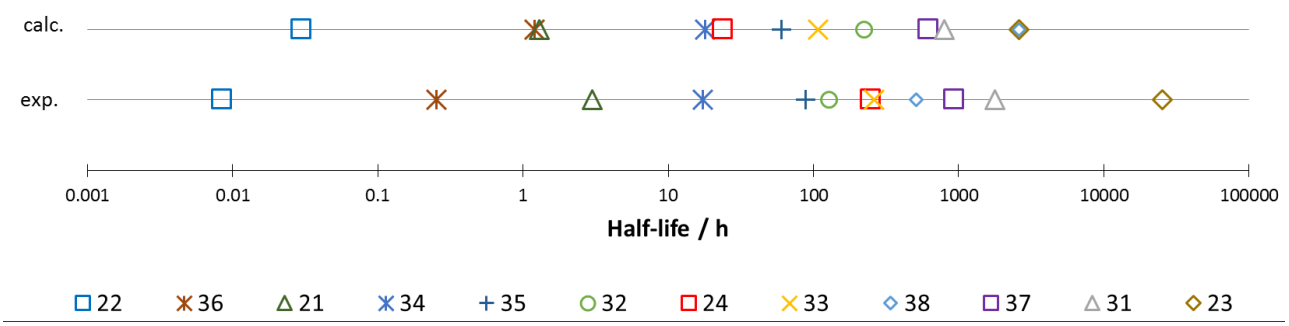


Figure 2.21. Comparison of calculated and thermal half-lives at 25 °C.

The lowest energy *Z*-isomer conformations (Table 2.12) matched those calculated previously using B3LYP/6-31G(d,p) and the relative energies were qualitatively consistent (Table 7.10, Appendix). Similarly, the energy barriers for the most stable transition states were consistent with the values calculated previously (Table 7.11, Appendix), in terms of the order of the relative energy barriers for the different compounds, although the PBE0-D3 values were lower than those calculated with B3LYP.

		*Z*-isomer SCF energy / kJ mol^{-1}	TS SCF energy / kJ mol^{-1}	
		Gas phase	Gas phase	PCM (MeCN)
	**21**	45.02	109.33	110.42
	**22**	57.24	96.44	96.61
	**23**	46.44	124.06	126.48
	**24**	55.98	109.83	112.01

Table 2.12. SCF energies of the most stable *Z*-conformers (relative to the *E*-isomer) in the gas phase and the lowest energy transition state (TS) SCF energy barriers for thermal isomerisation (relative to the *Z*-isomer) in both the gas phase and the PCM solvent model for acetonitrile. All calculated using PBE0-D3/6-13G**.

2.3.5.2 Non-covalent interactions and charge transfer

In order to understand the trends in thermal half-life, two key properties were studied computationally – non-covalent interactions (NCI) and charge transfer from the heteroaryl ring. Dr Julia Contreras-García and her co-workers have previously developed a computational approach

to analyse the NCIs in a molecule, enabling the attractive and repulsive integrated volumes to be obtained.[143,144] This method was carried out on the *E*- and *Z*-isomers of the azoheteroarenes developed in section 2.2 (compounds **21**-**24**); the difference between attractive and repulsive volumes (V) integrated along the NCI surface was calculated (Table 2.13) and compared to the internal (SCF) energy of the *Z*-isomers relative to the *E*-isomers (Table 2.12). By viewing the NCIs as a surface (Figure 2.22), it is clear that the *E*-isomers only provide small regions of NCI contacts, whereas for the *Z*-isomers, significant NCI regions are seen. The green regions correspond to weak dispersion-based interactions, and the red regions indicate intramolecular ring-centroid repulsions. For *Z*-**21** and *Z*-**23**, which adopt a T-shaped conformation with the phenyl ring orthogonal to the co-planar azoheteroarene (see section 2.2.5), there is a favourable CH···π-system interaction between the heteroaryl *ortho*-hydrogen and the phenyl ring (Figure 2.22, A).[145]

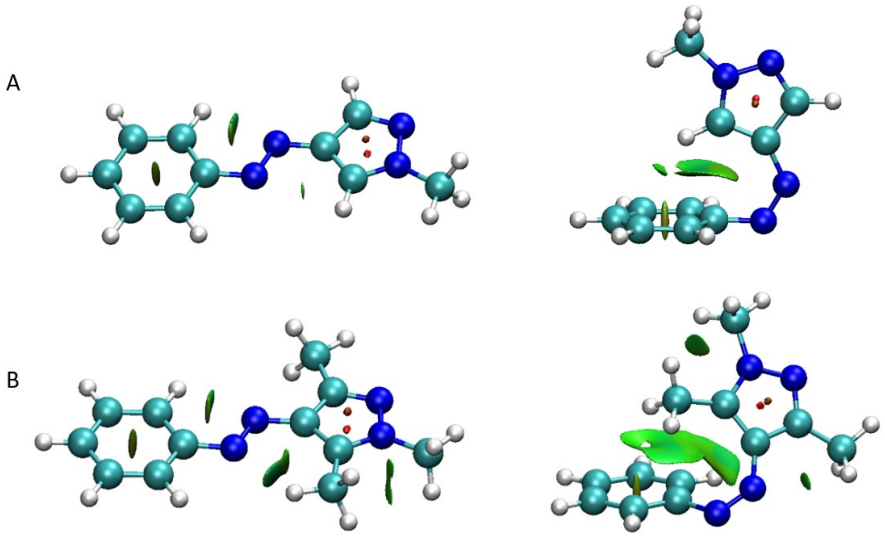


Figure 2.22. NCI surfaces for; A) *E*- and *Z*-**23**; B) *E*- and *Z*-**24**. Green regions are weak NCI contacts, red regions are strong, repulsive NCI contacts. Energy minimised structures were obtained using PBE0-D3/6-31G**.

Neither this T-shaped conformation nor CH···π-system interaction are possible for *Z*-**22** and *Z*-**24** due to the presence of the two *ortho*-methyls, however a large NCI surface is seen between the benzene ring and the methyl group facing it (Figure 2.22, B). Analysing the NCIs in more detail, azopyrrole **21** and azopyrazole **23** have very similar positive integrated volumes (Vpos−Vneg) to each other for both isomers, while the values for the bis(*o*-methylated) analogues **22** and **24** are also very similar to each other (Table 2.13). This is consistent with the relative internal (SCF) energies of the *Z*-isomers (Table 2.12) – **21** and **23** have similar energies, as do **22** and **24**. In general, although these values should not be taken as quantitative, large positive integrated volumes indicate destabilisation. For all four compounds, the *Z*-isomers have larger integrated volumes than the *E*-isomers, which is consistent with the *Z*-isomers being less stable than the *E*-isomers. In addition

to this, the difference between *E*- and *Z*-isomer integrated volumes is much smaller for **21** and **23** than for **22** and **24** (Table 2.13), presumably due to the stabilising effect of the CH···π-system interaction that is present in **21** and **23** only. This is also reflected in the *Z*-isomer stability, where *Z*-**22** and *Z*-**24** have a higher SCF energy relative to their *E*-isomers than *Z*-**21** and *Z*-**23** (Table 2.12).

This data clearly shows that NCIs contribute to the stability of the Z-isomers relative to the *E*-isomers. In terms of the relative energy barriers of the transition states (Table 2.12), the compounds with the non-covalent CH···π-system interaction have higher energy barriers than the heteroarenes lacking this interaction, as the favourable interaction has to be broken prior to reaching the transition state. The NCIs do not however explain the difference in transition state energy barrier between the different heteroaryl rings.

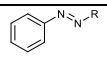
		Vpos—Vneg		Δ(Vpos—Vneg)	NPA Charge		ΔNPA
		E	*Z*	*Z—E*	*E*	*Z*	*E—Z*
21		28.78	29.28	0.50	0.2882	0.2731	0.015
22		37.38	38.43	1.05	0.3376	0.2624	0.075
23		26.63	26.85	0.22	0.2266	0.2131	0.014
24		34.89	36.63	1.74	0.2629	0.1946	0.068

Table 2.13. The difference between attractive and repulsive integrated volumes (V) in the NCI region, and the NPA charge calculated for the heteroarene fragment of photoswitches **21-24**. All values are for the lowest energy conformations and are in atomic units.

The charge transfer from the heteroaryl ring to the azo fragment can be estimated by carrying out natural population analysis (NPA) calculations.[146] This method sums the natural atomic charges of the atoms that make up the heteroarene, giving a value for the 'NPA charge', which is equivalent to the charge transfer (Table 2.13). The charge transfer was found to be greater in the *E*-isomers than in the *Z*-isomers of each photoswitch, as expected due to the interrupted conjugation in the T-shaped or distorted *Z*-isomer relative to the planar *E*-isomer. This difference in charge transfer between the two isomers was considerably larger for the *ortho*-methylated analogues (**22** and **24**). For both isomers, the charge transfer was considerably larger for the azopyrroles than the azopyrazoles – this is consistent with experimental evidence showing pyrroles to be better electron donors than pyrazoles,[114–116] and validates our explanation for the red-shifts in π-π* absorption maxima and the shorter thermal half-lives seen for the azopyrroles relative to the azopyrazoles (see sections 2.2.3 and 2.2.4). As mentioned previously, increased electron donation from the heteroaryl ring should stabilise the transition state, thus lowering the energy barrier and increasing the thermal isomerisation rate. It appears that both NCIs and charge transfer from the heteroarenes are

important factors in determining the thermal stability of the *Z*-isomer as, taken together, they correctly predict the order of the calculated transition state energy barriers (Table 2.12).

Examining the other azoheteroarenes that were studied experimentally (sections 2.3.3 and 2.3.4), similar trends were seen. In all cases, the presence of one or two *ortho*-hydrogens on the heteroarene led to *Z*-conformers with a T-shaped conformation, driven by the non-covalent CH···π-system interaction, and an increased *Z*-isomer stability was calculated relative to the compounds without this interaction. As discussed previously, certain substitution patterns prevented this T-shaped conformation, instead resulting in a twisted conformation. As well as the presence of two *ortho*-methyls, this was also observed for photoswitches where the *C*- or *N*-methyl in that position had been replaced with a basic nitrogen (Figure 2.23) – this accounts for the experimental observations of increased *Z*-isomer n-π* intensities relative to the *E*-isomers for these compounds. This twisted conformation also explains why the experimental thermal half-life of **32** fitted better into the bis(*o*-methylated) azopyrazole series (**24**, **32**), which adopt a twisted conformation, than the series with an *ortho*-hydrogen (**23**, **31**, **33**), which have the favourable CH···π-system NCI.

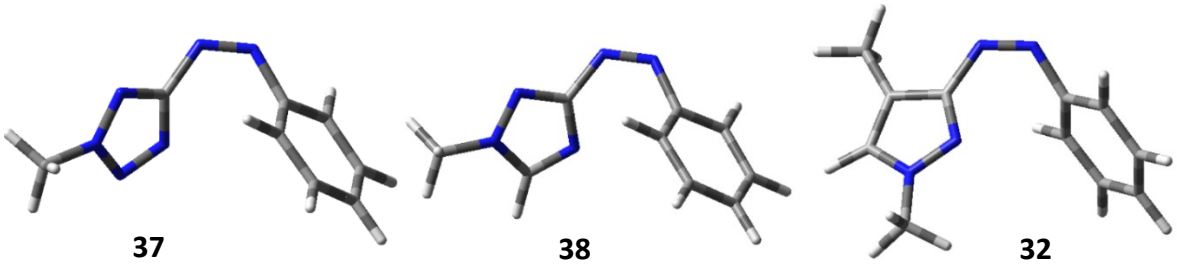


Figure 2.23. Energy minimised *Z*-conformers for compounds with two *ortho*-nitrogens (**37** and **38**) or one *ortho*-nitrogen and one *ortho*-methyl (**32**), calculated using PBE0-D3/6-13G**.

The NPA charges for the *Z*-isomers were analysed to identify whether they correctly predicted the effect that the azo group position on the heteroarene had on thermal half-life (Figure 2.24). If there is a correlation, an increase in NPA charge should lead to a decrease in thermal half-life. For the azopyrroles this was the case – the 2-pyrroles had larger NPA charges and shorter calculated and experimental thermal half-lives than the 3-pyrroles. There was not, however, a good correlation for the azopyrazoles. The 4-pyrazoles had the largest NPA charges, whereas the 5-pyrazoles had the shortest thermal half-lives. This indicates that there is another important factor that determines the effect that the azo position has on the half-life.

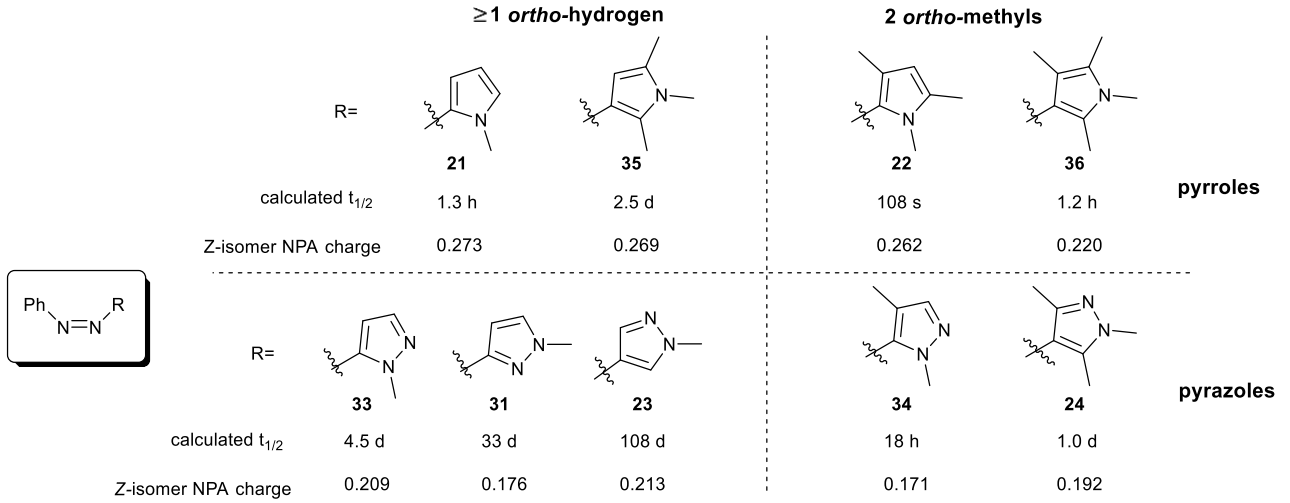


Figure 2.24. Comparison of *Z*-isomer NPA charges and calculated thermal half-lives for the different series of photoswitches. NPA charges are the Boltzmann weighted averages for the two *Z*-conformers. Half-lives are the Boltzmann weighted averages for the four transition states.

In addition to further study of these compounds, calculations are also being carried out on a range of other arylazoheteroarenes, including oxygen and sulfur-containing compounds, as well as compounds with different *ortho*-substitutions (such as *o*-halides), to widen the scope of the study. The arylazoimidazoles studied experimentally by Herges and Otsuki are also being included.[96,98] This ongoing work aims to identify other factors that are key to the observed thermal isomerisation rates. Some of the properties they have been focusing on are bond angle and distance asymmetry between the azo moiety and aryl rings, as well as N=N bond distance and Wiberg indices,[147] which can be used to measure the N=N bond order.

2.4 CONCLUSIONS

In the first part of this work (section 2.2), several novel azoheteroaryl photoswitches were developed with short and generally high yielding synthetic routes. The arylazopyrazoles in particular represent a previously unexplored class of azoheteroarene and were found to have desirable photochemical and thermal properties. Azopyrazole **24** was quantitatively photoswitched in both directions, which, to the best of our knowledge, is superior to all other azobenzenes reported to date.[60,61] Furthermore, azopyrazole **23** was found to have a very long thermal half-life (~1000 days), which is comparable to some of the slowest azo photoswitches published to date, and gives this compound class potential for use in applications such as optical data storage.[60,148] Computational studies and X-ray crystallography were used to visualise the conformations of these compounds and to understand how these conformations affected the photochemical properties. It was found that in contrast to the azobenzenes, the *Z*-isomers of 5-membered azoheteroarenes such as those developed here, are

able to adopt a conformation with a co-planar heteroarene-azo functionality approximately orthogonal to the phenyl group. This conformation results in a reduction of the *Z*-isomer n-π* absorbance intensity, due to this transition being symmetry forbidden. This effect can be readily tuned, using steric interactions alone, by addition of methyl substituents on the *ortho*-positions of the heteroaryl ring.

The computational methods used in this work accurately predicted the photochemical properties of these photoswitches, as well as the thermal kinetics of the azopyrroles. However, the thermal isomerisation rates calculated for the azopyrazoles did not match the experimental values well, suggesting that alternative methods needed to be identified. A wider range of arylazoheteroarenes were therefore synthesised and studied both photochemically and computationally (section 2.3) in order to understand the properties that affect thermal isomerisation rate and to find a computational method that accurately predicted these rates. Eight new analogues were successfully synthesised, with the azophenyl moiety attached at different positions on the heteroaryl ring and with different heteroaryl *ortho*-substitution patterns. These compounds obeyed the photochemical and thermal trends seen in section 2.2. Additionally, compounds with either two *ortho* basic nitrogens (**37** and **38**) or one *o*-nitrogen and one *o*-methyl (**32**) had similar thermal and photochemical properties to the bis(*o*-methylated) compounds, due to a similar twisted *Z*-isomer conformation. The T-shaped conformation that was adopted for all compounds with at least one *ortho*-hydrogen, with the phenyl ring perpendicular to the planar azoheteroarene, was found to be stabilised by a favourable CH···π-system non-covalent interaction. This interaction, together with the larger heteroaryl electron donation seen for the azopyrroles compared to the azopyrazoles, explained the general trends in thermal isomerisation rates seen, as well as the position of the π-π* transitions. The PBE0-D3 functional predicted the thermal half-lives more accurately than the B3LYP functional used in section 2.2, and in general the correct order of *Z*-isomer thermal stability was predicted.

In terms of changing the azo position on the heteroaryl ring, an initial attempt to attribute the trend in thermal isomerisation rate to an electron donation effect was unsuccessful for the azopyrazoles. Further work is being carried out to try to identify the cause of this trend and identify other important factors that control thermal isomerisation rate. A more comprehensive computational study is currently being undertaken on a wider scope of arylazoheteroarenes.

3 PHOTOSWITCHABLE HDAC INHIBITORS

3.1 INTRODUCTION

3.1.1 Epigenetics and cancer

Epigenetics is defined as 'the study of heritable changes in gene expression that occur independent to changes in the primary DNA sequence'.[149] In normal cells, these heritable changes are established during differentiation and are maintained during multiple cycles of cell division, so that cells containing the same genetic information have distinct characteristics.[149] The key epigenetic modifications are DNA methylation, histone post-translational modifications (PTMs), nucleosome positioning along the DNA, and incorporation of histone variants.[149–151] Together these mechanisms interact to create the epigenome. Aberrations to the epigenome can lead to inappropriate activation or silencing of genes, which can result in disease states. Epigenetic alterations, unlike genetic mutations, are reversible and this makes epigenetic mechanisms an attractive target for chemotherapy in diseases such as cancer.[149,152]

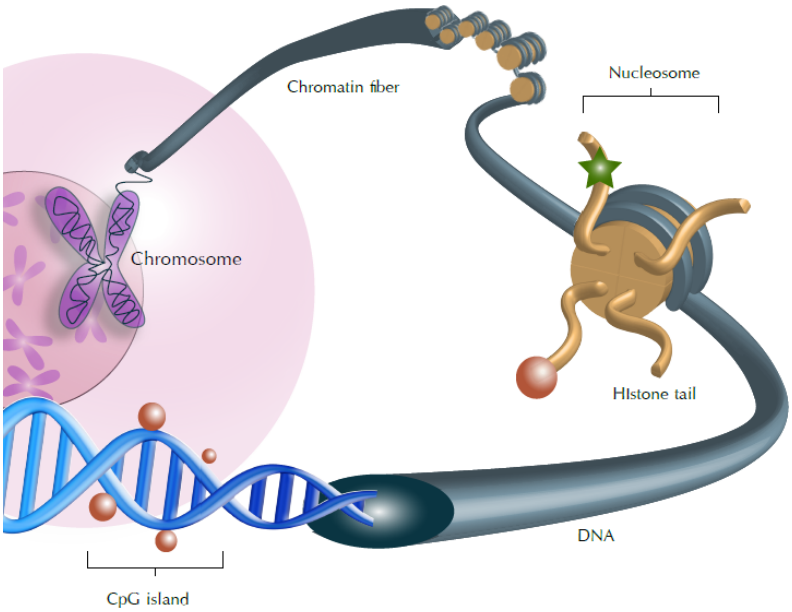


Figure 3.1. Schematic showing the organisation of DNA within chromatin and positioning of epigenetic modifications (red spheres and green star).

Within the nucleus, DNA is packaged into chromatin, a complex of DNA and protein. Chromatin consists of nucleosomes, which are made up of 146 base pairs of DNA wrapped around an octamer of core histone proteins, containing two each of histones H2A, H2B, H3 and H4 (Figure 3.1).[153] The repeating nucleosome cores are connected by stretches of linker DNA to assemble into higher order structures, which are further stabilised by the linker histone H1.[154] The organisation of DNA into its precise compact structure greatly influences the accessibility of certain parts of the DNA to transcription factors and thus modulates the activation or silencing of specific genes.[155]

3.1.1.1 Epigenetic mechanisms in normal cells

Focusing on the histones, these proteins have globular C-terminal domains and unstructured N-terminal tails, which protrude from the surface of chromatin and account for 25-30% of the mass of each histone protein.[156] There are at least eight possible PTMs that can take place on the tail, the most well understood being acetylation, methylation and phosphorylation.[157] There are two main functional consequences for the modification of histones. Firstly, histone PTMs modify the overall 3D structure of chromatin. For example, modifications such as acetylation and phosphorylation reduce the positive charge on the histones, which weakens the electrostatic interaction between the histones and DNA, leading to a less compact chromatin structure.[158] This is the active euchromatin state and is accessible for transcription. Conversely, heterochromatin has a compact structure and is therefore inaccessible to transcription factors – hypoacetylation and specific DNA methylation patterns are associated with this state.[157,158] The second function of histone modifications is for the recruitment or occlusion of proteins to chromatin. These proteins can then further modify chromatin, bringing about the activation or silencing of genes.[157] Histone modifications are highly dynamic and are regulated by the opposing action of different classes of enzymes.[158] For histone acetylation, these enzymes are the histone acetyltransferases (HATs) and the histone deacetylases (HDACs), of which I will be focusing on the latter.

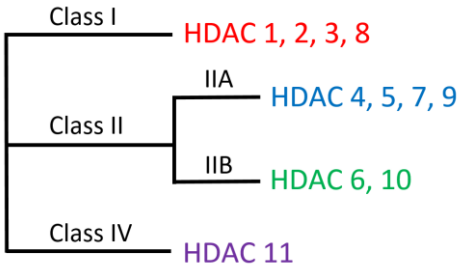
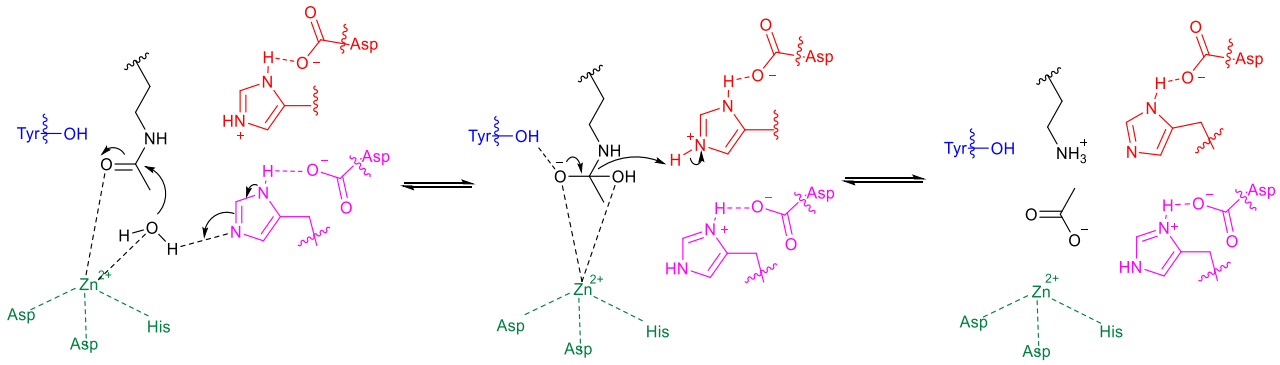


Figure 3.2. Phylogenetic tree of the classical HDAC family.

To date, 18 individual HDACs have been identified, which are split into the classical and Sirtuin families.[159] Classical HDACs are zinc-dependent enzymes with a Zn^{2+} ion in their active site, whereas Sirtuins require NAD^{+} as a cofactor. The HDAC family is grouped into classes I, II, III and IV, depending on the sequence homology to yeast analogues. Classes I, II and IV are classical HDACs (Figure 3.2), while class III are Sirtuins.[159] Class I and IV HDACs exist almost exclusively in the nucleus, whereas class II are able to shuttle between the nucleus and cytoplasm.[160] Crystal structures for several HDACs have been reported, as well as for histone deacetylase-like protein (HDLP), a bacterial enzyme which belongs to the HDAC superfamily.[161–163] The HDAC active site consists of an 11 Å deep tubular channel, at the base of which sits a Zn^{2+} ion. There is also a 14 Å internal channel at the foot

of the tubular channel. Crystal structures of enzyme-inhibitor complexes enabled the identification of important residues in the active site, from which a catalytic mechanism was proposed (Scheme 3.1).[161]



Scheme 3.1. Proposed catalytic mechanism of HDACs for the deacetylation of acetylated lysine.

3.1.1.2 The role of epigenetics in cancer

In recent years, epigenetic modifications and aberrations have played an important role in the initiation, development and progression of cancer. Prior to the formation of cancer ('oncogenesis'), global changes to the epigenome result in the dysregulation of gene expression that leads to the development and progression of cancer.[149,151] Epigenetic changes can occur in conjunction with genetic mutations or deletions and thus result in oncogenesis. As with genetic mutations, epigenetic changes can activate oncogenes and silence tumour suppressor genes. Cells with these epigenetic aberrations are selected for in the cancer cell population as they confer a growth advantage, leading to uncontrolled proliferation.[149]

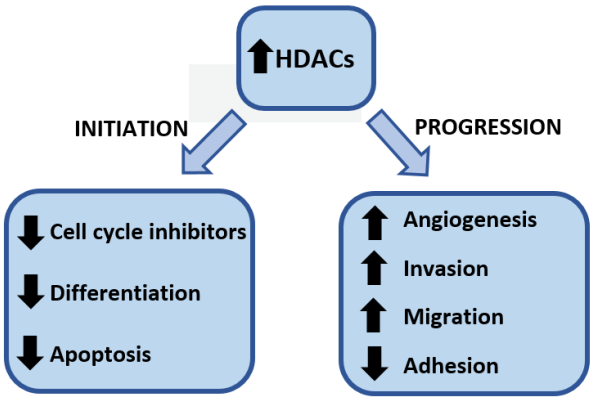


Figure 3.3. Schematic showing the effect of HDAC overexpression.

In addition to changes to other epigenetic modifications, such as DNA methylation and nucleosome positioning, cancer cells also show pronounced changes to histone modification patterns; HDACs are found overexpressed in many cancers.[164] This results in global loss of histone acetylation, which affects the expression of many genes involved in oncogenesis and cancer progression (Figure 3.3).[165]

In particular, HDAC overexpression is associated with increased proliferation, invasion, and advanced disease state, resulting in a poor prognosis.[159] The deacetylation of non-histone targets, such as transcription factors, also has a key role in the development of cancer. As with HDACs, HAT expression is altered in cancer, causing widespread changes in histone acetylation patterns. HAT function is believed to be linked to tumour suppression, hence dysregulation of HAT activity may lead to cancer.[166]

3.1.1.3 Epigenetic cancer therapy

Due to the reversibility of epigenetic changes and their prevalence in cancer, epigenetics is an extremely attractive new approach to cancer therapy.[149,151,152] HDAC inhibitors in particular are considered among the most promising candidates currently in development for cancer therapy.[166-168] There are four main classes of HDAC inhibitors that are either clinically approved or currently in clinical development, comprising hydroxamic acids, cyclic peptides, short chain fatty acids, and benzamides (Figure 3.4).[170] Hydroxamic acids are the most widely explored class and suberoylanilide hydroxamic acid (SAHA) was the first HDAC inhibitor to be approved by the FDA for the treatment of cutaneous T-cell lymphoma (CTCL).[170,171] These compounds are zinc-chelators so only inhibit the classical zinc-dependent HDACs.

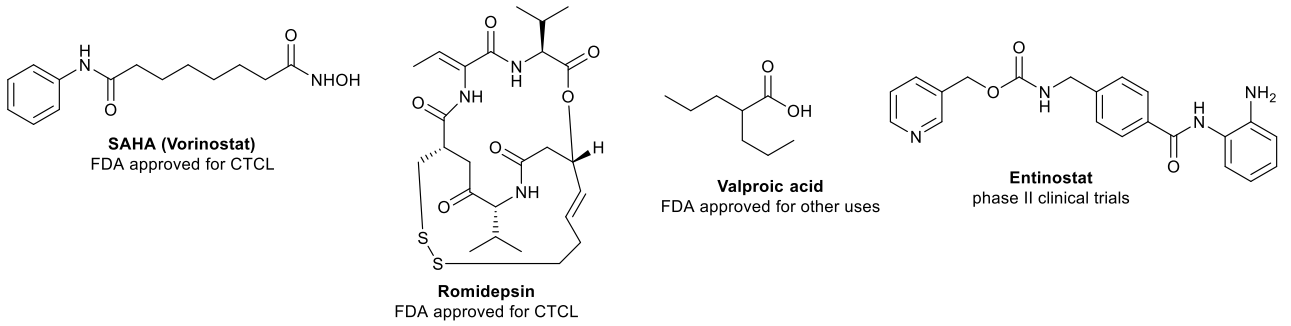


Figure 3.4. Examples of the four main classes of HDAC inhibitors that are clinically approved or in clinical development.

HDAC inhibitors have varying degrees of specificity; SAHA is a pan-HDAC inhibitor, whereas the benzamide Entinostat only inhibits class I HDACs,[170] and tubacin, a hydroxamic acid, is currently the only isoform specific HDAC inhibitor.[172] Several crystal structures of enzyme-inhibitor complexes have been reported for both hydroxamic acid and benzamide inhibitors (Figure 3.5).[161–163] The inhibitors were found to occupy the tubular active site channel and coordinate to the zinc in a bidentate fashion, with interactions between the inhibitor and key residues lining this hydrophobic channel and on the surface.[162] Unlike their hydroxamate counterparts, the benzamide inhibitors also occupy the internal cavity adjacent to the zinc active site (Figure 3.5, B).[163]

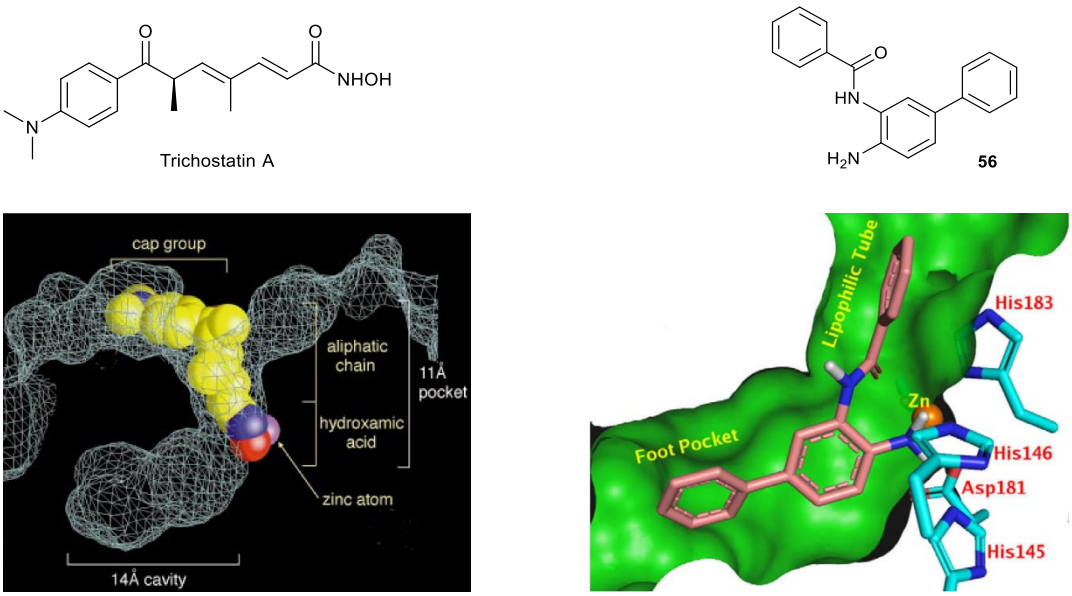


Figure 3.5. A) Crystal structure of HDLP and hydroxamic acid trichostatin A, showing occupation of the hydrophobic channel (taken from Finnin *et al*);[161] B) Crystal structure of HDAC2 and benzamide inhibitor **56**, showing occupation of both the hydrophobic channel and internal cavity (taken from Bressi *et al*).[163]

The majority of the classical HDAC inhibitors being developed have the same basic pharmacophore, consisting of a zinc-binding group (ZBG) that coordinates to the active site zinc, a capping unit that interacts with amino acids on the surface of the channel, and a linker that lies in the hydrophobic channel, positioning the ZBG and cap in the correct position (Figure 3.6).[171,173,174]



Figure 3.6. Pharmacophore for classical HDAC inhibitors.

HDAC inhibition causes hyperacetylation of the histones and this results in tumour regression *via* mechanisms such as inhibition of the cell cycle, induction of apoptosis, activation of the host immune response, and inhibition of angiogenesis (Figure 3.7).[168,169] This is achieved by the activation or deactivation of various genes that are involved in these processes, such as pro- and anti-apoptotic genes. One advantage of HDAC inhibitors is that they are relatively non-toxic to normal cells, despite the fact that they induce similar levels of hyperacetylation in these cells as in tumour cells.[168] This may be because HDAC inhibitors trigger a cell cycle checkpoint response in normal cells, which detects abnormal histone acetylation states, whereas this checkpoint is defective in a variety of tumour cell lines and results in aberrant mitosis, leading to cell death.[175]

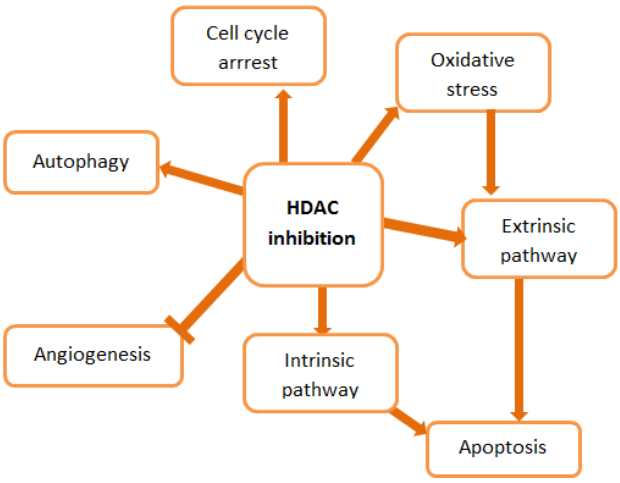


Figure 3.7. Mechanisms of cell death mediated by HDAC inhibition.

3.1.2 Photodynamic therapy

Photodynamic therapy (PDT) is an FDA approved treatment for several cancers, including oesophageal cancer and non-small cell lung cancer.[176] PDT involves the administration of a photosensitizer that accumulates in a specific target cell or tissue, followed by the localised administration of a specific wavelength of light, usually in the red to near-infrared region.[176] Following the absorption of light, the photosensitizer is transformed to a short-lived excited singlet state, which then undergoes intersystem crossing to a relatively long-lived excited triplet state (Figure 3.8).[177,178] This triplet state can either undergo a type 1 reaction, by reacting directly with cellular substrates to form radicals which then interact with oxygen to produce highly cytotoxic reactive oxygen species (ROS), or a type 2 reaction, whereby the excited state photosensitizer transfers its energy directly to oxygen, forming singlet oxygen which is itself a ROS.[177] Because cytotoxicity due to ROS is only observed in the specific regions that are exposed to light, PDT provides an excellent means to selectively destroy tumours through spatial control of tissue irradiation.

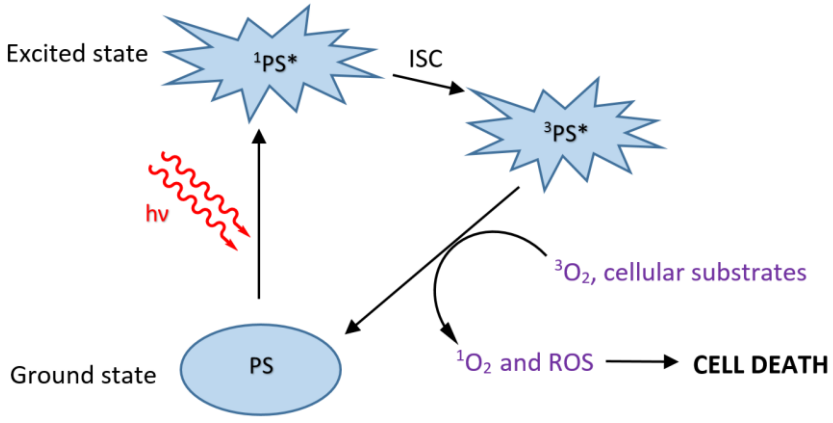


Figure 3.8. Mechanism of action of photodynamic therapy at the cellular level. PS = photosensitizer; ISC = intersystem crossing.

PDT was first proposed for use in the treatment of cancer in 1972 by Diamond and co-workers, due to the observation that the photosensitizer, a haematoporphyrin derivative (HPD), was found to localise selectively to tumours.[179] This is thought to be due to the high vascular permeability of HPD, its affinity for proliferating endothelium, and the lack of lymphatic drainage in tumours. There are three main mechanisms responsible for the anti-tumour effect of PDT.[178] Firstly, the ROS generated by PDT can kill the tumour cells directly. Secondly, PDT can damage the tumour-associated vasculature, leading to death of tumour tissue. Thirdly, PDT can activate an immune response against the tumour cells.[178] PDT efficacy is affected by a range of factors, including the type of sensitizer, its extracellular and intracellular localisation, the total dose administered, the total light exposure dose, oxygen availability, and the time between administration of drug and light exposure.[43]

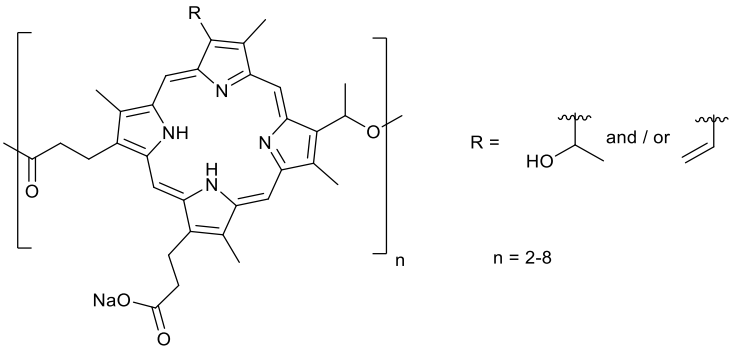


Figure 3.9. Structure of Photofrin®, a haematoporphyrin derivative.

There are several issues with the use of PDT for cancer treatment, one of which is the specificity and potency of the photosensitizers used. Though it is the most commonly used photosensitizer, Photofrin® (Figure 3.9) is not very selective for tumour cells over normal tissue and is absorbed by the skin, leading to long-lasting cutaneous photosensitivity.[180,181] Photofrin® also has a low molar absorption coefficient in the red light region of the spectrum and hence must be administered in high concentrations to have an effect, exacerbating the issue of cutaneous photosensitivity.[178] A more fundamental problem with PDT is its intrinsic requirement of oxygen for cytotoxicity, making it ineffective in hypoxic regions of tumours.[182]

There are several second generation photosensitizers that have been approved for use in PDT which have advantages over Photofrin. Verteporfin, a monomeric benzoporphyrin derivative, is rapidly absorbed by the tumour and rapidly cleared from the body, reducing patient photosensitivity.[183] Third generation photosensitizers are also in development, with a focus on improving the selectivity and specificity of the photosensitizer to enhance cellular uptake – due to the low solubility in aqueous media, photosensitizers cannot be delivered directly into the bloodstream

intravenously.[183] There are various targeted delivery strategies being researched in order to achieve this, including oil-in-water emulsions and nanoparticles or liposomes to act as carriers.[183,184] One concern of encapsulating the photosensitizer is that the observed singlet oxygen quantum yield may be decreased. Another alternative is to attach the photosensitizer directly to biologically active molecules, such as antibodies or receptor ligands.[183,184]

3.1.3 Photopharmacology

A significant issue with chemotherapy is its lack of selectivity, often resulting in off-target toxicity and debilitating side effects. This is particularly relevant in cancer chemotherapy, where tumour cells are derived from the host's normal cells. In order to improve selectivity, drugs need to be administered with high spatial and temporal precision, which can be a difficult task. PDT uses light to achieve selectivity for tumour cells, but has the disadvantage of being oxygen dependent and indiscriminately cytotoxic, as reactive oxygen species react with all components of the cell. Another way of accomplishing selectivity using light is by using photoswitchable inhibitors that are selective for a specific cellular target, such as a receptor or enzyme; this field of research is known as photopharmacology.[19,62] The concept involves administering a drug in its inactive conformation and giving it time to distribute around the body and accumulate in the target site. This site is then selectively irradiated to activate the drug at this location only (Figure 3.10). Because of the requirement of light to activate the drug, potential target sites must be accessible – either by being close to the skin surface or reachable by a fibre optic cable. The key steps involved in this process are identical to those of PDT, the only difference being the use of a photoswitchable inhibitor as opposed to a photosensitizer.

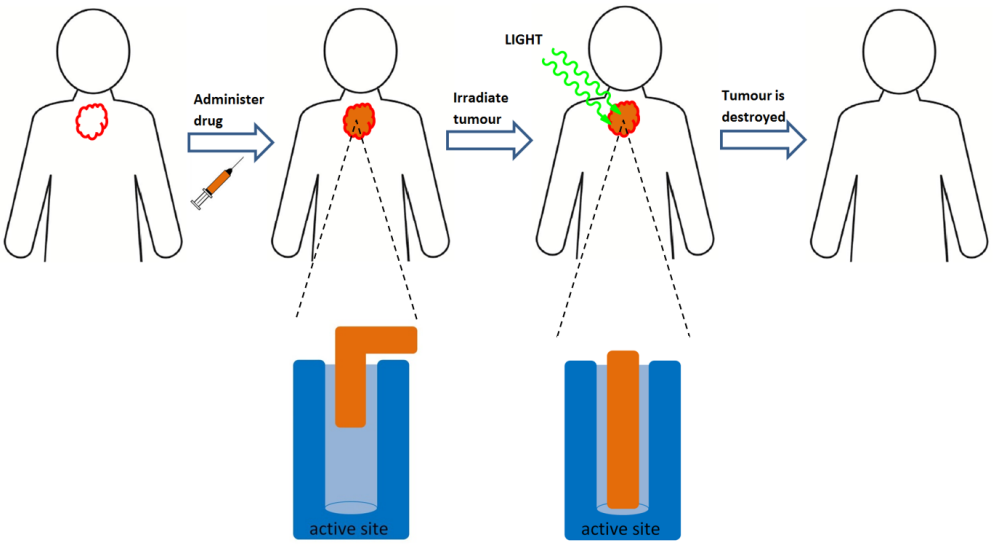


Figure 3.10. Illustration of the photopharmacology concept for destroying a tumour.

There are several different types of photosensitive molecule that can be used to interact with receptors or enzymes (Figure 3.11). The simplest method is using a caged ligand – this is a similar to using a prodrug, except that light is used to release the active molecule rather than the action of an enzyme.[185] Following release of the active molecule upon irradiation, it is able to interact with its biological target.[185,186] This approach is irreversible and also releases potentially toxic by-products on removal of the protecting group.[11] The second method is to use photoswitchable ligands. These ligands contain a photoswitchable portion that can alternate between two conformations, allowing reversible activation.[11] Finally, a photoswitchable tethered ligand can be used, whereby the ligand is covalently attached to its receptor by a photoswitch-containing tether. As the conformation of the tether changes, a biological response is reversibly triggered.[11,187] This last approach is generally used to probe biological systems (*i.e.* optochemical genetics) rather than in photopharmacology, due to the need for the ligand to be covalently tethered to the receptor of interest. There have been several reviews to date covering both photopharmacology and optochemical genetics.[11,19,31,62,187]

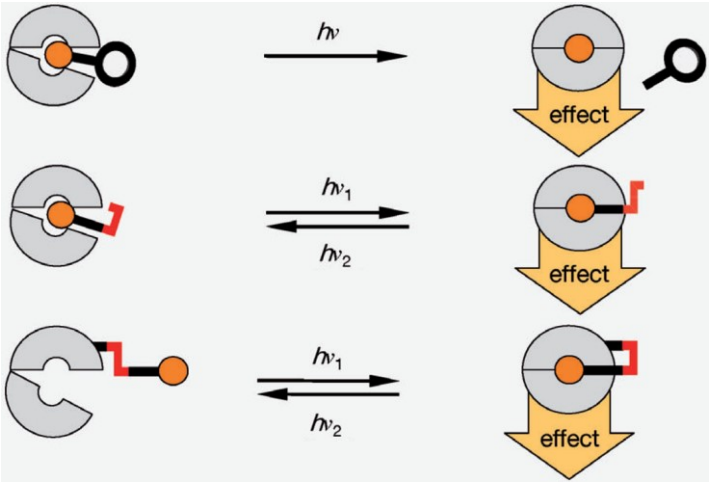


Figure 3.11. Three strategies using photosensitive ligands. A) A caged ligand cleaved with light, releasing the active form; B) A photoswitchable ligand reversibly activated by light; C) A photoswitchable ligand covalently tethered to the receptor. Adapted from Trauner *et al*.[11]

Azobenzenes have seen widespread use as photoswitchable ligands (both tethered and non-tethered), due to the pronounced change in shape that occurs upon isomerisation.[62,63,185-187] For use in photopharmacology, the ideal scenario is that the *Z*-isomer is the active form of the ligand, as this means that the thermally stable *E*-isomer can be administered as the inactive form, given time to accumulate in the target site, and then be selectively irradiated. In this situation, the thermal half-life needs to be long enough that the ligand can have its desired effect, but not so long that that the ligand is still in its active form during metabolism, where it may have off-target effects.[19] Alternatively a photoswitch with a fast thermal isomerisation rate could be used, and continuous or frequent irradiation could be carried out in order for the active

conformation to be present at the target site. The tunability of the *Z*-isomer thermal stability (see section 1.4) is an additional advantage of using azobenzenes.[25,31] In the alternative scenario, where the *Z*-isomer is the inactive form, the ligand would have to be irradiated prior to administering, and then irradiated at the target site to switch back to the *E*-isomer and activate the ligand. Tuning of the *Z*-isomer thermal stability is again required, as the thermal half-life needs to be long enough to ensure that the ligand is metabolised or excreted before any off-target effects occur due to isomerisation to the active *E*-isomer.

One issue with the use of azobenzenes *in vivo* is that the UV radiation required for *E*-*Z* isomerisation is cytotoxic due to the formation of reactive oxygen species, as mentioned in Chapter 1. Ideally absorption wavelengths need to be red-shifted away from cytotoxic regions and towards the infrared region, where tissue is relatively transparent (Figure 3.12). This can be achieved by altering the substitution pattern of the azobenzene, as discussed previously (section 1.4). In particular, the tetra-*o*-methoxyazobenzenes reported by Woolley and tetra-*o*-fluoroazobenzenes reported by Hecht can be photoswitched to either isomer with visible light while still maintaining long thermal half-lives.[54,57,60] This is in contrast to the push-pull azobenzenes which have red-shifted absorption spectra but fast thermal isomerisation rates.[25]

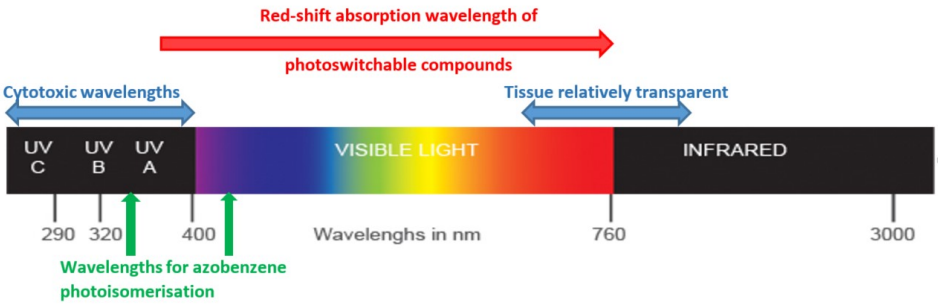


Figure 3.12. Illustration showing optimisation of photochemical properties of the azobenzene by red-shifting absorption wavelength.

3.1.4 Photoswitchable HDAC inhibitors

Given the Fuchter group's interest in epigenetics and more specifically HDAC inhibitors,[191,192] the decision was made to design and develop a photoswitchable HDAC inhibitor. HDAC inhibitors are well suited for this as: a) they have been extensively investigated and clinically validated, and hence are known to have a strong anti-tumourigenic effect;[167,170] b) the crystal structures of HDACs and HDAC-inhibitor complexes have been solved and the binding mode is well understood;[161–163,193] c) the pharmacophore of HDAC inhibition is known,[171,173,174] which will allow the design of photoswitchable variants of small molecule HDAC inhibitors with significant differences in potency between the two conformations, and; d) the cytotoxicity of HDAC inhibitors has been seen to

correlate well with their HDAC inhibitory potency, thus the two conformations of photoswitchable inhibitors should have different cytotoxicity profiles.[192] This should allow the selective destruction of tumour tissue, whilst leaving normal tissue unharmed, which is a major hurdle in conventional chemotherapy.

3.2 RESULTS AND DISCUSSION PART I: Azobenzene-based HDAC inhibitors

3.2.1 Preliminary work

An initial photoswitchable HDAC inhibitor (**57a**) was designed using known inhibitors as inspiration (Figure 3.13), consisting of a phenyl capping unit, an azobenzene linker, and a hydroxamic acid zinc binding group – this preliminary work was carried out by Dr Matthias Baud.[194] The tube-like entrance channel to the HDAC active site is approximately 5 Å wide at its narrowest point,[161] so only ligands with a cross-section smaller than this diameter are able to bind. Computational docking studies of *E*- and *Z*-**57a** with HDAC2 (pdb 3MAX)[163] indicated that when bound to the active site, *Z*-**57a** would have unfavourable steric interactions with amino acids lining the entrance channel, that would not be present in the *E*-**57a**–enzyme complex.[194] The two isomers should therefore exhibit two significantly different inhibitory activities, with the *Z*-isomer ideally being completely inactive. The preliminary study found *E*-**57a** to have an *in vitro* potency (IC_{50}) against HDAC1 of 0.478 µM.[194]

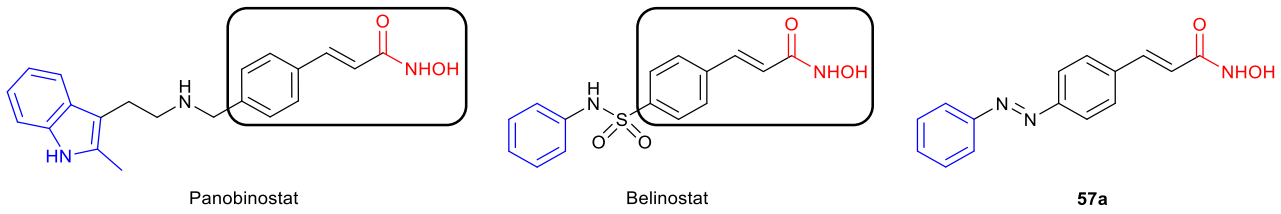


Figure 3.13. Initial photoswitchable HDAC inhibitor design (**57a**), incorporating the cinnamyl hydroxamic acid moiety seen in several HDAC inhibitors, such as Panobinostat and Belinostat. The cap, linker, and binding group sections of the inhibitors are highlighted in blue, black, and red respectively.

Irradiation of the **57a** at 355 nm led to a *Z*-rich photostationary state (PSS), while irradiation at 430 nm (or 532 nm) converted it back to an *E*-rich PSS (Figure 3.14). The thermal isomerisation half-life of *Z*-**57a** was approximately 29 hours at room temperature, demonstrating a comparable thermal stability to *Z*-azobenzene itself.[194] From this preliminary work, **57a** was identified as a suitable model compound.

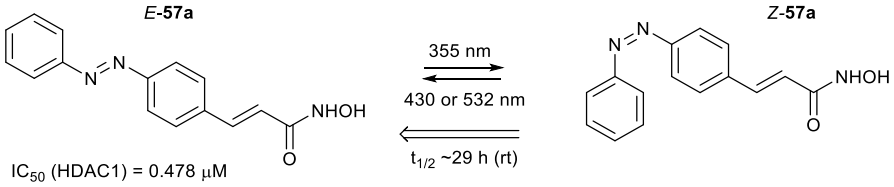


Figure 3.14. Photo- and thermal isomerisation of azobenzene **57a**.

3.2.2 Design of azobenzene HDAC inhibitors and stilbene isosteres

Initially, several analogues with *para*-substituents on the terminal aromatic ring were chosen for synthesis (Figure 3.15). The *tert*-butyl moiety (**57b**) will increase the steric hinderance on the terminal phenyl ring, and would therefore be expected to decrease the activity of the *Z*-isomer by inducing steric clashes with the amino acids lining the active site channel. The methoxy group (**57c**) was thought to decrease the lipophilicity of the molecule, and also provide an additional hydrogen bond acceptor.

Assessing the inhibitory activity of the *Z*-azobenzenes against HDACs is not as straightforward as for the *E*-isomers; firstly, quantitative photoswitching to the *Z*-isomer cannot be achieved, and secondly, the *Z*-isomer thermally isomerises back to the *E*-isomer. Both of these factors will affect the usefulness of the assay results. Therefore, stilbene isosteres **58a**-**c** (Figure 3.15) were prepared so that their inhibitory activity could be established as a model. *E*- and *Z*-stilbenes are both thermally stable and synthetically accessible, so this would allow the assay to be carried out on the pure *E*- and *Z*-isomers without any issue of thermal isomerisation. Comparison of the IC_{50} values for *E*-**58a**-**c** and *E*-**57a**-**c** would allow us to ascertain whether the alkene effectively mimics the azo functionality. If so, it would enable us to estimate the IC_{50} values for *Z*-**57a**-**c** from the *Z*-**58a**-**c** values.

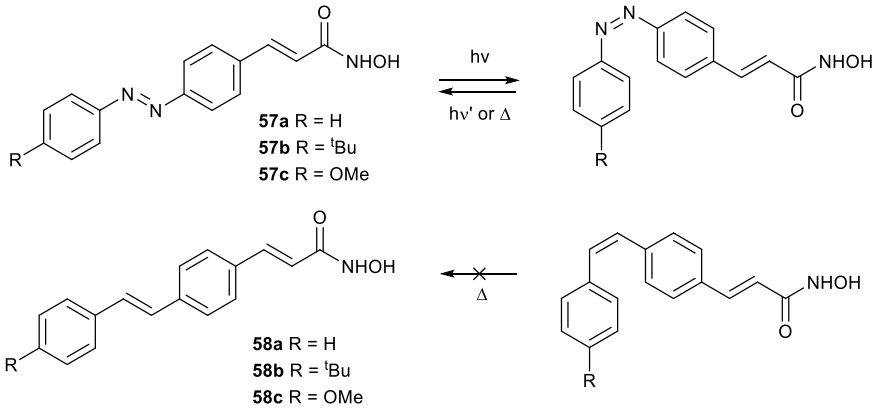
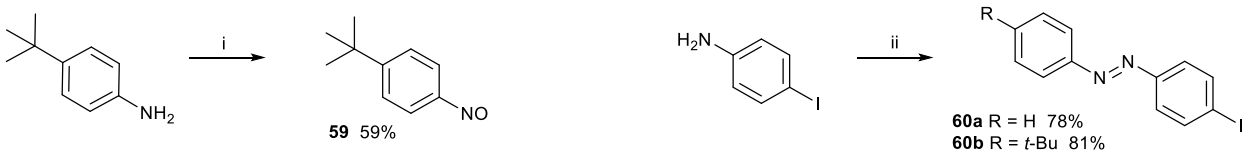


Figure 3.15. *E*- and *Z*-azobenzene HDAC inhibitors and thermally stable *E*- and *Z*-stilbene analogues.

3.2.3 Synthesis

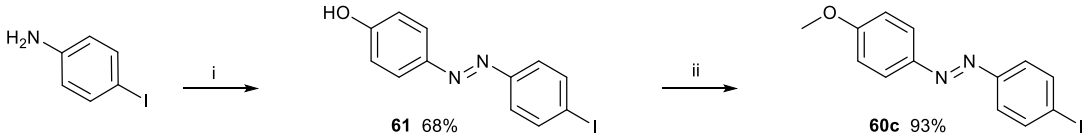
The azobenzene analogues **57a**-**c** were prepared using the general route developed in the preliminary studies.[194] Iodoazobenzenes **60a**-**b** were prepared in good yields by condensation of 4-iodoaniline with the appropriate nitrosobenzene in acetic acid *via* a Mills reaction (Scheme 3.2).[109,195] The *tert*-butylnitrosobenzene (**59**) required for the synthesis of **60b** is not commercially available, so was prepared by oxidation of 4-*tert*-butylaniline with Oxone®,[196] resulting in a green oil that decomposed slowly. Preparation of the methoxy iodoazobenzene analogue **60c** was

attempted by the same method, however oxidation of 4-methoxyaniline with Oxone® resulted in an inseparable mixture of the nitroso and nitro products.



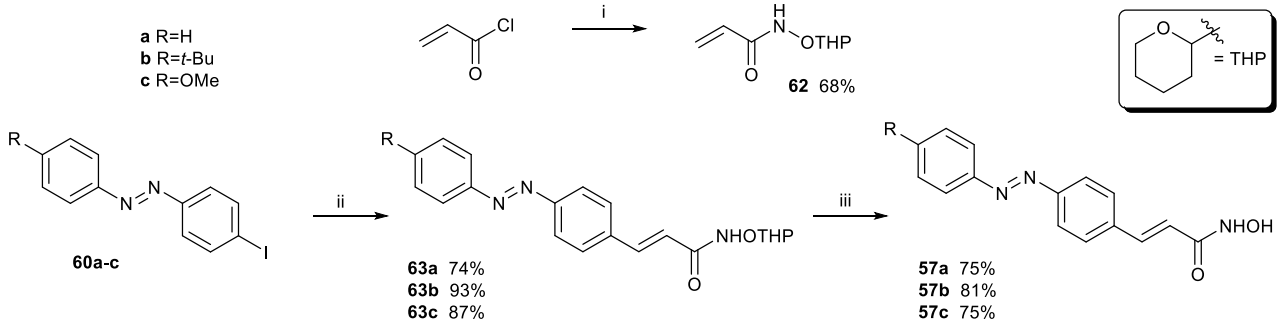
Scheme 3.2. Synthesis of iodoazobenzenes **60a**-**b**. Reagents and conditions: (i) aq. Oxone®, DCM, rt, o/n; (ii) nitrosobenzene or **59**, AcOH, 40 °C, o/n.

An alternative procedure reported by Tibiletti and co-workers using nitrosonium tetrafluoroborate and anisole was attempted,[197] but this also resulted in a mixture of nitroso and nitro products, both *ortho*- and *para*-substituted. The strong electron donating nature of the methoxy moiety is presumably the cause of over-oxidation to the nitrobenzene. Iodoazobenzene **60c** was instead prepared in two steps by first forming the diazonium salt from 4-iodoaniline, which underwent electrophilic aromatic substitution with phenol to afford **61**,[105] followed by methylation,[198] in an overall yield of 63% (Scheme 3.3).



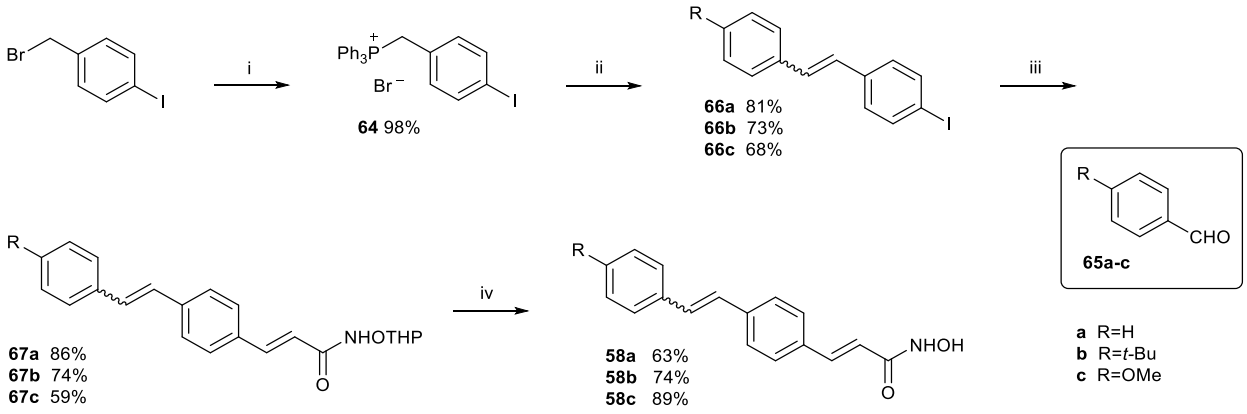
Scheme 3.3. Synthesis of iodoazobenzene **60c**. Reagents and conditions: (i) conc. HCl, aq. $NaNO_2$, 1:1 acetone:H_2O, 0 °C, 1 h; then phenol, Na_2CO_3, NaOH in 1:1 acetone:H_2O, 0 °C to rt, 3 h; (ii) K_2CO_3, Cs_2CO_3, DMF, MeI, rt, 6 h.

With iodoazobenzenes **60a**-**c** in hand, Heck coupling was carried out with THP-protected *N*-hydroxyacrylamide **62**, which was prepared from acryloyl chloride and THP-protected hydroxylamine in 68% yield (Scheme 3.4). Heck coupling between aryl halides and *N*-hydroxyacrylamide derivatives has previously been established,[199,200] including in the synthesis of HDAC inhibitors.[200] The Heck coupling furnished the protected hydroxamates **63a**-**c** in high yields, which were subsequently deprotected with catalytic pyridinium *p*-toluene sulfonate (PPTS) to afford hydroxamic acids **57a**-**c**. The overall yields for the synthesis of **57a**-**c** were 43%, 36%, and 41% respectively.



Scheme 3.4. Synthesis of azobenzene-based HDAC inhibitors. Reagents and conditions: (i) NH_2OTHP, NEt_3, DCM, 0 °C to rt, 24 h; (ii) **62**, $Pd(OAc)_2$, P(*o*-tol)$_3$, NEt_3, DMF, 100 °C, 24 h; (iii) cat. PPTS, 1:1 THF:*i*-PrOH, 80 °C, o/n (50 °C, 8 h for R=H).

Preparation of the stilbene isosteres commenced with a Wittig reaction between the benzyl phosphonium salt **64** and benzaldehydes **65a-c** (Scheme 3.5).[201] Iodostilbenes **66a**-**c** were afforded as a mixture of their *E*- and *Z*-isomers (Table 3.1). The variation in the required reaction time is presumably caused by the differences in reactivity of the aldehydes. Due to difficulties in separating the isomers at this stage, Heck coupling with THP-protected *N*-hydroxyacrylamide **62** was carried out on the isomeric mixtures of **66a**-**c** to give hydroxamates **67a**-**c** in 59-86% yield. THP deprotection was then carried out with catalytic PPTS to afford the final compounds **58a**-**c** as a mixture of isomers in yields of 63-89% (Scheme 3.5).



Scheme 3.5. Synthesis of stilbene analogues. Reagents and conditions: (i) PPh_3, PhMe, reflux, 8 h; (ii) **65a**-**c**, LiOH, *i*-PrOH, reflux; (iii) **62**, $Pd(OAc)_2$, P(*o*-tol)$_3$, NEt_3, DMF, 100 °C, 24 h; (iv) cat. PPTS, 1:1 THF:*i*-PrOH, 80 °C, o/n (50 °C for R=H).

Product	R	Reaction time / h	Yield / %	*E/Z*
66a	H	1	81	2:3
66b	^{t}Bu	1	73	2:3
66c	OMe	6	68	3:7

Table 3.1. Wittig reaction with different *para*-substituents.

The difference in solubility between the *E*- and *Z*-isomers of **58a**-**c** allowed them to be separated by filtration from DCM. The *E*-isomers were insoluble in DCM, whereas the *Z*-isomers were soluble; this difference in solubility was seen in the majority of solvents tested and is presumably due to the different conformations of the two isomers. The *E*-isomer is planar, hence there are extensive intermolecular interactions, such as π-π stacking, between the individual molecules, resulting in poor solubility, whereas the *Z*-isomer exists in a twisted conformation, resulting in weaker intermolecular interactions and the observed increase in solubility. The final compounds **58a**-**c** were afforded in overall yields of 44%, 40%, and 36% respectively.

3.2.4 Photoswitching

UV/vis spectra were recorded for azobenzenes **57a-c** in DMSO, due to lack of solubility in acetonitrile, and photoswitching was carried out using UVA (λ_{max} ~ 365 nm) or green (532 nm) light (Figure 3.16). Upon irradiation with UVA light, all three analogues were switched to PSSs containing 85-90% *Z*-isomer. Irradiating with 532 nm monochromatic light led to PSSs containing 74-82% *E*-isomer.

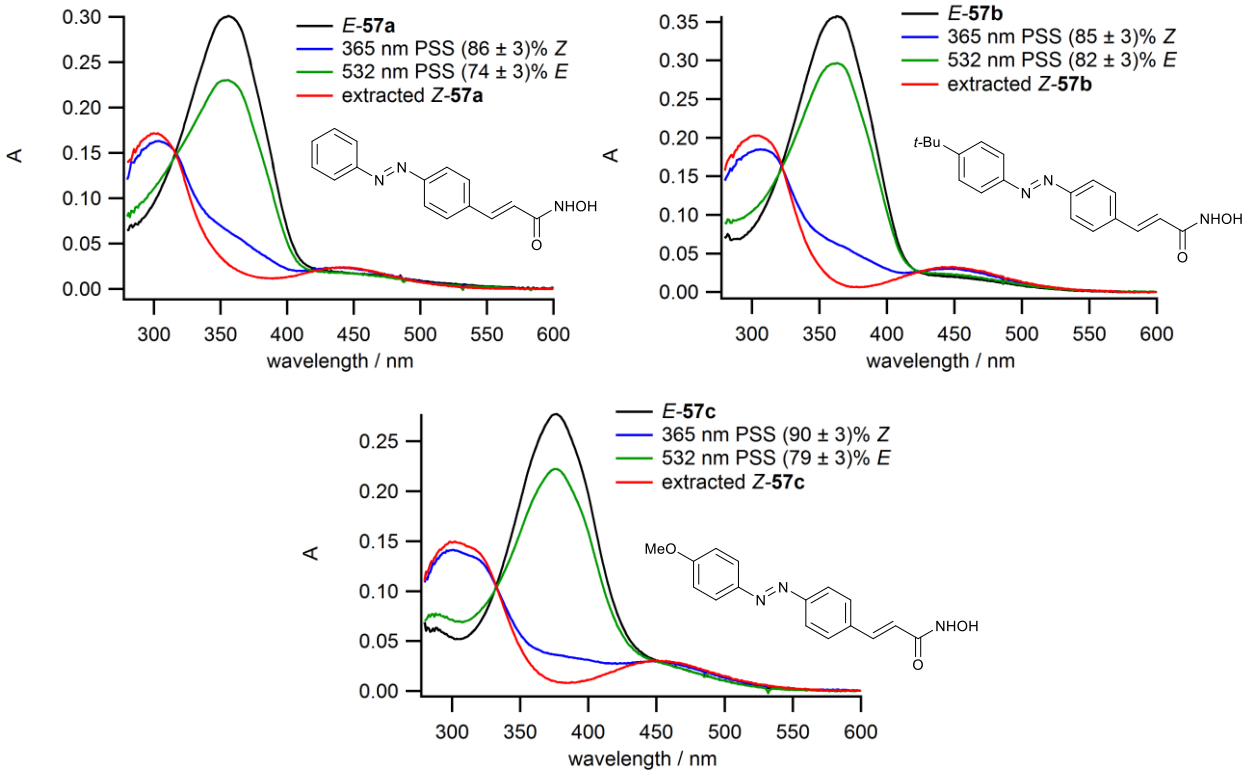


Figure 3.16. UV/vis spectra of **57a-c** recorded in DMSO at 1 × 10^{-5} M concentration; *E*-isomers, UVA (λ_{max} ~365 nm) and 532 nm PSS, and extracted pure *Z*-isomer spectra.

NMR spectroscopy was used to quantify the PSS compositions, from which the pure *Z*-isomer spectra were extracted (Figure 3.16). Previously, in section 2.2.3, this was achieved by recording a ^{1}H NMR of the *Z*-rich PSS at ~10^{-2} M concentration, however, for these compounds, the 365 nm (UVA) PSS was not reached after prolonged irradiation of the concentrated sample. Therefore, the *E/Z* composition of the irradiated concentrated sample was obtained by NMR (Figure 3.17, B), and the sample was diluted to 10^{-5} M to allow comparison with the spectra that had previously been recorded at 10^{-5} M (Figure 3.17, A). The *Z*-isomer spectrum and PSS compositions were then obtained as detailed in section 2.2.3.

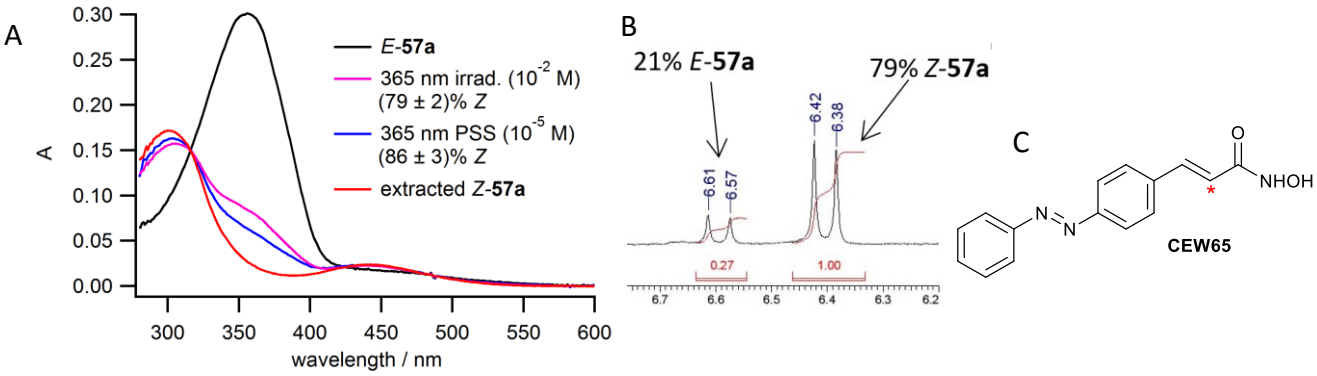


Figure 3.17. A) UV/vis spectra of **57a**; *E*-isomer, 365 nm PSS (irradiated at 10^{-5} M), the ~10^{-2} M NMR sample irradiated with 365 nm light (diluted to 10^{-5} M here) from which the *E/Z* compositions were obtained, and the extracted pure *Z*-isomer spectrum; B) The ratio of isomers present in the NMR spectrum, using the alkene signal shown in C). For full spectra for **57a**-**c** see Appendix 7.3.2.

The absorption maxima (λ_{max}) of the analogues were very similar (Table 3.2). The π-π* absorption maxima for *E*-**57b** and *E*-**57c** were slightly red-shifted relative to *E*-**57a**, due to the increased conjugation caused by the presence of *para*-electron donating groups (*tert*-butyl and methoxy for **57b** and **57c** respectively). The molar extinction coefficients (ε) were all fairly similar, with the majority within error margins of each other. λ_{max} and ε values for the *E*-isomer n-π* transitions have been included to give a rough idea of the position and intensities of these transitions, however they are not accurate due to the slight overlap in the π-π* and n-π* absorbances.

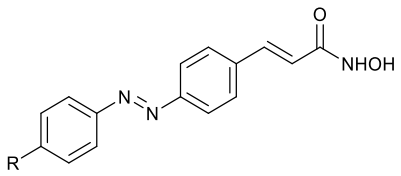
	E-isomer π-π*		*E*-isomer n-π*		*Z*-isomer π-π*		*Z*-isomer n-π*	
	λ_{max} / nm	$10^{-2} \times \varepsilon$ / M^{-1} cm^{-1}	λ_{max} / nm	$10^{-2} \times \varepsilon$ / M^{-1} cm^{-1}	λ_{max} / nm	$10^{-2} \times \varepsilon$ / M^{-1} cm^{-1}	λ_{max} / nm	$10^{-2} \times \varepsilon$ / M^{-1} cm^{-1}
57a	356	301 ± 41	440-450	18 ± 2.4 [a]	300	172 ± 24	443	23.8 ± 3.3
57b	363	357 ± 46	440-450	20 ± 2.6 [a]	304	203 ± 26	448	32.5 ± 4.2
57c	376	277 ± 29	440-450	34 ± 3.6 [a]	304	149 ± 16	451	31.0 ± 3.3

Table 3.2. Spectral data for **57a**-**c**. [a] There is still a small amount of π-π* absorbance at this wavelength, so these values are not accurate. All *Z*-isomer values are for the extracted *Z*-isomer spectrum.

3.2.5 Thermal isomerisation kinetics

The thermal isomerisation rates of the azobenzenes were measured in aqueous buffer at 30 °C, using UV/vis spectroscopy (Table 3.3). These conditions mimic those of the biological assay (see section 3.2.6). Azobenzene **57b** was found to be insufficiently soluble in the buffer, with either 100-fold or 10-fold dilutions from DMSO, therefore the kinetics were measured in DMSO. Kinetic data was also obtained for the other analogues in DMSO to allow comparison (Table 3.3). Azobenzenes **57b**-**c** both had faster thermal isomerisation rates than **57a**, due to the combination

of a *para*-electron donating group (*tert*-butyl or methoxy) and a *para*-electron withdrawing *N*-hydroxyacrylamide leading to a push-pull system.

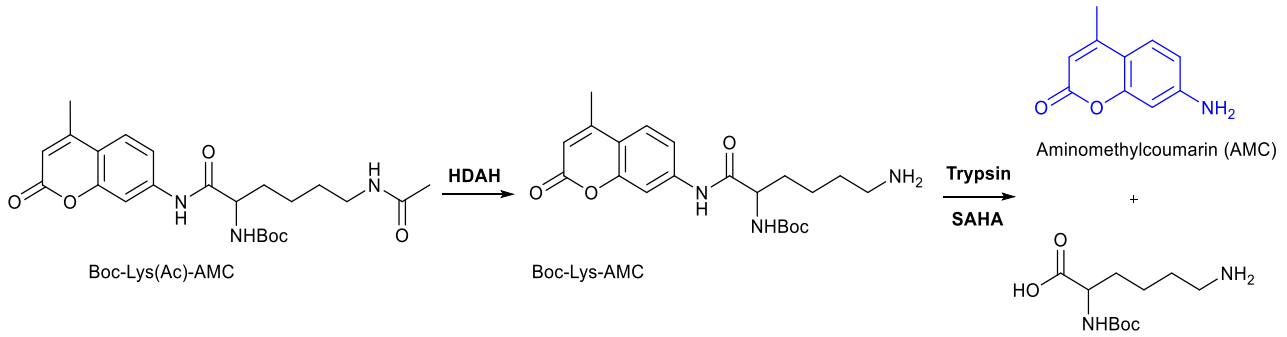


	R	Rate / s^{-1}		Half-life / h	
		buffer	DMSO	buffer	DMSO
57a	H	1.5×10^{-5}	2.2×10^{-5}	12.9	8.9
57b	*t*-Bu	- [a]	6.5×10^{-5}	- [a]	3.0
57c	OMe	3.4×10^{-5}	1.1×10^{-4}	5.7	1.6

Table 3.3. Thermal isomerisation kinetics at 30 °C. Graphs are provided in Appendix 7.3.2. [a] Not measured due to insolubility in buffer.

3.2.6 Biochemistry

All assays were carried out by either Dr Michael Korbus or Andreas Krämer in the Meyer-Almes group at the University of Applied Sciences, Darmstadt. The inhibitory activity of compounds **57a**-**c** and **58a**-**c** was initially tested against histone deacetylase-like amidohydrolase (HDAH) using a cell-free fluorogenic assay. HDAH is a bacterial enzyme with high sequence homology to the HDAC family,[202] and is one of several such enzymes to belong to the HDAC superfamily.[203] HDAH has been shown to be an excellent model for HDACs – a co-crystal structure has been obtained and the enzyme is well-established for use in biological assays.[192,204–208] The key steps of the fluorogenic assay are shown in Scheme 3.6.[192,209,210] The acetamide bond in the Boc-Lys(Ac)-AMC substrate is first cleaved by HDAH to release Boc-Lys-AMC. Trypsin (a peptidase) then cleaves the amide bond of the deacetylated substrate only, which releases the fluorescent molecule – aminomethylcoumarin (AMC). The activity of the enzyme is indirectly obtained by measuring the intensity of the fluorescence.[209,210] The assay can be carried out as either a continuous assay or an endpoint assay. In the continuous assay, the inhibitor and protein are incubated and the reaction is then started with the substrate and trypsin. The enzyme activity is determined from the slope of the fluorescence signal against time. In the endpoint assay, the reaction is carried out with the substrate only, and after a set time, a stop solution containing SAHA and trypsin is added. The enzyme activity is then determined by the final fluorescent signal. This second assay has to be used for human HDACs, as trypsin digests the enzyme so it cannot be present while the assay is taking place; this does not occur for the bacterial HDACs, so the continuous assay (which is more accurate) can be used.



Scheme 3.6. Key steps of the cell-free fluorogenic assay.

One caveat when using azobenzenes in fluorogenic assays is the need to ensure that the excitation and emission wavelengths of the fluorescent molecule do not cause photoisomerisation, which would affect the assay results. Another potential issue is that the azobenzene could quench the fluorescence of AMC, and hence reduce the fluorescent signal measured. With the endpoint assay, these potential issues are not a concern, as the fluorophore is not released until after the assay has been stopped, however with the continuous assay the fluorescent signal is measured during the course of the assay. The excitation and emission wavelengths of AMC are 340 and 460 nm respectively, which coincide with *E*- and *Z*-azobenzene absorbances. The intensity of the excitation wavelength is weak compared to the light sources used to switch azobenzene and the pulses are very short (nanoseconds to microseconds), so it is extremely unlikely that any photoisomerisation could occur. To check that fluorescence quenching was not occurring, the fluorescent signal of AMC was measured in the presence of different concentrations of inhibitor – signal intensity was found to be independent of inhibitor concentration.

	R	Compound	IC_{50} value / nM
Azobenzenes	H	*E*-**57a**	15.9
	t-Bu	*E*-**57b**	37.8
	OMe	*E*-**57c**	14.4
Stilbenes	H	*E*-**58a**	12.8
		Z-**58a**	6.8
	t-Bu	*E*-**58b**	27.1
		Z-**58b**	95.5
	OMe	*E*-**58c**	22.3
		Z-**58c**	13.5
		SAHA	37.3

Table 3.4. Initial fluorogenic assay of *E*-azobenzenes and *E*- and *Z*-stilbenes against HDAH.

In the initial continuous fluorogenic assay against HDAH, the *E*-azobenzenes **57a**-**c** and the *E*- and *Z*-stilbenes **58a**-**c** were tested. Both *E*-**57a**-**c** and *E*-**58a**-**c** were found to have excellent inhibitory activity with IC_{50} values between 13 and 38 nM (Table 3.4). The known HDAC inhibitor, SAHA, was

also assayed as a positive control and the azobenzenes were all found to have similar or improved IC_{50} values compared to its value. The similarity between the IC_{50} values for the *E*-stilbenes and *E*-azobenzenes suggests that the *E*-stilbenes are a suitable model for the *E*-azobenzenes, and accordingly the *Z*-stilbenes should be a suitable model for the *Z*-azobenzenes. The *Z*-stilbenes were expected to have poor inhibitory activity towards HDAH, due to a predicted steric clash between the terminal phenyl ring (*para*-substituted in the case of **58b**-**c**) and the amino acids lining the active site channel. *Z*-**58b** was found to have a 4-fold decrease in inhibition relative to *E*-**58b**, however *Z*-**58a** and *Z*-**58c** actually had slightly improved inhibition relative to their *E*-isomers. From these results it appears that the **58b** was the only analogue with a sufficiently sterically demanding *para*-substituent to induce unfavourable interactions upon the *Z*-isomer binding to the enzyme active site.

More recently, once the Meyer-Almes group had obtained the required set up in order to carry out photoswitching on the azobenzenes, additional assays were carried out on both the *E*- and *Z*-azobenzenes and stilbenes. The continuous fluorogenic assay was carried out with the following bacterial enzymes; HDAH, Pa0321, Pa3774, and Pa1409. The latter three enzymes are acetylpolyamine amidohydrolases (APAHs) obtained from *Pseudomonas aeruginosa* and they also belong to the HDAC superfamily.[203] *P. aeruginosa* is a pathogen that can cause severe and life threatening infections – it is responsible for hospital-acquired infections and is capable of becoming multi-drug resistant.[211] Targeting biofilms is a key strategy to treating these infections, as they are the cause of persistent infections and are resistant to conventional antibiotic treatments.[212] Since polyamines are known to be essential to the formation of biofilms,[213] and APAHs are involved in polyamine metabolism,[214] this family of enzymes has the potential to interfere with biofilm formation and therefore treat infections. The Meyer-Almes group have an interest in this family, having recently developed a new fluorescence lifetime-based binding assay for APAHs.[215] Assays were also carried out on human HDACs; class I (HDACs 1, 2, and 3) and class IIa (HDACs 4, 5, and 7), using the endpoint fluorogenic assay. Further assays are being carried out in order to improve the sigmoidal fits obtained for the IC_{50} curves and to confirm the reproducibility of the data for both the bacterial and human HDACs. Additional assays are also being carried out on HDACs 6 and 8.

The IC_{50} values (in µM) for both bacterial and human HDACs are shown in Table 3.5 and Table 3.6. For ease of comparison between the *E*- and *Z*-isomers of the azobenzenes and stilbenes, log IC_{50} values (in nM) were plotted for the different analogues (Figure 3.18).

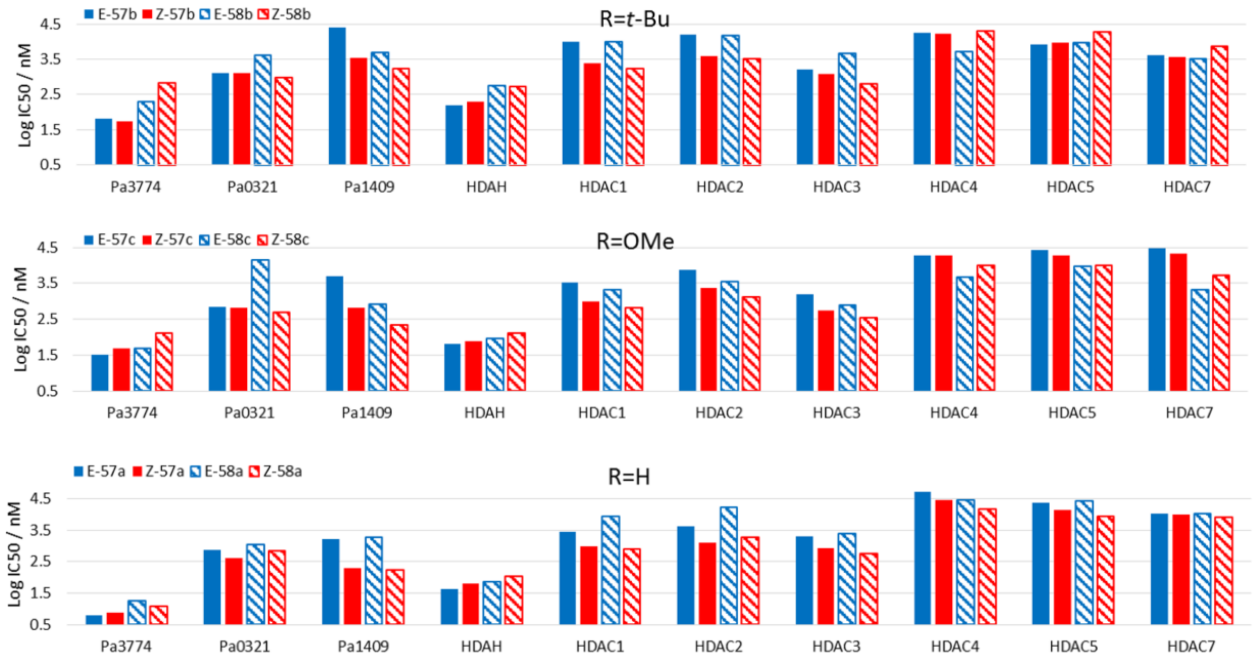
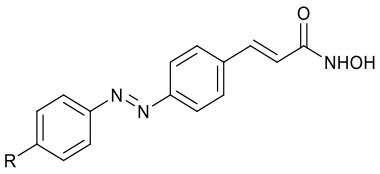
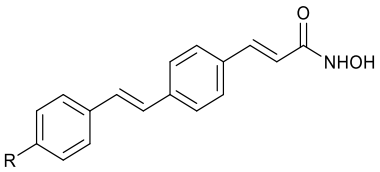


Figure 3.18. Log IC_{50} values for the *E*- and *Z*-azobenzenes and stilbenes with different R substituents, against bacterial and human HDACs.

The azobenzenes tested all achieved good inhibition of the bacterial HDACs (Table 3.5), with submicromolar IC_{50} values seen for the majority of inhibitor-enzyme combinations. The best inhibitory activities (*i.e.* smallest IC_{50} values) were achieved against Pa3774, however there was little difference in activity between the *E*- and *Z*-azobenzenes and only small activity differentials for the stilbenes. The best activity differentials for the azobenzenes were obtained for Pa1409, with the *Z*-azobenzenes 7- to 9-fold more active than the *E*-azobenzenes. The stilbenes also showed comparable activity differentials against Pa1409, however the best result was obtained against Pa0321, where *Z*-**58c** was 29-fold more active than *E*-**58c**. The best overall azobenzene-bacterial HDAC combination was Pa1409 and **57a** with IC_{50} values of 0.2 μM for the *Z*-isomer and 1.7 μM for the *E*-isomer. The *tert*-butyl analogues (**57b** and **58b**) had weaker inhibitory activity than the other compounds, presumably due to unfavourable interactions occurring in both isomers between the *tert*-butyl group and amino acids lining the active site channel. Additionally, for Pa0321 and Pa1409, the *Z*-azobenzene or *Z*-stilbene was always the more active isomer, whereas for Pa3774 and HDAH the *E*-isomer was the more active isomer in the majority of assays.





			IC_{50} value / μM			
		R	Pa3774	Pa0321	Pa1409	HDAH
Azobenzenes	*E*-**57a**	H	0.0063 ± 0.0002	0.75 ± 0.03	1.7 ± 0.2	0.042 ± 0.007
	Z-**57a**		0.0076 ± 0.0003	0.40 ± 0.02	0.20 ± 0.004	0.064 ± 0.007
			< 2-fold	2-fold	9-fold	< 2-fold
	E-**57b**	*t*-Bu	0.064 ± 0.005	1.3 ± 0.1	26 ± 2	0.16 ± 0.03
	Z-**57b**		0.056 ± 0.004	1.3 ± 0.07	3.5 ± 0.09	0.20 ± 0.03
			< 2-fold	< 2-fold	7-fold	< 2-fold
	E-**57c**	OMe	0.033 ± 0.002	0.68 ± 0.08	5.1 ± 0.2	0.063 ± 0.005
	Z-**57c**		0.048 ± 0.002	0.64 ± 0.04	0.67 ± 0.03	0.079 ± 0.006
			< 2-fold	< 2-fold	8-fold	< 2-fold
Stilbenes	*E*-**58a**	H	0.018 ± 0.0006	1.1 ± 0.1	1.9 ± 0.1	0.072 ± 0.01
	Z-**58a**		0.012 ± 0.0005	0.68 ± 0.03	0.17 ± 0.008	0.11 ± 0.02
			< 2-fold	< 2-fold	11-fold	< 2-fold
	E-**58b**	*t*-Bu	0.20 ± 0.01	4.2 ± 0.2	5.0 ± 0.2	0.57 ± 0.1
	Z-**58b**		0.67 ± 0.02	0.95 ± 0.04	1.7 ± 0.07	0.54 ± 0.05
			3-fold	4-fold	3-fold	< 2-fold
	E-**58c**	OMe	0.049 ± 0.002	14 ± 12	0.81 ± 0.02	0.090 ± 0.01
	Z-**58c**		0.13 ± 0.005	0.48 ± 0.03	0.22 ± 0.01	0.13 ± 0.02
			3-fold	29-fold	4-fold	< 2-fold
	SAHA		0.037 ± 0.003	0.50 ± 0.04	0.30 ± 0.04	0.095 ± 0.003

Table 3.5. IC_{50} values with standard errors for *E*- and *Z*-azobenzenes and stilbenes against bacterial HDACs, with SAHA as a positive control. Z-azobenzenes (*Z*-**57a**-**c**) refer to the 365 nm *Z*-rich PSS. Activity differential between the *E*- and *Z*-isomers is shown in purple. See Appendix 7.5 for graphs.

Comparing these assay results against HDAH with the assay carried out previously (Table 3.4), the new IC_{50} values were slightly higher than initial values recorded, but the majority were still within the same order of magnitude. The most noticeable deviation is that in the initial HDAH assay (Table 3.4), *Z*-**58b** was 4-fold less active than *E*-**58b**, whereas in the repeated assay, the difference in activity between the two isomers was negligible (Table 3.5). These differences may have been due to different batches of enzymes being used in the two assays – this is capable of leading to variation is results.[216] The more recent results (Table 3.5) are likely to be more reliable as the assays were not only carried out in triplicate, as the initial assays were, but experiments were also repeated if the data points did not produce satisfactory sigmoidal curves.

			IC_{50} value / μM					
		R	HDAC1	HDAC2	HDAC3	HDAC4	HDAC5	HDAC7
Azobenzenes	*E*-**57a**	H	2.9 ± 0.2	4.1 ± 0.2	2.0 ± 0.2	52 ± 0.1	24 ± 2	11 ± 1
	Z-**57a**		0.99 ± 0.04	1.3 ± 0.06	0.85 ± 0.05	28 ± 0.2	14 ± 0.8	10 ± 1
			3-fold	3-fold	2-fold	< 2-fold	< 2-fold	< 2-fold
	E-**57b**	*t*-Bu	10 ± 0.4	16 ± 0.8	1.6 ± 0.1	18 ± 1	8.3 ± 0.7	4.1 ± 0.3
	Z-**57b**		2.4 ± 0.08	3.8 ± 0.09	1.2 ± 0.08	17 ± 0.6	9.2 ± 1	3.7 ± 0.3
			4-fold	4-fold	< 2-fold	< 2-fold	< 2-fold	< 2-fold
	E-**57c**	OMe	3.4 ± 0.7	7.4 ± 0.3	1.6 ± 0.2	19 ± 1	27 ± 1	31 ± 2
	Z-**57c**		0.97 ± 0.06	2.3 ± 0.07	0.55 ± 0.04	19 ± 1	19 ± 0.7	21 ± 2
			4-fold	3-fold	3-fold	< 2-fold	< 2-fold	< 2-fold
Stilbenes	*E*-**58a**	H	8.5 ± 0.7	17 ± 0.7	2.4 ± 0.5	29 ± 0.06	27 ± 1	11 ± 0.7
	Z-**58a**		0.80 ± 0.03	1.9 ± 0.05	0.59 ± 0.03	15 ± 0.08	9.0 ± 0.7	8.0 ± 1
			11-fold	9-fold	4-fold	< 2-fold	3-fold	< 2-fold
	E-**58b**	*t*-Bu	10 ± 0.4	15 ± 0.3	4.5 ± 0.7	5.1 ± 0.2	9.1 ± 1	3.2 ± 0.2
	Z-**58b**		1.7 ± 0.08	3.2 ± 0.07	0.65 ± 0.05	20 ± 0.6	19 ± 7	7.3 ± 0.8
			6-fold	5-fold	7-fold	4-fold	2-fold	2-fold
	E-**58c**	OMe	2.1 ± 0.3	3.5 ± 0.07	0.78 ± 0.03	4.6 ± 0.2	9.7 ± 0.4	2.1 ± 0.1
	Z-**58c**		0.66 ± 0.03	1.3 ± 0.03	0.35 ± 0.01	10 ± 0.3	10 ± 0.6	5.4 ± 0.3
			3-fold	3-fold	2-fold	2-fold	< 2-fold	3-fold
	SAHA		0.062 ± 0.04	0.17 ± 0.008	0.054 ± 0.003	27 ± 4	24 ± 3	12 ± 0.9

Table 3.6. IC_{50} values with standard errors for *E*- and *Z*-azobenzenes and stilbenes against human HDACs, with SAHA as a positive control. Z-azobenzenes (*Z*-**57a**-**c**) refer to the 365 nm *Z*-rich PSS. Activity differential between the *E*- and *Z*-isomers is shown in purple. See Appendix 7.5 for graphs.

For the human HDAC assays carried out to date (Table 3.6 and Figure 3.18), weaker inhibitory activity was seen compared to the bacterial HDACs, with particularly poor inhibition of the class IIa HDACs (4, 5, 7). The best activity differentials for the azobenzenes were seen for HDACs 1 and 2, with a 4-fold decrease in activity for *Z*-**57b** compared to *E*-**57b**. This was the compound with the largest cap group. These results weren't matched as well by the stilbenes, where the best activity differentials were achieved for **58a** rather than **58b**. In all assays against the class I HDACs and the majority of assays against the class IIa HDACs, the *Z*-isomer was the more active isomer.

Across both bacterial and human HDAC assays, the *Z*-isomers of both the azobenzenes and stilbenes were generally more active than the *E*-isomers, especially where large activity differentials were achieved. These findings contradict our expectation that the *Z*-isomer would be a weaker inhibitor than the *E*-isomer (section 3.2.1).[194] Clearly, for the majority of inhibitor-enzyme combinations, there are more unfavourable interactions between the *E*-isomer and the active site channel than for the *Z*-isomer. In general, the IC_{50} values for the stilbenes were within an order of magnitude of the values for the azobenzenes and in most cases they predicted the trends seen in the azobenzenes

(Figure 3.18). The trends were less well predicted for the class IIa HDACs, where poor inhibitory activity was seen. For the majority of enzymes, the stilbenes predicted the correct order of inhibitory activity (*i.e.* lowest to highest IC_{50} value) seen for the azobenzenes, in terms of the different substitution patterns. Similarly for each substitution pattern, the correct order of activity was generally predicted in terms of the different enzymes (Figure 3.18). Larger *E*- and *Z*-isomer activity differentials were seen for the stilbenes compared to the azobenzenes. This is at least partially due to incomplete photoswitching to the *Z*-azobenzenes, so the IC_{50} values obtained are actually for the *Z*-rich photostationary states, rather than for the pure *Z*-isomers. Overall, these findings indicate that the *E*- and *Z*-stilbenes can be used as azobenzene mimics in order to identify trends in inhibitory activity. This is useful for initial assays, as it removes the requirement for photoswitching, and as both *E*- and *Z*-stilbenes are thermally stable, thermal isomerisation does not have to be taken into account.

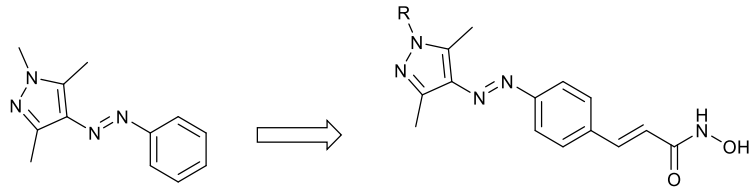
Since commencing this work, there have been publications from two research groups concerning photoswitchable HDAC inhibitors. This is perhaps unsurprising given the current growth in the field of photopharmacology and the ease at which an azobenzene can be incorporated into the HDAC inhibitor pharmacophore. In 2014, a patent for photoswitchable HDAC inhibitors was published.[217] The inventors, Mazitschek and co-workers, developed a wide range of azobenzene-containing hydroxamic acid and benzamide inhibitors, none of which contained the cinnamyl hydroxamic acid unit used in this work, for potential use in cancer chemotherapy. Further details of this research have just been published, focusing on photoswitchable benzamide inhibitors that have very fast thermal isomerisation rates, with an emphasis on controlling gene expression with light.[218] A paper has also been published by Feringa and co-workers on the development of photoswitchable HDAC inhibitors for use in photopharmacology.[219] They synthesised a range of different azobenzene-hydroxamic acid inhibitors, and carried out assays on class I and IIb HDACs. One of their inhibitors had the same structure as **57c**, and this actually gave the best results out of all their compounds. A 40-fold difference in activity was seen between the *E*- and *Z*-isomers for HDAC2 in the fluorogenic assay. In comparison, our assay of **57c** against HDAC2 only gave a 3-fold activity differential between *E*- and *Z*-isomers. Consistent with our work, the active isomer was found to be the *Z*-isomer for the class I HDACs (1, 2, and 3). They did not test class IIa enzymes, only class IIb, so further comparisons cannot be made. An *in vivo* assay was also carried out where, at a 100 μM concentration, the *Z*-isomer killed the majority of the cells while the *E*-isomer left nearly all the cells intact.[219] The stability

of their inhibitors towards reduction in the cellular environment was also tested by carrying out repeated photoswitching cycles in glutathione.

3.3 RESULTS AND DISCUSSION PART II: Arylazopyrazole-based HDAC inhibitors

3.3.1 Design of arylazopyrazole HDAC inhibitors

Extending the work on the azobenzene HDAC inhibitors, the azoheteroarene photoswitches developed in Chapter 2 were incorporated into the inhibitor scaffold. Several of these photoswitches had improved photoconversions and longer thermal half-lives compared to azobenzene – properties that are desirable for use in photopharmacology. Of the azoheteroarenes studied, arylazopyrazole **24** was chosen as this could be quantitatively photoswitched between both *E*- and *Z*-isomers and also had a slow thermal half-life of 10 days.



24

68a R = Me
68b R = benzyl
68c R = naphthyl

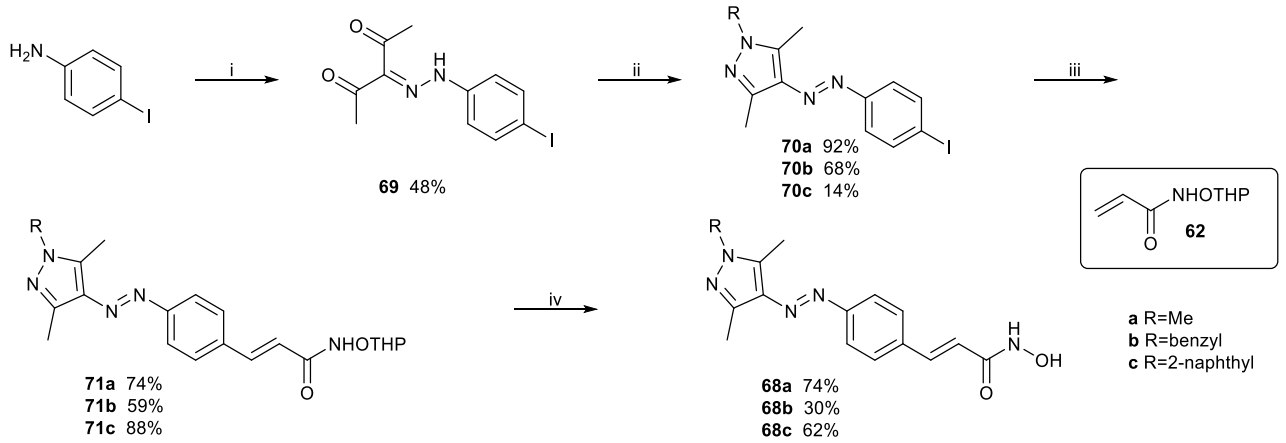
Figure 3.19. New HDAC inhibitor design incorporating azopyrazole **24**.

Three analogues were chosen initially, with different substituents at the pyrazole nitrogen (Figure 3.19). Given the results with the azobenzene HDAC inhibitors, benzyl and naphthyl substituents were chosen as they were expected to be bulky enough to cause unfavourable steric interactions between one isomer and the active site channel and therefore decrease the inhibitory activity seen relative to the other isomer. A methyl substituent was also chosen in order to provide a less bulky analogue for comparison. As mentioned in Chapter 2, the presence of an NH on the pyrazole ring can lead to fast *Z*-*E* thermal isomerisation rates through an azo-hydrazone tautomerisation mechanism, so the corresponding analogue was avoided.[97,101]

3.3.2 Synthesis

Azopyrazoles **70a**-**c** were prepared *via* the synthetic route used previously for the synthesis of **24**. The diazonium salt prepared from 4-iodoaniline was coupled with acetylacetone to give **69**, which was then condensed with the required hydrazine to give the azopyrazoles (Scheme 3.7). The yield obtained for the diazonium coupling was substantially lower than that obtained for the non-iodinated analogue **27** (see section 2.2.2), however, considering the availability of the starting materials for this particular substrate, time was not spent optimising the yield. Good yields were

obtained for **70a**-**b** in the pyrazole ring-forming step, with the yellow-orange products crystallising out of solution. For **70c** however, the suspension that formed during the reaction contained several yellow products, and several other compounds were also in solution, as identified by TLC and NMR spectroscopy. The reaction mixture was therefore concentrated and purified by column chromatography in order to obtain **70c** in 14% yield. With azopyrazoles **70a**-**c** in hand, Heck coupling was carried out with THP-protected *N*-hydroxyacrylamide **62** to afford **71a**-**c** in 59-88% yields (Scheme 3.7). A final THP deprotection using catalytic PPTS afforded the final compounds **68a**-**c** in 30-74% yield.



Scheme 3.7. Synthesis of arylazopyrazole-based HDAC inhibitors. Reagents and conditions. (i) aq. $NaNO_2$, conc. HCl, AcOH, 0 °C, 1 h; then add to acetylacetone, NaOAc, EtOH:H_2O, rt, 1 h; (ii) NH_2NHR, EtOH, reflux, 6 h – o/n; iii) **62**, NEt_3, P(o-tol)$_3$, DMF, 100 °C, 24 h; (iv) cat. PPTS, *i*-PrOH:THF, 50 °C, o/n.

3.3.3 Photoswitching

The UV/vis spectra of **68a**-**c** were measured in DMSO (Figure 3.20), due to limited solubility in acetonitrile, and all three compounds were photoswitched with UVA light (λ_{max} ~ 365 nm) and monochromatic green (532 nm) light. On irradiating with 365 nm light, the PSSs reached contained 93-97% *Z*-isomer; in comparison the azobenzene-based inhibitors studied in section 3.2.4 only contained 85-90% *Z*-isomer in their 365 nm PSSs. A similar improvement in photoconversion was seen upon irradiation with 532 nm light, with 92-93% *E*-isomer present in the azopyrazole PSSs (Figure 3.20) compared to 74-82% in the PSSs of the azobenzene-based inhibitors (section 3.2.4). These improved photoconversions for the azopyrazole-based inhibitors are due to better separation of absorbances between *E*- and *Z*-azopyrazole compared to *E*- and *Z*-azobenzene. PSS compositions were obtained by NMR and the *Z*-isomer spectra were extracted using the method described in section 2.2.3. The π-π* absorption maxima (λ_{max}) of all three analogues were red-shifted relative to the parent compound **24**; the *E*-isomer π-π* maxima were shifted by ~35 nm, while the *Z*-isomer π-π* maxima were shifted by ~20 nm. This was presumed to be due to the additional conjugation

of the *N*-hydroxyacrylamide with the π-system, rather than a solvent effect – the UV/vis spectra of **68a**-**c** were recorded in DMSO, whereas the spectra for **24** were recorded in acetonitrile. Spectra for **68a**-**c** were therefore re-measured in acetonitrile and a red shift of 10 – 30 nm was still observed.

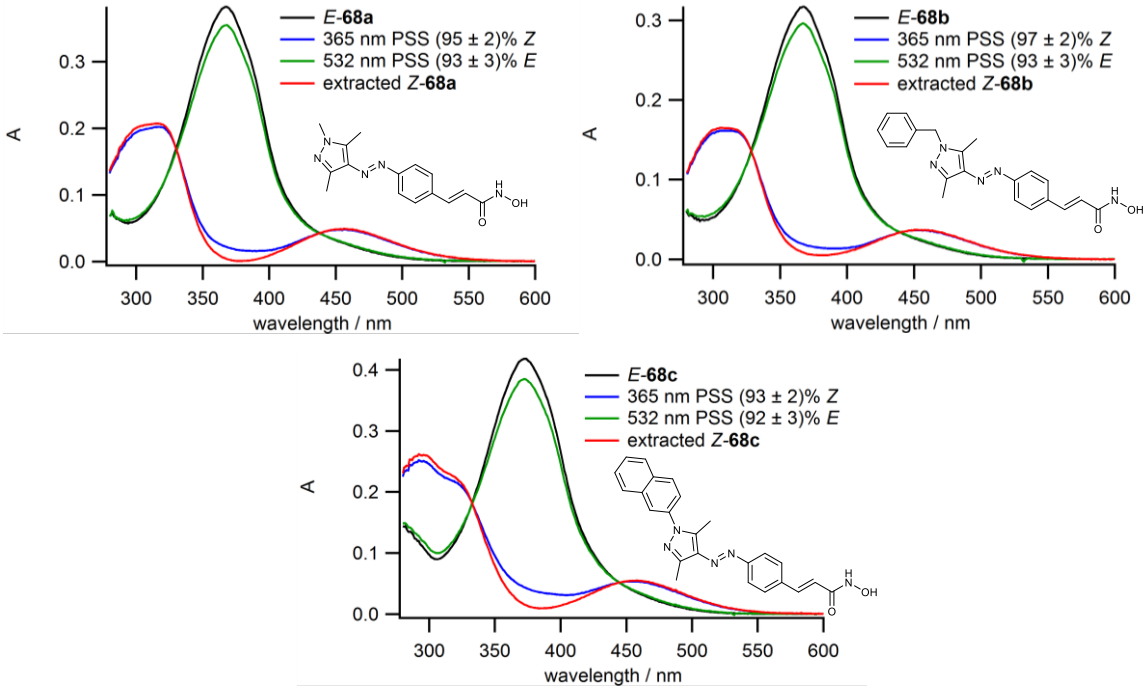


Figure 3.20. UV/vis spectra of **68a**-**c** recorded in DMSO at 1 × 10^{-5} M concentration; *E*-isomers, UVA (λ_{max} ~365 nm) and 532 nm PSSs, and extracted pure *Z*-isomer spectra.

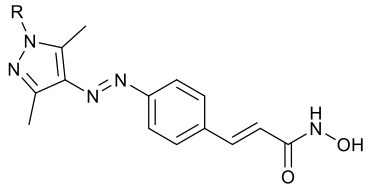
	E-isomer π-π*		*E*-isomer n-π*		*Z*-isomer π-π*		*Z*-isomer n-π*	
	λ_{max} / nm	$10^{-2} \times \varepsilon$ / M^{-1} cm^{-1}	λ_{max} / nm	$10^{-2} \times \varepsilon$ / M^{-1} cm^{-1}	λ_{max} / nm	$10^{-2} \times \varepsilon$ / M^{-1} cm^{-1}	λ_{max} / nm	$10^{-2} \times \varepsilon$ / M^{-1} cm^{-1}
68a	368	272 ± 15	440-450	26 ± 1.4 [a]	315	148 ± 8.1	457	35.1 ± 1.9
68b	367	331 ± 39	440-450	31 ± 3.6 [a]	~319	168 ± 20	452	38.6 ± 4.5
68c	373	432 ± 24	440-450	53 ± 2.9 [a]	~322	227 ± 13	458	56.7 ± 3.1

Table 3.7. Spectral data for **68a-c.** [a] There is still a small amount of π-π* absorbance at this wavelength, so these values are not accurate. All *Z*-isomer values are for the extracted *Z*-isomer spectrum.

3.3.4 Thermal isomerisation kinetics

The thermal isomerisation rates were measured at 30 °C using UV/vis spectroscopy. The isomerisation was studied in aqueous buffer for **68a** and **68b** (Table 3.8) so that the conditions were similar to those of the biological assays, however this was not possible for **68c** due to insolubility at the concentration used. The isomerisation rates were therefore also measured in DMSO for all three analogues. The half-lives were considerably shorter than for **24**, which had a half-life of 10 days in acetonitrile (taking into account the 5 °C increase in the temperature at which they were recorded).

This is presumably due to the presence of the electron withdrawing *N*-hydroxyacrylamide leading to a weak push-pull system with the weakly electron donating pyrazole ring.



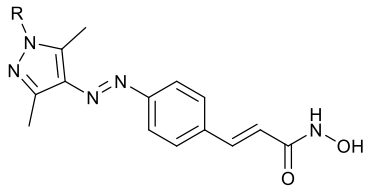
		Rate / s^{-1}		Half-life / h	
	R	buffer	DMSO	buffer	DMSO
68a	methyl	1.1×10^{-5}	1.8×10^{-5}	17.8	10.4
68b	benzyl	9.9×10^{-6}	1.4×10^{-5}	19.4	13.9
68c	2-naphthyl	- [a]	3.5×10^{-5}	- [a]	5.5

Table 3.8. Thermal isomerisation kinetics of **68a**-**c** at 30 °C. Graphs are provided in the Appendix 7.3.2. [a] Not measured due to insolubility in buffer.

3.3.5 Biochemistry

Assays were carried out by the Meyer-Almes group (University of Applied Sciences, Darmstadt). The azopyrazole inhibitors were tested against several bacterial HDACs, using the same continuous fluorogenic assay as was described previously (see section 3.2.6). The biochemical work is still ongoing in order to confirm the reproducibility of the results and obtain good sigmoidal fits for all IC_{50} curves. Assays are also being carried out on human HDACs 1-8.

In general, from the initial assay results, **68a**-**c** showed good inhibitory activity against the bacterial HDACs, with the majority of IC_{50} values sub-micromolar (Table 3.9). In addition to this, significant activity differentials were obtained for *E*- and *Z*-isomers of several inhibitor-enzyme combinations, as shown in purple in Table 3.9. The best results obtained were a 5-fold difference in activity between *E*- and *Z*-**68b** against Pa1409 and a 4-fold difference between *E*- and *Z*-**68c** against Pa0321 (Figure 3.1). For Pa0321 and Pa01409, the *Z*-isomer of all three compounds was a stronger inhibitor than the *E*-isomer. For Pa3774 and HDAH, the *E*-isomer was the stronger inhibitor for **68a** and **68b**, whereas for **68c**, which has the largest cap group, the *Z*-isomer was the stronger inhibitor. Indeed, **68c** was the only compound where the *Z*-isomer was more active than the *E*-isomer against all enzymes tested. This finding that the active isomer depends on the enzyme used is consistent with the results seen for the azobenzene-based HDAC inhibitors (section 3.2.6).



	R	IC$_{50}$ value / µM			
		Pa3774	Pa0321	Pa1409	HDAH
E-**68a**	methyl	0.062 ± 0.002	0.30 ± 0.02	0.53 ± 0.03	0.045 ± 0.002
Z-**68a**		0.10 ± 0.005	0.21 ± 0.01	0.27 ± 0.009	0.078 ± 0.004
		< 2-fold	< 2-fold	2-fold	< 2-fold
E-**68b**	benzyl	0.072 ± 0.004	0.50 ± 0.03	0.69 ± 0.02	0.053 ± 0.002
Z-**68b**		0.10 ± 0.007	0.20 ± 0.01	0.13 ± 0.007	0.14 ± 0.02
		< 2-fold	2-fold	5-fold	3-fold
E-**68c**	2-naphthyl	0.21 ± 0.01	0.81 ± 0.03	1.9 ± 0.1	1.2 ± 0.06
Z-**68c**		0.20 ± 0.02	0.22 ± 0.03	0.78 ± 0.04	0.63 ±0.03
		< 2-fold	4-fold	3-fold	2-fold
SAHA		0.037	0.49	0.28	0.037

Table 3.9. IC$_{50}$ values for **68a**-**c** against bacterial HDACs, with SAHA as a positive control. *Z*-**68a**-**c** refer to the 365 nm *Z*-rich PSS. Activity differential between the *E*- and *Z*-isomers is shown in purple. See Appendix 7.5 for all graphs.

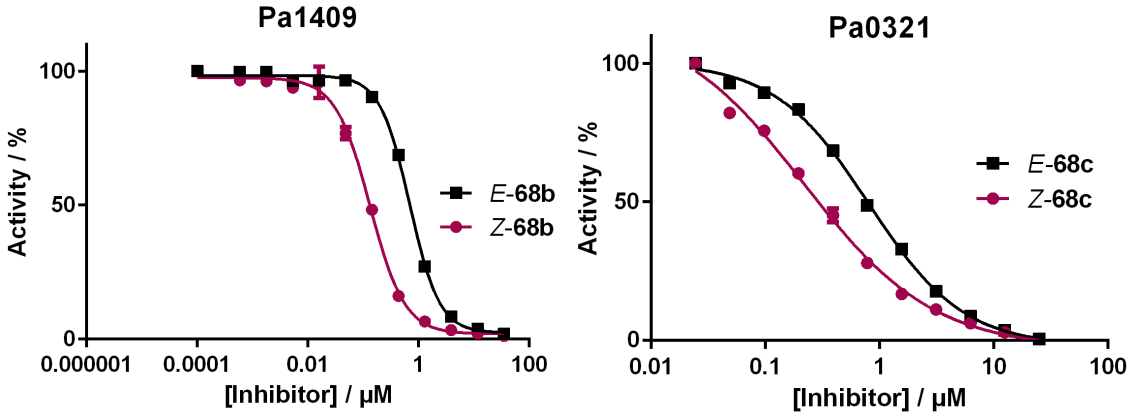


Figure 3.21. IC$_{50}$ curves for the best results.

Attempts were made to obtain inhibitor-enzyme crystal structures in order to better understand the binding in the active site. Successful crystal structures were obtained for *E*-**68a** bound to HDAH and to Pa3774 (Figure 3.22) at 1.8 and 2.6 Å resolution respectively, however attempts to crystallise the *Z*-isomers with the enzymes were unsuccessful. In addition to the zinc-chelation, several key interactions in the enzyme active site channel were identified from the crystal structures; these included π-interactions between the inhibitor aryl rings and phenylalanine residues, and hydrogen bonding between the methyl C-Hs and heteroatoms on the protein backbone or side chains. One

interesting observation, that may explain why in the majority of cases the *E*-isomer was less active than the *Z*-isomer, is that in the crystal structure the azoheteroaryl fragment is twisted out of planarity. It is however possible that this is only the case in the solid state and not in solution. The hydrophobicity of the channel (Figure 3.22, right) and its ability to accept or donate hydrogen bonds (Figure 3.22, left) were visualised and could potentially be used to redesign the ligands to maximise the interactions in the active site, in order to increase the activity of the *E*-isomer.

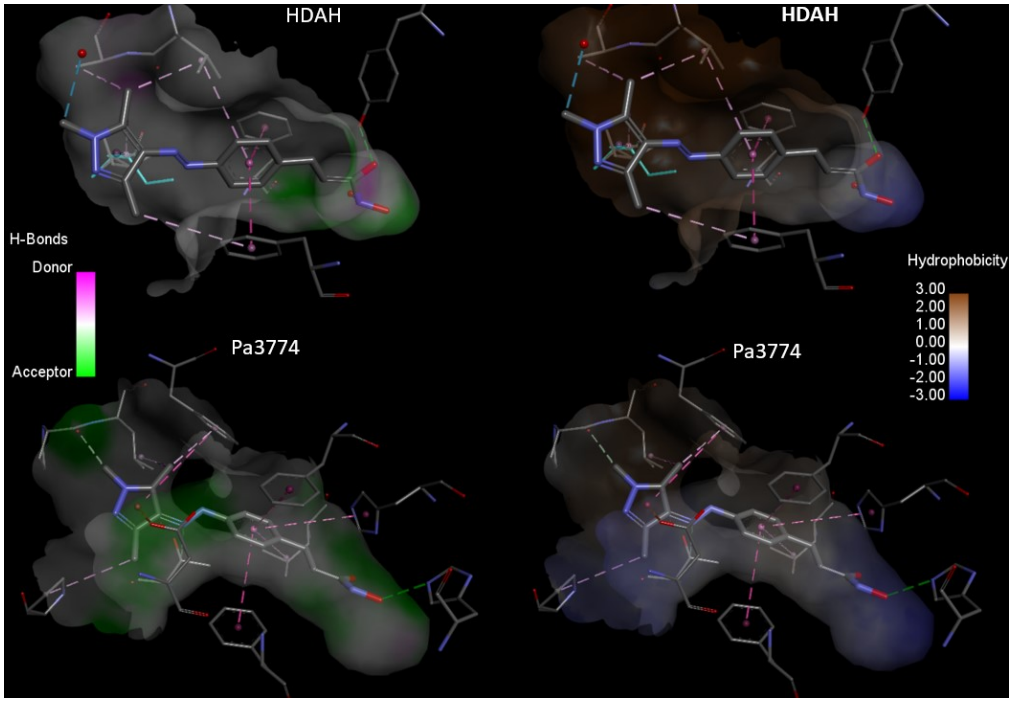


Figure 3.22. Enzyme-inhibitor crystal structures of **68a** with HDAH (top) and Pa3774 (bottom). H-bond donor and acceptor regions (left images) and hydrophobic regions (right images) of the binding pocket are shown.

3.4 RESULTS AND DISCUSSION PART III: Photoswitchable tethered HDAC inhibitors

3.4.1 Preliminary work

Previous work carried out by the Meyer-Almes group, has focused on the photocontrol of HDAH using a tethered azobenzene photoswitch (Figure 3.23).[220,221] HDAH has a very broad substrate scope consisting of various acetylated compounds such as polyamines, peptides, and various small molecule amines.[202] This property gives HDAH the potential to be used for light-controlled enzymatic deacetylation reactions in both industrial and biomedical applications. For example, the kinetic resolution of a racemic compound by deacetylation of one enantiomer only. The photoswitch used previously by the Meyer-Almes group was 4-phenylazomaleinanil (4-PAM) (Figure 3.23). Maleimides are commonly used for tethered photoswitches as they readily react with the sulfide moiety on cysteine residues.[11,31] In order to tether the photoswitch in the correct location on the enzyme, an HDAH variant was required that had an accessible cysteine close to the

active site and no other solvent accessible cysteines that the maleimide could react with. One solvent accessible cysteine was identified and replaced with a serine (C51S) to prevent the maleimide coupling to the enzyme in an undesired position.[220] This variant was then used as the template for other site-directed mutagenesis. This led to several HDAH variants with a single cysteine at a defined position close to the active site, which were covalently modified with 4-PAM.[220] Variants S20C and M30C showed a 40% and 50% reduction respectively in enzyme activity on switching from the *Z*-rich UVA (364 nm) PSS to the *E*-rich visible light (464 nm) PSS.[220] This was shown to be reversible by carrying out photoswitching cycles with UV and visible light. An interesting observation from this work was that the thermal half-life of enzyme-bound 4-PAM was up to 50-fold slower than its unbound counterpart.[220,221]

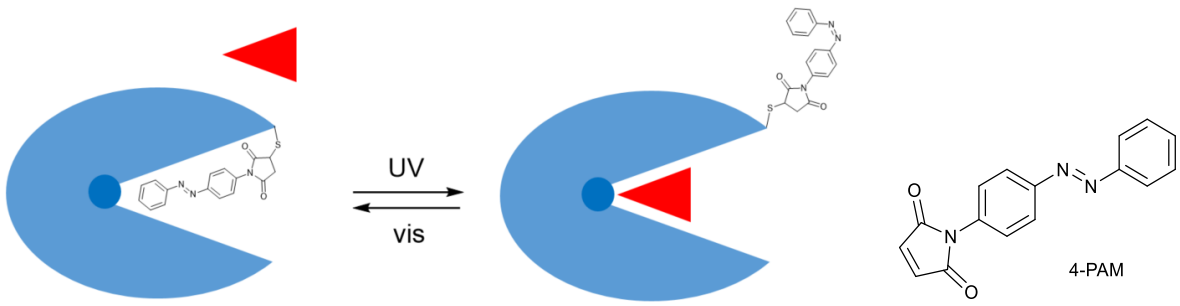


Figure 3.23. Schematic showing photocontrol of HDAH with a covalently tethered azobenzene, 4-PAM. Adapted from Korbus *et al.*[220]

The limitation of this system is that the reduction in activity is caused solely by the ability of one isomer to sterically block the entrance to the active site (Figure 3.23). By using a tethered photoswitch that contains a hydroxamic acid to bind to the active site zinc ion, an increased activity differential should be achievable upon photoisomerisation. Several different maleimide-containing HDAC inhibitor designs were proposed by the Meyer Almes group (Figure 3.24).

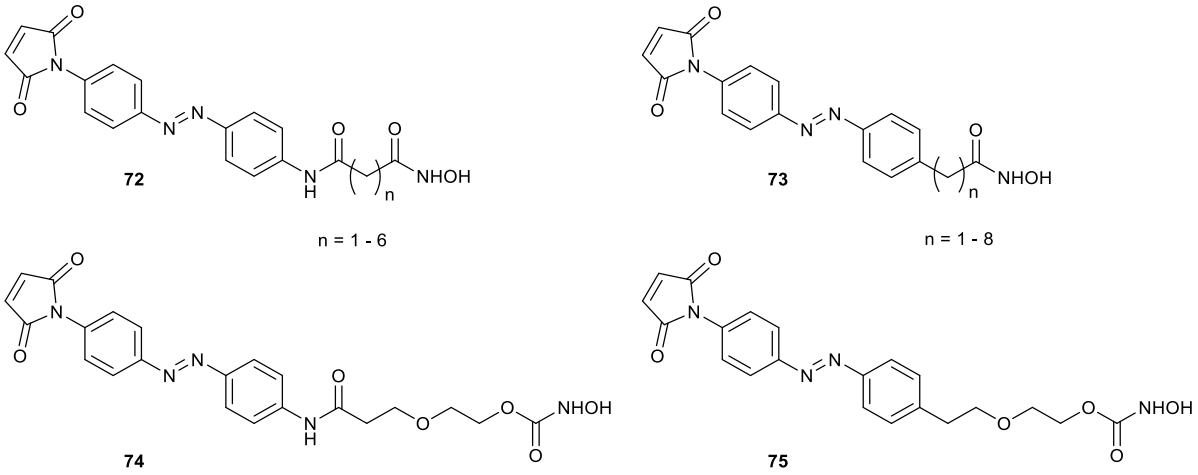


Figure 3.24. Proposed designs for photoswitchable tethered HDAC inhibitors.

For **72** and **73**, a range of alkyl linker lengths would be tested in order to identify the required length for optimum inhibition and activity differential. An alternative would be to include an ethylene glycol linker (**74** and **75**), with the aim of improving the solubility of the azobenzene derivatives, as this class of compound are known to have solubility issues. Indeed this was found previously with the azobenzene-based photoswitchable inhibitors developed in section 3.2.

One property to take note of is the residence time of the inhibitor in the active site. If the residence time is long, a very long irradiation time would be needed to ensure that no molecules remain bound to the active site for the length of the irradiation. Residence times of SAHA and dansyl ligands with different alkyl spacer lengths are shown in Table 3.10. These were measured by the Meyer-Almes lab using a FRET assay that they developed in order to study the kinetics of HDAC inhibition.[222,223] Dansyl derivatives with n = 2-3 spacer lengths would allow photoswitching timescales of ~1-2 minutes; shorter residence times than this would also be acceptable, however much longer times should be avoided as prolonged irradiation would be required.

Spacer length (n)	Residence time / min
2	0.83
3	1.1
4	3.5
5	4.2
6	11.3
SAHA	4

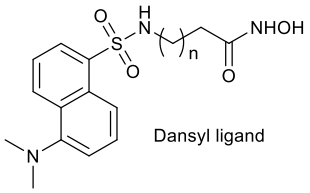
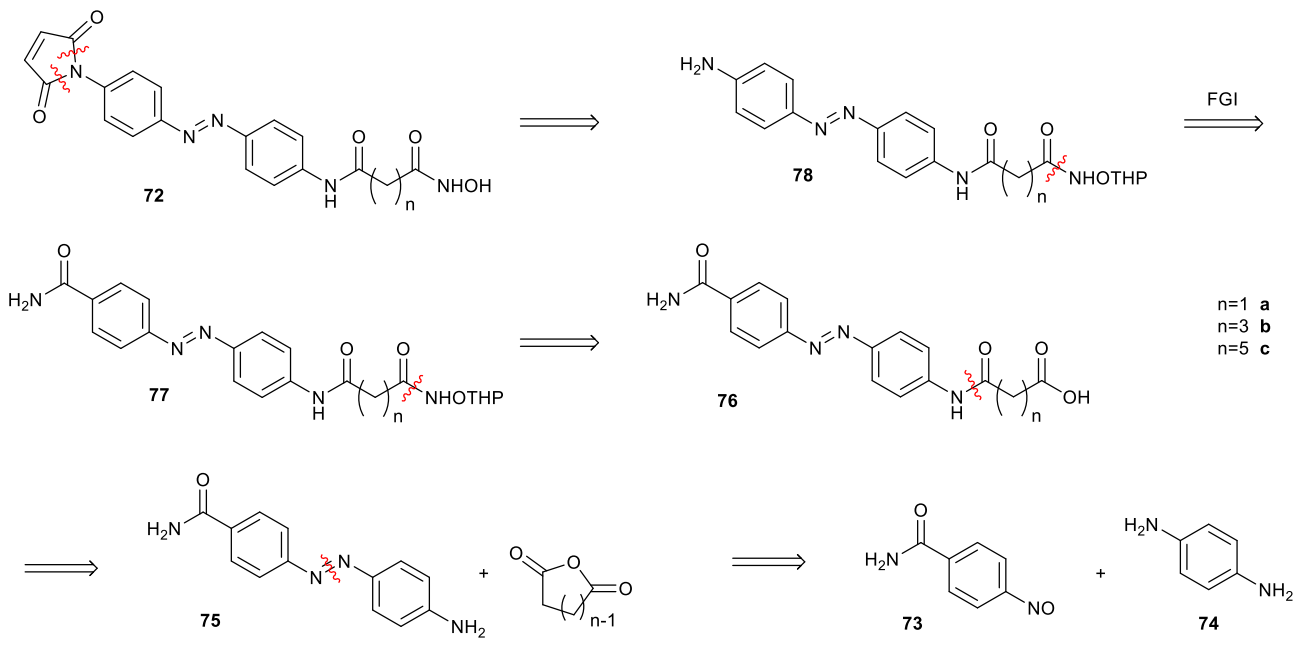


Table 3.10. Residence times of the HDAH-dansyl ligand complex with different alkyl spacer lengths.

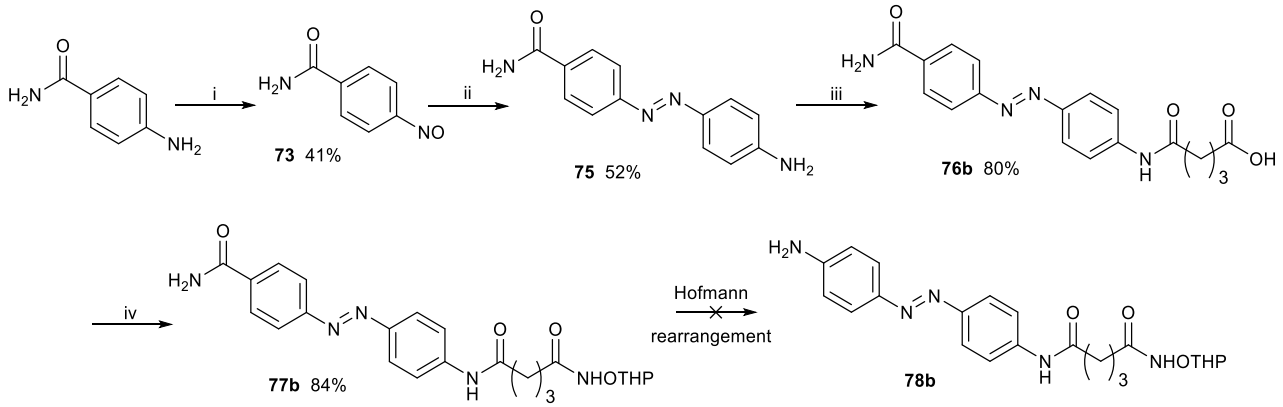
3.4.2 Synthesis

Of the proposed structures (Figure 3.24), compound **72** was selected for further study and a retrosynthesis was designed (Scheme 3.8). Azobenzene **75** should be readily accessible from the corresponding 4-nitrosobenzamide (**73**) and 1,4-diaminobenzene (**74**). Once azo formation has occurred on one of the amines of **74**, the molecule will be considerably less nucleophilic at the second amine, due to the presence of the electron withdrawing azo moiety; this should prevent a double condensation of two nitrosobenzenes on one molecule of diamine **74**. Following coupling with the relevant anhydride to give **76**, and formation of the THP-protected hydroxamic acid **77**, it was envisaged that a Hofmann rearrangement would give the primary amine **78**.[224] This could then be reacted with maleic anhydride to give the maleimide and a final THP deprotection would furnish **72**.



Scheme 3.8. Retrosynthetic analysis of **72**. FGI = functional group interconversion.

The three linker lengths chosen were n = 1, 3, 5 (**72a**-**c**). Initially, the n = 3 analogue **72b** was prepared to determine whether the proposed route would be viable (Scheme 3.9). Oxidation of 4-aminobenzamide with *m*CPBA gave nitrosobenzene **73**,[225] which was then coupled with 1,4-diaminobenzene *via* a Mills reaction to give azobenzene **75** in 52% yield. Refluxing this with glutaric anhydride in acetone gave carboxylic acid **76b** in 80% yield,[226] which underwent an amide-type coupling with THP-protected hydroxylamine to afford **77b** in 84% yield.[227]



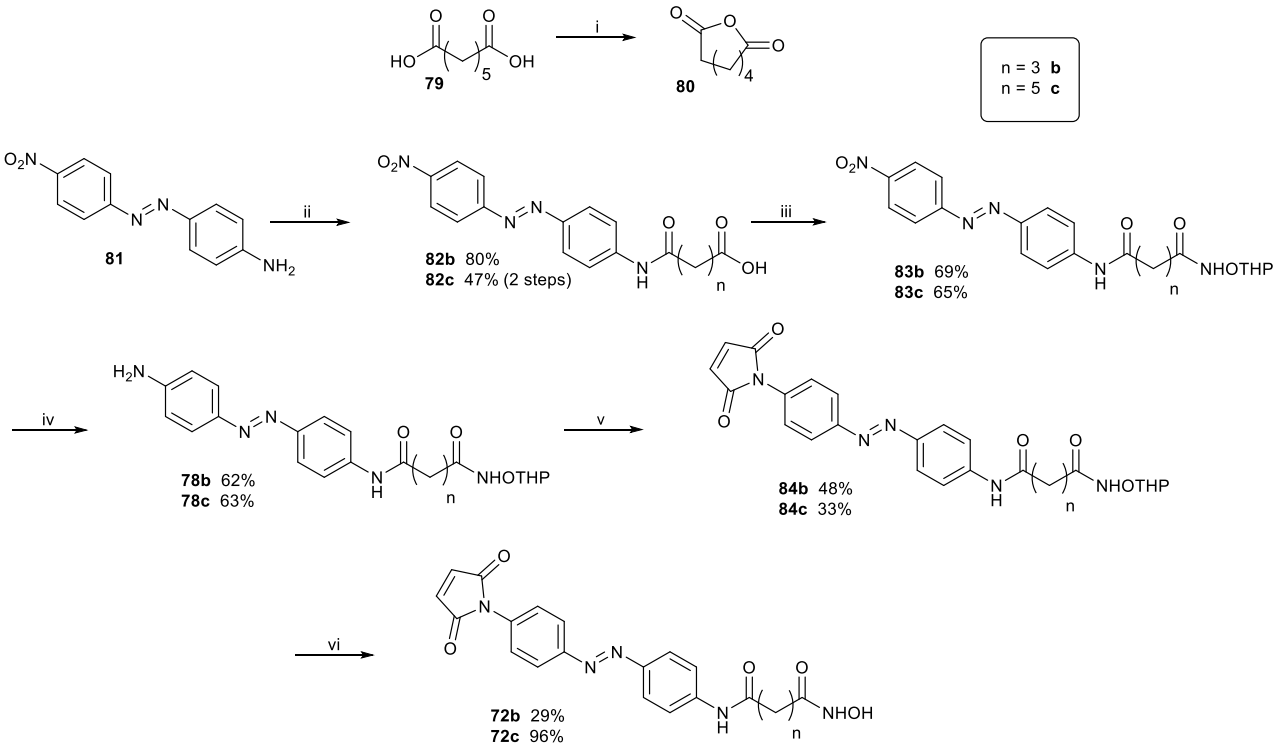
Scheme 3.9. 1st generation attempted synthesis of **72b**. Reagents and conditions: (i) *m*CPBA, MeCN, 60 °C, 1 h; (ii) 1,4-diaminoazobenzene (**74**), AcOH, 40 °C, overnight; (iii) glutaric anhydride, acetone, reflux, o/n; (iv) NH_2OTHP, HBTU, NEt_3, DMF, rt, o/n.

The next step was to carry out the Hofmann rearrangement to convert the amide to an amine. A range of literature conditions were attempted (Table 3.11), including one attempt to form the methyl carbamate, however all resulted in decomposition of the starting material.[228–231]

Conditions	Result
NaOCl, NaOH, dioxane/ H_2O, 60 °C [228]	decomposition
Br_2, NaOH, H_2O [229]	decomposition
sodium dichloroisocyanurate, NaOH, H_2O [230]	decomposition
N-bromosuccinimide, DBU, MeOH, Δ (to give the methyl carbamate) [231]	decomposition

Table 3.11. Attempted conditions for Hofmann rearrangement.

In light of these results, a different approach towards formation of **72b** was adopted, whereby a nitro group would be used instead of an amide – this could then be reduced to the amine prior to coupling with maleic anhydride. Commercially available azobenzene **81** was subjected to the same conditions as in the previous route; coupling with glutaric anhydride to give carboxylic acid **82b** in 80% yield,[226] followed by formation of the THP-protected hydroxamic acid **83b** in 69% yield (Scheme 3.10).

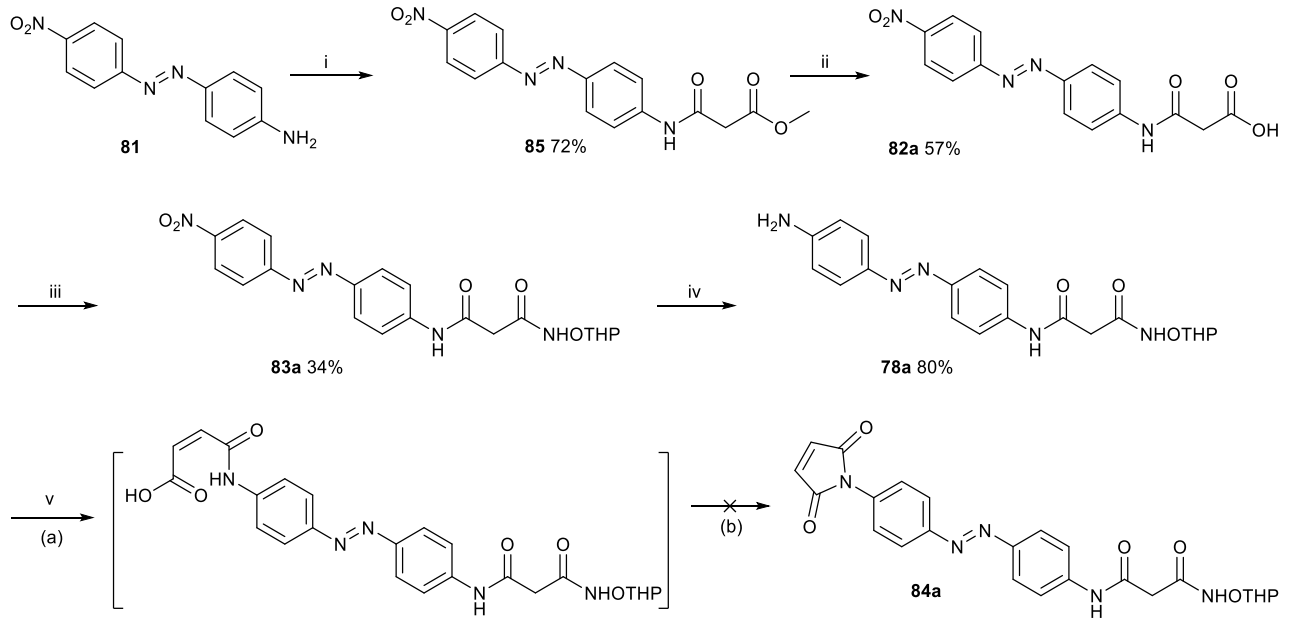


Scheme 3.10. 2nd generation synthesis of **72b-c.** Reagents and conditions: (i) Ac_2O, reflux, 4 h; (ii) glutaric anhydride or **79**, acetone, reflux, o/n; (iii) NH_2OTHP, HBTU, NEt_3, DMF, rt, o/n; (iv) Na_2S, 3:1 THF:H_2O, rt, 1–2 h; (v) a) maleic anhydride, AcOH, rt, 1 h; b) NaOAc, Ac_2O, DMF, rt, 1 h; (vi) cat. PPTS, 1:1 iPrOH:THF, 50 °C, o/n.

Reduction of the nitro group to an amine without reducing the azo moiety has been achieved in the literature using sodium sulfide.[232] This method was successful here, with complete conversion shown by NMR. Due to difficulties in partitioning the product into the organic phase during aqueous work up, an isolated yield of 62% was achieved for **78b**. The maleimide was then formed in two steps by reaction of **78b** with maleic anhydride to form the open chain maleamic acid, followed by

ring closure under basic conditions to give **84b** in 48% yield (Scheme 3.10).[233] THP deprotection with catalytic PPTS afforded the final product **72b**. Sequential trituration with ethyl acetate and water removed the majority of the impurities to give **72b** in 29% yield. A small amount of material was further purified by column chromatography to isolate the pure compound. Azobenzene **82c** (n = 5) was prepared similarly, however as pimelic anhydride (**80**) is not commercially available, it was prepared by refluxing pimelic acid (**79**) in acetic anhydride (Scheme 3.10).[234] This was then carried forward as the crude material and the following steps were carried out as before. Following the final deprotection step, purification by trituration was considerably more successful than for **72b** and the final product **72c** was obtained in 96% yield.

The synthetic route for compound **72a** (n = 1) was slightly different. Azobenzene **81** was coupled with methyl malonyl chloride to give the methyl ester **85**, followed by an ester hydrolysis with lithium hydroxide to afford carboxylic acid **82a** in 41% yield over the 2 steps (Scheme 3.11).[235,236]



Scheme 3.11. Synthetic route towards **72a**. Reagents and conditions: (i) methyl malonyl chloride, $NaHCO_3$, EtOAc, rt, 3 h; (ii) LiOH, 1:1 THF:H_2O, rt, 2 h; (iii) NH_2OTHP, HBTU, DMF, rt, o/n; (iv) Na_2S, 3:1 THF:H_2O, rt, 1 h; (v) a) maleic anhydride, AcOH, rt, 1 h; b) NaOAc, Ac_2O, DMF, rt.

This was then coupled with THP-protected hydroxylamine, using slightly modified conditions to those used for the preparation of **83b**-**c**; due to the 1,3-relationship between the amide and the carboxylic acid, the presence of base resulted in decomposition. Triethylamine was therefore omitted from the reaction and **83a** was afforded in a yield of 34%. Reduction of the nitro moiety using sodium sulfide proceeded in 80% yield to afford **78a**, however the next step was unsuccessful. After formation of the maleamic acid intermediate, basic conditions were required to facilitate ring closure to the maleimide. Again, the presence of base resulted in decomposition, presumably due

to deprotonation of the 1,3-dicarbonyl in the molecule causing side-reactions. Small amounts of the maleimide product were seen by NMR, however attempts to increase consumption of starting material by increasing reaction time led to decomposition. In light of the time already spent on the synthesis of these analogues, the biochemical studies were carried out on **72b**-**c** initially, and if the results indicated it would be worthwhile to test an analogue with a shorter alkyl linker, the synthesis of **72a** would be continued.

3.4.3 Photoswitching

The UV/vis spectra of **72b-c** were measured in DMSO (Figure 3.25). All three compounds were switched with UVA light (λ_{max} ~365 nm) and 532 nm monochromatic light. On irradiating with 365 nm light, the PSSs reached contained 88-89% *Z*-isomer, whereas irradiation with 532 nm light led to PSSs containing 83-84% *E*-isomer. The extracted *E*-isomer spectra and PSS compositions were obtained using the method established previously (see section 2.2.3). The positions of the absorption maxima and the molar extinction coefficients were found to be similar for the two analogues (Table 3.12).

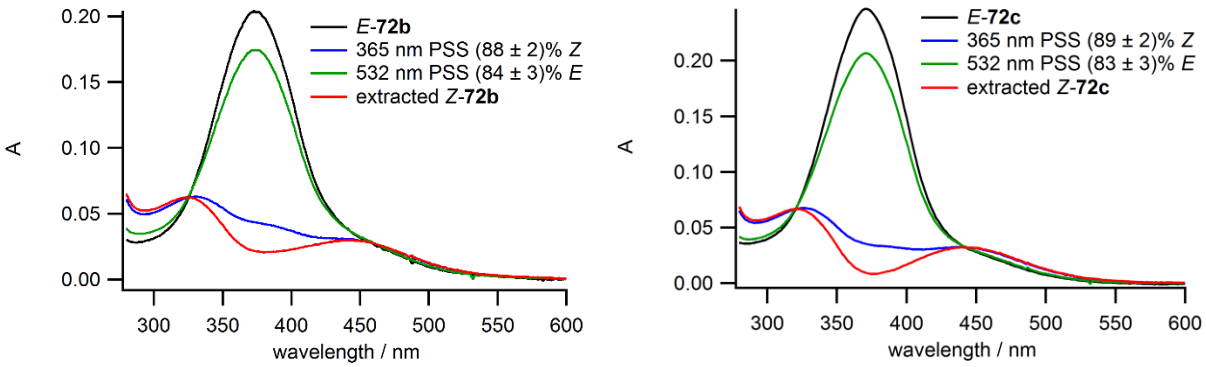


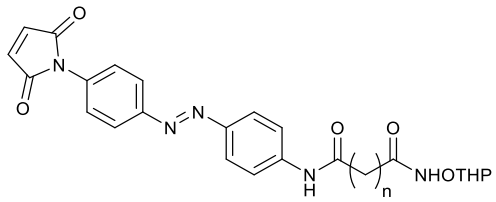
Figure 3.25. UV/vis spectra of **72b**-**c** recorded in DMSO at 1 × 10^{-5} M concentration; *E*-isomers, UVA (λ_{max} ~365 nm) and 532 nm PSSs, and extracted pure *Z*-isomer spectra.

	E-isomer π-π*		*E*-isomer n-π*		*Z*-isomer π-π*		*Z*-isomer n-π*	
	λ_{max} / nm	$10^{-2} \times \varepsilon$ / M^{-1} cm^{-1}	λ_{max} / nm	$10^{-2} \times \varepsilon$ / M^{-1} cm^{-1}	λ_{max} / nm	$10^{-2} \times \varepsilon$ / M^{-1} cm^{-1}	λ_{max} / nm	$10^{-2} \times \varepsilon$ / M^{-1} cm^{-1}
72b	373	204 ± 27	440-450	35 ± 4.6 [a]	323	62.3 ± 8.1	445	29.9 ± 3.9
72c	371	251 ± 15	440-450	31 ± 1.8 [a]	321	68.1 ± 4.0	443	32.9 ± 1.9

Table 3.12. Spectral data for **72b**-**c.** [a] There is still a small amount of π-π* absorbance at this wavelength, so these values are not accurate. All *Z*-isomer values are for the extracted *Z*-isomer spectrum.

3.4.4 Thermal isomerisation kinetics

The thermal half-lives of the compounds at 30 °C in aqueous buffer were found to be less than 1 hour (Table 3.13). The half-lives were also measured in DMSO and found to be considerably longer; 6 – 9 hours at 30 °C. The longer half-lives in DMSO allowed the PSS compositions to be quantified without the issue of thermal isomerisation occurring between the time at which the UV/vis and NMR spectra were recorded.



	Alkyl length, n	Rate / s^{-1}		Half-life / h	
		buffer	DMSO	buffer	DMSO
72b	3	1.0×10^{-3}	3.1×10^{-5}	0.19	6.2
72c	5	5.0×10^{-4}	2.3×10^{-5}	0.38	8.5

Table 3.13. Thermal isomerisation kinetics of **72b**-**c** at 30 °C. Graphs are provided in the Appendix 7.3.2.

3.4.5 Biochemistry

This work was performed by Andreas Krämer, led by Prof. Franz Meyer-Almes (University of Applied Sciences, Darmstadt). The maleimide HDAC inhibitors (**72b**-**c**) were tethered to the HDAH variants as described in section 3.4.1, using M30C and S20C variants as these gave the best results with 4-PAM.[220,221] Initially, **72b** was tethered to M30C and **72c** was tethered to S20C. In order to achieve *E*-*Z* photoisomerisation, the azobenzene-HDAH conjugates were irradiated with UVA light for 30 minutes and UV/vis spectra were recorded in order to confirm that the PSS had been reached. The continuous fluorogenic assay previously used in this work (see section 3.2.6) was carried out on the azobenzene-HDAH conjugates and also on the uncoupled HDAH as a control, with the relative fluorescence units (rfu) measured over time at different substrate concentrations (Figure 3.26). Michaelis-Menten kinetics were obtained from the exponential fitting of the data points (Table 3.14). V_{max} is the maximum enzyme rate and K_M is the substrate concentration at which rate = $V_{max}/2$. For the **72b**-M30C HDAH variant, a modest decrease in V_{max} and increase in K_M was seen relative to the values for the uncoupled enzyme, however there was no significant difference in the values between the *E*-isomer and the *Z*-rich PSS. For the **72c**-S20C HDAH variant, an approximately 5-fold decrease in V_{max} was seen relative to the uncoupled enzyme and a smaller change in K_M was seen. As with the previous conjugate, insignificant differences in the enzyme activity were seen for *E*-**72c** and the PSS; both the V_{max} and K_M values are within error of each other.

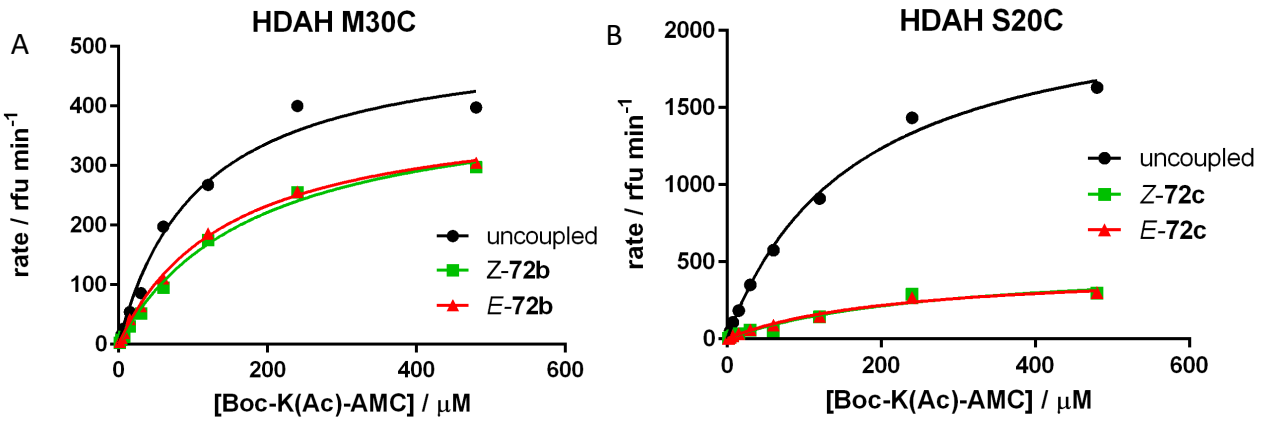


Figure 3.26. Assay results for enzymatic activity of the HDAH variants with *E*- and *Z*-**72b** or **72c** tethered, and of the uncoupled enzyme as a control. A) **72b** tethered to M30C; B) **72c** tethered to S20C. rfu = relative fluorescence units.

	HDAH M30C	
	V_{max} / rfu min^{-1}	K_m / μM
E-**72b** – HDAH	403 ± 11	147 ± 9.3
Z-**72b** – HDAH	422 ± 23	181 ± 22
Uncoupled HDAH	521 ± 38	109 ± 21

	HDAH S20C	
	V_{max} / rfu min^{-1}	K_m / μM
E-**72c** – HDAH	452 ± 44	218 ± 45
Z-**72c** – HDAH	494 ± 99	265 ± 107
Uncoupled HDAH	2248 ± 107	164 ± 18

Table 3.14. Michaelis-Menten kinetics for **72b**-**c** bound to the M30C or S20C HDAH mutant, with the uncoupled enzyme as a control.

Due to previous studies carried out by Meyer-Almes and co-workers confirming that 4-PAM was tethered to the active site cysteine,[220] it was assumed that this was also the case for **72b**-**c**, therefore the lack of activity differential between *E*- and *Z*-isomers was not the result of the malemide being tethered to a different residue. It is possible that the lack of activity differential between the two isomers was caused by long residence times of the *E*-isomer in the active site, however this is unlikely as irradiation was carried out for 30 minutes. Another possibility is that the relatively short half-lives of **72b** and **72c** in buffer (< 1 hour at 30 °C) could have led to predominantly *E*-isomer present in the irradiated sample, however the assay was started immediately following irradiation and the length of the assay was approximately 30 minutes, so this is unlikely to have been an issue. In addition to this, the previous work with 4-PAM found a 50-fold decrease in thermal isomerisation rate upon conjugation to the enzyme.[220,221] This was caused by interactions between the azobenzene and the enzyme, involving a hydrophobic cluster and a histidine residue, as identified using MD simulations.[221] It appears that these interactions would still occur for **72b**-**c**, however thermal isomerisation rates of the enzyme-inhibitor conjugates should still be measured to determine if this is the case. The most likely cause of the lack of activity differential between the *E*- and *Z*-isomers is that the cysteine residue was incorrectly positioned, so that neither isomer was able to bind to the active site zinc. This would explain the similar reduction in activity for both

isomers, as they could both be partially blocking the entrance to the active site, making it less accessible to the substrate.

3.5 CONCLUSIONS

First generation photoswitchable HDAC inhibitors based on azobenzenes were designed according to previous work and were successfully synthesised according to the established synthesis. *E*- and *Z*-stilbene isosteres were also synthesised to in order to establish whether their inhibitory activity could be used to predict the activity of the azobenzenes. This would mean that photoswitching wouldn't have to be carried out during initial assays and removes the complication of photostationary states and thermal isomerisation rates. Photochemical studies identified that UVA and green light were suitable for achieving *Z*- and *E*-rich PSS and thermal isomerisation rates were found to be sufficiently slow under the assay conditions that *Z*-*E* isomerisation should not be a significant issue during assaying of the *Z*-rich PSS. Assays were initially carried out on the *E*- and *Z*-stilbenes and the *E*-azobenzenes using HDAH. Further bacterial and human HDAC assays were then carried out on these compounds and also on a *Z*-rich mixture of azobenzene isomers, which was achieved by UVA irradiation. The azobenzenes were better inhibitors of the bacterial HDACs than the human HDACs, with the best result achieved for **57a** and Pa1409 (9-fold activity differential between isomers). In the majority of cases, the *Z*-isomer was more active than the *E*-isomer, which was opposite to the expected result – the bent *Z*-conformation was predicted to clash with the amino acids lining the active site channel. In general, the stilbene isosteres correctly predicted the trends in inhibition between the different enzymes and different *para*-substituted analogues, suggesting that they would be suited for use in preliminary assays to model the inhibitory activity of azobenzenes. Several assays are currently being repeated in order to improve the quality of the results. Additional assays are also being carried out on HDACs 6 and 8, which these compounds have yet to be tested against.

The second generation HDAC inhibitors were designed to incorporate the new arylazopyrazole photoswitches developed in Chapter 2. Three new analogues with different *N*-substituents on the pyrazole ring were successfully synthesised. Photochemical studies showed an increase in photoconversion compared to the azobenzene inhibitors upon irradiation with either UVA or green light, due to the improved separation of absorbances in the *E*- and *Z*-arylazopyrazoles relative to the *E*- and *Z*-azobenzenes. These compounds also had longer thermal half-lives under the assay conditions than the azobenzene-based HDAC inhibitors. Assays were again carried out on the *E*- and

Z-isomers and, as with the azobenzenes, all three analogues were found to be good inhibitors of the bacterial HDACs. The best activity differential was achieved for Pa1409 with **68b**, although the 5-fold difference in activity between *E*- and *Z*-**68b** was slightly less than the 9-fold difference achieved for Pa1409 with **57a**. As with the azobenzene-based inhibitors, several assays are currently being repeated in order to improve the quality of the results. Additional assays are also being carried out on the azopyrazole inhibitors against the human HDACs.

The potency of the photoswitchable inhibitors developed in this work towards bacterial HDACs, specifically the acetylpolyamine amidohydrolases, suggests potential use as antimicrobials. As mentioned in section 3.2.6, these compounds could be used to target biofilms, which are often responsible for persistent infections.

In continuation of previous work by the Meyer-Almes group, tethered photoswitchable HDAC inhibitors were designed with different length alkyl 'spacers'. Analogues with alkyl spacer lengths of n = 3 and n = 5 (**72b**-**c**) were successfully synthesised, however the n = 1 analogue (**72a**) was not prepared, due to problems with decomposition caused by the presence of the 1,3-dicarbonyl. Photoswitching using UVA and green light achieved >80% photoconversion between the two isomers. Short thermal half-lives were seen under the assay conditions, however these increased significantly on changing the solvent from aqueous buffer to DMSO. The photoswitches were successfully coupled to the HDAH enzyme, as shown by the reduction in enzyme activity compared to the uncoupled enzyme, however no significant difference in activity was observed for the *E*- and *Z*-isomers. To continue with this work, **72b** and **72c** should be tested on the other HDAH variants (**72b**–S20C and **72c**–M30C) to identify if the cysteine positioning relative to the active site is better for the different linker lengths. Alternatively other HDAH variants could be tested, such as D98C or E340C. These were not chosen initially as no difference in activity between *E*- and *Z*-isomers was seen in the previous work using 4-PAM.[220] It would also be useful to study the thermal isomerisation rates and the residence times of the conjugated compounds, to identify if either of these were the reason for the poor activity differential between the two isomers.

4 AZOBISIMIDAZOLE: A PHOTOSWITCHABLE BASE[ii]

4.1 INTRODUCTION

One way in which light can be used to perturb a system is to modulate pH, as mentioned briefly in section 1.5. This opportunity can, for example, lead to external control of the reaction rate of pH-dependent chemical and biochemical processes,[79,80,237] however this is currently limited by the availability of suitable photoresponsive acids or bases. The change in acidity or basicity of a photoactive molecule can be an irreversible process, for example through the release of a 'caged' proton upon irradiation with light. The most common example of this is the photoconversion of *o*-nitrobenzaldehyde (**86**) to *o*-nitrosobenzoic acid (**87**) (Figure 4.1).[237–239] Alternatively, the process can be reversible, allowing oscillation between two pH values rather than a one-off change in pH. One way by which this can be achieved is through generation of an excited state species that has a different acidity to the ground state species.[240–243] This has been reported for aromatic acids and bases, such as **88**, which have large differences in pK_a values between the ground and excited states, however the change in pH is transient, due the short lifetime of the excited state (Figure 4.1).[241,243]

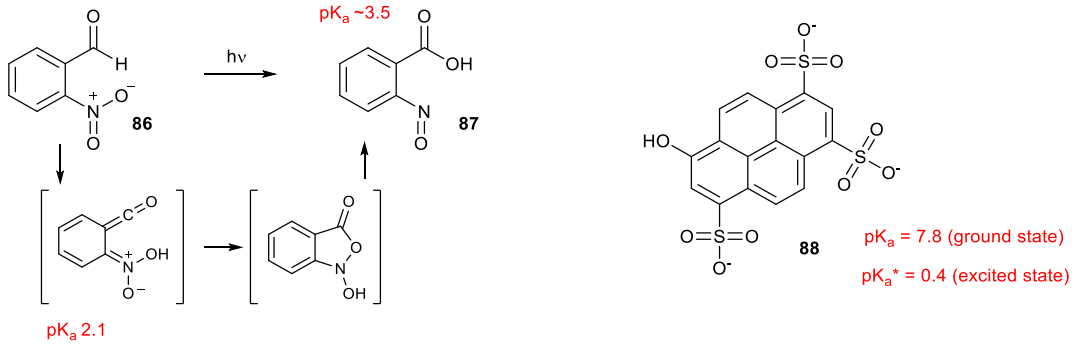


Figure 4.1. An example of an irreversible (left) and a reversible (right) photo acid, where the difference in acidity in the former is achieved by release of a 'caged' proton, and in the latter is achieved by population of an excited state.

More recently, a number of photoresponsive acids and bases have been reported in which the ground state acidity/basicity is changed through a reversible photoisomerisation.[79–81,244–246] A large number of these photoswitchable acids and bases have been azobenzenes, such as the examples reported by the Jullien and Hecht groups described in section 1.5.[80–84] The 2-hydroxyazobenzenes reported by Jullien undergo an increase in acidity on switching from the *E*- to the *Z*-isomer, due to additional stabilisation of the hydroxyl proton in the *E*-isomer by formation of a hydrogen bond to the azo nitrogen (Figure 1.13). This interaction is not possible in the *Z*-isomer due to the altered conformation, therefore the *Z*-isomer is more acidic and two distinct pK_a values are observed for

[ii] This chapter is based on the following publication: C. Weston, R. Richardson, M. Fuchter, *Chem. Commun.*, 2016, **52**, 4521–4524.

the two isomers. Another example that exploits hydrogen bonding to achieve a difference in pK_a between the *E*- and *Z*-isomers has been reported by Woolley and co-workers. They have developed azonium *p*-aminoazobenzenes such as **89** that have methoxy substituents on all four *ortho*-positions of the phenyl rings (Figure 4.2, A).[58,59] The azonium proton is able to hydrogen bond to one of the *ortho*-methoxy groups in *E*-**89** but not in *Z*-**89**, resulting in a pK_a shift of approximately 1.5 units between isomers. Hydrogen bonding to the azo group, however, is not the only plausible strategy for modifying azobenzene acidity/basicity. As mentioned previously (section 1.5), Hecht and co-workers have modulated the basicity of piperidine-containing azobenzenes through steric shielding in one isomer over the other (Figure 4.2, B).[80,83,84] Rather than attempt to achieve a pH jump, they have exploited the difference in pK_a to achieve photocontrol of a general base catalysed reaction. In general base catalysis, the reaction rate depends on the strength of the base (*i.e.* it is kinetically controlled), so a difference in pK_a values will affect the rate, whereas for specific base catalysis, the rate is independent on strength of the base, and instead depends on the pH of the system (*i.e.* thermodynamically controlled).[247] Using the Henry reaction as an example, Hecht and co-workers achieved a 9-fold increase in rate in the presence of the 365 nm PSS of **17** relative to *E*-**17**. On replacing the *tert*-butyl substituents with xylenes, a 28-fold increase in rate was achieved. For both analogues the PSS contained 90% *Z*-isomer.

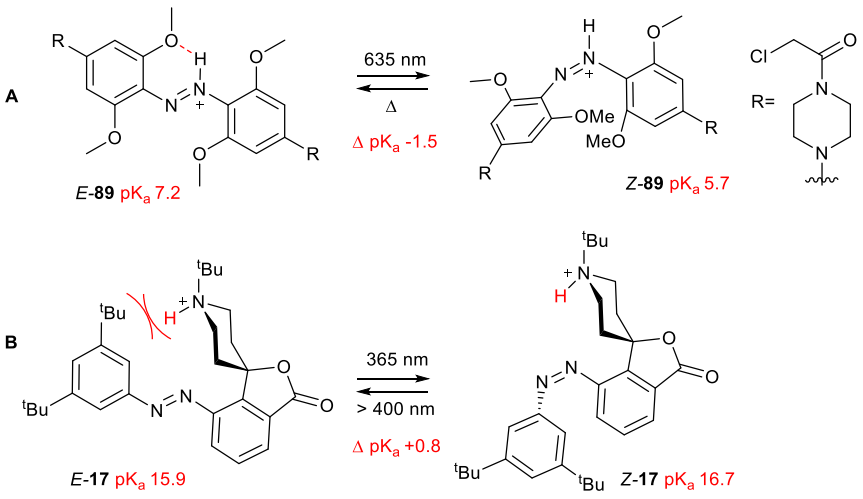


Figure 4.2. Previous azo photoswitchable bases reported by A) Woolley,[58] and; B) Hecht.[80]

Another interesting example where the conformation of the photoswitch is important, is the azobenzene dicarboxylic acid **90** reported by Bandyopadhyay and co-workers (Figure 4.3, A).[79] In the *E*-isomer, both carboxylic acids have the same pK_a, whereas in the *Z*-isomer two distinct deprotonation events occur. The authors have termed this compound a photoresponsive glycosidase mimic – the conformation of *Z*-**90** in its mono-deprotonated state allows it to catalyse the hydrolysis of a glucopyranoside (Figure 4.3, B).

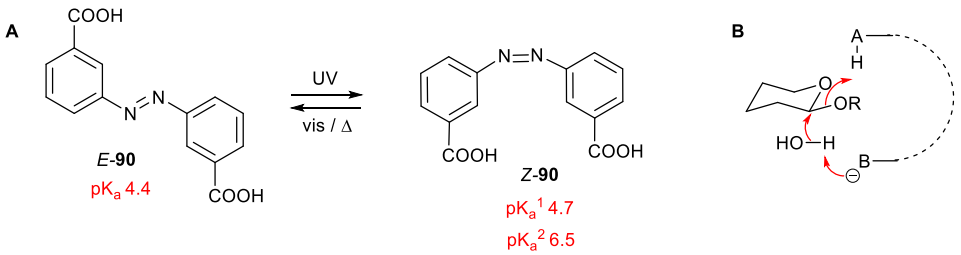


Figure 4.3. A) Photoswitchable glycosidase mimic **90** developed by the Bandyopadhyay group, and; B) Schematic of the glycosidase catalytic cycle.

As discussed in Chapter 2, novel azoheteroaryl photoswitches containing a phenyl ring and a 5-membered heteroarene were previously developed,[138] where photochemical and thermal properties could be altered by changing the nature of the heteroarene, the positioning of the azo group, and the *ortho*-substitution pattern on the heteroring. As well as affecting key properties, the presence of heteroatoms on at least one of the aryl rings can be exploited for use in applications such as spin-state switching. Herges and co-workers have developed azopyridines that act as photodissociable ligands through axial coordination of the pyridine nitrogen with a Ni-porphyrin.[14,248,249] The ligand is only able to coordinate to the complex in one conformation due to sterics, so photoswitching between the two isomers results in either a square planar low spin complex or a square pyramidal high spin complex. The Herges group have recently demonstrated that arylazoimidazoles can be used instead of azopyridines, and result in an improvement in ligand affinity.[96]

To date, although there have been several examples of photoswitchable acids and bases that are based on azobenzenes, there have been no examples of azoheteroarenes reported, despite the potential to utilise the presence of basic heteroatoms. Therefore, a photoswitchable Brønsted base of this class was designed, whereby a proton could be additionally stabilised in one isomer over the other, with the aim of achieving both a pH jump and photocontrol of a base catalysed reaction.

4.2 RESULTS AND DISCUSSION

4.2.1 Photoswitch design

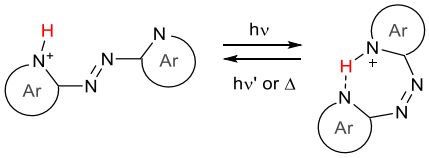


Figure 4.4. The required positioning of basic heteroatoms for a photoswitchable azoheteroaryl base.

In order to function as a photoswitchable base, heteroarenes are required on both sides of the azo group that have a basic atom in the correct position to allow stabilisation of a proton in one isomer. This can be achieved by having a basic nitrogen on both rings in the position adjacent to the azo group, so that in the protonated *Z*-isomer, the proton (on one heteroaryl ring) is additionally stabilised by a hydrogen bond to the basic nitrogen on the other ring (Figure 4.4). Imidazole was chosen as the heteroaryl ring, due to its high basicity relative to other heteroarenes.[102] Both azobis(2-imidazole) **91** and azobis(4-imidazole) **92** were considered to have the correct connectivity to enable proton stabilisation in the *Z*-isomer (Figure 4.5).

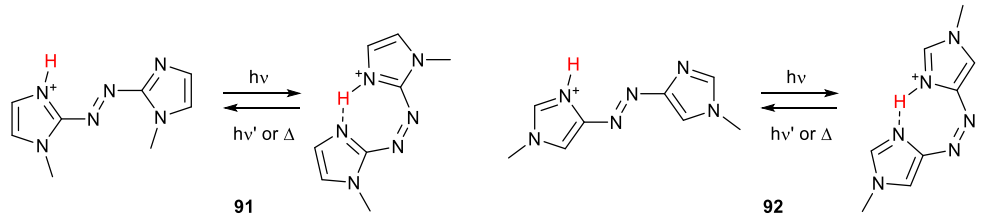


Figure 4.5. The two possible regioisomers of azobisimidazole that allow hydrogen bond stabilisation in the protonated *Z*-isomer.

DFT energy minimised conformations and TDDFT calculated UV/vis spectra were obtained for both these photoswitches in their neutral states using B3LYP/6-31G(d,p) and CAM-B3LYP/6-311G(2df,2p) respectively and the PCM solvent method for water (Figure 4.6). Two conformations were obtained for each isomer (see Appendix 7.4.2) and the calculated UV/vis spectra shown in Figure 4.6 are the Boltzmann weighted averages of the two conformations. Azobisimidazole **91**, which has the azo moiety attached at the 2-position of both imidazole moieties, was calculated to have a large n-π* absorbance in the *Z*-isomer, and hence good separation of absorbances between the *E*- and *Z*-isomers, which should allow for excellent photoconversion between isomers at different wavelengths. This large n-π* absorbance is due to the twisted conformation adopted by the *Z*-isomer (Figure 4.6, B), which minimises unfavourable steric interactions between a given *N*-methyl and the neighbouring aryl ring, and unfavourable lone pair interactions involving the basic imidazole nitrogens. Conversely, the energy minimised conformation of **92** led to a planar conformation for

the *Z*-isomer and hence a negligible n-π* absorbance was predicted on symmetry grounds (Figure 4.6). This planar conformation differs from the conformations seen for the azoheteroarenes that have one 5-membered and one 6-membered ring, where the 5-membered heteroarene, provided it has at least one *ortho*-hydrogen, sits co-planar to the azo group and the phenyl ring sits perpendicular to this in a T-shaped conformation (see Chapter 2). Presumably *Z*-**92** is able to adopt this planar conformation due to the reduced sterics of having two 5-membered rings, as well as the positioning of the C-H and nitrogen in the 5- and 3'-positions (Figure 4.6, B). In **91**, this planar conformation is unfavourable as either the *ortho*-methyls on each ring would be in close proximity to each other, causing unfavourable steric interactions, or the basic *ortho*-nitrogens would be close to each other, causing lone pair repulsion.

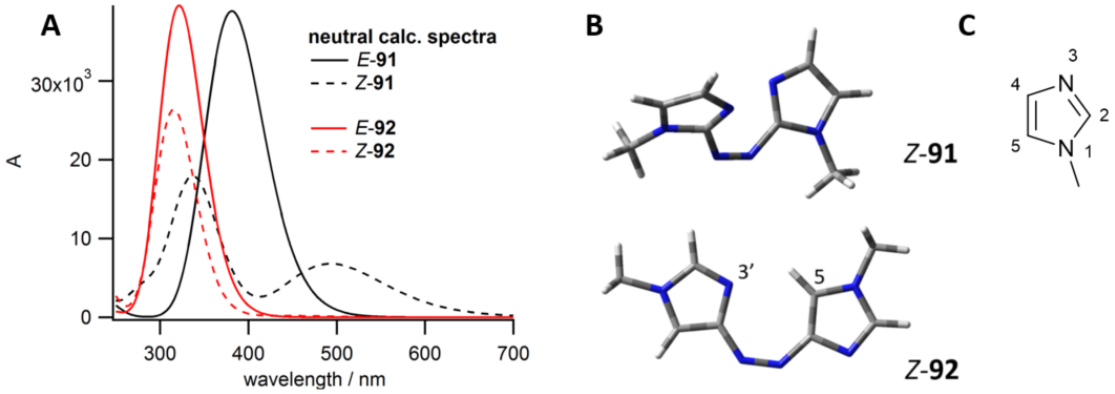


Figure 4.6. A) Calculated spectra for neutral **91** and **92** using CAM-B3LYP/6-311G(2df,2p) level of theory; B) Energy minimised conformations of *Z*-**91** and *Z*-**92** using B3LYP/6-31G(d,p); C) Numbering of the imidazole ring.

These calculations are consistent with the previous findings on the conformational preferences and resulting spectroscopic properties of the arylazoheteroarenes (Chapter 2) – when there is a mirror plane through the molecule, as with the planar *E*-isomers and *Z*-**92**, the n-π* transition is symmetry forbidden and no absorbance is predicted. Comparing the calculated *E*-isomer spectra, *E*-**91** had a significantly red-shifted π-π* absorbance relative to *E*-**92**, suggesting that visible light rather than UV light could be used for photoswitching. On the basis of the red-shifted *E*-isomer π-π* transition and the relatively intense *Z*-isomer n-π* transition, azobisimidazole **91** was chosen for further study. Energy minimised conformations and calculated UV/vis spectra were obtained for *E*-**91**H^+, protonated on either the azo or the imidazole nitrogen, and *Z*-**91**H^+ (Figure 4.7). These confirmed that in the *Z*-isomer, the proton would be stabilised by interacting with the basic nitrogens on both imidazole rings, resulting in a planar conformation and, in turn, a decreased n-π* absorbance. Indeed neutral *Z*-**91** was 52 kJ mol^{-1} less stable than *E*-**91**, whereas the protonated species *Z*-**91**H^+ was only 16 kJ mol^{-1} less stable than *E*-**91**H^+ (Table 7.13 and 7.14, Appendix).

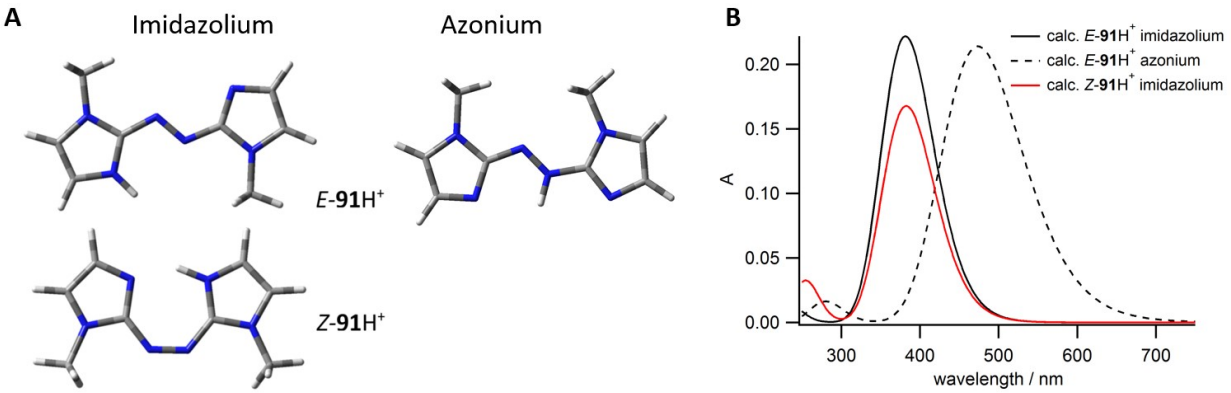
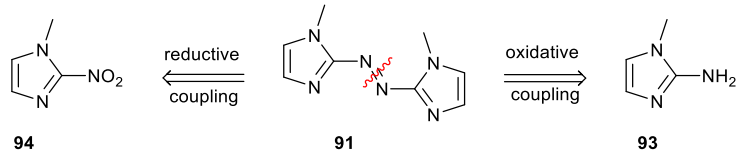


Figure 4.7. A) Energy minimised structures (B3LYP/6-31G(d,p)), and; B) Calculated UV/vis spectra (CAM-B3LYP/6-311G (2df,2p)); for protonated **91**.

The geometry optimisation of *E*-**91**H$^+$ protonated on either the imidazole or the azo nitrogen was carried out to confirm which protonation site was energetically favourable. For each protonation site three energy minimised conformers were located (see Appendix 7.4.2), from which the global minima were identified (Figure 4.7, A). The Gibbs free energy for *E*-**91**H$^+$ protonated on the imidazole was 44 kJ mol^{-1} lower than for protonation on the azo (Table 7.14, Appendix), indicating that protonation should occur on the imidazole ring. This is consistent with experimental data – imidazoles are generally several pK_a units more basic than azobenzenes. *N*-methyl imidazolium has a pK_a of 7.1,[250] whereas arylazoniums tend to have pK_a values below 3,[48–51] with the exception of systems such as those developed by Woolley and co-workers, where the azonium proton is stabilised in the *E*-isomer by hydrogen bonding (Figure 4.2, A).[58,59]

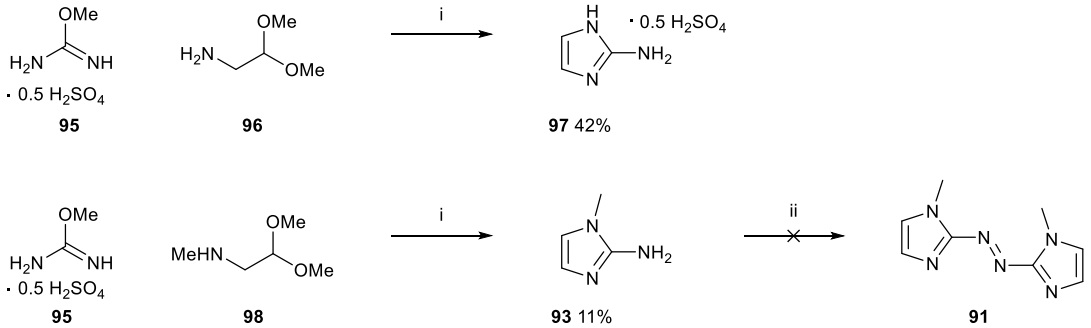
4.2.2 Synthesis

Two possible routes were envisaged for the synthesis of azobisimidazole **91** (Scheme 4.1); either oxidative coupling of aminoimidazole **93** or reductive coupling of nitroimidazole **94**. Both of these methods are well established for the synthesis of symmetric azobenzenes,[104] whereas for symmetric azoheteroarenes there is greater literature precedent for oxidative coupling. With regards to oxidative methods, examples include azobenzimidazoles, azopyrazoles and azoisoxazoles, including several analogues prepared from *N*-methylated aminoheteroarenes.[110,251,252] The oxidative route was therefore chosen, with *N*-methyl 2-aminoimidazole (**93**) as the precursor.



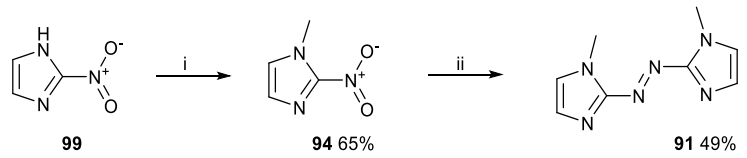
Scheme 4.1. Retrosynthetic strategies for azobisimidazole **91**.

A synthetic procedure developed by Weinmann and co-workers was used for the preparation of **93** (Scheme 4.2)**.**[253] In this procedure, 2-aminoacetaldehyde acetal **96** is reacted with *O*-methylisourea hemisulfate (**95**) under acidic conditions to give the 2-aminoimidazole hemisulfate salt **97**. In order to obtain the *N*-methyl analogue **93**, *N*-methylaminoacetaldehyde acetyl **98** was used in place of **96**. According to the literature procedure, the hemisulfate salt should precipitate out of the reaction mixture upon dropwise addition to ice-cold ethanol, however this could not be achieved for **93**. Instead the resulting solution was concentrated under reduced pressure and the product was obtained by column chromatography as the free amine in 11% yield. It was presumed that the addition of an *N*-methyl changed the solubility of the product sufficiently that it no longer precipitated out of ethanol. The reaction was repeated using the same reagents as the literature procedure (*i.e.* **96** rather than **98**) and the product did precipitate out of ice-cold ethanol, affording aminoimidazole **97** in 42% yield (Scheme 4.2), indicating that the literature conditions were not well suited to the methylated analogue. Oxidation of aminoimidazole **93** was first attempted using *tert*-butyl hypoiodite as the oxidant, formed *in situ* from *tert*-butyl hypochlorite and sodium iodide, according to the procedure developed by the Minakata lab for various azoheteroarenes.[110,251] This method was unsuccessful however and led to decomposition of the starting material. It is perhaps telling that no azoimidazoles were reported by Minakata and co-workers, and instead the closest analogues were azobenzimidazoles.[110] Although a variety of other conditions have been reported for oxidative coupling to give azoheteroarenes,[252,254,255] employing oxidants such as potassium permanganate or *tert*-butyl hydroperoxide, the reductive coupling route was explored first (Scheme 4.1) to see if that would hold any more success.



Scheme 4.2. Attempted synthesis of azobisimidazole **91** *via* oxidative coupling method. Reagents and conditions: (i) a) H_2O, 60 °C, o/n; b) H_2SO_4 added until pH 2.5, 100 °C, 8 h; (ii) *t*-BuOCl, NaI, MeCN, rt.

Commercially available 2-nitroimidazole **99** was *N*-methylated with methyl iodide to give **94** in 65% yield (Scheme 4.3). This was successfully reductively coupled to give **91** in 49% yield using zinc in aqueous ammonium chloride, according to a known procedure for a related nitroimidazole.[256]



Scheme 4.3. Synthesis of azobisimidazole **91** *via* reductive coupling method. Reagents and conditions. (i) MeI, K_2CO_3, MeCN, 0 – 65 °C, 3 h; (ii) NH_4Cl, Zn dust, H_2O, 45 °C, 1 h.

This demonstrated that the reductive coupling route could be used to prepare the azobisimidazole photoswitch in moderate yield without optimisation. In contrast, the oxidative coupling route appeared to be less suited to this compound, and would require considerable optimisation.

4.2.3 Photochemistry and pK_a determination

Irradiation was initially carried out on the neutral compound **91** in aqueous buffer at pH 9, where it was assumed to not be significantly protonated, using a range of wavelengths (Figure 4.8, A). The best *E*-*Z* photoconversion was achieved using a 408 nm laser diode, with an estimated PSS of (90 ± 3)% *Z*-isomer. The fast isomerisation rate of this compound (see below) meant that the PSS composition could not be quantified by NMR. Instead, the PSS composition was estimated by the method described previously in section 2.2.3 (see Appendix 7.3.3 for data) and used to obtain an estimated spectrum for the pure *Z*-isomer (Figure 4.8, A). Irradiation with 415 nm light generated by a dye laser resulted in a PSS of (79 ± 5)% *Z*-isomer; this wavelength was chosen to carry out further photoswitching due to the tunablity of the power using this light source. 532 nm irradiation of the n-π* absorbance of the *Z*-isomer resulted in quantitative switching of the azobisimidazole back to the *E*-isomer. This occurred at a considerably faster rate than that of the *Z*-*E* thermal isomerisation. Notably, *Z*-**91** has an intense n-π* absorbance (λ_{max} = 495 nm, ε = 8,000 M^{-1} cm^{-1}), much stronger than that seen for *Z*-azobenzenes (λ_{max} = ~450 nm, ε = 1,500 M^{-1} cm^{-1}).[25] This is in line with the DFT calculations that predict a twisted conformation.

The *Z*-*E* thermal isomerisation rate of neutral **91** was measured at 25 °C using UV/vis spectroscopy in aqueous buffer at pH 9 and the half-life was found to be 16 seconds. This is considerably faster than the thermal isomerisation of the unsymmetrical *N*-methyl(2-phenylazo)imidazole photoswitch reported by Araki and co-workers, which has a thermal half-life of 9 hours, albeit in toluene rather than water.[97] The half-life of **91** was also measured in acetonitrile and, at 2.9 minutes, was still considerably faster than the unsymmetrical analogue. This indicates that the move to a symmetric bisimidazole azo compound has a large impact on the energetics of thermal stability and presumably a similar trend would be seen for other azoheteroarenes.

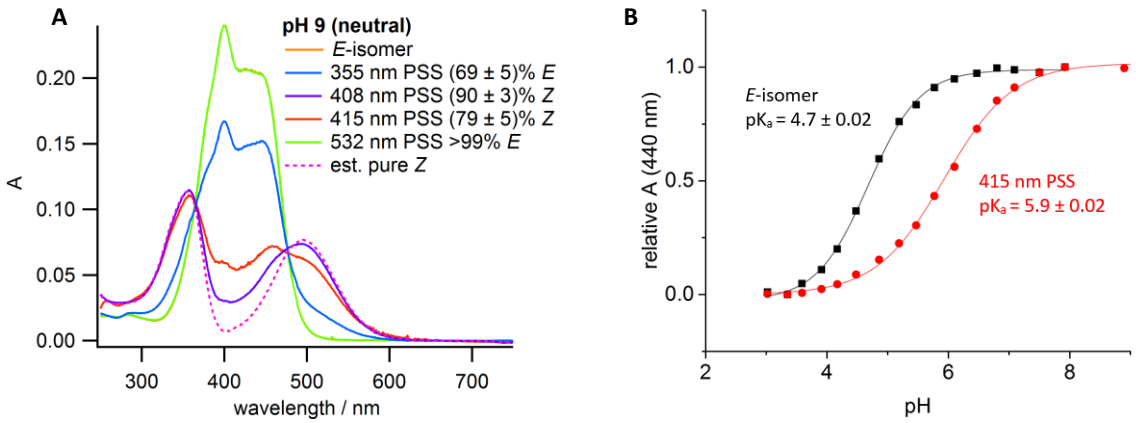


Figure 4.8. A) UV/vis spectra of the PSSs of **91** at different irradiation wavelengths, and estimated pure *Z*-isomer spectrum at 10^{-5} M; B) pH titration of *E*-**91** and the 415 nm PSS.

In order to determine the pK_a of both the *E*-isomer and the 415 nm PSS (79% *Z*), a pH titration was carried out on a buffered aqueous sample of **91**. At each pH increment the UV/vis spectra of the *E*-isomer and the PSS were measured. Due to the fast thermal isomerisation rate, the irradiated sample was allowed to thermally isomerise back to the *E*-isomer before adjusting the pH. The π-π* absorption maximum of the *E*-isomer at 440 nm was plotted against pH in order to obtain the corresponding titration curves (Figure 4.8, B). The pH titration confirmed that at pH 9 azobisimidazole **91** was indeed neutral, so the spectra recorded at that pH were of the purely neutral species (Figure 4.8, A). A pK_a value of 4.7 was obtained for the *E*-isomer and an apparent pK_a of 5.9 was obtained for the *E*/*Z* mixture present in the 415 nm PSS. By considering the PSS and the equilibria present in the system (Figure 4.9), equation 7 was derived (see Appendix 7.1 for derivation – carried out by Dr Robert Richardson), from which the pK_a of the *Z*-isomer was estimated as 6.0.

$$K_a^Z = \frac{K_a^E K_a^{PSS} R_{PSS}^{unprot}}{K_a^E + K_a^E R_{PSS}^{unprot} - K_a^{PSS}} \qquad (7)$$

where K_a is the dissociation constant for the conjugate acid of the *E*- or *Z*-isomer or PSS depending on the superscript, and R_{PSS}^{unprot} is the ratio of isomers in the PSS ([Z]/[E]).

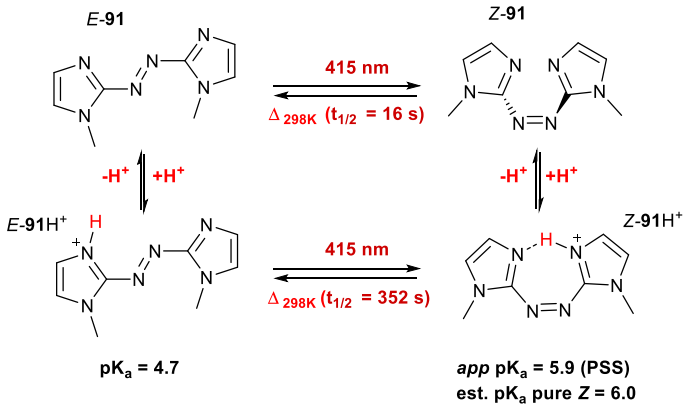


Figure 4.9. The photoswitch species present at different pHs and irradiation wavelengths. Thermal isomerisation rates and pK_a values are included.

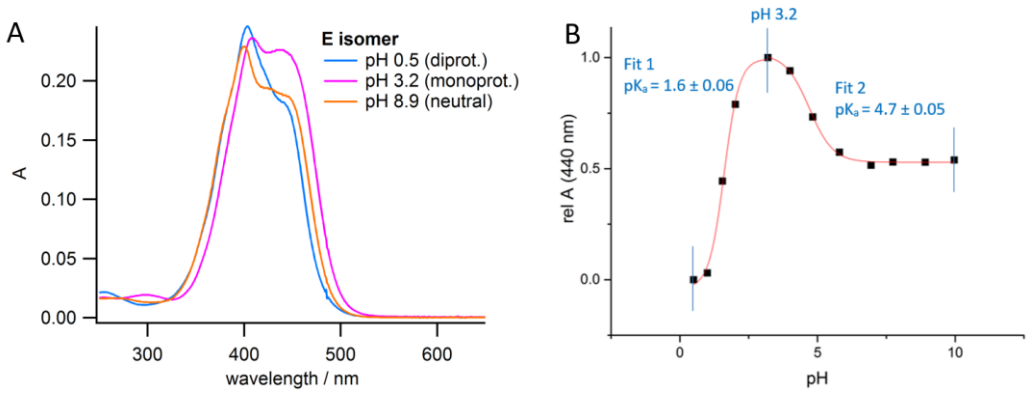


Figure 4.10. A) UV/vis spectra for neutral, mono- and di-protonated *E*-**91**; B) pH titration of *E*-**91** showing mono- and di-protonation events with sigmoidal fits.

A rough titration of the *E*-isomer, continued to a lower pH, showed a second protonation event which was assigned to protonation of the second imidazole ring, with a pK_a of approximately 1.6 (Figure 4.10). Given the results of the pH titration, mono-protonated *E*-**91** should be the only species present at pH 3, therefore further studies were carried out in acidic aqueous buffer at this pH. Irradiation at 415 nm led to a PSS with a very similar spectrum to that of the *E*-isomer (Figure 4.11). Although at first this appears to be a result of a PSS containing predominantly the *E*-isomer, it can instead be attributed to the fact that *E*-**91**H^+ and *Z*-**91**H^+ have very similar UV/vis spectra. This assignment is supported by TDDFT calculated spectra for the protonated *E*- and *Z*-isomers (Figure 4.11); the spectra of both isomers are highly similar due to their planar conformation (Figure 4.7), whereas for the neutral compound, *Z*-**91** adopts a twisted conformation which results in substantial differences betwen the *E*- and *Z*-isomer spectra (Figure 4.6). The protonated compound **91**H^+ was switched between two PSSs upon irradiation with 415 and 532 nm light, however due to the similarity in the *E* and *Z* spectra, the PSS compositions could not be estimated by the method used previously for the neutral compound. The thermal isomerisation rate in aqueous buffer at 25 °C was found to be approximately 20-fold slower than for the neutral compound, with a half-life of 352 seconds for **91**H^+ compared to 16 seconds for neutral **91**, however this was still too short to allow quantification of the PSSs by other methods such as NMR spectroscopy. The increased half-life of the *Z*-isomer upon protonation is attributed to the requirement to (partially) break the intramolecular hydrogen bond present in *Z*-**91**H^+ in either the rotation or inversion transition states for thermal *Z*-*E* isomerisation. This trend is opposite to that observed by Woolley and co-workers for their tetra(*o*-methoxy)aminoazobenzene photoswitches upon protonation (Figure 4.2), where the protonated *Z*-isomer has a much shorter half life than the neutral species.[58,59] This difference is due to the different protonation sites for the photoswitches; protonation of the azo group in the *ortho*-substituted aminoazobenzenes (Figure 4.2) increases the thermal *Z*-*E* isomerisation rate –

protonated azobenzenes in general undergo very fast thermal isomerisation, as discussed in section 1.3.[25] For the azobisimidazole, where protonation occurs on the imidazole nitrogen, the azo group is not involved in the protonation event.

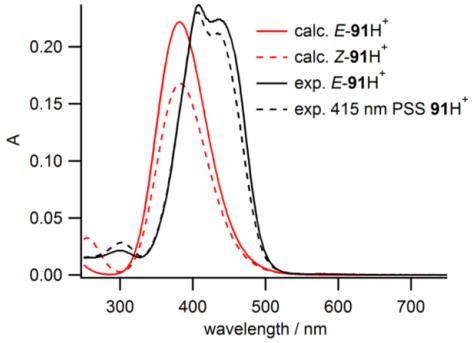


Figure 4.11. Comparison of experimental and calculated (CAM-B3LYP/6-311G(2df,2p) spectra for protonated **91**.

4.2.4 Computational NMR predictions

In order to provide further characterisation of the photoswitchable base, NMR spectra of the protonated species were recorded. Due to the fast thermal isomerisation rate of the *Z*-isomer, and the limitations of the equipment available, spectra were obtained for the *E*-isomer only. Computational NMR predictions were also carried out to provide further evidence for the protonation site on the *E*-isomer. This was carried out with the assistance of Dr Robert Richardson. The ^{13}C NMR chemical shifts for deuteronated *E*-**91** were compared to calculated chemical shifts for *E*-**91** protonated on either the imidazole or the azo. The NMR spectra were recorded in CD_3OD rather than D_2O due to a lack of solubility of the neutral compound at the concentrations required. Therefore geometry optimisations were repeated for the neutral and protonated species using the PCM method for methanol at the B3LYP/6−31G(d,p) level of theory (Table 7.16, Appendix). The gauge-including atomic orbital (GIAO) method was used for NMR chemical shift calculations, as this has been well established for predicting accurate chemical shifts, particularly for ^{13}C NMR.[257–260] The calculations were carried out at both B3LYP/6-311G(2df,2p) and mPW1PW91/6-311G(2df,2p) levels of theory to ensure that changing the functional didn't affect the results. NMR shielding tensors (σ) were calculated for the lowest energy conformers (which were the same as those found with water as the solvent model) and also for benzene as a reference. Chemical shifts (δ^x_{calc}) were obtained using equation 8 and the calculated shielding tensors (σ^{ref}) and experimental chemical shifts (δ^{ref}_{exp}) for benzene.[261]

$$\delta^x_{calc} = \delta^{ref}_{exp} + \sigma^{ref} - \sigma^x \qquad (8)$$

The calculated chemical shifts were then scaled relative to the calculated and experimental chemical shifts for neutral *E*-**91**. A graph of δ_{calc} vs δ_{exp} was plotted and the slope and intercept of the linear fit (Figure 7.44, Appendix) were used in equation 9 to give the scaled chemical shift.[257]

$$\delta_{scaled} = \frac{\delta_{calc} - intercept}{slope} \qquad (9)$$

The difference in experimental and calculated chemical shift was much smaller for the imidazolium calculated structure than the azonium (Figure 4.12), indicating that protonation had occurred on the imidazole nitrogen rather than the azo. The results for the two different functionals were almost identical, showing that changing the computational method had no effect on the findings. This data further confirms our hypothesis that protonation occurs on the imidazole rather than azo nitrogen.

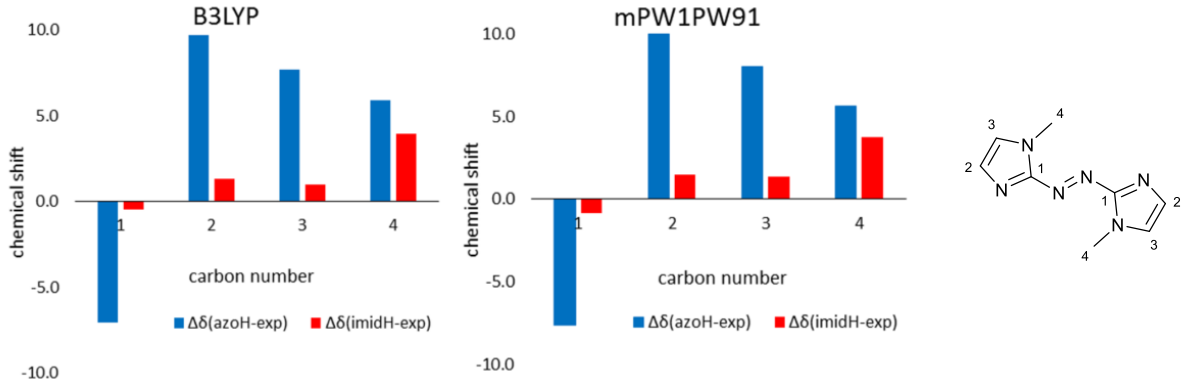


Figure 4.12. Difference in calculated chemical shift values for protonation on the azo (azoH) or imidazole (imidH) and the experimental (exp) chemical shifts for *E*-**91**H$^+$.

4.2.5 pH jump

Given the significant pK_a difference between the *E*- and *Z*-isomers of azobisimidazole **91**, an attempt was made to achieve reversible pH jump upon photoswitching. Photocontrol of solution pH has many potential uses, such as controlling the rate of a specific base catalysed reaction, or modulating enzyme activity.[237] In order to measure the pH of the solution a pH indicator was used; this would allow the pH of the sample to be quantified using UV/vis spectroscopy. This method has been established for measuring solution pH and pH jumps for several different systems.[246,262,263] Bromocresol purple (BCP) was chosen as it has a similar pK_a value to that of the photoswitch, and it has an absorption maxima at a wavelength where the azobisimidazole has a negligible absorbance. A pH titration was carried out on BCP (Figure 7.40, Appendix) and the extracted pK_a value of 6.8 was similar to the literature value of 6.2 – 6.4.[264]

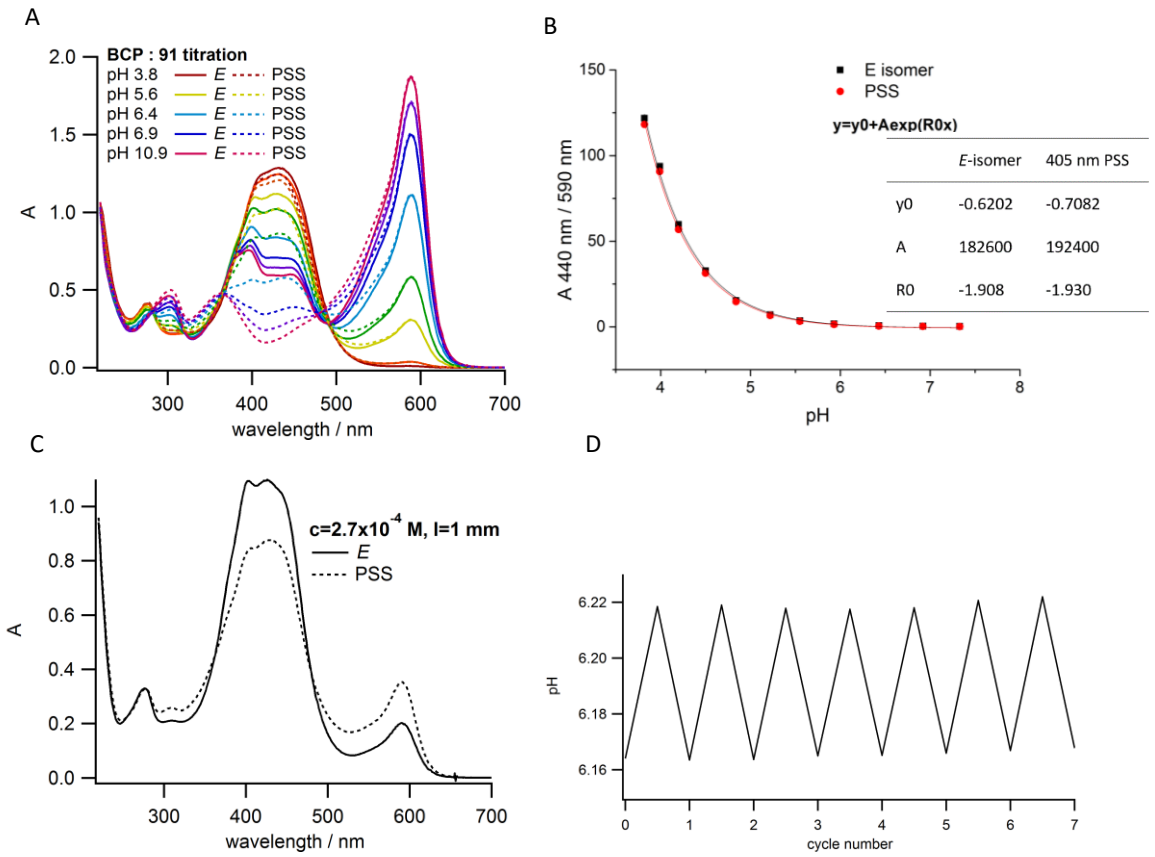


Figure 4.13. *E*-**91** and 405 nm PSS with equimolar BCP; A) pH titration; B) Exponential fit of $A_{440\ nm/590\ nm}$ against pH (440 nm and 590 nm correspond to **91** and BCP λ_{max} respectively); C) pH jump experiment at 2.7×10^{-4} M and 1 mm path length; D) pH oscillation with repeated cycles of photoswitching (405 nm / thermal).

	E-**91**	PSS
A (440 nm)	1.06	0.86
A (590 nm)	0.20	0.35
A (440/590 nm)	5.25	2.43
pH	5.42	5.71

Table 4.1. The absorbances at 440 nm and 590 nm obtained from the pH jump experiment for *E*-**91** and the 405 nm PSS (Figure 4.13, C), converted to pH using the values obtained from the exponential fit of the titration (Figure 4.13, B).

Prior to attempting the pH jump, pH titrations of both *E*-**91** and the 405 nm PSS with equimolar BCP were carried out (Figure 4.13, A). Irradiation was carried out with 405 nm light due to unavailability of the 415 nm light source used previously, at the time of the experiments. From this pH titration, a graph was plotted of the ratio of absorbance at 440 nm (*E*-**91** λ_{max}) and at 590 nm (BCP λ_{max}) versus pH and the exponential fit was obtained (Figure 4.13, B). Using this graph the pH value of a given sample of **91** and equimolar BCP could be extracted from its UV/vis spectrum. Irradiation of a 2.7×10^{-4} M aqueous solution of **91** at 405 nm resulted in an immediate change in the pH of the sample (Figure 4.13, C). A jump of 0.29 pH units was extracted (Table 4.1), which equates to a three-fold reduction in proton concentration in the PSS. In theory, using a 1:1 mixture of *E*-**91** and *E*-**91**H^+ as a buffer solution (*i.e.* [**91**] >> $[H^+]_{soln}$) should enable a pH jump equal to the difference in pK_a values

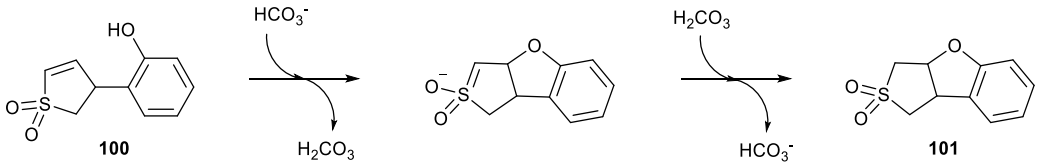
of the two isomers (ΔpK_a ~1.3). However, due to the concentrations being used, buffering by the indicator and potentially by carbonate is likely to decrease the range that can be obtained. Decreasing the concentration from 10^{-4} to 10^{-5} M concentration resulted in a decrease in the pH jump observed and similarly an increase in concentration would be expected to result in an increase in the pH jump. Unfortunately this could not be attempted due to the maximum absorption limit of UV/vis spectroscopy. The fast thermal isomerisation rate and small change in pH made other methods of pH detection, such as using a pH probe, impractical. In order to demonstrate the reproducibility of the pH jump, several repeated cycles of photoswitching were carried out (Figure 4.13, D). The pH jump was consistent each time, within 3% of the mean value, suggesting that no irreversible photochemistry involving the indicator was occurring.

4.2.6 Photocontrol of a cyclisation reaction

In order to further demonstrate the potential uses of the photoswitchable base, the photocontrol of a general base catalysed reaction was attempted. Theoretically, the more basic *Z*-isomer should catalyse such a reaction faster than the *E*-isomer and a difference in rate should be seen, as was observed in the piperidine-containing azobenzenes developed by Hecht and co-workers.[80,83,84] Several requirements need to be met when selecting an appropriate reaction. Firstly, a system is needed where the pK_a values are compatible with those of the photoswitch. Secondly, due to the short half-life of *Z*-**91**, the *Z*-isomer catalysed reaction has to be irradiated for the length of the reaction time. This means that reactions involving light sensitive reactants or products need to be avoided to prevent any side reactions or decomposition occurring during irradiation. If the photoswitch had a longer thermal half-life, as with Hecht's piperidine-containing azobenzenes,[80] photoisomerisation could be carried out prior to adding the photoswitch to the reaction, and a wider range of reactions would be accessible. Thirdly, the reaction conditions need to be adaptable to being carried out in a photoreactor, so a reaction is required that proceeds at room temperature and ideally is not air sensitive.

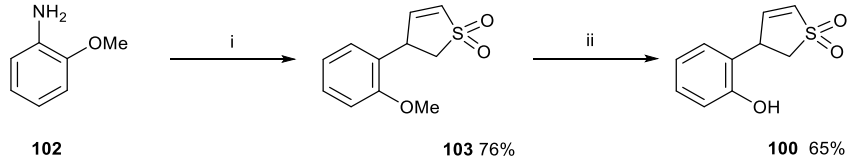
These requirements led to us choosing an intramolecular cyclisation reaction involving deprotonation of *ortho*-substituted phenol **100** to give tricyclic system **101**, reported by Chou and co-workers (Scheme 4.4).[265] The reported reaction was carried out for 20 hours at room temperature in a biphasic mixture of saturated aqueous $NaHCO_3$ and THF. $NaHCO_3$ has a very similar pK_a value to that of *Z*-**91** (pK_a = 6.3 and 6.0 respectively), therefore carrying out the reaction with *Z*-**91** as the base should result in a faster reaction rate than with *E*-**91**, which has a pK_a of 4.7. Due to the fairly long reported reaction time with excess $NaHCO_3$, the reaction was initially carried out in

the presence of one equivalent of **91**. This would hopefully result in sufficiently long reaction times to allow aliquots to be removed for monitoring by NMR and then be returned to the reaction mixture. Given the method for monitoring the reaction, deuterated solvents were selected for use.



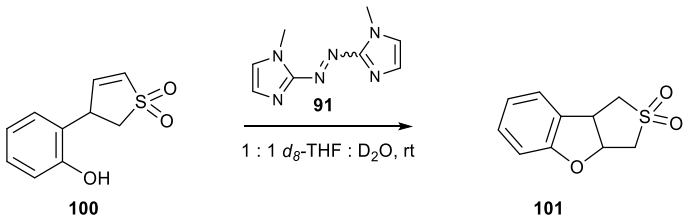
Scheme 4.4. Cyclisation reaction catalysed by $NaHCO_3$.

The starting material (**100**) for the cyclisation reaction was prepared in two steps according to the reported procedure (Scheme 4.5).[265] The tetrafluoroborate diazonium salt derived from *o*-anisidine (**102**) was prepared *in situ* and coupled with butadiene sulfone to give intermediate **103** in 76% yield, which was then demethylated with hydrobromic acid to afford **100** in 65% yield.



Scheme 4.5. Preparation of the starting material for the cyclisation reaction. Reagents and conditions: (i) aq. $NaNO_2$, 48% HBF_4, 0 °C, 1 h; then butadiene sulfone in MeOH, $Pd(OAc)_2$, reflux, 1 h; (ii) 47% HBr, reflux, 3 h.

With compound **100** in hand, the cyclisation reaction in the presence of *E*- or *Z*-**91** could be carried out (Scheme 4.6). Irradiation of the *E*-isomer to a *Z*-rich PSS was carried out once **91** was added to the reaction mixture, using a photoreactor fitted with visible light bulbs (λ_{max} ~420 nm). The reaction was stirred in a clear vial to enable irradiation of the entire sample. In order to ensure that all variables other than light were consistent between the *E*- and *Z*-**91** reactions, the *E*-**91** reaction (the 'dark' reaction) was also carried out in the photoreactor, but in an amber vial to prevent light reaching the sample. Both clear and amber vials were placed in water baths to try to maintain the same temperature for both reactions. The temperature in each vial was measured at intervals throughout the reaction time to ensure that there was no additional heating occurring in the irradiated sample. As mentioned above, the reactions were run in deuterated solvents (D_2O : d_8-THF) to allow analysis of the kinetics by proton NMR – the length of time that each aliquot was removed from the reaction was deemed sufficiently short relative to the overall reaction time to not adversely affect the results (<1% of the total time).



Scheme 4.6. Cyclisation reaction using *E*- or *Z*-**91** as the base.

The reactions were carried out under various conditions (Table 4.2) and the reaction rates were plotted (Figure 4.14). The results were not very consistent and in general did not fit the exponential curves very well. Experiment A and B were both degassed with argon, however, in experiment A, there was no difference in rate between the irradiated and dark reactions, while in experiment B, the irradiated reaction rate was twice as fast as the dark reaction. In experiment C, where the reaction was carried out under argon atmosphere but not degassed, the difference in rate was reversed – the dark reaction occurred at a faster rate than the irradiated reaction. It is possible that the difference in results is due to solvent evaporation during degassing leading to different ratios of D_2O : d_8-THF, although the solvent was cooled during degassing to try to avoid this. Experiment D was carried out under an air atmosphere with no degassing and also included control reactions, where no azobisimidazole was added. The irradiated and dark reaction with **91** present had very similar rates, comparable to experiment A. The controls were expected to have slow reaction rates compared to the reactions containing **91**, however the dark control reaction actually had the fastest rate, while the irradiated control reaction had a very slow rate that did not fit an exponential curve (Figure 4.14, D).

Experiment no.	Conditions	Reagents
A	Degassed w/ argon	**100** + **91**
B	Degassed w/ argon	**100** + **91**
C	Argon atmosphere	**100** + **91**
D	Air atmosphere	**100** + **91**, or **100** only (control)

Table 4.2. Reaction conditions for cyclisation reactions.

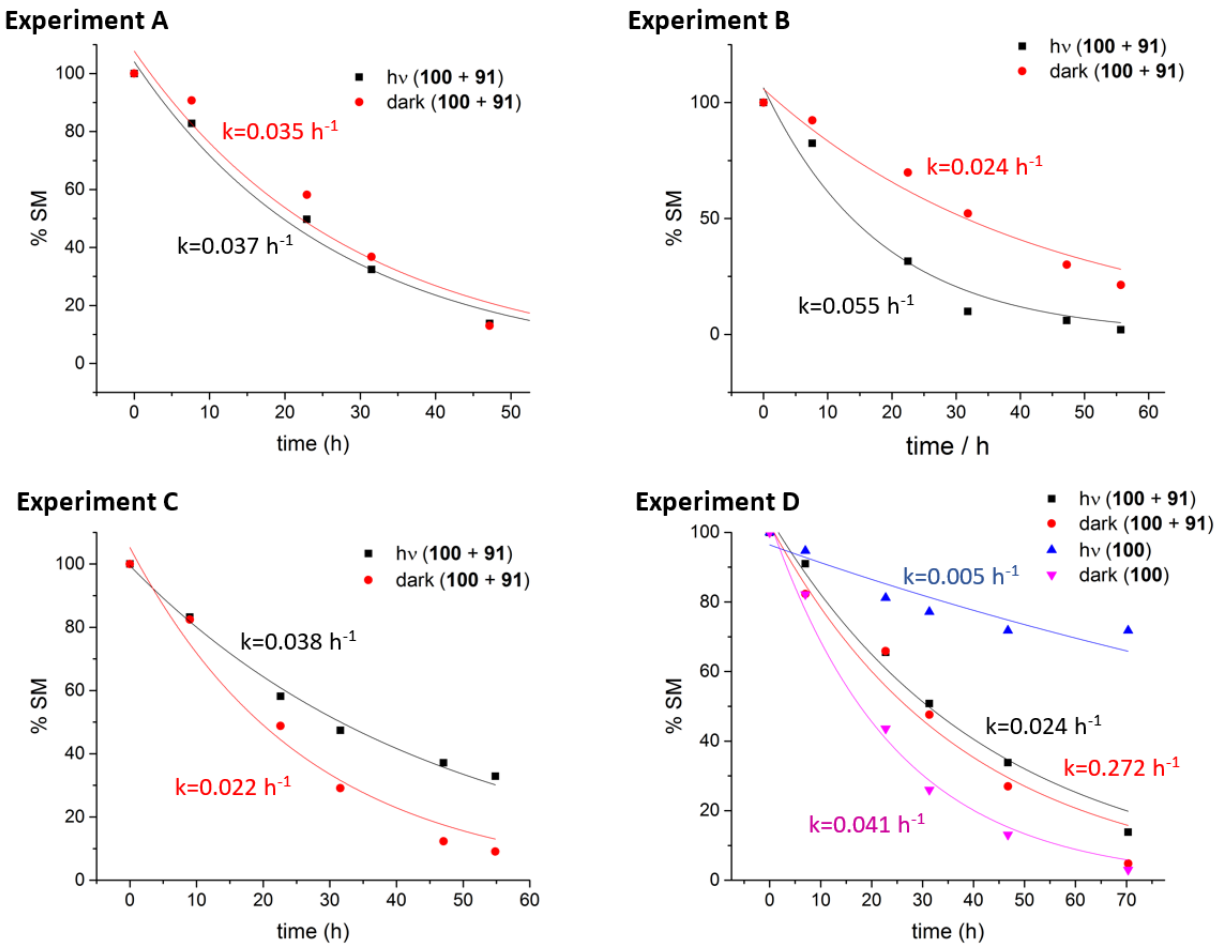


Figure 4.14. Reaction rates for irradiated and dark reactions.

In light of the conflicting results in experiments A to C, no further experimental work was carried out to try to explain the odd results obtained from the control reactions. It is possible that either the starting material or product is sensitive to the presence of oxygen, perhaps through the generation of singlet oxygen upon irradiation. Similarly, the inconsistent results may have been caused by off-target photochemistry involving the aromatic system or the sulfone, however neither should be excited by the irradiation wavelengths used in this work.[266,267] By integrating to the residual solvent peak, it did not appear that decomposition was occurring in either sample. Another potential explanation for the inconsistency in reaction rates is the difficulty in controlling the temperature during the reaction when one sample is being irradiated. Although temperature measurements taken throughout the reaction were consistent between the irradiated and dark reactions (within 1 °C), it is possible that localised heating was occurring that went undetected. Finally, the difference in pK_a values between the two isomers may not actually be sufficient to cause a significant enough change in reaction rate. The pK_a of phenol is approximately 10, so it may be that the difference in pK_a of 1.3 between *E*- and *Z*-**91** is not enough when the pK_a of the photoswitch is 4 – 5 orders of magnitude less than that of the phenol starting material. It is possible that

photocontrol of reaction rate could be achieved with the azobisimidazole if a different reaction was chosen. For example, one involving deprotonation of a carboxylic acid where the pK_a was much closer in value to the photoswitch, although care would have to be taken that the irradiation wavelengths used didn't cause unwanted photochemistry.

4.3 CONCLUSIONS

An azobisimidazole photoswitchable base was designed with basic nitrogens on the two imidazole rings, correctly positioned to stabilise a proton in the *Z*-isomer. This compound was readily accessible through a facile two-step synthesis. In contrast to the systems reported by Woolley,[58,59] the protonation event occurs on one of the imidazole rings and, in the *Z*-isomer, is additionally stabilised by the neighbouring imidazole ring, rather than through participation of the azo moiety. The protonation site was confirmed through computational analysis of the energy minimised conformations and by comparing calculated NMR chemical shifts with the experimental values. The hydrogen bond stabilisation resulted in the *Z*-isomer being over an order of magnitude more basic than the *E*-isomer. Furthermore, by avoiding protonation of the azo group, the thermal half-life of the protonated *Z*-isomer was increased relative to the neutral form. A pH jump was achieved upon irradiating an aqueous solution of the photoswitch, albeit smaller than the state of the art.[81,245] Increasing the concentration of the sample should in theory allow greater pH jumps to be achieved, however this was not possible with the current method of detection.

The attempted photocontrol of the base catalysed cyclisation reaction was unsuccessful, with highly variable results seen and unexpected reaction rates when controls were carried out. One limitation of the azobisimidazole photoswitch, with regards to this application, is the fast thermal half-life. If the thermal isomerisation rate were slower, the photoswitch could have been irradiated prior to starting the cyclisation reaction rather than requiring continuous irradiation throughout. This would have made it easier to ensure that the reaction conditions were consistent among the different samples and monitoring the reaction would have been more straightforward. A slow half-life would have also been a benefit for the pH jump experiments, as it would have allowed different methods of pH measurement, where higher concentrations could have been used.

In future work, other azoheteroarene photoswitches with correctly positioned basic heteroatoms could be studied to try to identify those with slower thermal isomerisation rates. Isomerisation rates could be predicted computationally using the methods developed in section 2.3.5.

5 EXPERIMENTAL

5.1 Synthesis – general methods

All reagents and solvents were supplied from commercial sources and used as received unless otherwise indicated. All reactions were carried out under N_2 unless specified otherwise. Reactions requiring anhydrous conditions were conducted in oven-dried glassware under an inert atmosphere (N_2 or Ar), and using anhydrous solvents. DCM, NEt_3, and pyridine were distilled over CaH_2. THF was distilled over Na/benzophenone. MeOH was distilled over Mg. Anhydrous chemicals were obtained commercially. All water used was distilled.

All reactions were monitored by thin-layer chromatography (TLC) using Merck silica gel 60 F254 plates (0.25 mm). TLC plates were visualized using UV light (254 nm) and/or by staining in potassium permanganate, ninhydrin, phosphomolybdic acid or vanillin, as appropriate. Flash column chromatography was performed using silica gel (Sigma-Aldrich) 40-63 μm 60 Å treated with a solvent system. The eluents used are specified in individual procedures. Solvents were removed by rotary evaporator at 40 °C or below and the compounds further dried using high vacuum pumps.

Melting points were obtained on a Reichert-Thermovar melting point apparatus and are uncorrected. Infrared spectra were recorded on a Perkin Elmer Frontier FT-IR Spectrometer. Reported absorptions are given in wavenumbers (cm^{-1}). Broad signals are labelled (br.). ^1H and ^{13}C NMR were recorded on a Bruker Advance 400 spectrometer at 400 MHz and 100 MHz respectively or a Bruker Advance 500 spectrometer at 500 MHz and 125 MHz respectively. Chemical shifts (δ) are quoted in ppm (parts per million) and referenced to residual solvent signals: ^1H δ = 7.27 ($CDCl_3$), 2.50 (d_6-DMSO), 3.31 (CD_3OD), 4.75 (D_2O); ^{13}C δ = 77.0 ($CDCl_3$), 39.51 (d_6-DMSO), 49.00 (CD_3OD). Coupling constants (*J*) are given in Hz. The following abbreviations are used to designate multiplicity within ^1H NMR analysis; s = singlet, d = double, t = triplet, q = quartet, quin = quintet, m = multiplet, br. = broad signal, *app* = apparent. Any signals corresponding to more than one carbon within ^{13}C NMR analysis are quantified in brackets. Low and high resolution mass spectra (EI, CI, ESI, APCI) were recorded by the Imperial College London Department of Chemistry Mass Spectroscopy Service using a Micromass Autospec Premier and Micromass LCT Premier spectrometer.

5.2 Synthesis – experimental procedures

5.2.1 General procedures

General procedure A – *diazonium coupling*

According to a modified literature procedure,[101] 12 M HCl (0.42 mL/mmol) was added to a suspension of aniline (1.0 equiv.) in water (1 mL/mmol) at 0 °C and the mixture was stirred for 5 min. $NaNO_2$ (1.1 equiv.) in water (1 mL/mmol) was added dropwise and the resulting solution was stirred at 0 °C for 1 h. A suspension of the appropriate pyrrole derivative (1.0 equiv.) in MeOH (6 mL/mmol) and pyridine (1 mL/mmol) was added, resulting in the formation of an orange-red precipitate. The suspension was stirred for 1 h at 0 °C, then concentrated under reduced pressure. The resulting residue was extracted with EtOAc (3 × 10 mL/mmol), washed with brine, dried over $MgSO_4$, and concentrated under reduced pressure to afford the crude product. Purification methods are specified in individual procedures.

General procedure B – *N-methylation*

Sodium hydride (60% dispersion in mineral oil) (2.0 equiv.) was added in several aliquots to a solution of the appropriate azopyrrole derivative (1.0 equiv.) in anhydrous THF (5 mL/mmol) at 0 °C and the mixture was stirred at 0 °C for 30 min. Methyl iodide (2.05 equiv.) was added dropwise and the resulting solution was stirred at 60 °C for 1 h. After cooling, the reaction mixture was quenched with water (10 mL/mmol) and extracted with DCM (2 × 10 mL/mmol). The combined organic layers were washed with water and brine, then dried over $MgSO_4$ and concentrated under reduced pressure to afford the crude product, which was purified by flash column chromatography (eluent systems are specified in individual procedures).

General procedure C – *modified Mills reaction*

According to a modified literature procedure,[108] a solution of the appropriate aminoheteroarene (1.1 equiv.) and nitrosobenzene (1.0 equiv.) in a 1 : 1 mixture of toluene and 40% aq. NaOH (2 mL/mmol) was stirred at 80 °C for the required time (specified in individual procedures). The reaction mixture was cooled, diluted with water (2 mL/mmol) and extracted with EtOAc (3 × 5 mL/mmol). The combined organic layers were washed with brine, dried over $MgSO_4$, and concentrated under reduced pressure to afford the crude product, which was purified by flash column chromatography (eluent systems are specified in individual procedures).

General procedure D – *Heck reaction*

According to a procedure developed in the Fuchter group,[194] NEt_3 (3.0 equiv.), tri(*o*-tolyl)phosphine (0.1 equiv.), and $Pd(OAc)_2$ (0.05 equiv.) were added to a solution of the appropriate azobenzene derivative (1.0 equiv.) and THP-protected *N*-hydroxyacrylamide **62** (1.5 equiv.) in anhydrous DMF (4 mL/mmol). The resulting mixture was stirred at 100 °C for 24 h, then quenched with water (20 mL/mmol) and extracted with DCM (2 × 20 mL/mmol). The combined organic layers were washed sequentially with 5% aq. LiCl and brine, dried over $MgSO_4$ and concentrated under reduced pressure to afford the crude product, which was purified by flash column chromatography (eluent systems are specified in individual procedures).

General procedure E – *THP deprotection*

According to a procedure developed in the Fuchter group,[194] a solution of the appropriate THP-protected hydroxamate derivative (1.0 equiv.) and PPTS (0.1 equiv.) in a 1 : 1 mixture of *i*-PrOH and THF (20 mL/mmol) was heated for the required time (specified in individual procedures) and concentrated under reduced pressure. Purification methods are specified in individual procedures.

General procedure F – *Wittig reaction*

According to a modified literature procedure,[6] LiOH (1.5 equiv.) was added to a stirred suspension of phosphonium ylide **64** (1.1 equiv.) in *i*-PrOH (4 mL/mmol). After 15 min, the appropriate benzaldehyde derivative (1.0 equiv.) was added and the reaction mixture was heated under reflux for the required time (specified in individual procedures). This was quenched with water and extracted with EtOAc (3 × 30 mL/mmol). The combined organic phases were washed with brine until neutral, dried over $MgSO_4$, and concentrated under reduced pressure to afford the crude product, which was purified by flash column chromatography to give the product as a mixture of *E*- and *Z*-isomers. Small aliquots of each isomer were separated by chromatography to allow characterisation.

General procedure G – *amide coupling*

According to a modified literature procedure,[227] *O*-(tetrahydropyran-2-yl)-hydroxylamine (1.2 equiv.), NEt_3 (2.0 equiv.), and HBTU (1.2 equiv.), were added to the appropriate azobenzene-carboxylic acid derivative (1.0 equiv.) in DMF (4 mL/mmol) and the solution was stirred at rt overnight. Purification method is specified in individual procedures.

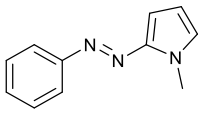
General procedure H – *nitro reduction*

According to a modified literature procedure,[232] sodium sulfide (3.0 equiv.) was added to the appropriate *p*-nitroazobenzene derivative (1.0 equiv.) in a 3 : 1 mixture of THF and water

(4 mL/mmol) and stirred for the required time at rt (specified in individual procedures). The reaction mixture was diluted with water and extracted with EtOAc (2 × 10 mL/mmol). The aqueous phase was saturated with NaCl and further extracted with EtOAc (3 × 10 mL/mmol). The combined organic layers were washed with brine, dried over $MgSO_4$, and concentrated under reduced pressure.

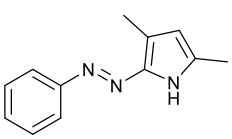
5.2.2 Arylazopyrazoles and pyrroles

(*E*)-1-Methyl-2-(phenyldiazenyl)-1*H*-pyrrole (21)



Compound **21** was prepared according to a modified literature procedure for a related compound.[105] 12 M HCl (2.8 mL) was added to a suspension of aniline (0.50 mL, 5.5 mmol, 1.2 equiv.) in a 1 : 1 mixture of acetone and water (20 mL) at 0 °C and the mixture was stirred for 5 min. $NaNO_2$ (0.44 g, 6.4 mmol, 1.4 equiv.) in water (4 mL) was added dropwise and the resulting solution was stirred at 0 °C for 1 h, then transferred by cannula into a suspension of *N*-methylpyrrole (0.41 mL, 4.6 mmol, 1.0 equiv.) and Na_2CO_3 (0.97 g, 9.15 mmol, 2.0 equiv.) in a 1 : 1 mixture of acetone and water (20 mL), resulting in formation of an orange precipitate. The mixture was stirred at rt for 1 h and concentrated under reduced pressure. The residue was extracted with DCM (3 × 50 mL) and the combined organic layers were washed with brine, dried over $MgSO_4$, and concentrated under reduced pressure. Purification by flash column chromatography (pentane : Et_2O, 50 : 1) afforded **21** as an orange solid (0.44 g, 52%). R_f 0.29 (pentane : Et_2O, 50 : 1); m.p. 40 – 42 °C (DCM-pentane); IR (neat) 1496, 1347, 1326, 1038, 767; ^{1}H NMR (400 MHz, $CDCl_3$) δ 7.82 (d, *J* = 7.3 Hz, 2H, 2 × phenyl-CH), 7.47 (t, *J* = 7.3 Hz, 2H, 2 × phenyl-CH), 7.37 (t, *J* = 7.3 Hz, 1H, phenyl-CH), 6.95 (br. t, *J* = 2.0 Hz, 1H, pyrrole-CH), 6.72 (dd, *J* = 4.4, 1.5 Hz, 1H, pyrrole-CH), 6.30 (dd, *J* = 4.2, 2.7 Hz, 1H, pyrrole-CH), 3.98 (s, 3H, CH_3); ^{13}C NMR (100 MHz, $CDCl_3$) δ 153.6, 146.5, 129.3, 129.0 (2C), 126.8, 122.0 (2C), 110.2, 100.0, 33.4; MS (ESI) *m/z* 186 $(M+H)^+$; HRMS (ESI) *m/z* calc. for $C_{11}H_{12}N_3$ 186.1031, found: 186.0997.

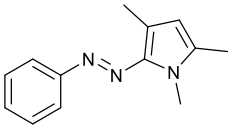
(*E*)-3,5-Dimethyl-2-(phenyldiazenyl)-1*H*-pyrrole (**26**)



Following general procedure A, diazonium coupling with 2,4-dimethylpyrrole (0.56 mL, 5.5 mmol) gave the crude product as a brown solid. Purification by flash column chromatography

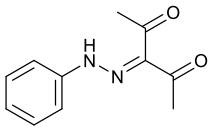
(pentane : Et_2O, 10 : 1) afforded **26** as a brown solid (0.78 g, 71%). R_f 0.31 (pentane : Et_2O, 10 : 1) m.p. 102 – 104 °C (DCM-pentane); IR (neat) 3170, 1466, 1343, 1138, 819; ^{1}H NMR (400 MHz, $CDCl_3$) δ 8.86 (br. s, 1H, NH), 7.76 (d, *J* = 7.5 Hz, 2H, 2 × phenyl-CH), 7.44 (t, *J* = 7.5 Hz, 2H, 2 × phenyl-CH), 7.30 (t, *J* = 7.5 Hz, 1H, phenyl-CH), 5.95 (s, 1H, pyrrole-CH), 2.42 (s, 3H, CH_3), 2.31 (s, 3H,CH_3); ^{13}C NMR (100 MHz, $CDCl_3$) δ 153.1, 142.5, 135.1, 130.2, 129.0 (2C), 128.2, 121.5 (2C), 112.2, 13.4, 10.7; MS (APCI) *m/z* 200 $(M+H)^+$; HRMS (APCI) *m/z* calc. for $C_{12}H_{14}N_3$ 200.1182, found: 200.1178.

(*E*)-1,3,5-Trimethyl-2-(phenyldiazenyl)-1*H*-pyrrole (**22**)



Methylation of azopyrrole **26** was carried out following general procedure B, but with 1.8 equiv. of both NaH (60% dispersion in mineral oil) and methyl iodide and a reaction time of 2 h. Purification by flash column chromatography (pentane : Et_2O, 10 : 1) afforded **22** as an orange solid (0.32 g, 58%). R_f 0.59 (pentane : Et_2O, 10 : 1); m.p. 62 – 64 °C (DCM-pentane); IR (neat) 1468, 1347, 1138, 766; ^{1}H NMR (400 MHz, $CDCl_3$) δ 7.75 (d, *J* = 7.5 Hz, 2H, 2 × phenyl-CH), 7.43 (t, *J* = 7.5 Hz, 2H, 2 × phenyl-CH), 7.29 (t, *J* = 7.5 Hz, 1H, phenyl-CH), 5.93 (s, 1H, pyrrole-CH), 3.82 (s, 3H, NCH_3), 2.41 (s, 3H, CH_3), 2.30 (s, 3H, CH_3); ^{13}C NMR (100 MHz, $CDCl_3$) δ 154.3, 141.8, 135.1, 128.8 (2C), 127.9, 121.3 (2C), 118.4, 112.1, 30.3, 14.1, 12.7; MS (ESI) *m/z* 214 $(M+H)^+$; HRMS (ESI) *m/z* calc. for $C_{13}H_{16}N_3$ 214.1344, found: 214.1354.

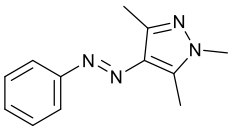
3-(2-Phenylhydrazono)pentane-2,4-dione[106] **(27)**



$NaNO_2$ (0.61 g, 8.8 mmol, 1.2 equiv.) in water (2.5 mL) was added dropwise to a solution of aniline (0.70 mL, 7.4 mmol, 1.0 equiv.) in AcOH (10 mL) and 12 M HCl (1.7 mL) at 0 °C. The resulting solution was stirred at 0 °C for 1 h, then transferred by cannula into a suspension of pentan-2,4-dione (0.98 mL, 9.6 mmol, 1.3 equiv.) and NaOAc (1.81 g, 22.1 mmol, 3 equiv.) in EtOH (7 mL) and water (4 mL), forming a yellow precipitate. The reaction mixture was stirred for 1 h at rt and the precipitate was collected by filtration, washed sequentially with water, a 1 : 1 mixture of water and EtOH, and hexane, then dried under vacuum to afford **27** as a yellow solid (1.50 g, quant.). ^{1}H NMR (400 MHz, $CDCl_3$) δ 14.76 (br. s, 1H, NH), 7.43 – 7.42 (m, 4H, 4 × phenyl-CH), 7.23 – 7.21 (m, 1H, phenyl-CH),

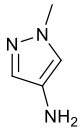
2.62 (s, 3H, CH_3), 2.51 (s, 3H, CH_3); ^{13}C NMR (100 MHz, $CDCl_3$) δ 198.0, 197.1, 141.6, 133.3, 129.7 (2C), 125.9, 116.3 (2C), 31.7, 26.7; MS (ESI) *m/z* 205 $(M+H)^+$; HRMS (ESI) *m/z* calc. for $C_{11}H_{13}N_2O_2$ 205.0977, found: 205.0983.

(*E*)-1,3,5-Trimethyl-4-(phenyldiazenyl)-1*H*-pyrazole[268] (24)



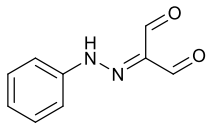
Methylhydrazine (0.30 mL, 5.78 mmol, 1.0 equiv.) was added to a solution of **27** (1.18 g, 5.78 mmol, 1.0 equiv.) in EtOH (30 mL) and heated under reflux for 3 h. Concentration under reduced pressure afforded **24** as a yellow-orange solid (1.22 g, quant.). IR (neat) 1551, 1507, 1416, 759; ^{1}H NMR (400 MHz, $CDCl_3$) δ 7.79 (d, *J* = 7.3 Hz, 2H, 2 × phenyl-CH), 7.47 (t, *J* = 7.3 Hz, 2H, 2 × phenyl-CH), 7.38 (t, *J* = 7.3 Hz, 1H, phenyl-CH), 3.80 (s, 3H, NCH_3), 2.59 (s, 3H, CH_3), 2.51 (s, 3H, CH_3); ^{13}C NMR (100 MHz, $CDCl_3$) δ 153.6, 142.4, 138.8, 135.1, 129.3, 128.9 (2C), 121.8 (2C), 36.0, 13.9, 10.0; MS (ESI) *m/z* 215 $(M+H)^+$; HRMS (ESI) *m/z* calc. for $C_{12}H_{15}N_4$ 215.1297, found: 215.1294.

1-Methyl-1*H*-pyrazol-4-amine[269] (29)



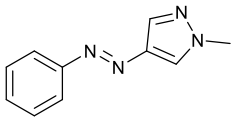
K_2CO_3 (3.45 g, 24.9 mmol, 2.0 equiv.) and methyl iodide (0.86 mL, 13.8 mmol, 1.1 equiv.) were added to a solution of 4-nitropyrazole (**28**) (1.41 g, 12.5 mmol, 1.0 equiv.) in MeCN (50 mL). The resulting suspension was stirred at 60 °C overnight, then cooled to rt, diluted with EtOAc (50 mL) and washed with water (2 × 50 mL). The organic phase was dried over $MgSO_4$ and concentrated under reduced pressure. The resulting crude residue was taken up in anhydrous MeOH (60 mL, purged with N_2) and 10% Pd/C (0.26 g) was added. H_2 was bubbled through the resulting suspension for 5 min and the reaction mixture was then stirred under a H_2 atmosphere overnight. Filtration through celite and concentration under reduced pressure gave the crude product. Purification by flash column chromatography (0.03 M NH_3 in DCM : MeOH, 95 : 5) afforded **29** as a purple oil (0.71 g, 58%). R_f 0.23 (0.03 M NH_3 in DCM : MeOH, 95 : 5); ^{1}H NMR (400 MHz, $CDCl_3$) δ 7.15 (s, 1H, CH), 6.99 (s, 1H, CH), 3.80 (s, 3H, CH_3), 2.88 (br. s, 2H, NH_2); ^{13}C NMR (100 MHz, $CDCl_3$) δ 131.1, 129.0, 119.4, 39.0; MS (ESI) *m/z* 98 $(M+H)^+$; HRMS (ESI) *m/z* calc. for $C_4H_8N_3$ 98.0718, found: 98.0703.

2-(2-Phenylhydrazono)malonaldehyde[112] (30)



$NaNO_2$ (0.83 g, 12.1 mmol, 1.1 equiv.) in water (2.5 mL) was added dropwise to a solution of aniline (1.0 mL, 10.9 mmol, 1.0 equiv.) in water (20 mL) and 12 M HCl (2.2 mL) at 0 °C. The resulting solution was stirred at 0 °C for 1 h, then transferred by cannula into a suspension of 3-dimethylaminoacrolein (1.1 mL, 10.9 mmol, 1.0 equiv.) and NaOAc (0.22 g, 2.64 mmol, 3.0 equiv.) in EtOH (30 mL), forming a brown precipitate. The reaction mixture was stirred for 1 h at rt and the precipitate was collected by filtration, washed with water and dried under vacuum to afford **30** as an amorphous brown solid (0.86 g, 45%). ^{1}H NMR (400 MHz, $CDCl_3$) δ 14.64 (br. s, 1H, NH), 10.0 (s, 1H, CHO), 9.64 (s, 1H, CHO), 7.52 (d, *J* = 8.0 Hz, 2H, 2 × phenyl-CH), 7.46 (t, *J* = 8.0 Hz, 2H, 2 × phenyl-CH), 7.29 (t, *J* = 8.0 Hz, 1H, phenyl-CH); ^{13}C NMR (100 MHz, $CDCl_3$) δ 189.7, 186.7, 140.6, 133.3, 129.8 (2C), 127.3, 116.9 (2C); MS (ESI) *m/z* 177 $(M+H)^+$; HRMS (ESI) *m/z* calc. for $C_9H_9N_2O_2$ 177.0664, found: 177.0666.

(*E*)-1-Methyl-4-(phenyldiazenyl)-1*H*-pyrazole (23)



Following general procedure C, nitrosobenzene (0.25 g, 2.3 mmol) and **29** (0.25 g, 2.6 mmol) in a 1 : 1 mixture of 1 : 1 pyridine and 40% aq. NaOH (6 mL) were heated for 2 h. Purification by flash column chromatography (pentane : Et_2O, 10 : 1) afforded **23** as an orange solid (144 mg, 33%).

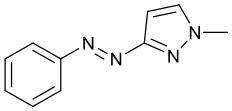
or

Methylhydrazine (0.08 mL, 1.5 mmol, 1.0 equiv.) was added to a solution of **30** (0.26 g, 1.5 mmol, 1.0 equiv.) in EtOH (10 mL) and heated under reflux for 1 h. Once cooled, the reaction mixture was concentrated under reduced pressure, redissolved in EtOAc (10 mL), washed sequentially with water (2 × 10 mL) and brine (10 mL), dried over $MgSO_4$ and concentrated under reduced pressure to afford **23** as an orange solid (0.26 g, 55%).

R_f 0.2 (pentane : Et_2O, 3 : 1); m.p. 50 – 52 °C (DCM-pentane); IR (neat) 1528, 1462, 1155, 1016, 764; ^{1}H NMR (400 MHz, $CDCl_3$) δ 8.03 (s, 1H, pyrazole-CH), 7.98 (s, 1H, pyrazole-CH), 7.80 (d, *J* = 7.3 Hz, 2H, 2 × phenyl-CH), 7.49 (t, *J* = 7.3 Hz, 2H, 2 × phenyl-CH), 7.43 (t, *J* = 7.3 Hz, 1H, phenyl-CH), 3.99 (s, 3H, CH_3); ^{13}C NMR (100 MHz, $CDCl_3$) δ 152.9, 141.9, 133.4, 130.2, 129.0 (2C), 126.8, 122.2 (2C), 39.6; MS (ESI) *m/z* 187 $(M+H)^+$; HRMS (ESI) *m/z* calc. for $C_{10}H_{11}N_4$ 187.0984, found: 187.0982.

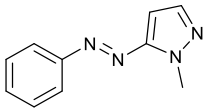
5.2.3 Further study of arylazoheteroarenes

(*E*)-1-Methyl-3-(phenyldiazenyl)-1*H*-pyrazole (31)



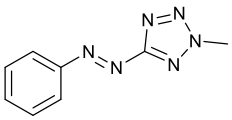
Following general procedure C, 1-methyl-1*H*-pyrazol-3-amine (**39**) (0.45 g, 4.63 mmol) and nitrosobenzene (0.45 g, 4.21 mmol) were heated for 6 h, to give the crude product as a brown solid. Purification by flash column chromatography (pentane : DCM, 1 : 2) afforded **31** as an orange solid (0.23 g, 27%). R_f 0.15 (pentane : DCM, 1 : 2); m.p. 86 – 88 °C (DCM-pentane); IR (neat) 1473, 1364, 1302, 1208, 1050; ^{1}H NMR (400 MHz, $CDCl_3$) δ 7.95 (d, *J* = 6.8 Hz, 2H, 2 × phenyl-CH), 7.57 – 7.40 (m, 3H, 3 × phenyl-CH), 7.37 (d, *J* = 2.4 Hz, 1H, pyrazole-CH), 6.64 (d, *J* = 2.4 Hz, 1H, pyrazole-CH), 3.99 (s, 3H, CH_3); ^{13}C NMR (100 MHz, $CDCl_3$) δ 163.6, 152.6, 131.7, 131.0, 128.9 (2C), 122.8 (2C), 96.0, 39.5; MS (ESI) *m/z* 187 $(M+H)^+$; HRMS (ESI) *m/z* calc. for $C_{10}H_{11}N_4$ 187.0984, found: 187.0978.

(*E*)-1-Methyl-5-(phenyldiazenyl)-1*H*-pyrazole (33)



Following general procedure C, 1-methyl-1*H*-pyrazol-5-amine (**40**) (100 mg, 1.03 mmol) and nitrosobenzene (100 mg, 0.94 mmol) were heated overnight. Purification by flash column chromatography (pentane : EtOAc, 20 : 1) afforded **33** as an orange solid (104 mg, 60%). R_f 0.15 (pentane : EtOAc, 20 : 1); m.p. 48 – 50 °C (DCM-pentane); IR (neat) 1583, 1509, 1399, 1289, 789; ^{1}H NMR (400 MHz, $CDCl_3$) δ 7.91 (dd, *J* = 8.3, 2.0 Hz, 2H, 2 × phenyl-CH), 7.57 (d, *J* = 2.1 Hz, pyrazole-CH), 7.56 – 7.50 (m, 3H, 3 × phenyl-CH), 6.57 (d, *J* = 2.1 Hz, 1H, pyrazole-CH), 4.26 (s, 3H, CH_3); ^{13}C NMR (100 MHz, $CDCl_3$) δ 153.1, 152.8, 139.1, 131.5, 129.1 (2C), 122.8 (2C), 93.7, 36.1; MS (ESI) *m/z* 187 $(M+H)^+$; HRMS (ESI) *m/z* calc. for $C_{10}H_{11}N_4$ 187.0984, found: 187.0992.

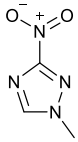
(*E*)-2-Methyl-5-(phenyldiazenyl)-2*H*-tetrazole (37)



Following general procedure C, 2-methyl-2*H*-tetrazol-5-amine (**41**) (110 mg, 1.11 mmol) and nitrosobenzene (108 mg, 1.01 mmol) were heated for 5 h. Purification by flash column chromatography (pentane : DCM, 1 : 1) afforded **37** as an orange solid (0.14 g, 74%). R_f 0.15

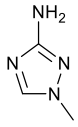
(pentane : DCM, 1 : 1); m.p. 101 – 103 °C (DCM-pentane); IR (neat) 1489, 1442, 1386, 1151, 780; ^{1}H NMR (400 MHz, $CDCl_3$) δ 8.10 (dd, *J* = 7.8, 2.0 Hz, 2H, 2 × phenyl-CH), 7.62 – 7.54 (m, 3H, 3 × phenyl-CH), 4.49 (s, 3H, CH_3); ^{13}C NMR (100 MHz, $CDCl_3$) δ 171.8, 152.5, 133.4, 129.3 (2C), 123.9 (2C), 40.2; MS (ESI) *m/z* 189 $(M+H)^+$; HRMS (ESI) *m/z* calc. for $C_8H_9N_6$ 189.0889, found: 189.0889.

1-Methyl-3-nitro-1*H*-1,2,4-triazole[130] (43)



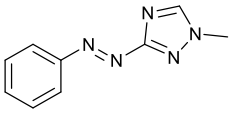
A solution of LiOH (0.21 g, 8.76 mmol, 1.0 equiv.) and dimethyl sulfate (0.83 mL, 8.76 mmol, 1.0 equiv.) in EtOH (2 mL) was added to a suspension of 3-nitro-1*H*-1,2,4-triazole (**42**) (1.00 g, 8.76 mmol, 1.0 equiv.) in EtOH (5 mL) and the mixture was stirred at 75 °C overnight. The resulting salt was filtered off and the filtrate was concentrated under reduced pressure. DCM was added to the residue and this was washed sequentially with dilute aq. Na_2CO_3 (10 mL) and water (10 mL), then dried over $MgSO_4$ and concentrated under reduced pressure to afford the crude product as a mixture of regioisomers (3-nitro **43** : 5-nitro ratio, 2 : 1). Purification by flash column chromatography (DCM : MeOH, 99 : 1) gave **43** as a white solid (0.37 g, 33%). R_f 0.30 (DCM : MeOH, 99 : 1); ^{1}H NMR (400 MHz, $CDCl_3$) δ 8.20 (s, 1H, CH), 4.08 (s, 3H, CH_3); ^{13}C NMR (100 MHz, $CDCl_3$) δ 162.7, 145.3, 37.7; MS (CI) *m/z* 146 $(M+NH_4)^+$; HRMS (CI) *m/z* calc. for $C_3H_8N_5O_2$ 146.0678, found: 146.0682.

1-Methyl-1*H*-1,2,4-triazol-3-amine[133] (44)



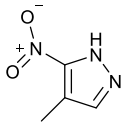
Nitrotriazole **43** (145 mg, 1.13 mmol, 1.0 equiv.) was added to 10% Pd/C (12 mg) and hydrazine monohydrate (0.13 mL, 2.6 mmol, 2.3 equiv.) in anhydrous MeOH (1.5 mL, purged with N_2) and the resulting mixture was heated under reflux for 3 h. After cooling, the reaction mixture was filtered through celite and washed with MeOH. The filtrate was concentrated under reduced pressure to afford **44** as a white solid (100 mg, 90%). ^{1}H NMR (400 MHz, $CDCl_3$) δ 7.62 (s, 1H, CH), 3.82 (br. s, 2H, NH_2), 3.71 (s, 3H, CH_3); ^{13}C NMR (100 MHz, $CDCl_3$) δ 163.6, 142.6, 35.8; MS (EI) *m/z* 98 $(M)^+$; HRMS (EI) *m/z* calc. for $C_3H_6N_4$ 98.0592, found: 98.0598.

(*E*)-1-Methyl-3-(phenyldiazenyl)-1*H*-1,2,4-triazole (38)



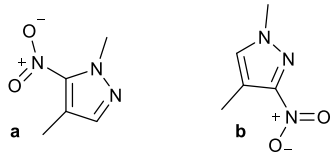
Following general procedure C, aminotriazole **44** (60 mg, 0.61 mmol) and nitrosobenzene (60 mg, 0.56 mmol) were heated for 6 h. Purification by flash column chromatography (DCM : MeOH, 99 : 1) afforded **38** as an orange solid (60 mg, 57%). R_f 0.12 (DCM : MeOH, 99 : 1); m.p. 129 – 131 °C (DCM-pentane); IR (neat) 1501, 1343, 1215, 1046, 776; ^{1}H NMR (400 MHz, $CDCl_3$) δ 8.14 (s, 1H, triazole-CH), 8.09 – 8.05 (m, 2H, 2 × phenyl-CH), 7.54 – 7.50 (m, 3H, 3 × phenyl-CH), 4.06 (s, 3H, CH_3); ^{13}C NMR (100 MHz, $CDCl_3$) δ 169.3, 152.5, 144.8, 132.3, 129.1 (2C), 123.6 (2C), 36.9; MS (ESI) *m/z* 188 $(M+H)^+$; HRMS (ESI) *m/z* calc. for $C_9H_{10}N_5$ 188.0936, found: 188.0935.

4-Methyl-5-nitro-1*H*-pyrazole[134] (47)



Nitric acid (70%, 5.5 mL, 61 mmol, 1.0 equiv.) and acetic anhydride (11.5 mL, 122 mmol, 2.0 equiv.) were added to a solution of 4-methylpyrazole (**45**) (5.00 g, 60.9 mmol, 1.0 equiv.) in AcOH (19 mL). The resulting solution was stirred at rt for 2 h, then diluted with water (20 mL) and extracted with EtOAc (3 × 20 mL), dried over $MgSO_4$, and concentrated under reduced pressure to afford crude 1-nitro-4-methylpyrazole (**46**). This was redissolved in benzonitrile (25 mL) and stirred at 160 °C for 6 h. Once the reaction mixture was cooled to rt, hexane (100 mL) was added and the resulting precipitate was filtered off to give **47** as a cream solid (0.93 g, 12%). ^{1}H NMR (400 MHz, $CDCl_3$) δ 13.19 (br. s, 1H, NH), 7.71 (s, 1H, CH), 2.44 (s, 3H, CH_3); ^{13}C NMR (100 MHz, $CDCl_3$) δ 154.0, 131.9, 114.1, 9.6; MS (EI) *m/z* 127 $(M)^+$; HRMS (EI) *m/z* calc. for $C_4H_5N_3O_2$ 127.0382, found: 127.0386.

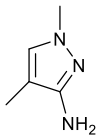
1,4-Dimethyl-3/5-nitro-1*H*-pyrazole[270] (48)



Following a modified literature procedure for 1-methyl-3-nitrotriazole **43**,[130] dimethyl sulfate (1.0 mL, 11 mmol, 2.0 equiv.) was added dropwise to a solution of nitropyrazole **47** (0.70 g, 5.5 mmol, 1.0 equiv.) and LiOH (0.26 mg, 11 mmol, 2.0 equiv.) in EtOH (20 mL) at rt and the reaction mixture was stirred at 75 °C overnight. The solvent was removed under reduced pressure and DCM

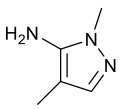
was added to the yellow residue. This was washed sequentially with dilute aq. Na_2CO_3 (15 mL) and water (15 mL), dried over $MgSO_4$, and concentrated under reduced pressure to afford **48** as a mixture of regioisomers. Kugelrohr distillation (80 °C, 8×10^{-1} mbar) gave 5-nitropyrazole **48b** as a clear oil (0.18 g). 3-nitropyrazole **48a**, was obtained as a white solid from the residue (0.53 g), giving a combined yield of 91% (**48a** : **48b** ratio, 3 : 1). Recrystallisation of **48a** by vapour diffusion of pentane into DCM gave a white square crystal, from which the absolute structure was unambiguously determined by X-ray crystallography (Appendix 7.2). **1,4-Dimethyl-3-nitropyrazole (48a)** m.p. 86 – 88 °C (DCM-pentane); IR (neat) 1576, 1506, 1343, 1314, 1191, 1024, 845; ^{1}H NMR (400 MHz, $CDCl_3$) δ 7.27 (d, *J* = 1.0 Hz, 1H, CH), 3.93 (s, 3H, NCH_3), 2.31 (d, *J* = 1.0 Hz, 3H, CH_3); ^{13}C NMR (100 MHz, $CDCl_3$) δ 153.3, 132.2, 115.1, 40.1, 9.5; MS (CI) *m/z* 159 $(M+NH_4)^+$; HRMS (CI) *m/z* calc. for $C_5H_{11}N_4$ 159.0882, found: 159.0877. **1,4-Dimethyl-5-nitropyrazole (48b)** ^{1}H NMR (400 MHz, $CDCl_3$) δ 7.35 (d, *J* = 0.4 Hz, 1H, CH), 4.20 (s, 3H, NCH_3), 2.34 (d, *J* = 0.4 Hz, 3H, CH_3); ^{13}C NMR (100 MHz, $CDCl_3$) δ 143.3, 138.9, 118.5, 41.3, 10.5.

1,4-Dimethyl-1*H*-pyrazol-3-amine[271] **(49)**



A solution of **48a** (33 mg, 0.23 mmol) in anhydrous MeOH (2 mL, purged with N_2) was added to 10% Pd/C (5 mg) at rt. H_2 gas was bubbled through the suspension for 5 min, and the mixture was then stirred for 4 h under H_2 atmosphere (1 atm). The reaction mixture was filtered through a celite plug and concentrated under reduced pressure to afford **49** as a white solid (24 mg, 92%). IR (neat) 3326 (br.), 3224 (br.), 1618, 1505, 1442; ^{1}H NMR (400 MHz, $CDCl_3$) δ 6.91 (s, 1H, CH), 3.67 (s, 3H, NCH_3), 2.57 (br. s, 2H, NH_2), 1.92 (s, 3H, CH_3); ^{13}C NMR (100 MHz, $CDCl_3$) δ 152.5, 129.9, 101.6, 38.2, 7.4; MS (EI) *m/z* 111 $(M)^+$; HRMS (EI) *m/z* calc. for $C_5H_9N_3$ 111.0796, found: 111.0791.

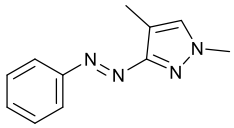
1,4-Dimethyl-1*H*-pyrazol-5-amine[271] **(50)**



Following the procedure described for the preparation of aminopyrazole **49**, a suspension of nitropyrazole **48b** (0.18 g, 1.28 mmol) and 10% Pd/C (20 mg) in MeOH (5 mL) was stirred for 4 h under H_2 atmosphere to afford **50** as a white solid (0.14 g, 98%). IR (neat) 3371 (br.), 3124 (br.), 3083 (br.), 1642, 1585, 1535, 1408, 975; ^{1}H NMR (400 MHz, $CDCl_3$) δ 7.11 (s, 1H, CH), 3.65 (s. 3H, NCH_3),

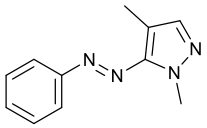
3.27 (br. s, 2H, NH_2), 1.90 (s, 3H, CH_3); ^{13}C NMR (100 MHz, $CDCl_3$) δ 141.3, 138.2, 100.1, 34.5, 7.9; MS (CI) *m/z* 112 $(M+H)^+$; HRMS (CI) *m/z* calc. for $C_5H_{10}N_3$ 112.0875, found: 112.0881.

(*E*)-1,4-Dimethyl-3-(phenyldiazenyl)-1*H*-pyrazole (32)



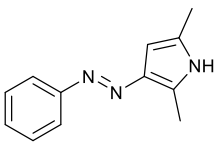
Following general procedure C, aminopyrazole **49** (50 mg, 0.45 mmol) and nitrosobenzene (44 mg, 0.41 mmol) were heated overnight. Purification by flash column chromatography (pentane : EtOAc, 20 : 1) afforded **32** as an orange oil (32 mg, 36%). R_f 0.31 (pentane : EtOAc, 20 : 1); IR (neat) 1471, 1360, 1318, 1179, 816; ^1H NMR (400 MHz, $CDCl_3$) δ 8.04 - 7.88 (m, 2H, 2 × phenyl-CH), 7.57 – 7.41 (m, 3H, 3 × phenyl-CH), 7.22 (s, 1H, pyrazole-CH), 3.97 (s, 3H, NCH_3), 2.36 (s, 3H, CH_3); ^{13}C NMR (100 MHz, $CDCl_3$) δ 159.4, 153.1, 131.1, 130.6, 128.9 (2C), 122.7 (2C), 112.7, 39.5, 9.5; MS (ESI) *m/z* 201 $(M+H)^+$; HRMS (ESI) *m/z* calc. for $C_{11}H_{13}N_4$ 201.1140, found: 201.1136.

(*E*)-1,4-Dimethyl-5-(phenyldiazenyl)-1*H*-pyrazole (34)



Following general procedure C, aminopyrazole **50** (55 mg, 0.49 mmol) and nitrosobenzene (48 mg, 0.45 mmol) were heated overnight. Purification by flash column chromatography (pentane : EtOAc, 20 : 1) afforded **34** as an orange oil (53 mg, 59%). R_f 0.21 (pentane : EtOAc, 20 : 1); IR (neat) 1553, 1434, 1401, 1302, 1007; ^1H NMR (400 MHz, $CDCl_3$) δ 7.94 – 7.81 (m, 2H, 2 × phenyl-CH), 7.56 – 7.43 (m, 3H, 3 × phenyl-CH), 7.38 (s, 1H, pyrazole-CH), 4.19 (s, 3H, NCH_3), 2.33 (s, 3H, CH_3); ^{13}C NMR (100 MHz, $CDCl_3$) δ 153.3, 148.5, 139.8, 131.0, 129.1 (2C), 122.4 (2C), 109.0, 36.7, 10.6; MS (ESI) *m/z* 201 $(M+H)^+$; HRMS (ESI) *m/z* calc. for $C_{11}H_{13}N_4$ 201.1140, found: 201.1143.

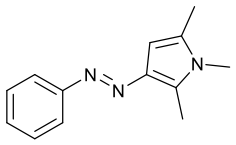
(*E*)-2,5-Dimethyl-3-(phenyldiazenyl)-1*H*-pyrrole (54)



Following general procedure A, diazonium coupling with 2,5-dimethylpyrrole (0.30 mL, 3.0 mmol) gave the crude product as a brown oil. Purification by flash column chromatography (pentane : EtOAc, 20 : 1) afforded **54** as an orange solid (0.56 g, 95%). R_f 0.20 (pentane : EtOAc,

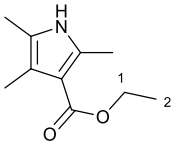
20 : 1); m.p. 108 – 109 °C (DCM-pentane); IR (neat) 3206, 3097, 2982, 1524, 1400, 1265, 989; ^{1}H NMR (400 MHz, $CDCl_3$) δ 7.93 (br. s, 1H, NH), 7.80 (td, *J* = 8.3, 1.0 Hz, 2H, 2 × phenyl-CH), 7.45 (d, *J* = 7.3 Hz, 2H, 2 × phenyl-CH), 7.33 (tt, *J* = 6.8, 1.0 Hz, 1H, phenyl-CH), 6.26 (dd, *J* = 2.9, 1.0 Hz, 1H, pyrrole-CH), 2.60 (s, 3H, CH_3), 2.25 (s, 3H, CH_3); ^{13}C NMR (100 MHz, $CDCl_3$) δ 153.8, 140.8, 133.8, 128.8 (2C), 128.5, 128.5, 121.8 (2C), 95.8, 13.1, 10.6; MS (ESI) *m/z* 200 $(M+H)^+$; HRMS (ESI) *m/z* calc. for $C_{12}H_{14}N_3$ 200.1188, found: 200.1199.

(*E*)-1,2,5-Trimethyl-3-(phenyldiazenyl)-1*H*-pyrrole (35)



Methylation of azopyrrole **54** (0.14 g, 0.70 mmol) was carried out following general procedure B. Purification by flash column chromatography (pentane : EtOAc, 20 : 1) afforded **35** as an orange solid (95 mg, 64%). R_f 0.19 (pentane : EtOAc, 20 : 1); m.p. 81 – 83 °C (DCM-pentane); IR (neat) 1532, 1400, 1345, 772; ^{1}H NMR (400 MHz, $CDCl_3$) δ 7.79 (d, *J* = 7.5 Hz, 2H, 2 × phenyl-CH), 7.44 (t, *J* = 7.5 Hz, 2H, 2 × phenyl-CH), 7.32 (t, *J* = 7.5 Hz, 1H, phenyl-CH), 6.30 (d, *J* = 1.0 Hz, 1H, pyrrole-CH), 3.47 (s, 3H, NCH_3), 2.59 (s, 3H, CH_3), 2.25 (s, 3H, CH_3); ^{13}C NMR (100 MHz, $CDCl_3$) δ 154.0, 140.0, 135.8, 130.5, 128.8 (2C), 128.2, 121.7 (2C), 95.2, 30.2, 12.4, 9.8; MS (ESI) *m/z* 214 $(M+H)^+$; HRMS (ESI) *m/z* calc. for $C_{13}H_{16}N_3$ 214.1344, found: 214.1347.

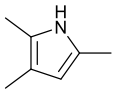
Ethyl 2,4,5-trimethyl-1*H*-pyrrole-3-carboxylate[136] (52)



A solution of ethyl 4-methylpyrrole-3-carboxylate (**51**) (0.90 g, 5.87 mmol) and paraformaldehyde (0.99 g) in AcOH (16.2 mL), hydriodic acid (16.2 mL) and hypophosphoric acid (3.2 mL) was stirred at rt for 2 h. The reaction mixture was then poured onto water (50 mL) and aq. NH_4OH was added until the solution was basic. This was then extracted with DCM (3 × 50 mL), dried over $MgSO_4$, and concentrated under reduced pressure. Purification by flash column chromatography (pentane : EtOAc, 20 : 1) afforded **52** as a white solid (0.95 g, 89%). R_f 0.14 (pentane : EtOAc, 20 : 1); ^{1}H NMR (400 MHz, $CDCl_3$) δ 7.68 (br. s, 1H, NH), 4.27 (q, *J* = 7.2 Hz, 2H, C(1)H_2), 2.46 (s, 3H, CH_3), 2.15 (s, 3H, CH_3), 2.12 (s, 3H, CH_3), 1.35 (t, *J* = 7.2 Hz, 3H, C(2)H_3); ^{13}C NMR (100 MHz, $CDCl_3$) δ 166.4,

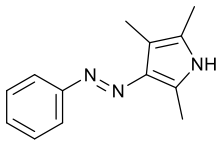
133.5, 121.9, 116.1, 110.9, 58.9, 14.5, 13.9, 10.9, 10.5; MS (ESI) *m/z* 182 $(M+H)^+$; HRMS (ESI) *m/z* calc. for $C_{10}H_{16}NO_2$ 182.1181, found: 182.1175.

2,3,5-Trimethyl-1*H*-pyrrole (53)[272]



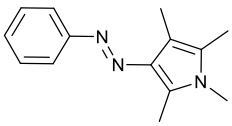
A solution of pyrrole **52** (0.91 g, 5.0 mmol) in conc. H_2SO_4 (2.8 mL), EtOH (10 mL) and water (0.25 mL) was heated under reflux for 1 h and once cooled was poured onto water (20 mL). This was extracted with DCM (3 × 20 mL), dried over $MgSO_4$, and concentrated under reduced pressure to afford **53** as a brown oil (0.27 g). This was carried forward to the next step as the crude material. ^{1}H NMR (400 MHz, $CDCl_3$) δ 5.64 (d, *J* = 2.4 Hz, 1H, CH), 2.21 (s, 3H, CH_3), 2.14 (s, 3H, CH_3), 1.97 (s, 3H, CH_3).

(*E*)-2,3,5-Trimethyl-4-(phenyldiazenyl)-1*H*-pyrrole (55)



Following general procedure A, diazonium coupling with 2,3,5-trimethylpyrrole **53** (0.27 g, 2.5 mmol) gave the crude product as a brown oil. Purification by flash column chromatography (pentane : EtOAc, 20 : 1) afforded **55** as an red-orange oil (0.18 g, 17% over two steps). R_f 0.18 (pentane : EtOAc, 20 : 1); IR (neat) 3406, 1478, 1457, 1390, 1221; ^{1}H NMR (400 MHz, $CDCl_3$) δ 7.76 (dd, *J* = 7.8, 1.5 Hz, 2H, 2 × phenyl-CH), 7.69 (br. s, 1H, NH), 7.44 (t, *J* = 7.8 Hz, 2H, 2 × phenyl-CH), 7.32 (tt, *J* = 7.8, 2.0 Hz, 1H, phenyl-CH), 2.57 (s, 3H, CH_3), 2.27 (s, 3H, CH_3), 2.17 (s, 3H, CH_3); ^{13}C NMR (100 MHz, $CDCl_3$) δ 154.2, 138.2, 131.1, 128.7 (2C), 128.2, 123.7, 121.5 (2C), 108.2, 11.3, 11.0, 10.6; MS (ESI) *m/z* 214 $(M+H)^+$; HRMS (ESI) *m/z* calc. for $C_{13}H_{16}N_3$ 214.1344, found: 214.1345.

(*E*)-1,2,3,5-Tetramethyl-4-(phenyldiazenyl)-1*H*-pyrrole (36)

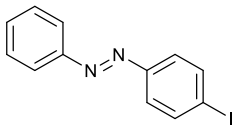


Methylation of azopyrrole **55** (0.18 g, 0.84 mmol) was carried out following general procedure B. Purification by flash column chromatography (pentane : EtOAc, 50 : 1) afforded **36** as an orange solid (105 mg, 55%). R_f 0.25 (pentane : EtOAc, 50 : 1); m.p. 84 – 86 °C (DCM-pentane); IR (neat)

1524, 1384, 1347, 1192, 767; ^{1}H NMR (400 MHz, $CDCl_3$) δ 7.76 (dd, *J* = 7.8, 1.5 Hz, 2H, 2 × phenyl-CH), 7.43 (t, *J* = 7.8 Hz, 2H, 2 × phenyl-CH), 7.30 (d, *J* = 7.8 Hz, 1H, phenyl-CH), 3.46 (s, 3H, NCH_3), 2.57 (s, 3H, CH_3), 2.30 (s, 3H, CH_3), 2.16 (s, 3H, CH_3); ^{13}C NMR (100 MHz, $CDCl_3$) δ 154.4, 137.6, 133.9, 128.7 (2C), 127.9, 126.1, 121.4 (2C), 107.3, 30.3, 11.5, 9.9, 9.2; MS (ESI) *m/z* 228 $(M+H)^+$; HRMS (ESI) *m/z* calc. for $C_{14}H_{18}N_3$ 228.1501, found: 228.1494.

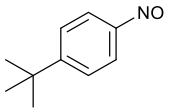
5.2.4 Photoswitchable azobenzene-based HDAC inhibitors

(*E*)-1-(4-Iodophenyl)-2-phenyldiazene[195] (60a)



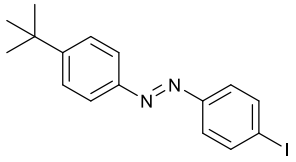
A solution of 4-iodoaniline (2.43 g, 11.1 mmol, 1.0 equiv.) and nitrosobenzene (1.44 g, 13.4 mmol, 1.2 equiv.) in AcOH (90 mL) was stirred at 40 °C overnight. The resulting dark red reaction mixture was quenched with water (400 mL) and extracted with DCM (2 × 400 mL). The combined organic layers were washed with brine (400 mL), dried over $MgSO_4$ and concentrated under reduced pressure. Purification by flash column chromatography (PE : EtOAc, 70 : 1) yielded **60a** as an orange solid (3.24 g, 78%). R_f 0.29 (PE : EtOAc, 70 : 1); ^{1}H NMR (400 MHz, $CDCl_3$) δ 7.93 (d, *J* = 8.3 Hz, 2H, 2 × Ar-CH), 7.88 (d, *J* = 8.3 Hz, 2H, 2 × Ar-CH), 7.67 (d, *J* = 8.3 Hz, 2H, 2 × Ar-CH), 7.55 – 7.50 (m, 3H, 3 × Ar-CH); ^{13}C NMR (100 MHz, $CDCl_3$) δ 152.4, 151.9, 138.3 (2C), 131.4, 129.1 (2C), 124.5 (2C), 122.9 (2C), 97.6; MS (ESI) *m/z* 309 $(M+H)^+$; HRMS (ESI) *m/z* calc. for $C_{12}H_{10}N_2I$ 308.9889, found: 308.9894.

1-(*tert*-Butyl)-4-nitrosobenzene[196] (59)



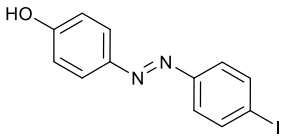
A solution of Oxone® (6.10 g, 19.9 mmol, 2.0 equiv.) in water (50 mL) was added to a solution of 4-(*tert*-butyl)aniline (1.48 g, 9.93 mmol, 1.0 equiv.) in DCM (50 mL). The reaction mixture was stirred overnight under argon. The two phases were separated and the organic phase was washed with water (50 mL), dried over $MgSO_4$ and concentrated under reduced pressure. Purification by flash column chromatography (PE : EtOAc, 20 : 1) yielded **59** as a green oil (0.96 g, 59%). R_f 0.58 (PE : EtOAc, 20 : 1); ^{1}H NMR (400 MHz, $CDCl_3$) δ 7.86 (d, *J* = 8.6 Hz, 2H, 2 × Ar-CH), 7.63 (d, *J* = 8.6 Hz, 2H, 2 × Ar-CH), 1.39 (s, 9H, 3 × CH_3); ^{13}C NMR (100 MHz, $CDCl_3$) δ 165.2, 159.8, 126.1 (2C), 121.0 (2C), 35.6, 31.0 (3C); MS (EI) *m/z* 163 $(M)^+$; HRMS (EI) *m/z* calc. for $C_{10}H_{13}NO$ 163.0997, found: 163.0993.

(*E*)-1-(4-(*Tert*-butyl)phenyl)-2-phenyldiazene[198] (60b)



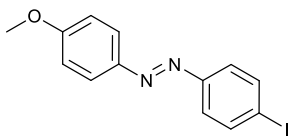
Following the procedure for the preparation of azobenzene **60a**, 4-iodoaniline (1.04 g, 4.75 mmol) and *tert*-butylnitrosobenzene **59** (0.93 g, 5.70 mmol) in AcOH (40 mL) were stirred at 40 °C overnight, resulting in a dark red solution. Purification by flash column chromatography (100% PE) yielded **60b** as an orange solid (1.42 g, 81%). R_f 0.18 (100% PE); IR (neat) 1655, 1624, 1475, 1003; ^{1}H NMR (400 MHz, $CDCl_3$) δ 7.87 (*app*-dd, *J* = 8.8, 2.4 Hz, 4H, 4 × Ar-CH), 7.66 (d, *J* = 8.3 Hz, 2H, 2 × Ar-CH), 7.55 (d, *J* = 8.3 Hz, 2H, 2 × Ar-CH), 1.39 (s, 9H, 3 × CH_3); ^{13}C NMR (100 MHz, $CDCl_3$) 155.0, 152.0, 150.4, 138.3 (2C), 126.1 (2C), 124.4 (2C), 122.7 (2C), 97.2, 35.0, 31.2 (3C); MS (ESI) *m/z* 365 $(M+H)^+$; HRMS (ESI) *m/z* calc. for $C_{16}H_{18}N_2I$ 365.0515, found: 365.0493.

(*E*)-4-((4-Iodophenyl)diazenyl)phenol[105] (61)



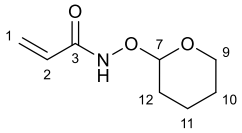
12 M HCl (2.7 mL) was added dropwise to a suspension of 4-iodoaniline (1.33 g, 6.07 mmol, 1.2 equiv.) in a 1 : 1 mixture of acetone and water (15 mL) at 0 °C and stirred for 5 min. $NaNO_2$ (0.49 g, 7.09 mmol, 1.4 equiv.) in water (4 mL) was added dropwise, and the resulting solution was stirred at 0 °C for 1 h, then transferred by cannula into a suspension of phenol (0.48 g, 5.06 mmol, 1.0 equiv.), Na_2CO_3 (1.07 g, 10.1 mmol, 2.0 equiv.), and NaOH (0.81 g, 20.2 mmol, 4.0 equiv.) in a 1 : 1 mixture of acetone and water (15 mL) at 0 °C. The resulting dark red-brown suspension was stirred at rt for 3 h. Acetone was removed under vacuum and the residue was quenched with 1 M HCl, followed by extraction with DCM (3 × 100 mL). The combined organic layers were washed with brine, dried over $MgSO_4$ and concentrated under reduced pressure. Purification by flash column chromatography (PE : EtOAc, 4 : 1) afforded **61** as a dark red solid (1.34 g, 68%). R_f 0.5 (PE : EtOAc, 4 : 1); ^{1}H NMR (400 MHz, $CDCl_3$) δ 7.89 (d, *J* = 8.8 Hz, 2H, 2 × Ar-CH), 7.85 (d, *J* = 8.8 Hz, 2H, 2 × Ar-CH), 7.62 (d, *J* = 8.8 Hz, 2H, 2 × Ar-CH), 6.96 (d, *J* = 8.8 Hz, 2H, 2 × Ar-CH), 5.04 (s, 1H, OH); ^{13}C NMR (100 MHz, $CDCl_3$) 158.5, 152.0, 147.1, 138.3 (2C), 125.2 (2C), 124.2 (2C), 115.9 (2C), 96.8; MS (ESI) *m/z* 325 $(M+H)^+$; HRMS (ESI) *m/z* calc. for $C_{12}H_{10}N_2OI$ 324.9838, found: 324.9835.

(*E*)-1-(4-Iodophenyl)-2-(4-methoxyphenyl)diazene[198] (60c)



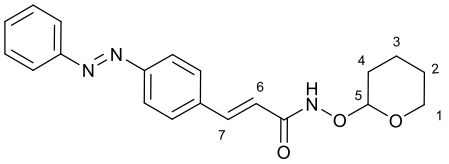
Azobenzene **61** (1.15 g, 3.55 mmol, 1.0 equiv.) was added to a suspension of K_2CO_3 (0.98 g, 7.10 mmol, 2.0 equiv.) and Cs_2CO_3 (0.58 g, 1.77 mmol, 0.5 equiv.) in anhydrous DMF (18 mL). After 10 min, methyl iodide (0.44 mL, 7.1 mmol, 2.0 equiv.) was added and the resulting mixture was stirred at rt for 6 h. This was then quenched with water (80 mL) and extracted with EtOAc (5 × 40 mL). The combined organic layers were washed with brine, dried over $MgSO_4$ and concentrated under reduced pressure. Purification by flash column chromatography (PE : EtOAc, 17 : 1) afforded **60c** as an orange solid (1.12 g, 93%). R_f 0.5 (PE : EtOAc, 17 : 1); IR (neat) 1601, 1492, 1457; ^{1}H NMR (400 MHz, $CDCl_3$) δ 7.93 (d, *J* = 8.8 Hz, 2H, 2 × Ar-CH), 7.85 (d, *J* = 8.8 Hz, 2H, 2 × Ar-CH), 7.63 (d, *J* = 8.8 Hz, 2H, 2 × Ar-CH), 7.03 (d, *J* = 8.8 Hz, 2H, 2 × Ar-CH), 3.91 (s, 3H, OCH_3); ^{13}C NMR (100 MHz, $CDCl_3$) δ 162.3, 152.0, 146.8, 138.2 (2C), 124.9 (2C), 124.2 (2C), 114.3 (2C), 96.7, 55.6; MS (ESI) *m/z* 339 $(M+H)^+$; HRMS (ESI) *m/z* calc. for $C_{13}H_{12}N_2OI$ 338.9994, found: 338.9998.

***N*-((Tetrahydro-2*H*-pyran-2-yl)oxy)acrylamide[7] (62)**



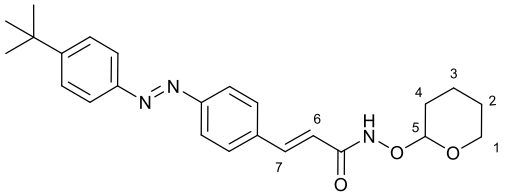
A solution of acryloyl chloride (1.43 mL, 18.0 mmol, 1.05 equiv.) in anhydrous DCM (20 mL) was added dropwise to an ice-cold solution of *O*-(tetrahydro-2*H*-pyran-2-yl)hydroxylamine (2.00g, 17.1 mmol, 1.0 equiv.) and NEt_3 (2.62 mL, 18.8 mmol, 1.1 equiv.) in anhydrous DCM (150 mL). The resulting solution was stirred at rt for 24 h and then washed with water (100 mL). The aqueous layer was washed with DCM (100 mL) and the combined organic layers were dried over $MgSO_4$. Concentration under reduced pressure and purification by flash column chromatography (PE : EtOAc, 3 : 7) yielded **62** as a white solid (1.98 g, 68%). R_f 0.42 (PE : EtOAc, 3 : 7); m.p. 156 – 158 °C (cyclohexane); IR (neat) 3146 (br.), 1658, 1628, 1533, 1409; ^{1}H NMR (400 MHz, $CDCl_3$) δ 8.47 (s, 1H, NH), 6.43 (d, *J* = 16.6 Hz, 1H, C(1)H_a), 6.18 – 5.97 (m, 1H, C(2)H), 5.75 (d, *J* = 10.3 Hz, 1H, C(1)H_b), 5.05 – 4.93 (m, 1H, C(7)H), 4.02 – 3.92 (m, 1H, C(9)H_a), 3.68 – 3.63 (m, 1H, C(9)H_b), 1.93 – 1.55 (m, 6H, C(10)H_2, C(11)H_2 & C(12)H_2); ^{13}C NMR (100 MHz, $CDCl_3$) δ 163.3, 128.1, 127.0, 102.7, 62.6, 28.0, 25.0, 18.6; MS (CI) *m/z* 189 $(M+NH_4^+)$; HRMS (CI) *m/z* calc. for $C_8H_{17}N_2O_3$ 189.1239, found: 189.1238.

(*E*)-3-(4-((*E*)-Phenyldiazenyl)phenyl)-*N*-((tetrahydro-2*H*-pyran-2-yl)oxy)acrylamide (63a)



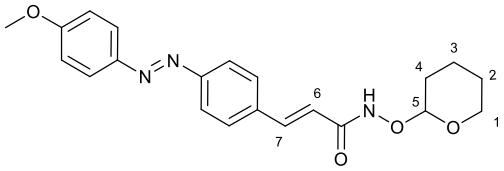
Following general procedure D, azobenzene **60a** (1.01 g, 3.28 mmol) was coupled with THP-protected *N*-hydroxyacrylamide **62** (0.84 g, 4.92 mmol) and purified by flash column chromatography (PE : EtOAc, 3 : 2) to give **63a** as an orange solid (0.85 g, 74%). R_f 0.32 (PE : EtOAc, 3 : 2); m.p. 92 – 94 °C (EtOAc); IR (neat) 3200 (br.), 1655, 1624, 1204; ^{1}H NMR (400 MHz, d_6-DMSO) δ 11.34 (s, 1H, NH), 7.93 (*app*-t, *J* = 9.3 Hz, 4H, 4 × Ar-CH), 7.81 (d, *J* = 7.8 Hz, 2H, 2 × Ar-CH), 7.65 – 7.56 (m, 4H, 3 × Ar-CH & C(7)H), 6.64 (d, *J* = 16.1 Hz, 1H, C(6)H), 4.95 – 4.92 (m, 1H, C(5)H), 4.02 – 3.93 (m, 1H, C(1)H_a), 3.59 – 3.51 (m, 1H, C(1)H_b), 1.76 – 1.50 (m, 6H, C(2)H_2, C(3)H_2 & C(4)H_2); ^{13}C NMR (100 MHz, d_6-DMSO) δ 162.2, 152.2, 152.0, 138.4, 137.6, 131.8, 129.6 (2C), 128.8 (2C), 123.2 (2C), 122.7 (2C), 120.6, 101.1, 61.4, 27.8, 24.7, 18.3; MS (ESI) *m/z* 352 $(M+H)^+$; HRMS (ESI) *m/z* calc. for $C_{20}H_{22}N_3O_3$ 352.1661, found: 352.1679.

(*E*)-3-(4-((*E*)-(4-(*tert*-Butyl)phenyl)diazenyl)phenyl)-*N*-((tetrahydro-2H-pyran-2-yl)oxy)acrylamide (63b)



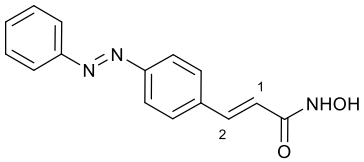
Following general procedure D, azobenzene **60b** (0.96 g, 2.63 mmol) was coupled with THP-protected *N*-hydroxyacrylamide **62** (0.67 g, 3.94 mmol) and purified by flash column chromatography (PE : EtOAc, 7 : 3) to give **63b** as an orange solid (1.00 g, 93%). R_f 0.25 (PE : EtOAc, 7 : 3); m.p. 174 – 176 °C (EtOAc); IR (neat) 3164 (br.), 1670, 1654, 1620, 1530; ^{1}H NMR (500 MHz, d_6-DMSO) δ 11.31 (s, 1H, NH), 7.91 (d, *J* = 8.0 Hz, 2H, 2 × Ar-CH), 7.85 (d, *J* = 8.5 Hz, 2H, 2 × Ar-CH), 7.80 (d, *J* = 8.0 Hz, 2H, 2 × Ar-CH), 7.63 (d, *J* = 8.5 Hz, 2H, 2 × Ar-CH), 7.58 (d, *J* = 15.8 Hz, 1H, C(7)H), 6.64 (d, *J* = 15.8 Hz, 1H, C(6)H), 4.96 – 4.91 (m, 1H, C(5)H), 4.01 – 3.91 (m, 1H, C(1)H_a), 3.58 – 3.50 (m, 1H, C(1)H_b), 1.75 – 1.49 (m, 6H, C(2)H_2, C(3)H_2 & C(4)H_2), 1.34 (s, 9H, 3 × CH_3); ^{13}C NMR (125 MHz, d_6-DMSO) δ 162.2, 154.9, 152.3, 150.0, 138.4, 137.4, 128.7 (2C), 126.3 (2C), 123.1 (2C), 122.5 (2C), 120.4, 101.0, 61.4, 34.8, 30.9 (3C), 27.8, 24.6, 18.3; MS (ESI) *m/z* 408 $(M+H)^+$; HRMS (ESI) *m/z* calc. for $C_{24}H_{30}N_3O_3$ 408.2287, found: 408.2285.

(*E*)-3-(4-((*E*)-(4-Methoxyphenyl)diazenyl)phenyl)-*N*-((tetrahydro-2*H*-pyran-2-yl)oxy)acrylamide (63c)



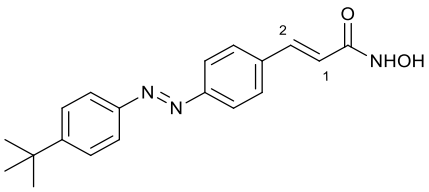
Following general procedure D, azobenzene **60c** (0.82 g, 2.43 mmol) was coupled with THP-protected *N*-hydroxyacrylamide **62** (0.62 g, 3.64 mmol) and purified by flash column chromatography (PE : EtOAc, 2 : 3) to give **63c** as an orange solid (0.81 g, 87%). R_f 0.5 (PE : EtOAc, 2 : 3); m.p. 112 – 114 °C (EtOAc); IR (neat) 3165 (br.), 1652, 1601, 1504; ^{1}H NMR (400 MHz, d_6 DMSO) δ 11.33 (s, 1H, NH), 7.92 (d, *J* = 9.1 Hz, 2H, 2 × Ar-CH), 7.88 (d, *J* = 8.3 Hz, 2H, 2 × Ar-CH), 7.78 (d, *J* = 8.3 Hz, 2H, 2 × Ar-CH), 7.58 (d, *J* = 16.1 Hz, 1H, C(7)H), 7.15 (d, *J* = 9.1 Hz, 2H, 2 × Ar-CH), 6.62 (d, *J* = 16.1 Hz, 1H, C(6)H), 4.95 – 4.91 (m, 1H, C(5)H), 4.01 – 3.92 (m, 1H, C(1)H_a), 3.88 (s, 3H, OCH_3), 3.58 – 3.52 (m, 1H, C(1)H_b), 1.75 – 1.49 (m, 6H, C(2)H_2, C(3)H_2 & C(4)H_2); ^{13}C NMR (100 MHz, d_6-DMSO) δ 162.2 (2C), 152.4, 146.3, 138.4, 136.9, 128.7 (2C), 124.7 (2C), 122.8 (2C), 120.2, 114.7 (2C), 101.0, 61.4, 55.7, 27.8, 24.6, 18.3; MS (ESI) *m/z* 382 $(M+H)^+$; HRMS (ESI) *m/z* calc. for $C_{21}H_{24}N_3O_4$ 382.1767, found: 382.1770.

(*E*)-*N*-Hydroxy-3-(4-((*E*)-phenyldiazenyl)phenyl)acrylamide (57a)



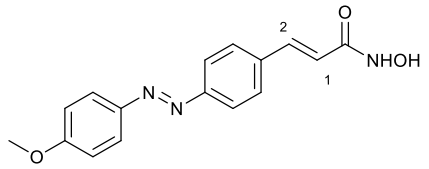
Following general procedure E, deprotection of THP-hydroxamate **63a** (0.73 g, 2.08 mmol) was carried out at 50 °C for 8 h. Purification by flash column chromatography (DCM : MeOH : AcOH, 92 : 8 : 0.5) yielded **57a** as a dark orange amorphous solid (0.42 g, 75%). R_f 0.44 (DCM : MeOH, 92 : 8); IR (neat) 3238 (br.), 1655, 1597, 1567, 1499; ^{1}H NMR (400 MHz, d_6-DMSO) δ 11.03 – 10.63 (br. s, 1H, NH), 9.30 – 9.00 (br. s, 1H, OH), 7.92 (*app*-t, *J* = 8.8 Hz, 4H, 4 × Ar-CH), 7.79 (d, *J* = 8.3 Hz, 2H, 2 × Ar-CH), 7.64 – 7.58 (m, 3H, 3 × Ar-CH), 7.53 (d, *J* = 15.7 Hz, 1H, C(2)H), 6.59 (d, *J* = 15.7 Hz, 1H, C(1)H); ^{13}C NMR (125 MHz, d_6-DMSO) δ 162.3, 152.0, 152.0, 137.9, 137.0, 131.7, 129.5 (2C), 128.6 (2C), 123.2 (2C), 122.6 (2C), 121.0; MS (ESI) *m/z* 266 $(M–H)^-$; HRMS (ESI) *m/z* calc. for $C_{15}H_{12}N_3O_2$ 266.0930, found: 266.0929.

(*E*)-3-(4-((*E*)-(4-(*tert*-Butyl)phenyl)diazenyl)phenyl)-*N*-hydroxyacrylamide (57b)



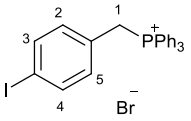
Following general procedure E, deprotection of THP-hydroxamate **63b** (0.76 g, 1.87 mmol) was carried out at 80 °C overnight. Purification by flash column chromatography (DCM : MeOH : AcOH, 94 : 6 : 0.5) yielded **57b** as a dark orange amorphous solid (0.49 g, 81%). R_f 0.33 (DCM : MeOH, 94 : 6); IR (neat) 3212 (br.), 1644, 1610, 1542, 1387; ^{1}H NMR (400 MHz, d_6-DMSO) δ 10.84 (br. s, 1H, NH), 9.14 (br. s, 1H, OH), 7.91 (d, *J* = 8.5 Hz, 2H, 2 × Ar-CH), 7.85 (d, *J* = 8.5 Hz, 2H, 2 × Ar-CH), 7.78 (d, *J* = 8.5 Hz, 2H, 2 × Ar-CH), 7.63 (d, *J* = 8.5 Hz, 2H, 2 × Ar-CH), 7.54 (d, *J* = 16.1 Hz, 1H, C(2)H), 6.58 (d, *J* = 16.1 Hz, 1H, C(1)H), 1.34 (s, 9H, 3 × CH_3); ^{13}C NMR (125 MHz, d_6-DMSO) δ 162.3, 154.8, 152.1, 150.0, 137.6, 137.1, 128.6 (2C), 126.3 (2C), 123.1 (2C), 122.5 (2C), 120.9, 34.8, 30.9 (3C); MS (ESI) *m/z* 324 $(M+H)^+$; HRMS (ESI) *m/z* calc. for $C_{19}H_{22}N_3O_2$ 324.1712, found: 324.1719.

(*E*)-*N*-Hydroxy-3-(4-((*E*)-(4-methoxyphenyl)diazenyl)phenyl)acrylamide (57c)



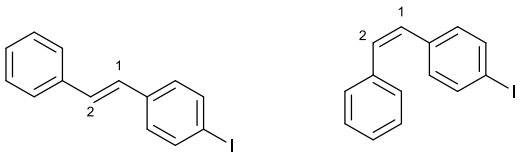
Following general procedure E, deprotection of THP-hydroxamate **63c** (0.70 g, 1.84 mmol) was carried out at 80 °C for 8 h. Purification by flash column chromatography (DCM : MeOH : AcOH, 92 : 8 : 0.5) yielded **57c** as a dark orange amorphous solid (0.41 g, 75%). R_f 0.42 (DCM : MeOH, 92 : 8); IR (neat) 3246 (br.), 1661, 1600, 1584, 1498; ^{1}H NMR (400 MHz, d_6-DMSO) δ 10.84 (br. s, 1H, NH), 9.13 (br. s, 1H, OH), 7.92 (d, *J* = 9.1 Hz, 2H, 2 × Ar-CH), 7.88 (d, *J* = 8.3 Hz, 2H, 2 × Ar-CH), 7.77 (d, *J* = 8.3 Hz, 2H, 2 × Ar-CH), 7.53 (d, *J* = 15.7 Hz, 1H, C(2)H), 7.15 (d, *J* = 9.1 Hz, 2H, 2 × Ar-CH), 6.57 (d, *J* = 15.7 Hz, 1H, C(1)H), 3.88 (s, 3H, OCH_3); ^{13}C NMR (125 MHz, d_6-DMSO) δ 162.4, 162.2, 152.2, 146.3, 137.2, 137.1, 128.5 (2C), 124.7 (2C), 122.8 (2C), 120.6, 114.7 (2C), 55.7; MS (ESI) *m/z* 298 $(M+H)^+$; HRMS (ESI) *m/z* calc. for $C_{16}H_{16}N_3O_3$ 298.1192, found: 298.1190.

(4-Iodobenzyl)triphenylphosphonium bromide[1,2] **(64)**



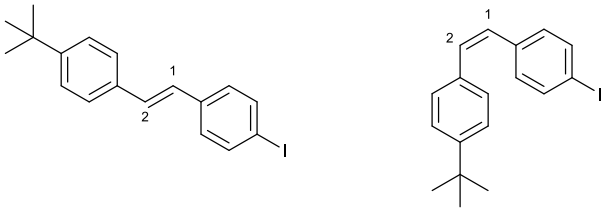
4-Iodobenzyl bromide (3.16 g, 10.6 mmol, 1.0 equiv.) and triphenylphosphine (3.07 g, 11.7 mmol, 1.1 equiv.) were added to toluene (60 mL) and heated under reflux for 8 h. The resulting precipitate was collected by filtration, washed sequentially with toluene and diethyl ether, and dried under vacuum to yield **64** as a colourless solid (6.43 g, 98%). IR (neat) 1588, 1485, 1436, 1110; ^{1}H NMR (400 MHz, $CDCl_3$) δ 7.87 – 7.73 (m, 9H, 9 × Ar-CH), 7.71 – 7.60 (m, 6H, 6 × Ar-CH), 7.45 (d, *J* = 8.3 Hz, 2H, C(3)H & C(4)H), 6.91 (dd, *J* = 8.3, 2.5 Hz, 2H, C(2)H & C(5)H), 5.52 (d, *J* = 14.7 Hz, C(1)H_2); ^{13}C NMR (100 MHz, $CDCl_3$) δ 137.5 (d, *J* = 3.5 Hz, 2C), 134.9 (d, *J* = 3.5 Hz, 3C), 134.3 (d, *J* = 10.4 Hz, 6C), 133.3 (d, *J* = 6.9 Hz, 2C), 130.0 (d, *J* = 12.1 Hz, 6C), 127.0 (d, *J* = 8.7 Hz, 1C), 117.3 (d, *J* = 86.7 Hz, 3C), 94.3 (d, *J* = 5.2 Hz, 1C), 29.8 (d, *J* = 46.8 Hz, 1C); ^{31}P NMR (162 MHz, $CDCl_3$) δ 23.0; MS (ESI) *m/z* 479 $(M\text{-}Br)^+$.

(*E/Z*)-1-Iodo-4-styrylbenzene[3-5] **(66a)**



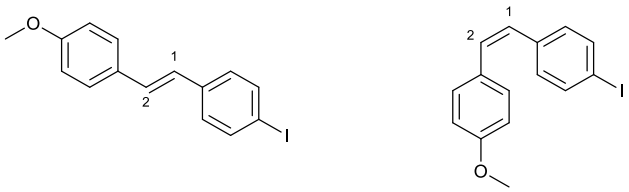
Following general procedure F for benzaldehyde (**65b**) (0.63 mL, 6.21 mmol) with a reaction time of 1 h, purification by flash column chromatography (100% PE) afforded *E*- and *Z*-**66a** as a white solid and colourless oil respectively (1.70 g, 81%; *E* : *Z* ratio, 2 : 3). ***E*-isomer** R_f 0.71 (100% PE); ^{1}H NMR (400 MHz, $CDCl_3$) δ 7.69 (d, *J* = 8.3 Hz, 2H, 2 × Ar-CH), 7.51 (d, *J* = 7.1 Hz, 2H, 2 × Ar-CH), 7.37 (t, *J* = 7.1 Hz, 2H, 2 × Ar-CH), 7.30 – 7.25 (m, 3H, 3 × Ar-CH), 7.12 (d, *J* = 16.4 Hz, 1H, C(1)H or C(2)H), 7.03 (d, *J* = 16.4 Hz, 1H, C(1)H or C(2)H); ^{13}C NMR (100 MHz, $CDCl_3$) δ 137.7 (2C), 136.9, 136.8, 129.5, 128.7 (2C), 128.2 (2C), 127.9, 127.5, 126.6 (2C), 92.8; MS (EI) *m/z* 306 $(M)^+$; HRMS (EI) *m/z* calc. for $C_{14}H_{11}I$ 305.9906, found: 305.9908. ***Z*-isomer** R_f 0.50 (100% PE); ^{1}H NMR (400 MHz, $CDCl_3$) δ 7.55 (d, *J* = 8.3 Hz, 2H, 2 × Ar-CH), 7.26 – 7.21 (m, 5H, 5 × Ar-CH), 6.99 (d, *J* = 8.3 Hz, 2H, 2 × Ar-CH), 6.64 (d, *J* = 12.2 Hz, 1H, C(1)H or C(2)H), 6.50 (d, *J* = 12.2 Hz, 1H, C(1)H or C(2)H); ^{13}C NMR (100 MHz, $CDCl_3$) δ 137.3 (2C), 136.8, 136.7, 131.1, 130.7 (2C), 129.0, 128.8 (2C), 128.3 (2C), 127.3, 92.5; MS (EI) *m/z* 306 $(M)^+$; HRMS (EI) *m/z* calc. for $C_{14}H_{11}I$ 305.9906, found: 305.9914

(*E/Z*)-1-(*tert*-Butyl)-4-(4-iodostyryl)benzene[273] **(66b)**



Following general procedure F for 4-(*tert*-butyl)benzaldehyde (**65b**) (1.0 mL, 6.10 mmol) with a reaction time of 1 h, purification by flash column chromatography (100% PE) afforded *E*- and *Z*-**66b** as white solids (1.78 g, 73%; *E* : *Z* ratio, 2 : 3). ***E*-isomer** R_f 0.35 (100% PE); m.p. 157 – 160 °C (PE); IR (neat) 1505, 1483, 969; ^{1}H NMR (400 MHz, $CDCl_3$) δ 7.68 (d, *J* = 8.3 Hz, 2H, 2 × Ar-CH), 7.46 (d, *J* = 8.6 Hz, 2H, 2 × Ar-CH), 7.39 (d, *J* = 8.6 Hz, 2H, 2 × Ar-CH), 7.25 (d, *J* = 8.3 Hz, 2H, 2 × Ar-CH), 7.11 (d, *J* = 16.1 Hz, 1H, C(1)H or C(2)H), 6.99 (d, *J* = 16.1 Hz, 1H, C(1)H or C(2)H), 1.34 (s, 9H, 3 × CH_3); ^{13}C NMR (100 MHz, $CDCl_3$) δ 151.1, 137.7 (2C), 137.1, 134.1, 129.3, 128.1 (2C), 126.7, 126.3 (2C), 125.7 (2C), 92.5, 34.6, 31.3 (3C); MS (EI) *m/z* 362 $(M)^+$; HRMS (EI) calc. for $C_{18}H_{19}I$ 362.0532, found: 362.0532. ***Z*-isomer** R_f 0.58 (100% PE); m.p. 46 – 48 °C (PE); IR (neat) 1508, 1480, 1461, 1004; ^{1}H NMR (400 MHz, $CDCl_3$) δ 7.56 (d, *J* = 8.3 Hz, 2H, 2 × Ar-CH), 7.26 (d, *J* = 7.8 Hz, 2H, 2 × Ar-CH), 7.17 (d, *J* = 7.8 Hz, 2H, 2 × Ar-CH), 7.03 (d, *J* = 8.3 Hz, 2H, 2 × Ar-CH), 6.59 (d, *J* = 12.5 Hz, 1H, C(1)H or C(2)H), 6.45 (d, *J* = 12.5 Hz, 1H, C(1)H or C(2)H), 1.31 (s, 9H, 3 × CH_3); ^{13}C NMR (100 MHz, $CDCl_3$) δ 150.4, 137.3 (2C), 137.0, 133.7, 130.9, 130.7 (2C), 128.5 (2C), 128.3, 125.2 (2C), 92.4, 34.6, 31.3 (3C); MS (EI) *m/z* 362 $(M)^+$; HRMS (EI) *m/z* calc. for $C_{18}H_{19}I$ 362.0532, found: 362.0533.

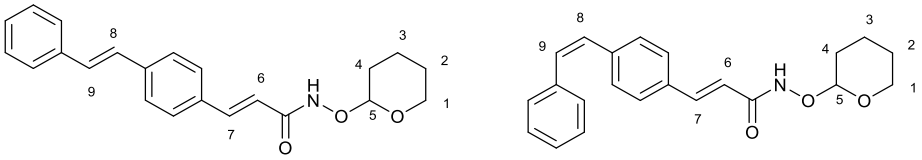
(*E/Z*)-1-Iodo-4-(4-methoxystyryl)benzene[3] **(66c)**



Following general procedure F for 4-methoxybenzaldehyde (**65c**) (0.52 mL, 4.24 mmol) with a reaction time of 6 h, purification by flash column chromatography (PE : EtOAc, 100 : 1) afforded *E*- and *Z*-**66c** as a white solid and colourless oil respectively (0.96 g, 68%; *E*: *Z* ratio, 3 : 7). ***E*-isomer** R_f 0.16 (PE : EtOAc, 100 : 1); IR (neat) 1603, 1509, 1460, 1250; ^{1}H NMR (400 MHz, $CDCl_3$) δ 7.68 (d, *J* = 8.3 Hz, 2H, 2 × Ar-CH), 7.46 (d, *J* = 8.6 Hz, 2H, 2 × Ar-CH), 7.24 (d, *J* = 8.3 Hz, 2H, 2 × Ar-CH), 7.08 (d, *J* = 16.1 Hz, 1H, C(1)H or C(2)H), 6.91 (d, *J* = 8.6 Hz, 2H, 2 × Ar-CH), 6.89 (d, *J* = 16.1 Hz, 1H, C(1)H or C(2)H), 3.84 (s, 3H, OCH_3); ^{13}C NMR (100 MHz, $CDCl_3$) δ 159.5, 137.7 (2C), 137.2, 129.7, 129.0,

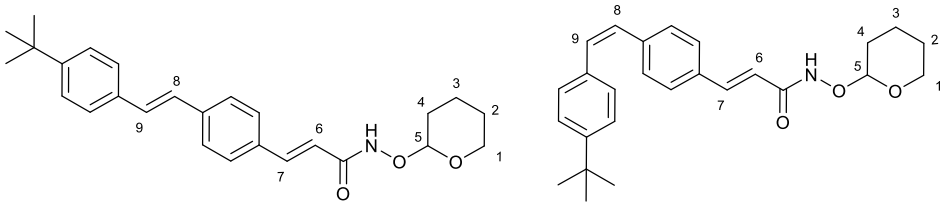
128.0 (2C), 127.8 (2C), 125.4, 114.2 (2C), 92.1, 55.3; MS (CI) *m/z* 337 $(M+H)^+$; MS (CI) *m/z* calc. for $C_{15}H_{14}OI$ 337.0089, found: 337.0061. ***Z*-isomer** R_f 0.26 (PE : EtOAc, 100 : 1); IR (neat) 1606, 1509, 1480, 1247; ^1H NMR (400 MHz, $CDCl_3$) δ 7.56 (d, *J* = 8.6 Hz, 2H, 2 × Ar-CH), 7.17 (d, *J* = 8.6 Hz, 2H, 2 × Ar-CH), 7.02 (d, *J* = 8.6 Hz, 2H, 2 × Ar-CH), 6.78 (d, *J* = 8.6 Hz, 2H, 2 × Ar-CH), 6.56 (d, *J* = 12.2 Hz, 1H, C(1)H or C(2)H), 6.40 (d, *J* = 12.2 Hz, 1H, C(1)H or C(2)H), 3.80 (s, 3H, OCH_3); ^{13}C NMR (100 MHz, $CDCl_3$) δ 158.8, 137.3 (2C), 137.1, 130.7 (2C), 130.6, 130.1 (2C), 129.2, 127.5, 113.7 (2C), 92.2, 55.2; MS (CI) *m/z* 337 $(M+H)^+$; HRMS (CI) *m/z* calc. for $C_{15}H_{14}OI$ 337.0089, found: 337.0121.

(*E*)-3-(4-((*E/Z*)-Styryl)phenyl)-*N*-((tetrahydro-2*H*-pyran-2-yl)oxy)acrylamide (67a)



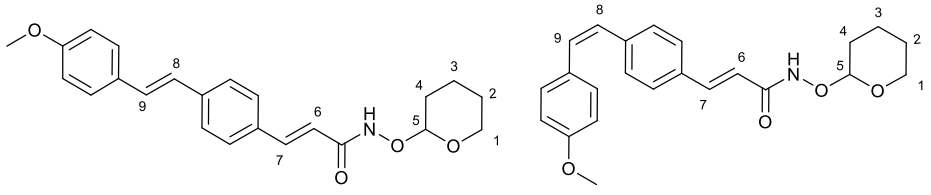
Following general procedure D, the isomeric mixture of stilbene **66a** (1.70 g, 5.55 mmol) was coupled with THP-protected *N*-hydroxyacrylamide **62** (1.43 g, 8.33 mmol) and purified by flash column chromatography (PE : EtOAc, 3: 2) to afford an isomeric mixture of *E*- and *Z*-**67a** as orange solids (1.67 g, 86%; *E : Z* ratio, 9 : 11). Small aliquots of each isomer were separated by chromatography to allow characterisation. ***E*-isomer** R_f 0.31 (PE : EtOAc, 3: 2); m.p. 156 – 158 °C (EtOAc); IR (neat) 3186 (br.), 1653, 1620, 1438, 1113; ^1H NMR (500 MHz, d_6-DMSO) δ 11.22 (s, 1H, NH), 7.66 (d, *J* = 8.3 Hz, 2H, 2 × Ar-CH), 7.62 (d, *J* = 8.1 Hz, 2H, 2 × Ar-CH), 7.58 (d, *J* = 8.3 Hz, 2H, 2 × Ar-CH), 7.49 (d, *J* = 15.9 Hz, 1H, C(7)H), 7.39 (t, *J* = 8.1 Hz, 2H, 2 × Ar-CH), 7.34 (d, *J* = 16.5 Hz, 1H, C(8)H or C(9)H), 7.31 – 7.26 (m, 2H, Ar-CH & C(8)H or C(9)H), 6.52 (d, *J* = 15.9 Hz, 1H, C(6)H), 4.93 – 4.90 (m, 1H, C(5)H), 4.00 – 3.94 (m, 1H, $C(1)H_a$), 3.56 – 3.52 (m, 1H, $C(1)H_b$), 1.74 – 1.51 (m, 6H, $C(2)H_2$, $C(3)H_2$ & $C(4)H_2$) ; ^{13}C NMR (125 MHz, d_6-DMSO) δ 162.6, 139.0, 138.4, 136.9, 133.9, 129.5, 128.7 (2C), 128.1, 127.9, 127.7 (2C), 127.0 (2C), 126.6 (2C), 118.3, 101.0, 61.4, 27.8, 24.7, 18.3; MS (ESI) *m/z* 372 $(M+Na)^+$; HRMS (ESI) *m/z* calc. for $C_{22}H_{23}NO_3Na$ 372.1576, found: 372.1581. ***Z*-isomer** R_f 0.42 (PE : EtOAc, 3 : 2); m.p. 45 – 47 °C (EtOAc); IR (neat) 3171 (br.), 1656, 1620, 1509; ^1H NMR (400 MHz, d_6-DMSO) δ 11.23 (s, 1H, NH), 7.48 – 7.42 (m, 3H, C(7)H & 2 × Ar-CH), 7.30 – 7.23 (m, 7H, 7 × Ar-CH), 6.70 (d, *J* = 12.2 Hz, 1H, C(8)H or C(9)H), 6.64 (d, *J* = 12.2 Hz, 1H, C(8)H or C(9)H), 6.46 (d, *J* = 15.7 Hz, 1H, C(6)H), 4.92 – 4.89 (m, 1H, C(5)H), 3.99 – 3.91 (m, 1H, $C(1)H_a$), 3.56 – 3.50 (m, 1H, $C(1)H_b$), 1.73 – 1.49 (m, 6H, $C(2)H_2$, $C(3)H_2$ & $C(4)H_2$); ^{13}C NMR (125 MHz, d_6-DMSO) δ 162.5, 138.9, 138.2, 136.7, 133.5, 130.9, 129.4, 129.1 (2C), 128.5 (2C), 128.4 (2C), 127.6, 127.4 (2C), 118.6, 101.0, 61.4, 27.8, 24.6, 18.3; MS (ESI) *m/z* 372 $(M+Na)^+$; HRMS (ESI) *m/z* calc. for $C_{22}H_{23}NO_3Na$ 372.1576, found: 372.1570.

(*E*)-3-(4-((*E/Z*)-4-(*tert*-Butyl)styryl)phenyl)-*N*-((tetrahydro-2*H*-pyran-2-yl)oxy)acrylamide (67b)



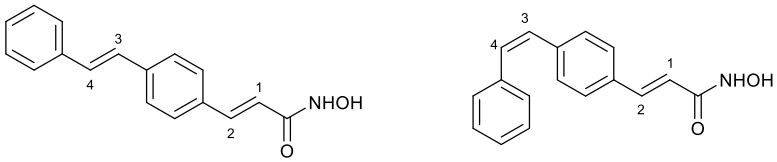
Following general procedure D, the isomeric mixture of stilbene **66b** (1.66 g, 4.58 mmol) was coupled with THP-protected *N*-hydroxyacrylamide **62** (1.18 g, 6.87 mmol) and purified by flash column chromatography (PE : EtOAc, 3 : 2) to afford an isomeric mixture of *E*- and *Z*-**67b** as yellow solids (1.38 g, 74%; *E* : *Z* ratio, 2 : 3). Small aliquots of each isomer were separated by chromatography to allow characterisation. ***E*-isomer** R_f 0.39 (PE : EtOAc, 3 : 2); m.p. 188 – 190 °C (EtOAc); IR (neat) 3173 (br.), 1654, 1628, 1517; ^{1}H NMR (400 MHz, d_6-DMSO) δ 11.21 (br. s, 1H, NH), 7.63 (d, *J* = 8.3 Hz, 2H, 2 × Ar-CH), 7.57 (d, *J* = 8.3 Hz, 2H, 2 × Ar-CH), 7.53 (d, *J* = 8.5 Hz, 2H, 2 × Ar-CH), 7.47 (d, *J* = 15.5 Hz, 1H, C(7)H), 7.39 (d, *J* = 8.5 Hz, 2H, 2 × Ar-CH), 7.30 (d, *J* = 16.4 Hz, 1H, C(8)H or C(9)H), 7.20 (d, *J* = 16.4 Hz, 1H, C(8)H or C(9)H), 6.50 (d, *J* = 15.5 Hz, 1H, C(6)H), 4.93 – 4.87 (m, 1H, C(5)H), 3.99 – 3.92 (m, 1H, C(1)H_a), 3.55 – 3.50 (m, 1H, C(1)H_b), 1.74 – 1.49 (m, 6H, C(2)H_2, C(3)H_2 & C(4)H_2), 1.28 (s, 9H, 3 × CH_3); ^{13}C NMR (100 MHz, d_6-DMSO) δ 162.7, 150.6, 139.0, 138.6, 134.1, 133.7, 129.3, 128.1 (2C), 126.9 (3C), 126.4 (2C), 125.5 (2C), 118.3, 101.0, 61.4, 34.4, 31.1 (3C), 27.8, 24.7, 18.3; MS (ESI) *m/z* 428 $(M+Na)^+$; HRMS (ESI) *m/z* calc. for $C_{26}H_{31}NO_3Na$ 428.2202, found: 428.2204. ***Z*-isomer** R_f 0.50 (PE : EtOAc, 3 : 2); m.p. 146 – 148 °C (EtOAc); IR (neat) 3153 (br.), 1656, 1621, 1512; ^{1}H NMR (400 MHz, d_6-DMSO) δ 11.23 (br. s, 1H, NH), 7.49 – 7.42 (m, 3H, 2 × Ar-CH & C(7)H), 7.29 (d, *J* = 8.3 Hz, 4H, 4 × Ar-CH), 7.17 (d, *J* = 8.3 Hz, 2H, 2 × Ar-CH), 6.63 (d, *J* = 12.7 Hz, 1H, C(8)H or C(9)H), 6.59 (d, *J* = 12.7 Hz, 1H, C(8)H or C(9)H), 6.48 (d, *J* = 15.6 Hz, 1H, C(6)H), 4.92 – 4.89 (m, 1H, C(5)H), 3.99 – 3.91 (m, 1H, C(1)H_a), 3.56 – 3.50 (m, 1H, C(1)H_b), 1.75 – 1.49 (m, 6H, C(2)H_2, C(3)H_2 & C(4)H_2), 1.25 (s, 9H, 3 × CH_3); ^{13}C NMR (100 MHz, d_6-DMSO) δ 162.6, 150.0, 139.0, 138.5, 133.7, 133.5, 130.7, 129.0 (2C), 128.8, 128.3 (2C), 127.7 (2C), 125.2 (2C), 118.6, 101.0, 61.4, 34.3, 31.0 (3C), 27.8, 24.7, 18.3; MS (ESI) *m/z* 428 $(M+Na)^+$; HRMS (ESI) *m/z* calc. for $C_{26}H_{31}NO_3Na$ 428.2202, found: 428.2209.

(*E*)-3-(4-((*E/Z*)-4-Methoxystyryl)phenyl)-*N*-((tetrahydro-2H-pyran-2-yl)oxy)acrylamide (67c)



Following general procedure D, the isomeric mixture of stilbene **66c** (0.96 g, 2.86 mmol) was coupled with THP-protected *N*-hydroxyacrylamide **62** (0.73 g, 4.29 mmol) and purified by flash column chromatography (PE : EtOAc, 1 : 1) to afford an isomeric mixture of *E*- and *Z*-**67c** as yellow solids (0.65 g, 59%; *E* : *Z* ratio, 1 : 4). Small aliquots of each isomer were separated by chromatography to allow characterisation. ***E*-isomer** R_f 0.25 (PE : EtOAc, 1 : 1); m.p. 172 – 174 °C (EtOAc); IR (neat) 3189 (br.), 1688, 1653, 1593, 1514; ^{1}H NMR (400 MHz, d_6-DMSO) δ 11.24 (br. s, 1H, NH), 7.62 – 7.53 (m, 6H, 6 × Ar-CH), 7.47 (d, *J* = 15.7 Hz, 1H, C(7)H), 7.27 (d, *J* = 16.1 Hz, 1H, C(8)H or C(9)H), 7.11 (d, *J* = 16.1 Hz, 1H, C(8)H or C(9)H), 6.95 (d, *J* = 8.4 Hz, 2H, 2 × Ar-CH), 6.51 (d, *J* = 15.7 Hz, 1H, C(6)H), 4.92 – 4.88 (m, 1H, C(5)H), 3.99 – 3.90 (m, 1H, C(1)H_a), 3.78 (s, 3H, OCH_3), 3.56 – 3.50 (m, 1H, C(1)H_b), 1.74 – 1.49 (m, 6H, C(2)H_2, C(3)H_2 & C(4)H_2); ^{13}C NMR (125 MHz, d_6-DMSO) δ 162.7, 159.2, 139.1, 138.9, 133.4, 129.5, 129.2, 128.0 (2C), 128.0 (2C), 126.6 (2C), 125.4, 118.0, 114.2 (2C), 101.0, 61.4, 55.2, 27.8, 24.7, 18.3; MS (ESI) *m/z* 380 $(M+H)^+$; HRMS (ESI) *m/z* calc. for $C_{23}H_{26}NO_4$ 380.1862, found: 380.1873. ***Z*-isomer** R_f 0.34 (PE : EtOAc, 1 : 1); m.p. 46 – 49 °C (EtOAc); IR (neat) 3185 (br.), 1656, 1621, 1602, 1510; ^{1}H NMR (400 MHz, d_6-DMSO) δ 11.25 (br. s, 1H, NH), 7.48 – 7.43 (m, 3H, 2 × Ar-CH & C(7)H), 7.28 (d, *J* = 8.3 Hz, 2H, 2 × Ar-CH), 7.18 (d, *J* = 8.3 Hz, 2H, 2 × Ar-CH), 6.84 (d, *J* = 8.3 Hz, 2H, 2 × Ar-CH), 6.61 (d, *J* = 12.2 Hz, 1H, C(8)H or C(9)H), 6.52 (d, *J* = 12.2 Hz, 1H, C(8)H or C(9)H), 6.46 (d, *J* = 16.1 Hz, 1H, C(6)H), 4.92 – 4.89 (m, 1H, C(5)H), 4.00 – 3.93 (m, 1H, C(1)H_a), 3.73 (s, 3H, OCH_3), 3.56 – 3.51 (m, 1H, C(1)H_b), 1.75 – 1.49 (m, 6H, C(2)H_2, C(3)H_2 & C(4)H_2); ^{13}C NMR (100 MHz, d_6-DMSO) δ 162.6, 158.6, 139.0, 138.6, 133.3, 130.5, 129.9 (2C), 129.0 (2C), 128.8, 127.7, 127.7 (2C), 118.5, 113.8 (2C), 101.0, 61.4, 55.0, 27.8, 24.6, 18.3; MS (ESI) *m/z* 380 $(M+H)^+$; HRMS (ESI) *m/z* calc. for $C_{23}H_{26}NO_4$ 380.1862, found: 380.1870.

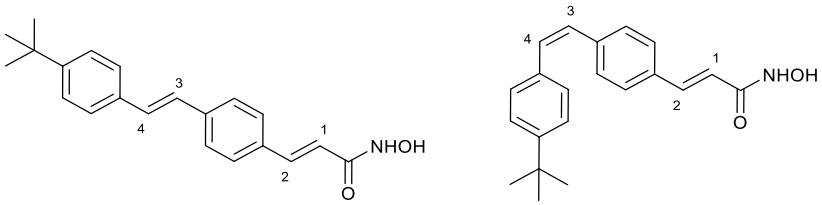
(*E*)-*N*-Hydroxy-3-(4-((*E/Z*)-styryl)phenyl)acrylamide (58a)



Following general procedure E, deprotection of the isomeric mixture of THP-hydroxamate **67a** (1.67 g, 4.78 mmol) was carried out at 50 °C for 8 h. Purification by flash column chromatography (DCM : MeOH : AcOH, 92 : 8 : 0.5) yielded an isomeric mixture of *E*- and *Z*-**58a** as a dark orange solid (0.80 g, 63%; *E* : *Z* ratio, 3 : 7). This was triturated with DCM and the remaining solid was filtered and repeatedly washed with DCM to yield *E*-**58a** as an orange solid. The filtrate was concentrated under reduced pressure to yield *Z*-**58a** as an orange solid. ***E*-isomer** R_f 0.41 (DCM : MeOH, 92 : 8); m.p. 192

– 194 °C (MeOH); IR (neat) 3248 (br.), 2620, 1664, 1560, 1447, 1417; ^{1}H NMR (400 MHz, d_6-DMSO) δ 10.82 (br. s, 1H, NH), 9.03 (br. s, 1H, OH), 7.64 (*app*-t, *J* = 9.0 Hz, 4H, 4 × Ar-CH), 7.57 (d, *J* = 7.3 Hz, 2H, 2 × Ar-CH), 7.45 (d, *J* = 15.7 Hz, 2H, C(2)H), 7.38 (t, *J* = 7.3 Hz, 2H, 2 × Ar-CH), 7.32 – 7.26 (m, 3H, Ar-CH, C(3)H & C(4)H), 6.47 (d, *J* = 15.7 Hz, 1H, C(1)H); ^{13}C NMR (125 MHz, d_6-DMSO) δ 162.8, 138.2, 137.9, 136.9, 134.1, 129.4, 128.8 (2C), 128.0 (2C), 127.9, 127.8, 127.0 (2C), 126.6 (2C), 118.8; MS (CI) *m/z* 266 $(M+H)^+$; HRMS (CI) *m/z* calc. for $C_{17}H_{16}NO_2$ 266.1181, found: 266.1176. ***Z*-isomer** R_f 0.67 (DCM : MeOH, 92 : 8); m.p. 48 – 51 °C (DCM); IR (neat) 3190 (br.), 2859, 1650, 1600, 1509, 1491; ^{1}H NMR (400 MHz, d_6-DMSO) δ 7.44 (d, *J* = 7.8 Hz, 2H, 2 × Ar-CH), 7.38 (d, *J* = 15.9 Hz, 1H, C(2)H), 7.30 – 7.23 (m, 7H, 7 × Ar-CH), 6.69 (d, *J* = 11.7 Hz, 1H, C(3)H or C(4)H), 6.63 (d, *J* = 11.7 Hz, 1H, C(3)H or C(4)H), 6.42 (d, *J* = 15.9 Hz, 1H, C(1)H); ^{13}C NMR (100 MHz, d_6-DMSO) δ 162.7, 137.9, 137.7, 136.7, 133.8, 130.9, 129.5, 129.1 (2C), 128.5 (2C), 128.5 (2C), 127.5 (3C), 119.1; MS (ESI) *m/z* 226 $(M+H)^+$; HRMS (ESI) *m/z* calc. for $C_{17}H_{16}NO_2$ 266.1181, found: 266.1186.

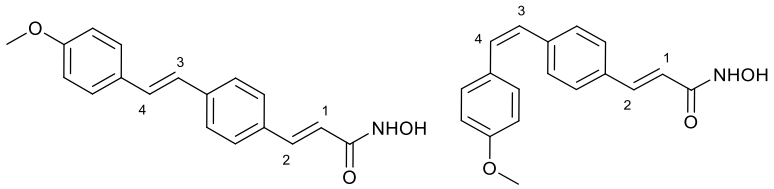
(*E*)-3-(4-((*E/Z*)-4-(*tert*-Butyl)styryl)phenyl)-*N*-hydroxyacrylamide (58b)



Following general procedure E, deprotection of the isomeric mixture of THP-hydroxamate **67b** (0.34 g, 0.84 mmol) was carried out at 80 °C overnight. Purification by flash column chromatography (DCM : MeOH : AcOH, 93 : 7 : 0.5) and separation of isomers, as detailed for **58a**, afforded *E*- and *Z*-**58b** as a pale pink solid and a dark orange solid respectively (0.20 g, 74%; *E : Z* ratio, 9 : 11). ***E*-isomer** R_f 0.35 (DCM : MeOH, 93 : 7); m.p. 196 – 198 °C (MeOH); IR (neat) 3217 (br.), 1643, 1596, 1388; ^{1}H NMR (400 MHz, d_6-DMSO) δ 10.75 (br. s, 1H, NH), 9.06 (br. s, 1H, OH), 7.63 (d, *J* = 8.3 Hz, 2H, 2 × Ar-CH), 7.55 (*app*-t, *J* = 8.3 Hz, 4H, 4 × Ar-CH), 7.45 (d, *J* = 15.6 Hz, 1H, C(2)H), 7.41 (d, *J* = 8.3 Hz, 2H, 2 × Ar-CH), 7.31 (d, *J* = 16.6 Hz, 1H, C(3)H or C(4)H), 7.21 (d, *J* = 16.6 Hz, 1H, C(3)H or C(4)H), 6.47 (d, *J* = 15.6 Hz, 1H, C(1)H), 1.29 (s, 9H, 3 × CH_3); ^{13}C NMR (125 MHz, d_6-DMSO) δ 162.8, 150.5, 138.4, 137.9, 134.1, 133.9, 129.2, 127.9 (2C), 126.9, 126.8 (2C), 126.4 (2C), 125.5 (2C), 118.6, 34.4, 31.0 (3C); MS (ESI) *m/z* 322 $(M+H)^+$; HRMS (ESI) *m/z* calc. for $C_{21}H_{24}NO_2$ 322.1807, found: 322.1824. ***Z*-isomer** R_f 0.42 (DCM: MeOH, 93 : 7); m.p. 60 – 63 °C (DCM); IR (neat) 3200 (br.), 1654, 1600, 1512; ^{1}H NMR (400 MHz, d_6-DMSO) δ 10.92 – 10.58 (br. s, 1H, NH), 9.27 – 8.89 (br. s, 1H, OH), 7.46 (d, *J* = 8.3 Hz, 2H, 2 × Ar-CH), 7.39 (d, *J* = 16.1 Hz, 1H, C(1)H), 7.29 (d, *J* = 8.3 Hz, 2H, 2 × Ar-CH), 7.28 (d, *J* = 8.3 Hz, 2H, 2 × Ar-CH), 7.18 (d, *J* = 8.3 Hz, 2H, 2 × Ar-CH), 6.62 (d, *J* = 12.2 Hz, 1H, C(3)H or C(4)H),

6.58 (d, *J* = 12.2 Hz, 1H, C(3)H or C(4)H), 6.43 (d, *J* = 16.1 Hz, 1H, C(2)H), 1.25 (s, 9H, 3 × CH_3); ^{13}C NMR (125 MHz, d_6-DMSO) δ 162.7, 150.0, 138.3, 137.8, 133.7 (2C), 130.6, 128.9 (2C), 128.8, 128.3 (2C), 127.5 (2C), 125.1 (2C), 118.9, 34.3, 31.0 (3C); MS (ESI) *m/z* 322 $(M+H)^+$; HRMS (ESI) *m/z* calc. for $C_{21}H_{24}NO_2$ 322.1807, found: 322.1800.

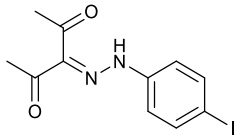
(*E*)-*N*-Hydroxy-3-(4-((*E/Z*)-4-methoxystyryl)phenyl)acrylamide (58c)



Following general procedure E, deprotection of the isomeric mixture of THP-hydroxamate **67c** (0.48 g, 1.26 mmol) was carried out at 80 °C overnight, resulting in the formation of *E*-**58c** as a white precipitate (80 mg) which was removed by filtration. The filtrate was purified by flash column chromatography (DCM : MeOH : AcOH, 94 : 6 : 0.5), and washed with pentane to yield *Z*-**58c** as a dark orange solid (0.25 g), giving a combined yield of 89% (*E : Z* ratio, 1 : 3). ***E*-isomer** m.p. 190 – 192 °C (*i*-PrOH-THF); IR (neat) 3251 (br.), 2688, 1662, 1595, 1573, 1514; ^1H NMR (400 MHz, d_6-DMSO) δ 10.72 (s, 1H, NH), 9.01 (s, 1H, OH), 7.61 – 7.53 (m, 6H, 6 × Ar-CH), 7.45 (d, *J* = 15.9 Hz, 1H, C(2)H), 7.27 (d, *J* = 16.2 Hz, 1H, C(3)H or C(4)H), 7.11 (d, *J* = 16.2 Hz, 1H, C(3)H or C(4)H), 6.96 (d, *J* = 8.8 Hz, 2H, 2 × Ar-CH), 6.46 (d, *J* = 15.9 Hz, 1H, C(1)H), 3.78 (s, 3H, OCH_3); ^{13}C NMR (400 MHz, d_6-DMSO) δ 162.9, 159.2, 138.6, 138.0, 133.6, 129.5, 129.1, 128.0 (2C), 127.9 (2C), 126.6 (2C), 125.5, 118.5, 114.2 (2C), 55.2; MS (ESI) *m/z* 296 $(M+H)^+$; HRMS (ESI) *m/z* calc. for $C_{18}H_{18}NO_3$ 296.1287, found: 296.1308. ***Z*-isomer** R_f 0.31 (DCM : MeOH, 96 : 4); m.p. 48 – 50 °C (DCM); IR (neat) 3184 (br.), 1650, 1600, 1509, 1249; ^1H NMR (400 MHz, d_6-DMSO) δ 10.75 (br. s, 1H, NH), 9.05 (br. s, 1H, OH), 7.46 (d, *J* = 7.8 Hz, 2H, 2 × Ar-CH), 7.41 (d, *J* = 15.7 Hz, 1H, C(2)H), 7.27 (d, *J* = 7.8 Hz, 2H, 2 × Ar-CH), 7.18 (d, *J* = 8.3 Hz, 2H, 2 × Ar-CH), 6.84 (d, *J* = 8.3 Hz, 2H, 2 × Ar-CH), 6.60 (d, *J* = 12.2 Hz, 1H, C(3)H or C(4)H), 6.51 (d, *J* = 12.2 Hz, 1H, C(3)H or C(4)H), 6.42 (d, *J* = 15.7 Hz, 1H, C(1)H), 3.73 (s, 3H, OCH_3); ^{13}C NMR (125 MHz, d_6-DMSO) δ 162.7, 158.6, 138.3, 137.8, 133.5, 130.4, 129.9 (2C), 128.9 (2C), 128.8, 127.8, 127.5 (2C), 118.9, 113.8 (2C), 55.0; MS (ESI) *m/z* 296 $(M+H)^+$; HRMS (ESI) *m/z* calc. for $C_{18}H_{18}NO_3$ 296.1287, found: 296.1284.

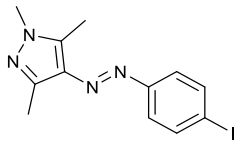
5.2.5 Photoswitchable arylazopyrazole-based HDAC inhibitors

3-(2-(4-Iodophenyl)hydrazono)pentane-2,4-dione[274] (69)



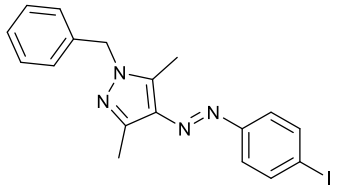
A solution of $NaNO_2$ (3.60 g, 52.2 mmol, 1.2 equiv.) in water (10 mL) was added dropwise to a solution of 4-iodoaniline (9.52 g, 43.5 mmol, 1.0 equiv.) in 12 M HCl (10 mL) and AcOH (60 mL) and stirred for 1 h at 0 °C. This solution was then transferred by cannula into a solution of 2,4-pentanedione (5.81 mL, 56.6 mmol, 1.3 equiv.) and NaOAc (1.07 g, 130.5 mmol, 3 equiv.) in 2 : 1 EtOH : water (65 mL), resulting in the formation of a yellow precipitate. After stirring at rt for 1 h, the precipitate was filtered off, washed with water, and dried under vacuum to afford **69** as a yellow solid (6.87 g, 48%). IR (neat) 1667, 1620, 1505, 1353, 813; ^{1}H NMR (400 MHz, $CDCl_3$) δ 14.65 (s, 1H, NH), 7.72 (d, *J* = 8.8 Hz, 2H, 2 × Ar-CH), 7.18 (d, *J* = 8.8 Hz, 2H, 2 × Ar-CH), 2.61 (s, 3H, CH_3), 2.49 (s, 3H, CH_3); ^{13}C NMR (100 MHz, $CDCl_3$) δ 198.2, 196.9, 141.3, 138.6 (2C), 133.5, 117.9 (2C), 89.3, 31.7, 26.6; MS (ESI) *m/z* 331 $(M+H)^+$; HRMS (ESI) *m/z* calc. for $C_{11}H_{12}N_2O_2I$ 330.9944, found: 330.9962.

(*E*)-4-((4-Iodophenyl)diazenyl)-1,3,5-trimethyl-1*H*-pyrazole (70a)



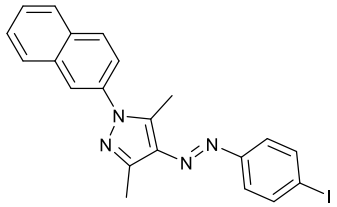
Methylhydrazine (0.13 mL, 2.4 mmol, 1.0 equiv.) was added to a solution of **69** (0.80 g, 2.4 mmol, 1.0 equiv.) in EtOH (20 mL) and the resulting solution was heated under reflux overnight. Concentration under reduced pressure and recrystallisation from MeOH afforded **70a** as a yellow solid (0.76 g, 92%). m.p. 104 – 106 °C (MeOH); IR (neat) 1727, 1407, 1390, 1235, 835; ^{1}H NMR (400 MHz, $CDCl_3$) δ 7.79 (d, *J* = 8.3 Hz, 2H, 2 × Ar-CH), 7.52 (d, *J* = 8.3 Hz, 2H, 2 × Ar-CH), 3.79 (s, 3H, NCH_3), 2.58 (s, 3H, CH_3), 2.49 (s, 3H, CH_3); ^{13}C NMR (100 MHz, $CDCl_3$) δ 153.0, 142.5, 139.2, 138.0 (2C), 135.1, 123.5 (2C), 95.1, 36.0, 13.9, 10.0; MS (ESI) *m/z* 341 $(M+H)^+$; HRMS (ESI) *m/z* calc. for $C_{12}H_{14}N_4I$ 341.0263, found: 341.0263.

(*E*)-1-Benzyl-4-((4-iodophenyl)diazenyl)-3,5-dimethyl-1*H*-pyrazole (70b)



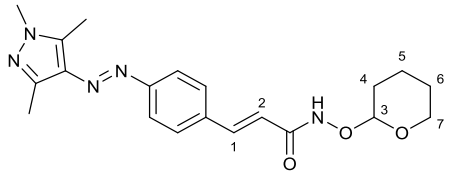
Benzylhydrazine dihydrochloride (0.12 g, 0.60 mmol, 1.0 equiv.) and NEt_3 (0.16 mL, 1.2 mmol, 2.0 equiv.) were added to a solution of **69** (0.20 g, 0.60 mmol, 1.0 equiv.) in EtOH (5 mL) and heated under reflux overnight. Orange crystals formed on cooling, and were filtered under vacuum and washed with MeOH (5 mL) to afford **70b** as an orange solid (0.17 g, 68%). m.p. 134 – 136 °C (MeOH); IR (neat) 1496, 1453, 1412, 1387; ^{1}H NMR (400 MHz, $CDCl_3$) δ 7.79 (d, *J* = 8.6 Hz, 2H, 2 × phenyl-CH), 7.52 (d, *J* = 8.6 Hz, 2H, 2 × phenyl-CH), 7.36 – 7.29 (m, 3H, 3 × benzyl-CH), 7.17 (d, *J* = 7.3 Hz, 2H, 2 × benzyl-CH), 5.30 (s, 2H, CH_2), 2.54 (s, 3H, CH_3), 2.52 (s, 3H, CH_3); ^{13}C NMR (100 MHz, $CDCl_3$) δ 153.0, 142.8, 139.4, 138.1 (2C), 136.1, 135.5, 128.9 (2C), 127.9, 126.8 (2C), 123.5 (2C), 95.2, 53.1, 14.1, 10.0; MS (ESI) *m/z* 417 $(M+H)^+$; HRMS (ESI) *m/z* calc. for $C_{18}H_{18}N_4I$ 417.0576, found: 417.0582.

(*E*)-4-((4-Iodophenyl)diazenyl)-3,5-dimethyl-1-(naphthalen-2-yl)-1*H*-pyrazole (70c)



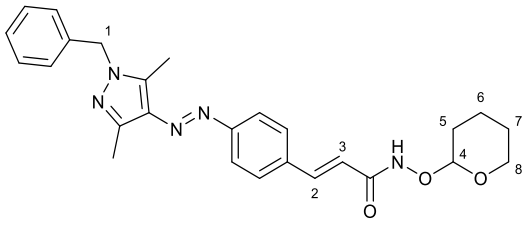
2-Naphthylhydrazine hydrochloride (1.25 g, 6.39 mmol, 1.0 equiv.) and NEt_3 (0.89 mL, 6.39 mmol, 1.0 equiv.) were added to a solution of **69** (2.11 g, 6.39 mmol, 1.0 equiv.) in EtOH (30 mL) and heated under reflux for 6 h. The resulting suspension was concentrated under reduced pressure and purified by flash column chromatography (pentane : EtOAc, 15 : 1) to afford **70c** as an orange solid (0.40 g, 14%). R_f 0.35 (pentane : EtOAc, 15 : 1) ; m.p. 136 – 138 °C (MeOH); IR (neat) 1510, 1404, 1340; ^{1}H NMR (400 MHz, $CDCl_3$) δ 8.00 (d, *J* = 8.8 Hz, 1H, naphthyl-CH), 7.96 – 7.91 (m, 3H, 3 × naphthyl-CH), 7.83 (d, *J* = 8.8 Hz, 2H, 2 × phenyl-CH), 7.65 (dd, *J* = 8.8, 2.4 Hz, 1H, naphthyl-CH), 7.60 – 7.57 (m, 4H, 2 × phenyl-CH & 2 × naphthyl-CH), 2.73 (s, 3H, CH_3), 2.62 (s, 3H, CH_3); ^{13}C NMR (100 MHz, $CDCl_3$) δ 153.0, 144.2, 139.8, 138.1 (2C), 136.4, 136.3, 133.1, 132.5, 129.3, 128.1, 127.9, 127.0, 126.8, 123.6 (2C), 123.1, 123.0, 95.5, 14.2, 11.5; MS (ESI) *m/z* 453 $(M+H)^+$; HRMS (ESI) *m/z* calc. for $C_{21}H_{18}N_4I$ 453.0576, found: 453.0578.

(*E*)-*N*-((Tetrahydro-2*H*-pyran-2-yl)oxy)-3-(4-((*E*)-(1,3,5-trimethyl-1*H*-pyrazol-4-yl)diazenyl)phenyl)acrylamide (71a)



Following general procedure D, azopyrazole **70a** (0.24 g, 0.71 mmol) was coupled with THP-protected *N*-hydroxyacrylamide **62** (0.18 g, 1.1 mmol) and purified by flash column chromatography (pentane : EtOAc, 1 : 3) to afford **71a** as an orange solid (0.20 g, 74%). R_f 0.19 (pentane : EtOAc, 1 : 3); m.p. 162 – 164 °C (EtOAc); IR (neat) 3144 (br.), 1655, 1620, 1520, 1399; ^{1}H NMR (400 MHz, *d*$_6$-DMSO) δ 11.28 (s, 1H, NH), 7.76 (d, *J* = 8.3 Hz, 2H, 2 × Ar-CH), 7.71 (d, *J* = 8.3 Hz, 2H, 2 × Ar-CH), 7.54 (d, *J* = 15.6 Hz, 1H, C(1)H), 6.57 (d, *J* = 15.6 Hz, 1H, C(2)H), 4.94 – 4.91 (m, 1H, C(3)H), 3.98 – 3.94 (m, 1H, C(7)H_a), 3.56 – 3.53 (m, 1H, C(7)H_b), 3.33 (s, 3H, NCH_3), 2.56 (s, 3H, CH_3), 2.38 (s, 3H, CH_3), 1.72 – 1.51 (m, 6H, C(4)H_2, C(5)H_2 & C(6)H_2); ^{13}C NMR (100 MHz, *d*$_6$-DMSO) 162.4, 153.5, 140.5, 140.0, 138.7, 135.5, 134.7, 128.6 (2C), 121.9 (2C), 119.4, 101.0, 61.4, 36.0, 27.8, 24.6, 18.3, 13.8, 9.5; (ESI) *m/z* 384 $(M+H)^+$; HRMS (ESI) *m/z* calc. for $C_{20}H_{26}N_5O_3$ 384.2036, found: 384.2036.

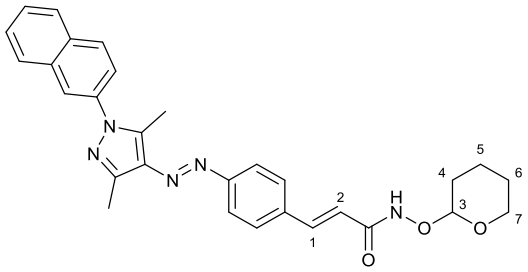
***(E)*-3-(4-((*E*)-(1-Benzyl-3,5-dimethyl-1*H*-pyrazol-4-yl)diazenyl)phenyl)-*N*-((tetrahydro-2*H*-pyran-2-yl)oxy)acrylamide (71b)**



Following general procedure D, azopyrazole **70b** (0.46 g, 1.1 mmol) was coupled with THP-protected *N*-hydroxyacrylamide **62** (0.28 g, 1.7 mmol) and purified by flash column chromatography (pentane : EtOAc, 1 : 2) to afford **71b** as an orange solid (0.30 g, 59%). R_f 0.6 (pentane : EtOAc, 1 : 2); m.p. 178 – 180 °C (EtOAc); IR (neat) 3120 (br.), 1650, 1422, 1407; ^{1}H NMR (400 MHz, *d*$_6$-DMSO) δ 11.29 (s, 1H, NH), 7.78 (d, *J* = 8.8 Hz, 2H, 2 × phenyl-CH), 7.73 (d, *J* = 8.8 Hz, 2H, 2 × phenyl-CH), 7.55 (d, *J* = 15.6 Hz, 1H, C(2)H), 7.37 (t, *J* = 7.3 Hz, 2H, 2 × benzyl-CH), 7.31 (t, *J* = 7.3 Hz, 1H, benzyl-CH), 7.22 (d, *J* = 7.3 Hz, 2H, 2 × benzyl-CH), 6.58 (d, *J* = 15.6 Hz, 1H, C(3)H), 5.35 (s, 2H, C(1)H_2), 4.94 – 4.92 (m, 1H, C(4)H), 3.99 – 3.94 (m, 1H, C(8)H_a), 3.56 – 3.54 (m, 1H, C(8)H_b), 2.57 (s, 3H, CH_3), 2.41 (s, 3H, CH_3), 1.73 – 1.55 (m, 6H, C(5)H_2, C(6)H_2 & C(7)H_2); ^{13}C NMR (100 MHz, *d*$_6$-DMSO) δ 162.4, 153.4, 141.1, 140.1, 138.6, 136.7, 135.7, 134.9, 128.7 (2C), 128.6 (2C), 127.6, 127.1 (2C), 122.0, 119.5,

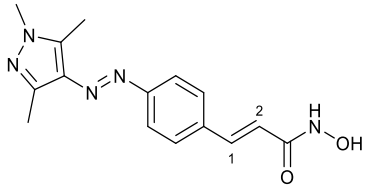
101.0, 61.4, 52.1, 27.8, 24.7, 18.3, 14.0, 9.6; MS (ESI) *m/z* 460 $(M+H)^+$; HRMS (ESI) *m/z* calc. for $C_{26}H_{30}N_5O_3$ 460.2349, found: 460.2349.

(*E*)-3-(4-((*E*)-(3,5-Dimethyl-1-(naphthalen-2-yl)-1*H*-pyrazol-4-yl)diazenyl)phenyl)-*N*-((tetrahydro-2*H*-pyran-2-yl)oxy)acrylamide (71c)



Following general procedure D, azopyrazole **70c** (0.31 g, 0.69 mmol) was coupled with THP-protected *N*-hydroxyacrylamide **62** (0.18 g, 1.0 mmol) and purified by flash column chromatography (pentane : EtOAc, 2 : 1) to afford **71c** as an orange solid (0.30 g, 88%). R_f 0.14 (pentane : EtOAc, 2 : 1); m.p. 172 – 174 °C (EtOAc); IR (neat) 3110 (br.), 1652, 1600, 1515, 1489, 1337; ^{1}H NMR (400 MHz, *d*$_6$-DMSO) δ 11.30 (br. s, 1H, NH), 8.21 (d, *J* = 2.4 Hz, 1H, naphthyl-CH), 8.13 (d, *J* = 8.8 Hz, 1H, naphthyl-CH), 8.09 – 8.04 (m, 2H, 2 × naphthyl-CH), 7.85 (d, *J* = 8.3 Hz, 2H, 2 × phenyl-CH), 7.79 (dd, *J* = 8.8, 2.4 Hz, 1H, naphthyl-CH), 7.75 (d, *J* = 8.3 Hz, 2H, 2 × phenyl-CH), 7.64 – 7.62 (m, 2H, 2 × naphthyl-CH), 7.56 (d, *J* = 16.4 Hz, 1H, C(1)H), 6.60 (d, *J* = 16.4 Hz, 1H, C(2)H), 4.94 – 4.92 (m, 1H, C(3)H), 3.99 – 3.95 (m, 1H, C(7)H_a), 3.56 – 3.52 (m, 1H, C(7)H_b), 2.76 (s, 3H, CH_3), 2.54 (s, 3H, CH_3), 1.74 – 1.50 (m, 6H, C(4)H_2, C(5)H_2 & C(6)H_2); ^{13}C NMR (125 MHz, *d*$_6$-DMSO) δ 162.4, 153.4, 142.6, 140.7, 138.7, 136.1 (2C), 136.0, 132.8, 132.1, 129.2, 128.7 (2C), 128.2, 127.8, 127.2, 127.0, 122.9, 122.6, 122.3 (2C), 119.7, 101.1, 61.4, 27.8, 24.7, 18.3, 14.2, 11.1; MS (ESI) *m/z* 496 $(M+H)^+$; HRMS (ESI) *m/z* calc. for $C_{29}H_{30}N_5O_3$ 496.2349, found: 496.2348.

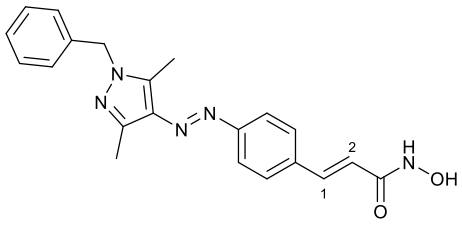
(*E*)-*N*-Hydroxy-3-(4-((E)-(1,3,5-trimethyl-1*H*-pyrazol-4-yl)diazenyl)phenyl)acrylamide (68a)



Following general procedure E, deprotection of THP-hydroxamate **71a** (0.19 g, 0.50 mmol) was carried out at 50 °C overnight. Concentration under reduced pressure, followed by trituration with EtOAc and water sequentially, afforded **68a** as an amorphous orange solid (0.11 g, 74%). IR (neat) 3400 – 2500 (br.), 1651, 1614, 1515, 1402; ^{1}H NMR (400 MHz, *d*$_6$-DMSO) δ 10.80 (br. s, 1H, NH or

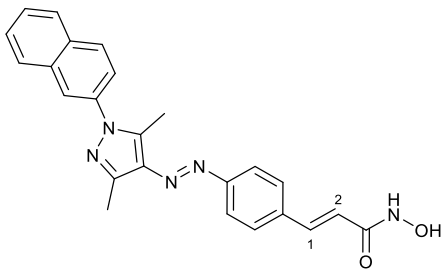
OH), 7.75 (d, *J* = 8.3 Hz, 2H, 2 × Ar-CH), 7.70 (d, *J* = 8.3 Hz, 2H, 2 × Ar-CH), 7.51 (d, *J* = 15.6 Hz, 1H, C(1)H), 6.53 (d, *J* = 15.6 Hz, 1H, C(2)H), 3.74 (s, 3H, NCH_3), 2.56 (s, 3H, CH_3), 2.38 (s, 3H, CH_3); ^{13}C NMR (100 MHz, d_6-DMSO) δ 162.6, 153.3, 140.4, 139.9, 137.5, 135.8, 134.6, 128.5 (2C), 121.9 (2C), 119.8, 36.0, 13.8, 9.5; MS (ESI) *m/z* 300 $(M+H)^+$; HRMS (ESI) *m/z* calc. for $C_{15}H_{18}N_5O_2$ 300.1461, found: 300.1470.

(*E*)-3-(4-((*E*)-(1-Benzyl-3,5-dimethyl-1*H*-pyrazol-4-yl)diazenyl)phenyl)-*N*-hydroxyacrylamide (68b)



Following general procedure E, deprotection of THP-hydroxamate **71b** (0.29 g, 0.63 mmol) was carried out at 50 °C overnight. Concentration under reduced pressure, followed by trituration with EtOAc and water sequentially, afforded **68b** as an amorphous orange solid (70 mg, 30%). IR (neat) 3320 – 2500 (br.), 1652, 1620, 1401; ^1H NMR (400 MHz, d_6-DMSO) δ 10.81 (br. s, 1H, NH or OH), 7.76 (d, *J* = 8.4 Hz, 2H, 2 × phenyl-CH), 7.70 (d, *J* = 8.4 Hz, 2H, 2 × phenyl-CH), 7.51 (d, *J* = 15.9 Hz, 1H, C(1)H), 7.36 (t, *J* = 7.4 Hz, 1H, 2 × benzyl-CH), 7.30 (t, *J* = 7.4 Hz, 1H, benzyl-CH), 7.21 (d, J = 7.4 Hz, 2H, 2 × benzyl-CH), 6.53 (d, J = 15.9 Hz, 1H, C(2)H), 5.34 (s, 2H, CH_2), 2.56 (s, 3H, CH_3), 2.41 (s. 3H, CH_3); ^{13}C NMR (100 MHz, d_6-DMSO) δ 162.5, 153.3, 141.1, 140.1, 137.5, 136.7, 135.9, 134.9, 128.7 (2C), 128.5 (2C), 127.6, 127.1 (2C), 122.0 (2C), 119.9, 52.1, 14.0, 9.6; MS (ESI) *m/z* 376 $(M+H)^+$; HRMS (ESI) *m/z* calc. for $C_{21}H_{22}N_5O_2$ 376.1774, found: 376.1774.

(*E*)-3-(4-((*E*)-(3,5-Dimethyl-1-(naphthalen-2-yl)-1*H*-pyrazol-4-yl)diazenyl)phenyl)-*N*-hydroxyacrylamide (68c)

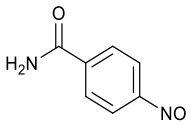


Following general procedure E, deprotection of THP-hydroxamate **71c** (0.29 g, 0.59 mmol) was carried out at 50 °C overnight. Concentration under reduced pressure, followed by trituration with EtOAc and water sequentially, afforded **68c** as an amorphous orange solid (0.15 g, 62%). IR (neat)

3314 (br.), 3053 (br.), 1599, 1512, 1397; ^{1}H NMR (400 MHz, d_6-DMSO) δ 10.84 (br. s, 1H, NH), 9.13 (br. s, 1H, OH), 8.20 (d, *J* = 2.1 Hz, 1H, naphthyl-CH), 8.12 (d, *J* = 8.6 Hz, 1H, naphthyl-CH), 8.08 – 8.03 (m, 2H, 2 × naphthyl-CH), 7.83 (d, *J* = 8.5 Hz, 2H, 2 × phenyl-CH), 7.79 (dd, *J* = 8.6, 2.1 Hz, 1H, naphthyl-CH), 7.74 (d, *J* = 8.5 Hz, 2H, 2 × phenyl-CH), 7.64 – 7.61 (m, 2H, 2 × naphthyl-CH), 7.53 (d, *J* = 15.6 Hz, 1H, C(1)H), 6.55 (d, *J* = 15.6 Hz, 1H, C(2)H), 2.75 (s, 3H, CH_3), 2.53 (s, 3H, CH_3); ^{13}C NMR (100 MHz, d_6-DMSO) δ 162.6, 153.3, 142.5, 140.7, 137.5, 136.3, 136.0, 135.9, 132.8, 132.0, 129.2, 128.6 (2C), 128.2, 127.8, 127.1, 126.9, 122.8, 122.5, 122.2 (2C), 120.1, 14.2, 11.1; MS (ESI) *m/z* 412 $(M+H)^+$; HRMS (ESI) *m/z* calc. for $C_{24}H_{22}N_5O_2$ 412.1774, found: 412.1774.

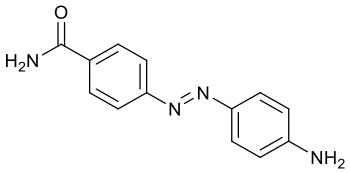
5.2.6 Photoswitchable tethered HDAC inhibitors

4-Nitrosobenzamide[225] (73)



mCPBA (4.94 g, 22.1 mmol, 2.0 equiv.) in MeCN (50 mL) was added to 4-aminobenzamide (1.50 g, 11.0 mmol, 1.0 equiv.) in MeCN (300 mL) and stirred at 60 °C for 1 h. The reaction mixture was then poured onto 2% aq. NaOH (400 mL), and extracted with EtOAc until the organic layer was clear. The combined organic layers were washed with water (200 mL) and brine (200 mL), then dried over $MgSO_4$ and concentrated under reduced pressure. The precipitate was triturated with EtOAc and filtered under vacuum to afford **73** as a cream solid (0.68 g, 41%). ^{1}H NMR (400 MHz, d_6-DMSO) δ 8.30 (br. s, 1H, NH), 8.17 (d, *J* = 8.3 Hz, 2H, 2 × Ar-CH), 8.02 (d, *J* = 8.3 Hz, 2H, 2 × Ar-CH), 7.74 (br. s, 1H, NH); ^{13}C NMR (100 MHz, d_6-DMSO) δ 166.6, 165.2, 140.3, 129.1, 120.5; MS (ESI) *m/z* 151 $(M+H)^+$; HRMS (ESI) *m/z* calc. for $C_7H_7N_2O_2$ 151.0508, found: 151.0481.

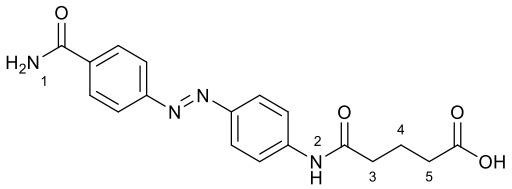
(*E*)-4-((4-Aminophenyl)diazenyl)benzamide (75)



A solution of **73** (2.30 g, 15.3 mmol, 1.2 equiv.) and 1,4-diaminobenzene (**74**) (1.38 g, 12.8 mmol, 1.0 equiv.) in AcOH (100 mL) was stirred at 40 °C for 4 h. The solvent was removed under vacuum and the resulting black residue was triturated with EtOAc. The remaining solid was removed by filtration and the filtrate was washed sequentially with water (2 × 50 mL) and brine (50 mL), dried

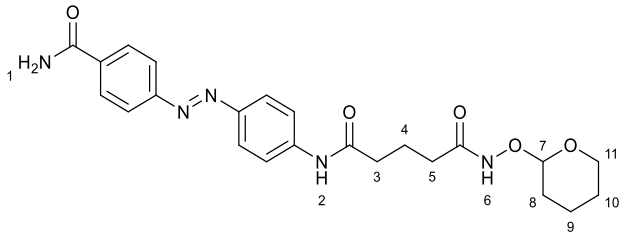
over $MgSO_4$, and concentrated under reduced pressure to afford **75** as a brown solid (1.92 g, 52%). m.p. 217 – 219 °C (EtOAc); IR (neat) 3442 (br.), 3310 (br.), 3198 (br.), 1594, 1413, 1282, 1106, 865; ^{1}H NMR (400 MHz, CD_3OD) δ 7.98 (d, *J* = 8.8 Hz, 2H, 2 × Ar-CH), 7.84 (d, *J* = 8.8 Hz, 2H, 2 × Ar-CH), 7.75 (d, *J* = 8.8 Hz, 2H, 2 × Ar-CH), 6.74 (d, *J* = 8.8 Hz, 2H, 2 × Ar-CH); ^{13}C NMR (100 MHz, CD_3OD) δ 171.8, 156.6, 154.4, 145.7, 135.2, 129.7 (2C), 126.7 (2C), 122.9 (2C), 115.0 (2C); MS (ESI) *m/z* 241 $(M+H)^+$; HRMS (ESI) *m/z* calc. for $C_{13}H_{13}N_4O$ 241.1089, found: 241.1107.

(*E*)-5-((4-((4-Carbamoylphenyl)diazenyl)phenyl)amino)-5-oxopentanoic acid (76b)



Following a modified literature procedure,[226] glutaric anhydride (0.36 g, 3.1 mmol, 1.5 equiv.) was added to a solution of **75** (0.51 g, 2.1 mmol, 1.0 equiv.) in acetone (20 mL) and the solution was heated under reflux overnight. The resulting precipitate was filtered off and washed with acetone to afford **76b** as an orange solid (0.60 g, 80%). m.p. 260 – 262 °C (acetone); IR (neat) 3410 (br.), 3307 (br.), 3209 (br.), 1694, 1658, 1525, 1410, 864; ^{1}H NMR (400 MHz, *d*$_6$-DMSO) δ 10.33 (s, 1H, N(2)H or OH), 8.13 (br. s, 1H, N(1)H$_a$), 8.06 (d, *J* = 8.3 Hz, 2H, 2 × Ar-CH), 7.90 (*app*-t, *J* = 8.8 Hz, 4H, 4 × Ar-CH), 7.84 (d, *J* = 8.8 Hz, 2H, 2 × Ar-CH), 7.51 (br. s, 1H, N(1)H$_b$), 2.42 (t, *J* = 7.4 Hz, 2H, C(3)H$_2$ or C(5)H$_2$), 2.28 (t, *J* = 7.4 Hz, 2H, C(3)H$_2$ or C(5)H$_2$), 1.83 (quin, *J* = 7.4 Hz, 2H, C(4)H$_2$); ^{13}C NMR (100 MHz, *d*$_6$-DMSO) δ 174.5, 171.7, 167.5, 153.7, 147.6, 142.9, 136.0, 128.9 (2C), 124.1 (2C), 122.2 (2C), 119.4 (2C), 35.7, 33.2, 20.5; MS (ESI) *m/z* 355 $(M+H)^+$; HRMS (ESI) *m/z* calc. for $C_{18}H_{19}N_4O_4$ 355.1406, found: 355.1440.

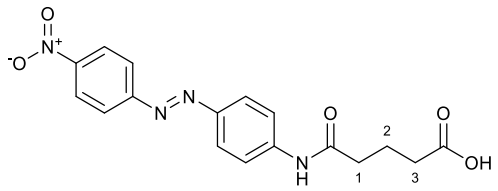
(*E*)-*N*1-(4-((4-Carbamoylphenyl)diazenyl)phenyl)-*N*5-((tetrahydro-2*H*-pyran-2-yl)oxy)glutaramide (77b)



Following general procedure G, **76b** (0.52 g, 1.47 mmol) was coupled with NH_2OTHP (0.21 g, 1.76 mmol). Solvent was removed under vacuum and the residue was triturated with EtOAc. The solid was filtered off and dried under vacuum to afford **77b** as an amorphous brown solid (0.56 g,

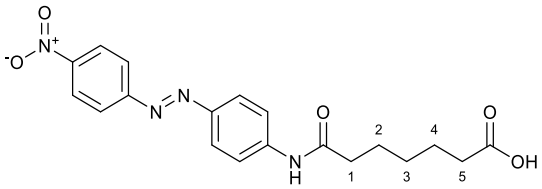
84%). IR (neat) 3394 (br.), 3298 (br.), 3189 (br.), 1647, 1529, 1409, 843; ^{1}H NMR (400 MHz, d_6-DMSO) δ 10.98 (s, 1H, N(2)H or N(6)H), 10.32 (s, 1H, N(2)H or N(6)H), 8.13 (br. s, 1H, N(1)H_a), 8.06 (d, J = 8.8 Hz, 2H, 2 × Ar-CH), 7.90 (*app*-t, J = 8.8 Hz, 4H, 4 × Ar-CH), 7.84 (d, J = 8.8 Hz, 2H, 2 × Ar-CH), 7.53 (br. s, 1H, N(1)H_b), 4.84 – 4.82 (m, 1H, C(7)H), 3.94 – 3.88 (m, 1H, C(11)H_a), 3.51 – 3.48 (m, 1H, C(11)H_b), 2.39 (t, J = 7.4 Hz, 2H, C(3)H_2 or C(5)H_2), 2.07 (t, J = 7.4 Hz, 2H, C(3)H_2 or C(5)H_2), 1.83 (quin, J = 7.4 Hz, 2H, C(4)H_2), 1.67 – 1.48 (m, 6H, C(8)H_2, C(9)H_2 & C(10)H_2); ^{13}C NMR (100 MHz, d_6-DMSO) δ 171.4, 168.7, 167.2, 153.5, 147.5, 142.9, 136.0, 128.8 (2C), 124.0 (2C), 122.1 (2C), 119.2 (2C), 100.9, 61.3, 35.6, 31.5, 27.8, 24.7, 20.8, 18.3; MS (ESI) *m/z* 454 $(M+H)^+$; HRMS (ESI) *m/z* calc. for $C_{23}H_{28}N_5O_5$ 454.2090 , found: 454.2075.

(*E*)-5-((4-((4-Nitrophenyl)diazenyl)phenyl)amino)-5-oxopentanoic acid (82b)



Following a modified literature procedure,[226] glutaric anhydride (0.71 g, 6.2 mmol, 1.5 equiv.) was added to (*E*)-4-((4-nitrophenyl)diazenyl)aniline (**81**) (1.00 g, 4.1 mmol, 1.0 equiv.) in acetone (40 mL) and the solution was heated under reflux overnight. The resulting precipitate was filtered off and washed with acetone to afford **82b** as an orange solid (1.18 g, 80%). m.p. 200 – 202 °C (acetone); IR (neat) 3311 (br.), 1699, 1523, 1344, 1210, 858; ^{1}H NMR (400 MHz, d_6-DMSO) δ 10.62 (s, 1H, NH or OH), 8.42 (d, J = 9.3 Hz, 2H, 2 × Ar-CH), 8.04 (d, J = 9.3 Hz, 2H, 2 × Ar-CH), 7.96 (d, J = 9.3 Hz, 2H, 2 × Ar-CH), 7.87 (d, J = 9.3 Hz, 2H, 2 × Ar-CH), 2.42 (t, J = 7.6 Hz, 2H, C(1)H_2 or C(3)H_2), 2.24 (t, J = 7.3 Hz, 2H, C(1)H_2 or C(3)H_2), 1.82 (quin, J = 7.3 Hz, 2H, C(2)H_2); ^{13}C NMR (100 MHz, d_6-DMSO) δ 174.2, 171.5, 155.4, 148.1, 147.4, 143.6, 125.1 (2C), 124.6 (2C), 123.2 (2C), 119.2 (2C), 35.6, 33.0, 20.3; MS (ESI) *m/z* 357 $(M+H)^+$; HRMS (ESI) *m/z* calc. for $C_{17}H_{17}N_4O_5$ 357.1199, found: 357.1207.

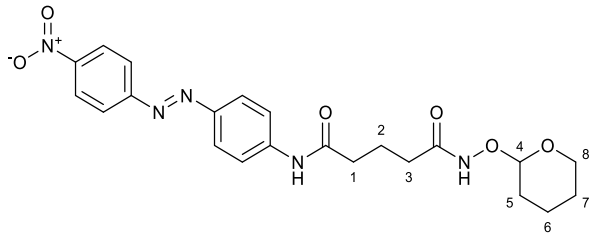
(*E*)-7-((4-((4-Nitrophenyl)diazenyl)phenyl)amino)-7-oxoheptanoic acid (82c)



Following modified literature procedures,[226,234] pimelic acid (**79**) (1.66 g, 10.4 mmol, 1.0 equiv.) in Ac_2O (5 mL) was heated under reflux for 4 h, followed by removal of solvent under vacuum to afford

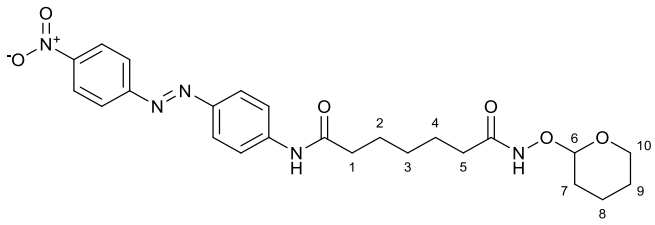
pimelic anhydride (**80**) as a white solid. This was added to a solution of (*E*)-4-((4-nitrophenyl)diazenyl)aniline (**81**) (3.78 g, 15.6 mmol, 1.5 equiv.) in acetone (100 mL) and the resulting mixture was heated under reflux overnight. Concentration under reduced pressure and purification by flash column chromatography (DCM : MeOH, 96 : 4) afforded **82c** as an orange-red solid (1.89 g, 47%). R_f 0.21 (DCM : MeOH, 96 : 4); m.p. 170 – 172 °C (DCM); IR (neat) 3312 (br.), 1708, 1595, 1501, 1300; ^{1}H (100 MHz, d_6-DMSO) δ 10.36 (s, 1H, NH or OH), 8.43 (d, *J* = 8.8 Hz, 2H, 2 × Ar-CH), 8.05 (d, *J* = 8.8 Hz, 2H, 2 × Ar-CH), 7.96 (d, *J* = 9.1 Hz, 2H, 2 × Ar-CH), 7.87 (d, *J* = 9.1 Hz, 2H, 2 × Ar-CH), 2.37 (t, *J* = 7.3 Hz, 2H, C(1)H_2 or C(5)H_2), 2.20 (t, *J* = 7.3 Hz, 2H, C(1)H_2 or C(5)H_2), 1.62 (quin, *J* = 7.3 Hz, 2H, C(2)H_2 or C(4)H_2), 1.51 (quin, *J* = 7.3 Hz, 2H, C(2)H_2 or C(4)H_2), 1.33 (quin, *J* = 7.3 Hz, 2H, C(3)H_2); ^{13}C NMR (100 MHz, d_6-DMSO) δ 171.9 (2C), 155.3, 148.1, 147.4, 143.7, 125.1 (2C), 124.5 (2C), 123.2 (2C), 119.2 (2C), 36.4, 33.7, 28.1, 24.7, 24.3; MS (ESI) *m/z* 385 $(M+H)^+$; HRMS (ESI) *m/z* calc. for $C_{19}H_{21}N_4O_5$ 385.1512, found: 385.1505.

(*E*)-*N*1-(4-((4-Nitrophenyl)diazenyl)phenyl)-*N*5-((tetrahydro-2*H*-pyran-2-yl)oxy)glutaramide (83b)



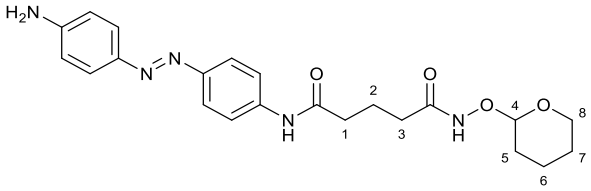
Following general procedure G, **82b** (1.15 g, 3.23 mmol) was coupled with NH_2OTHP (0.45 g, 3.87 mmol). Solvent was removed under vacuum and the residue was triturated with EtOAc. The solid was filtered off and dried under vacuum to afford **83b** as a red solid (1.01 g, 69%). m.p. 136 – 138 °C (EtOAc); IR (neat) 3311 (br.), 1698, 1666, 1517, 1340, 1136, 859; ^{1}H NMR (400 MHz, d_6-DMSO) δ 10.99 (s, 1H, NH), 10.38 (s, 1H, NH), 8.42 (d, *J* = 9.0 Hz, 2H, 2 × Ar-CH), 8.04 (d, *J* = 9.0 Hz, 2H, 2 × Ar-CH), 7.96 (d, *J* = 9.3 Hz, 2H, 2 × Ar-CH), 7.87 (d, *J* = 9.3 Hz, 2H, 2 × Ar-CH), 4.83 – 4.81 (m, 1H, C(4)H), 3.93 – 3.88 (m, 1H, C(8)H_a), 3.51 – 3.47 (m, 1H, C(8)H_b), 2.39 (t, *J* = 7.5 Hz, 2H, C(1)H_2 or C(3)H_2), 2.07 (t, *J* = 7.5 Hz, 2H, C(1)H_2 or C(3)H_2), 1.83 (quin, *J* = 7.5 Hz, 2H, C(2)H_2), 1.66 – 1.46 (m, 6H, C(5)H_2, C(6)H_2 & C(7)H_2); ^{13}C NMR (100 MHz, d_6-DMSO) δ 171.5, 168.7, 155.4, 148.1, 147.4, 143.7, 125.1 (2C), 124.6 (2C), 123.3 (2C), 119.3 (2C), 100.9, 61.3, 35.6, 31.5, 27.8, 24.7, 20.8, 18.3; MS (ESI) *m/z* 456 $(M+H)^+$; HRMS (ESI) *m/z* calc. for $C_{22}H_{26}N_5O_6$ 456.1883, found: 456.1879.

(*E*)-*N*1-(4-((4-Nitrophenyl)diazenyl)phenyl)-*N*7-((tetrahydro-2*H*-pyran-2-yl)oxy)heptanediamide (83c)



Following general procedure G, **82c** (1.58 g, 4.11 mmol) was coupled with NH_2OTHP (0.58 g, 4.94 mmol). Solvent was removed under vacuum and the residue was triturated with EtOAc. The solid was filtered off and dried under vacuum to afford **83c** as an orange solid (1.28 g, 65%). m.p. 61 – 63 °C (EtOAc); IR (neat) 3213 (br.), 1661, 1517, 1342; ^{1}H NMR (400 MHz, $CDCl_3$) δ 8.46 (br. s, 1H, NH), 8.38 (d, *J* = 9.1 Hz, 2H, 2 × Ar-CH), 8.01 (d, *J* = 9.1 Hz, 2H, 2 × Ar-CH), 7.97 (d, *J* = 8.8 Hz, 2H, 2 × Ar-CH), 7.81 (d, *J* = 8.8 Hz, 2H, 2 × Ar-CH), 4.97 – 4.95 (m, 1H, C(6)H), 3.98 – 3.91 (m, 1H, C(10)H_a), 3.67 – 3.61 (m, 1H, C(10)H_b), 2.45 (t, *J* = 7.3 Hz, 2H, C(1)H_2 or C(5)H_2), 2.23 – 2.16 (m, 2H, C(1)H_2 or C(5)H_2), 1.85 – 1.54 (m, 10H, C(7)H_2, C(8)H_2, C(9)H_2, C(2)H_2 & C(4)H_2), 1.46 (quin, *J* = 7.3 Hz, 2H, C(3)H_2); ^{13}C (100 MHz, $CDCl_3$) δ 171.8, 170.6, 155.9, 148.6, 148.4, 142.2, 124.7 (4C), 123.3 (2C), 119.7 (2C), 102.5, 62.6, 37.2, 32.7, 28.1, 28.0, 24.9, 24.7, 24.0, 18.5; MS (ESI) *m/z* 484 $(M+H)^+$; HRMS (ESI) *m/z* calc. for $C_{24}H_{30}N_5O_6$ 484.2196, found: 484.2201.

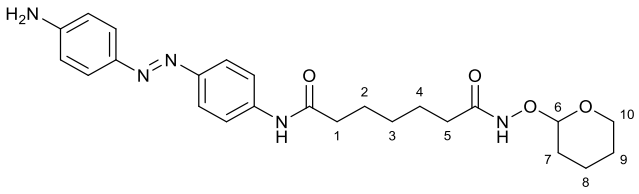
(*E*)-*N*1-(4-((4-Aminophenyl)diazenyl)phenyl)-*N*5-((tetrahydro-2*H*-pyran-2-yl)oxy)glutaramide (78b)



Following general procedure H, reduction of *p*-nitroazobenzene **83b** (1.54 g, 3.46 mmol) was carried out for 1 h to afford **78b** as an amorphous red solid (0.91 g, 62%). IR (neat) 3354 (br.), 3223 (br.), 1664, 1595, 1528, 1505; ^{1}H NMR (400 MHz, d_6-DMSO) δ 10.97 (s, 1H, NH), 10.14 (s, 1H, NH), 7.74 (d, *J* = 9.3 Hz, 2H, 2 × Ar-CH), 7.70 (d, *J* = 9.3 Hz, 2H, 2 × Ar-CH), 7.62 (d, *J* = 8.8 Hz, 2H, 2 × Ar-CH), 6.65 (d, *J* = 8.8 Hz, 2H, 2 × Ar-CH), 6.02 (br. s, 2H, NH_2), 4.83 – 4.81 (m, 1H, C(4)H), 3.94 – 3.88 (m, 1H, C(8)H_a), 3.51 – 3.47 (m, 1H, C(8)H_b), 2.35 (t, *J* = 7.4 Hz, 2H, C(1)H_2 or C(3)H_2), 2.06 (t, *J* = 7.4 Hz, 2H, C(1)H_2 or C(3)H_2), 1.82 (quin, *J* = 7.4 Hz, 2H, C(2)H_2), 1.67 – 1.47 (m, 6H, C(5)H_2, C(6)H_2 & C(7)H_2); ^{13}C NMR (100 MHz, d_6-DMSO) δ 171.0, 168.7, 152.4, 147.9, 142.8, 140.5, 124.8 (2C), 122.5 (2C),

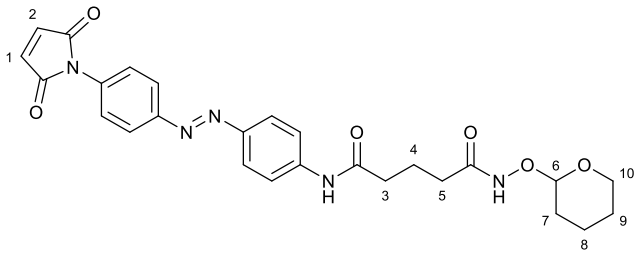
119.2 (2C), 113.4 (2C), 100.8, 61.2, 35.5, 31.5, 27.8, 24.7, 20.9, 18.3; MS (ESI) *m/z* 426 $(M+H)^+$; HRMS (ESI) *m/z* calc. for $C_{22}H_{28}N_5O_4$ 426.2141, found: 426.2134.

(*E*)-*N*1-(4-((4-Aminophenyl)diazenyl)phenyl)-*N*7-((tetrahydro-2*H*-pyran-2-yl)oxy)heptanediamide (78c)



Following general procedure H, reduction of *p*-nitroazobenzene **83c** (1.26 g, 2.61 mmol) was carried out for 2 h, affording **78c** as an amorphous orange solid (0.75 g, 63%). IR (neat) 3311 (br.), 3237 (br.), 1665, 1599, 1530; ^{1}H NMR (400 MHz, d_6-DMSO) δ 10.92 (s, 1H, NH), 10.11 (s, 1H, NH), 7.75 (d, *J* = 9.3 Hz, 2H, 2 × Ar-CH), 7.71 (d, *J* = 9.3 Hz, 2H, 2 × Ar-CH), 7.62 (d, *J* = 8.8 Hz, 2H, 2 × Ar-CH), 6.66 (d, *J* = 8.8 Hz, 2H, 2 × Ar-CH), 6.02 (s, 2H, NH_2), 4.81 – 4.79 (m, 1H, C(6)H), 3.94 – 3.88 (m, 1H, C(10)H_a), 3.50 – 3.47 (m, 1H, C(10)H_b), 2.33 (t, *J* = 7.5 Hz, 2H, C(1)H_2 or C(5)H_2), 2.00 (t, *J* = 7.5 Hz, 2H, C(1)H_2 or C(5)H_2), 1.67 – 1.47 (m, 10H, C(7)H_2, C(8)H_2, C(9)H_2, C(2)H_2, C(4)H_2), 1.29 (quin, *J* = 7.5 Hz, 2H, C(3)H_2); ^{13}C (100 MHz, d_6-DMSO) δ 171.4, 169.0, 152.3, 147.9, 142.9, 140.6, 124.8 (2C), 122.5 (2C), 119.2 (2C), 113.4 (2C), 100.8, 61.3, 36.4, 36.3, 32.1, 28.1, 27.8, 24.8, 24.7, 18.3; MS (ESI) *m/z* 454 $(M+H)^+$; HRMS (ESI) *m/z* calc. for $C_{24}H_{32}N_5O_4$ 454.2454, found: 454.2461.

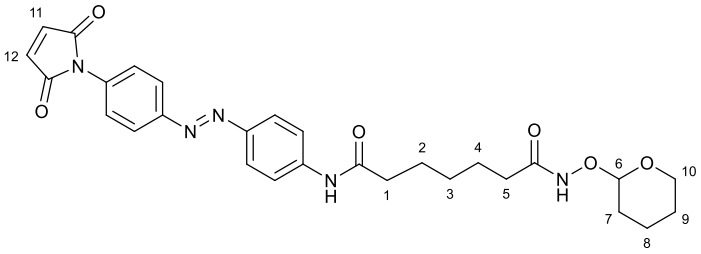
(*E*)-*N*1-(4-((4-(2,5-Dioxo-2,5-dihydro-1*H*-pyrrol-1-yl)phenyl)diazenyl)phenyl)-*N*5-((tetrahydro-2*H*-pyran-2-yl)oxy)glutaramide (84b)



Following a modified literature procedure,[233] maleic anhydride (0.22 g, 2.2 mmol, 1.1 equiv.) was added to **78b** (0.86 g, 2.0 mmol, 1.0 equiv.) in AcOH (50 mL) and the red solution was stirred at rt for 1 h, forming an orange precipitate. This was filtered off and redissolved in DMF (15 mL) and acetic anhydride (0.5 mL). NaOAc (84 mg, 1.0 mmol, 0.5 equiv.) was added and the reaction mixture was stirred at rt for 1 h. The mixture was poured onto water and extracted with EtOAc (3 × 25 mL). The combined organic layers were washed with 5% aq. LiCl, dried over $MgSO_4$, and concentrated

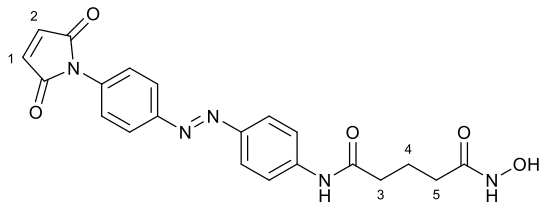
under reduced pressure to afford **84b** as an amorphous orange solid (0.49 g, 48%). IR (neat) 3312 (br.), 1707, 1665, 1594, 1527, 1398; ^{1}H NMR (400 MHz, d_6-DMSO) δ 10.99 (s, 1H, NH), 10.31 (s, 1H, NH), 7.96 (d, *J* = 8.8 Hz, 2H, 2 × Ar-CH), 7.90 (d, *J* = 9.3 Hz, 2H, 2 × Ar-CH), 7.83 (d, *J* = 9.3 Hz, 2H, 2 × Ar-CH), 7.57 (d, *J* = 8.8 Hz, 2H, 2 × Ar-CH), 7.24 (s, 2H, C(1)H & C(2)H), 4.84 – 4.82 (m, 1H, C(6)H), 3.94 – 3.89 (m, 1H, C(10)H_a), 3.52 – 3.49 (m, 1H, C(10)H_b), 2.39 (t, *J* = 7.3 Hz, 2H, C(3)H_2 or C(5)H_2), 2.07 (t, *J* = 7.3 Hz, 2H, C(3)H_2 or C(5)H_2), 1.83 (quin, *J* = 7.3 Hz, 2H, C(4)H_2), 1.68 – 1.47 (m, 6H, C(7)H_2, C(8)H_2 & C(9)H_2); ^{13}C NMR (125 MHz, d_6-DMSO) δ 171.3, 169.7 (2C), 168.6, 150.6, 147.3, 142.6, 134.9 (2C), 133.7, 127.2 (2C), 123.8 (2C), 122.7 (2C), 119.2 (2C), 100.8, 61.2, 35.5, 31.4, 27.8, 24.7, 20.8, 18.3; MS (ESI) *m/z* 506 $(M+H)^+$; HRMS (ESI) *m/z* calc. for $C_{26}H_{28}N_5O_6$ 506.2040, found: 506.2038.

(*E*)-*N*1-(4-((4-(2,5-Dioxo-2,5-dihydro-1*H*-pyrrol-1-yl)phenyl)diazenyl)phenyl)-*N*7-((tetrahydro-2*H*-pyran-2-yl)oxy)heptanediamide (84c)



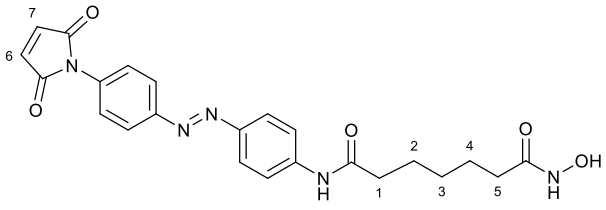
Following the procedure described for the preparation of maleimide **84b**, *p*-aminoazobenzene **78c** (0.73 g, 1.61 mmol) was reacted with maleic anhydride (0.17 g, 1.8 mmol), affording **84c** as an amorphous orange solid (0.28 g, 33%). IR (neat) 3317 (br.), 1709, 1662, 1500, 1373; ^{1}H (400 MHz, d_6-DMSO) δ 10.93 (s, 1H, NH), 10.29 (s, 1H, NH), 7.97 (d, *J* = 8.8 Hz, 2H, 2 × Ar-CH), 7.91 (d, *J* = 8.8 Hz, 2H, 2 × Ar-CH), 7.85 (d, *J* = 8.8 Hz, 2H, 2 × Ar-CH), 7.59 (d, *J* = 8.8 Hz, 2H, 2 × Ar-CH), 7.25 (s, 2H, C(11)H & C(12)H), 4.81 – 4.89 (m, 1H, C(6)H), 3.94 – 3.89 (m, 1H, C(10)H_a), 3.51 – 3.48 (m, 1H, C(10)H_b), 2.37 (t, *J* = 7.5 Hz, 2H, C(1)H_2 or C(5)H_2), 2.01 (t, *J* =7.5 Hz, 2H, C(1)H_2 or C(5)H_2), 1.67 – 1.51 (m, 10H, C(2)H_2, C(4)H_2, C(7)H_2, C(8)H_2, C(9)H_2), 1.30 (quin, *J* = 7.5 Hz, 2H, C(3)H_2); ^{13}C (100 MHz, d_6-DMSO) δ 171.8, 169.7 (2C), 169.0, 162.3, 150.7, 147.3, 142.7, 134.9 (2C), 127.2 (2C), 123.8 (2C), 122.7 (2C), 119.2 (2C), 100.8, 61.3, 36.4, 35.8, 32.0, 30.8, 28.1, 27.8, 24.7, 18.3; MS (ESI) *m/z* 534 $(M+H)^+$; HRMS (ESI) *m/z* calc. for $C_{28}H_{32}N_5O_6$ 534.2353, found: 532.2333.

(*E*)-*N*1-(4-((4-(2,5-Dioxo-2,5-dihydro-1*H*-pyrrol-1-yl)phenyl)diazenyl)phenyl)-*N*5-hydroxyglutaramide (72b)



Following general procedure E, deprotection of THP-hydroxamate **84b** (0.48 g, 0.96 mmol) was carried out at 50 °C overnight. Concentration under reduced pressure, followed by sequential trituration with EtOAc and water, afforded **72b** as an orange solid (140 mg, 85% pure by NMR, 29% yield) with a small impurity still present. Further purification of 50 mg by flash column chromatography (DCM : MeOH : AcOH, 94 : 6 : 0.1) afforded the pure product as an amorphous orange solid (20 mg). R_f 0.25 (94 : 6, DCM : MeOH); IR (neat) 3500 – 2700 (br.), 1703, 1662, 1501, 1403; ^{1}H NMR (400 MHz, *d*$_6$-DMSO) δ 10.40 (s, 1H, NH), 10.30 (s, 1H, NH), 8.70 (s, 1H, OH), 7.96 (t, *J* = 8.6 Hz, 2H, 2 × Ar-CH), 7.89 (d, *J* = 9.1 Hz, 2H, 2 × Ar-CH), 7.85 (d, *J* = 9.1 Hz, 2H, 2 × Ar-CH), 7.57 (d, *J* = 8.6 Hz, 2H, 2 × Ar-CH), 7.23 (s, 2H, C(1)H & C(2)H), 2.38 (t, *J* = 7.8 Hz, 2H, C(3)H_2 or C(5)H_2), 2.02 (t, *J* = 6.4 Hz, 2H, C(3)H_2 or C(5)H_2), 1.83 (quin, *J* = 7.3 Hz, 2H, C(4)H_2); ^{13}C NMR (125 MHz, *d*$_6$-DMSO) δ 171.3, 169.7 (2C), 168.7, 150.7, 147.3, 142.6, 134.9 (2C), 133.7, 127.2 (2C), 123.8 (2C), 122.7 (2C), 119.2 (2C), 35.7, 31.6, 21.0; MS (ESI) *m/z* 422 $(M+H)^+$; HRMS (ESI) *m/z* calc. for $C_{21}H_{20}N_5O_5$ 422.1464, found: 422.1480.

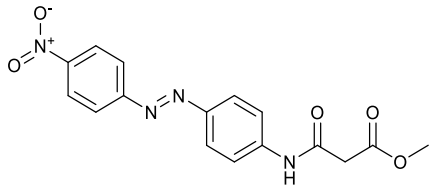
(*E*)-*N*1-(4-((4-(2,5-Dioxo-2,5-dihydro-1*H*-pyrrol-1-yl)phenyl)diazenyl)phenyl)-*N*7-hydroxyheptanediamide (72c)



Following general procedure E, deprotection of THP-hydroxamate **84c** (0.26 g, 0.49 mmol) was carried out at 50 °C overnight. Concentration under reduced pressure, followed by sequential trituration with EtOAc and water, afforded **72c** as an amorphous brown solid (0.21 g, 96%). IR (neat) 3300 – 2900 (br.), 1707, 1594, 1499, 1375; ^{1}H NMR (400 MHz, *d*$_6$-DMSO) δ 10.35 (s, 1H, NH), 10.28 (s, 1H, NH), 7.96 (d, *J* = 8.9 Hz, 2H, 2 × Ar-CH), 7.90 (d, *J* = 8.9 Hz, 2H, 2 × Ar-CH), 7.83 (d, *J* = 8.9 Hz, 2H, 2 × Ar-CH), 7.57 (d, *J* = 8.9 Hz, 2H, 2 × Ar-CH), 7.24 (s, 2H, C(6)H & C(7)H), 2.36 (t, *J* = 7.2 Hz, 2H,

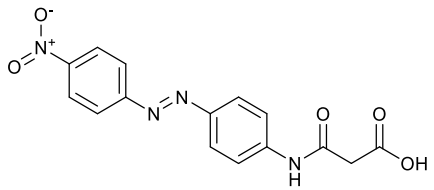
C(1)H_2 or C(5)H_2), 1.96 (t, *J* = 7.2 Hz, 2H, C(1)H_2 or C(5)H_2), 1.60 (quin, *J* = 7.2 Hz, 2H, C(2)H_2 or C(4)H_2), 1.53 (quin, *J* = 7.2 Hz, 2H, C(2)H_2 or C(4)H_2), 1.29 (quin, *J* = 7.2 Hz, 2H, C(3)H_2); ^{13}C NMR (100 MHz, d_6-DMSO) δ 171.8, 169.7 (2C), 169.0, 150.7, 147.3, 142.7, 134.9 (2C), 133.7, 127.2 (2C), 123.8 (2C), 122.7 (2C), 119.2 (2C), 36.4, 32.1, 28.2, 24.9, 24.7; MS (ESI) *m/z* 513 $(M+MeCN+Na)^+$; HRMS (ESI) *m/z* calc. for $C_{25}H_{26}N_6O_5Na$ 513.1862, found: 513.1849.

(*E*)-Methyl 3-((4-((4-nitrophenyl)diazenyl)phenyl)amino)-3-oxopropanoate (85)



Following a modified literature procedure,[235] methyl malonyl chloride (4.4 mL, 40 mmol, 1.5 equiv.) was added slowly to (*E*)-4-((4-nitrophenyl)diazenyl)aniline (**81**) (6.56 g, 27.1 mmol, 1.0 equiv.) and $NaHCO_3$ (2.50 g, 29.8 mmol, 1.1 equiv.) in EtOAc (250 mL) at 0°C. After 15 min the reaction mixture was warmed to rt and left to stir for 3 h. Glycine (2.03 g, 27.1 mmol, 1 equiv.) and 2M aq. $NaHCO_3$ (100 mL) was added and the resulting mixture stirred for 1 h. The biphasic mixture was then separated and the aqueous layer was further extracted with EtOAc (2 × 100 mL). The combined organic layers were dried over $MgSO_4$, and concentrated under reduced pressure to afford the crude product. Purification by flash column chromatography (DCM : MeOH, 98 : 2) afforded **85** as an orange solid (6.68 g, 72%). R_f 0.35 (DCM : MeOH, 98 : 2); m.p. 161 – 163 °C (DCM); IR (neat) 3243 (br.), 1712, 1683, 1522, 1343; ^{1}H NMR (400 MHz, $CDCl_3$) δ 9.59 (s, 1H, NH), 8.38 (d, *J* = 9.1 Hz, 2H, 2 × Ar-CH), 8.01 (*app*-t, *J* = 9.1 Hz, 4H, 4 × Ar-CH), 7.79 (d, *J* = 9.1 Hz, 2H, 2 × Ar-CH), 3.85 (s, 3H, CH_3), 3.56 (s, 2H, CH_2); ^{13}C NMR (100 MHz, $CDCl_3$) δ 170.5, 162.9, 155.8, 149.0, 148.5, 141.2, 124.8 (4C), 123.3 (2C), 120.1 (2C), 52.9, 41.1; MS (ESI) *m/z* 343 $(M+H)^+$; HRMS (ESI) *m/z* calc. for $C_{16}H_{15}N_4O_5$ 343.1042, found: 343.1049.

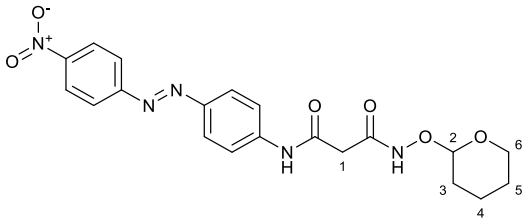
(*E*)-3-((4-((4-Nitrophenyl)diazenyl)phenyl)amino)-3-oxopropanoic acid (82a)



Following a modified literature procedure,[236] LiOH (1.84 g, 76.5 mmol, 5.0 equiv.) was added to a solution of **85** (5.23 g, 15. 3 mmol, 1.0 equiv.) in a 1 : 1 mixture of THF and water and the resulting

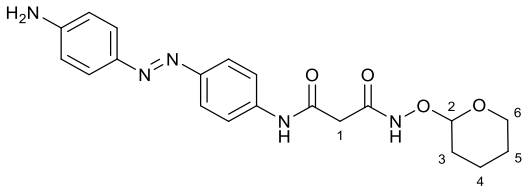
mixture was stirred at rt for 2 h. After neutralising with 3 M HCl, the precipitate was filtered off to afford **82a** as an amorphous red solid (2.87 g, 57%). IR (neat) 3600 – 2500 (br.), 1709, 1597, 1522, 1303; ^{1}H NMR (400 MHz, d_6-DMSO) δ 12.75 (br. s, 1H, NH or OH), 10.63 (s, 1H, NH or OH), 8.43 (d, *J* = 8.8 Hz, 2H, 2 × Ar-CH), 8.05 (d, *J* = 8.8 Hz, 2H, 2 × Ar-CH), 7.98 (d, *J* = 8.8 Hz, 2H, 2 × Ar-CH), 7.86 (d, *J* = 8.8 Hz, 2H, 2 × Ar-CH), 3.43 (s, 2H, CH_2); ^{13}C NMR (100 MHz, d_6-DMSO) δ 169.1, 165.3, 155.3, 148.2, 147.7, 143.2, 125.1 (2C), 124.6 (2C), 123.3 (2C), 119.3 (2C), 44.2; MS (ESI) *m/z* 329 $(M+H)^+$; HRMS (ESI) *m/z* calc. for $C_{15}H_{13}N_4O_5$ 329.0886, found: 329.0887.

(*E*)-*N*1-(4-((4-Nitrophenyl)diazenyl)phenyl)-*N*3-((tetrahydro-2*H*-pyran-2-yl)oxy)malonamide (83a)



Following general procedure G but without the presence of base, **82a** (3.37 g, 10.3 mmol) was coupled with NH_2OTHP (1.44 g, 12.3 mmol). The red solution was quenched with water (50 mL) and extracted with EtOAc (3 × 50 mL). The combined organic layers were washed with 5% aq. LiCl (2 × 50 mL), dried over $MgSO_4$, and concentrated under reduced pressure to afford the crude product. Purification by flash column chromatography (pentane : EtOAc, 2 : 1) afforded **83a** as a red solid (1.50 g, 34%). R_f 0.55 (pentane : EtOAc, 2 : 1); m.p. 226 – 228 °C (EtOAc); IR (neat) 3111 (br.), 1703, 1654, 1516, 1491, 1338, 1307; ^{1}H NMR (400 MHz, d_6-DMSO) δ 11.25 (s, 1H, NH), 10.59 (s, 1H, NH), 8.42 (d, *J* = 8.8 Hz, 2H, 2 × Ar-CH), 8.04 (d, *J* = 8.8 Hz, 2H, 2 × Ar-CH), 7.98 (d, *J* = 8.8 Hz, 2H, 2 × Ar-CH), 7.85 (d, *J* = 8.8 Hz, 2H, 2 × Ar-CH), 4.87 – 4.85 (m, 1H, C(2)H), 3.95 – 3.89 (m, 1H, C(6)H_a), 3.55 – 3.51 (m, 1H, C(6)H_b), 3.25 (s, 2H, C(1)H_2), 1.69 – 1.50 (m, 6H, C(3)H_2, C(4)H_2 & C(5)H_2); ^{13}C NMR (125 MHz, d_6-DMSO) δ 165.8, 163.4, 155.5, 148.3, 147.8, 143.2, 125.2 (2C), 124.7 (2C), 123.4 (2C), 119.5 (2C), 101.2, 61.5, 42.3, 27.8, 24.8, 18.3; MS (ESI) *m/z* 428 $(M+H)^+$; HRMS (ESI) *m/z* calc. for $C_{20}H_{22}N_5O_6$ 428.1570, found: 428.1573.

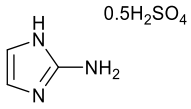
(*E*)-*N*1-(4-((4-Aminophenyl)diazenyl)phenyl)-*N*3-((tetrahydro-2*H*-pyran-2-yl)oxy)malonamide (78a)



Following general procedure H, reduction of *p*-nitroazobenzene **83a** (0.70 g, 1.64 mmol) was carried out for 1 h, affording **78a** as an amorphous orange solid (0.52 g, 80%). ^{1}H NMR (400 MHz, $CDCl_3$) δ 11.23 (s, 1H, NH), 10.35 (s, 1H, NH), 7.75 – 7.72 (m, 4H, 4 × Ar-CH), 7.63 (d, *J* = 8.8 Hz, 2H, 2 × Ar-CH), 6.65 (d, *J* = 8.8 Hz, 2H, 2 × Ar-CH), 6.04 (br. s, 2H, NH_2), 4.87 – 4.85 (m, 1H, C(2)H), 3.96 – 3.90 (m, 1H, C(6)H_a), 3.55 – 3.52 (m, 1H, C(6)H_b), 3.21 (s, 2H, C(1)H_2), 1.69 – 1.50 (m, 6H, C(3)H_2, C(4)H_2 & C(5)H_2); ^{13}C NMR (125 MHz, *d*$_6$-DMSO) δ 165.2, 163.4, 152.5, 148.2, 142.8, 140.1, 124.9 (2C), 122.5 (2C), 119.3 (2C), 113.4 (2C), 101.0, 61.3, 42.1, 27.7, 24.7, 18.2; MS (ESI) *m/z* 398 $(M+H)^+$; HRMS (ESI) *m/z* calc. for $C_{20}H_{24}N_5O_4$ 398.1828, found: 398.1821.

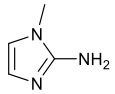
5.2.7 Azobisimidazole: A photoswitchable base

1*H*-Imidazol-2-amine[253] (97)



A solution of *o*-methylisourea hemisulfate (**95**) (2.83 g, 19.3 mmol, 1.0 equiv.) and 2-aminoacetaldehyde dimethyl acetal (**96**) (2.53 mL, 23.2 mmol, 1.2 equiv.) in water (15 mL) was stirred at 50 °C overnight, then cooled to rt. 5 M H_2SO_4 was added dropwise until a pH of 2.5 was reached, and the reaction mixture was stirred at 100 °C for 6 h, resulting in a yellow solution. Once cooled to rt, this was transferred by cannula into ice-cold EtOH (30 mL), forming a white precipitate. The suspension was stirred at 0 °C for 20 min, filtered, and dried under vacuum to afford **97** as a white solid (1.08 g, 42%). ^{1}H NMR (400 MHz, D_2O) δ 6.66 (s, 2H, 2 × CH); ^{13}C NMR (100 MHz, D_2O) δ 146.6, 112.8 (2C); MS (CI) *m/z* 84 $(M+H)^+$; HRMS (CI) *m/z* calc. for $C_3H_6N_3$ 84.0562, found: 84.0552.

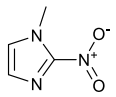
1-Methyl-1*H*-imidazol-2-amine[275] (93)



Following a modified literature procedure,[253] a solution of *o*-methylisourea hemisulfate (**95**) (15.30 g, 43.0 mmol, 1.0 equiv.) and (methylamino)acetaldehyde dimethyl acetal (**98**) (6.7 mL, 52 mmol, 1.2 equiv.) in water (50 mL) was stirred at 60 °C overnight, then cooled to rt. 5 M H_2SO_4 was added dropwise until a pH of 2.5 was reached, and the reaction mixture was stirred at 100 °C for 8 h while maintaining pH 2.5, resulting in a yellow solution. Concentration under reduced pressure and purification by flash column chromatography (0.03 M NH_3 in DCM : MeOH, 9 : 1) afforded **93** as a white solid (0.47 g, 11%). ^{1}H NMR (400 MHz, CD_3OD) δ 6.41 (d, *J* = 2.7 Hz, 1H, CH),

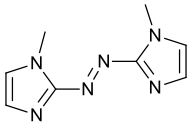
6.37 (d, *J* = 2.7 Hz, 1H, CH), 3.23 (s, 3H, CH_3); ^{13}C NMR (100 MHz, CD_3OD) δ 155.8, 114.6, 109.2, 30.2; MS (EI) *m/z* 97 $(M)^+$; HRMS (EI) *m/z* calc. for $C_4H_7N_3$ 97.0640, found: 97.0651.

1-Methyl-2-nitro-1*H*-imidazole[276] (94)



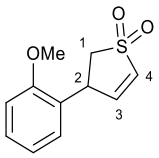
Methyl iodide (1.5 mL, 23.6 mmol, 1.2 equiv.) was added dropwise to a suspension of 2-nitroimidazole (**99**) (2.23 g, 19.7 mmol, 1.0 equiv.) and K_2CO_3 (4.08 g, 29.6 mmol, 1.5 equiv.) in MeCN (30 mL) at 0 °C and the reaction mixture was stirred at 65 °C for 3 h. The reaction was quenched with water (30 mL) and concentrated under reduced pressure. The resulting residue was diluted with water (20 mL) and extracted with EtOAc (4 × 50 mL), and the combined organic layers were dried over $MgSO_4$ and concentrated under reduced pressure to afford **94** as an off-white solid (1.64 g, 65%). ^{1}H NMR (400 MHz, $CDCl_3$) δ 7.15 (d, *J* = 1.0 Hz, 1H, CH), 7.07 (d, *J* = 1.0 Hz, 1H, CH), 4.09 (s, 3H, CH_3); ^{13}C NMR (100 MHz, $CDCl_3$) δ 145.1, 128.2, 126.9, 37.5; MS (CI) *m/z* 145 $(M+NH_4)^+$; HRMS (CI) *m/z* calc. for $C_4H_9N_4O_2$ 145.0726 found: 145.0731.

(*E*)-1,2-Bis(1-methyl-1*H*-imidazol-2-yl)diazene (91)



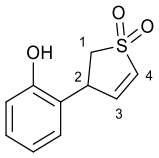
Following a modified literature procedure,[256] nitroimidazole **94** (0.74 g, 5.82 mmol, 1.0 equiv.) and Zn dust (0.76g, 11.6, 2.0 equiv.) were added to a solution of 0.1 M aq. NH_4Cl (70 mL) at 45 °C, resulting in the immediate formation of an orange solution, which was left to stir at 45 °C for 1 h. The solid was filtered off and the filtrate was extracted with $CHCl_3$ (2 × 50 mL). The combined organic layers were dried over $MgSO_4$ and concentrated under reduced pressure. Purification by flash column chromatography (DCM : MeOH, 95 : 5) afforded **91** as an orange solid (0.27 g, 49%). R_f 0.16 (DCM : MeOH, 95 : 5); m.p. 224 – 225 °C (DCM-pentane); IR (neat) 1679, 1473, 1388, 1287, 1166; ^{1}H NMR (400 MHz, $CDCl_3$) δ 7.32 (d, *J* = 1.0 Hz, 2H, 2 × CH), 7.20 (d, *J* = 1.0 Hz, 2H, 2 × CH), 4.09 (s, 6H, 2 × CH_3); ^{13}C NMR (100 MHz, $CDCl_3$) δ 153.5 (2C), 131.0 (2C), 124.6 (2C), 32.9 (2C); MS (ESI) *m/z* 191 $(M+H)^+$; HRMS (ESI) *m/z* calc. for $C_8H_{11}N_6$ 191.1045, found: 191.1037.

3-(2-Methoxyphenyl)-2,3-dihydrothiophene 1,1-dioxide[265] (103)



A solution of $NaNO_2$ (0.67 g, 9.73 mmol, 1.1 equiv.) in water (5 mL) at 0 °C was added to a solution of *o*-anisidine (**102**) (1.0 mL, 8.85 mmol, 1.0 equiv.) in 48% HBF_4 (5 mL) and the resulting solution was stirred for 1 h at 0 °C. A solution of butadiene sulfone (1.46 g, 12.4 mmol, 1.4 equiv.) in MeOH (5 mL), followed by $Pd(OAc)_2$ (99 mg, 0.44 mmol, 0.05 equiv.), was added to the reaction mixture and heated under reflux for 1 h. The reaction was quenched with water (15 mL), and extracted with DCM (3 × 15 mL). The combined organic layers were dried over $MgSO_4$, and concentrated under reduced pressure to give the crude product as a white solid. Purification by flash column chromatography (pentane : EtOAc, 3 : 1) gave **103** as a white solid (1.51 g, 76%). R_f 0.6 (pentane : EtOAc, 3 : 1); ^{1}H NMR (400 MHz, $CDCl_3$) δ 7.31 (dt, *J* = 7.9, 1.7 Hz, 1H, phenyl-CH), 7.12 (dd, *J* = 7.6, 1.7 Hz, 1H, phenyl-CH), 6.96 (dt, *J* = 7.6, 1.0 Hz, 1H, phenyl-CH), 6.91 (d, *J* = 8.3 Hz, 1H, phenyl-CH), 6.81 – 6.71 (m, 2H, C(3)H & C(4)H), 4.77 – 4.67 (m, 1H, C(2)H), 3.86 (s, 3H, CH_3), 3.70 (dd, *J* = 13.7, 8.3 Hz, 1H, C(1)H_a), 3.15 (dd, *J* = 13.7, 5.4 Hz, 1H, C(1)H_b); ^{13}C NMR (100 MHz, $CDCl_3$) δ 156.7, 142.2, 131.6, 129.4, 127.7, 127.0, 121.1, 110.8, 55.4, 54.8, 39.0; MS (CI) *m/z* 242 $(M+NH_4)^+$; HRMS (CI) *m/z* calc. for $C_{11}H_{16}NO_3S$ 242.0851, found: 242.0845.

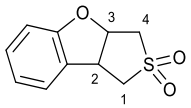
3-(2-Hydroxyphenyl)-2,3-dihydrothiophene 1,1-dioxide[265] (100)



A solution of **103** (0.31 g, 1.38 mmol) in 47% aq. HBr (5 mL) was heated under reflux for 3 h. The reaction mixture was then cooled to 0 °C and quenched with dilute aq. $NaHCO_3$. This was then extracted with DCM (3 × 10 mL), dried over $MgSO_4$, and concentrated under reduced pressure to give the crude product. Purification by flash column chromatography (pentane : EtOAc, 3 : 1) gave **100** as a white solid (0.19 g, 65%). R_f 0.4 (pentane : EtOAc, 3 : 1); ^{1}H NMR (400 MHz, $CDCl_3$) δ 7.20 (dt, *J* = 7.6, 1.7 Hz, 1H, phenyl-CH), 7.12 (dd, *J* = 7.6, 1.7 Hz, 1H, phenyl-CH), 6.95 (dt, *J* = 7.7, 1.0 Hz, 1H, phenyl-CH), 6.82 – 6.80 (m, 2H, phenyl-CH & C(3)H or C(4)H), 6.77 (dd, *J* = 6.8, 2.4 Hz, 1H, C(3)H or C(4)H), 5.45 (br. s, 1H, OH), 4.72 (tdd, *J* = 8.4, 5.6, 2.6 Hz, 1H, C(2)H), 3.74 (dd, *J* = 13.7, 8.8 Hz, 1H, C(1)H_a), 3.24 (dd, *J* = 13.7, 5.4 Hz, 1H, C(1)H_b); ^{13}C NMR (100 MHz, $CDCl_3$) δ 153.1, 142.2, 131.6,

129.4, 128.2, 125.3, 121.6, 115.6, 54.6, 39,1; MS (CI) *m/z* 228 $(M+NH_4)^+$; HRMS (CI) *m/z* calc. for $C_{10}H_{14}NO_3S$ 228.0694, found: 228.0685.

1,3,3a,8b-Tetrahydrothieno[3,4-b]benzofuran 2,2-dioxide[265] **(101)**



Bisazoimidazole **91** (1.0 equiv.) was added to a solution of **100** (1.0 equiv.) in a 1 : 1 mixture of d_8-THF and D_2O (0.015 M) under the conditions specified in section 4.2.6. Aliquots were removed for analysis by ^1H NMR at regular intervals and returned to the reaction mixture. On completion of the reaction, the mixture was quenched with 3 M HCl and extracted with 3 × EtOAc, dried over $MgSO_4$, and concentrated under reduced pressure to give the crude product as a white solid. Yields of isolated product were not calculated due to known loss of material during repeated transfer of sample from the reaction vial to the NMR tubes. ^1H NMR (400 MHz, $CDCl_3$) δ 7.25 – 7.19 (m, 2H, 2 × phenyl-CH), 6.96 (dt, *J* = 7.3, 1.0 Hz, 1H, phenyl-CH), 6.85 (d, *J* = 8.3 Hz, 1H, phenyl-CH), 5.52 – 5.47 (m, 1H, C(3)H), 4.30 (*app*-q, *J* = 8.5 Hz, 1H, C(2)H), 3.63 – 3.54 (m, 2H, C(1)H_a and C(4)H_a), 3.44 (dd, *J* = 14.2, 3.9 Hz, 1H, C(4)H_b), 3.16 (dd, *J* = 13.7, 7.3 Hz, 1H, C(1)H_b); ^{13}C NMR (100 MHz, $CDCl_3$) δ 158.8, 129.9, 126.8, 124.8, 121.9, 110.4, 80.2, 54.8, 54.7, 42.0; MS (CI) *m/z* 211 $(M+H)^+$; HRMS (CI) *m/z* calc. for $C_{10}H_{11}O_3S$ 211.0429, found: 211.0424.

5.3 Photochemistry

5.3.1 General methods

All samples were prepared and stored in the dark, as far as practicable. UV/vis spectra were measured at ~10^{-5} M concentration unless specified otherwise. Compounds with thermal half-lives of <1 day at rt were left in the dark for 5 half-lives to ensure that pure *E*-isomer was present – the *E*-isomer spectra were deemed to be >99% *E.* For compounds with half-lives of >1 day at rt, the ^{1}H NMRs of the freshly synthesised compounds were found to have <2% *Z*-isomer (with the exception of **23** which contained 6% *Z*-isomer). Therefore the *E*-isomer spectra were deemed to be >98% *E*. (94% *E* for **23** – the pure *E*-isomer spectrum was obtained using equation 2 below).

Irradiation at 532 nm or 355 nm was performed using the 2nd or 3rd harmonic of a Nd:YAG (Continuum Surelite I) laser. Irradiation at 408 nm was performed using a 408 nm laser diode at 3.5 mW. Irradiation at 405 nm was performed using a 405 nm laser diode at approx. 20 mW. Other laser wavelengths were generated using a Lambda Physik tuneable dye laser, pumped by the suitable Nd:YAG harmonic. UV spectra were recorded on a Agilent 8453 photodiode array spectrophotometer, with samples held in a 4 window 1 cm × 1 cm quartz Suprasil cuvette (unless specified otherwise), thermostatted with a Peltier temperature controller. The sample was irradiated in the UV/vis spectrometer sample chamber with the light entering at ~90° to the spectrometer probe light. Irradiation was continued during acquisition of the UV/vis spectrum when determining photostationary states (PSSs) and photochemical timecourses.

Broadband lamp photoswitching was also carried out with a Luzchem 4V photoreactor fitted with broadband UVA, UVB or visible (λ_{max} ~ 420 nm) fluorescent lamps.

Quantitative (or near-quantitative) photoswitching to the *Z*-isomer was identified by an area of near-zero absorbance at a wavelength where the *E*-isomer absorbed. For all compounds, the most *Z*-rich PSS was quantified by either NMR or estimated by UV/vis spectroscopy (as described in section 2.2.3), depending on the thermal isomerisation rate of the compound. The pure *Z*-isomer spectra were extracted / estimated using the *E*-isomer spectrum and the quantified PSS. All other PSS ratios were assigned by interpolating between the *E*- and *Z*-isomer spectra using the following equation:

$$f_{PSS} = \frac{A_{PSS} - A_Z}{A_E - A_Z} \qquad (10)$$

Where f_{PSS} is the fraction of *E*-isomer present in the PSS; and A_{PSS}, A_E, and A_Z are the absorbances at the π-π* *E*-isomer absorption maximum.

5.3.2 Quantification of PSS composition by NMR spectroscopy

A concentrated solution (10^{-3} to 10^{-2} M) of the photoswitch in deuterated solvent was irradiated with the required wavelength of light and the ratio of isomers present was determined by ^{1}H NMR (see Appendix 7.3). At this concentration, the sample was above the maximum absorbance limit of the UV/vis spectrometer, so to determine that the PSS had been reached, the sample was diluted to ~10^{-5} M and irradiated again to ensure no further change to the spectrum occurred. The error on the % *E*-isomer present as determined by NMR was given as 2% due to the limit of detection of NMR.

By subtracting the spectrum of the authentic *E*-isomer from this PSS spectrum using equation 2, a spectrum for the pure *Z*-isomer was obtained with an estimated 3% uncertainty in the absorbance due to the uncertainty in the NMR measurement.

$$A_Z = \frac{A_{PSS} - A_E \times f}{1 - f} \qquad (2)$$

Where f = fraction of *E*-isomer present in the PSS, and A = absorbance in the PSS, *E*, or *Z* spectrum.

This method was used for **21**, **23**, **24**, **31**-**34**, **37**, **38,** and all HDAC inhibitors. The UVA PSS composition of **23** and **24** was also obtained using this method.

For the azobenzene HDAC inhibitors (**57a**-**c**) the PSS was not reached after 30 min of irradiation of the concentrated sample. The ratio of isomers present in the irradiated sample was quantified by NMR. The diluted UV/vis spectrum of this sample was then used to obtain the pure *Z*-isomer spectrum and from this the ratio of isomers present in the PSS was determined (see Appendix 7.3.2).

5.3.3 Estimation of PSS composition by UV/vis spectroscopy

This method was used for compounds whose thermal isomerisation was too fast to allow analysis by NMR. The spectrum of the *Z*-isomer was estimated based on the PSS with the highest concentration of *Z*-isomer. Initially, the fraction of *E*-isomer present in this PSS was estimated from the absorbance at the *E*-isomer absorption maximum. Using this estimate, the spectrum of the authentic *E*-isomer was subtracted from that of the PSS, using equation 2. This estimate for the residual *E*-isomer fraction was then varied until a range was obtained that predicted a sensible UV/vis spectrum for the pure *Z*-isomer (see Appendix 7.3). The maximum fraction of *E*-isomer in the PSS was taken as the highest value that ensured that the absorbance remained positive at all wavelengths. The minimum fraction of *E*-isomer in the PSS was taken as the lowest value that

ensured that no obvious π- π* absorbance from the *E*-isomer remained in the spectrum. The centre point of this range was taken as the pure *Z*-isomer spectrum and from this the % *Z*-isomer in the PSS was assigned with a 3% uncertainty in absorbance (see Appendix 7.3). The other PSS ratios were assigned by interpolating between these values using equation 10 with an estimated absolute uncertainty of about 5%.

This method was used for **22**, **35**, **36**, and **91**.

5.3.4 Photoisomerisation quantum yields

In order to obtain quantum yields (for **21**-**24**), the timecourse of photoisomerisation was followed by UV/vis spectroscopy (see Appendix 7.3), at a known laser power and known sample concentrations; extinction coefficients were obtained from the absorbances measured at 10^{-5} M where possible. When absorbances were low at the irradiation wavelength, the extinction coefficient was obtained from the absorbance at higher concentration. The extinction coefficient for **23** at 532 nm was too small to be determined accurately, so quantum yields were not calculated at this wavelength. Instead 415 nm light was used to obtain a *Z*-*E* quantum yield.

For compound **22** (which had a fast thermal isomerisation rate), when switching to pure *E*-isomer at 532 nm, the thermal rate constant (0.0326 ± 0.0007) s^{-1} was subtracted from the observed rate constant (0.120 ± 0.004) s^{-1} during the photochemistry to give a pure photochemical rate constant (0.088 ± 0.004) s^{-1} that was used in the quantum yield calculation. At other wavelengths, the switching of **22** was incomplete, and no useful quantum yield could be obtained due to the competing thermal isomerisation.

5.3.5 Thermal isomerisation kinetics

Kinetics were followed by either UV/vis or ^{1}H NMR spectroscopy. For compounds with half-lives of <15 days, kinetics were measured at 25 °C (excepting for the HDAC inhibitors which were measured at 30 °C). For compounds with very long half-lives (>15 days), kinetics were measured by NMR at a range of higher temperatures, from which the kinetics at 25 °C were extrapolated. The kinetics of the azoheteroarenes (Chapter 2) were measured in MeCN, the kinetics of the HDAC inhibitors (Chapter 3) were measured in DMSO and/or phosphate buffer (pH 7.2), and the kinetics of azobisimidazole **91** (Chapter 4) were measured in water or MeCN.

5.3.6 pK_a titration

A 1×10^{-2} M stock solution of **91** in MeOH was prepared and diluted 1000-fold into 10 mM phosphate-citrate buffer (~pH 3) to 100 mL volume. This solution was kept in the dark and the pH was measured using a pH meter. The UV/vis spectrum of a 4 mL aliquot was recorded for both the *E*-isomer and the PSS, following 15 seconds irradiation with 415 nm light. This aliquot was then returned to the main sample and given time to thermally isomerise back to the *E*-isomer. Aqueous NaOH was then added to increase the pH and the process was repeated.

5.3.7 pH jump

Initially a pH titration of the pH indicator (BCP) was carried out in the buffer to check the pK_a value obtained. For the pH jump experiments a stock solution of BCP sodium salt (1.1×10^{-3} M) and **91** (1.1×10^{-3} M) in MeOH was prepared. The pH titration was carried out in buffer (40-fold dilution to 2.7×10^{-5} M) on both the *E*-isomer and the PSS (using the 405 nm laser diode). The absorbance at 590 nm was the same for the *E* isomer and the PSS at all pHs, indicating that the indicator was not affected by irradiation. A graph was plotted of the ratio of absorbance at 440 nm (π-π* *E*-**91**) and absorbance at 590 nm (BCP) versus pH and the exponential fit was obtained for both *E*-**91** and the PSS (Figure 4.13). The pH jump experiment was carried out using the same stock solution, but diluted into water (4-fold dilution to 2.7×10^{-4} M) in a 1 mm path length cuvette and pH values for the *E* isomer and the PSS were extracted using the exponential equation obtained from the graph.

5.4 Computational

5.4.1 Arylazopyrazoles and pyrroles

The computational work detailed below was carried out with the aid of Dr Robert Richardson.

Geometry optimisation and TDDFT calculations

DFT calculations were performed in Gaussian09 (revision C01).[277] Geometry optimisations and frequency calculations (unscaled) were performed at the B3LYP/6−31G(d,p) level[278,279] using a PCM continuum solvent model[280] for acetonitrile, as shown to give good results by Jones and co-workers.[46] TDDFT calculations were performed at the CAM-B3LYP/6−311G(2df,2p) level,[281] using the same solvent model. TDDFT calculated excitation energies are unscaled.

SCF energies, enthalpies and free energies are calculated relative to the lowest energy conformer of the *E*-isomer of the compound (Appendix 7.4). Only two conformers were located for each compound. K_{eq} is determined as the equilibrium constant between both calculated conformers. The enthalpy, free energy and K_{eq} are given at 25 °C.

Calculated UV/vis spectra

After TDDFT calculations of the excitation energies, the spectra were simulated using the Gaussview 5 program, with default peak widths and unscaled excitation energies. The Boltzmann factors of the energy minimised structures of each isomer were used to obtain the weighted average TDDFT spectrum. The spectra were scaled so that the maximum peak height was equal to that of the equivalent experimental spectrum for easy comparison.

Dihedral drives

Energy minimised structures were obtained at constrained NNHet dihedral angles (increased by 10° increments). TDDFT calculations were carried out on each energy minimised structure in order to obtain the n-π* oscillator strengths at each dihedral angle. Graphs of dihedral angle vs. relative energy, oscillator strength and population fraction were plotted (Figures 2.13 and 7.43). All computational dihedral angles were plotted as 180 – θ to give minima between 0 and 90°.

5.4.2 Further study of arylazoheteroarenes

The computational work detailed below was carried out by Joaquín Calbo (University of Valencia) and Dr Julia Contreras-García (Pierre and Marie Curie University).

Theoretical calculations were performed in Gaussian 09 (revision D01).[277] All the possible conformers both in the *Z*- and *E*-isomers were fully optimized using the hybrid exchange-correlation

PBE0 functional[140] with the Grimme dispersion correction in its latest version (D3).[141] The split-valence Pople's basis set 6-31G** was used throughout.[282] Transition states were optimised by using the Berny algorithm at the same level of theory.[283] Theoretical calculations were carried out in gas phase unless otherwise specified.

Atomic charges were calculated by performing a Natural Bond Orbital (NBO) analysis.[146,284–288] The Natural Population Analysis (NPA) charges were summed over the atoms in the heteroarene.

The non-covalent index (NCI) for the different compounds was computed using the NCIPLOT program.[144] The NCI visualisation index is based on the density and its derivatives, enabling the identification of non-covalent interactions. It is based on the peaks that appear in the reduced density (RDG) at low densities (ρ). The molecular electron density computed in the SCF procedure at the PBE0/6-31G** level was used. The density and RDG cutoffs were kept at their default values. The NCI volumes and charges where integrated according to the expressions

$$V_{\mathrm{NCI}} = \int_{\Omega_{\mathrm{NCI}}} \mathrm{d}\,\vec{r}$$

$$q_{\mathrm{NCI}} = \int_{\Omega_{\mathrm{NCI}}} \rho(\vec{r})\,\mathrm{d}\,\vec{r}$$

by numerical integration through summation over a cubic grid with 0.1 a.u. increments.

5.4.3 Azobisimidazole: A photoswitchable base

The computational work detailed below was carried out with the aid of Dr Robert Richardson.

Geometry optimisation and TDDFT calculations were carried out as detailed in section 5.4.1, but using the PCM method for water.

GIAO ^{13}C NMR Calculations

Geometry optimisations were repeated for the neutral and protonated species using the PCM method for methanol at the B3LYP/6−31G(d,p) level of theory.[278,279] The GIAO method was used for NMR chemical shift calculations,[260,289] at both the B3LYP/6-311G(2df,2p) and mPW1PW91/6-311G(2df,2p) levels to ensure that changing the functional didn't alter the results significantly. NMR shielding tensors (σ) were calculated for the lowest energy conformers and also for benzene as a reference. Chemical shifts were obtained using the calculated tensor and experimental chemical shifts for benzene.[261] The calculated chemical shifts were then scaled (eq. 9) using the calculated and experimental values for neutral *E*-**91**, by plotting a graph of δ_{calc} vs δ_{exp} and obtaining the slope and intercept of the linear fit.[257]

$$\delta_{scaled} = \frac{\delta_{calc} - intercept}{slope} \qquad (9)$$

5.5 Biochemistry

The work detailed below was carried out by Dr Michael Korbus and Andreas Krämer, led by Prof. Meyer-Almes at the University of Applied Sciences, Darmstadt, Germany.

5.5.1 General methods

Standard chemicals and solvents were purchased at the highest available level of purity from Sigma-Aldrich (USA), Merck (Germany), Roth (Germany), and Fisher Scientific (Germany). SAHA was purchased from Cayman Chemical (USA). Boc-Lys(Ac)-AMC and Boc-Lys(TFA)-AMC were obtained from Bachem (Germany). Trypsin from bovine pancreas was obtained from AppliChem (Germany). The HDAH enzyme used was *FB188*-HDAH-wt unless specified otherwise. AMC release was measured on a PheraStar Fluorescence Spectrometer (BMG Labtech). All experiments were carried out in triplicate (at least). In all assays, the activity of the enzyme without the presence of an inhibitor was also measured.

For the assays carried out on the non-tethered inhibitors, the stock solutions (10 mM in DMSO) were incubated at 60 °C for 30 min prior to use to ensure that only the *E*-isomer was present. After the inhibitors were dissolved in the desired assay buffer, the solution was split into two aliquots. One aliquot was kept in the dark, and the other was irradiated for at least 15 min at 365 nm to reach the *Z*-rich PSS. All further preparation and measurements were performed in the dark.

5.5.2 Continuous HDAC assay

This assay was carried out for all bacterial HDACs. The reaction buffer contained 20 mM HEPES pH 8, 50 mM NaCl, 0.001 Pluronic. The bacterial HDAC homologues Pa3774, Pa1409, Pa0321 and HDAH were purified as described elsewhere.[215,290] The IC_{50} values of the described inhibitors were determined using a standard fluorogenic enzyme activity assay.[291] The final protein concentrations were 50 nM for Pa3774, Pa1409 and Pa0321 and 100 nM for HDAH. For the assays with Pa3774, Pa1409 and Pa0321, the substrate used was Boc-Lys(TFA)-AMC at a final concentration of 20 µM and for the assays with HDAH, the substrate was Boc-Lys(Ac)-AMC at a concentration of 40 µM. Each enzyme was added to serial dilutions of the desired inhibitor and incubated for 30 min at 30°C. The reaction was started by adding the fluorogenic substrate along with trypsin (0.5 mg/mL final concentration). SAHA was also tested on the enzymes as a reference to the tested inhibitors.

The fluorescent signal was recorded at set intervals. The enzyme activity in terms of relative fluorescent units per second was determined from the slope of the linear initial phase of the kinetics and normalised with respect to percent of uninhibited enzyme activity. The normalised fluorescence

intensities were plotted versus the concentration of test compounds and fitted to a four-parameter logistic model[292] to calculate the IC_{50} values.

5.5.3 Endpoint HDAC assay

This assay was carried out for all human HDACs. The reaction buffer contained 25 mM Tris-HCl pH 8, 137 mM NaCl, 2.7 mM KCl and 1 mM $MgCl_2$. The human HDACs were all purchased from BPS Bioscience (USA) and used according to their instructions. The final concentration used in the assay was 1-2 nM. The substrate used was Boc-Lys(Ac)-AMC at a concentration of 30 µM. The preparation for the assay was as described for the continuous assay (section 5.5.2), with the exception that it was carried out in two steps. Since trypsin digests the HDAC enzymes, only Boc-Lys(Ac)-AMC was added to the mixture of HDAC and inhibitor and incubated for 1 h at 30 °C. Afterwards the assay was stopped by adding 20 µl of the stop solution, containing 2.5 mg/mL trypsin and 10 µM SAHA. SAHA was also tested on the enzymes as a reference to the inhibitors.

Once a plateau in fluorescence intensity had been reached, the intensity was averaged over at least 5 min and normalised with respect to percent of uninhibited enzyme activity. Results were plotted as detailed above (section 5.5.2).

5.5.4 Chemical modification of HDAH variants[220,221]

The covalent modification of cysteines by photoswitchable HDAC inhibitors **72b**-**c** was carried out in 40 mM sodium phosphate buffer pH 7.2, containing 150 mM NaCl and 1 mM EDTA (MC buffer) in the presence of 8% DMSO. 30 µM of each HDAH variant (M30C, S20C) were modified with a 4-fold molar excess of the inhibitor at 23 °C for 2 h. Unreacted maleimido groups were deactivated by a 110-fold molar excess of dithiothreitol at 23 °C for 30 min. Samples were centrifuged (15 min, 10 000 g, 23 °C) and the supernatant purified using a gel-filtration column (NAP-10 column; GE Healthcare, UK). Photoswitch-modified HDAH variants were confirmed by UV/vis measurements.

5.5.5 Measurement of Michaelis-Menten kinetics[220,221]

Photoswitch/HDAH variant conjugate (1 µM) was irradiated by UVA light for ~ 30 min. Additionally, a non-irradiated and unmodified sample of each HDAH variant was measured as a reference. Michaelis-Menten-parameters were determined by following the product formation under steady-state conditions by employing the continuous fluorogenic assay used previously (section 5.5.2). The enzyme activity in terms of relative fluorescent units per second was determined from the slope of the linear initial phase of the kinetics. The normalised fluorescence signal was plotted against the

substrate concentration [Boc-Lys(Ac)-AMC]. Michaelis-Menten-parameters (K_m and V_{max}) were obtained by fitting the resulting curves to the Michaelis-Menten equation.

6 REFERENCES

1 H. Follmann and C. Brownson, *Naturwissenschaften*, 2009, **96**, 1265–1292.

2 M. F. Hohmann-Marriott and R. E. Blankenship, *Annu. Rev. Plant Biol.*, 2011, **62**, 515–548.

3 D. Osorio and M. Vorobyev, *Vis. Res.*, 2008, **48**, 2042–2051.

4 C. L. Partch, C. B. Green and J. S. Takahashi, *Trends Cell Biol.*, 2014, **24**, 90–99.

5 M. Fernández-Suárez and A. Y. Ting, *Nat. Rev. Mol. Cell Biol.*, 2008, **9**, 929–943.

6 R. Y. Tsien, *Annu. Rev. Biochem.*, 1998, **67**, 509–44.

7 D. Chudakov, M. Matz, S. Lukyanov and K. Lukyanov, *Physiol. Rev.*, 2010, **90**, 1103–1163.

8 M. Zimmer, *Chem. Soc. Rev.*, 2009, **38**, 2823–2832.

9 G. Miesenböck, *Science*, 2009, **326**, 395–399.

10 K. Deisseroth, *Nat. Methods*, 2011, **8**, 26–29.

11 T. Fehrentz, M. Schönberger and D. Trauner, *Angew. Chem., Int. Ed.*, 2011, **50**, 12156–12182.

12 C. E. Wayne and R. P. Wayne, *Photochemistry*, Oxford University Press, 1996.

13 H. Bouas-Laurent and H. Dürr, *Photochromism: Molecules and Systems*, Elsevier, revised ed.

14 S. Thies, H. Sell, C. Bornholdt, C. Schütt, F. Köhler, F. Tuczek and R. Herges, *Chem. - A Eur. J.*, 2012, **18**, 16358–16368.

15 T. Hugel, N. B. Holland, A. Cattani, L. Moroder, M. Seitz and H. E. Gaub, *Science*, 2002, **296**, 1103–1106.

16 W. R. Browne and B. L. Feringa, *Nat. Nanotechnol.*, 2006, **1**, 25–35.

17 K. Matsuda and M. Irie, *Polyhedron*, 2005, **24**, 2477–2483.

18 M. Alemani, M. V. Peters, S. Hecht, K. H. Rieder, F. Moresco and L. Grill, *J. Am. Chem. Soc.*, 2006, **128**, 14446–14447.

19 W. A. Velema, W. Szymanski and B. L. Feringa, *J. Am. Chem. Soc.*, 2014, **136**, 2178–2191.

20 H. Bouas-Laurent and H. Dürr, *Pure Appl. Chem.*, 2001, **73**, 639–665.

21 C. Brieke, F. Rohrbach, A. Gottschalk, G. Mayer and A. Heckel, *Angew. Chem., Int. Ed.*, 2012, **51**, 8446–8476.

22 J. W. Verhoeven, *Pure Appl. Chem.*, 1996, **68**, 2223–2286.

23 A. M. Brouwer, *Pure Appl. Chem.*, 2011, **83**, 2213–2228.

24 E. Fischer, *J. Phys. Chem.*, 1967, **71**, 3704–3706.

25 H. M. D. Bandara and S. C. Burdette, *Chem. Soc. Rev.*, 2012, **41**, 1809–1825.

26 M. Irie, T. Fukaminato, K. Matsuda and S. Kobatake, *Chem. Rev.*, 2014, **114**, 12174–12277.

27 R. Klajn, *Chem. Soc. Rev.*, 2014, **43**, 148–184.

28 A. Santiago and R. S. Becker, *J. Am. Chem. Soc.*, 1968, **90**, 3654–3658.

29 S. Kawata and Y. Kawata, *Chem. Rev.*, 2000, **100**, 1777–1788.

30 J. Garcia-Amorós, M. Díaz-Lobo, S. Nonell and D. Velasco, *Angew. Chem., Int. Ed.*, 2012, **51**, 12820–12823.

31 A. A. Beharry and G. A. Woolley, *Chem. Soc. Rev.*, 2011, **40**, 4422–4437.

32 T. Nägele, R. Hoche, W. Zinth and J. Wachtveitl, *Chem. Phys. Lett.*, 1997, **272**, 489–495.

33 G. S. Hartley and R. J. W. Le Fèvre, *J. Chem. Soc.*, 1939, 531–535.

34 R. J. W. Le Fevre and J. Northcott, *J. Chem. Soc.*, 1953, 867–870.

35 E. R. Talaty and J. C. Fargo, *Chem. Commun.*, 1967, 65–66.

36 G. S. Hartley, *J. Chem. Soc.*, 1938, 633–642.

37 C. A. Winkler, J. Halpern and G. W. Brady, *Can. J. Res., Sect. B*, 1950, **28B**, 140–155.

38 Y. Dou, Y. Hu, S. Yuan, W. Wu and H. Tang, *Mol. Phys.*, 2009, **107**, 181–190.

39 C. R. Crecca and A. E. Roitberg, *J. Phys. Chem. A*, 2006, **110**, 8188–8203.

40 I. Conti, M. Garavelli and G. Orlandi, *J. Am. Chem. Soc.*, 2008, **130**, 5216–5230.

41 H. Rau and E. Lüddecke, *J. Am. Chem. Soc.*, 1982, **104**, 1616–1620.

42 T. Ikegami, N. Kurita, H. Sekino and Y. Ishikawa, *J. Phys. Chem. A*, 2003, **107**, 4555–4562.

43 A. Cembran, F. Bernardi, M. Garavelli, L. Gagliardi and G. Orlandi, *J. Am. Chem. Soc.*, 2004, **126**, 3234–3243.

44 J. Dokić, M. Gothe, J. Wirth, M. V Peters, J. Schwarz, S. Hecht and P. Saalfrank, *J. Phys. Chem. A*, 2009, **113**, 6763–6773.

45 A. A. Blevins and G. J. Blanchard, *J. Phys. Chem. B*, 2004, **108**, 4962–4968.

46 N. Wazzan, P. R. Richardson and A. C. Jones, *Photochem. Photobiol. Sci.*, 2010, **9**, 968–974.

47 V. Smrecki, G. Baranovic, G. Keresztury and Z. Meic, *J. Mol. Struct.*, 1997, **408-409**, 405–408.

48 G. E. Lewis, *J. Org. Chem.*, 1960, **25**, 2193–2195.

49 T. Stoyanova, S. Stoyanov, L. Antonov and V. Petrova, *Dyes Pigm.*, 1996, **31**, 1–12.

50 S. Stoyanov, L. Antonov, T. Stoyanova and V. Petrova, *Dyes Pigm.*, 1996, **32**, 171–185.

51 A. A. M. Prabhu, G. Venkatesh, R. K. Sankaranarayanan, S. Siva and N. Rajendiran, *Indian J. Chem., Sect. A Inorg., Bio-inorg., Phys., Theor. Anal. Chem.*, 2010, **49**, 407–417.

52 N. K. Joshi, M. Fuyuki and A. Wada, *J. Phys. Chem. B*, 2014, **118**, 1891–1899.

53 T. Asano and T. Okada, *J. Org. Chem.*, 1984, **49**, 4387–4391.

54 A. A. Beharry, O. Sadovski and G. A. Woolley, *J. Am. Chem. Soc.*, 2011, **133**, 19684–19687.

55 S. Samanta, A. A. Beharry, O. Sadovski, T. M. McCormick, A. Babalhavaeji, V. Tropepe and G. A. Woolley, *J. Am. Chem. Soc.*, 2013, **135**, 9777–9784.

56 S. Samanta, T. M. McCormick, S. K. Schmidt, D. S. Seferos and G. A. Woolley, *Chem. Commun.*, 2013, **49**, 10314–10316.

57 M. Dong, A. Babalhavaeji, S. Samanta, A. A. Beharry and G. A. Woolley, *Acc. Chem. Res.*, 2015, **48**, 2662–2670.

58 S. Samanta, A. Babalhavaeji, M.-X. Dong and G. A. Woolley, *Angew. Chem., Int. Ed.*, 2013, **52**, 14127–14130.

59 M. Dong, A. Babalhavaeji, M. J. Hansen, L. Kalman and G. A. Woolley, *Chem. Commun.*, 2015, **51**, 12981–12984.

60 D. Bléger, J. Schwarz, A. M. Brouwer and S. Hecht, *J. Am. Chem. Soc.*, 2012, **134**, 20597–20600.

61 R. Siewertsen, H. Neumann, B. Buchheim-Stehn, R. Herges, C. Näther, F. Renth and F. Temps, *J. Am. Chem. Soc.*, 2009, **131**, 15594–15595.

62 J. Broichhagen, J. A. Frank and D. Trauner, *Acc. Chem. Res.*, 2015, **48**, 1947–1960.

63 M. Stein, S. J. Middendorp, V. Carta, E. Pejo, D. E. Raines, S. A. Forman, E. Sigel and D. Trauner, *Angew. Chem., Int. Ed.*, 2012, **51**, 10500–10504.

64 W. A. Velema, J. P. van der Berg, M. J. Hansen, W. Szymanski, A. J. M. Driessen and B. L. Feringa, *Nat. Chem.*, 2013, **5**, 924–928.

65 A. D. Abell, M. A. Jones, A. T. Neffe, S. G. Aitken, T. P. Cain, R. J. Payne, S. B. McNabb, J. M. Coxon, B. G. Stuart, D. Pearson, H. Y.-Y. Lee and J. D. Morton, *J. Med. Chem.*, 2007, **50**, 2916–2920.

66 W. Szymański, J. M. Beierle, H. A. V Kistemaker, W. A. Velema and B. L. Feringa, *Chem. Rev.*, 2013, **113**, 6114–6178.

67 G. A. Woolley, *Acc. Chem. Res.*, 2005, **38**, 486–493.

68 S.-L. Dong, M. Löweneck, T. E. Schrader, W. J. Schreier, W. Zinth, L. Moroder and C. Renner, *Chem. - A Eur. J.*, 2006, **12**, 1114–1120.

69 C. J. Bruns and J. F. Stoddart, *Acc. Chem. Res.*, 2014, **47**, 2186–2199.

70 S. Tsuda, Y. Aso and T. Kaneda, *Chem. Commun.*, 2006, 3072–3074.

71 T. Ikeda and O. Tsutsumi, *Science*, 1995, **268**, 1873–1875.

72 A. Sobolewska, S. Bartkiewicz, J. Mysliwiec and K. D. Singer, *J. Mater. Chem. C*, 2014, **2**, 1409–1412.

73 A. Shishido, *Polym. J.*, 2010, **42**, 525–533.

74 S. Hvilsted, C. Sánchez and R. Alcalá, *J. Mater. Chem.*, 2009, **19**, 6641–6648.

75 A. S. Matharu, S. Jeeva and P. S. Ramanujam, *Chem. Soc. Rev.*, 2007, **36**, 1868–1880.

76 M. Eich, J. H. Wendorff, B. Reck and H. Ringsdorf, *Macromol. Rapid Commun.*, 1987, **8**, 59–63.

77 M. Eich and J. H. Wendorff, *Macromol. Rapid Commun.*, 1987, **63**, 59–63.

78 E. Lorincz, P. Koppa, G. Erdei, A. Süto, F. Ujhelyi, P. Várhegyi, P. S. Ramanujam and P. I. Richter, *'Azobenzene Polyesters for Polarization Holographic Storage: Part II. Technology and System' Volume II of Handbook of Organic Electronics and Photonics*, American Scientific Publishers, 2007.

79 M. Samanta, V. S. R. Krishna and S. Bandyopadhyay, *Chem. Commun.*, 2014, **50**, 10577–10579.

80 M. V Peters, R. S. Stoll, A. Kühn and S. Hecht, *Angew. Chem., Int. Ed.*, 2008, **47**, 5968–5972.

81 M. Emond, T. Le Saux, S. Maurin, J.-B. Baudin, R. Plasson and L. Jullien, *Chem. - A Eur. J.*, 2010, **16**, 8822–8831.

82 M. Emond, J. Sun, J. Grégoire, S. Maurin, C. Tribet and L. Jullien, *Phys. Chem. Chem. Phys.*, 2011, **13**, 6493–6499.

83 R. S. Stoll and S. Hecht, *Org. Lett.*, 2009, **11**, 4790–4793.

84 R. S. Stoll, M. V Peters, A. Kuhn, S. Heiles, R. Goddard, M. Buhl, C. M. Thiele and S. Hecht, *J. Am. Chem. Soc.*, 2009, **131**, 357–367.

85 M. M. M. Raposo, A. M. F. P. Ferreira, M. Amaro, M. Belsley and J. C. V. P. Moura, *Dyes Pigm.*, 2009, **83**, 59–65.

86 P. J. Coelho, L. M. Carvalho, A. M. C. Fonseca and M. M. M. Raposo, *Tet. Lett.*, 2006, **47**, 3711–3714.

87 P. J. Coelho, L. M. Carvalho, J. C. V. P. Moura and M. M. M. Raposo, *Dyes Pigm.*, 2009, **82**, 130–133.

88 M. M. M. Raposo, M. C. R. Castro, A. M. C. Fonseca, P. Schellenberg and M. Belsley, *Tetrahedron*, 2011, **67**, 5189–5198.

89 M. M. M. Raposo, A. M. C. Fonseca, M. C. R. Castro, M. Belsley, M. F. S. Cardoso, L. M. Carvalho and P. J. Coelho, *Dyes Pigm.*, 2011, **91**, 62–73.

90 M. M. M. Raposo, M. C. R. Castro, M. Belsley and A. M. C. Fonseca, *Dyes Pigm.*, 2011, **91**, 454–465.

91 M. M. M. Raposo, A. M. R. C. Sousa, A. M. C. Fonseca and G. Kirsch, *Tetrahedron*, 2005, **61**, 8249–8256.

92 M. M. M. Raposo, A. M. F. P. Ferreira, M. Belsley and J. C. V. P. Moura, *Tetrahedron*, 2008, **64**, 5878–5884.

93 R. W. Boyd and G. L. Fischer, *Nonlinear Optical Materials*, 2nd edn., 2001.

94 J. Garcia-Amorós, M. C. R. Castro, P. Coelho, M. M. M. Raposo and D. Velasco, *Chem. Commun.*, 2013, **49**, 11427–11429.

95 J. Garcia-Amorós, A. Bučinskas, M. Reig, S. Nonell and D. Velasco, *J. Mater. Chem. C*, 2014, **2**, 474–480.

96 T. Wendler, C. Schütt, C. Näther and R. Herges, *J. Org. Chem.*, 2012, **77**, 3284–3287.

97 J. Otsuki, K. Suwa, K. Narutaki, C. Sinha, I. Yoshikawa and K. Araki, *J. Phys. Chem. A*, 2005, **109**, 8064–8069.

98 J. Otsuki, K. Suwa, K. K. Sarker and C. Sinha, *J. Phys. Chem. A*, 2007, **111**, 1403–1409.

99 B. A. Trofimov, E. Y. Schmidt, A. I. Mikhaleva, A. M. Vasil'tsov, A. B. Zaitsev, N. S. Smolyanina, E. Y. Senotrusova, A. V. Afonin, I. A. Ushakov, K. B. Petrushenko, O. N. Kazheva, O. A. Dyachenko, V. V. Smirnov, A. F. Schmidt, M. V. Markova and L. V. Morozova, *Eur. J. Org. Chem.*, 2006, **2006**, 4021–4033.

100 Y. Y. Rusakov, L. B. Krivdin, E. Y. Senotrusova, E. Y. Schmidt, A. M. Vasiltsov, A. I. Mikhaleva, B. A. Trofimov, O. A. Dyachenko, A. N. Chekhlov and O. N. Kazheva, 2007, 142–151.

101 J. Chen and Z. Yin, *Dyes Pigm.*, 2014, **102**, 94–99.

102 T. Eicher, H. Siegfried and A. Speicher, *The Chemistry of Heterocycles: Structure, Reactions, Syntheses, and Applications*, Wiley-VCH, Weinheim, Germany, 3rd edn., 2012.

103 H. V. Patel, K. A. Vyas, S. P. Pandey and P. S. Fernandes, *Synth. Commun.*, 1992, **22**, 3081–3087.

104 E. Merino, *Chem. Soc. Rev.*, 2011, **40**, 3835–3853.

105 G. Leriche, G. Budin, L. Brino and A. Wagner, *Eur. J. Org. Chem.*, 2010, 4360–4364.

106 US Pat., US2010197651 A1, 2010.

107 N. Campbell, A. W. Henderson and D. Taylor, *J. Chem. Soc.*, 1953, 1281–1285.

108 E. V Brown, *J. Heterocycl. Chem.*, 1969, **6**, 571–573.

109 C. Mills, *J. Chem. Soc. Trans.*, 1894, **67**, 925–933.

110 S. Okumura, C.-H. Lin, Y. Takeda and S. Minakata, *J. Org. Chem.*, 2013, **78**, 12090–12105.

111 Y. Shvo and D. Czarkie, *J. Organomet. Chem.*, 1989, **368**, 357–365.

112 S. Makhseed, H. M. E. Hassaneen and M. H. Elnagdi, *Z. Naturforsch*, 2007, **62b**, 529–536.

113 C. Hansch, A. Leo and R. W. Taft, *Chem. Rev.*, 1991, **91**, 165–195.

114 E. A. Hill, M. L. Gross, M. Stasiewicz and M. Manion, *J. Am. Chem. Soc.*, 1969, **91**, 7381–7392.

115 D. S. Noyce, *J. Org. Chem.*, 1976, **41**, 3640–3642.

116 L. I. Belenkii and N. D. Chuvylkin, *Chem. Heterocycl. Compd.*, 1996, **32**, 1319–1343.

117 E. V Brown and G. R. Granneman, *J. Am. Chem. Soc.*, 1975, **97**, 621–627.

118 P. Bortolus and S. Monti, *J. Phys. Chem.*, 1979, **83**, 648–652.

119 C. Reichardt, *Solvents and Solvent Effects in Organic Chemistry*, Wiley-VCH, Weinheim, Germany, 3rd edn., 2003.

120 H. Tian and S. Yang, *Chem. Soc. Rev.*, 2004, **33**, 85–97.

121 P. D. Wildes, J. G. Pacifici, G. Irick Jr. and D. G. Whitten, *J. Am. Chem. Soc.*, 1971, **93**, 2004–2008.

122 N. J. Bunce, G. Ferguson, C. L. Forber and G. J. Stachnyk, *J. Org. Chem.*, 1987, **52**, 394–398.

123 D. Gegiou, K. A. Muszjat and E. Fischer, *J. Am. Chem. Soc.*, 1968, **90**, 3907–3918.

124 N. Nishimura, T. Suavosm and H. Yamanaka, *Bull. Chem. Soc. Jpn.*, 1976, **49**, 1381–1387.

125 H. Nishioka, X. Liang and H. Asanuma, *Chem. - A Eur. J.*, 2010, **16**, 2054–2062.

126 D. Jacquemin, J. Preat, E. A. Perpète, D. P. Vercauteren, J.-M. André, I. Ciofini and C. Adamo, *Int. J. Quantum Chem.*, 2011, **111**, 4224–4240.

127 F. Zapata, M. Á. Fernández-González, D. Rivero, Á. Álvarez, M. Marazzi and L. M. Frutos, *J. Chem. Theory Comput.*, 2014, **10**, 312–323.

128 L. Briquet, D. P. Vercauteren, E. A. Perpète and D. Jacquemin, *Chem. Phys. Lett.*, 2006, **417**, 190–195.

129 J. W. Robinson, *Atomic Spectroscopy*, Marcel Dekker Inc., New York, 2nd edn., 1996.

130 G. T. Sukhanov and A. Y. Lukin, *Chem. Heterocycl. Compd.*, 2005, **41**, 861–865.

131 L. I. Bagal, M. S. Pevzner, N. I. Sheludyakova and V. M. Kerusov, *Chem. Heterocycl. Compd.*, 1970, **6**, 245–248.

132 R. W. Middleton, H. Monney and J. Parrick, *Synthesis*, 1984, 740–742.

133 US Pat., US20060160857, 2006.

134 J. W. A. M. Janssen, H. J. Koeners, C. G. Kruse and L. Habraken, *J. Org. Chem*, 1973, **38**, 1777–1782.

135 C. L. Habraken and P. Cohen-Fernandes, *J. Chem. Soc., Chem. Commun.*, 1972, 37–38.

136 US Pat., US4070366 A, 1978.

137 G. P. Stahly, E. M. Marlett and G. E. Nelson, *J. Org. Chem.*, 1983, **48**, 4423–4426.

138 C. Weston, R. Richardson, P. Haycock, A. White and M. Fuchter, *J. Am. Chem. Soc.*, 2014, **136**, 11878–11881.

139 J. P. Perdew, M. Ernzerhof and K. Burke, *J. Chem. Phys.*, 1996, **105**, 9982–9985.

140 C. Adamo and V. Barone, *J. Chem. Phys.*, 1999, **110**, 6158–6170.

141 S. Grimme, J. Antony, S. Ehrlich and H. Krieg, *J. Chem. Phys.*, 2010, **132**, 154104–154119.

142 S. Grimme, S. Ehrlich and L. Goerigk, *J. Comput. Chem.*, 2011, **32**, 1456–1465.

143 E. R. Johnson, S. Keinan, P. Mori Sánchez, J. Contreras García, A. J. Cohen and W. Yang, *J. Am. Chem. Soc.*, 2010, **132**, 6498–6506.

144 J. Contreras-Garcia, E. R. Johnson, S. Keinan, R. Chaudret, J. P. Piquemal, D. N. Beratan and W. Yang, *J. Chem. Theory Comput.*, 2011, **7**, 625–632.

145 M. Nishio, *Phys. Chem. Chem. Phys.*, 2011, **13**, 13873–13900.

146 A. E. Reed, R. B. Weinstock and F. Weinhold, *J. Chem. Phys.*, 1985, **83**, 735–746.

147 K. B. Wiberg, *Tetrahedron*, 1968, **24**, 1083–1096.

148 Y. Wu, Y. Xie, Q. Zhang, H. Tian, W. Zhu and A. D. Q. Li, *Angew. Chem.*, 2014, **126**, 2122–2126.

149 S. Sharma, T. K. Kelly and P. A. Jones, *Carcinogenesis*, 2010, **31**, 27–36.

150 C. A. Iacobuzio-Donahue, *Annu. Rev. Pathol.*, 2009, **4**, 229–249.

151 M. A. Dawson and T. Kouzarides, *Cell*, 2012, **150**, 12–27.

152 C. B. Yoo and P. A. Jones, *Nat. Rev. Drug Discov.*, 2006, **5**, 37–50.

153 P. Marks, R. A. Rifkind, V. M. Richon, R. Breslow, T. Miller and W. K. Kelly, *Nat. Rev. Cancer*, 2001, **1**, 194–202.

154 K. Luger, a W. Mäder, R. K. Richmond, D. F. Sargent and T. J. Richmond, *Nature*, 1997, **389**, 251–260.

155 G. Felsenfeld and M. Groudiner, *Nature*, 2003, **421**, 444–448.

156 B. D. Strahl and C. D. Allis, *Nature*, 2000, **403**, 41–45.

157 T. Kouzarides, *Cell*, 2007, **128**, 693–705.

158 A. J. Bannister and T. Kouzarides, *Cell Res.*, 2011, **21**, 381–395.

159 O. Witt, H. E. Deubzer, T. Milde and I. Oehme, *Cancer Lett.*, 2009, **277**, 8–21.

160 A. J. M. de Ruijter, A. H. van Gennip, H. N. Caron, S. Kemp and A. B. P. van Kuilenburg, *Biochem. J.*, 2003, **370**, 737–749.

161 M. S. Finnin, J. R. Donigian, a Cohen, V. M. Richon, R. a Rifkind, P. a Marks, R. Breslow and N. P. Pavletich, *Nature*, 1999, **401**, 188–193.

162 A. Vannini, C. Volpari, G. Filocamo, E. C. Casavola, M. Brunetti, D. Renzoni, P. Chakravarty, C. Paolini, R. De Francesco, P. Gallinari, C. Steinkühler and S. Di Marco, *Proc. Natl. Acad. Sci. U. S. A.*, 2004, **101**, 15064–15069.

163 J. C. Bressi, A. J. Jennings, R. Skene, Y. Wu, R. Melkus, R. De Jong, S. O'Connell, C. E. Grimshaw, M. Navre and A. R. Gangloff, *Bioorg. Med. Chem. Lett.*, 2010, **20**, 3142–3145.

164 M. Nakagawa, Y. Oda, T. Eguchi, S.-I. Aishima, T. Yao, F. Hosoi, Y. Basaki, M. Ono, M. Kuwano, M. Tanaka and M. Tsuneyoshi, *Oncol. Rep.*, 2007, **18**, 769–774.

165 M. A. Glozak and E. Seto, *Oncogene*, 2007, **26**, 5420–5432.

166 S. Y. Roth, J. M. Denu and C. D. Allis, *Annu. Rev. Biochem.*, 2001, **70**, 81–120.

167 H.-J. Kim and S.-C. Bae, *Am. J. Transl. Res.*, 2011, **3**, 166–179.

168 R. W. Johnstone, *Nat. Rev. Drug Discov.*, 2002, **1**, 287–299.

169 J. S. Carew, F. J. Giles and S. T. Nawrocki, *Cancer Lett.*, 2008, **269**, 7–17.

170 J. M. Wagner, B. Hackanson, M. Lübbert and M. Jung, *Clin. Epigenetics*, 2010, **1**, 117–136.

171 T. A. Miller, D. J. Witter and S. Belvedere, *J. Med. Chem.*, 2003, **46**, 5097–5116.

172 S. J. Haggarty, K. M. Koeller, J. C. Wong, C. M. Grozinger and S. L. Schreiber, *Proc. Natl. Acad. Sci. U. S. A.*, 2003, **100**, 4389–4394.

173 M. Jung, K. Hoffmann, G. Brosch and P. Loidl, *Bioorg. Med. Chem. Lett.*, 1997, **7**, 1655–1658.

174 A. Mai, S. Massa, D. Rotili, I. Cerbara, S. Valente, R. Pezzi, S. Simeoni and R. Ragna, *Med. Res. Rev.*, 2005, **25**, 261–309.

175 L. Qiu, A. Burgess, D. P. Fairlie, H. Leonard, P. G. Parsons and B. G. Gabrielli, *Mol. Biol. Cell*, 2000, **11**, 2069–2083.

176 P. Agostinis, K. Berg, K. a Cengel, T. H. Foster, A. W. Girotti, S. O. Gollnick, S. M. Hahn, M. R. Hamblin, A. Juzeniene, D. Kessel, M. Korbelik, J. Moan, P. Mroz, D. Nowiz, J. Piette, B. C. Willson and J. Golab, *Am. Cancer Soc.*, 2011, **61**, 250–281.

177 W. Henderson and J. Dougherty, *Photochem. Photobiol.*, 1992, **55**, 145–157.

178 D. E. J. G. J. Dolmans, D. Fukumura and R. K. Jain, *Nat. Rev. Cancer*, 2003, **3**, 375–380.

179 I. Diamond, A. F. Mcdonagh, C. B. Wilson, S. G. Granelli, S. Nielsen and R. Jaenicke, *Lancet*, 1972, **300**, 1175–1177.

180 A. Orenstein, G. Kostenich, L. Roitman, Y. Shechtman, Y. Kopolovic, B. Ehrenberg and Z. Malik, *Br. J. Cancer*, 1996, **73**, 937–944.

181 S.-I. Moriwaki, J. Misawa, Y. Yoshinari, I. Yamada, M. Takigawa and Y. Tokura, *Photodermatol., Photoimmunol. Photomed.*, 2001, **17**, 241–243.

182 B. W. Henderson and V. H. Fingar, *Cancer Res.*, 1987, **47**, 3110–3114.

183 L. B. Josefsen and R. W. Boyle, *Met. Based. Drugs*, 2008, **2008**.

184 N. Shirasu, S. O. Nam and M. Kuroki, *Anticancer Res.*, 2013, **33**, 2823–2832.

185 G. C. R. Ellis-Davies, *Nat. Methods*, 2007, **4**, 619–628.

186 J. W. Walker, J. a McCray and G. P. Hess, *Biochemistry*, 1986, **25**, 1799–805.

187 J. Broichhagen and D. Trauner, *Curr. Opin. Chem. Biol.*, 2014, **21**, 121–127.

188 E. V. A. Bartels, N. H. Wassermann and B. F. Erlanger, 1971, **68**, 1820–1823.

189 A. Mourot, T. Fehrentz, Y. Le Feuvre, C. M. Smith, C. Herold, D. Dalkara, F. Nagy, D. Trauner and R. H. Kramer, *Nat. Methods*, 2012, **9**, 396–404.

190 J. H. Harvey and D. Trauner, *ChemBioChem*, 2008, **9**, 191–193.

191 M. G. J. Baud, P. Haus, T. Leiser, F.-J. Meyer-Almes and M. J. Fuchter, *ChemMedChem*, 2013,

8, 149–156.

192 M. G. J. Baud, T. Leiser, P. Haus, S. Samlal, A. C. Wong, R. J. Wood, V. Petrucci, M. Gunaratnam, S. M. Hughes, L. Buluwela, F. Turlais, S. Neidle, F. J. Meyer-Almes, A. J. P. White and M. J. Fuchter, *J. Med. Chem.*, 2012, **55**, 1731–1750.

193 S. Haider, C. G. Joseph, S. Neidle, C. a. Fierke and M. J. Fuchter, *Bioorg. Med. Chem. Lett.*, 2011, **21**, 2129–2132.

194 M. G. J. Baud, PhD thesis, Imperial College London, 2011.

195 M. Volgraf, P. Gorostiza, S. Szobota, M. R. Helix, E. Y. Isacoff and D. Trauner, *J. Am. Chem. Soc.*, 2007, **129**, 260–261.

196 D. Bléger, J. Dokić, M. V. Peters, L. Grubert, P. Saalfrank and S. Hecht, *J. Phys. Chem. B*, 2011, **115**, 9930–9940.

197 F. Tibiletti, M. Simonetti, K. M. Nicholas, G. Palmisano, M. Parravicini, F. Imbesi, S. Tollari and A. Penoni, *Tetrahedron*, 2010, **66**, 1280–1288.

198 U. Siemeling, C. Bruhn, M. Meier and C. Schirrmacher, *Z. Naturforsch*, 2008, **63b**, 1395–1401.

199 H. Dalton King, D. J. Denhart, J. A. Deskus, J. L. Ditta, J. R. Epperson, M. A. Higgins, J. E. Kung, L. R. Marcin, C. P. Sloan, G. K. Mattson, T. F. Molski, R. G. Krause, R. L. Bertekap, N. J. Lodge, R. J. Mattson and J. E. Macor, *Bioorg. Med. Chem. Lett.*, 2007, **17**, 5647–5651.

200 J. C. Bressi, R. de Jong, Y. Wu, A. J. Jennings, J. W. Brown, S. O'Connell, L. W. Tari, R. J. Skene, P. Vu, M. Navre, X. Cao and A. R. Gangloff, *Bioorg. Med. Chem. Lett.*, 2010, **20**, 3138–3141.

201 R. Antonioletti, F. Bonadies, A. Ciammaichella and A. Viglianti, *Tetrahedron*, 2008, **64**, 4644–4648.

202 C. Hildmann, M. Ninkovic, R. Dietrich, D. Wegener, D. Riester, T. Zimmermann, O. M. Birch, C. Bernegger, P. Loidl and A. Schwienhorst, *J. Bacteriol.*, 2004, **186**, 2328–2339.

203 D. D. Leipe and D. Landsman, *Nucleic Acids Res.*, 1997, **25**, 3693–3697.

204 T. K. Nielsen, C. Hildmann, A. Dickmanns, A. Schwienhorst and R. Ficner, *J. Mol. Biol.*, 2005, **354**, 107–120.

205 C. Hildmann, D. Wegener, D. Riester, R. Hempel, A. Schober, J. Merana, L. Giurato, S. Guccione, T. K. Nielsen, R. Ficner and A. Schwienhorst, *J. Biotechnol.*, 2006, **124**, 258–70.

206 S. Schäfer, L. Saunders, E. Eliseeva, A. Velena, M. Jung, A. Schwienhorst, A. Strasser, A. Dickmanns, R. Ficner, S. Schlimme, W. Sippl, E. Verdin and M. Jung, *Bioorg. Med. Chem.*, 2008, **16**, 2011–2033.

207 P. M. Lombardi, K. E. Cole, D. P. Dowling and D. W. Christianson, *Curr. Opin. Struct. Biol.*, 2011, **21**, 735–743.

208 J. Sykora and F. J. Meyer-Almes, *Biochemistry*, 2010, **49**, 1418–1424.

209 D. Wegener, F. Wirsching, D. Riester and A. Schwienhorst, *Chem. Biol.*, 2003, **10**, 61–68.

210 D. Wegener, C. Hildmann, D. Riester and A. Schwienhorst, *Anal. Biochem.*, 2003, **321**, 202–208.

211 V. Aloush, S. Navon-venezia, Y. Seigman-igra, S. Cabili and Y. Carmeli, *Antimicrob. Agents Chemother.*, 2006, **50**, 43–48.

212 U. Römling and C. Balsalobre, *J. Intern. Med.*, 2012, **272**, 541–561.

213 C. N. Patel, B. W. Wortham, J. L. Lines, J. D. Fetherston, R. D. Perry and M. A. Oliveira, *J. Bacteriol.*, 2006, **188**, 2355–2363.

214 P. J. Large, *FEMS Microbiol. Rev.*, 1992, **88**, 249–262.

215 C. Meyners, R. Wawrzinek, A. Krämer, S. Hinz, P. Wessig and F. J. Meyer-Almes, *Anal. Bioanal. Chem.*, 2014, **406**, 4889–4897.

216 D. W. Moss, *J. Clin. Path.*, 1970, **4**, 22–30.

217 US Pat., US2016022817 A1, 2016.

218 S. A. Reis, B. Ghosh, J. A. Hendricks, D. M. Szantai-Kis, L. Törk, K. N. Ross, J. Lamb, W. Read-Button, B. Zheng, H. Wang, C. Salthouse, S. J. Haggarty and R. Mazitschek, *Nat. Chem. Biol.*, 2016, **12**, 317–323.

219 W. Szymanski, M. E. Ourailidou, W. a. Velema, F. J. Dekker and B. L. Feringa, *Chem. - A Eur. J.*, 2015, **21**, 16517–16524.

220 M. Korbus, G. Balasubramanian, F. Müller-Plathe, H. Kolmar and F.-J. Meyer-Almes, *Biol. Chem.*, 2014, **395**, 401–412.

221 M. Korbus, S. Backé and F.-J. Meyer-Almes, *J. Mol. Recognit.*, 2015, **28**, 201–209.

222 C. Meyners, M. G. J. Baud, M. J. Fuchter and F. J. Meyer-Almes, *J. Mol. Recognit.*, 2014, **27**, 160–172.

223 C. Meyners, M. G. J. Baud, M. J. Fuchter and F.-J. Meyer-Almes, *Anal. Biochem.*, 2014, **460**, 39–46.

224 A. W. Hofmann, *Ber. Dtsch. Chem. Ges.*, 1881, **14**, 2725–2736.

225 E. Johnson and D. Campbell, *J. Org. Chem.*, 1982, **3**, 4664–4670.

226 D. Burdulene, I. Z. Stumbryavichyute, Z. Talaikite, G. V Vladyko, E. I. Boreko and L. V Korobchenko, *Pharm. Chem. J.*, 1997, **30**, 680–682.

227 S. Mahboobi, A. Sellmer, M. Winkler, E. Eichhorn, H. Pongratz, T. Ciossek, T. Baer, T. Maier and T. Beckers, *J. Med. Chem.*, 2010, **53**, 8546–8555.

228 US Pat., US2003092712 A1, 2003.

229 Br. Pat., GB2026481 A, 1980.

230 B. Staskun, *J. Org. Chem.*, 1988, **53**, 5287–5291.

231 X. Huang, M. Seid and J. W. Keillor, *J. Org. Chem.*, 1997, **62**, 7495–7496.

232 M. Schönberger and D. Trauner, *Angew. Chem., Int. Ed.*, 2014, **53**, 3264–3267.

233 S. Muramatsu, K. Kinbara, H. Taguchi, N. Ishii and T. Aida, *J. Am. Chem. Soc.*, 2006, **128**, 3764–9.

234 J. A. Cisneros, E. Björklund, I. González-Gil, Y. Hu, Á. Canales, F. J. Medrano, A. Romero, S. Ortega-Gutiérrez, C. J. Fowler and M. L. López-Rodríguez, *J. Med. Chem.*, 2012, **55**, 824–836.

235 P. G. Jagtap, G. J. Southan, E. Baloglu, S. Ram, J. G. Mabley, A. Marton, A. Salzman and C. Szabó, *Bioorganic Med. Chem. Lett.*, 2004, **14**, 81–85.

236 S. Dallavalle, R. Cincinelli, R. Nannei, L. Merlini, G. Morini, S. Penco, C. Pisano, L. Vesci, M. Barbarino, V. Zuco, M. De Cesare and F. Zunino, *Eur. J. Med. Chem.*, 2009, **44**, 1900–1912.

237 S. Kohse, A. Neubauer, A. Pazidis, S. Lochbrunner and U. Kragl, *J. Am. Chem. Soc.*, 2013, **135**,

9407–9411.

238 M. V. George and J. C. Scaiano, *J. Phys. Chem.*, 1980, **84**, 492–495.

239 S. Abbruzzetti, M. Carcelli, D. Rogolino and C. Viappiani, *Photochem. Photobiol. Sci.*, 2003, **2**, 796–800.

240 L. G. Arnaut and S. J. Formosinho, *J. Photochem. Photobiol. A Chem.*, 1993, **75**, 1–20.

241 E. Pines and D. Huppert, *J. Phys. Chem.*, 1983, **87**, 4471–4478.

242 J. H. Clark, S. L. Shapiro, A. J. Campillo and K. R. Winn, *J. Am. Chem. Soc.*, 1979, 746–748.

243 R. M. D. Nunes, M. Pineiro and L. G. Arnaut, *J. Am. Chem. Soc.*, 2009, **131**, 9456–9462.

244 S. H. Kawai, S. L. Gilat and J. Lehn, *Eur. J. Org. Chem.*, 1999, 2359–2366.

245 Z. Shi, P. Peng, D. Strohecker and Y. Liao, *J. Am. Chem. Soc.*, 2011, **133**, 14699–14703.

246 N. Abeyrathna and Y. Liao, *J. Am. Chem. Soc.*, 2015, **137**, 11282–11284.

247 R. Stewart, *The Proton: Applications to Organic Chemistry*, Academic Press Inc. (London) Ltd., UK edn., 1985.

248 F. Matino, G. Schull, U. Jana, F. Köhler, R. Berndt and R. Herges, *Chem. Commun.*, 2010, **46**, 6780–6782.

249 S. Thies, H. Sell, C. Schütt, C. Bornholdt, C. Näther, F. Tuczek and R. Herges, *J. Am. Chem. Soc.*, 2011, **133**, 16243–16250.

250 J. A. Dean, *Lange's Handbook of Chemistry*, McGraw-Hill, New York, 12th edn., 1979.

251 Y. Takeda, S. Okumura and S. Minakata, *Angew. Chem., Int. Ed.*, 2012, **51**, 7804–7808.

252 B. Jiang, Y. Ning, W. Fan, S.-J. Tu and G. Li, *J. Org. Chem.*, 2014, **79**, 4018–4024.

253 H. Weinmann, M. Harre, K. Koenig, E. Merten and U. Tilstam, *Tet. Lett.*, 2002, **43**, 593–595.

254 Y.-C. Li, C. Qi, S.-H. Li, H.-J. Zhang, C.-H. Sun, Y.-Z. Yu and S.-P. Pang, *J. Am. Chem. Soc.*, 2010, **132**, 12172–12173.

255 G. Steinhauser, G. Giester, C. Wagner, P. Weinberger, B. Zachhuber, G. Ramer, M. Villa and B. Lendl, *Inorg. Chem.*, 2012, **51**, 6739–6745.

256 E. Gattavecchia and D. Tonelli, *J. Chem. Soc. Perkin Trans. 2*, 1986, 689–693.

257 S. G. Smith, R. S. Paton, J. W. Burton and J. M. Goodman, *J. Org. Chem.*, 2008, **73**, 4053–4062.

258 D. C. Braddock and H. S. Rzepa, *J. Nat. Prod.*, 2008, **71**, 728–730.

259 G. Bifulco, P. Dambruoso, L. Gomez-Paloma and R. Riccio, *Chem. Rev.*, 2007, **107**, 3744–3779.

260 Y. Cao, M. D. Beachy, D. A. Braden, L. Morrill, M. N. Ringnalda and R. A. Friesner, *J. Chem. Phys.*, 2005, **122**, 224110–224116.

261 K. O. Jeon, J. S. Yu and C. K. Lee, *Heterocycles*, 2003, **60**, 2685–2705.

262 M. Gutman and E. Pines, *J. Am. Chem. Soc.*, 1981, **103**, 3709–3713.

263 W. Yao and R. H. Byrne, *Environ. Sci. Technol.*, 2001, **35**, 1197–1201.

264 R. W. Sabnis, *Handbook of acid-base indicators*, CRC Press, Boca Raton, 2007.

265 C.-W. Ko and T. Chou, *J. Org. Chem.*, 1998, **63**, 4645–4653.

266 G. Némethy and A. Ray, *J. Phys. Chem.*, 1973, **77**, 64–68.

267 P. Klán and J. Wirz, *Photochemistry of Organic Compounds: From Concepts to Practice*, John Wiley & Sons Ltd, 1st edn., 2009.

268 H. V Patel, K. A. Vyas, S. P. Pandey and P. S. Fernandes, *Synth. Commun.*, 1992, **22**, 3081–3087.

269 Korean Pat., KR20130094693 A, 2013.

270 P. Ravi, G. M. Gore, A. K. Sikder and S. P. Tewari, *Synth. Commun.*, 2012, **42**, 3463–3471.

271 G. Ege and H. Franz, *J. Heterocycl. Chem.*, 1982, **19**, 1267–1273.

272 D. A. Lightner and L. K. Low, *J. Heterocycl. Chem.*, 1975, **12**, 793–795.

273 F. W. Patureau, C. Nimphius and F. Glorius, *Org. Lett.*, 2011, **13**, 6346–6349.

274 E. Opozda and E. Śledziewska, *J. Prakt. Chem.*, 1991, **333**, 601–606.

275 B. A. Tertov, V. V. Burykin and A. V. Koblik, *Khim. Geterotsikl. Soedin.*, 1972, 1552–1554.

276 J. O'Connell, J. Parquette and W. Yelle, *Synthesis*, 1988, 767–771.

277 Gaussian 09, M. J. Frisch, G. W. Trucks, H. B. Schlegel, G. E. Scuseria, M. A. Robb, J. R. Cheeseman, G. Scalmani, V. Barone, B. Mennucci, G. A. Petersson, H. Nakatsuji, M. Caricato, X. Li, H. P. Hratchian, A. F. Izmaylov, J. Bloino, G. Zheng, J. L. Sonnenberg, M. Hada, M. Ehara, K. Toyota, R. Fukuda, J. Hasegawa, M. Ishida, T. Nakajima, Y. Honda, O. Kitao, H. Nakai, T. Vreven, J. A. Montgomery, Jr., J. E. Peralta, F. Ogliaro, M. Bearpark, J. J. Heyd, E. Brothers, K. N. Kudin, V. N. Staroverov, R. Kobayashi, J. Normand, K. Raghavachari, A. Rendell, J. C. Burant, S. S. Iyengar, J. Tomasi, M. Cossi, N. Rega, J. M. Millam, M. Klene, J. E. Knox, J. B. Cross, V. Bakken, C. Adamo, J. Jaramillo, R. Gomperts, R. E. Stratmann, O. Yazyev, A. J. Austin, R. Cammi, C. Pomelli, J. W. Ochterski, R. L. Martin, K. Morokuma, V. G. Zakrzewski, G. A. Voth, P. Salvador, J. J. Dannenberg, S. Dapprich, A. D. Daniels, Ö. Farkas, J. B. Foresman, J. V. Ortiz, J. Cioslowski, and D. J. Fox, Gaussian, Inc., Wallingford CT, 2009.

278 C. Lee, C. Hill and N. Carolina, *Phys. Rev. B*, 1988, **37**, 785–789.

279 A. D. Becke, *J. Chem. Phys.*, 1993, **98**, 5648–5652.

280 S. Miertuš, E. Scrocco and J. Tomasi, *Chem. Phys.*, 1981, **55**, 117–129.

281 M. J. G. Peach, T. Helgaker, P. Sałek, T. W. Keal, O. B. Lutnaes, D. J. Tozer and N. C. Handy, *Phys. Chem. Chem. Phys.*, 2006, **8**, 558–562.

282 M. M. Francl, W. J. Pietro, W. J. Hehre, J. S. Binkley, M. S. Gordon, J. D. Douglas and J. A. Pople, *J. Chem. Phys.*, 1982, **77**, 3654–3665.

283 H. B. Schlegel, *J. Comput. Chem.*, 1982, **3**, 214–218.

284 J. P. Foster and F. Weinhold, *J. Am. Chem. Soc.*, 1980, **102**, 7211–7218.

285 A. E. Reed and F. Weinhold, *J. Chem. Phys.*, 1983, **78**, 4066–4073.

286 P. W. Abegg and T.-K. Ha, *Mol. Phys.*, 1974, **27**, 763–767.

287 J. E. Carpenter and F. Weinhold, *J. Mol. Struct.*, 1988, **169**, 41–62.

288 A. E. Reed, L. a Curtiss and F. Weinhold, *Chem. Rev.*, 1988, **88**, 899–926.

289 K. Wolinski, J. F. Hinton and P. Pulay, *J. Am. Chem. Soc.*, 1990, **112**, 8251–8260.

290 T. K. Nielsen, C. Hildmann, D. Riester, D. Wegener, A. Schwienhorst and R. Ficner, *Acta Crystallogr., Sect. F Struct. Biol. Cryst. Commun.*, 2007, **63**, 270–273.

291 D. Wegener, C. Hildmann, D. Riester, A. Schober, F.-J. Meyer-Almes, H. E. Deubzer, I. Oehme, O. Witt, S. Lang, M. Jaensch, V. Makarov, C. Lange, B. Busse and A. Schwienhorst, *Biochem. J.*, 2008, **413**, 143–150.

292 A. Vlund, *Biometrics*, 1978, **34**, 357–365.

293 S. R. Logan, *J. Chem. Educ.*, 1997, **74**, 1303.

294 C. Weston, R. Richardson and M. Fuchter, *Chem. Commun.*, 2016, **52**, 4521–4524.

295 R. D. Stolow, *J. Am. Chem. Soc.*, 1959, **81**, 5806–5811.

296 R. D. Richardson, M. G. J. Baud, C. E. Weston, H. S. Rzepa, M. K. Kuimova and M. J. Fuchter, *Chem. Sci.*, 2015, **6**, 3853–3862.

7 APPENDIX

7.1 Equation derivations

All derivations were performed by Dr Robert Richardson, a member of the Fuchter group.

7.1.1 Thermal isomerisation kinetics

The thermal isomerisation is a first order process, following an exponential decay that can be expressed as:

$A = A_o e^{-kt}$ where A = absorbance at time t; A_o = absorbance at t=0; k = rate constant; t = time

Rearranging this equation and taking the natural log of both sides gives: $\ln\left(\frac{A}{A_o}\right) = -kt$

Which can be rewritten as: $lnA = -kt + lnA_o$

This equation is known as the integrated form of the first-order rate equation.

This can then be arranged to solve for t:

$t = -(lnA - lnA_o)/k$

For calculating the thermal half-life, A_o =2 and A=1 so:

$t_{1/2} = -\ln(1/2)/k$ or $t_{1/2} = \ln(2)/k$

7.1.2 Photoisomerisation quantum yields[138]

The rate of a unidirectional photochemical reaction initiated with monochromatic light is given by:[293]

$$r_{A\to B} = \frac{q_{in}\Phi_{A\to B}}{V}(1 - 10^{-\varepsilon_A[A]l}) \quad \text{(A1)}$$

When the absorbance is much less than 0.43, Taylor expansion of the exponential and truncation at the linear term gives an approximate first-order rate equation A2 from which an expression relating the quantum yield to an observed first-order rate constant, photon flux and measurable properties of the sample can be derived equation 3:

$$r_{A\to B} = \frac{q_{in}\Phi_{A\to B}\varepsilon_A l}{V}[A] \quad \text{(A2)}$$

$$\Phi_{A\to B} = \frac{k\,V}{q_{in}\varepsilon_A l \ln 10} \quad (3)$$

where Φ = quantum yield; k = rate constant (obtained from the exponential fit of a graph of A vs. time); V = sample volume; ε= molar extinction coefficient; l = pathlength; and q = molar photon flux.

Where the photoswitching is incomplete, the kinetics of approach to the PSS from one direction must be considered. For a reaction starting at pure *E*-isomer generating a photostationary state of composition, *R*:

$$R = \left.\frac{[Z]}{[E]}\right|_{PSS} \quad \text{(A3)}$$

The rate law for the formation of *Z*-isomer is:

$$[Z] = \frac{k_f}{k_f + k_r} c_{total}\left(1 - e^{-(k_f + k_r)t}\right) \quad \text{(A4)}$$

where c_{total} is the total concentration of the photoswitch and k_f and k_r are the first order approximate rate constants for the forward and reverse photochemical reactions under the low absorption approximation discussed above. An exponential fit to the time course of the photochemistry gives an observed rate constant ($k_{obs} = k_r + k_f$) equal to sum of the forward and back rate constants. At the PSS:

$$R = \frac{k_f}{k_r} \quad \text{(A5)}$$

Rearranging (A5) and substituting into the expression for k_{obs} gives:

$$k_r = \frac{k_{obs}}{R + 1} \quad \text{(A6)}$$

$$k_f = \frac{k_{obs}}{\frac{1}{R} + 1} \quad \text{(A7)}$$

Then equation 3 can be used to determine the quantum yields for the forward and reverse processes from these rate constants. Uncertainties on all these values were estimated by error propagation by standard techniques.

The maximum absorbance at the pump wavelength was around or below 0.1 or 0.2 for all compounds and good exponential fits were obtained for all compounds (Figure 7.18), confirming the validity of the low absorbance approximation in all cases presented here.

Molar photon flux was calculated using equation A8:

$$q_{in} = \frac{P\lambda}{hcN_A} \quad \text{(A8)}$$

where P = power (of the laser); λ = pump wavelength; h = Planck's constant; c = speed of light; and N_A = Avogadro's number.

7.1.3 pK_a equation derivation[294]

To measure the pK_a of the *Z*-isomer given the thermal isomerisation rate present in these species directly was not possible, given the large similarity between the UV/vis spectra for three of the four species under study. Stolow[295] investigated the effect of 4-substitution on the pK_a of cyclohexanecarboxylic acids by treating a system (Figure 7.1) involving multiple thermodynamic equilibria where eq and ax are the conformers with the axial and equatorial carboxylate groups.

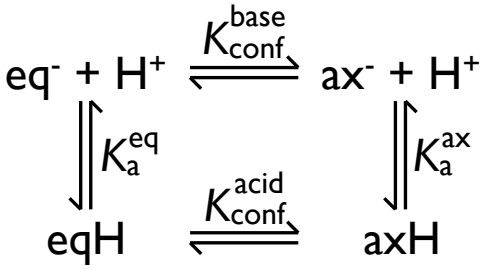


Figure 7.1. A system involving multiple thermodynamic equilibria

Where in that case, an apparent acidity constant K_a of the rapidly equilibrating system (that is measured by pH titration) is a weighted average of the K_a values, K_a^{ax} and K_a^{eq} of a conformationally locked cyclohexanecarboxylic acid where the weighting depends on the equilibration ratio (e.g., K_{base}^{conf}) of the equatorial and axial conformers.

Naively extending this approach to photochemistry by replacing the conformer equilibrium constants with PSS ratios could lead to problems given the fundamentally different nature of such a photochemical switching regarding the non-applicability of the principles of microscopic reversibility and detailed balance to the photoswitchable base. For the system in Figure 7.2, we repeat the derivation by Stolow and address the limitations of such an approach.

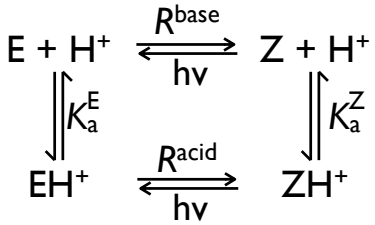


Figure 7.2. Photoswitching involving additional equilibria

Where the acidity constants for the *E*- and Z-isomers are pH and irradiation independent and defined as:

$$K_a^E = \frac{[E][H]}{[EH^+]} \qquad \text{(A9)}$$

$$K_a^Z = \frac{[Z][H]}{[ZH^+]} \quad \text{(A10)}$$

and the ratios present in the photostationary state, R, in both the acidic and basic forms are given by:

$$R^{acid} = \frac{[ZH^+]}{[EH^+]} \quad \text{(A11)}$$

$$R^{base} = \frac{[Z]}{[E]} \quad \text{(A12)}$$

and are not (yet) assumed to be pH independent. We assume that:

1. The rate of proton exchange in the acid/base reactions is much faster than rate of the bulk photochemistry[296] so the relative concentrations of acidic and basic forms of either isomer is determined only by the K_a and the pH of the medium.
2. The thermal isomerisation of *Z* and *Z*H$^+$ is not significant compared to the equivalent photochemical step (both should show first-order kinetics provided that the solution absorbance is low)[296]. This was demonstrated for the high and low pH cases by increasing the laser power until the UV spectrum of the steady state solution is unchanged.

From equations A9-A12, we see that:

$$\frac{R^{base}}{R^{acid}} = \frac{[Z]}{[E]}\frac{[EH^+]}{[ZH^+]} = \frac{[Z][H^+]}{[ZH^+]}\frac{[EH^+]}{[E][H^+]} = \frac{K_a^Z}{K_a^E} \quad \text{(A13)}$$

hence that R_{base} / R_{acid} must be independent of pH (even if the individual ratios are pH dependent) and determined by the relative pK_a values present. In our system at high pH we measure R^{base} = 3.76 at pH 10. Given we know that $pK_a^Z > pK_a^E$ (hence $K_a^Z << K_a^E$) this must mean that $R^{acid} >> 3.76$ at pH 10, hence $[ZH^+]/[EH^+] >> 1$ at pH 10.

If we can assume that R^{base} *(and hence, from equation A13,* R^{acid}*) is independent of pH,* this leads to the (perhaps counter-intuitive) result that the low pH PSS is essentially pure ZH$^+$. The reliability of this is discussed later.

We define the apparent K_a (K_a') of the interconverting system akin to Stolow that can be determined by a titration under irradiating conditions:

$$K_a' = \frac{\big([E]+[Z]\big)[H^+]}{[EH^+]+[ZH^+]} \quad \text{(A14)}$$

As the acid/base equilibria are fully established, we can substituted for [EH$^+$] and [ZH$^+$] using equations A9 and A10:

$$K_a' = \frac{([E]+[Z])[H^+]}{\frac{[E][H^+]}{K_a^E}+\frac{[Z][H^+]}{K_a^Z}} = \frac{(K_a^E K_a^Z([E]+[Z])}{K_a^Z[E]+K_a^E[Z]} \qquad \text{(A15)}$$

Then, substituting for [Z] using equation A12:

$$K_a' = \frac{K_a^E K_a^Z([E]+[E]R^{base})}{K_a^Z[E]+K_a^E[E]R^{base}} = \frac{K_a^E K_a^Z(1+R^{base})}{K_a^Z+K_a^E R^{base}} \qquad \text{(A16)}$$

Equation A16 can then be rearranged to solve for K_a':

$$K_a^Z = \frac{K_a^E K_a' R^{base}}{K_a^E + K_a^E R^{base} - K_a'} \qquad (7)$$

If we can assume that R^{base} *(and hence, from equation A13,* R^{acid}*) is independent of pH*, then we can used R^{base} = 3.76 (as determined at pH 9) along with pK_a^E = 4.7, pK_a' = 5.9 from the dark and light titrations to give pK_a^Z = 6.0. The reliability of this assumption is discussed later.

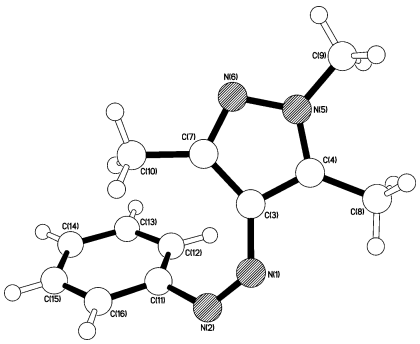
Unlike in the equilibrium situation in Figure 7.1, where the equilibrium ratios are determined only by the energies of the various species and not by the mechanisms through which they are formed, this may not apply to the photochemistry situation in which extra mechanisms may be possible for forwards and back reactions at different pH.

For example, excitation of *E*H$^+$ could be followed by an excited state proton transfer from EH^{+}* to the medium to generate *E** that can then undergo further photochemical reactions, the quantum yield of forming *Z*H$^+$ from exciting *E*H$^+$ may depend on pH and buffer concentration affecting the rates in one direction only (microscopic reversibility does not apply here). This could lead to different ratios of R^{base} and R^{acid} although a full quantitative assessment of this affect would be complicated. However, the isomerisation reaction of these species are typically ultrafast with excited state lifetimes well under 1 ns,[32] so the significance of any diffusion controlled proton transfer with buffers in millimolar concentrations is likely to be negligible.

According to equation A16, if R^{base} in pH dependant, K_a' must also be pH dependant given that the individual K_a values are pH independent. This would suggest that the pH titration curve (Figure 4.8) may differ in shape (*i.e.*, it may be be flatter or sharper than the one for titration in the dark). This appears not to be the case, so the conclusions presented here are likely to be good estimates.

7.2 X-ray crystallography

Z-23



Formula	C10 H10 N4	
Formula weight	186.22	
Temperature	173 K	
Diffractometer, wavelength	Agilent Xcalibur 3 E, 0.71073 Å	
Crystal system, space group	Monoclinic, P 21/c	
Unit cell dimensions	a = 11.2431(7) Å	□ = 90°
	b = 10.1867(6) Å	□ = 104.512(7)°
	c = 8.9687(6) Å	□ = 90°
Volume, Z	994.41(11) Å^3, 4	
Density (calculated)	1.244 Mg/m^3	
Absorption coefficient	0.080 mm^{-1}	
F(000)	392	
Crystal colour / morphology	Yellow platy needles	
Crystal size	0.53 x 0.39 x 0.07 mm^3	
□ range for data collection	2.739 to 28.046°	
Index ranges	-12<=h<=13, -8<=k<=12, -11<=l<=6	
Reflns collected / unique	3120 / 1952 [R(int) = 0.0117]	
Reflns observed [F>4□(F)]	1485	
Absorption correction	Analytical	
Max. and min. transmission	0.995 and 0.966	
Refinement method	Full-matrix least-squares on F^2	
Data / restraints / parameters	1952 / 0 / 129	
Goodness-of-fit on F^2	1.021	
Final R indices [F>4□(F)]	R1 = 0.0430, wR2 = 0.0913	
R indices (all data)	R1 = 0.0613, wR2 = 0.1014	
Largest diff. peak, hole	0.153, -0.140 eÅ^{-3}	
Mean and maximum shift/error	0.000 and 0.000	

Table 7.1. Crystal data and structure refinement for **23**

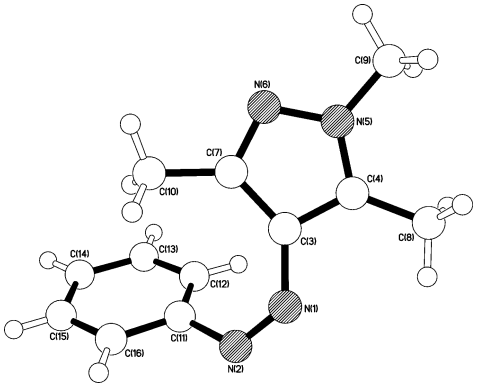
N(1)-N(2)	1.2578(19)
N(1)-C(3)	1.411(2)
N(2)-C(9)	1.439(2)
C(3)-C(4)	1.378(2)
C(3)-C(7)	1.416(2)
C(4)-N(5)	1.330(2)
N(5)-N(6)	1.3643(17)
N(5)-C(8)	1.455(2)
N(6)-C(7)	1.321(2)
C(9)-C(14)	1.379(2)
C(9)-C(10)	1.385(2)
C(10)-C(11)	1.377(2)
C(11)-C(12)	1.379(3)
C(12)-C(13)	1.378(3)
C(13)-C(14)	1.380(3)

Table 7.2. Bond lengths [Å] for **23**

N(2)-N(1)-C(3)	123.88(14)
N(1)-N(2)-C(9)	121.28(14)
C(4)-C(3)-N(1)	119.08(14)
C(4)-C(3)-C(7)	104.28(14)
N(1)-C(3)-C(7)	136.56(16)
N(5)-C(4)-C(3)	107.46(14)
C(4)-N(5)-N(6)	112.16(13)
C(4)-N(5)-C(8)	128.90(14)
N(6)-N(5)-C(8)	118.93(13)
C(7)-N(6)-N(5)	104.89(13)
N(6)-C(7)-C(3)	111.19(15)
C(14)-C(9)-C(10)	120.58(17)
C(14)-C(9)-N(2)	119.30(16)
C(10)-C(9)-N(2)	119.82(15)
C(11)-C(10)-C(9)	119.46(17)
C(10)-C(11)-C(12)	120.22(19)
C(13)-C(12)-C(11)	120.00(18)
C(12)-C(13)-C(14)	120.32(19)
C(9)-C(14)-C(13)	119.40(19)

Table 7.3. Bond angles [°] for **23**

Z-**24**



Formula	C12 H14 N4
Formula weight	214.27
Temperature	173 K
Diffractometer, wavelength	Agilent Xcalibur 3 E, 0.71073 Å
Crystal system, space group	Orthorhombic, P b c a
Unit cell dimensions	a = 9.3288(5) Å □ = 90°
	b = 8.9949(4) Å □ = 90°
	c = 27.0230(13) Å □ = 90°
Volume, Z	2267.53(18) $Å^3$, 8
Density (calculated)	1.255 Mg/m^3
Absorption coefficient	0.079 mm^{-1}
F(000)	912
Crystal colour / morphology	Orange blocks
Crystal size	0.51 x 0.41 x 0.20 mm^3
□ range for data collection	2.653 to 28.115°
Index ranges	-4<=h<=11, -11<=k<=11, -35<=l<=20
Reflns collected / unique	5056 / 2316 [R(int) = 0.0231]
Reflns observed [F>4□(F)]	1881
Absorption correction	Analytical
Max. and min. transmission	0.984 and 0.972
Refinement method	Full-matrix least-squares on F^2
Data / restraints / parameters	2316 / 0 / 148
Goodness-of-fit on F^2	1.044
Final R indices [F>4□(F)]	R1 = 0.0457, wR2 = 0.1032
R indices (all data)	R1 = 0.0599, wR2 = 0.1114
Largest diff. peak, hole	0.240, -0.199 $eÅ^{-3}$
Mean and maximum shift/error	0.000 and 0.000

Table 7.4. Crystal data and structure refinement for **24**

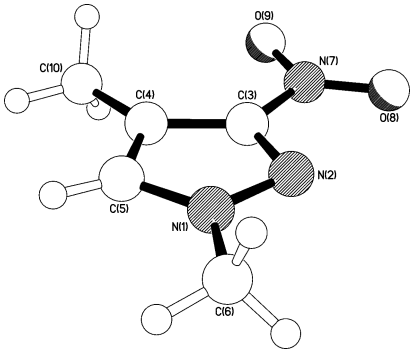
N(1)-N(2)	1.2592(19)
N(1)-C(3)	1.4140(19)
N(2)-C(11)	1.439(2)
C(3)-C(4)	1.391(2)
C(3)-C(7)	1.425(2)
C(4)-N(5)	1.3370(19)
C(4)-C(8)	1.483(2)
N(5)-N(6)	1.3617(18)
N(5)-C(9)	1.451(2)
N(6)-C(7)	1.324(2)
C(7)-C(10)	1.490(2)
C(11)-C(12)	1.383(2)
C(11)-C(16)	1.384(2)
C(12)-C(13)	1.387(2)
C(13)-C(14)	1.382(2)
C(14)-C(15)	1.378(2)
C(15)-C(16)	1.383(2)

Table 7.5,Bond lengths [Å] for **24**

N(2)-N(1)-C(3)	125.34(13)
N(1)-N(2)-C(11)	122.11(14)
C(4)-C(3)-N(1)	117.56(13)
C(4)-C(3)-C(7)	105.44(13)
N(1)-C(3)-C(7)	136.40(14)
N(5)-C(4)-C(3)	106.13(13)
N(5)-C(4)-C(8)	122.94(14)
C(3)-C(4)-C(8)	130.92(15)
C(4)-N(5)-N(6)	112.66(13)
C(4)-N(5)-C(9)	127.79(14)
N(6)-N(5)-C(9)	119.52(14)
C(7)-N(6)-N(5)	105.91(12)
N(6)-C(7)-C(3)	109.79(13)
N(6)-C(7)-C(10)	117.96(14)
C(3)-C(7)-C(10)	132.02(15)
C(12)-C(11)-C(16)	120.74(15)
C(12)-C(11)-N(2)	121.93(14)
C(16)-C(11)-N(2)	116.97(15)
C(11)-C(12)-C(13)	119.01(15)
C(14)-C(13)-C(12)	120.51(16)
C(15)-C(14)-C(13)	119.85(16)
C(14)-C(15)-C(16)	120.34(16)
C(15)-C(16)-C(11)	119.44(16)

Table 7.6. Bond angles [°] for **24**

48a



Formula	C5 H7 N3 O2
Formula weight	141.14
Temperature	173(2) K
Diffractometer, wavelength	Agilent Xcalibur 3 E, 0.71073 Å
Crystal system, space group	Monoclinic, P 21/c
Unit cell dimensions	a = 8.0120(5) Å □ = 90°
	b = 11.4910(6) Å □ = 113.418(8)°
	c = 7.7899(5) Å □ = 90°
Volume, Z	658.10(8) Å^3, 4
Density (calculated)	1.424 Mg/m^3
Absorption coefficient	0.113 mm^{-1}
F(000)	296
Crystal colour / morphology	Colourless tablets
Crystal size	0.83 x 0.55 x 0.23 mm^3
□ range for data collection	2.771 to 28.334°
Index ranges	-6<=h<=10, -14<=k<=14, -10<=l<=9
Reflns collected / unique	2259 / 1316 [R(int) = 0.0279]
Reflns observed [F>4□(F)]	1130
Absorption correction	Analytical
Max. and min. transmission	0.973 and 0.943
Refinement method	Full-matrix least-squares on F^2
Data / restraints / parameters	1316 / 0 / 94
Goodness-of-fit on F^2	1.106
Final R indices [F>4□(F)]	R1 = 0.0415, wR2 = 0.1114
R indices (all data)	R1 = 0.0479, wR2 = 0.1173
Largest diff. peak, hole	0.216, -0.279 eÅ^{-3}
Mean and maximum shift/error	0.000 and 0.000

Table 7.7. Crystal data and structure refinement for **48a**.

N(1)-N(2)	1.3382(16)
N(1)-C(5)	1.3514(19)
N(1)-C(6)	1.4600(19)
N(2)-C(3)	1.3359(18)
C(3)-C(4)	1.403(2)
C(3)-N(7)	1.4340(18)
C(4)-C(5)	1.380(2)
C(4)-C(10)	1.493(2)
N(7)-O(8)	1.2272(17)
N(7)-O(9)	1.2296(16)

Table 7.8. Bond lengths [Å] for **48a**

N(2)-N(1)-C(5)	112.91(12)
N(2)-N(1)-C(6)	119.68(12)
C(5)-N(1)-C(6)	127.38(13)
C(3)-N(2)-N(1)	102.71(12)
N(2)-C(3)-C(4)	114.48(12)
N(2)-C(3)-N(7)	118.35(13)
C(4)-C(3)-N(7)	127.17(13)
C(5)-C(4)-C(3)	101.75(13)
C(5)-C(4)-C(10)	127.07(14)
C(3)-C(4)-C(10)	131.15(13)
N(1)-C(5)-C(4)	108.15(13)
O(8)-N(7)-O(9)	123.25(13)
O(8)-N(7)-C(3)	119.44(13)
O(9)-N(7)-C(3)	117.31(13)

Table 7.9. Bond angles [°] for **48a**

7.3 Photochemistry

7.3.1 Novel azoheteroaryl photoswitches

Quantification of PSS composition by NMR

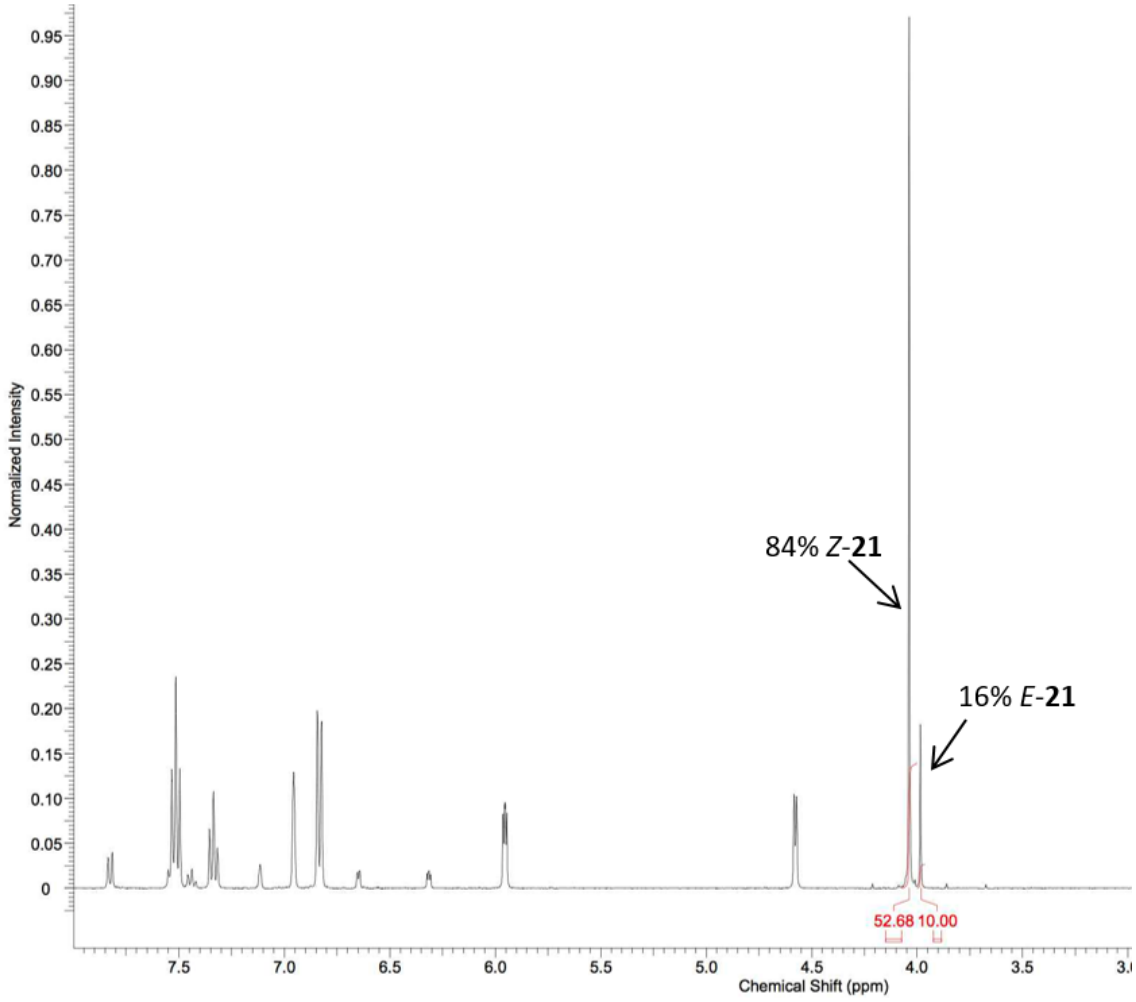


Figure 7.3. ^{1}H NMR of **21** at 415 nm PSS in d_3-MeCN at ~10^{-2}M concentration.

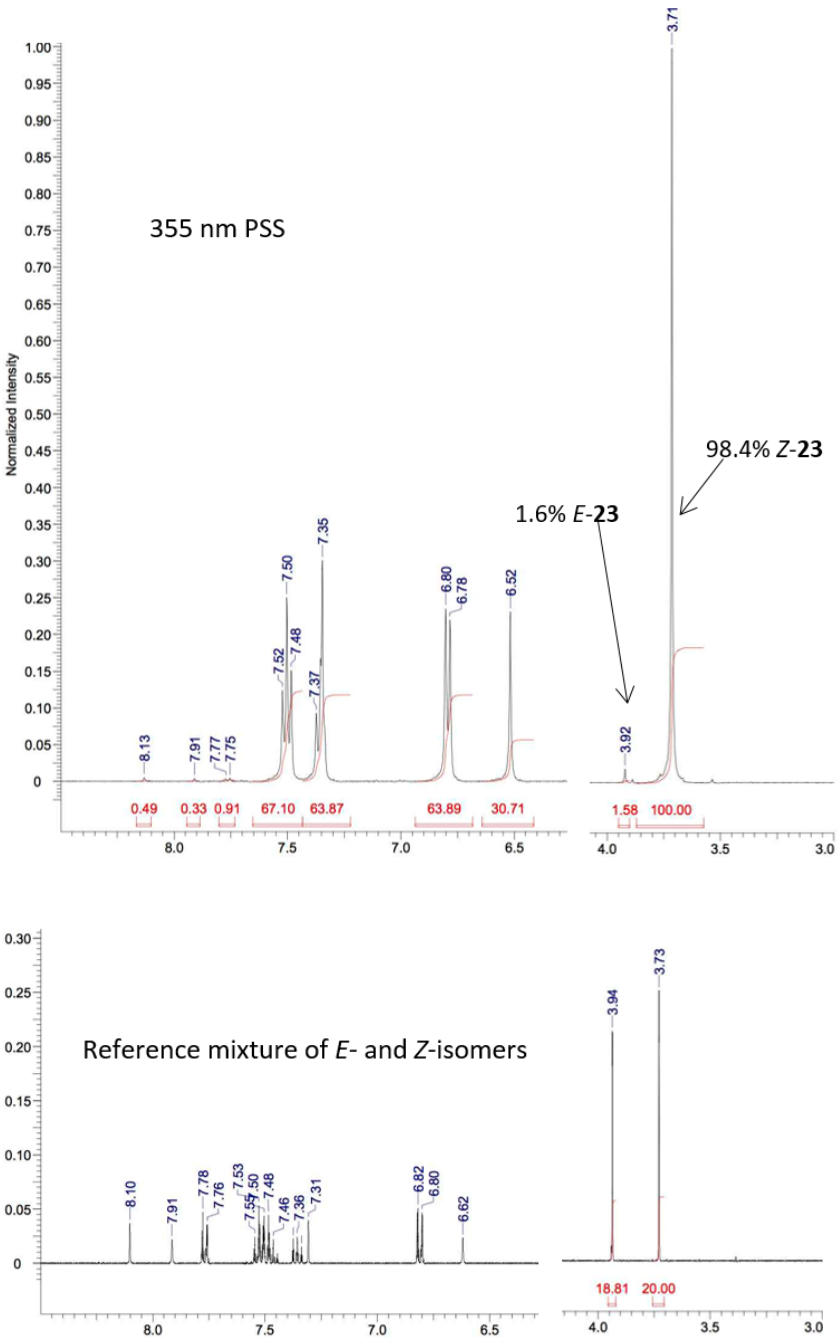


Figure 7.4. ^{1}H NMR of the 355 nm PSS of **23** in d_3-MeCN at ~10^{-2}M concentration, with a reference spectrum (containing 52% *Z*-**23**) to show both *E*- and *Z*-isomer peaks.

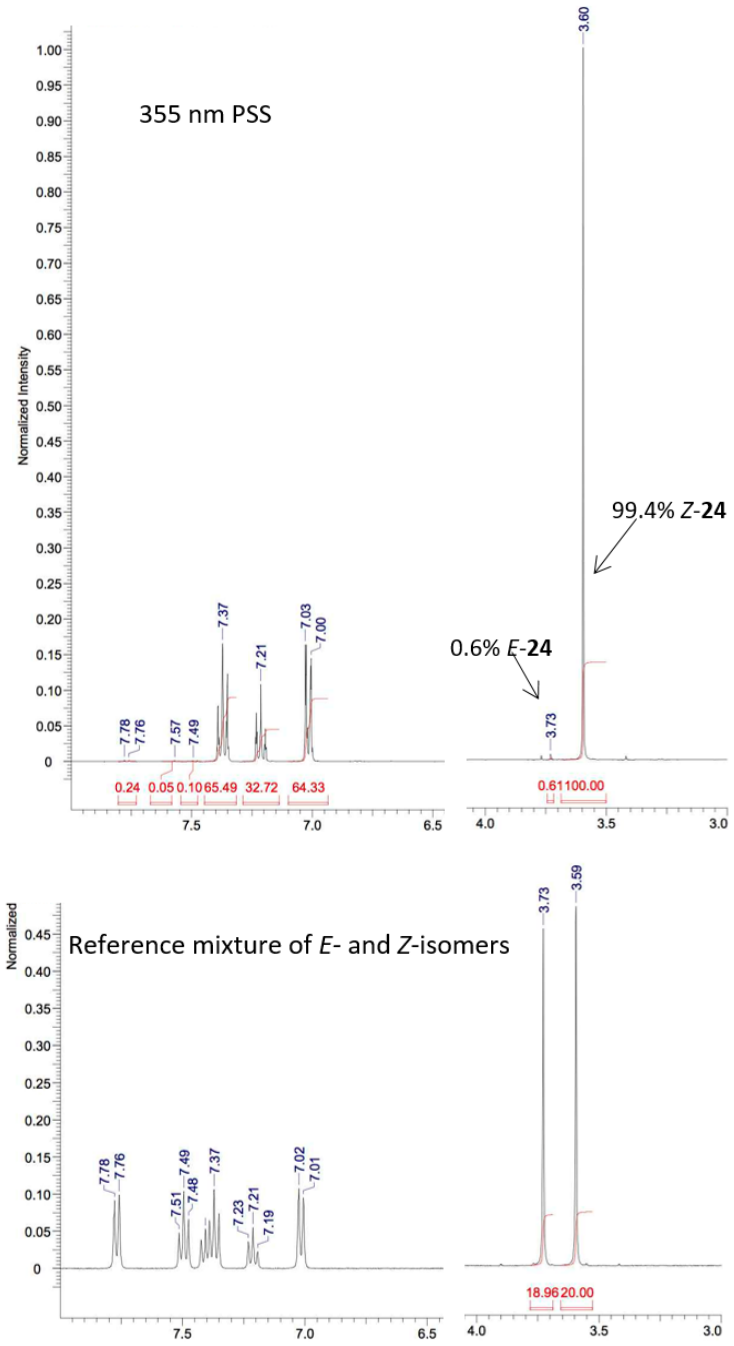


Figure 7.5. ^{1}H NMR of the 355 nm PSS of **24** in d_3-MeCN at ~10^{-2}M concentration, with a reference spectrum (containing 51% *Z*-**24**) to show both *E*- and *Z*-isomer peaks.

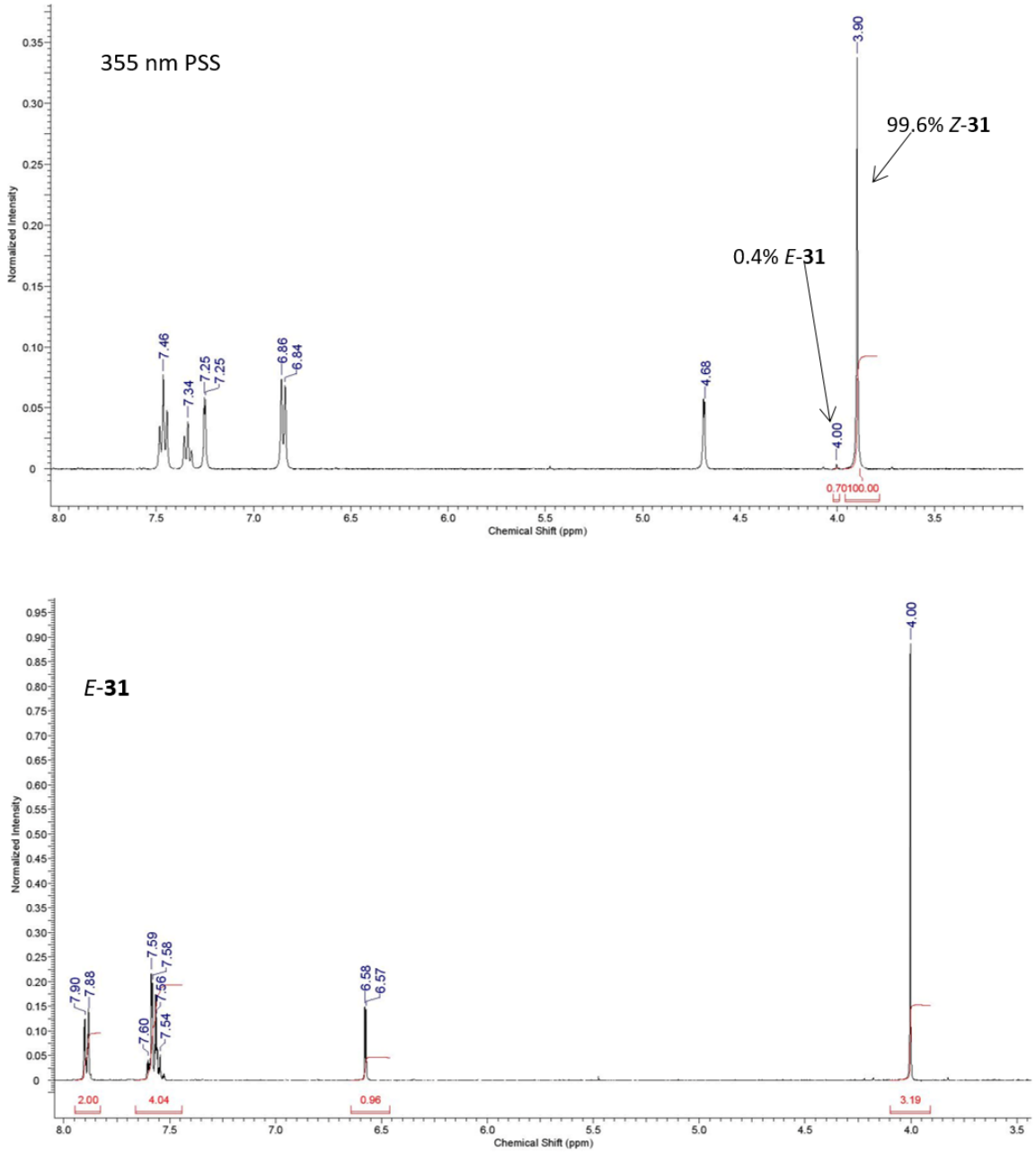


Figure 7.6. ^{1}H NMR of the 355 nm PSS of **31** in d_3-MeCN at 5 x 10^{-3} M concentration, with a reference spectrum to show *E*-isomer peaks.

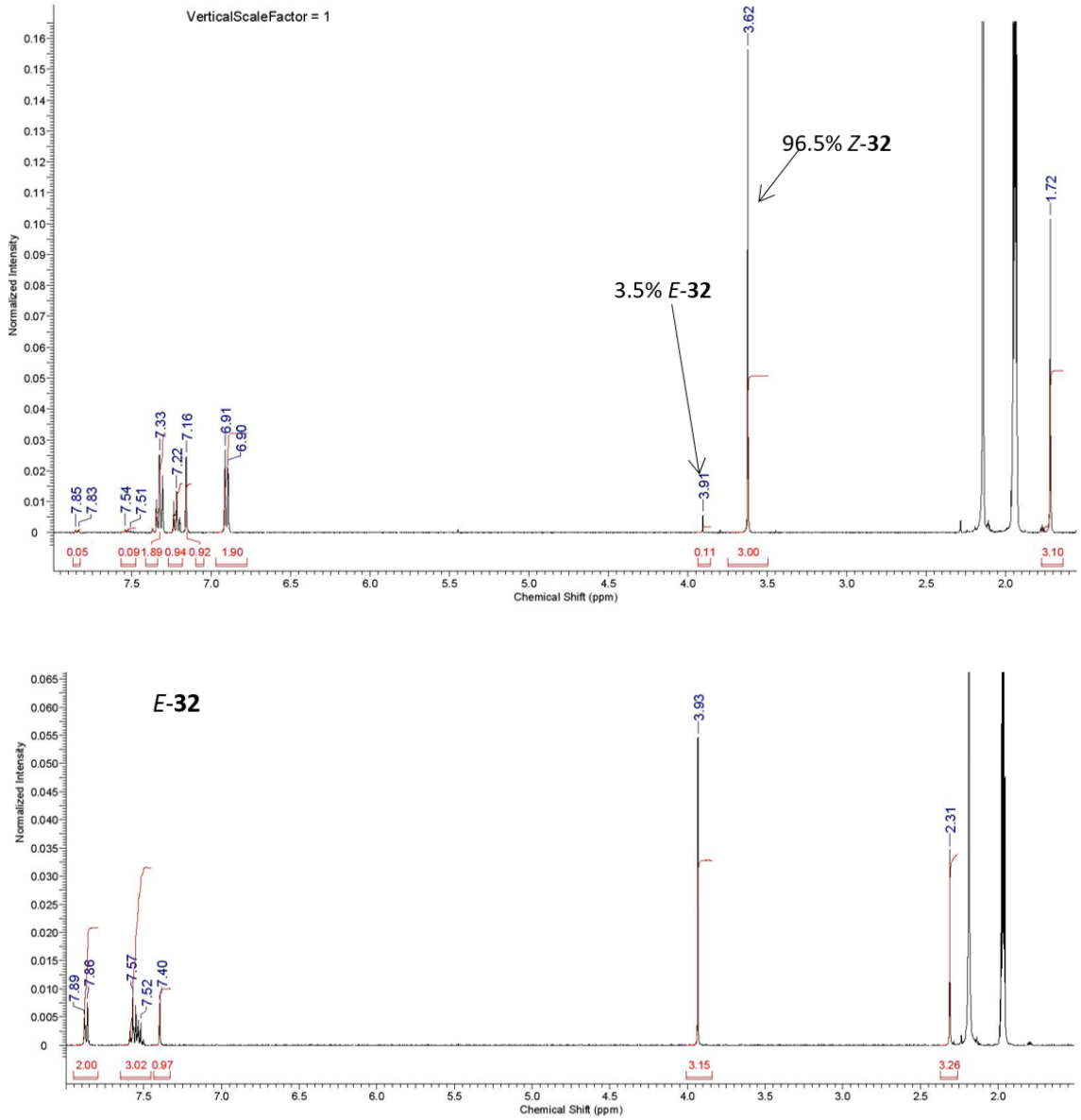


Figure 7.7. ^{1}H NMR of the 355 nm PSS of **32** in d_3-MeCN at 4.6 x 10^{-3} M concentration, with a reference spectrum to show *E*-isomer peaks.

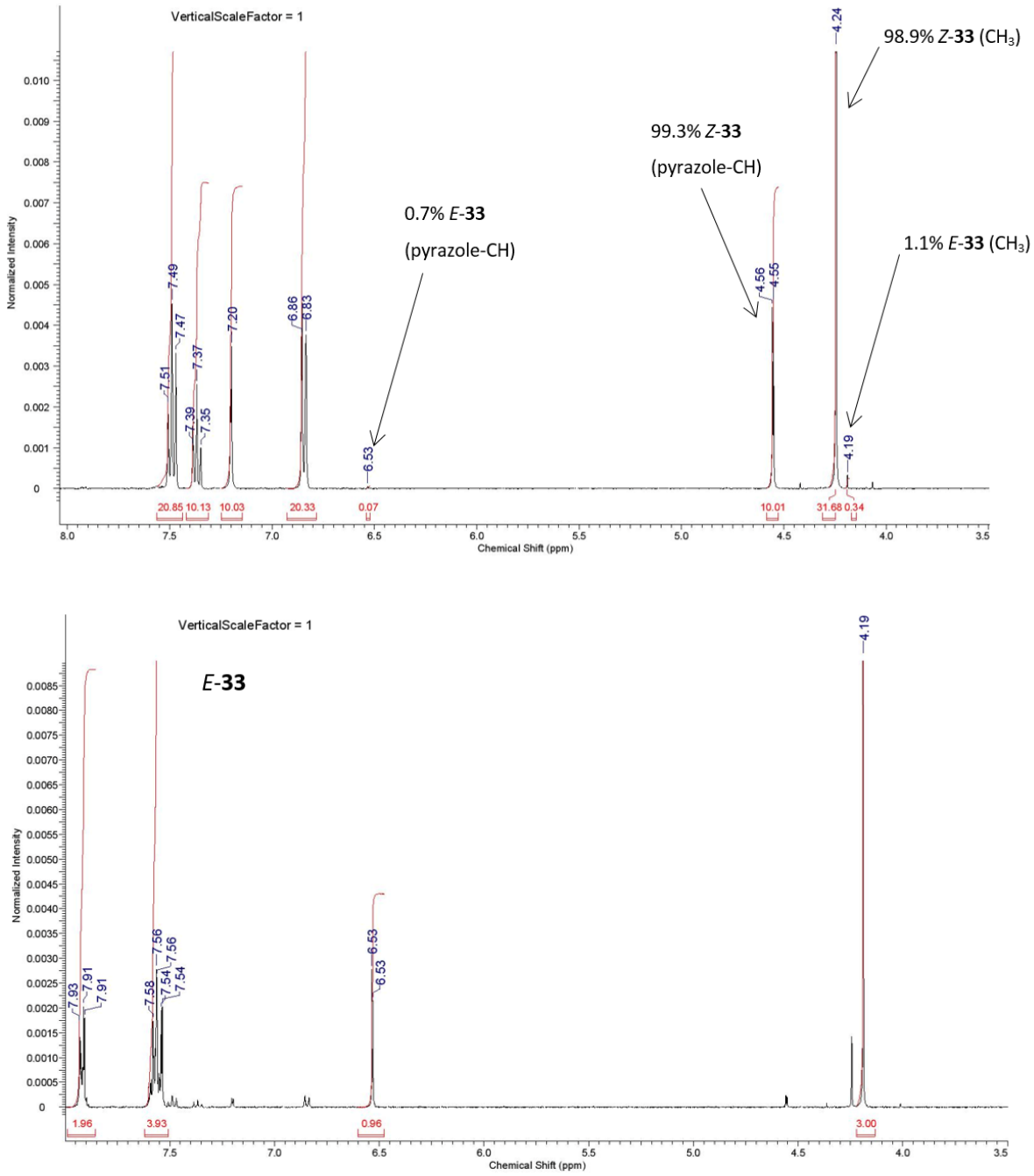


Figure 7.8. ^{1}H NMR of the 355 nm PSS of **33** in d_3-MeCN at 5.4 x 10^{-3} M concentration, with a reference spectrum to show *E*-isomer peaks. Due to the closeness in methyl shifts for the *E* and *Z* isomer, the pyrazole-CH peak was also integrated.

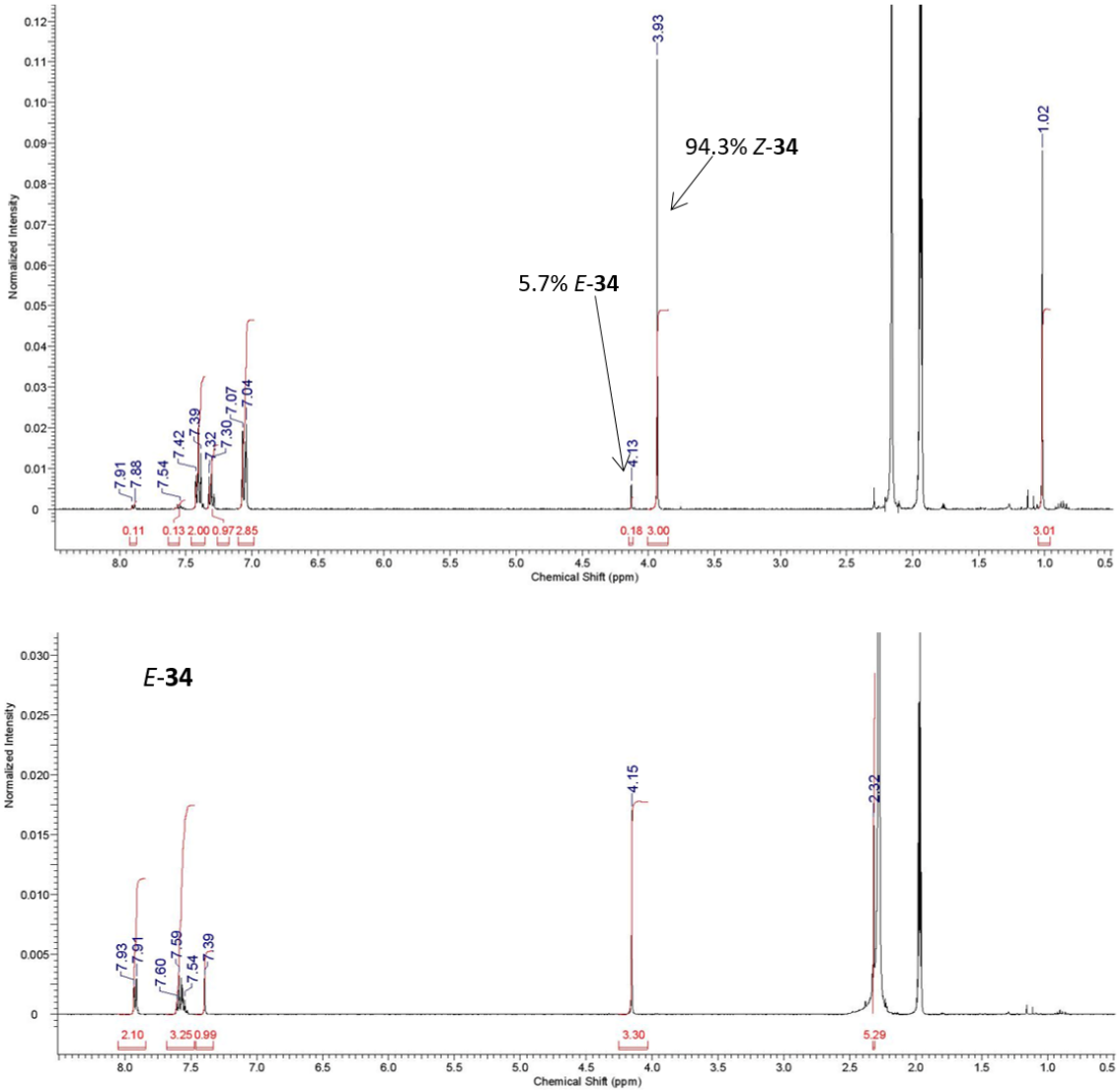


Figure 7.9. ^{1}H NMR of the 355 nm PSS of **34** in d_3-MeCN at 6.5 x 10^{-3} M concentration, with a reference spectrum to show *E*-isomer peaks.

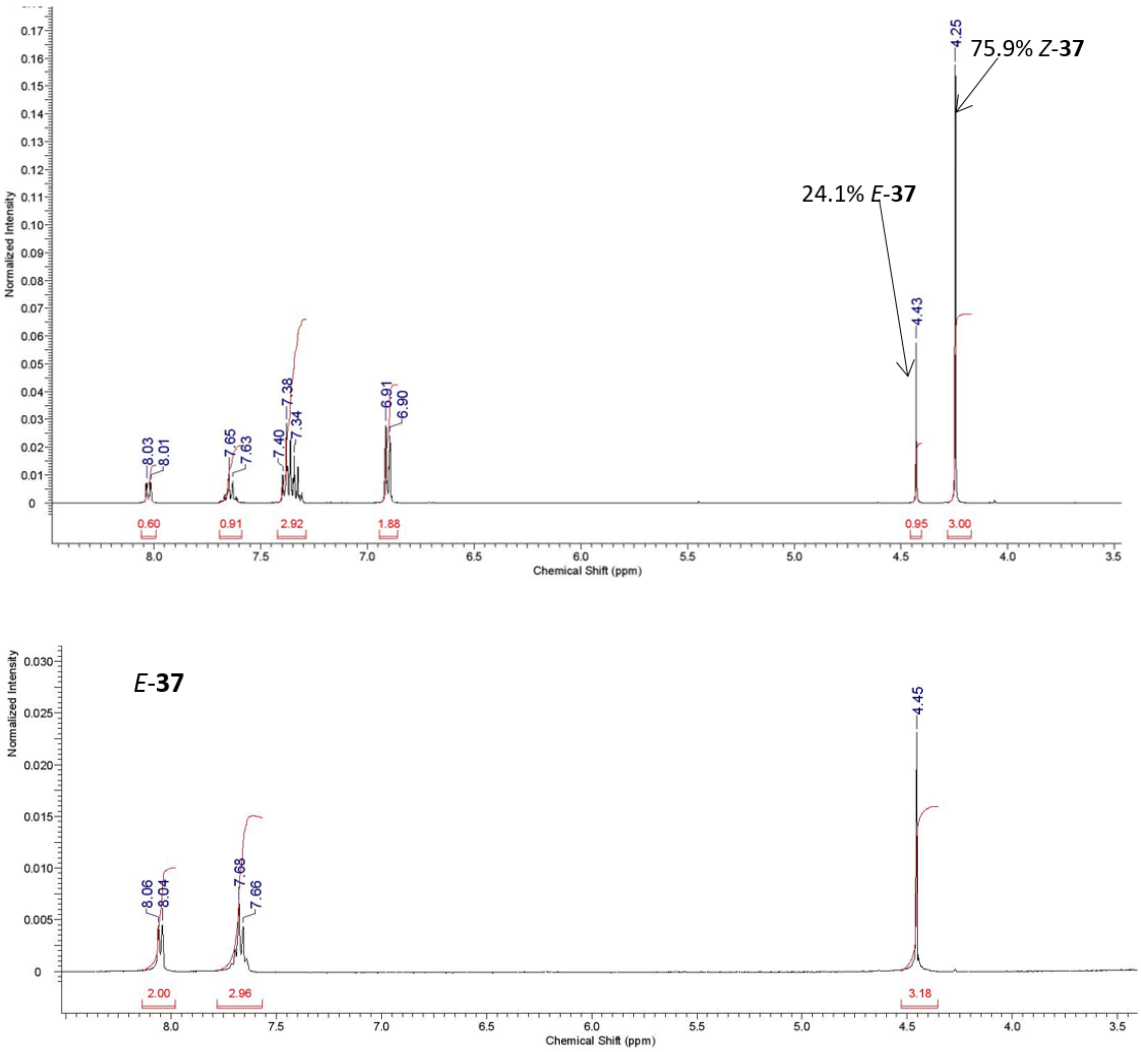


Figure 7.10. ^{1}H NMR of the 355 nm PSS of **37** in d_3-MeCN at 7.4 x 10^{-3} M concentration, with a reference spectrum to show *E*-isomer peaks.

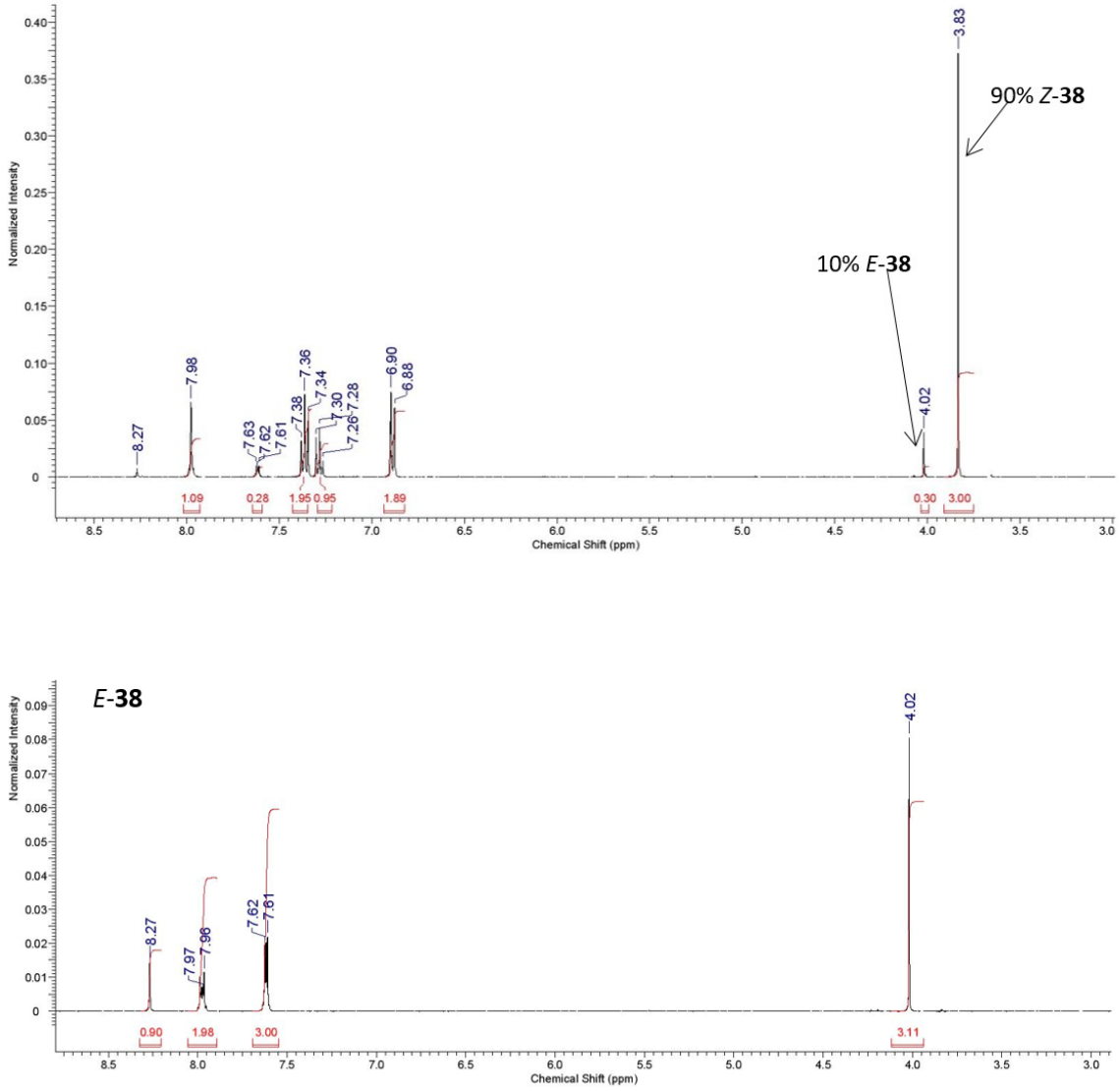


Figure 7.11. ^{1}H NMR of the 355 nm PSS of **38** in d_3-MeCN at 6.4 x 10^{-3} M concentration, with a reference spectrum to show *E*-isomer peaks.

Photostationary states following broadband irradiation

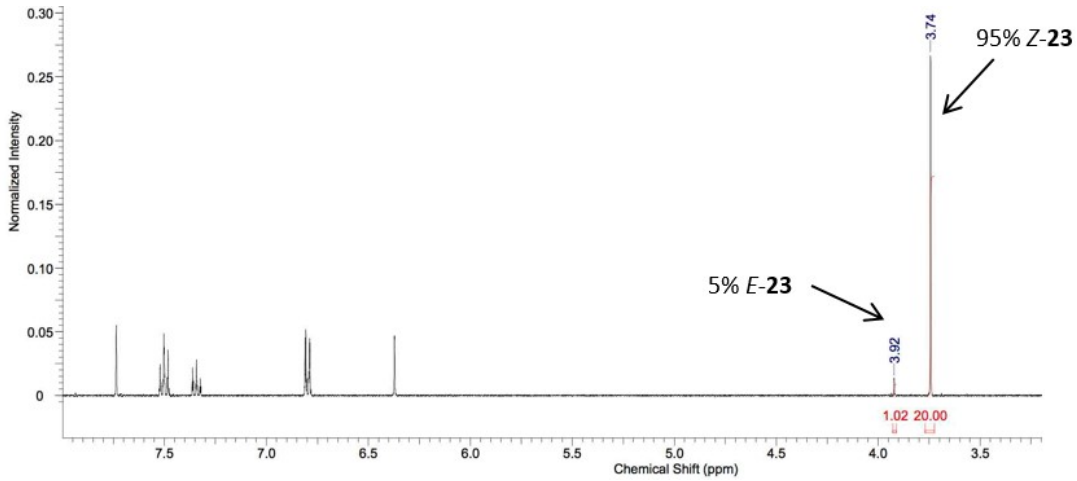


Figure 7.12. PSS of **23** in d_3-MeCN using broadband UVA light with a 330-620 nm filter, containing 95% *Z*-**23.**

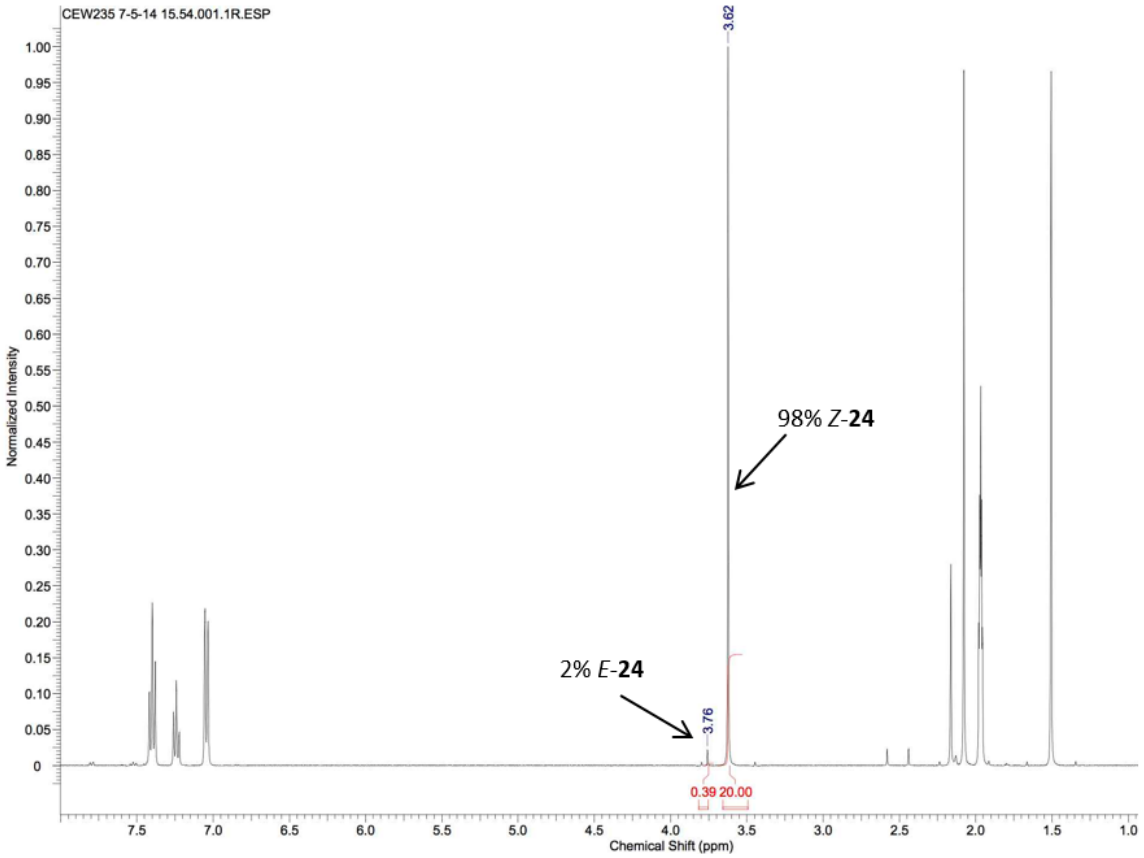


Figure 7.13. PSS of **24** in d_3-MeCN using broadband UVA light with a 330-620 nm filter, containing 98% *Z*-**24.**

Estimation of PSS composition by UV/vis for fast thermally isomerising compounds

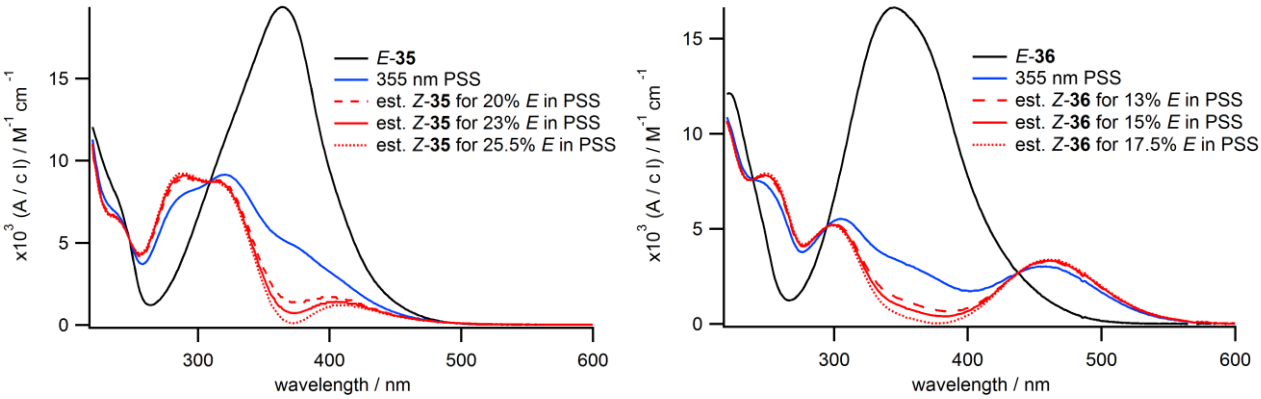


Figure 7.14. Estimating the pure *Z*-spectrum of **35** and **36**.

UV/vis spectra

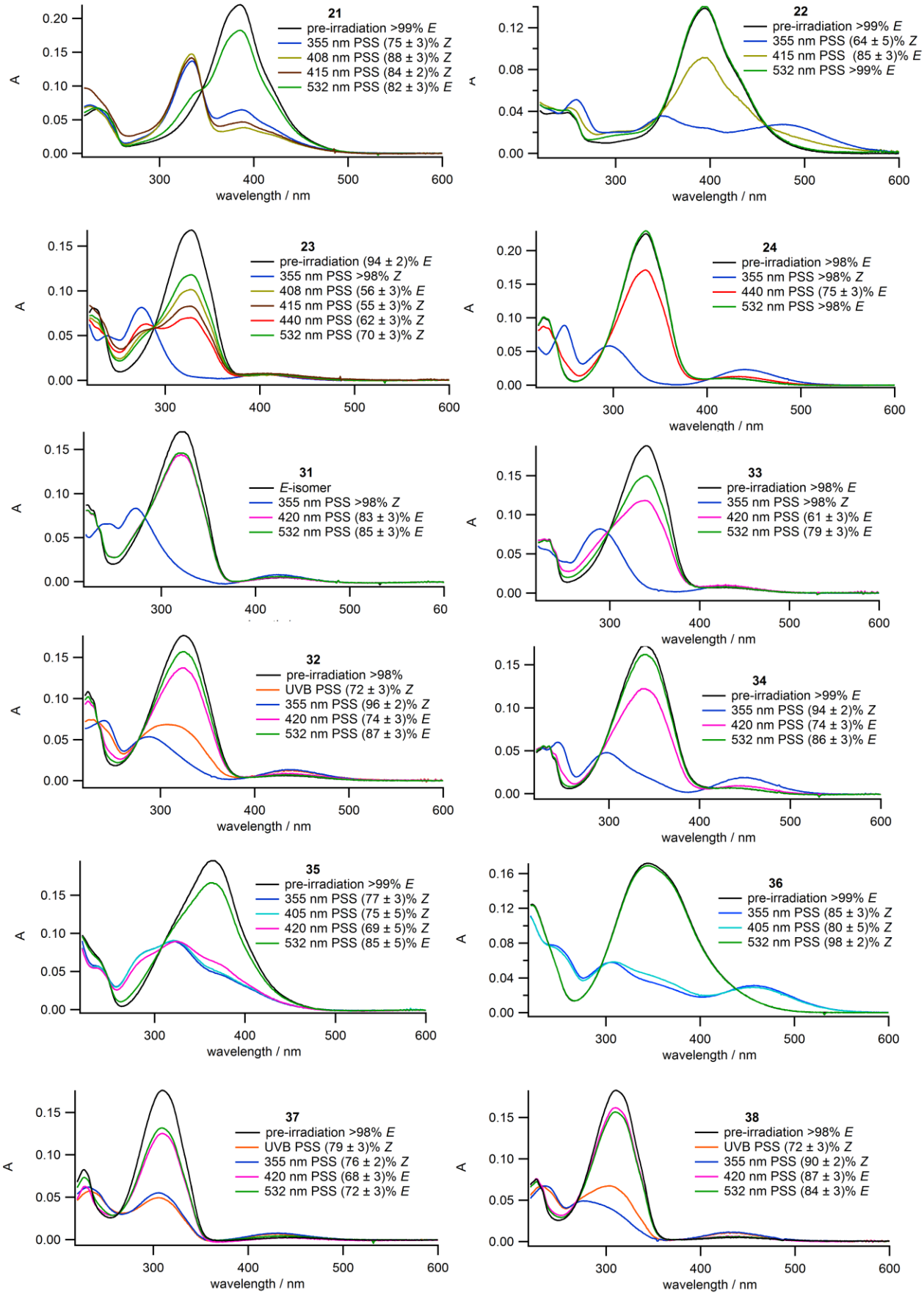


Figure 7.15. PSS of photoswitches at several different irradiation wavelengths.

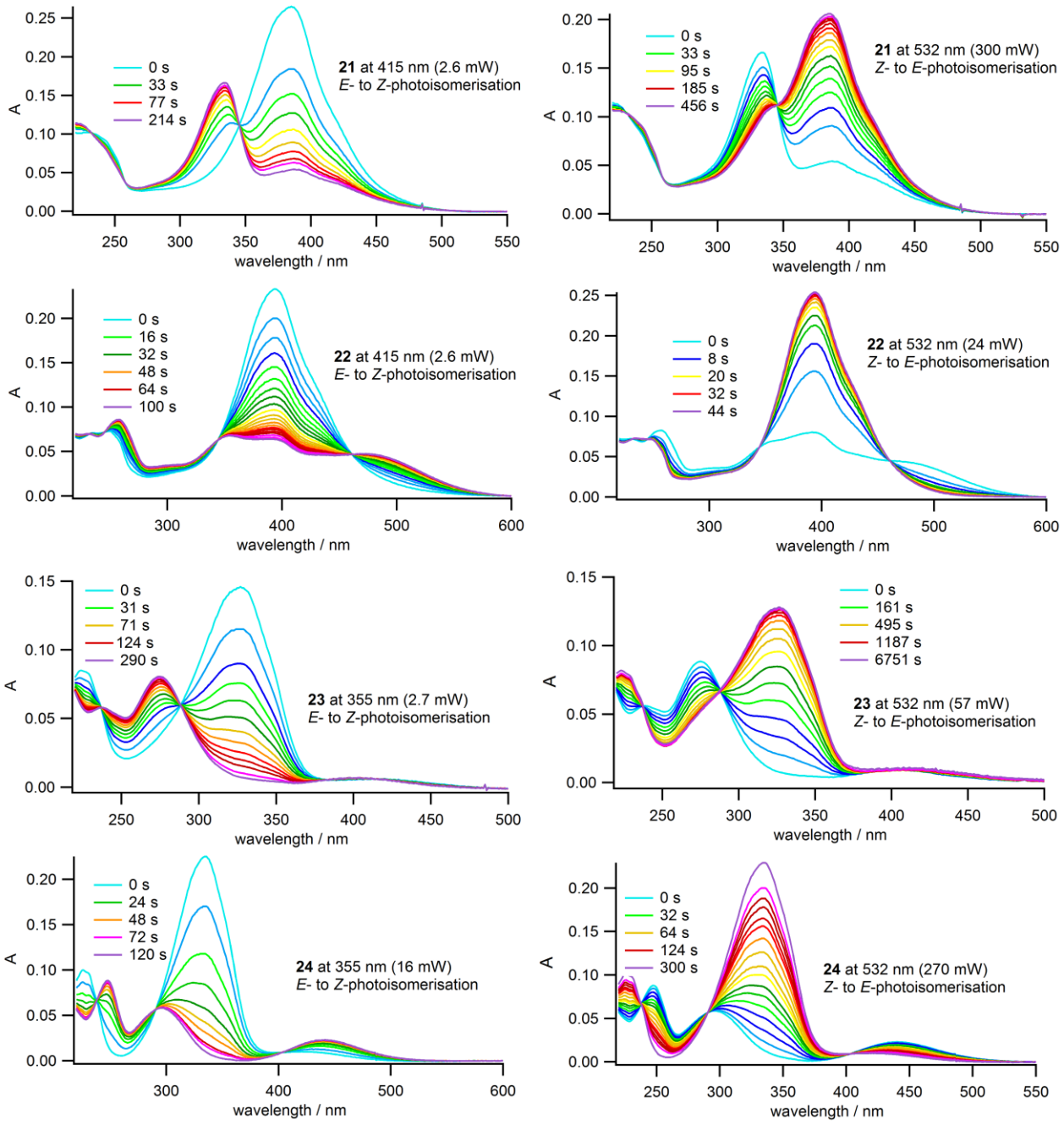


Figure 7.16. Time-resolved UV/vis spectra for photoisomerisation of **21**-**24** used for quantum yield calculations.

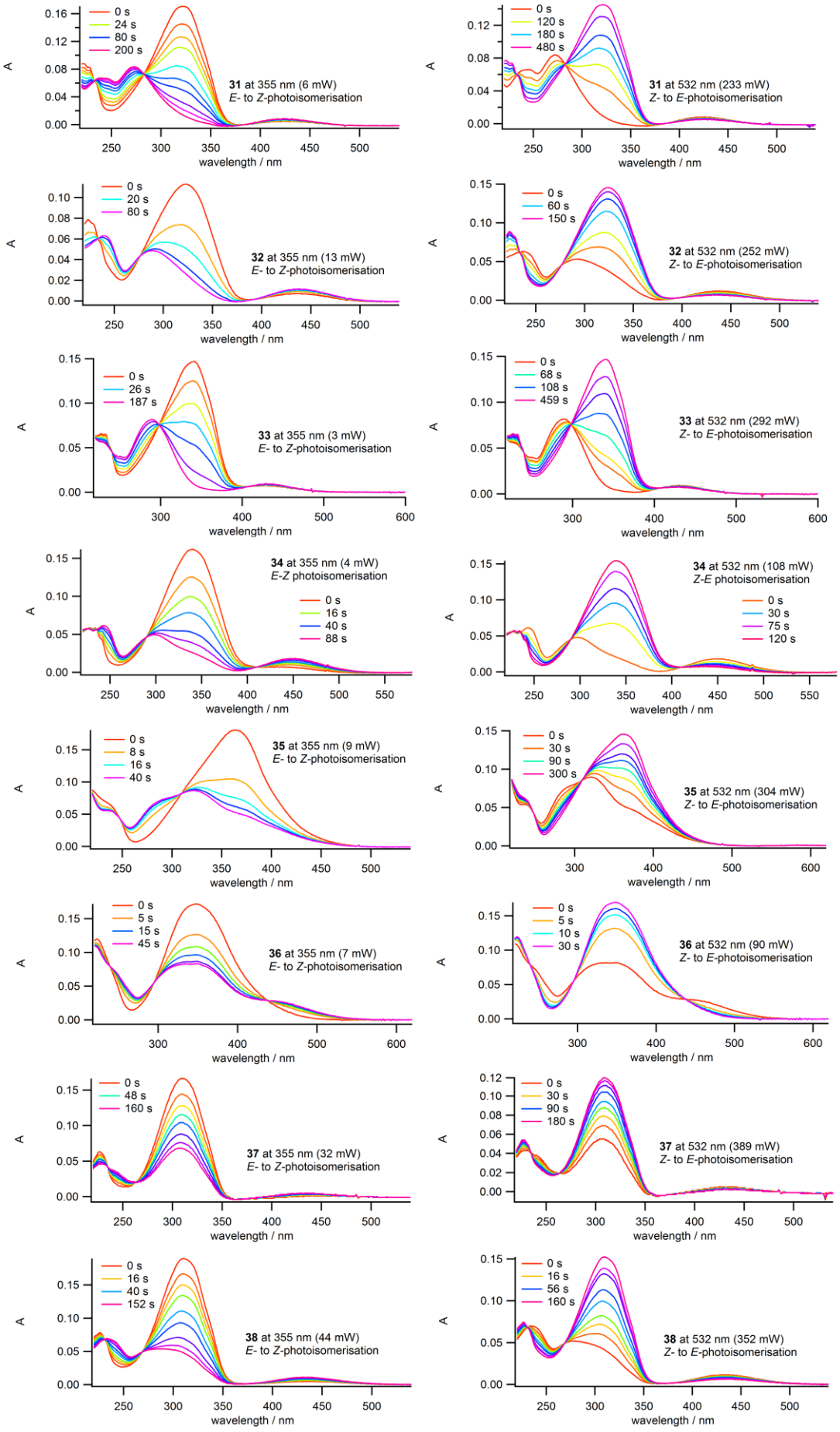


Figure 7.17. Time-resolved UV/vis spectra for photoisomerisation of **31**-**38**.

Photoisomerisation kinetics

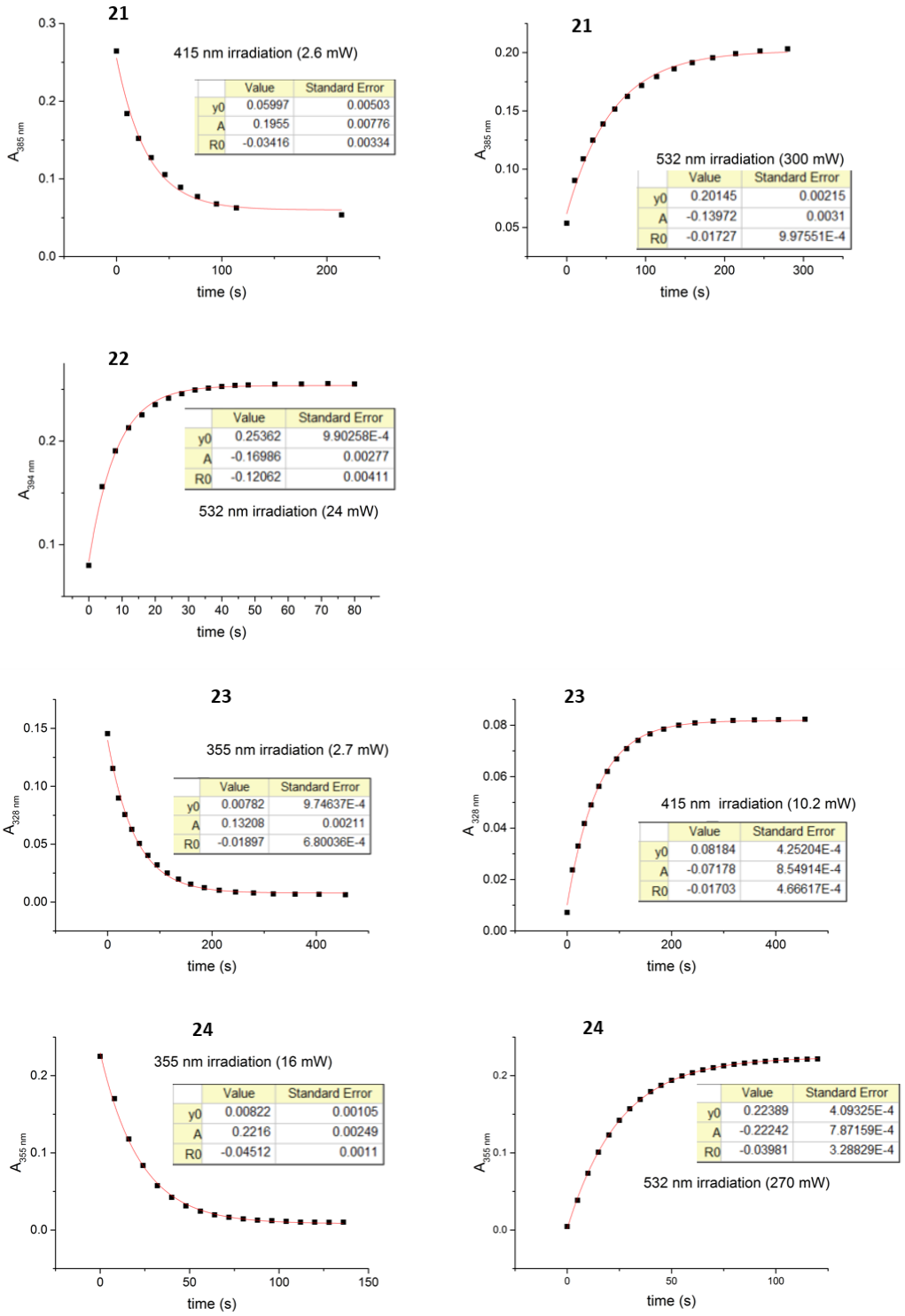


Figure 7.18. Kinetics for photoisomerisation in acetonitrile, used for quantum yield calculations.

Thermal isomerisation kinetics

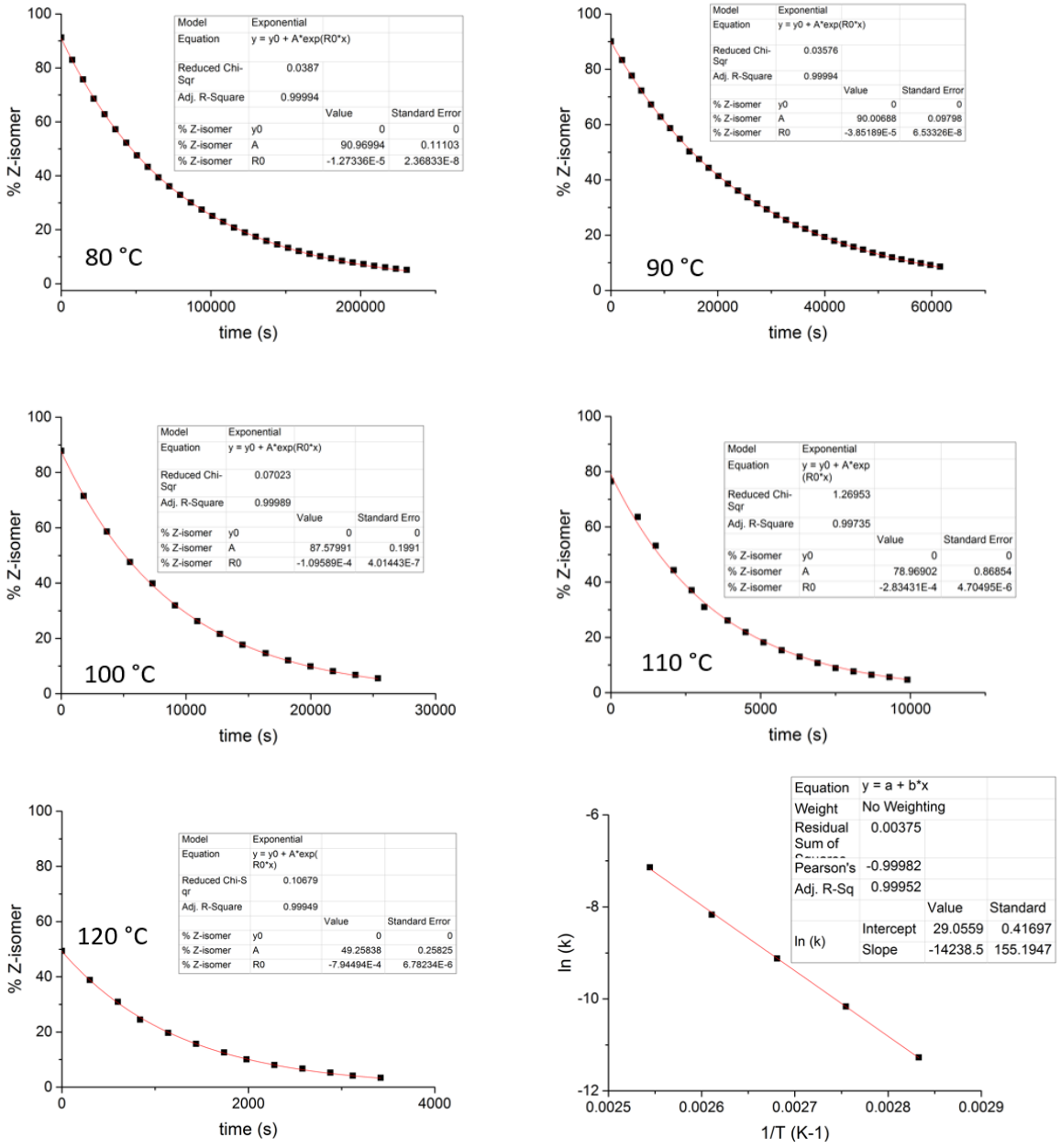


Figure 7.19.Thermal isomerisation of **23** at a range of temperatures in d_6-DMSO and Eyring plot.

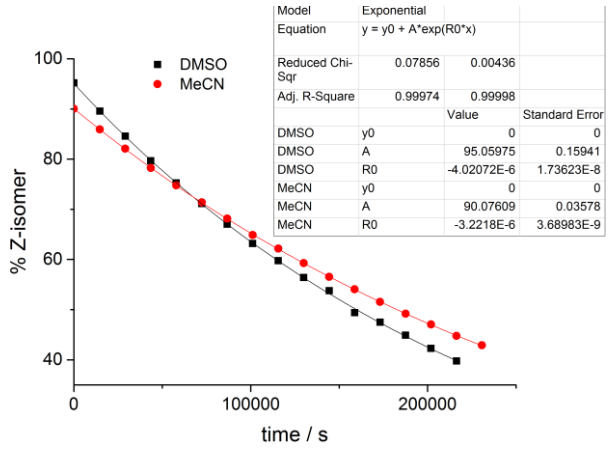


Figure 7.20. Thermal isomerisation of **23** at 70 °C in d_6-DMSO and d_3-acetonitrile, to allow comparison between the two solvents.

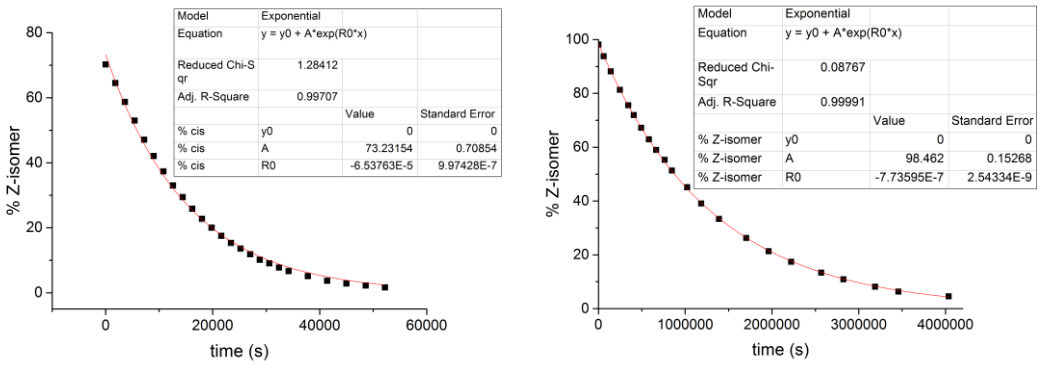


Figure 7.21. Thermal isomerisation of **21** (left) and **24** (right) in d_3-acetonitrile at 25 °C, monitored by NMR.

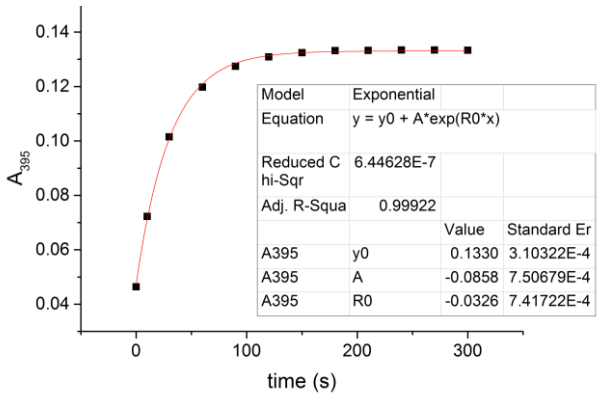


Figure 7.22. Thermal isomerisation of **22** in acetonitrile at 25 °C, monitored by UV/vis spectroscopy.

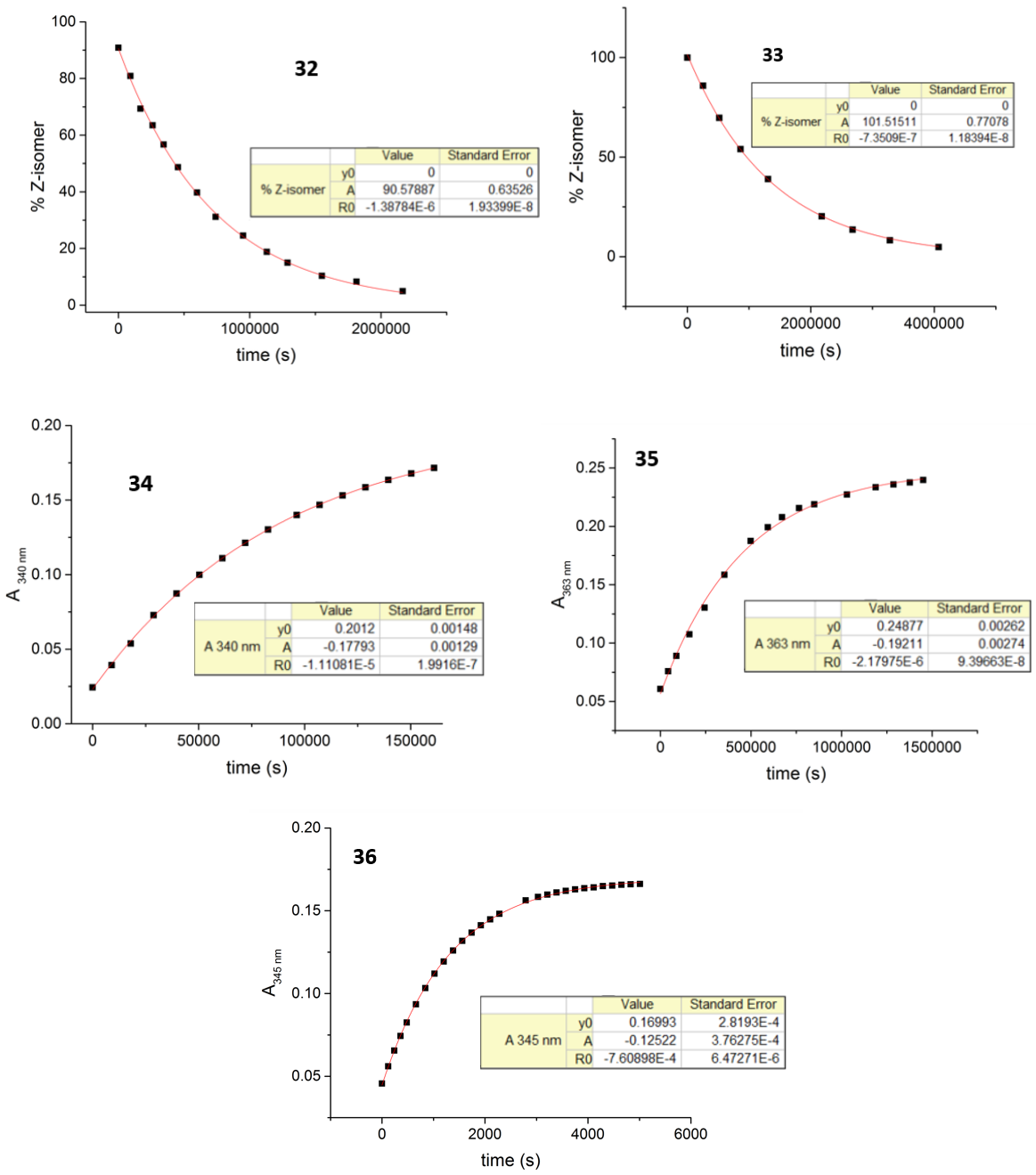


Figure 7.23. Thermal isomerisation of **32**-**36** in acetonitrile at 25 °C.

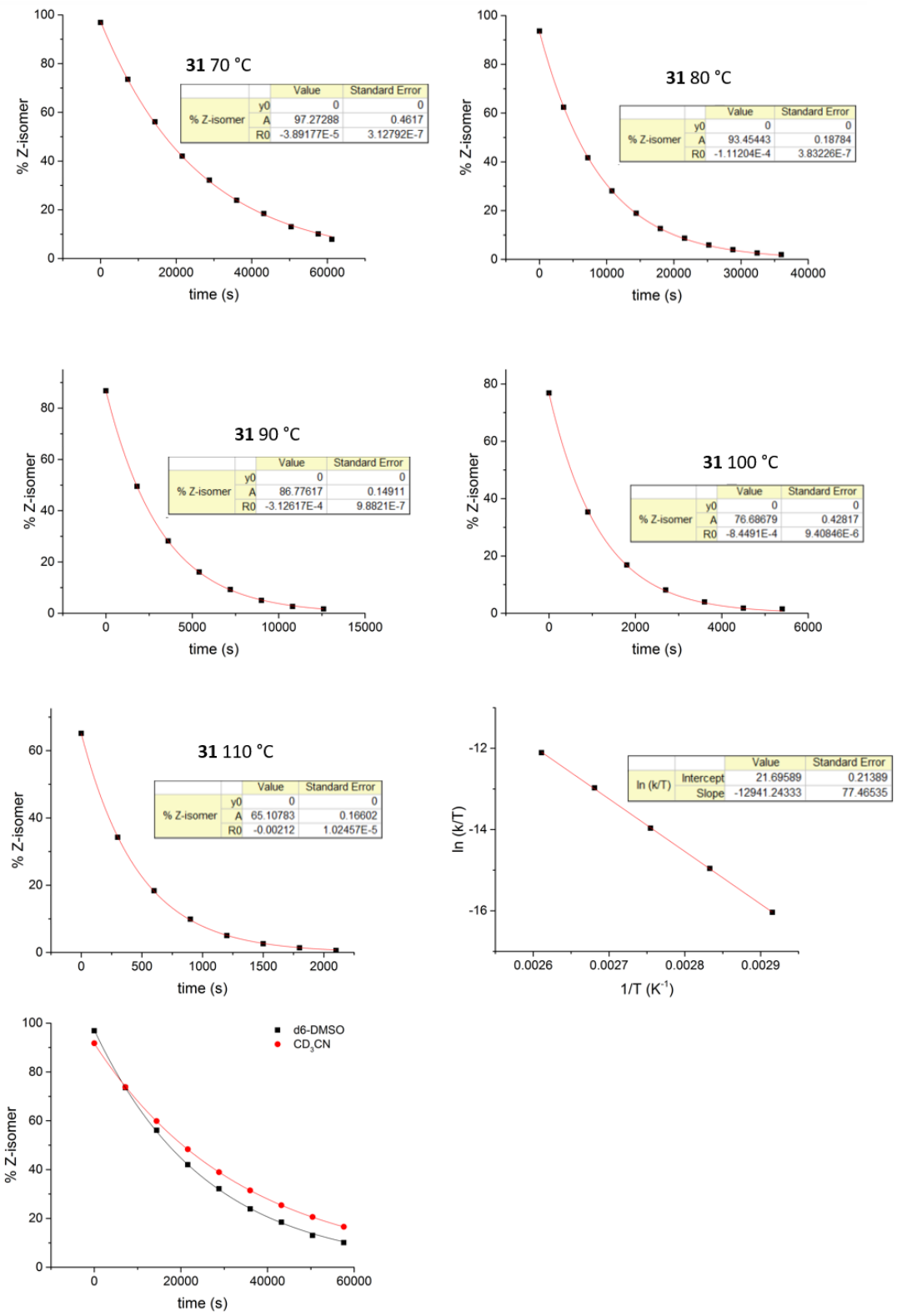


Figure 7.24. Thermal isomerisation of **31** at a range of temperatures in d_6-DMSO and Eyring plot, and comparison of rates in d_6-DMSO and d_3-MeCN at 70 °C.

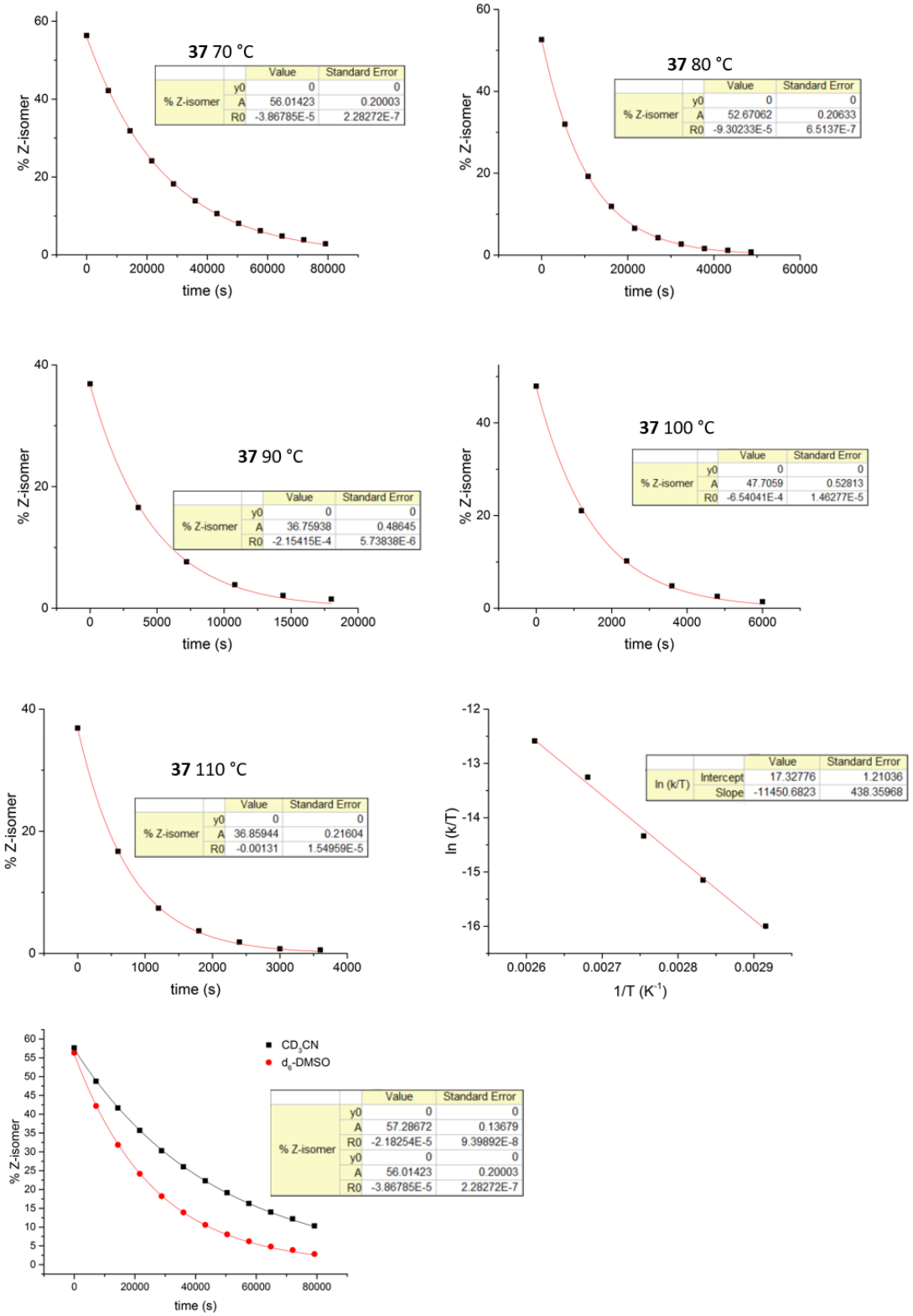


Figure 7.25. Thermal isomerisation of **37** at a range of temperatures in *d*$_6$-DMSO and Eyring plot, and comparison of rates in *d*$_6$-DMSO and *d*$_3$-MeCN at 70 °C.

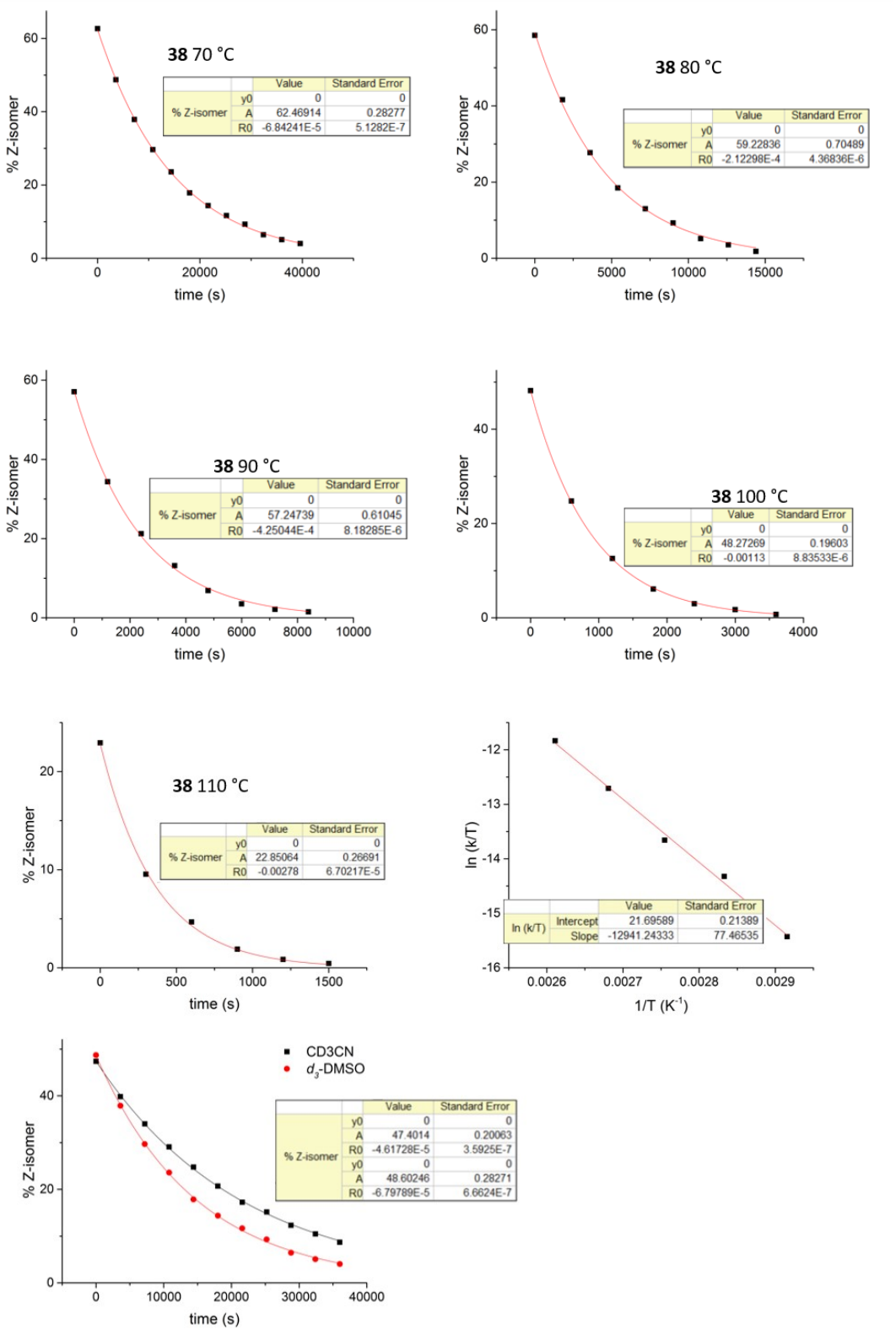


Figure 7.26. Thermal isomerisation of **38** at a range of temperatures in d_6-DMSO and Eyring plot, and comparison of rates in d_6-DMSO and d_3-MeCN at 70 °C.

7.3.2 Photoswitchable HDAC inhibitors

Quantification of PSS composition by NMR

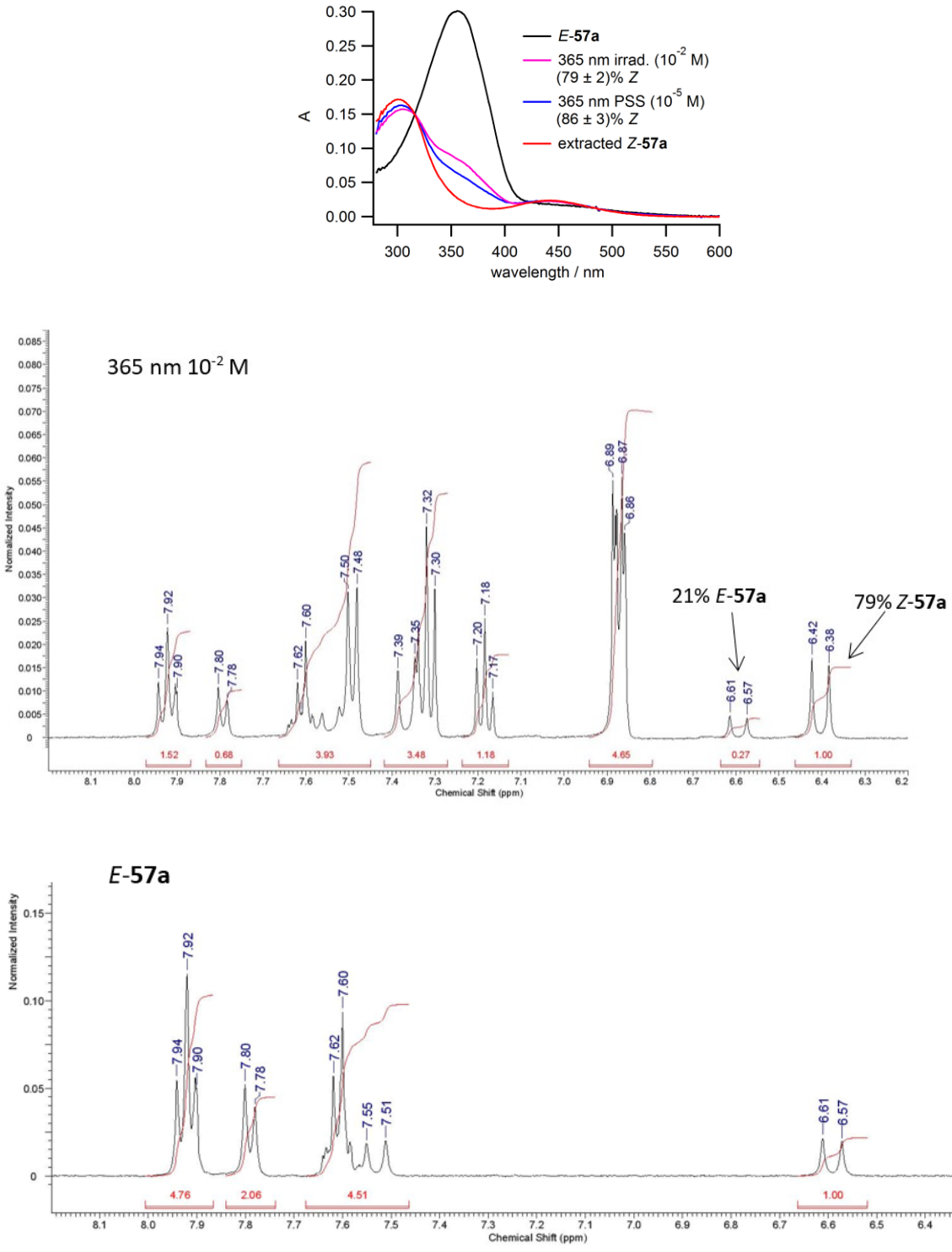


Figure 7.27. Top) UV/vis spectra of *E*-**57a**, the 365 nm PSS at 10^{-5} M, and the spectrum following 365 nm irradiation at 10^{-2} M (PSS not reached); Middle) ^{1}H NMR of **57a** in d_6-DMSO at ~10^{-2} M concentration after 365 nm irradiation; Bottom) Reference spectrum to show *E*-isomer peaks.

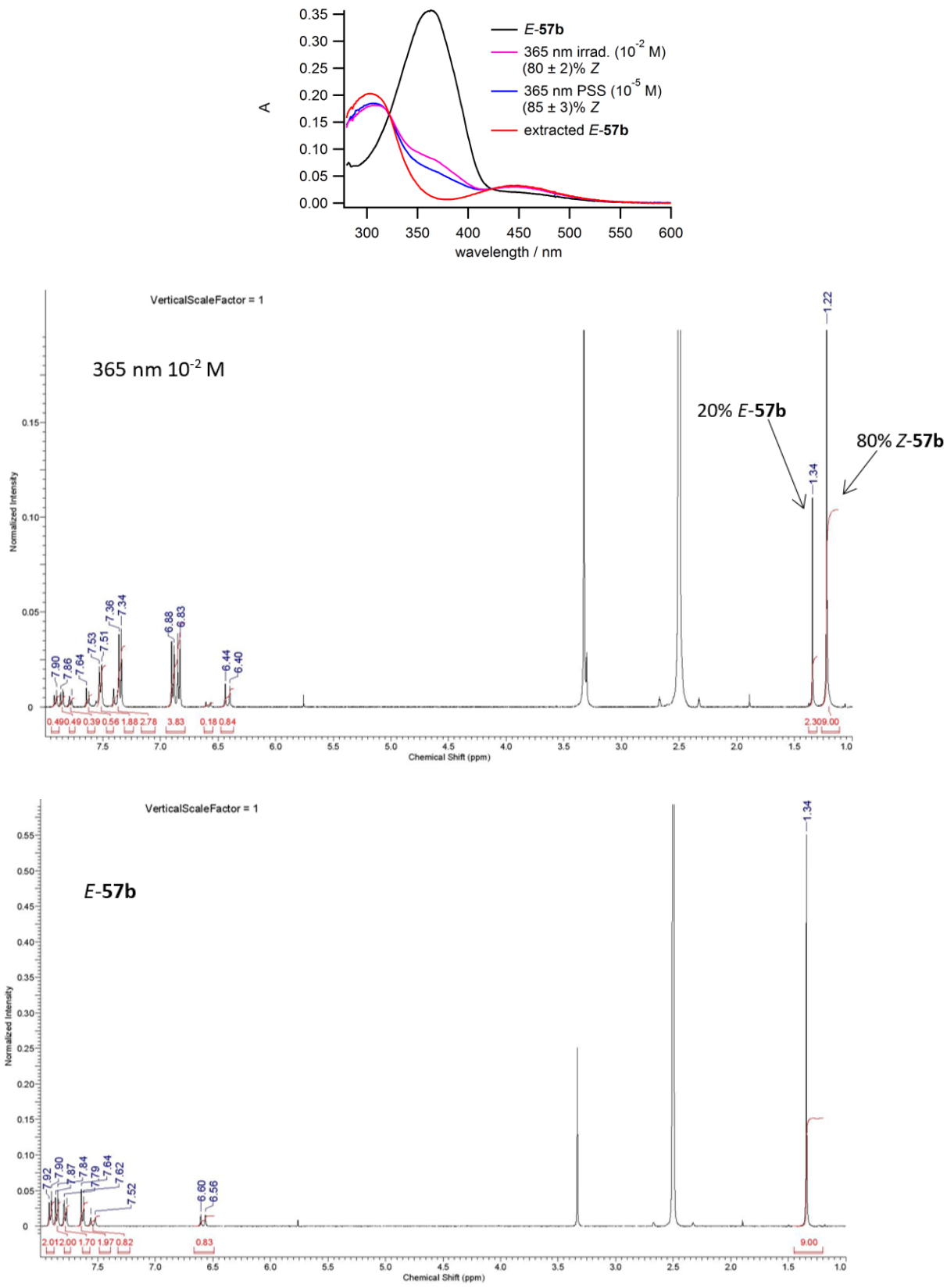


Figure 7.28. Top) UV/vis spectra of *E*-**57b**, the 365 nm PSS at 10^{-5} M, and the spectrum following 365 nm irradiation at 10^{-2} M (PSS not reached); Middle) ^{1}H NMR of **57b** in d_6-DMSO at ~10^{-2} M concentration after 365 nm irradiation; Bottom) Reference spectrum to show *E*-isomer peaks.

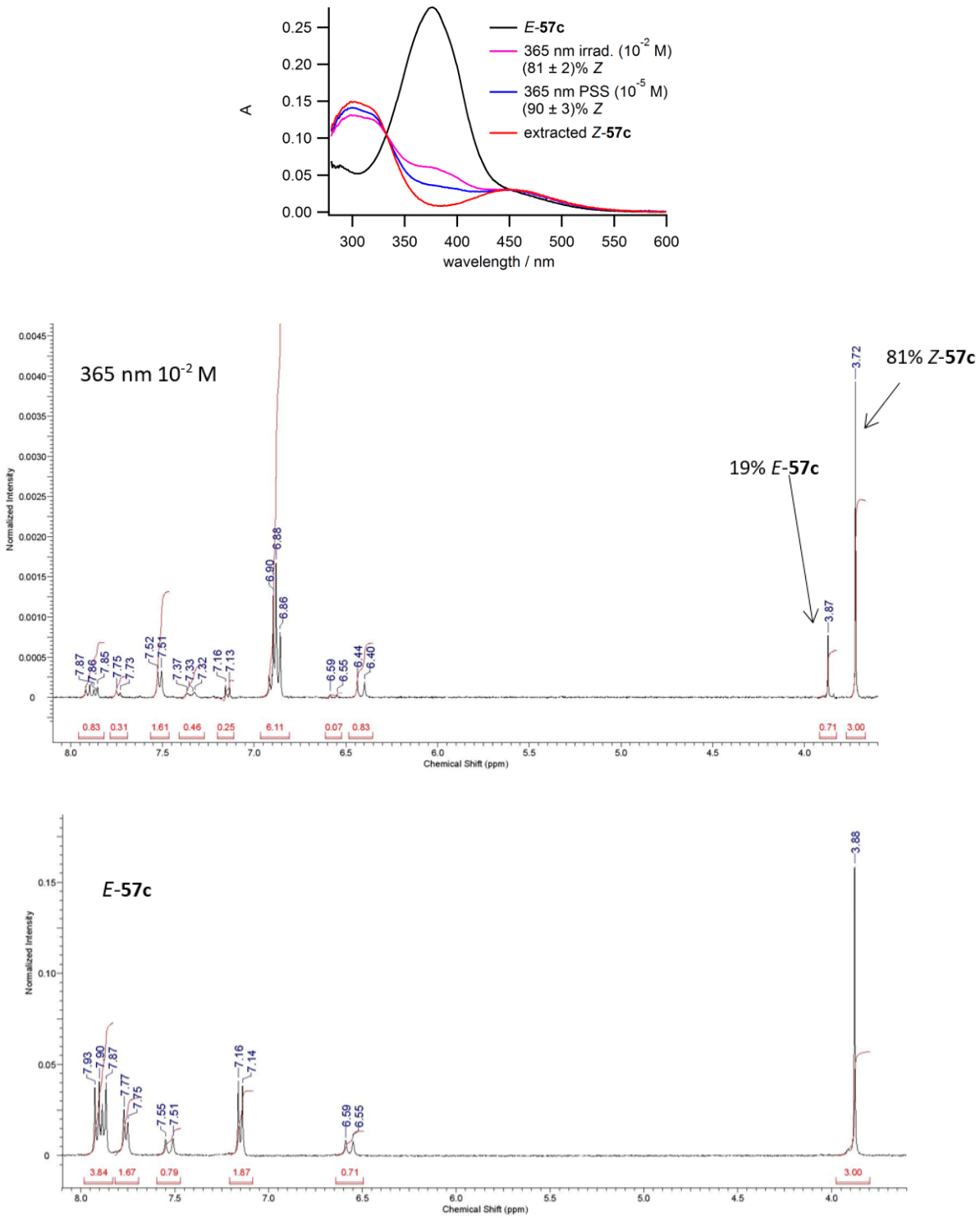


Figure 7.29. Top) UV/vis spectra of *E*-**57c**, the 365 nm PSS at 10^{-5} M, and the spectrum following 365 nm irradiation at 10^{-2} M (PSS not reached); Middle) ^{1}H NMR of **57c** in d_6-DMSO at ~10^{-2} M concentration after 365 nm irradiation; Bottom) Reference spectrum to show *E*-isomer peaks.

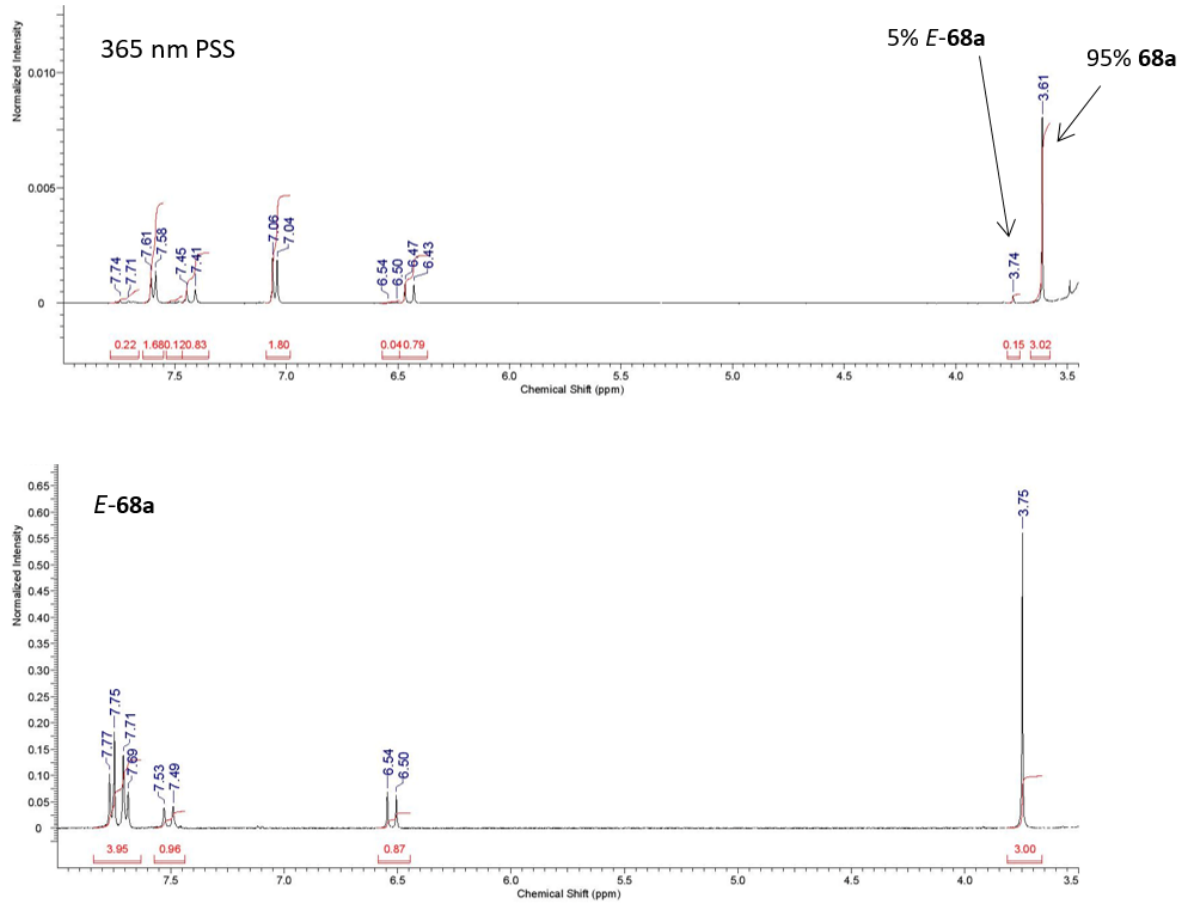


Figure 7.30. ^{1}H NMR of the 365 nm PSS of **68a** in d_6-DMSO at ~10^{-2} M concentration, with a reference spectrum to show *E*-isomer peaks.

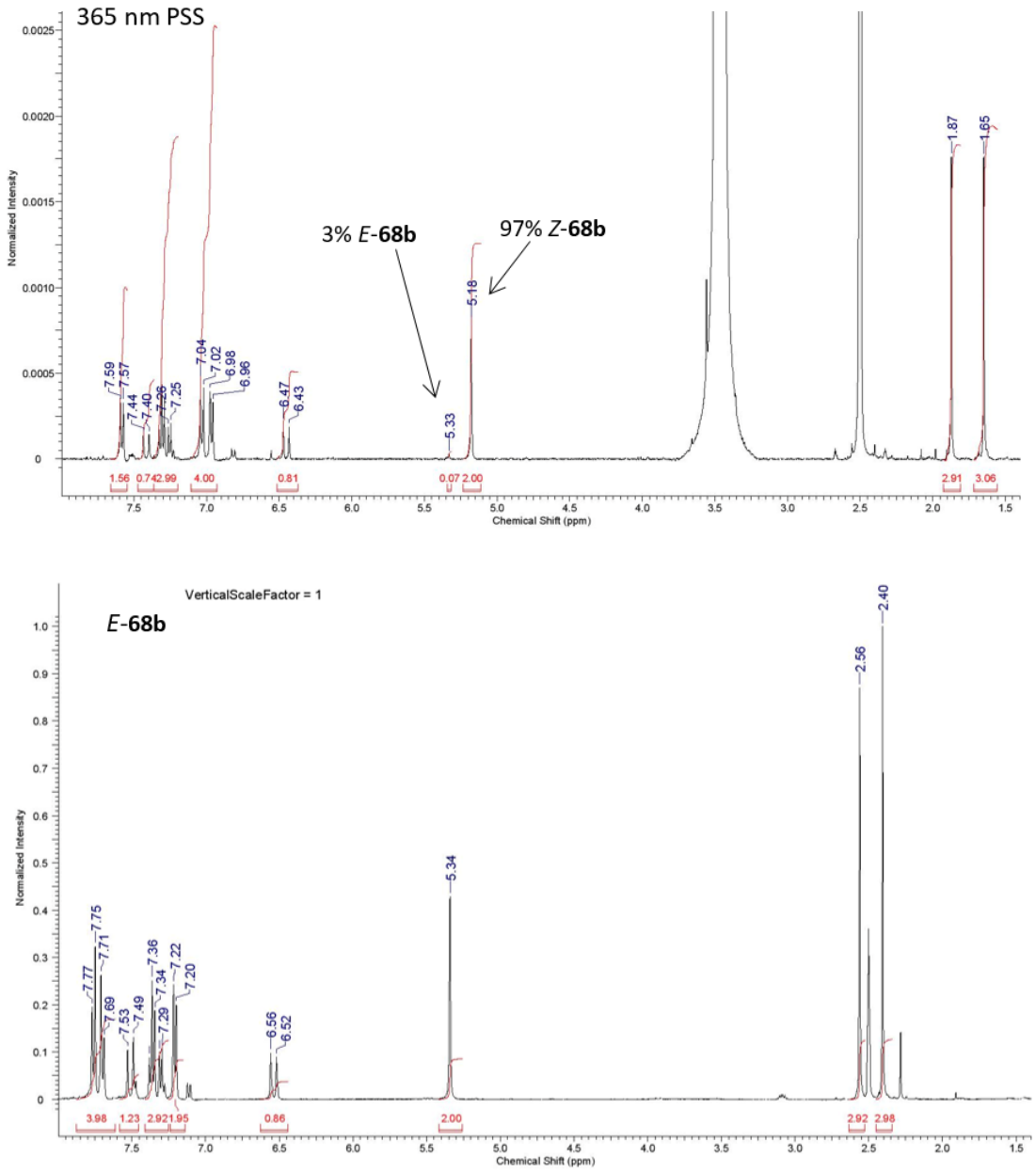


Figure 7.31. ^{1}H NMR of the 365 nm PSS of **68b** in d_6-DMSO at ~10^{-2} M concentration, with a reference spectrum to show *E*-isomer peaks.

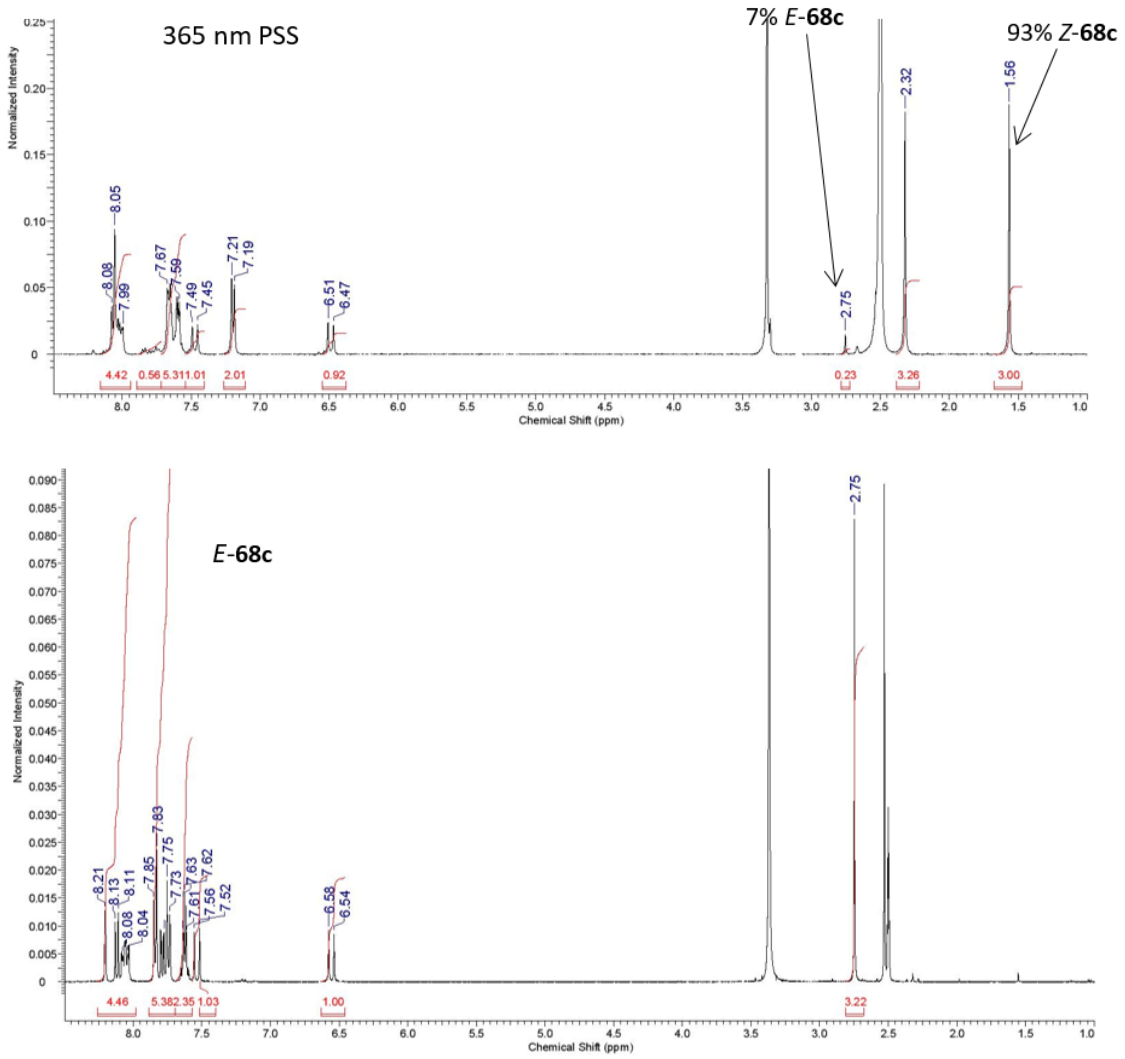


Figure 7.32.[1]H NMR of the 365 nm PSS of **68c** in d_6-DMSO at ~10^{-2} M concentration, with a reference spectrum to show *E*-isomer peaks.

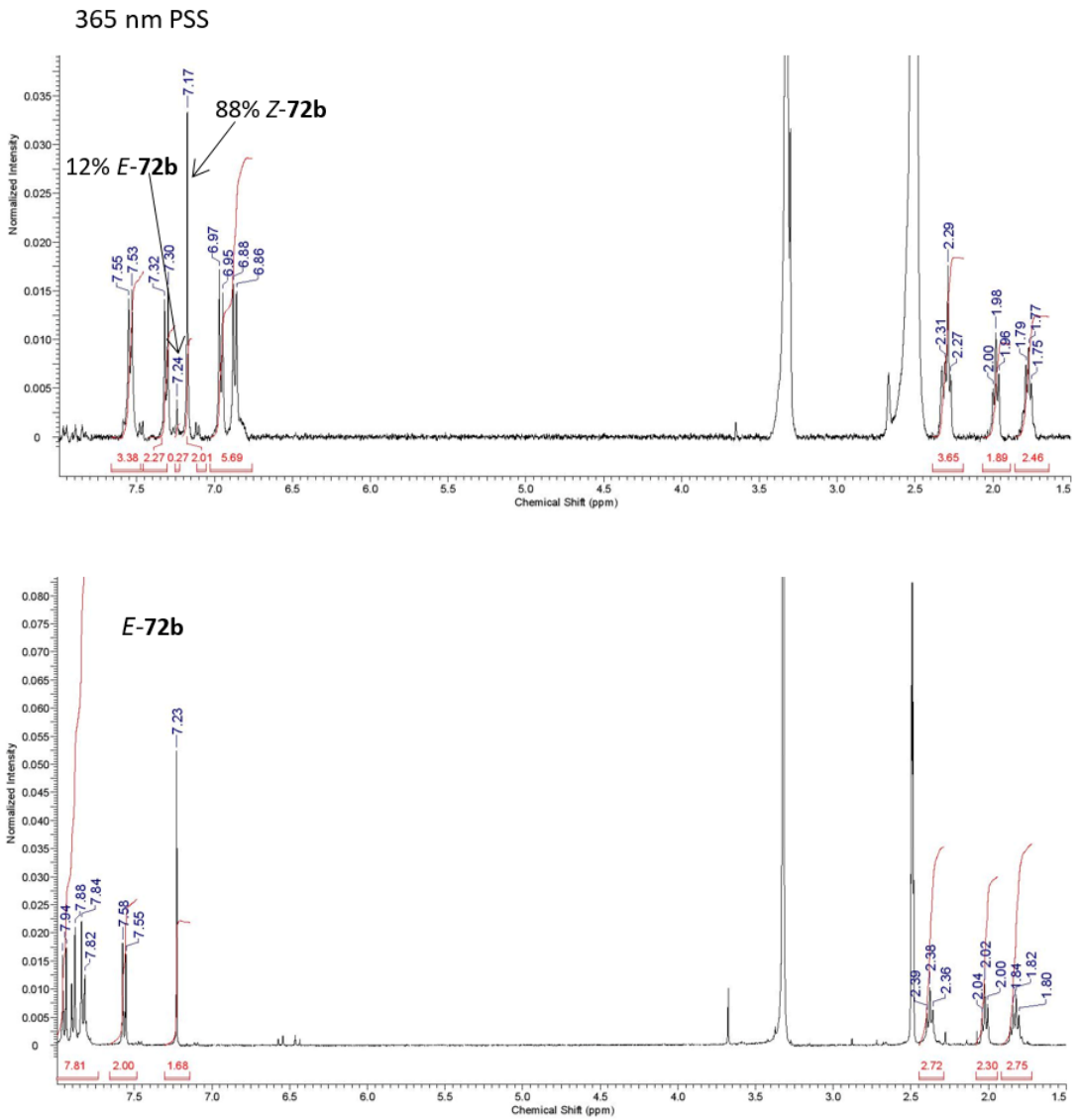


Figure 7.33.[1]H NMR of the 365 nm PSS of **72b** in d_6-DMSO at ~10^{-2} M concentration, with a reference spectrum to show *E*-isomer peaks.

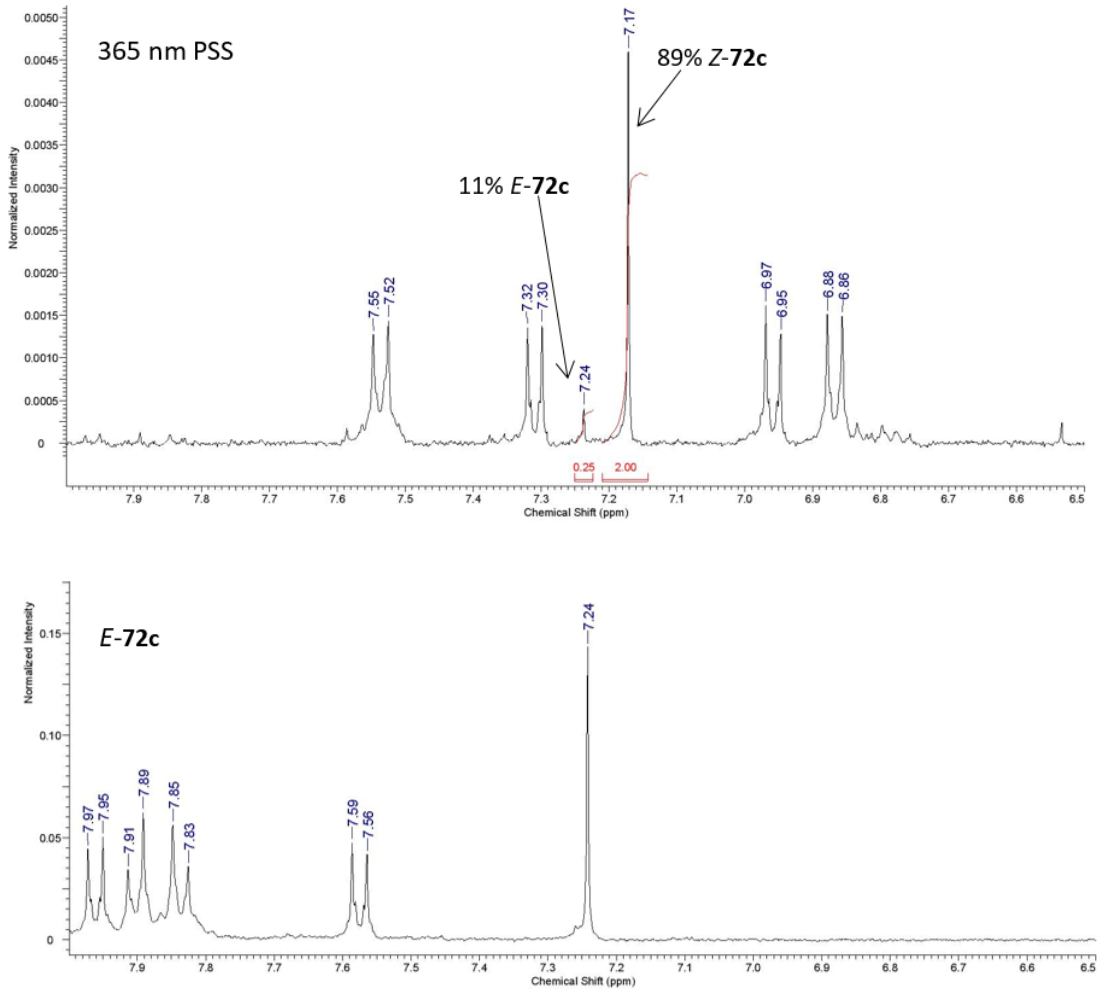


Figure 7.34. ^{1}H NMR of the 365 nm PSS of **72c** in d_6-DMSO at ~10^{-2} M concentration, with a reference spectrum to show *E*-isomer peaks.

Thermal isomerisation kinetics

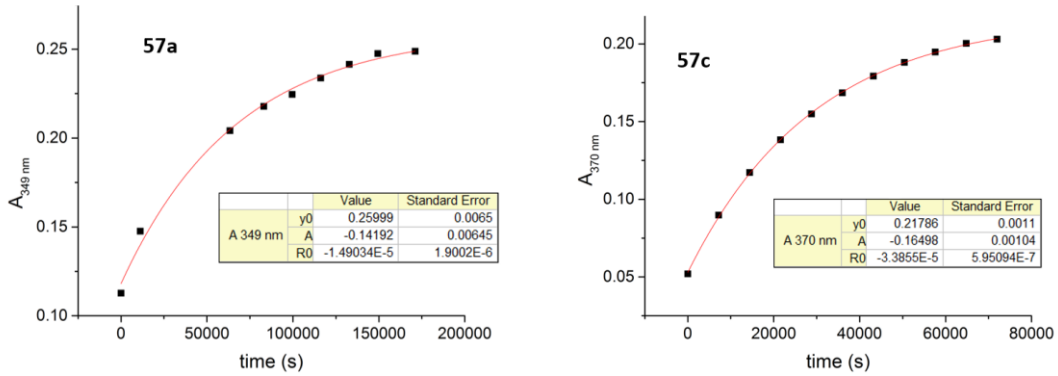


Figure 7.35. Thermal isomerisation rates for azobenzene HDAC inhibitors in aqueous buffer at 30 °C.

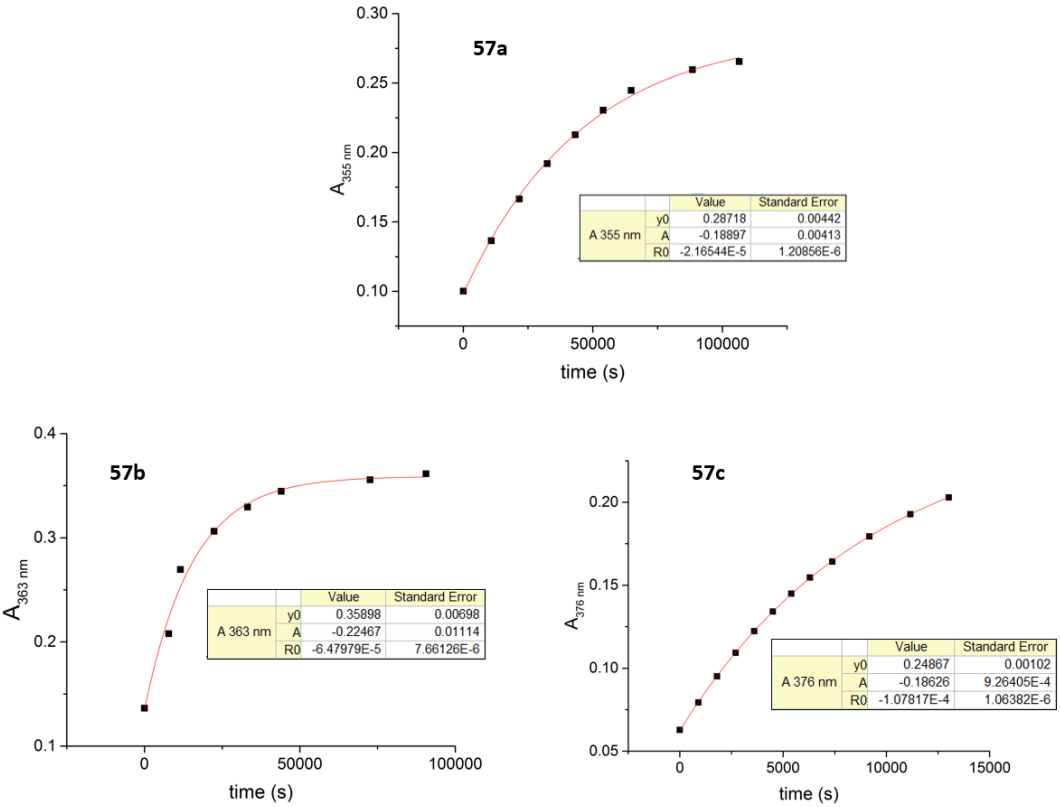


Figure 7.36. Thermal isomerisation rates for azobenzene HDAC inhibitors in DMSO at 30 °C.

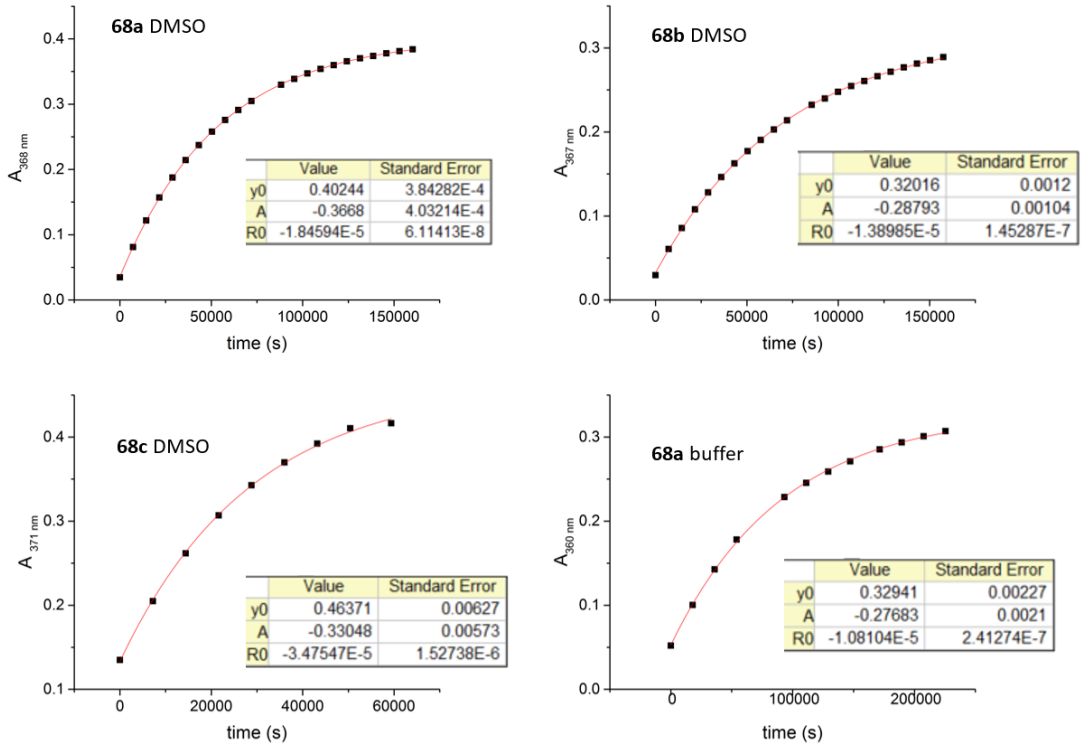


Figure 7.37. Thermal isomerisation rates for pyrazole HDAC inhibitors in DMSO or aqueous buffer at 30 °C.

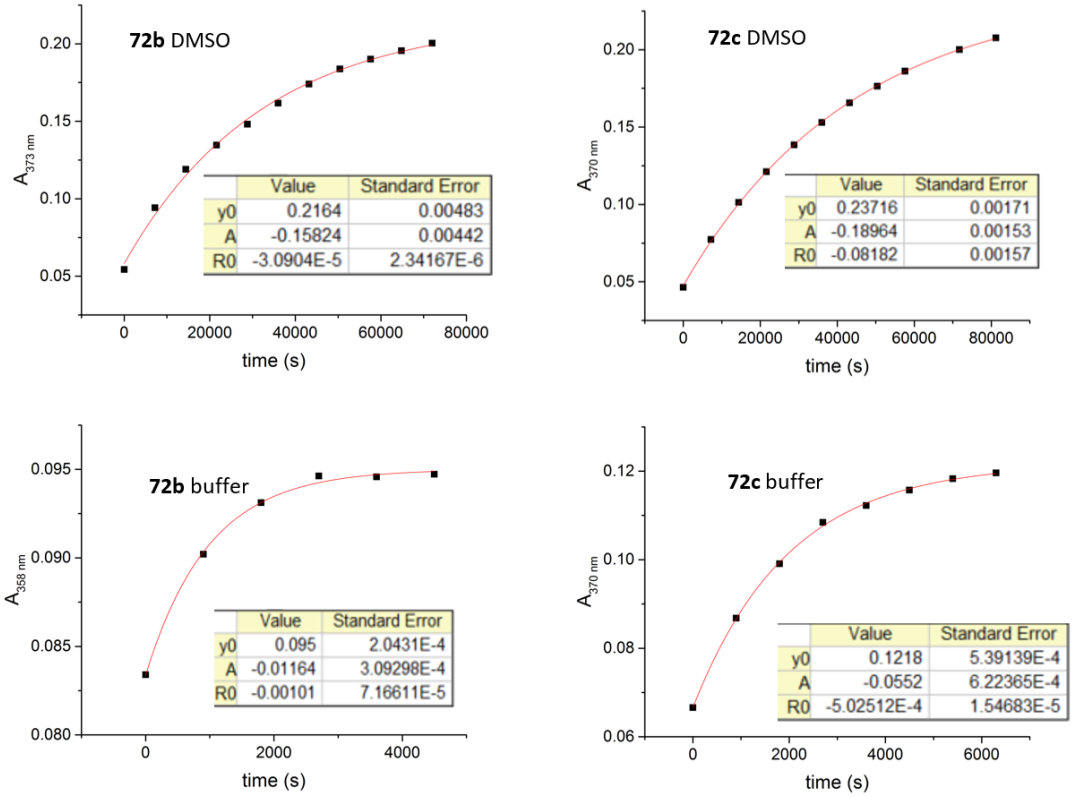


Figure 7.38. Thermal isomerisation rates for tethered HDAC inhibitors in DMSO or aqueous buffer at 30 °C.

7.3.3 Azobisimidazole: A photoswitchable base

Estimation of PSS compositions by UV/vis spectroscopy

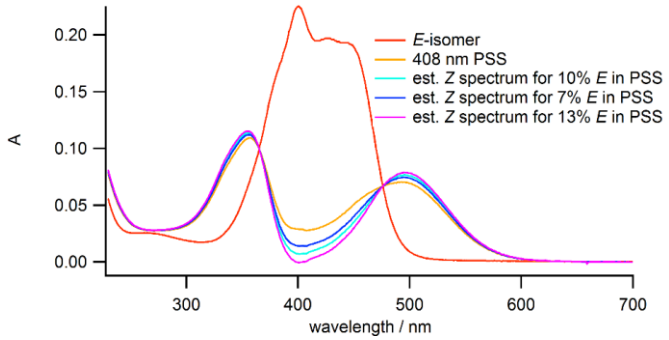


Figure 7.39. Estimating pure *Z*-spectrum of **91**

pH titrations

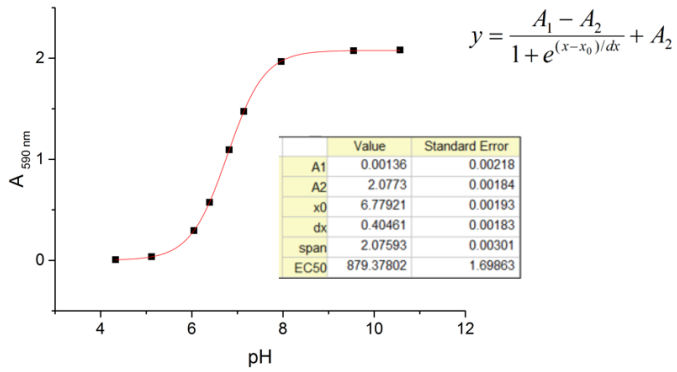


Figure 7.40. Bromocresol purple pH titration.

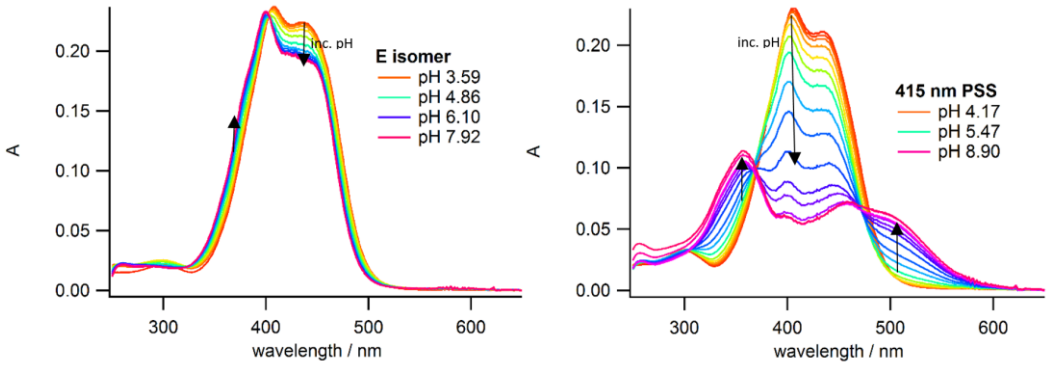


Figure 7.41. Spectra for *E*-**91** and 415 nm PSS pH titration (mono-protonation of the azobisimidazole).

Thermal isomerisation kinetics

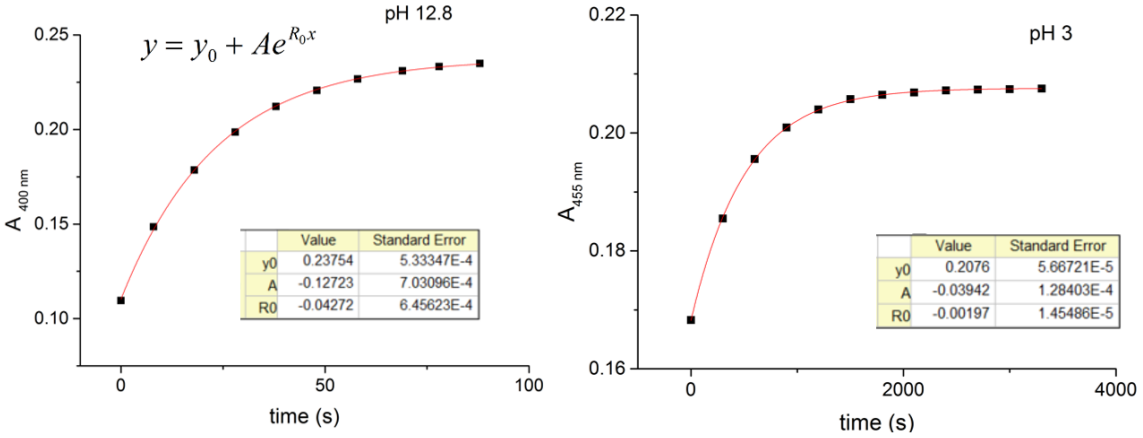


Figure 7.42. Thermal isomerisation of **1** at 25 °C in phosphate/citrate buffer, at pH 12.8 (neutral **91**) and pH 3 (protonated **91**).

7.4 Computational

7.4.1 Novel azoheteroaryl photoswitches: Arylazopyrazoles and pyrroles

Energy minimised structures and excitation data

compound	conformation	Dihedral angle	SCF energy / kJ mol^{-1}	Enthalpy / kJ mol^{-1}	Free Energy / kJ mol^{-1}	K_{eq}
E-**21**	1	0.0	4.9	7.4	4.3	1.7×10^{-1}
	2	**180.0**	**0.0**	**0.0**	**0.0**	**1**
Z-**21**	**1**	**180.0**	**49.4**	**51.5**	**45.8**	$\mathbf{9.5\times10^{-9}}$
	2	-36.8	76.2	77.5	76.7	3.5×10^{-14}
E-**22**	1	0.0	7.0	7.2	7.1	5.7×10^{-2}
	2	**180.0**	**0.0**	**0.0**	**0.0**	**1**
Z-**22**	**1**	**-36.9**	**65.0**	**64.1**	**69.6**	$\mathbf{6.3\times10^{-13}}$
	2	151.0	74.9	74.1	80.6	7.3×10^{-15}
E-**23**	1	0.0	0.0	0.0	0.4	8.5×10^{-1}
	2	**180.0**	**1.6**	**1.4**	**0.0**	**1**
Z-**23**	1	0.0	50.9	50.3	49.1	2.5×10^{-9}
	2	**180.0**	**50.4**	**49.6**	**48.3**	$\mathbf{3.4\times10^{-9}}$
E-**24**	1	0.2	0.0	0.0	2.1	4.3×10^{-1}
	2	**177.8**	**5.2**	**5.1**	**0.0**	**1**
Z-**24**	**1**	**152.9**	**63.3**	**62.4**	**68.0**	$\mathbf{1.2\times10^{-12}}$
	2	-43.4	66.2	65.1	69.3	7.1×10^{-13}

Table 7.10. Calculated data for the energy minimised structures of **21**-**24** using B3LYP/6-31G(d,p) and PCM model for acetonitrile. For each isomer, the lowest energy conformer is in bold.

		Mechanism	SCF energy / kJ mol^{-1}	Enthalpy / kJ mol^{-1}	Free Energy / kJ mol^{-1}	Activation Energy / kJ mol^{-1}	k / s^{-1}
21	1	Rot.	165.4	161.6	156.5		
	2	Rot.	169.9	166.2	164.5		
	3	**Inv.**	**150.4**	**146.3**	**140.5**	**94.7**	**1.53 x 10^{-4}**
	4	Inv.	163.9	159.9	159.0		
22	1	Rot.	151.5	144.9	149.4		
	2	Rot.	157.7	151.5	156.2		
	3	**Inv.**	**149.6**	**143.3**	**148.5**	**78.9**	**9.23 x 10^{-2}**
	4	Inv.	154.2	147.5	151.8		
23	**1**	**Inv.[a]**	**167.6**	**161.3**	**160.6**	**112.3**	**1.28 x 10^{-7}**
	2	Inv.[a]	169.6	163.4	162.1		
	3	Inv.	175.8	169.3	170.3		
	4	Inv.	175.9	169.4	170.7		
24	**1**	**Inv.[a]**	**165.2**	**159.1**	**158.6**	**90.6**	**8.21 x 10^{-4}**
	2	Inv.[a]	171.2	165.2	164.7		
	3	Inv.	173.3	166.6	167.7		
	4	Inv.	173.8	167.1	169.9		

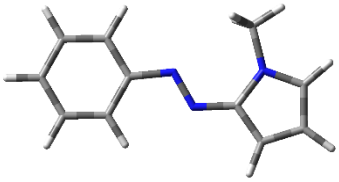
Table 7.11. Calculated data for the energy minimised transition states of **21**-**24** using B3LYP/6-31G(d,p) and PCM model for acetonitrile. For each isomer, the lowest energy transition state is in bold. Energies are given relative to the lowest energy conformer of the *E*-isomer of each compound. [a] No rotation transition state found – rotation input geometry optimised to an inversion transition state.

	Cmpd no.	n-π* λ_{max} / nm	n-π* f	π –π* λ_{max} / nm	π –π* f	λ_{max} separation / nm
E-isomers	**21**	428	0	372	0.92	56
	22	425	0	383	0.97	42
	23	426	0	326	0.89	100
	24	427	0.0017	334	0.86	93
Z-isomers	**21**	407	0.0023	298	0.52	109
	22	485	0.14	323	0.30	162
	23	396	0.0026	252	0.53	144
	24	454	0.058	283	0.32	171

Table 7.12. Calculated λ_{max} and oscillator strength (f) for n-π* and π-π* excitation (for the energy minimised structures of **21**-**24**). These are quoted for the lowest energy conformers (as highlighted in table S1). The differences in values for each conformer of an isomer are less than the predicted error of the method.

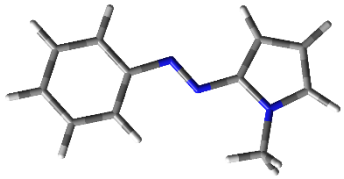
Structures and Cartesian coordinates for optimised geometry

E-**21 (1)**



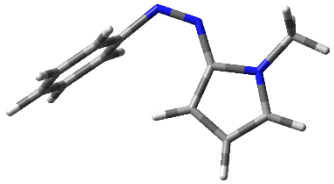
C	-1.855892	-0.503253	-0.000009
N	-2.597739	0.683238	-0.000012
C	-3.919469	0.351734	0.000053
C	-4.059878	-1.032176	0.000056
C	-2.764559	-1.569982	0.000027
H	-2.473239	-2.610745	0.000041
H	-4.997068	-1.569547	0.000080
H	-4.673569	1.126219	0.000170
C	-2.108242	2.059847	-0.000047
H	-1.498933	2.252967	0.883509
H	-2.974649	2.723080	-0.000090
H	-1.498946	2.252858	-0.883638
N	-0.500087	-0.678117	-0.000002
N	0.236245	0.363202	-0.000106
C	1.626652	0.092654	-0.000069
C	2.201435	-1.192328	-0.000067
C	3.585410	-1.331771	-0.000013
C	4.415179	-0.202999	0.000058
C	3.848526	1.073615	0.000089
C	2.462275	1.220657	0.000021
H	2.002389	2.204078	0.000034
H	4.485147	1.953307	0.000158
H	5.494523	-0.321252	0.000104
H	4.024854	-2.325234	-0.000032
H	1.551948	-2.059985	-0.000103

(2)



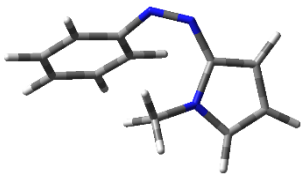
C	-2.420171	-1.535961	0.000060
C	-1.812783	-0.272210	-0.000110
N	-2.825169	0.684636	-0.000456
C	-4.024644	0.047588	-0.000319
C	-3.807749	-1.330169	0.000066
N	-0.511886	0.155278	-0.000236
N	0.367161	-0.767625	0.000468
C	1.704884	-0.308496	0.000195
C	2.685173	-1.313924	0.000106
C	4.039018	-0.982195	-0.000125
C	4.428436	0.359095	-0.000217
C	3.454436	1.366294	-0.000090
C	2.101926	1.042379	0.000116
C	-2.641182	2.132517	0.000365
H	-1.886458	-2.474419	0.000131
H	-4.580533	-2.085932	0.000276
H	-4.947772	0.608992	-0.000334
H	-3.092373	2.570255	0.894296
H	-3.103546	2.572173	-0.886827
H	-1.574022	2.343515	-0.005970
H	2.359795	-2.349625	0.000205
H	4.788205	-1.768160	-0.000230
H	5.481997	0.621682	-0.000353
H	3.756650	2.409704	-0.000111
H	1.343256	1.816286	0.000208

Z-**21 (1)**



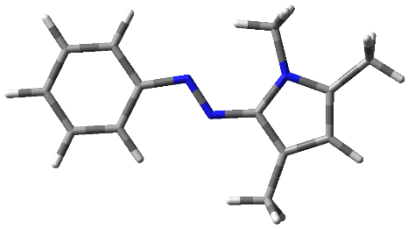
C	1.350973	-0.112197	-0.000123
C	0.811923	1.190834	-0.000037
C	1.887163	2.089051	0.000217
C	3.060869	1.336279	0.000282
N	2.742357	0.021481	0.000045
C	3.699674	-1.080420	0.000143
H	4.704716	-0.658478	0.000107
H	3.568268	-1.701959	0.887475
H	3.568274	-1.702101	-0.887086
H	4.093087	1.655409	0.000473
H	1.831959	3.168301	0.000324
H	-0.234630	1.444115	-0.000195
N	0.904548	-1.416071	-0.000411
N	-0.304136	-1.792601	-0.000440
C	-1.968030	-0.457944	1.213150
C	-3.097909	0.361170	1.208047
C	-3.664152	0.777603	0.000245
C	-3.097758	0.361994	-1.207784
C	-1.967879	-0.457098	-1.213302
C	-1.390720	-0.854628	-0.000168
H	-1.527877	-0.790461	2.148343
H	-3.537868	0.671540	2.151364
H	-4.545032	1.412075	0.000405
H	-3.537610	0.673012	-2.150937
H	-1.527585	-0.788980	-2.148655

(2)



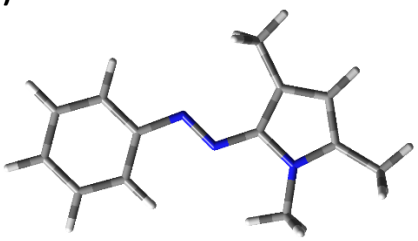
H	1.102361	-1.296562	2.545725
H	-0.307017	-1.186566	1.460452
H	0.350136	0.274059	2.228011
C	0.608337	-0.688768	1.786403
N	1.533236	-0.492209	0.672326
C	2.576226	-1.338280	0.408019
H	2.677880	-2.261310	0.960829
C	3.405427	-0.770169	-0.546515
H	4.297604	-1.221390	-0.956352
C	2.880307	0.502622	-0.840152
H	3.260913	1.234989	-1.537805
N	0.935386	1.814830	-0.148942
C	1.700569	0.654224	-0.107529
N	-0.323280	1.899834	-0.037572
C	-1.218635	0.793459	-0.130252
C	-2.387504	0.863125	0.644626
H	-2.496038	1.678235	1.353464
C	-3.379117	-0.105759	0.508906
H	-4.268715	-0.056310	1.129507
H	-4.018321	-1.871429	-0.555483
C	-3.238807	-1.125272	-0.437161
C	-2.097690	-1.169010	-1.244417
H	-1.994943	-1.944536	-1.997663
H	-0.206735	-0.260082	-1.727865
C	-1.084865	-0.223886	-1.092512

E-**22 (1)**



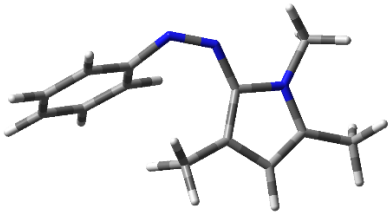
C	1.320213	0.365653	-0.000028
N	2.128382	-0.785684	-0.000044
C	3.438013	-0.392237	0.000017
C	3.491640	1.000722	0.000010
C	2.176094	1.488892	0.000017
C	1.737856	2.920989	-0.000022
H	2.119323	3.451247	-0.880224
H	0.649165	2.993866	-0.000305
H	2.118815	3.451204	0.880438
H	4.402326	1.584230	0.000003
C	4.562867	-1.373402	-0.000014
H	4.535835	-2.024862	0.881622
H	5.516066	-0.841722	0.000026
H	4.535872	-2.024764	-0.881731
C	1.714832	-2.189404	0.000078
H	2.102042	-2.696085	0.889233
H	2.102622	-2.696387	-0.888647
H	0.630462	-2.228178	-0.000268
N	-0.033073	0.495914	-0.000058
N	-0.778379	-0.543921	0.000026
C	-2.165885	-0.264208	-0.000028
C	-2.735506	1.023578	0.000047
C	-4.118965	1.171752	0.000060
C	-4.957014	0.049535	-0.000016
C	-4.396628	-1.230058	-0.000039
C	-3.011470	-1.385895	-0.000034
H	-2.559880	-2.373365	-0.000053
H	-5.038034	-2.106481	-0.000070
H	-6.035628	0.174421	-0.000015
H	-4.551132	2.168609	0.000115
H	-2.082651	1.888594	0.000112

(2)



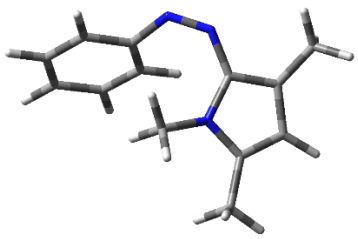
C	3.218206	1.143102	-0.000224
C	2.210766	0.163565	0.000015
C	2.578589	-1.196154	0.000247
C	3.923359	-1.552879	0.000224
C	4.922460	-0.571148	-0.000024
C	4.563504	0.778922	-0.000254
N	0.884969	0.655391	0.000020
N	-0.014521	-0.256271	-0.000013
C	-1.307947	0.159652	0.000025
N	-2.307581	-0.823417	-0.000037
C	-3.527059	-0.220560	-0.000036
C	-3.324565	1.163243	0.000037
C	-1.945733	1.421945	0.000082
C	-2.080121	-2.262842	-0.000129
C	-4.805858	-0.990982	-0.000088
C	-1.293790	2.769489	0.000176
H	-2.051756	3.558158	0.000231
H	-0.648991	2.905564	0.874771
H	-0.648980	2.905678	-0.874392
H	-4.114232	1.903187	0.000066
H	-4.894173	-1.636210	-0.882307
H	-5.652265	-0.301660	-0.000081
H	-4.894207	-1.636272	0.882084
H	-2.520892	-2.721051	-0.889872
H	-2.520999	-2.721181	0.889493
H	-1.006544	-2.437097	-0.000082
H	2.919864	2.187046	-0.000391
H	5.330821	1.547506	-0.000446
H	5.969446	-0.859013	-0.000035
H	4.199201	-2.603817	0.000414
H	1.802779	-1.952871	0.000450

Z-**22 (1)**



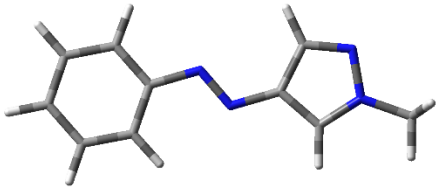
C	-1.044112	0.367927	-0.363504
N	-2.366873	0.556010	0.067206
C	-2.995465	-0.650972	0.142154
C	-2.103428	-1.621695	-0.308702
C	-0.877705	-1.009882	-0.632064
C	0.288897	-1.710226	-1.259843
H	0.707829	-1.135020	-2.090951
H	1.104512	-1.877774	-0.547753
H	-0.026824	-2.682811	-1.647509
C	-2.923595	1.831906	0.496964
H	-2.366835	2.630223	0.008325
H	-3.973824	1.890120	0.206921
H	-2.846837	1.956973	1.582157
C	-4.393079	-0.810153	0.644606
H	-4.499298	-0.454671	1.676526
H	-5.117011	-0.256999	0.034825
H	-4.672507	-1.865270	0.621578
H	-2.332972	-2.673940	-0.414194
N	-0.353351	1.521920	-0.666591
N	0.905911	1.666732	-0.727505
C	1.847917	0.751692	-0.174680
C	1.725499	0.233037	1.127088
C	2.777407	-0.486644	1.690957
C	3.954453	-0.710771	0.969546
C	4.082513	-0.185888	-0.319431
H	3.147255	0.996853	-1.868348
C	3.046878	0.559607	-0.879537
H	4.996715	-0.344231	-0.884007
H	4.766960	-1.278013	1.412902
H	2.677832	-0.873182	2.701214
H	0.818120	0.407478	1.695219

(2)



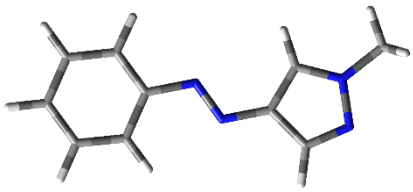
H	3.178127	3.138573	0.514479
C	2.304708	2.830261	-0.063505
H	2.456457	3.164952	-1.097437
H	1.430714	3.363993	0.325519
C	2.144290	1.347953	0.029448
N	1.056393	0.689386	-0.489610
C	0.086831	1.317984	-1.384292
H	-0.745363	1.754759	-0.827201
H	0.580462	2.097848	-1.966532
H	-0.305899	0.573943	-2.075291
C	1.256104	-0.690294	-0.317683
C	2.501793	-0.876006	0.305924
C	3.024063	0.407650	0.554693
H	3.956094	0.641118	1.051661
C	3.089081	-2.196391	0.697867
H	4.179668	-2.178100	0.608864
H	2.694392	-2.996926	0.066744
H	2.854105	-2.456021	1.737567
N	0.464777	-1.752486	-0.694567
N	-0.803816	-1.793131	-0.782657
C	-1.680388	-0.827912	-0.208370
C	-1.492641	-0.280108	1.074338
H	-0.582014	-0.488092	1.625434
C	-2.489306	0.509277	1.645288
H	-2.340968	0.917498	2.640884
C	-3.672424	0.777374	0.949510
H	-4.439683	1.400866	1.397879
C	-3.867341	0.222603	-0.318756
H	-4.788304	0.413632	-0.861677
C	-2.889517	-0.592652	-0.884006
H	-3.040788	-1.052868	-1.855791

E-**23 (1)**



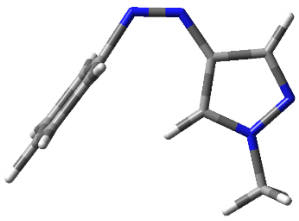
C	-2.407055	-1.145394	0.001197
C	-1.950102	0.184988	0.000208
C	-2.876984	1.237322	-0.000850
C	-4.245648	0.970142	-0.001168
C	-4.696820	-0.351258	-0.000264
C	-3.773157	-1.405067	0.000956
N	-0.585725	0.575766	0.000446
N	0.238955	-0.386983	-0.000569
C	1.573154	-0.002777	-0.000127
C	2.629809	-0.914522	-0.001178
N	3.765632	-0.192317	-0.000356
N	3.528630	1.151001	0.001190
C	2.207151	1.271963	0.001325
C	5.137202	-0.676193	-0.000604
H	-5.761709	-0.563305	-0.000423
H	1.743863	2.247919	0.002378
H	2.627622	-1.994154	-0.002356
H	-2.501730	2.255934	-0.001475
H	-4.957208	1.790133	-0.002069
H	-4.125581	-2.432426	0.001770
H	-1.682422	-1.951350	0.002154
H	5.657379	-0.317455	0.890097
H	5.657282	-0.317076	-0.891209
H	5.124762	-1.765711	-0.000803

(2)



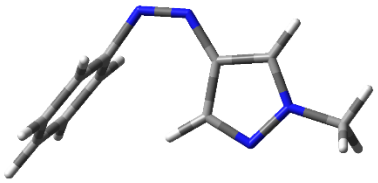
H	-5.417110	0.966796	0.890688
C	-4.819204	1.170515	-0.000053
H	-5.417300	0.966484	-0.890592
H	-4.508202	2.214646	-0.000268
N	-3.633201	0.327254	-0.000051
N	-3.779811	-1.028020	-0.000048
C	-2.538343	-1.501997	-0.000001
H	-2.353764	-2.567883	0.000008
C	-1.579970	-0.457239	0.000047
C	-2.345120	0.715372	-0.000004
H	-2.052349	1.753394	0.000003
N	-0.206343	-0.662917	0.000116
N	0.488988	0.396923	0.000128
C	1.892189	0.186251	0.000049
C	2.518934	-1.073284	0.000002
C	3.907238	-1.151891	-0.000064
C	4.685360	0.013602	-0.000083
C	4.065524	1.264823	-0.000035
C	2.673816	1.350669	0.000031
H	2.168816	2.311574	0.000071
H	4.663867	2.170718	-0.000048
H	5.768810	-0.057658	-0.000134
H	4.390932	-2.124356	-0.000098
H	1.906322	-1.967323	0.000022

Z-**23 (1)**



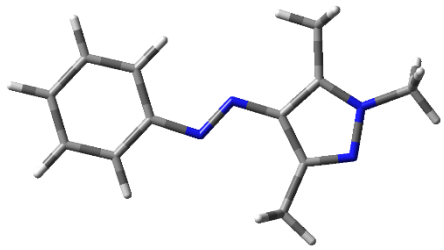
C	2.725634	-1.146906	0.000238
C	1.313460	-0.985196	-0.000091
C	1.135093	0.410880	-0.000182
N	2.366582	0.948801	0.000096
N	3.360952	0.015193	0.000320
N	0.493190	-2.119797	-0.000215
N	-0.765810	-2.108497	-0.000191
C	-1.515492	-0.882391	-0.000039
C	-1.937340	-0.326631	-1.214276
C	-2.752108	0.806515	-1.208162
C	-3.158134	1.379011	0.000216
C	-2.751669	0.806543	1.208477
C	-1.936903	-0.326579	1.214340
H	-3.794176	2.258625	0.000341
C	2.719480	2.361322	-0.000388
H	0.256442	1.033009	-0.000571
H	3.272446	-2.080300	0.000495
H	-1.623568	-0.780342	-2.149282
H	-3.071786	1.240212	-2.151059
H	-3.071050	1.240282	2.151456
H	-1.622763	-0.780266	2.149236
H	1.804759	2.952874	0.000169
H	3.307196	2.593404	0.889991
H	3.305976	2.593201	-0.891638

(2)



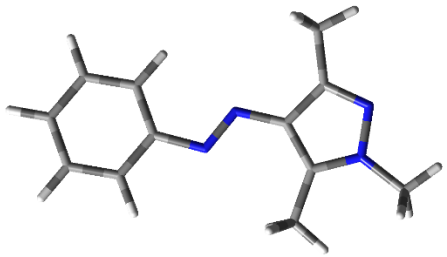
N	2.066120	-1.382284	0.000825
N	3.063719	-0.451415	0.000160
C	2.589698	0.801608	-0.000370
C	1.192887	0.718384	-0.000114
C	0.935044	-0.690181	0.000631
H	-0.006576	-1.214997	0.001068
H	3.231699	1.669623	-0.000934
C	4.451016	-0.890791	0.000256
H	4.647874	-1.490251	0.891309
H	5.096968	-0.013402	-0.000113
H	4.647810	-1.490933	-0.890356
N	0.457443	1.910960	-0.000465
N	-0.798768	1.987770	-0.000332
C	-1.636831	0.819873	-0.000140
C	-2.102157	0.299954	1.213924
C	-3.002997	-0.765969	1.208132
C	-3.452201	-1.305598	-0.000052
C	-3.001578	-0.767242	-1.208329
C	-2.100720	0.298606	-1.214231
H	-1.752072	0.726079	-2.149283
H	-1.754679	0.728440	2.148948
H	-3.355583	-1.173168	2.151157
H	-4.154868	-2.132983	-0.000071
H	-3.353131	-1.175491	-2.151287

E-**24 (1)**



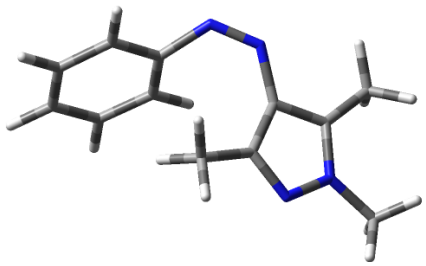
C	1.288371	-0.048038	0.000322
C	2.331849	0.891531	-0.003535
N	3.473069	0.174843	-0.010436
N	3.249490	-1.178271	-0.005773
C	1.931261	-1.331421	-0.001123
C	1.330452	-2.700295	-0.001299
H	0.691489	-2.851118	-0.876661
H	2.124002	-3.451701	-0.003606
H	0.695045	-2.852729	0.876345
C	4.838342	0.673897	0.009944
H	5.498921	-0.175336	-0.156964
H	4.986774	1.410928	-0.782814
H	5.073536	1.132628	0.974887
C	2.280470	2.381291	0.001995
H	1.238537	2.703203	-0.006799
H	2.765665	2.796352	0.892298
H	2.783226	2.804314	-0.874713
N	-0.034396	0.347907	0.000499
N	-0.895531	-0.585687	0.002576
C	-2.244538	-0.141544	0.001589
C	-2.653053	1.204507	-0.002812
C	-4.008781	1.515937	-0.003968
C	-4.972452	0.499090	-0.000803
C	-4.570287	-0.838137	0.003505
C	-3.212671	-1.156629	0.004666
H	-2.877781	-2.189288	0.007892
H	-5.311832	-1.631295	0.005883
H	-6.028592	0.751284	-0.001842
H	-4.321253	2.556313	-0.007455
H	-1.899934	1.983758	-0.005393

(2)



H	-5.406618	-0.561146	0.006481
H	-4.618086	-1.829865	-0.960423
H	-4.596997	-1.921315	0.820114
C	-4.561810	-1.245986	-0.038163
N	-3.353526	-0.433163	-0.009681
N	-3.482959	0.932760	0.025235
C	-2.242571	1.403195	0.035143
C	-1.298908	0.334385	0.008990
C	-2.069097	-0.847509	-0.021076
C	-1.662587	-2.281916	-0.063666
H	-1.143483	-2.562726	0.858259
H	-0.955075	-2.450186	-0.879619
H	-2.521157	-2.943185	-0.195573
H	-2.907539	3.429455	0.060525
H	-1.413972	3.148806	0.978183
H	-1.362798	3.185825	-0.781964
C	-1.967856	2.873102	0.074906
N	0.064825	0.550916	0.007717
N	0.798186	-0.486941	0.027255
C	2.192653	-0.220596	0.008170
C	3.023356	-1.347156	0.101177
C	4.410396	-1.204565	0.091350
C	4.979797	0.066052	-0.015684
C	4.153686	1.193394	-0.113015
C	2.769376	1.057879	-0.102042
H	2.121222	1.923045	-0.179164
H	4.596248	2.181637	-0.199604
H	6.059469	0.181007	-0.025727
H	5.044811	-2.082613	0.165854
H	2.559672	-2.325414	0.182432

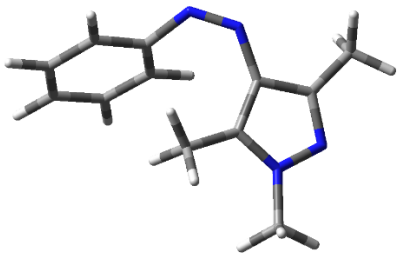
Z-**24**[*] **(1)**



C	-1.036073	0.501808	-0.389906
C	-2.340192	0.598820	0.119150
N	-2.837641	-0.655729	0.114213
N	-1.968482	-1.562026	-0.419779
C	-0.866733	-0.883229	-0.727766
C	0.249798	-1.586302	-1.435448
H	0.605247	-1.004404	-2.290869
H	1.108366	-1.754503	-0.778853
H	-0.106707	-2.553645	-1.796803
H	-4.925218	-0.468907	0.259823
H	-4.275511	-2.125737	0.257603
H	-4.130341	-1.114482	1.717513
C	-4.120913	-1.111890	0.623449
C	-3.077934	1.795336	0.615904
H	-4.103864	1.820772	0.235882
H	-3.129627	1.816035	1.710613
H	-2.557539	2.696253	0.285364
N	-0.311684	1.676116	-0.652789
N	0.942883	1.790418	-0.640899
C	1.834236	0.804079	-0.114259
C	1.658828	0.236002	1.158283
C	2.653776	-0.580571	1.693958
C	3.819645	-0.847342	0.969758
C	4.000657	-0.267531	-0.289211
C	3.024957	0.574714	-0.818932
H	2.518013	-1.009335	2.682479
H	0.759072	0.446255	1.726015
H	4.586996	-1.489838	1.390239
H	4.909622	-0.458351	-0.851754
H	3.165655	1.055077	-1.782362

[*]Images in the main text are the enantiomer of this structure, for comparison with the x-ray structure.

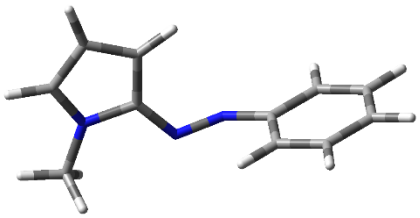
(2)



C	-2.880329	-0.406903	-0.968447
C	-1.733490	-0.802913	-0.264914
C	-1.585429	-0.439401	1.083706
C	-2.562766	0.340596	1.700191
C	-3.682812	0.773777	0.983964
C	-3.836957	0.398575	-0.353283
N	-0.874076	-1.749615	-0.911491
N	0.383813	-1.721936	-0.854017
C	1.157974	-0.660971	-0.353099
C	1.079453	0.733118	-0.511719
N	2.217991	1.219210	0.040460
N	3.033720	0.245430	0.540056
C	2.412854	-0.899747	0.280395
C	2.664618	2.603808	0.079158
C	0.090958	1.608903	-1.208106
C	2.994954	-2.218415	0.679233
H	0.583598	2.463370	-1.679379
H	-0.431170	1.048805	-1.985095
H	-0.666081	1.991847	-0.514278
H	2.917372	2.964377	-0.922468
H	1.892092	3.245711	0.508150
H	3.552998	2.637718	0.707460
H	2.907078	-2.940356	-0.138535
H	2.473957	-2.645558	1.543449
H	4.048990	-2.101637	0.940621
H	-3.003280	-0.732539	-1.996871
H	-4.711086	0.718261	-0.912478
H	-4.436161	1.386254	1.469508
H	-2.449419	0.609460	2.746242
H	-0.723197	-0.779896	1.646144

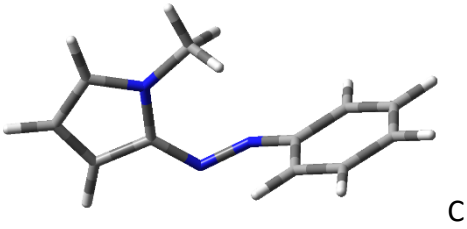
Structures and Cartesian coordinates for transition states

21 TS1



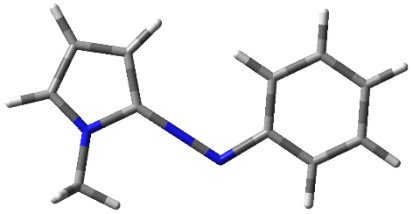
C	2.261398	1.611342	-0.118981
C	1.370748	0.495009	-0.080113
C	1.938678	-0.803132	0.058570
C	3.315207	-0.962055	0.152834
C	4.186476	0.135131	0.117781
C	3.634256	1.413629	-0.017647
N	0.042831	0.661857	-0.152765
N	-0.842668	1.575119	-0.230567
C	-1.261817	1.966876	-1.452554
N	-2.314178	2.886488	-1.521126
C	-2.549005	3.166636	-2.813900
C	-1.667779	2.424087	-3.624592
C	-0.866316	1.668907	-2.779704
C	-3.003683	3.468133	-0.371413
H	5.259964	-0.002980	0.193334
H	-0.088368	0.968993	-3.046917
H	-1.644710	2.451609	-4.704292
H	-3.317905	3.870361	-3.099662
H	1.848528	2.609393	-0.226179
H	4.285329	2.284884	-0.045793
H	3.716611	-1.967534	0.256939
H	1.277156	-1.663188	0.089205
H	-3.383030	2.675140	0.273720
H	-2.321495	4.099333	0.201023
H	-3.834695	4.069577	-0.738219

21 TS2



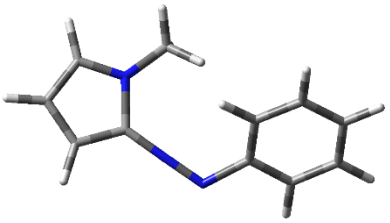
C			
2.405307	1.625973	-0.061860	
C	1.482620	0.535821	-0.060881
C	2.013074	-0.783478	0.013412
C	3.384351	-0.986472	0.092374
C	4.287017	0.086170	0.105005
C	3.773169	1.384454	0.028572
N	0.159588	0.739954	-0.125065
N	-0.706900	1.675910	-0.134224
C	-1.169223	2.192879	-1.291806
N	-0.771568	1.931819	-2.615721
C	-1.516397	2.707820	-3.428991
C	-2.408369	3.488027	-2.676453
C	-2.201681	3.158905	-1.343595
C	0.236177	0.976079	-3.073369
H	5.356109	-0.086647	0.170494
H	-2.702983	3.548462	-0.469271
H	-3.112923	4.197952	-3.083444
H	-1.379512	2.666396	-4.500966
H	2.021154	2.639765	-0.117451
H	4.449431	2.236562	0.035563
H	3.757013	-2.006656	0.147997
H	1.326449	-1.624153	0.009717
H	1.224746	1.255299	-2.704941
H	-0.005504	-0.025766	-2.715599
H	0.236719	0.984142	-4.163599

21 TS3



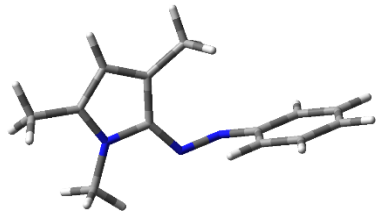
C	2.616717	0.923066	-1.157737
C	1.427236	0.451916	-0.530364
N	1.866521	-0.609841	0.344638
C	3.195013	-0.748463	0.234625
C	3.697061	0.187887	-0.685257
N	0.186563	0.800411	-0.615472
N	-1.029819	1.146955	-0.687535
C	-1.335356	2.199793	-1.617001
C	-2.675375	2.615048	-1.625034
C	-3.096561	3.625731	-2.487056
C	-2.182784	4.228829	-3.356530
C	-0.846463	3.812536	-3.356308
C	-0.421527	2.805176	-2.493018
H	-2.507957	5.015269	-4.030860
C	0.978239	-1.395466	1.185466
H	0.610789	2.474748	-2.494169
H	-0.135113	4.276316	-4.034085
H	-4.135418	3.942705	-2.483157
H	-3.368130	2.130292	-0.943120
H	2.643546	1.730493	-1.875635
H	4.737547	0.294320	-0.956885
H	3.730706	-1.496896	0.803123
H	1.278718	-1.324252	2.233515
H	-0.027566	-0.990675	1.069185
H	0.981784	-2.444870	0.879549

21 TS4



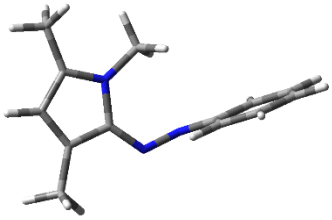
C	-0.738399	2.300581	-2.991679
C	-1.366960	2.143325	-1.746393
C	-2.495724	2.918150	-1.440143
C	-2.951063	3.880470	-2.338591
C	-2.309811	4.051332	-3.570614
C	-1.211756	3.250406	-3.897383
N	-1.015752	1.126743	-0.796712
N	0.196478	0.777371	-0.734703
C	1.450410	0.470055	-0.637256
C	2.042698	-0.721214	-0.133334
C	3.420778	-0.651759	-0.310407
C	3.702213	0.602707	-0.869038
N	2.557916	1.269610	-1.108224
C	2.477612	2.664699	-1.513117
H	-2.673870	4.791201	-4.276904
H	0.091414	1.651622	-3.254213
H	-0.728791	3.359189	-4.864358
H	-3.810280	4.493900	-2.083367
H	-2.991896	2.759240	-0.487034
H	1.467561	-1.543338	0.269670
H	4.158601	-1.398838	-0.055113
H	4.663167	1.057189	-1.070219
H	2.562771	3.331176	-0.649152
H	1.518293	2.842429	-1.997664
H	3.284064	2.883397	-2.214888

22 TS1



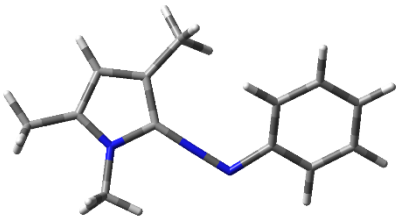
C	-0.926613	1.522560	-2.833396
C	-1.263883	1.853861	-1.468928
N	-2.252073	2.868224	-1.518856
C	-2.497760	3.174280	-2.800956
C	-1.696183	2.345130	-3.630634
N	-0.892668	1.401359	-0.286991
N	-0.073292	0.381798	-0.204859
C	1.268044	0.382004	-0.096983
C	2.049691	1.578799	-0.113461
C	3.433814	1.524083	0.027131
C	4.110758	0.309075	0.174484
C	3.352738	-0.872548	0.180738
C	1.971652	-0.851162	0.050402
C	-2.859786	3.495852	-0.348546
H	5.190639	0.279944	0.278871
C	0.036069	0.470300	-3.265728
H	-1.708723	2.373089	-4.711622
C	-3.462674	4.230965	-3.211762
H	1.545320	2.533859	-0.226226
H	3.993965	2.457323	0.018555
H	3.852142	-1.832943	0.291094
H	1.400695	-1.775320	0.060941
H	-2.516547	2.955993	0.531244
H	-2.556642	4.543325	-0.275486
H	-3.948082	3.437414	-0.416742
H	-3.516188	4.289290	-4.299250
H	-3.160108	5.210928	-2.825485
H	-4.466187	4.024408	-2.823845
H	0.010251	0.346589	-4.350889
H	1.058347	0.720237	-2.962210
H	-0.198166	-0.485059	-2.782956

22 TS2



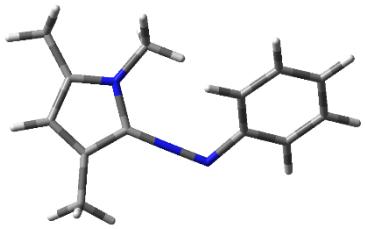
C	-2.096945	3.170873	-1.322146
C	-1.133357	2.103001	-1.304833
N	-0.760961	1.847657	-2.651891
C	-1.440322	2.701042	-3.443699
C	-2.262359	3.533306	-2.643550
N	-0.737651	1.516087	-0.190503
N	0.055869	0.475421	-0.192738
C	1.396391	0.421163	-0.090857
C	2.217697	1.589454	-0.028257
C	3.599714	1.478437	0.101974
C	4.234742	0.233836	0.158936
C	3.437485	-0.919303	0.083487
C	2.057532	-0.842541	-0.037887
C	0.165916	0.810980	-3.105160
H	5.313188	0.160803	0.256152
C	-2.733312	3.760790	-0.107295
H	-2.905170	4.308856	-3.035682
C	-1.321662	2.722513	-4.929458
H	1.744549	2.566340	-0.065629
H	4.191242	2.390330	0.157829
H	3.904704	-1.901151	0.121823
H	1.455471	-1.745271	-0.089409
H	1.178166	1.032013	-2.761285
H	-0.137495	-0.155099	-2.701453
H	0.150687	0.776406	-4.193100
H	-3.732499	4.139371	-0.336532
H	-2.797566	3.023784	0.695672
H	-2.140321	4.603073	0.268895
H	-1.933541	3.529071	-5.334641
H	-0.285560	2.880942	-5.246883
H	-1.662077	1.779325	-5.370656

22 TS3



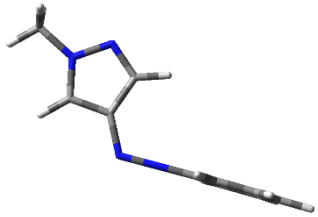
C	-0.646231	2.402518	-2.820219
C	-1.350182	2.189262	-1.625174
C	-2.515950	2.929742	-1.374703
C	-2.942141	3.901879	-2.277491
C	-2.228019	4.124112	-3.459655
C	-1.085627	3.363633	-3.729773
N	-1.033272	1.171526	-0.665950
N	0.180572	0.802840	-0.595464
C	1.426137	0.490854	-0.501486
C	2.641523	1.064665	-1.007955
C	3.701461	0.309260	-0.520859
C	3.192032	-0.739102	0.272843
N	1.854305	-0.636185	0.311732
C	0.937218	-1.517328	1.009962
H	-2.565784	4.873009	-4.169691
H	0.225389	1.794408	-3.034545
H	-0.540470	3.515221	-4.657485
H	-3.834532	4.483338	-2.063636
H	-3.066239	2.733930	-0.458634
C	2.745825	2.279562	-1.876048
H	4.754653	0.479530	-0.701665
C	3.948124	-1.815827	0.978493
H	1.165379	-1.548000	2.078904
H	-0.067890	-1.118739	0.867818
H	0.980331	-2.534031	0.607832
H	5.019319	-1.697394	0.805612
H	3.769656	-1.790124	2.059664
H	3.650917	-2.810130	0.625350
H	3.753152	2.701154	-1.826784
H	2.542223	2.041569	-2.927560
H	2.031906	3.050825	-1.577968

22 TS4



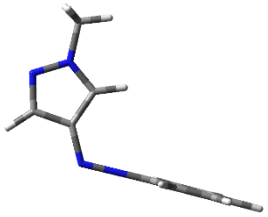
N	2.582619	1.264787	-1.198336
C	1.481472	0.568950	-0.552654
C	2.074637	-0.571251	0.079450
C	3.438501	-0.553037	-0.193509
C	3.728958	0.601345	-0.943713
N	0.236505	0.896488	-0.602174
N	-0.976368	1.268791	-0.625204
C	-1.364030	2.205531	-1.637565
C	-0.808996	2.243878	-2.927252
C	-1.323862	3.117010	-3.885941
C	-2.392185	3.961973	-3.571725
C	-2.959565	3.912778	-2.293414
C	-2.462088	3.027962	-1.339456
C	2.498732	2.580249	-1.808979
H	-2.788850	4.641716	-4.319728
H	0.000265	1.565014	-3.177224
H	-0.895927	3.131392	-4.884550
H	-3.794898	4.561053	-2.044328
H	-2.902989	2.964807	-0.348593
C	1.295561	-1.597456	0.835678
H	4.178855	-1.275093	0.124281
C	5.066020	1.100533	-1.382026
H	3.016659	3.330521	-1.203030
H	1.448513	2.855769	-1.886254
H	2.937713	2.569524	-2.810213
H	1.858402	-1.962908	1.699796
H	0.345714	-1.179202	1.179937
H	1.062899	-2.467852	0.209493
H	5.292824	2.077803	-0.939093
H	5.845352	0.399513	-1.077735
H	5.116677	1.220107	-2.470236

23 TS1



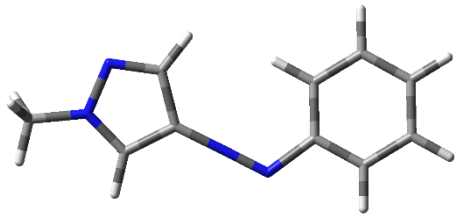
C	-1.331333	0.427917	3.079880
C	-1.628809	0.823447	1.776567
C	-2.848500	0.164197	1.466138
N	-3.262560	-0.570946	2.489113
N	-2.321719	-0.395249	3.463035
N	-0.803950	1.697552	1.041617
N	-1.159892	1.983117	-0.103626
C	-1.543833	2.291169	-1.338830
C	-1.115772	1.508763	-2.450336
C	-1.508897	1.863839	-3.735152
C	-2.321727	2.976758	-3.976788
C	-2.741533	3.742320	-2.883473
C	-2.372892	3.424530	-1.581751
C	-2.480949	-1.077909	4.738796
H	-2.618946	3.239445	-4.986337
H	-2.705243	4.026166	-0.743084
H	-3.374458	4.612094	-3.041209
H	-1.168409	1.250155	-4.565477
H	-0.485623	0.643578	-2.276707
H	-2.499738	-2.157785	4.579149
H	-1.641326	-0.818304	5.382601
H	-3.414476	-0.764676	5.210363
H	-0.501090	0.681553	3.721731
H	-3.420723	0.204202	0.549773

23 TS2



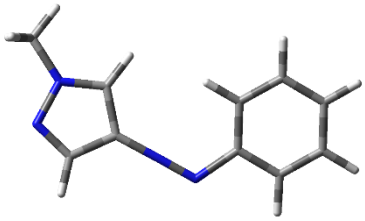
C	-1.195700	0.124362	3.050883
C	-1.519926	0.586050	1.752607
C	-2.655067	-0.143892	1.386886
N	-2.928494	-0.951675	2.424492
N	-2.049212	-0.807490	3.458083
N	-0.783369	1.575698	1.070875
N	-1.162033	1.896072	-0.057515
C	-1.570825	2.242040	-1.274752
C	-1.070143	1.571669	-2.428233
C	-1.492179	1.966718	-3.692130
C	-2.403638	3.012879	-3.871888
C	-2.894657	3.668182	-2.737409
C	-2.500469	3.306970	-1.454547
H	-2.722112	3.308085	-4.865850
H	-2.888287	3.823309	-0.583493
H	-3.604876	4.483999	-2.846887
H	-1.094852	1.438905	-4.555554
H	-0.362852	0.759440	-2.302683
H	-0.378185	0.442840	3.683358
H	-3.252747	-0.131772	0.488281
C	-4.014445	-1.914492	2.545672
H	-4.608259	-1.892206	1.632670
H	-3.602885	-2.915016	2.691821
H	-4.642990	-1.652993	3.399108

23 TS3



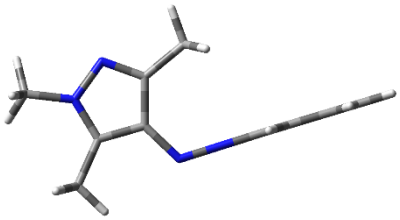
C	-1.298622	-1.138241	1.941648
C	-1.662579	-0.128489	1.042264
C	-3.003400	0.266145	0.944906
C	-3.968485	-0.354686	1.734294
C	-3.605346	-1.373742	2.623049
C	-2.267268	-1.764555	2.724989
N	-0.563935	0.449715	0.294624
N	-0.867131	1.264125	-0.611127
C	-1.172510	2.102791	-1.584901
C	-0.264274	2.852857	-2.381412
N	-0.987123	3.570857	-3.239739
N	-2.341147	3.358285	-3.106155
C	-2.456772	2.492216	-2.118540
C	-0.525107	4.511955	-4.249260
H	-4.361974	-1.855834	3.234794
H	-3.273258	1.063555	0.261194
H	-5.007180	-0.044801	1.661290
H	-1.980972	-2.552657	3.415189
H	-0.250934	-1.418204	2.005949
H	-0.935933	5.502292	-4.042656
H	0.563026	4.552378	-4.221292
H	-0.856154	4.181799	-5.235844
H	-3.435097	2.145000	-1.811857
H	0.814711	2.897959	-2.349457

23 TS4



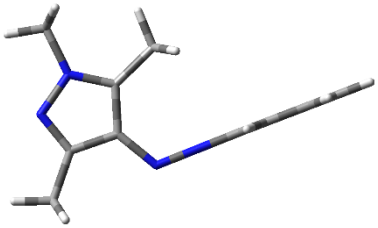
C	2.158669	-0.252013	0.195578
C	1.502394	0.715381	-0.650597
C	2.586704	1.275360	-1.382372
N	3.699557	0.672966	-0.962730
N	3.462055	-0.280049	0.002661
N	0.214268	1.001801	-0.705842
N	-1.009261	1.281567	-0.731647
C	-1.437966	2.232984	-1.736422
C	-2.778326	2.627794	-1.641810
C	-3.311024	3.533582	-2.558059
C	-2.508467	4.039652	-3.584454
C	-1.172107	3.635344	-3.688599
C	-0.635975	2.737278	-2.768746
C	5.071805	0.908759	-1.386923
H	1.691551	-0.914184	0.913597
H	-2.920858	4.741790	-4.302792
H	0.394889	2.410598	-2.848043
H	-0.550550	4.021957	-4.491329
H	-4.348945	3.842279	-2.475371
H	-3.381688	2.213969	-0.838820
H	5.499605	-0.020138	-1.768815
H	5.073485	1.664070	-2.171811
H	5.664349	1.257688	-0.538596
H	2.605588	2.052164	-2.132502

24 TS1



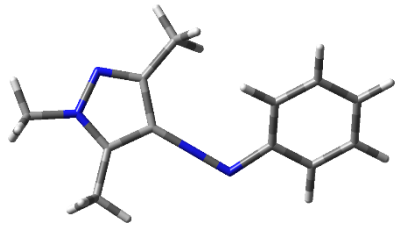
C	-0.799075	2.030505	-2.680007
C	-1.200474	2.285903	-1.329584
C	-2.439141	2.938826	-1.414059
N	-2.707349	3.032782	-2.729689
N	-1.719573	2.491456	-3.514967
N	-0.620049	2.012808	-0.087346
N	0.472019	1.436975	-0.048450
C	1.645317	0.818428	-0.006659
C	2.863613	1.560719	-0.008241
C	4.080792	0.893084	0.056030
C	4.154554	-0.502874	0.121154
C	2.959203	-1.230555	0.120495
C	1.719905	-0.604769	0.057776
H	5.113340	-1.007781	0.170090
C	-3.326801	3.452415	-0.332255
C	-3.844729	3.676783	-3.368131
C	0.431524	1.355772	-3.194593
H	2.821524	2.643330	-0.056658
H	4.993094	1.484661	0.053151
H	2.985578	-2.316491	0.168591
H	0.801469	-1.181507	0.059977
H	-2.876838	3.231297	0.636215
H	-3.468330	4.535265	-0.412619
H	-4.316044	2.984156	-0.371696
H	0.408213	1.331918	-4.286319
H	1.337207	1.879997	-2.872947
H	0.508876	0.329424	-2.821479
H	-3.958336	3.245000	-4.361578
H	-4.749364	3.494074	-2.786426
H	-3.684073	4.755331	-3.456802

24 TS2



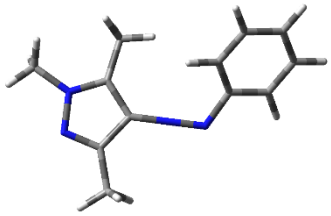
C	-3.520893	-2.660210	1.444328
C	-3.246135	-1.273453	1.636564
C	-4.305003	-0.339011	1.433703
C	-5.565042	-0.791423	1.060934
C	-5.835587	-2.151672	0.874021
C	-4.796138	-3.067640	1.071376
N	-2.142436	-0.635651	2.005958
N	-0.971028	-0.446210	2.351750
C	0.008146	-0.242857	1.374723
C	-0.054187	-0.203513	-0.032253
N	1.211380	0.028558	-0.429941
N	2.097472	0.143957	0.613702
C	1.373455	-0.019807	1.712335
C	-1.206489	-0.368663	-0.965138
C	1.992802	0.038392	3.072387
C	1.717626	0.164060	-1.790439
H	-6.825132	-2.487274	0.582923
H	-2.726725	-3.381895	1.601368
H	-4.976478	-4.130715	0.931428
H	-6.352697	-0.056661	0.912743
H	-4.110611	0.718008	1.579020
H	-1.677389	-1.347143	-0.828648
H	-1.975017	0.385119	-0.767667
H	-0.896797	-0.278764	-2.007368
H	3.064927	0.226342	2.985475
H	1.545681	0.834271	3.676121
H	1.844874	-0.901013	3.614120
H	2.787735	0.346572	-1.713695
H	1.545707	-0.751442	-2.361299
H	1.241626	1.005441	-2.299414

24 TS3



C	-0.664193	2.371661	-2.825204
C	-1.394003	2.235953	-1.637140
C	-2.540883	3.014550	-1.434075
C	-2.924616	3.958826	-2.385124
C	-2.186268	4.104982	-3.563903
C	-1.062314	3.301787	-3.784390
N	-1.111160	1.250542	-0.617851
N	0.076702	0.848629	-0.527316
C	1.330480	0.468702	-0.379677
C	2.567759	1.050638	-0.876446
N	3.609904	0.354855	-0.464054
N	3.096146	-0.699759	0.270464
C	1.765844	-0.662926	0.378253
C	2.754479	2.291289	-1.687967
C	0.948106	-1.656532	1.121090
C	4.013338	-1.682008	0.827836
H	-2.492272	4.829880	-4.312226
H	0.192968	1.728896	-2.993784
H	-0.501031	3.396834	-4.709759
H	-3.802041	4.575372	-2.212682
H	-3.109548	2.872374	-0.519339
H	1.286682	-1.759301	2.157323
H	-0.092543	-1.325683	1.120205
H	0.995910	-2.648731	0.657947
H	3.813943	2.552029	-1.732945
H	2.391044	2.156691	-2.712297
H	2.201326	3.130986	-1.258127
H	5.019173	-1.396123	0.524727
H	3.950594	-1.693069	1.919177
H	3.784713	-2.679645	0.444333

24 TS4



C	-2.683301	2.828073	-1.460879
C	-1.481422	2.176546	-1.766772
C	-0.833736	2.447180	-2.980310
C	-1.369890	3.386968	-3.860473
C	-2.548256	4.066193	-3.534724
C	-3.203738	3.783920	-2.331673
N	-1.056317	1.160155	-0.831773
N	0.167975	0.880855	-0.805032
C	1.457263	0.612854	-0.747426
C	2.573397	1.398113	-1.181954
N	3.665378	0.690731	-0.865105
N	3.379988	-0.529525	-0.279676
C	2.066184	-0.575679	-0.181969
C	2.616887	2.766167	-1.764366
C	1.352349	-1.755537	0.389064
H	-2.960710	4.799791	-4.220794
H	0.065555	1.896247	-3.236076
H	-0.873319	3.584860	-4.806249
H	-4.123169	4.303607	-2.078247
H	-3.186389	2.579624	-0.530612
H	3.010657	3.493725	-1.045098
H	1.609242	3.078979	-2.040866
H	3.255466	2.803642	-2.653042
H	2.049780	-2.404369	0.922864
H	0.565931	-1.429139	1.076725
H	0.867653	-2.344792	-0.397512
C	5.058482	1.089550	-0.991830
H	5.666495	0.190835	-0.898897
H	5.232950	1.548572	-1.966598
H	5.334090	1.798423	-0.205090

Dihedral drives

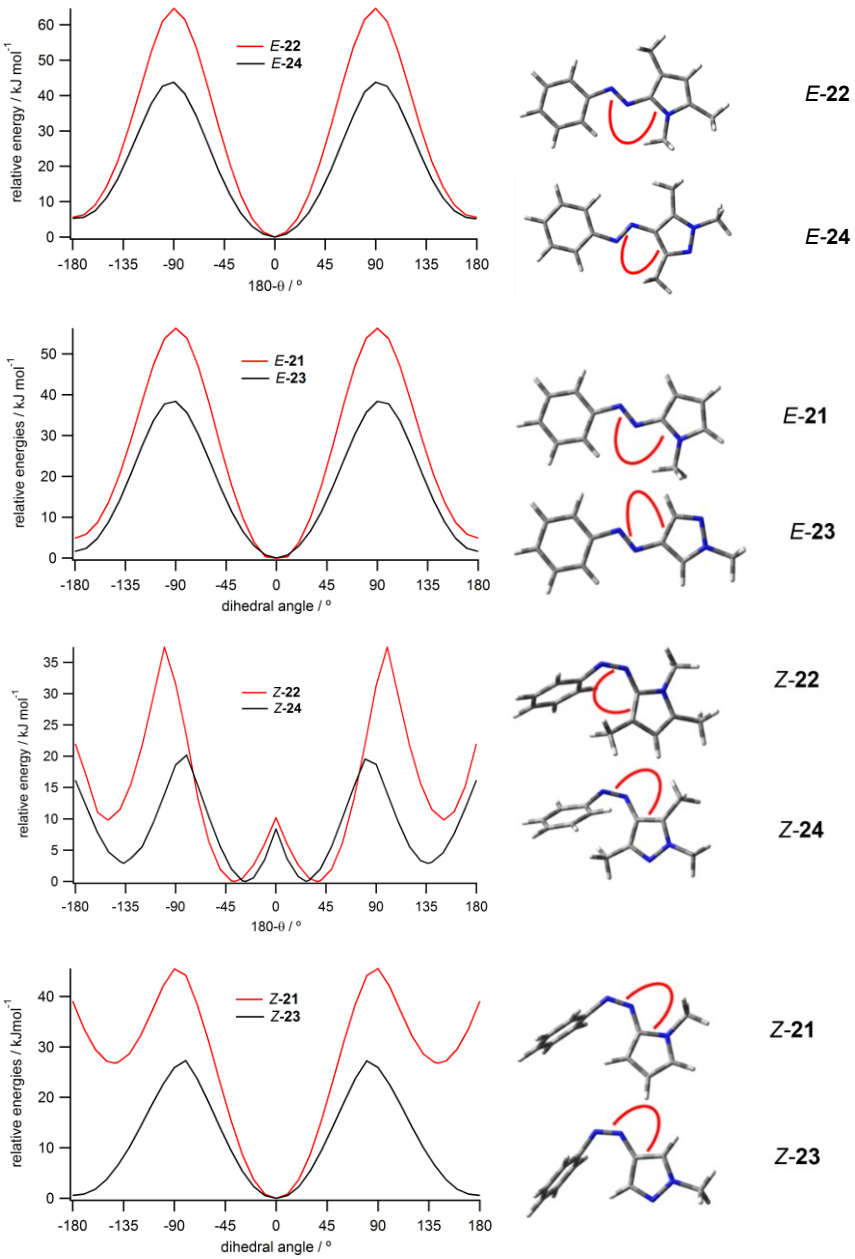


Figure 7.43. Dihedral angle vs. relative energy. Calculated using B3LYP/6-31G(d,p). Minimised structures show the dihedral angles that have been constrained for each isomer. All computational dihedral angles are plotted as 180 – θ to give minima between 0 and 90 °, and for consistency with the main text.

7.4.2 Azobisimidazole: A photoswitchable base

Energy minimised structures and excitation data

compound		Dihedral angles / ° (N=C-N=N)		SCF energy / kJ mol^{-1}	ΔH / kJ mol^{-1}	ΔG / kJ mol^{-1}	K_{eq}	Population fraction
E-**91**	**1**	**0.0**	**0.0**	**0.0**	**0.0**	**0.0**	**1**	**0.997**
	2	0.0	180.0	7.3	4.9	14.3	3.1 x 10^{-3}	0.003
Z-**91**	**1**	**-28.8**	**-28.8**	**51.4**	**50.2**	**52.0**	**7.7 x 10^{-10}**	**0.996**
	2	-11.9	134.0	61.2	60.4	65.5	3.3 x 10^{-12}	0.004
E-**92**	**1**	**0.0**	**0.0**	**0.0**	**0.0**	**0.0**	**1**	**0.756**
	2	0.0	180.0	1.1	1.4	2.8	3.2 x 10^{-1}	0.224
Z-**92**	1	-31.7	-31.7	56.0	55.0	54.2	3.2 x 10^{-10}	0.021
	2	**0.0**	**180.0**	**49.5**	**48.7**	**44.7**	**1.5 x 10^{-8}**	**0.979**

Table 7.13. Calculated data for the energy minimised structures of **91** and **92**, using B3LYP/6-13G(d,p) and the PCM for water. For each isomer the lowest energy conformer is in bold. The population fraction is the normalised Boltzmann factor at 25 °C. ΔH = enthalpy, ΔG = Gibbs free energy.

compound		Dihedral angles / ° (N=C-N=N)		SCF energy / kJ mol^{-1}	ΔH / kJ mol^{-1}	ΔG / kJ mol^{-1}	K_{eq}	Population fraction
E-**91**H$^+$ (imidazolium)	**1**	**0.0**	**0.0**	**0.0**	**0.0**	**0.0**	**1**	**0.970**
	2	0.0	180.0	10.8	10.5	12.0	7.9 x 10^{-3}	0.008
	3	0.0	180.0	5.4	5.3	9.4	2.3 x 10^{-2}	0.022
E-**91**H$^+$ (azolium)	1	0.0	0.0	49.7	50.0	51.0	1.1 x 10^{-9}	0.064[a]
	2	**0.0**	**180.0**	**42.1**	**42.9**	**44.4**	1.7 x 10^{-8}	**0.936[a]**
	3	4.4	-178.0	89.2	89.1	95.4	1.9 x 10^{-17}	0.000[a]
Z-**91**H$^+$	**1**	**-1.1**	**1.1**	**16.3**	**13.7**	**16.0**	**1.6 x 10^{-3}**	**1.000**
	2	-2.8	117.9	53.5	52.7	52.4	6.4 x 10^{-10}	0.000
E-**91** (1) relative to *E*-**91**H$^+$imidazolium (1)				1204.4	1168.1	1167.4		

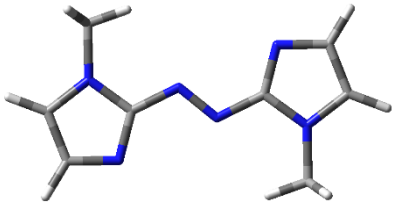
Table 7.14. Calculated data for the energy minimised structures of **91**H$^+$, using B3LYP/6-13G(d,p) and PCM for water. For each isomer the lowest energy conformer is in bold. The population fraction is the normalised Boltzmann factor at 25 °C. ΔH = enthalpy, ΔG = Gibbs free energy. [a] Normalised relative to azonium K_{eq} only. Population fractions for azonium conformers when normalised to imidazolium *E*-**91**H$^+$ are 0.000.

Cmpd no.	n-π* λ_{max} / nm	n-π* f	π –π* λ_{max} / nm	π –π* f	λ_{max} separation / nm
E-**91**	430	0	381	0.96	49
Z-**91**	493	0.17	338	0.44	155
E-**91**H$^+$ (imidazolium)	427	0	400	0.96	27
E-**91**H$^+$ (azolium)	-	-	484	0.90	
Z-**91**H$^+$	453	0.002	383	0.72	70

Table 7.15. Calculated λ_{max} and oscillator strength (f) for n-π* and π-π* excitation (for the energy minimised structures). These are quoted for the lowest energy conformers.

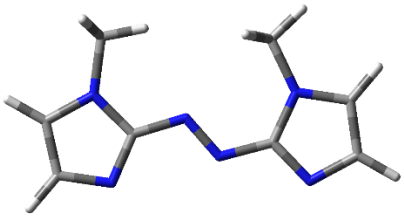
Structures and Cartesian coordinates for optimised geometry

E-**91** (1)



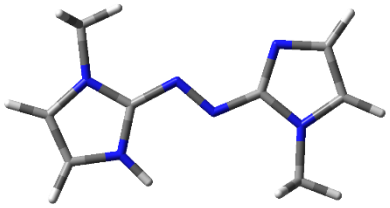
N	-1.190727	-1.482699	1.645622
C	-2.167682	-0.924858	0.924677
N	-3.352582	-0.875743	1.630590
C	-3.103483	-1.429786	2.851870
C	-1.766867	-1.795741	2.837656
N	-2.158711	-0.419104	-0.355971
N	-1.036698	-0.492219	-0.956841
C	-1.027736	0.013418	-2.237534
N	-2.004846	0.570618	-2.958767
C	-1.428671	0.883636	-4.150792
C	-0.091865	0.518342	-4.164694
N	0.157280	-0.035378	-2.943284
C	1.434774	-0.572807	-2.481363
C	-4.629814	-0.337359	1.169087
H	0.673334	0.605909	-4.920825
H	-1.209039	-2.267556	3.635317
H	-3.868601	-1.517197	3.608094
H	-1.986628	1.354965	-4.948649
H	1.750708	-1.392436	-3.130440
H	2.195037	0.211268	-2.493315
H	1.302108	-0.939481	-1.465856
H	-5.390829	-1.120678	1.182060
H	-4.944560	0.483056	1.817760
H	-4.497419	0.028521	0.153256

E-**91** (2)



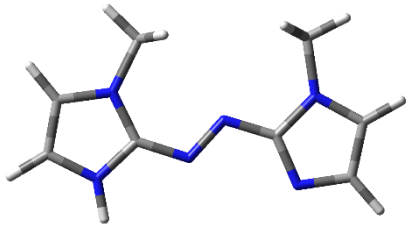
N	0.112717	0.018219	-3.047517
C	-1.060956	0.056724	-2.324024
N	-2.051533	0.611075	-3.027050
C	-1.496128	0.933612	-4.227284
C	-0.158975	0.576616	-4.263420
N	-1.059833	-0.453217	-1.041193
N	-2.184186	-0.379383	-0.440612
C	-2.229768	-0.875246	0.841626
N	-1.224304	-1.455513	1.601141
C	-1.791274	-1.774857	2.802945
C	-3.115105	-1.379868	2.733313
N	-3.380825	-0.825873	1.522734
C	1.404454	-0.510742	-2.618577
H	0.595055	0.671568	-5.029659
H	-1.220412	-2.245272	3.589466
H	-3.870453	-1.474806	3.501103
H	-2.070071	1.405278	-5.013508
H	1.712867	-1.322948	-3.280518
H	2.157506	0.280025	-2.642591
H	1.304447	-0.886965	-1.603478
C	0.174388	-1.706861	1.256115
H	0.653042	-2.180019	2.113972
H	0.240110	-2.366442	0.390414
H	0.682964	-0.770932	1.023332

E-**91**H$^+$ (imidazolium)



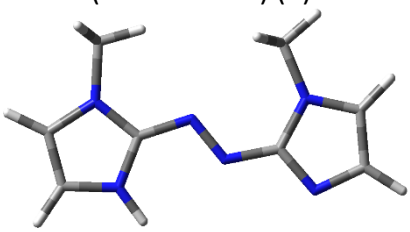
N	0.154504	-0.083114	-2.940424
C	-1.069947	0.012315	-2.295748
N	-2.001288	0.570244	-3.091624
C	-1.363947	0.829371	-4.245485
C	-0.020646	0.430749	-4.173819
N	-1.156732	-0.442621	-1.026326
N	-2.303954	-0.340639	-0.455930
C	-2.277076	-0.830241	0.822322
N	-1.25241	-1.373208	1.512129
C	-1.68008	-1.729062	2.768491
C	-3.00154	-1.392397	2.843353
N	-3.35797	-0.836819	1.630983
C	-4.68988	-0.335730	1.277241
C	1.39170	-0.635163	-2.384783
H	0.77895	0.482406	-4.896810
H	-1.02644	-2.183262	3.494289
H	-3.70929	-1.500921	3.648720
H	-1.86059	1.285669	-5.090852
H	2.16964	-0.564227	-3.143227
H	1.686839	-0.066858	-1.502189
H	1.240513	-1.679732	-2.110826
H	-5.410438	-1.150957	1.351632
H	-4.963653	0.467576	1.962190
H	-4.654149	0.039215	0.257159
H	-0.324835	-1.481831	1.121462

E-**91**H$^+$ (imidazolium) (2)



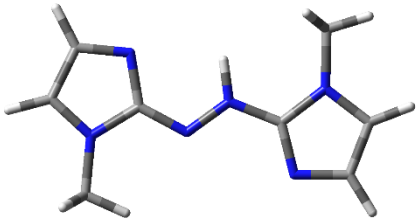
N	-2.593140	0.599842	-0.031990
C	-1.586312	-0.300269	-0.021860
N	-2.157829	-1.532982	-0.020328
C	-3.530016	-1.378307	-0.029731
C	-3.803690	-0.040226	-0.037057
N	-0.293771	0.146261	-0.015376
N	0.594563	-0.780507	-0.005913
C	1.881968	-0.357942	0.000610
N	2.885029	-1.314453	0.010977
C	4.055468	-0.643580	0.015661
C	3.725582	0.718373	0.007898
N	2.391482	0.886814	-0.001330
C	2.705858	-2.766978	0.015971
C	-1.473216	-2.832166	-0.010636
H	5.010083	-1.147140	0.023871
H	-4.193920	-2.227212	-0.030407
H	-4.741345	0.489262	-0.045237
H	4.413563	1.552618	0.008797
H	2.161882	-3.076967	-0.876952
H	3.689274	-3.234043	0.024521
H	2.150019	-3.069364	0.904180
H	-2.238007	-3.607088	-0.012486
H	-0.843966	-2.925467	-0.894789
H	-0.855510	-2.918306	0.882346
H	-2.434782	1.600064	-0.035274

E-**91**H$^+$ (imidazolium) (3)



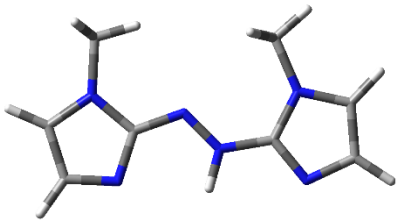
N	0.133569	0.025471	-3.080073
C	-0.940703	-0.000126	-2.264122
N	-1.972216	0.552196	-2.934298
C	-1.556553	0.933993	-4.187075
C	-0.234703	0.603604	-4.279187
N	-0.912129	-0.512601	-0.992847
N	-2.062394	-0.418808	-0.424465
C	-2.187157	-0.884960	0.837133
N	-1.229156	-1.477474	1.659559
C	-1.858929	-1.763237	2.820043
C	-3.184540	-1.339045	2.678811
N	-3.377443	-0.803175	1.463813
C	1.471399	-0.476639	-2.750469
H	0.466621	0.729608	-5.087254
H	-1.345803	-2.233497	3.645733
H	-3.973268	-1.411961	3.414294
H	-2.217727	1.399862	-4.898480
H	1.741784	-1.264585	-3.454299
H	2.187784	0.343073	-2.815394
H	1.450735	-0.873067	-1.738517
C	0.181477	-1.757782	1.378823
H	0.612089	-2.227986	2.262100
H	0.265239	-2.427366	0.522888
H	0.708825	-0.830069	1.156937
H	-2.896843	0.649434	-2.532566

E-**91**H$^+$ (azolium) (1)



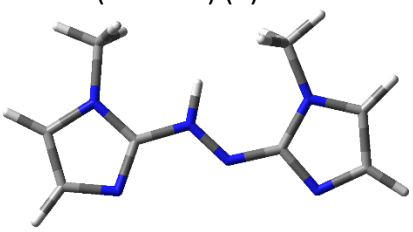
N	-3.405184	-0.835304	1.664380
C	-2.257610	-0.859929	0.886083
N	-1.216068	-1.400120	1.549862
C	-1.700699	-1.720682	2.754243
C	-3.066093	-1.376149	2.846205
N	-2.272023	-0.384274	-0.361867
N	-1.157977	-0.452186	-1.000979
C	-1.019046	-0.001052	-2.296819
N	0.185091	-0.087956	-2.951766
C	-0.039367	0.442486	-4.190369
C	-1.374071	0.823160	-4.216927
N	-1.978171	0.542988	-3.031592
C	1.454038	-0.628327	-2.454523
C	-4.720596	-0.321122	1.270703
H	0.743553	0.504515	-4.929793
H	-1.095647	-2.179468	3.523446
H	-3.770687	-1.486651	3.656468
H	-1.910280	1.281333	-5.035273
H	2.194719	-0.534378	-3.246489
H	1.796047	-0.061475	-1.586020
H	1.345399	-1.684744	-2.200014
H	-5.454299	-1.125908	1.328627
H	-5.004976	0.491636	1.939964
H	-4.653971	0.046412	0.249272
H	-0.346207	-0.859041	-0.521113

E-**91**H$^+$ (azolium) (2)



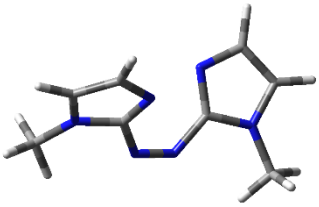
N	0.154269	0.035634	-3.120069
C	-0.968873	0.025848	-2.309803
N	-2.035873	0.566934	-2.926665
C	-1.591521	0.924500	-4.138450
C	-0.227769	0.601868	-4.279437
N	-0.917243	-0.480499	-1.070214
N	-2.015372	-0.439273	-0.405880
C	-2.189636	-0.899713	0.876017
N	-1.241539	-1.480895	1.676812
C	-1.891055	-1.764656	2.846144
C	-3.202958	-1.338253	2.689889
N	-3.381441	-0.799572	1.457555
C	1.489128	-0.468552	-2.783218
H	0.452484	0.741043	-5.105903
H	-1.381189	-2.234426	3.672881
H	-4.005801	-1.401006	3.409762
H	-2.226741	1.393708	-4.876338
H	1.763615	-1.259464	-3.482138
H	2.209536	0.348035	-2.843062
H	1.464349	-0.864173	-1.770799
C	0.169946	-1.760272	1.393043
H	0.598853	-2.230109	2.276471
H	0.254839	-2.434849	0.540723
H	0.699935	-0.832314	1.176907
H	-2.856873	-0.034405	-0.837210

E-**91**H$^+$ (azolium) (3)



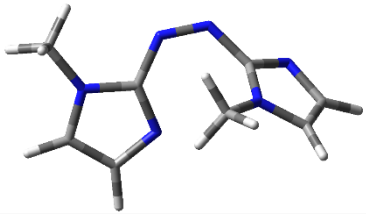
N	-2.738797	0.587156	-0.044876
C	-1.728835	-0.339717	0.012870
N	-2.163435	-1.585725	0.098220
C	-3.520456	-1.469076	0.095884
C	-3.897518	-0.138691	0.009372
N	-0.395052	0.044925	-0.013309
N	0.541011	-0.836153	-0.038028
C	1.838882	-0.547427	-0.028293
N	2.517623	0.682387	0.045490
C	3.827003	0.386588	0.017926
C	3.933253	-1.015293	-0.075333
N	2.725814	-1.573256	-0.098263
C	-2.637009	2.045222	-0.148902
H	-4.864237	0.339273	-0.017027
H	4.587126	1.152352	0.068902
H	4.846010	-1.592223	-0.121499
H	-4.165274	-2.333568	0.158660
H	-3.641890	2.445965	-0.268385
H	-2.196302	2.466129	0.757491
H	-2.045956	2.323652	-1.023758
C	1.970186	2.038495	0.157986
H	2.800880	2.736554	0.244342
H	1.402116	2.294885	-0.739405
H	1.355397	2.125103	1.057364
H	-0.201051	1.045939	-0.010380

Z-**91** (1)



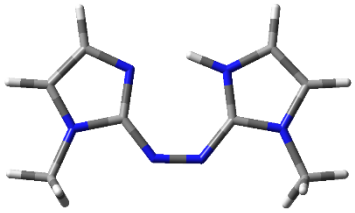
C	0.282617	-0.015127	0.400565
N	0.475741	0.291265	1.685619
C	1.812847	0.511223	1.803723
C	2.451404	0.333866	0.587019
N	1.469884	0.024950	-0.307789
C	1.645977	-0.267387	-1.726319
H	3.490157	0.393842	0.300353
N	-0.881806	-0.108894	-0.343794
N	-2.028098	-0.418331	0.106068
C	-2.284299	-1.017447	1.328413
N	-3.594489	-0.988850	1.770657
C	-3.660026	-1.807476	2.859256
C	-2.388945	-2.337128	3.012179
N	-1.542169	-1.844520	2.068513
H	-2.060921	-3.051097	3.755602
H	-4.570514	-1.938639	3.423695
C	-4.681659	-0.189195	1.216280
H	2.263437	0.791905	2.746175
H	2.470128	0.332092	-2.114357
H	1.865382	-1.327270	-1.880048
H	0.723897	-0.014206	-2.248147
H	-5.622405	-0.724008	1.351022
H	-4.742599	0.781919	1.714623
H	-4.490242	-0.034700	0.155090

Z-**91** (2)



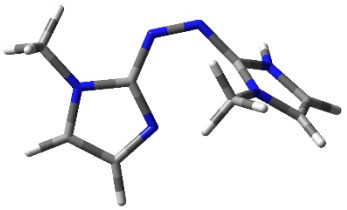
N	-1.559275	-2.098675	2.017395
C	-2.195964	-1.174028	1.224506
N	-3.312376	-0.722958	1.783740
C	-3.362942	-1.328154	3.013839
C	-2.306681	-2.194926	3.169576
N	-1.888191	-0.890880	-0.121790
N	-0.751335	-0.497574	-0.524795
C	0.283534	-0.077238	0.287423
N	0.317468	0.223987	1.590683
C	1.545979	0.759596	1.802081
C	2.279719	0.783857	0.623332
N	1.470152	0.263490	-0.335885
C	1.811867	0.062217	-1.742511
H	3.282548	1.118988	0.407352
H	-2.038485	-2.880085	3.959347
H	-4.162896	-1.127701	3.713292
H	1.858510	1.107674	2.776923
H	2.415370	0.902657	-2.086573
H	2.374880	-0.865862	-1.867997
H	0.889395	0.005140	-2.316858
C	-0.361196	-2.873586	1.722368
H	-0.442745	-3.848087	2.205188
H	-0.276307	-3.023859	0.645341
H	0.529407	-2.355442	2.084640

Z-**91**H$^+$ (1)



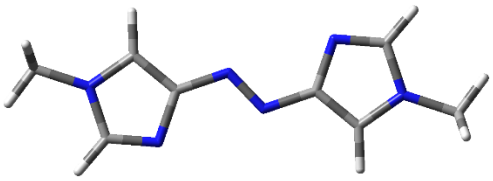
C	0.531970	-0.309220	0.327092
N	0.618739	0.201467	1.576756
C	1.756395	0.943508	1.689804
C	2.393866	0.891421	0.473495
N	1.629258	0.119142	-0.357462
C	1.945946	-0.222107	-1.748554
H	3.317062	1.341496	0.146757
N	-0.375643	-1.100067	-0.329225
N	-1.452499	-1.603098	0.142714
C	-1.968581	-1.489262	1.396142
N	-3.156064	-2.158363	1.633138
C	-3.501870	-1.921014	2.916809
C	-2.511135	-1.097752	3.451078
N	-1.578389	-0.838858	2.514639
H	-2.451070	-0.697322	4.452278
H	-4.395668	-2.332635	3.359374
C	-3.886872	-2.988586	0.672547
H	2.030320	1.448570	2.601470
H	2.732968	0.448182	-2.088876
H	2.288852	-1.256063	-1.806321
H	1.055827	-0.096480	-2.362025
H	-4.850278	-3.245969	1.109365
H	-4.035089	-2.432101	-0.251773
H	-3.322350	-3.898063	0.462591
H	-0.142508	-0.017598	2.269227

Z-**91**H$^+$ (2)



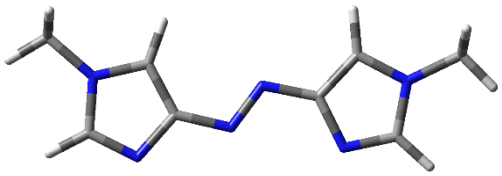
N	-1.612551	-2.265822	2.088652
C	-2.058260	-1.352497	1.207532
N	-3.107734	-0.728886	1.765688
C	-3.309193	-1.210171	3.046440
C	-2.374174	-2.175538	3.246340
N	-1.746201	-1.259162	-0.158795
N	-0.657656	-0.758328	-0.585914
C	0.278083	-0.165971	0.202118
N	0.275434	0.075180	1.523765
C	1.418312	0.740325	1.765605
C	2.144082	0.916695	0.580051
N	1.416692	0.346398	-0.400244
C	1.780796	0.251851	-1.816107
H	3.093207	1.394776	0.390980
H	-2.185127	-2.811105	4.095565
H	-4.089425	-0.831697	3.684831
H	1.693985	1.076524	2.755247
H	2.159846	1.217160	-2.151435
H	2.548682	-0.512759	-1.948678
H	0.892697	-0.018293	-2.382448
C	-0.462863	-3.147701	1.889158
H	-0.620578	-4.059659	2.462785
H	-0.383126	-3.397158	0.831349
H	0.446445	-2.644866	2.223454
H	-3.645708	-0.005544	1.305970

E-**92** (1)



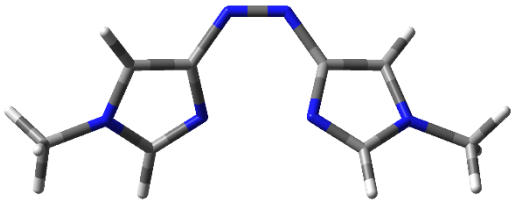
H	4.228687	1.918811	0.190032
C	3.532600	1.093346	0.120230
N	2.221493	1.186595	0.117437
C	1.779819	-0.121603	0.011892
C	2.859065	-0.989793	-0.047600
N	3.974549	-0.201270	0.022558
H	2.907865	-2.064252	-0.131087
C	5.363474	-0.645849	-0.001667
H	5.563635	-1.310873	0.841369
H	6.011144	0.227921	0.071877
H	5.577290	-1.171496	-0.934948
N	0.466321	-0.575300	-0.033625
N	-0.421616	0.332437	0.030477
C	-1.735088	-0.121311	-0.015007
N	-2.176705	-1.429523	-0.120575
C	-3.487815	-1.336333	-0.123293
H	-4.183864	-2.161830	-0.193086
C	-2.814369	0.746835	0.044567
N	-3.929814	-0.041738	-0.025526
H	-2.863216	1.821287	0.128117
C	-5.318749	0.402817	-0.001442
H	-5.966412	-0.471021	-0.074191
H	-5.519072	1.067188	-0.844957
H	-5.532407	0.929177	0.931462

E-**92** (2)



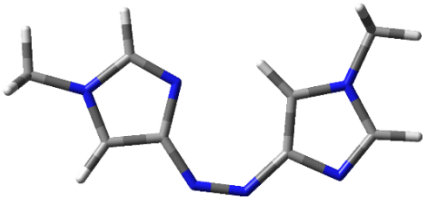
C	-2.688618	0.946364	0.006139
C	-1.817535	-0.131945	-0.079786
N	-2.526961	-1.314640	-0.153513
C	-3.791622	-0.954512	-0.112827
N	-3.943960	0.404076	-0.016198
N	-0.424482	-0.190213	-0.100949
N	0.136526	0.948697	-0.028706
C	1.524689	0.936289	-0.046573
C	2.272534	2.101915	0.025326
N	3.580609	1.706534	-0.018188
C	3.572637	0.337804	-0.113263
N	2.358867	-0.165229	-0.133380
C	4.756813	2.568281	0.027274
C	-5.206014	1.133263	0.050187
H	-2.515623	2.007568	0.078050
H	1.977090	3.136634	0.100877
H	-4.645425	-1.617175	-0.148521
H	4.494630	-0.226201	-0.163786
H	-6.026762	0.417029	0.010596
H	-5.268372	1.697713	0.983186
H	-5.290459	1.821278	-0.793902
H	4.752393	3.260325	-0.817661
H	4.774348	3.136561	0.959802
H	5.649336	1.944745	-0.027144

Z-**92** (1)



N	-1.532098	-1.834862	1.825292
C	-2.368972	-1.023137	1.081328
C	-3.621732	-0.959101	1.671371
N	-3.532797	-1.704692	2.815684
C	-2.262992	-2.220655	2.847305
N	-2.124751	-0.490037	-0.192456
N	-0.983306	-0.169178	-0.638404
C	0.170547	-0.015128	0.143412
N	0.243249	0.417892	1.454863
C	1.528081	0.572658	1.684694
N	2.302326	0.262712	0.596536
C	1.440519	-0.086721	-0.407690
H	1.777182	-0.362534	-1.394785
H	-4.525057	-0.447545	1.377962
C	3.757953	0.308164	0.521439
H	-1.945074	-2.884971	3.639855
C	-4.584931	-1.918196	3.802585
H	1.969891	0.920526	2.608985
H	-4.211032	-2.592545	4.573323
H	-4.870464	-0.970799	4.265594
H	-5.461534	-2.367204	3.330428
H	4.075156	0.990368	-0.270365
H	4.147238	0.664394	1.475451
H	4.160099	-0.687754	0.321709

Z-**92** (2)



C	1.587890	0.513309	-0.579644
C	0.615462	-0.052287	0.240479
N	1.196471	-0.439991	1.439412
C	2.464604	-0.114494	1.329144
N	2.754325	0.467505	0.122347
N	-0.686239	-0.126924	-0.249961
N	-1.738708	-0.589681	0.289926
C	-1.923885	-1.170615	1.546909
N	-3.242302	-1.561085	1.783469
C	-3.244574	-2.078767	2.985855
N	-2.000198	-2.055232	3.564338
C	-1.149591	-1.481989	2.664885
C	-1.649775	-2.548776	4.892187
C	4.062423	0.943470	-0.317663
H	1.518135	0.925309	-1.574106
H	-0.100926	-1.332805	2.851805
H	-4.100663	-2.489315	3.504464
H	3.227737	-0.269617	2.079740
H	-2.546048	-2.953288	5.362889
H	-0.898533	-3.338103	4.817403
H	-1.258664	-1.736037	5.508271
H	4.022773	2.014296	-0.527430
H	4.785890	0.760784	0.476844
H	4.374864	0.409065	-1.217126

GIAO ^{13}C NMR Calculations

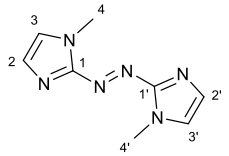
Energy minimised structures

SCF energies, enthalpies and free energies are calculated relative to the lowest energy conformer of each species. Population fraction is the normalised Boltzmann factor at 25 °C.

	compound		SCF energy / kJ mol^{-1}	Enthalpy / kJ mol^{-1}	Free Energy / kJ mol^{-1}	Population fraction
neutral	*E*-**91**	**1**	**0.0**	**0.0**	**0.0**	**0.978**
		2	7.4	7.4	9.4	0.022
	Z-**91**	**1**	**0.0**	**0.0**	**0.0**	**0.996**
		2	10.0	10.4	13.7	0.004
protonated	*E*-**91**H$^+$ (imidazolium)	**1**	**0.0**	**0.0**	**0.0**	**0.971**
		2	10.8	10.6	12.1	0.007
		3	5.4	5.3	9.4	0.022
	E-**91**H$^+$ (azolium)	1	7.6	7.2	6.7	0.062
		2	**0.0**	**0.0**	**0.0**	**0.938**
	Z-**91**H$^+$	**1**	**0.0**	**0.0**	**0.0**	**1.000**

Table 7.16. Calculated data for the energy minimised structures of **91** with methanol as the solvent model. For each isomer, the lowest energy conformer is in bold.

NMR shielding tensors and chemical shifts



		Shielding tensor (σ)			
		C1/C1’	C2/C2’	C3/C3’	C4/C4’
B3LYP	*E*-**91** (neutral)	21.85	52.40	44.58	150.36
	E-**91** imidH$^+$	24.46	48.03	46.98	147.50
	E-**91** azoH$^+$	31.69	38.87	39.62	145.38
mPW1PW91	*E*-**91** (neutral)	27.34	56.46	49.30	154.29
	E-**91** imidH$^+$	29.87	52.58	51.27	151.51
	E-**91** azoH$^+$	37.19	43.38	44.05	149.48

Table 7.17. Calculated shielding tensors.

		Scaled chemical shifts (δ)			
		C1/C1’	C2/C2’	C3/C3’	C4/C4’
B3LYP	*E*-**91** (neutral)	153.49	125.56	132.71	35.98
	E-**91** imidH$^+$	151.10	129.55	130.51	38.60
	E-**91** azoH$^+$	144.49	137.92	137.24	40.54
mPW1PW91	*E*-**91** (neutral)	153.03	126.15	132.75	35.86
	E-**91** imidH$^+$	150.69	129.73	130.94	38.43
	E-**91** azoH$^+$	143.93	138.22	137.61	40.30

Table 7.18. Calculated and scaled chemical shifts.

	B3LYP		mPW1PW91	
Carbon number	Δδ(azoH-exp)	Δδ(imidH-exp)	Δδ(azoH-exp)	Δδ(imidH-exp)
1/1’	-7.07	-0.46	-7.63	-0.87
2/2’	9.70	1.33	10.00	1.51
3/3’	7.69	0.96	8.06	1.39
4/4’	5.90	3.96	5.66	3.79

Table 7.19. Difference in calculated and experimental ^{13}C NMR shifts for *E*-**91**H$^+$, with protonation on either the azo or the imidazole nitrogen. Experimental values are for the deuteronated imidazolium ion.

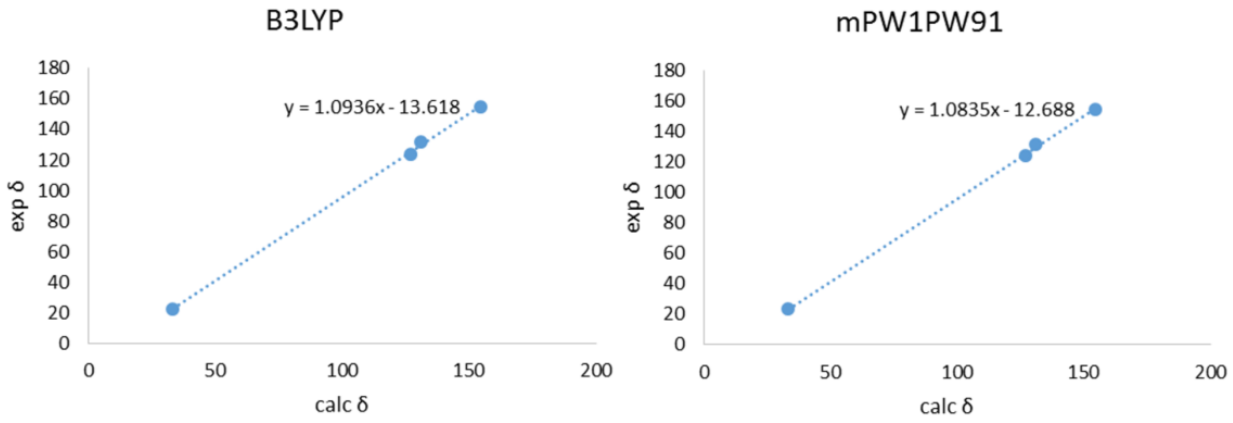


Figure 7.44. Calculated vs. experimental ^{13}C chemical shifts for neutral *E*-**91**.

7.5 Biochemistry

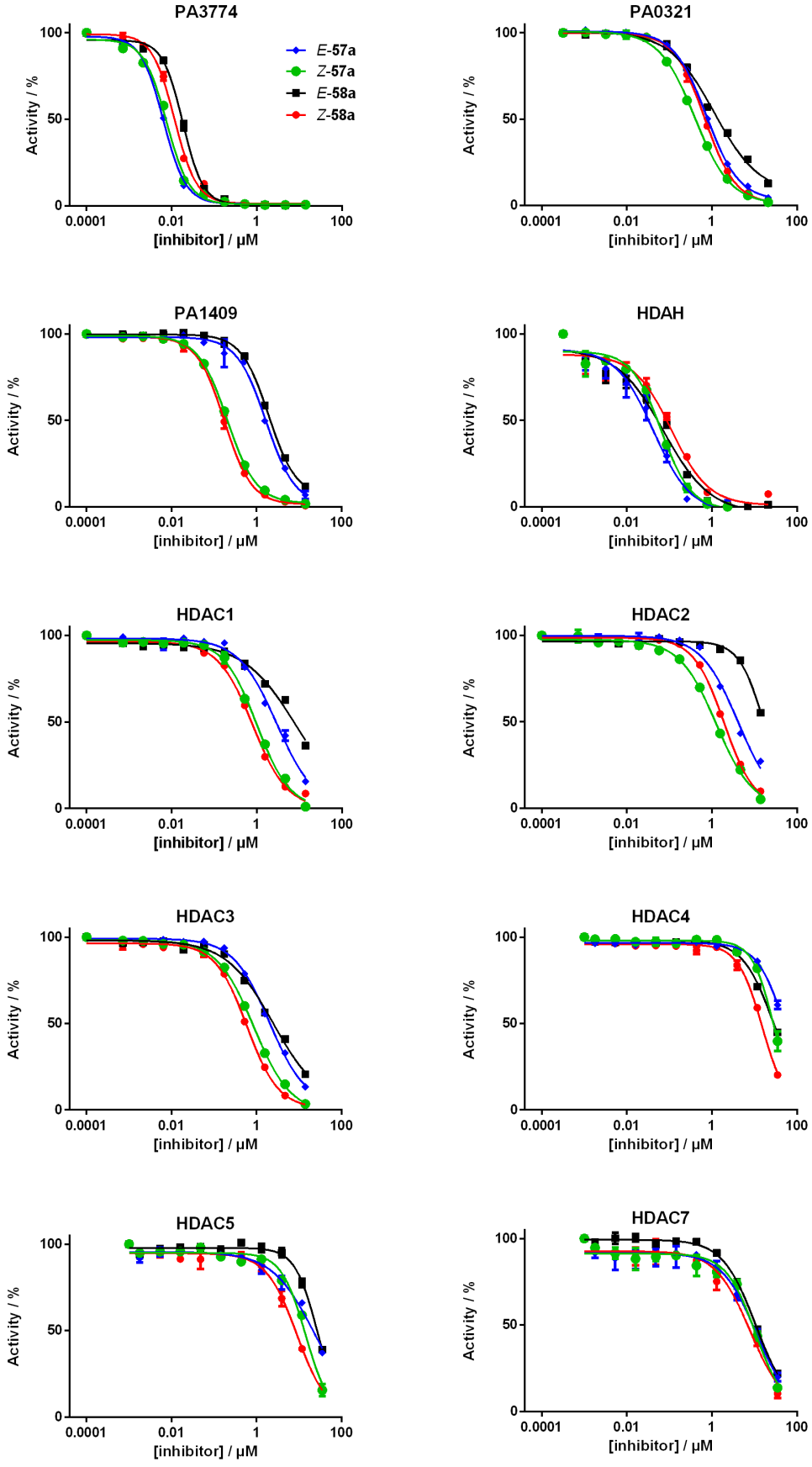


Figure 7.45. IC_{50} curves for **57a** and **58a** against human and bacterial HDACs.

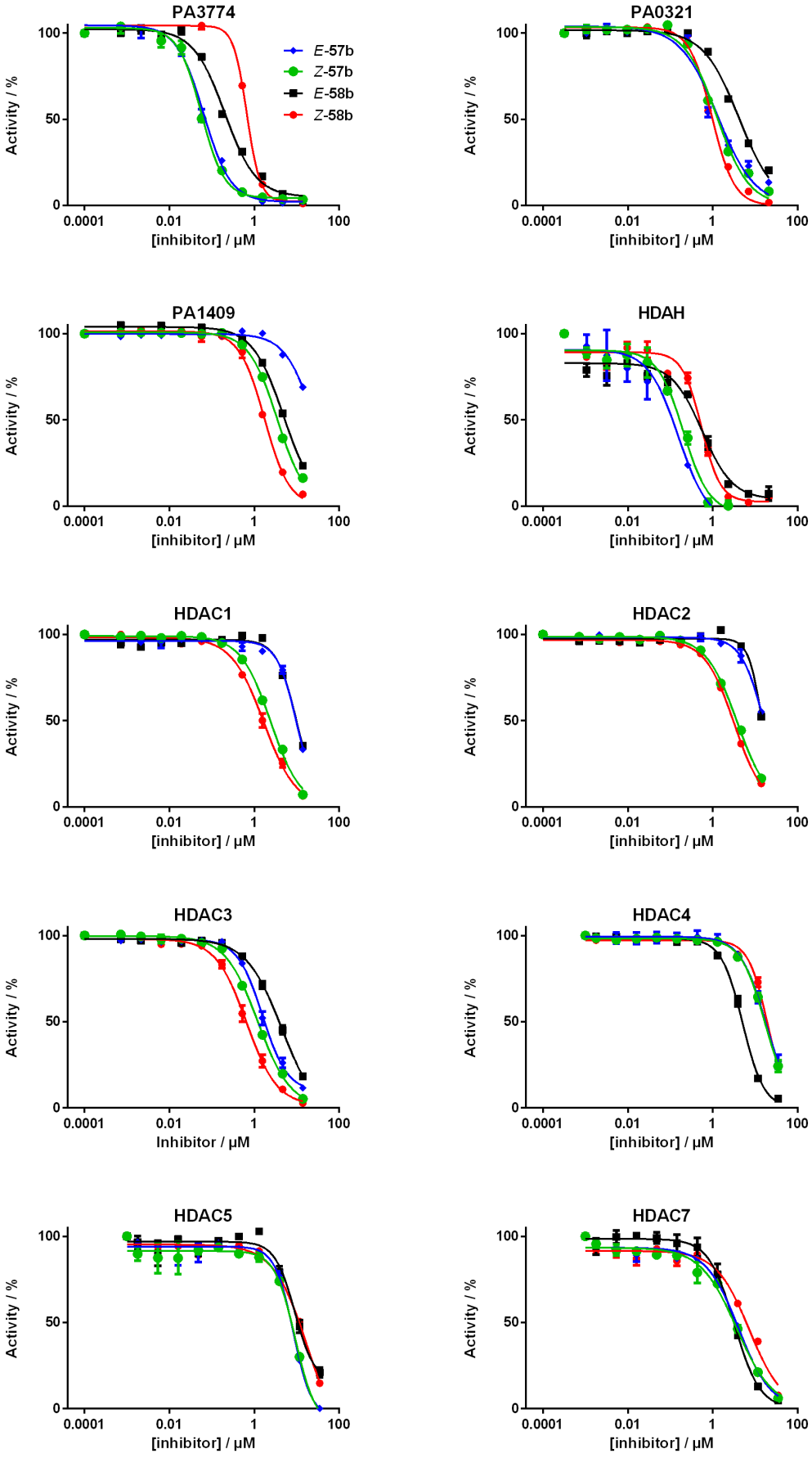


Figure 7.46. IC_{50} curves for **57b** and **58b** against human and bacterial HDACs.

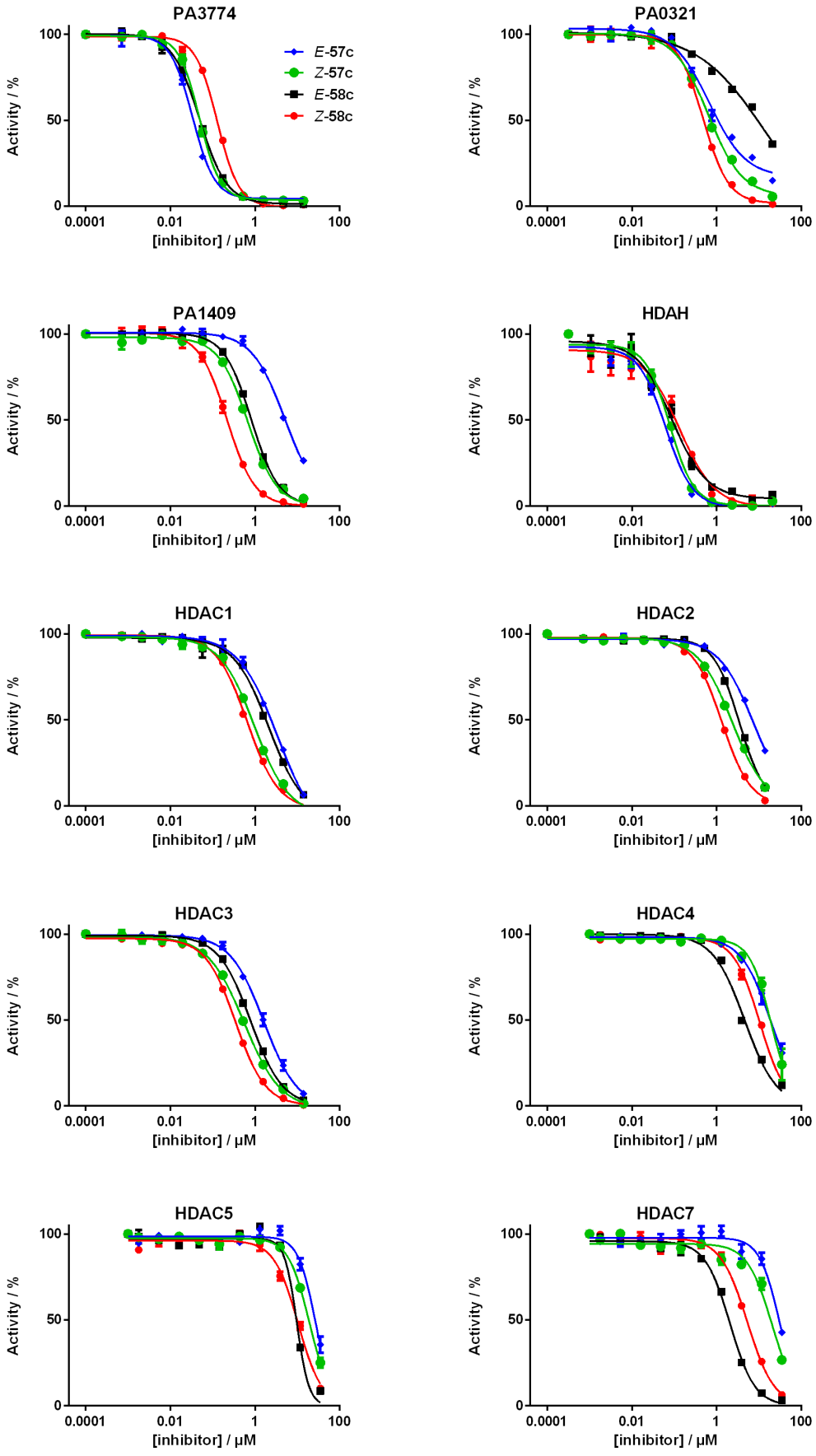


Figure 7.47. IC_{50} curves for **57c** and **58c** against human and bacterial HDACs.

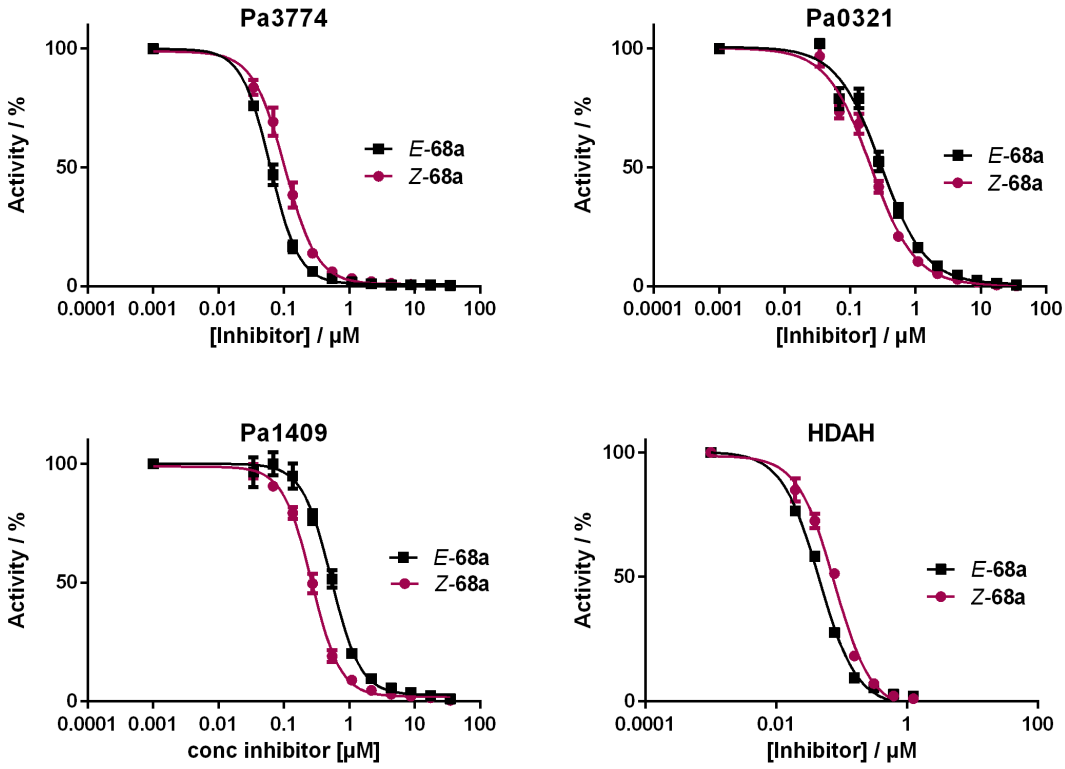


Figure 7.48. IC_{50} curves for **68a** against bacterial HDACs.

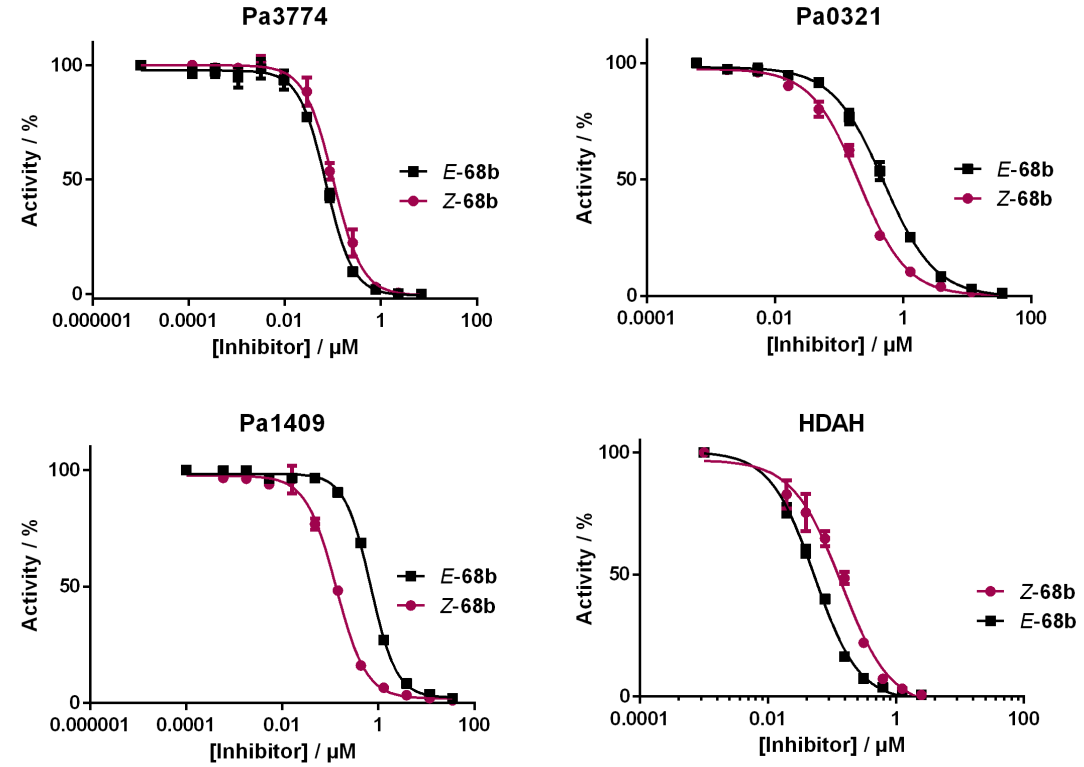


Figure 7.49. IC_{50} curves for **68b** against bacterial HDACs.

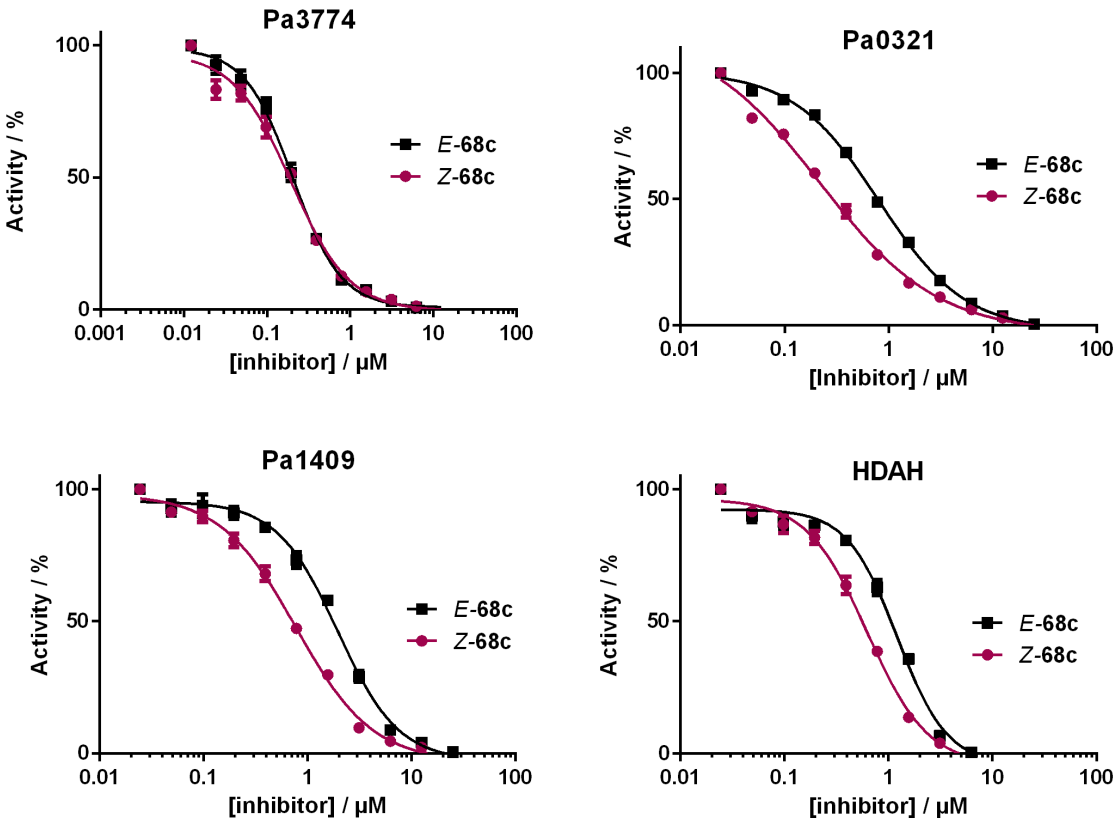


Figure 7.50. IC_{50} curves for **68c** against bacterial HDACs.